Bulletin 40
Part 2
(of 7 Parts)

THE SHOCK AND VIBRATION BULLETIN

DECEMBER 1969

A Publication of
THE SHOCK AND VIBRATION
INFORMATION CENTER
U.S. Naval Research Laboratory, Washington, D.C.

Office of
The Director of Defense
Research and Engineering

DISCLAIMER NOTICE

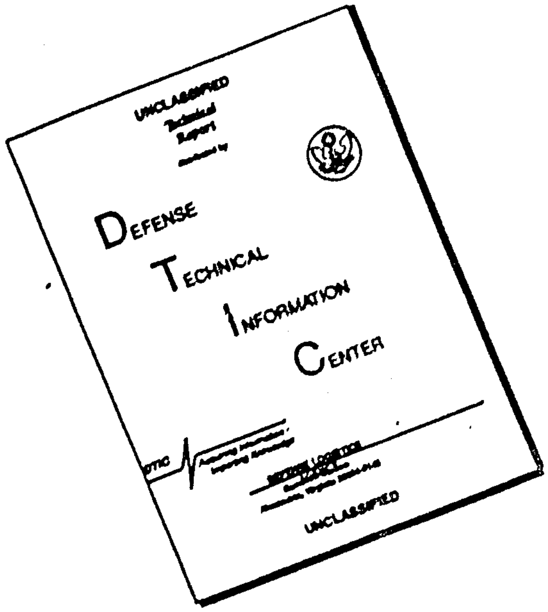

THIS DOCUMENT IS BEST QUALITY AVAILABLE. THE COPY FURNISHED TO DTIC CONTAINED A SIGNIFICANT NUMBER OF PAGES WHICH DO NOT REPRODUCE LEGIBLY.

SYMPOSIUM MANAGEMENT

THE SHOCK AND VIBRATION INFORMATION CENTER

William W. Mutch, Director
Henry C. Pusey, Coordinator
Rudolph H. Volin, Coordinator
Edward H. Schell, Coordinator
Katherine G. Jahnel, Clerk Typist

Bulletin Production

Graphic Arts Branch, Technical Information Division,
Naval Research Laboratory

Bulletin 40
Part 2
(of 7 Parts)

THE SHOCK AND VIBRATION BULLETIN

DECEMBER 1969

A Publication of
THE SHOCK AND VIBRATION
INFORMATION CENTER
Naval Research Laboratory, Washington, D.C.

The 40th Symposium on Shock and Vibration was held at the Chamberlin Hotel, Fort Monroe, Virginia and the NASA Langley Research Center, Hampton, Virginia, on 21-23 October 1969. The National Aeronautics and Space Administration was host.

Office of
The Director of Defense
Research and Engineering

CONTENTS

PART 2

Shock

*This paper not presented at Symposium.

PART 1

CLASSIFIED
(Unclassified Titles)

*This paper not presented at Symposium.

PART 3

Vibration

*This paper not presented at Symposium.

---

*This paper not presented at Symposium.

PART 4

Dynamics

*This paper not presented at Symposium.

PART 5

Damping and Isolation

*This paper not presented at Symposium.

*This paper not presented at Symposium.

PART 6

Transportation

*This paper not presented at Symposium.

PART 7

Instrumentation and Data Analysis

*This paper not presented at Symposium.

Ship Shock

SUPPLEMENT

*This paper not presented at Symposium.

ERRATUM

The following corrections should be made in the text of the paper "The Critical Damping Calculator and a Comparison of Selected Structural Damping Evaluation Systems," by B. E. Douglas as printed in Shock and Vibration Bulletin 38, Part 3, November 1968.

Page 89, top of second column, the equation should read:

$$M\ddot{x} + C\dot{x} + Kx = Fe^{i\omega t}$$

Page 90, Eq. (2) should read:

$$\frac{(C/C_c)^2}{1-(C/C_c)^2} = \left(\frac{1}{2.72n}\log_{10}\frac{A_1}{A_2}\right)^2$$

Page 91, Eq. (3) should read:

$$Z = \sqrt{KM}\left[4\left(\frac{C}{C_c}\right)^2 - 2 + \omega^2\frac{M}{K} + \frac{K}{M}\frac{1}{\omega^2}\right]^{1/2}$$

Eq. (4) should read:

$$\frac{C}{C_c} = 0.29\left[\omega^2\frac{M}{K} + \frac{K}{M}\frac{1}{\omega^2} - 2\right]^{1/2}$$

SHOCK

AN EXPERIMENTAL APPROACH TO UNDERSTANDING SHOCK RESPONSE

Merval W. Oleson
Naval Research Laboratory
Washington, D.C.

Those with experience will probably agree that attempts to interpret most measured shock response data in a meaningful fashion — that is, to develop understanding — are always difficult and frequently futile. Many carefully planned measurement programs have produced ambiguous, obscure, and nonrelevant final reports. Indeed, recognition of such limited results has precluded measurement attempts in many other programs.

It is the author's contention in this paper that our problems stem from attempts to interpret the measured response data in terms of the primary parameter of measurement — usually acceleration or velocity — whereas the parameter most readily related to the actual structure is that of differential displacement across structural elements. In addition to numerous illustrations from a successful measurement program, various arguments are offered to justify this contention.

In practice, differential displacement is not always feasible as a direct measurement, particularly across those structural elements which are very stiff. In such cases displacement information can be inferred on the basis of differential velocities, and sometimes even on the basis of acceleration. However, it is important to keep in mind that the approach to interpretation still proceeds from the differential displacement parameter rather than from the inertially measured velocity or acceleration parameters. Such a conceptual distinction may sound overly fine, but nevertheless has real significance to the mental framework on which interpretive understanding is developed.

Among factors which determine the potential combat superiority of a Naval ship is its ability to sustain the effects of an enemies weapons with its own maneuverability and offensive capability unimpaired. For this reason, equipments destined for use aboard ships of the United States Navy are required to meet minimum standards of "shock hardness," standards which are intended to ensure that vital equipment and the ship itself will survive the effects of severe underwater shock due to a mine or other near-miss explosion. For items below about 60,000 pounds weight, acceptance standards are based on one of several shock test procedures spelled out in MIL-S-901C [1]. Heavier items are presently qualified on the basis of calculation, although it is probable that larger test machines, capable of accommodating equipments of up to 160 tons, will be available in the foreseeable future.

In most cases, the ability or inability of an equipment to perform its designed function after being subjected to a stipulated series of mechanical shocks is prima facie evidence for acceptance or rejection. As applied to mechanically simple structures, there seems little reason to dispute such a criterion. However, when the engineering and economic investment is substantial, it is usual for technically concerned participants to require instrumentation on the equipment undergoing qualification test, with a view towards obtaining more information than that produced by the blind legalism of a go no-go result. Unfortunately, experience suggests that the inclusion of such instrumentation is — by itself — no guarantee of information.

In this connection, one might pose the question — "for what specific purpose are measuring instruments installed during the shock test of shipboard equipment?" At the conceptual level the question is not difficult to answer — "to gain an understanding of the structural behavior under shock on the basis of measured data" — for it is from such an understanding that one can identify and correct deficiencies, develop guidelines for future design, and generally improve the shock survival potential of the equipment and of the ship which depends upon it. It is at the implementing level, where the easy words must be replaced by equipment, techniques, and results — by transducers and that form of cryptoanalysis peculiar to interpreting shock records, that "understanding on the basis of measured data" becomes formidable. So formidable in fact that we have learned methods of evasion; don't install instrumentation, thereby avoiding an embarrassing problem in interpretation — report oscillographic results as "raw data" and let somebody else worry about interpretation — or report extensive tabulations of the establishment parameters (peak g, peak velocities, frequencies, etc.) with the implication that any competent reader will understand their significance. The familiarity of these stratagems is itself a measure of the difficulty of the problem.

Some years ago, attempts to understand structural behavior on the basis of experimental measurements led more-or-less accidently to a new approach, one that was conditioned largely by concurrent instrumentation developments [2]. More recently, this approach has developed into what appears as a significantly improved method for the interpretation of such measurements, and it is this result which will be presented here. Since the interpretive technique evolved largely as a result of instrumentation developments, it will be necessary to treat some characteristics of this instrumentation. However, rather than trace the evolutionary association, a qualitative rationale for the technique will be suggested on the basis of the objective of shock response measurement.

UNDERSTANDING OF STRUCTURAL BEHAVIOR

The proposition can be simply stated — the most understandable format for measured data is that in which dimensional change across elements of the structure under test is presented in a time domain.

Recall the assertion of a measurement objective stated above — "to gain an understanding of the structural behavior under shock on the basis of measured data." One may reasonably ask what there is about structural behavior that can be understood — what parameters can contribute significantly to our insight into the performance of an equipment under shock loading? While this question is not necessarily susceptible to a universally satisfactory answer, one possibility is to view the equipment behavior in terms of a failure criteria. The equipment should perform its designed function in the shock environment without malfunction or breakage. Now malfunction or breakage are usually related to dimensional change — deformations sufficient to cause rupture or misalignment of critical parts. These deformations may be moderately large in the case of soft limber structures, or may be very small in the case of stiff structures. They may be linear in the case of loads below the elastic limit, or may be nonlinear in the case of loads above the elastic limit, sliding joints, mechanical stops, etc. In any event, the deformation of elements of the structure is one link associating the incident shock and the equipment performance.

Actually, the equipment designer must have given some thought (no matter how cursory) to structural deformation before fabrication, and to the extent that actual loads and deformations are distributed throughout the structure in accordance with his assumptions, satisfactory performance should be assured. The fact that actual performance is sometimes unsatisfactory, stems largely from the difficulty of accurately predicting the distribution of loads in real structures which tend to be mechanically complex. Excessive deformation or rupture of parts of the structure are evidence that the designers assumptions or simplifications were incorrect. Experimental measurements which identify or anticipate such excessive deformations of structural elements are clearly of key importance in understanding structural behavior.

Consider for a moment the dynamic structural-analysis problem which parallels the problem of interpreting experimental data. In current practice, a complicated structure is, after a series of simplifying assumptions, decomposed into a mathematical model (the normal mode model) which consists of a group of uncoupled linear oscillators. Each mathematical oscillator is the analog of a single-degree-of-freedom (sdof) mechanical system. The mass element of each sdof system is now mathematically driven at a specified "shock design value" having the dimensions of acceleration, and the coupled (but still simplified) model of the original structure is recomposed. Predicted loads on elements of this model are calculated on the basis of properly combined normal mode responses [3]. Hidden in this analytical procedure is the fact that the shock design values actually derive from dimensional change across the spring elements of a set of synthetic sdof systems, the dimensional changes having been scaled by a radial frequency multiplier to produce design values with the dimensions of acceleration [4]. Similarly, the combined responses associated with the recomposed model relate directly to deformations between the foundation or input point of the model, and various points on the model [5]. It is worth emphasizing. The analysts stress calculations derive directly from predicted dimensional changes across elements or between points of the model, and not from the calculated motion response at any one point on the model.

Thus, though not superficially obvious, the methods of structural analysis have anticipated the experimental technique proposed above.

But there is a significant difference between the analytical problem and the experimental problem; where the analyst is usually forced into making simplifying assumptions for the purposes of modeling a complex structure, the experimental problem is one in which there is no choice but to deal with the real complex structure. Where the analyst has the uncomfortable problem of deciding, before-the-fact, the critical structural elements which his model must incorporate, the experimentalist has the problem of separating, after-the-fact, the meaningful content of his measured data from the insignificant. This is the problem which separates men from the machines of data processing. Judgement, intuition, interpretation, insight — however one addresses the human faculty which translates measured data into a usable understanding of structural behavior, this faculty can be aided by processing of the data from one format to others but cannot be supplanted by such processing. Recognizing this limitation, we look for that format which can most easily be associated with structural detail, and once again identify bending, stretching, internal collision — that is dimensional change across structural elements — as such a format.

At this point it may be appropriate to attach a more specific meaning to the phrase — "understanding of structural behavior" — a phrase which has so far been loosely employed to suggest some type of useful insight. As employed in this paper, "understanding" relates individually and collectively to salient mechanical response characteristics of a particular structure under shock, and implies achieving a sufficient grasp of the nature of each such characteristic to explain cause and effect. The implicit assumption is that useful insight can be built by steps, each step corresponding to the explanation of behavior attributable to some element or subelement of the total structure.

Understanding may take the form of experimental confirmation of design predictions, or it may be an empiricism constructed to fit the observational evidence. In the first case the cause and effect explanation stems from the designers equations, and in the second case it must be generated by the experimentalists imagination. However, observe that the problem of interpreting experimental data is common to both cases.

While understanding in the above sense is unique to a particular structure, the methods by which understanding is evolved need not be. In the experimental context these methods involve a mental exercise; one in which all of the available facts — design predictions, drawings, physical observations of the structure, and measured data in all practical formats — are considered in a series of associative frameworks until a tenable cause and effect explanation appears. It is the theme of this paper that the associative interpretation is most obvious to the imagination if measured data is available in a relative displacement format

PRACTICAL ASPECTS OF MEASUREMENT

If the reader recognizes more than sophistry in the above arguments, he may also recognize that the implementation problem in "understanding" has been shifted from one in data interpretation to one in instrumentation. It is here that the instrumentation developments at the Naval Research Laboratory must catch up with the argument. The sequence went somewhat as follows:

- For a particular shock test, accelerometer transducers were applied to a structure too flimsy to accommodate the more commonly employed velocity transducers.

- The accelerometer signal was electronically filtered to remove high frequency mechanical signals.

- The filter was exchanged for an electronic integrator, which not only served to remove high frequency signal components, but also produced a record in the more "understandable" velocity parameter.

- Improvements in the electronic integrating equipment allowed cascaded integration which produced not only a velocity record, but also an inertial displacement record [6,7].

- Inertial displacement records from two or more gages were electronically combined to produce records of bending, stretching, collision, etc. [8].

There is no intention to minimize the time (a decade) or effort spanned by the above evolution, but instrumentation development is not the theme of this paper. Nor is it intended to suggest that the instrumentation, at its current state of development, is completely satisfactory — only that it has been employed to considerable advantage in some measurement programs, and to less, but still useful advantage in others. Further comment regarding limitations of the instrumentation will appear in succeeding sections.

With this instrumentation system, dimensional change is obtained as the second integral of an algebraic combination of measured accelerations taken at points on the structure. The number of ways in which dimensional change can be experimentally defined (degrees of freedom) is determined by the number of feasible combinations. For example, consider a simple beam instrumented with four gages whose sensitive axes are perpendicular to the beam length and which are positioned at intervals along the length of the beam. Any one gage can define only inertial translation at its attachment point. Using any combination of two gages, both beam translation and beam rotation can be defined. With three gages in combination, deflection of a point on the beam relative to a line between two other points can be defined by eliminating both translational and rotational components in the resulting record, a presentation which can identify the first bending mode of the beam. If all four gages are used in the proper combination, the lowest bending mode can also be eliminated, thus allowing potential identification of bending in the second and higher modes. As another example, consider an open rectangular frame structure. Shearing deformation (into a parallelogram shape) of the frame can be measured as the differential rotation of adjacent frame elements, where the rotation of each element is obtained from a pair of gages perpendicular to the element and spaced along its length.

It is not difficult to recognize that considerations of accuracy impose a limit on the gage combinations which are of practical value. In any subtractive process, small percentage inaccuracies in the subtrahend and the minuend tend to result in a much larger percentage inaccuracy in the difference. Thus the requirement on absolute accuracy of independent motion measurements must be quite stringent if acceptable accuracy is to be maintained in their differential. Some of the sources of inaccuracy in the practical system are obvious and others are a bit subtle. To list the main ones:

- Transducer calibration accuracy.

- Nonlinearity in the transducer or in the electronics.

- Zero stability of the transducer and the electronics. (Instability causes an apparent shift in inertial reference.)

- Cross axis sensitivity of the transducer.

- Angular misalignment of transducers whose signals are to be combined.

- Cantilever flexibility of the transducer on its attachment point. (This important source of error is particularly subtle. Synchronous rotational oscillation of the sensitive axis of the transducer produces rectification of a component of the cross axis drive.)

- Calibration accuracy of the cascaded integrators.

- Integration interval for which the integrators can maintain a stable inertial reference.

- Accuracy with which separate signals can be reduced to a common scale factor and electronically combined.

While the accuracy problem is a formidable one, experience has shown that it is manageable.

If the difference measurement is comparatively large, such as deflection across a low frequency shock mount, the accuracy with which it can be defined is potentially better than that where the difference is small. Unfortunately, the dimensional changes associated with stiff elements of a structure tend to be small, and must necessarily, in some parts of the structure, become too small for accurate definition.

However, one may observe that dimensional change between two points on a structure can be recognized from the difference in velocity between the same points. Velocity, being progressively less sensitive to the lower frequency components of dimensional change, is also less difficult to measure accurately in those regions of the structure where dimensional change is most difficult to measure. The fact that dimensional change must be inferred from relative velocities does complicate interpretation, but when viewed in relation to the structure between the points of measurement, can be productive of understanding. Similarly, dimensional change may sometimes be detected from an acceleration record — for example, an internal collision may sometimes be detected by the appearance of an otherwise unexplained oscillatory transient in the acceleration signal.

Acceleration, velocity, and displacement — all of the mechanical motion parameters appear to be useful for interpretation, and it might almost seem that some of the steam has disappeared from the original proposition. But not so. In the first place, the usefulness of the measurements is in the inverse order — displacement, velocity, and lastly acceleration. In the second place, displacement and velocity records are employed for defining differential motions rather than inertial motion at a single point. (One may note that the differential acceleration parameter is seldom useful, since the nodes of the very high structural frequencies, emphasized in the acceleration parameter, tend to be so physically close that a prohibitive number of gages would be necessary for reasonable definition.) A distinction between the usefulness of parameters, based primarily on the sequence in which they are considered, may sound overdrawn. Nevertheless, this distinction has real significance to the mental framework on which interpretive understanding is developed.

In the opinion of the author, the preceding paragraph identifies an important point relative to contemporary difficulties in the interpretation of measured shock data. The structural response parameter commonly measured in much current shock work — acceleration — is also the least productive of understanding. Since the primary measured parameter is the most obvious for subsequent study, but also the most difficult to relate to structural behavior, perhaps we can point to one reason as to why many experimental shock studies have been of limited value.

ILLUSTRATIONS OF THE INTERPRETIVE METHOD

To illustrate the experimental approach, selected segments from a set of records obtained during a recently completed series of shock evaluation tests have been chosen. From these segments — reproduced here from actual field transcriptions — plus an abbreviated description of the physical structures involved and of the instrumentation employed, interpretations made during the field operations will be sketched. In spite of the limited scope, it is hoped that the reader will sense a growing insight into the structural behavior such as the test crew acquired during the program.

Physical Configuration

The evaluation tests were aimed at establishing satisfactory shock mitigating performance of three versions of a surface-to-air missile stowage system. Stowed missiles, gripped at two support planes by rubber faced handling bands, were installed in a matrix framework each column of which was supported from the deck on two rubber shock isolating mounts (Fig. 1). In addition to the vertical mounts, athwartship shock isolating mounts were attached between the outboard vertical members of the stowage framework and the ships bulkhead to prevent toppling instability when only one or two matrix columns were occupied by stowed missiles. Members of the framework were held together by athwartship tensioning bolts, vertical clamping screws, and pinned joints, such that on-loading and off-loading of the stowed missiles could be efficiently accomplished. The design intent was that the missile/framework assembly behave as a rigid mass load atop the comparatively soft rubber mounts.

For purposes of performance evaluation, a partially completed matrix of each version of the stowage system, loaded with a mix of inert missiles, dynamically simulated missile shapes, or inert booster motors as appropriate, was attached to a section of simulated ships deck, and installed in the Floating Shock Platform (FSP) of MIL-S-901C (Fig. 2). Explosive charges were detonated in the water at various standoff distances from the FSP to provide a controlled shock input.

Scheduling of the series was arranged to provide at least one full day between successive

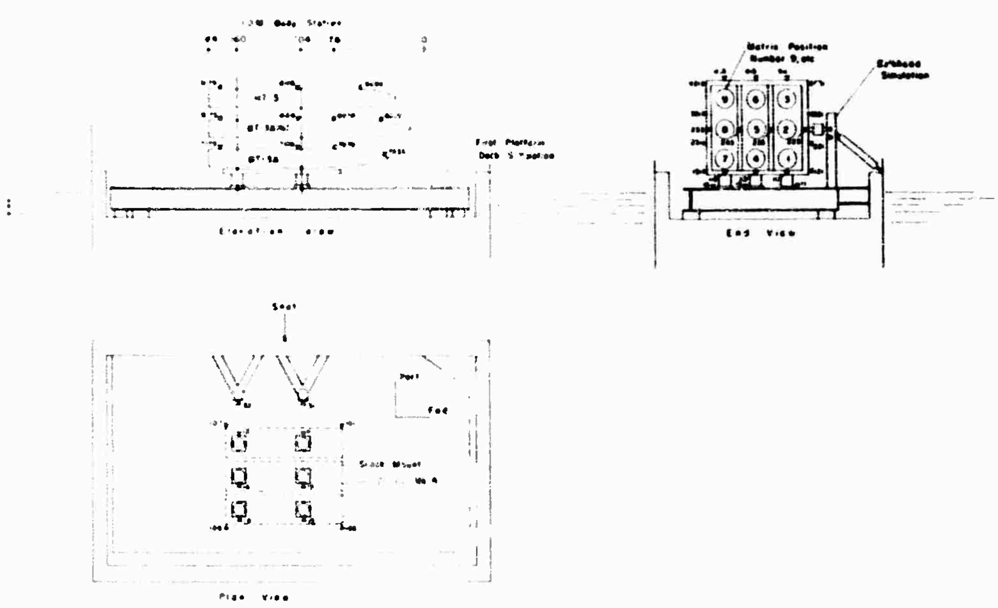

Fig. 1 - In this schematic drawing, a "cradle type" shock-mitigating missile stowage assembly is shown installed in a Floating Shock Platform (FSP). Each vertical column of missiles in the matrix is supported on two rubber shock mounts. To simulate the dynamic characteristics of a shipboard installation, a section of ships deck is welded to the FSP along the port edge, and supported on pedestals at the two starboard corners.

shocks, for the purposes of reducing instrumental data, correcting instrumentation deficiencies, and making such modifications to the structure as were indicated and feasible.

Instrumentation

Time-history records from 64 to 67 channels of instrumentation were obtained during 16 separate shock tests. Some 85% of the gages were bridge type (strain gage or piezoresistive) accelerometers, installed at various positions on the FSP, the simulated decking, the stowage framework, and the stowed missiles. It was from these accelerometers that most of the useful data were obtained. Signals from ±2500 g accelerometers, attached at severe shock points on the FSP and on the simulated decking, were integrated once prior to recording on magnetic tape and integrated a second time on reproduction to produce simultaneous transcriptions of velocity and displacement. Signals from ±25 g to ±100 g accelerometers, attached at points on the mitigated assembly, were recorded directly and subsequently double integrated on reproduction to produce simultaneous transcriptions of acceleration, velocity, and displacement. Following the preliminary scaling, reading, and inspection of each of these two or three parameter transcriptions, signals from selected gage combinations were electronically combined in a weighted adder/subtractor to produce differential displacement records of bending, stretching, etc. (Fig. 3).

Three features of the instrumentation system were of particular importance to the way in which measured data were processed and interpreted:

- In a practical circuit, electronic component stability and noise impose a limit on the period over which signal integration is feasible. For this reason, the integrators of the instrumentation system included a second-order low frequency cutoff, which caused a systematic drift of the apparent reference point in inertial space, from which the transient motion was initiated. A correction for the drift is calculable but was infrequently performed since the errors were small for short time intervals and could usually be discounted in reading the records for longer intervals [9]. However, the rate of error accumulation was higher for the prerecording integration (integrator period of 1.6 seconds) than for postintegration (integrator period of 4 seconds), a complication dictated by

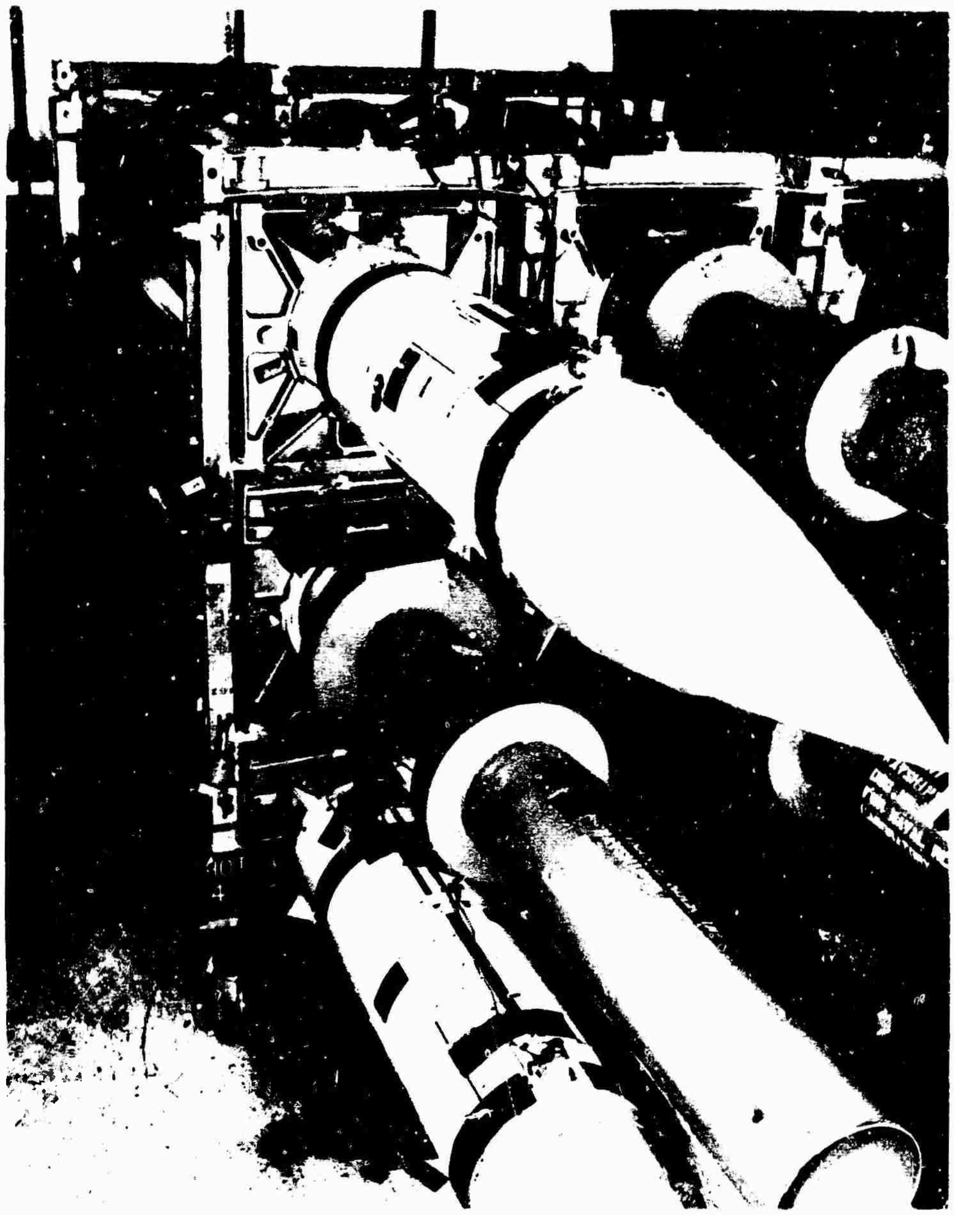

Fig. 2 - A typical assembly of two inert operational missiles and seven dynamically simulated missile mockups in a 3 by 3 matrix is pictured. Components of the stowage system are pinned and clamped to provide a rigid structure, but one which can be quickly assembled or disassembled.

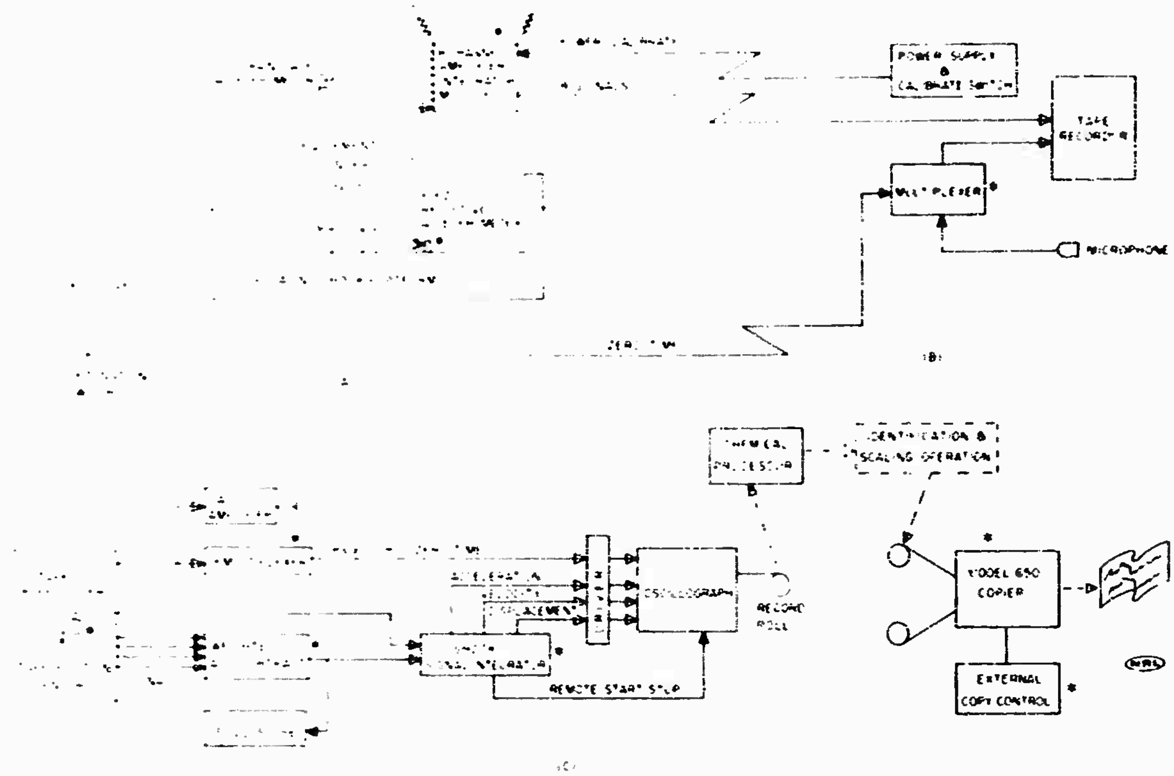

Fig. 3 - Shock input and response motions were measured (A) with accelerometer transducers, recorded (B) on magnetic tape, and reproduced (C) through electronic equipment which produced transcriptions of either inertial or differential acceleration, velocity, and displacement parameters. Additional copies of properly scaled transcriptions were available to participants within a few hours after each test. Items identified by an asterisk were developed particularly for this shock measuring system.

the greater dynamic signal ranges produced by those gages installed at severe shock locations. Consequently, any comparison between uncorrected deck motion records and the stowage system records required that the systematic error be discounted.

• Various factors such as electronic noise, minor electrical or mechanical overload, slight angular misalignment of the transducer, and calibration inaccuracies, sometimes produced nonsystematic drifts in the inertial reference of the combined records. Such drifts could occur both before and after initiation of transient motion. The problem can be put into perspective by noting that, in the presence of peak accelerations of up to 100 g on the mitigated structure and several thousand g at the more severe deck locations, an equivalent acceleration error of 0.2 g in the combined signals could produce as much as 3.5 inches error in the inertial reference point at the end of 300 milliseconds. In practice, the resultant errors were generally less than this, and could usually be discounted by proper interpretation.

• Characteristically, the initial transcription, scaling, and reading of the instrumental records from any one test was completed within six to seven hours. The efficiency with which these more routine phases of processing could be accomplished, allowed interpretive study of the records to proceed concurrently with the test operations. In turn, immediate physical accessibility of the test structure and the opportunity to introduce instrumentation changes during succeeding tests were important aids to interpretation.

Motions in the Vertical Direction and Mount Characteristics

When excited by an underwater shock, the FSP responds with vertical athwartship, and roll motions. In the records of Figs. 4 and 5,

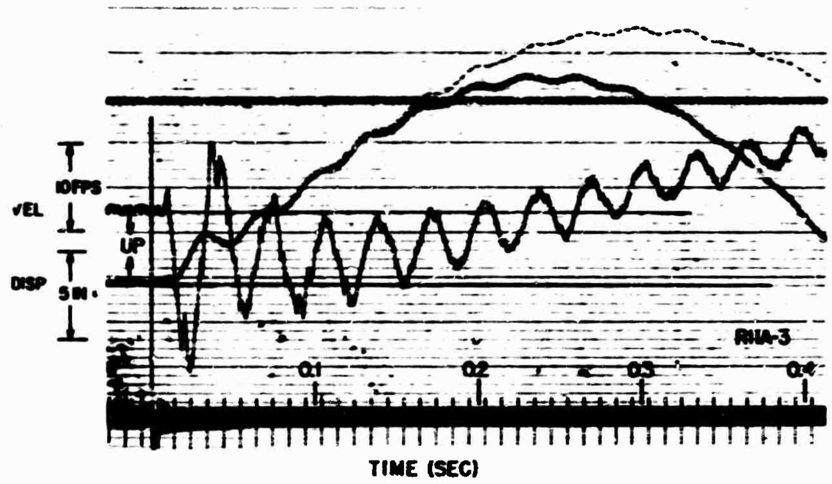

Fig. 4 - Average vertical translation of the deck under the stowage system. Because of the comparatively severe shock environment, signals from the acceleration transducers on the deck were integrated once prior to recording, and were subsequently reproduced as time-records of velocity and displacement. The dotted line shows the effect of a calculated first-order correction which accounts for the low frequency characteristics of the first integrator circuitry.

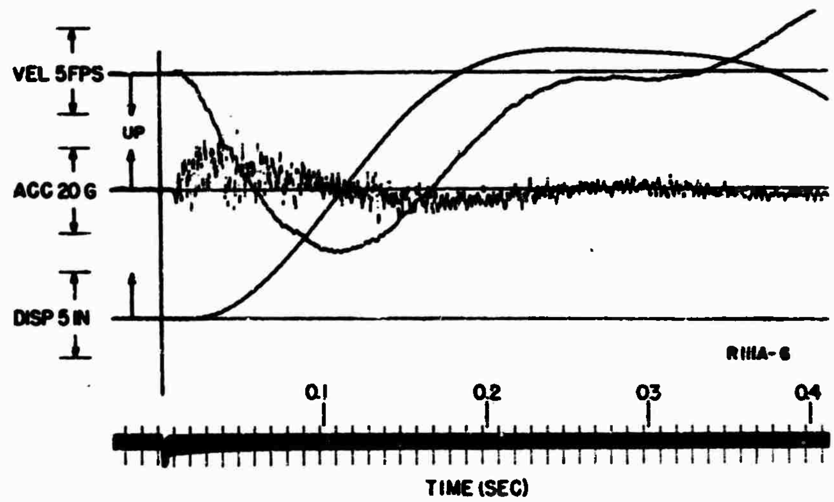

Fig. 5 - Average vertical translation of the mitigating stowage system. Acceleration signals from gages located on the stowage assembly were recorded directly, allowing reproduction in a three-parameter format.

coupled roll motions have been eliminated by summing the response of four spatially distributed gages to show only the averaged vertical input and response motions through the geometrical center of the stowage system. This type of presentation provided a comparison between the experimental data and an analytical model of the system which predicted uncoupled modal responses in various rotational and translational axes. By comparing the two records, it is immediately clear that the very vigorous 30 cps deck oscillation of Fig. 4 has been effectively isolated from the stowage assembly as shown by the records of Fig. 5.

Diaphragming of the simulated ships decking in its 30 cps mode is shown in more detail by the records of Fig. 6. Relative to a plane through the corners of the deck, a point near one of the rubber mounts is seen to have an initial peak downward deflection of 1-1/2 inches, followed by a lightly damped decaying oscillation. A revised inertial reference baseline has been drawn on the displacement trace of this record to discount the physically unrealizable drift otherwise indicated.

Axial deflection of a rubber shock mount was obtained by subtracting measured inertial motion at the deck attachment point from that at the stowage attachment point. In Fig. 7, this deflection has been plotted against measured acceleration at the top of the mount to confirm proper performance of these vitally important elements of the stowage system. By estimating the portion of total system load supported on each mount, the measured acceleration-deflection characteristic could be converted to a force-deflection curve and compared with the design value for dynamic stiffness of the mount. As shown on the figure, the measured stiffness was slightly nonlinear, and, on the average was somewhat less than that employed for design purposes.

Bending of a Stowed Missile and a Handling Band Problem

Because of the fact that the center of gravity of each stowed missile was quite close to its forward support plane, the airframe acted as a cantilever beam to support much of the weight. In Fig. 8, records from three gages along the length of one missile were combined to show vertical bending of the cantilevered forward end off a line through the two support planes. Of particular interest in this record is the absence of any sustained modal oscillation, indicating either a lack of significant drive at the modal frequency or high internal damping in the missile structure.

In attempting to understand certain features of the missile bending record, such as the two cycles of increased amplitude oscillation which appear about 60 milliseconds after the initial input (Fig. 8), an otherwise unrecognized problem in handling band tolerance was uncovered. The records of Fig. 9 were obtained from two

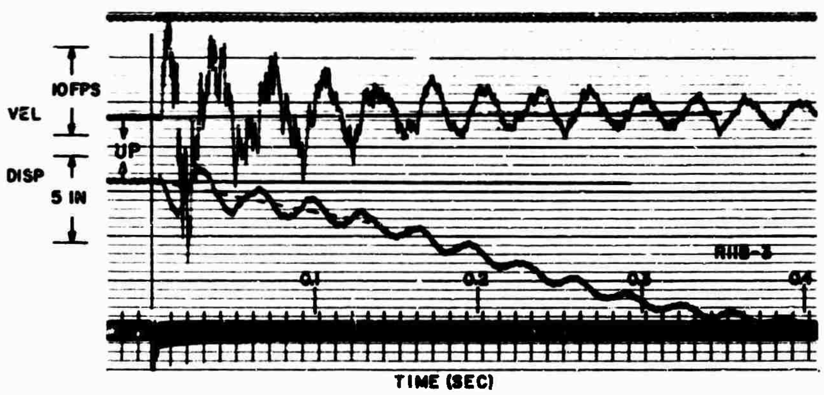

Fig. 6 - Bending of the deck surface in a diaphragm mode occurred at a frequency slightly above 30 cps, as shown by this record of differential translation near the center relative to port and starboard corners. An unrealistic drift in the differential displacement trace is a characteristic result of nonlinear overload in one of the accelerometers or its associated electronics. In many instances such drifts may be partially compensated by estimating a revised inertial reference baseline based on physical possibilities for structural deformation.

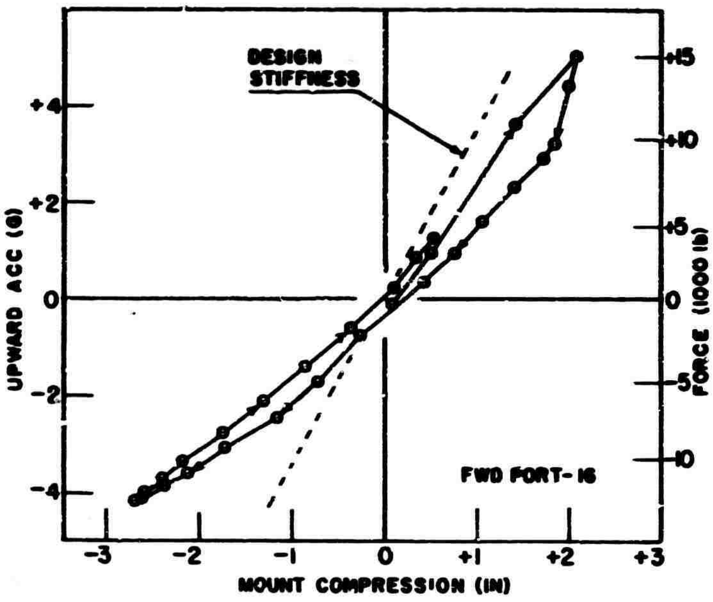

Fig. 7 - Dynamic response characteristics of a rubber shock mount were obtained from two gages, one located at the deck attachment and another at the stowage system attachment. Data points shown on this plot were taken at 10 millisecond intervals.

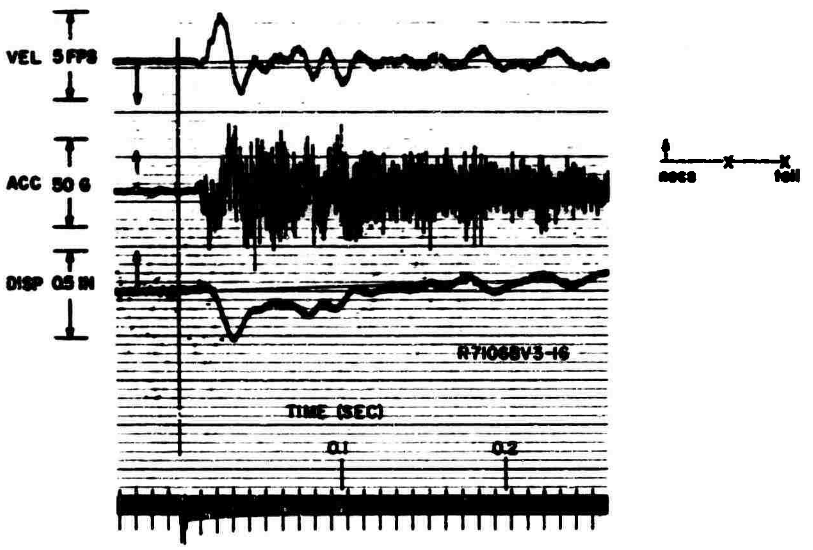

Fig. 8 - Three vertical gages positioned along the axis of one of the stowed missiles were algebraically combined to produce this record which shows bending of the cantilevered nose off a line through the two support points. At 200 milliseconds, an inertial vertical translation of the entire missile of about 15 inches has been almost entirely suppressed to emphasize the much smaller bending deflection.

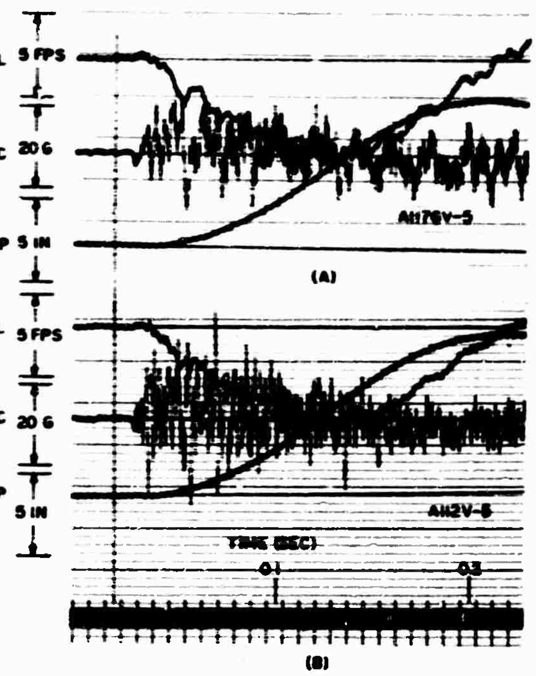

Fig. 9 - Undesirable collisions between a missile and its poorly fitted handling band were initially detected as a difference in the velocity-time traces across the handling band. The difference in velocity trace detail on the missile (A) and on the stowage system below the handling band (B) necessarily implies differential motion. The waveshape of the missile velocity trace suggests collisions.

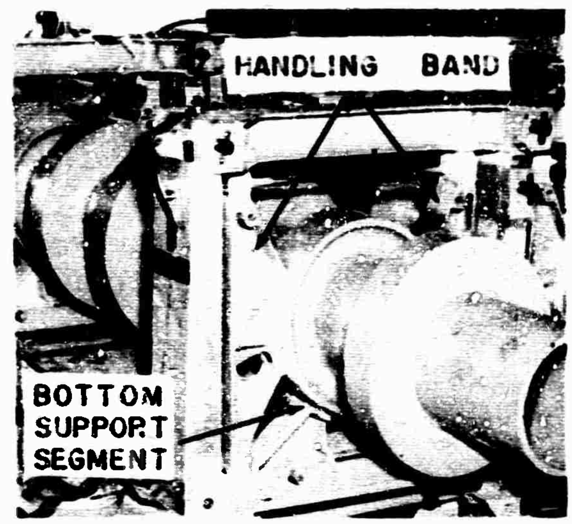

Fig. 10 - Structural behavior, hypothesized from the records of Fig. 9, was confirmed by physical inspection. Bottom support segments of some of the handling bands made no contact with the missile periphery under quiescent conditions.

gages, one on the missile near its after support plane and the other on the stowage framework adjacent to the after handling band. Careful comparison of the velocity traces indicated not only that differential motion was present, but also suggested that impulsive energy was being transferred between the missile and the stowage framework. On succeeding inspection of the structure, it was established that the lower support surfaces of some of the handling bands were not in contact with the missile periphery (Fig. 10). Under shock loading, the rubber facing on the side support surfaces deformed in shear, allowing subsequent collisions between the missile airframe and the bottom support surfaces.

Oscillatory Roll of a Booster Motor in its Handling Bands

Rotational response of the assembled stowage system occurred about an axis in the fore and aft direction. Measured roll records defining this motion were obtained by combining sets of either vertical or athwartship gages; the booster stowage system roll record of Fig. 11 was obtained from four vertical gages located above the shock mounts. Similarly, roll records for one of the stowed boosters, obtained from two athwartship gages on the booster diameter, are shown in Fig. 12. Comparison of the traces of these two figures, and particularly the velocity traces, again indicates differential motion. In this case, a lightly damped 29 cps rotational mode of the booster on its rubber faced handling bands was being excited. Confirmation of this instrumental evidence was obtained by observing crack lines in a layer of paint applied at the juncture between the booster case and its handling band (Fig. 13). The mechanism by which the rolling mode was excited was never clearly delineated, though evidence suggested that it originated with the vigorous flexing of the deck at 30 cps, and was coupled into the stowage system via the simulated bulkhead pedestals and the athwartship stabilizing mounts.

Bending of Vertical Frame Members and Athwartship Tensioning Integrity

Two important considerations during design of the stowage system had involved possible effects of athwartship loading on the cross sectional rigidity of the stowage framework; one related to bending and shearing deformation

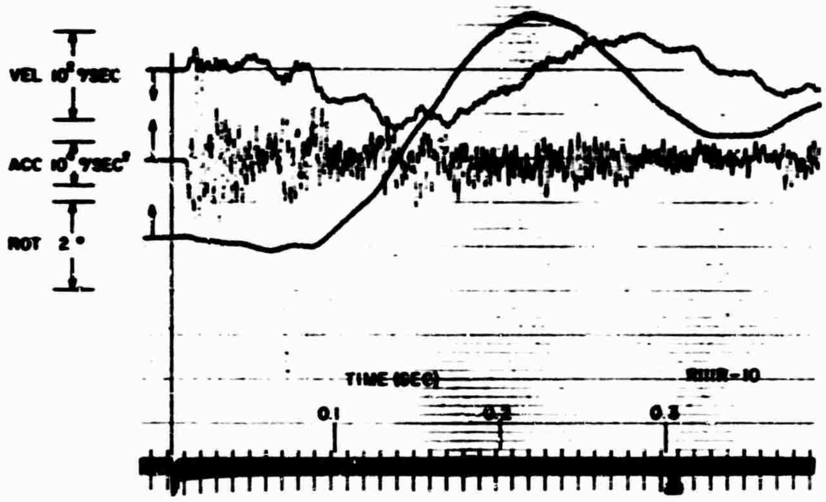

Fig. 11 - Averaged roll motion of the booster stowage system about an axis in the fore-and-aft direction was obtained by an algebraic combination of four vertically oriented gages above the shock mounts

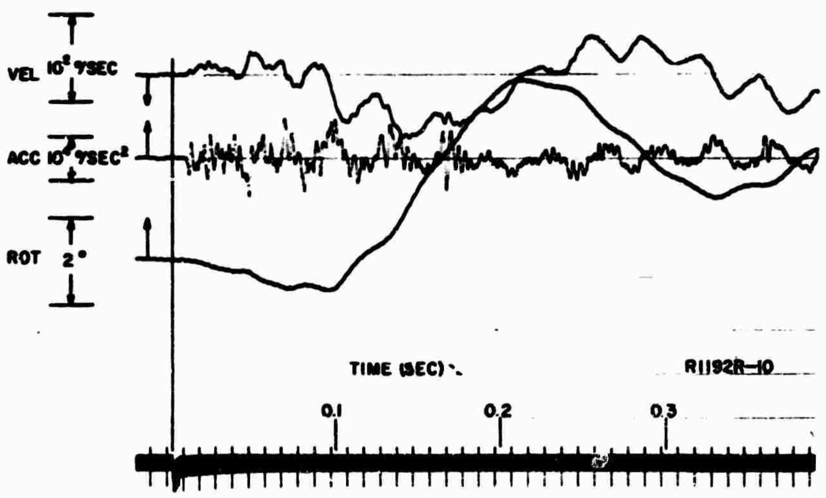

Fig. 12 - Though the system design assumed rigid restraint of the stowed boosters, measurements established that an oscillatory rotational motion of the booster within its rubber faced handling bands actually occurred. This differential motion is evidenced by comparing the angular velocity of a booster shown here with the angular velocity of the stowage system framework as shown in the preceding figure.

Fig. 13 - Cracks in a paint film at the junction between the booster case and its handling band surface tend to confirm the behavior as hypothesized from instrumental data

of the verticals, and the other related to the clamping tension required in long assembly bolts to maintain rigidity in the face of inertial reaction loads imposed by the stowed missiles.

Bending records of both the port and the starboard vertical uprights of one stowage system are shown in Fig. 14. In each case, bending was obtained as the relative displacement of an athwartship gage located at the center of the upright off a line between two other gages located at the top and bottom ends. Discounting small baseline drifts in the traces, the indicated maximum bending was less than 0.1 inch on a 56-inch vertical baseline. Further, both the bending-deflection and the more sensitive bending-velocity records from the two opposite sides of the system compare in great detail, thus showing that athwartship clamping integrity was indeed maintained.

Excessive Clearance in a Pinned Joint

All of the rigid body modes of the stowage systems were designed to be below about 8 cps, such that the stowed missiles would be substantially isolated from any input components of higher frequency. However, early in the test series, high frequency acceleration components observed by athwartship gages attached to the missiles, were cause for concern because of their associated high g levels. Even higher athwartship levels were observed on the stowage framework itself. The source of this problem was identified by studying selected athwartship records at comparatively late times after shock incidence. In the traces of Fig. 15, note that the transient bursts in the acceleration trace coincide with lower frequency maxima and minima in the velocity trace. A physical interpretation of this evidence suggested internal collision within the pinned joints which coupled the athwartship stabilizer mounts to the system framework (Fig. 16). With each load reversal at these joints, the loosely fitted pins transferred from one side of their clearance holes to the other, thus producing an acceleration transient. As an effective temporary fix, shim stock was introduced into the pinned joints to reduce the clearance and thus the severity of the collisions.

In summary, interpretations of the measured data have led to:

- Identification of the mechanisms of prominent driving motions.
- Verification of calculated performance of the system on the basis of its rigid body modes.
- Quantitative definition of the shock mount characteristics.
- Delineation of shock effects on the stowed missiles, whose protection was the primary purpose of system design.
- Identification, for subsequent correction, of several anomolous characteristics which might otherwise have compromised performance of the system.

It may be of some interest to speculate on how much of this understanding would have accrued, had the measured data been interpreted only in

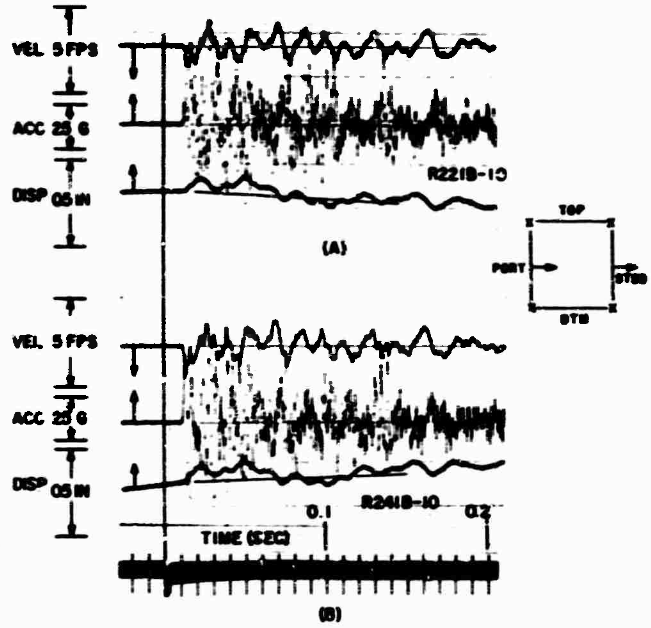

Fig. 14 - These two sets of records show bending of the forward-port (A) and the forward-starboard (B) vertical members of the stowage framework as the motion of the center of each member off a line between its ends. The similarity in velocity trace detail across the 65-inch width of the system confirmed proper performance of athwartship tensioning bolts.

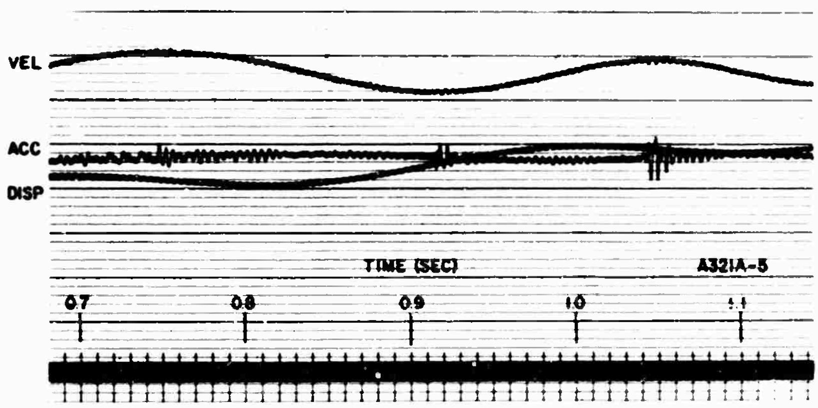

Fig. 15 - The source of high level high frequency athwartship acceleration components throughout the stowage system was identified from records such as this. The isolated bursts of transient acceleration, coinciding with lower frequency velocity maxima, were clearly related to a change in the direction of athwartship restraining forces on the entire system.

Fig. 16 - Dominant athwartship restraint on the stowage system was established by these "stabilizer" mounts. Excessive clearance in the pinned joints between the mounts and the system upright resulted in vigorous rattling and the consequent introduction of undesirably high acceleration peaks.

terms of the peak values, prominent frequencies, and time-history records of measured accelerations such as those shown in Fig. 9.

One might be struck by the similarity of the foregoing illustrations to an actual test report on the stowage system, rather than the generalities usually associated with descriptions of a method. Indeed, the illustrations have been rather directly abstracted from a test report [10]. In this connection, two points made earlier may be reemphasized:

- While the details of such understanding as has been developed are uniquely related to the particular test structure, the methods employed to gain this understanding are applicable to other structures as well.

- Each increment of understanding was the result of an imaginative conjunction of several bits of evidence stemming from a variety of sources, sources certainly not restricted to the dimensional change format taken as the theme of this paper. However, in each case, the mental approach from which interpretation grew had dimensional change, whether measured or inferred, as its foundation.

OTHER DATA FORMATS

In reviewing this report in an early draft form, one associate of the author took some exception to the proposition introduced near the beginning, which commenced "The most understandable format...", etc. The objection arose, quite reasonably, from past experience in shock measurement programs in which other data formats had been of obvious value, and a consequent reaction to what appeared as an extreme claim for the dimensional change format. If this claim were presented in the exclusive sense, that is to deny the value of other data formats, then indeed the objection would be justified. But such is not the case. As a matter of fact, the possibility of just such a confusion is the major reason why several earlier paragraphs were devoted to defining the meaning of "understanding" as it applies to the experimental shock problem.

One may recognize several interrelated facets of the broader structural shock response problem. Insofar as each of these facets depends on a measured data input, their legitimate requirements for data in a particular format may be quite dissimilar. To develop an empirically based understanding of the shock behavior of any particular structure is one such facet, and clearly an important one. On the other hand, the decomposition of time-history records into shock spectra is a necessary format in connection with current design analysis methods; the tabulation of peak values, sometimes within specified frequency bands, may be an important format for comparison with limiting criteria based on such values; and the definition of relative shock inputs to somewhat dissimilar structural targets may be most conveniently based on an inertial value read from one of the measured motion parameters. Further, any-one, or all of these formats may actually be of considerable value in connection with the problem addressed by this paper.

Yet, of the conventional data formats, all having been regularly employed for several years, none has lent itself so readily to interpretation in terms of structural response characteristics as that proposed here. It is for this reason that the dimensional change format has been called "The most understandable."

ANALYSIS VS EXPERIMENT

Having taken the opportunity of a partial departure from the technical theme to answer one anticipated objection, there remains an additional topic of a somewhat similar nature which can be addressed in conclusion.

As an experimentally oriented researcher, the author has frequently been exposed to the charge that instrumentation of a structure which has not been the subject of prior analysis is an expensive exercise in futility. A countercharge is that most tested structures are not actually subjected to analytical study; if they are, the multitude of assumptions tend to divorce the analysis from reality, and that, in any event, failure to exploit an expensive shock test for what empirical information it can produce is also uneconomical. While both of these contentions may have some justification, one suspects that they are more than likely the ritualistic ploys of a game played by individuals with a vested interest in either analysis or in experiment. With only a little imagination, one can assume that the analysts and the experimentalists chose up sides in the middle ages as philosophers on the one hand, and craftsmen on the other. Over the years, the initial status gap has been closed by both the commercial and the scientific contributions of an experimental technology, until today's inheritors are of sufficiently equal prestige to make such a contest possible.

Unfortunately, this game, if such it is, tends to obscure and compromise both the individual and the cooperative contributions of the contestants.

In an article titled "The Unity of Science-Technology," M. Kranzberg, Professor of History at Case Institute of Technology, repeatedly emphasizes the notion that ". two or more good men, particularly if they have different backgrounds, are more creative in problem-solving than one good man by himself; . . ." [11]. Reason verifies this statement. In the present context, a cooperative interplay between accurate structural analysis and meaningful experimental understanding must certainly be of mutual benefit. Yet, if the key adjectives "accurate" and "meaningful" of the preceding sentence do indeed apply, then one must also recognize the fact that both analysis and experiment are capable of independent contribution.

The goal of this paper has been to put more "meaning" in the term "meaningful understanding" as it applies to experimental shock measurement, thus improving both its individual and its cooperative stature.

To quote once more from Professor Kranzberg's article, "... for to a considerable degree modern science is *measurement* and the *analysis of such measurement*, and there are many fields of science whose progress — if not their very existence — is owing to the development of instrumentation."

REFERENCES

1. MIL-S-901C(NAVY) 15 Jan. 1963, "Military Specification Shock Tests, H.I. (High Impact); Shipboard Machinery, Equipment and Systems, Requirements For." Superseding MIL-S-901B(NAVY) of 9 April 1954

2. M.W. Oleson, "Shock Instrumentation Development and Random Vibration Research," Report of NRL Progress, July 1963, pp. 32-38

3. R.O. Belsheim and G.J. O'Hara, "Shock Design of Shipboard Equipment - Part I - Dynamic Design-Analysis Method," NRL Report 5545, Sept. 16, 1960; also published as NAVSHIPS 250-423-30, May 1961

4. G. J. O'Hara, "Shock Spectra and Design Shock Spectra," NRL Report 5386, Nov. 12, 1959

5. R.E. Blake and E.S. Swick, "Dynamics of Linear Elastic Structures," NRL Report 4420, Oct. 7, 1954

6. M.W. Oleson, "Integration and Double Integration - A Practical Technique," Shock and Vibration Bulletin 35, Part 4, Feb. 1966, pp. 1-10

7. M.W. Oleson, "Shock Signal Integrator; Description, Operation, and Schematics," NRL Memo Report 1903, July 1968

8. M.W. Oleson, "Components of a New Shock Measurement System," Report of NRL Progress, Oct. 1967, pp. 16-27

9. S.I. Gendler and M.W. Oleson, "Shock Instrumentation Development (Correction of Integrated Records)," Report of NRL Progress, Sept. 1965, pp. 22-26

10. R.L. Bort, "SAM Shock Stowage Program - Results of Shock Evaluation of Cradle Type Tartar Terrier Mitigating Stowage System," NRL Memo Report 2016, July 1969

11. Melvin Kranzberg, "The Unity of Science-Technology," American Scientist, Vol. 55, No. 1, March 1967, pp. 48-65

DISCUSSION

Mr. Neubert (Pennsylvania State Univ.): Since you were talking about bending deformations, why have you not included the bending strain as one of the primary quantities to measure? People use acceleration to predict relative displacement and then strain. It would seem that, in a lot of measurement situations, it would help the analyst to know what the measured strain is.

Mr. Oleson: Are you talking about a strain of the kind you would measure with a strain gage? (Yes.) This is a logical question to ask in view of the theme of this paper. However, the problem with using a strain gage in this approach, is that the strain gage measurement is meaningful only at the instrumented point. With a collection of motion measuring gages, which are intelligently positioned on the structure, we can define not what happens at a point, but rather what happens across various structural elements. To illustrate, how would one install a strain gage to identify dimensional change associated with the handling-band junction where rattling occurred? There is no way in which a strain gage could be used for that purpose.

Mr. Neubert: But, on the other hand, it would seem logical to back up the bending displacement of the missiles themselves by measured strains. Accelerations give part of the picture, but it seems to me that strain gages would help complete the picture.

Mr. Oleson: I am not really sure that I understand your question. I have no objection to using strain gages. I think that they can produce very valuable information. In the text of this paper I have tried to point out that one can and should use data in every form and of every type that is available. The more one knows about the structure, the better are his chances of understanding its behavior under shock. Thus, neither strain measurements nor inertial acceleration measurements are actually precluded. However, of the various possible data formats, I do contend that the dimensional change format, which identifies stretching, bending, rattling, etc. across structural elements, is the single most useful format in any attempts to interpret structural behavior on the basis of experimental data.

Mr. Neubert: I guess my main point is that for analysis purposes we use accelerations to predict strains. It would be helpful if more people would actually measure strains, so that we could determine whether the predictions were correct. It seems that there is a hesitancy to measure strain as compared to measuring acceleration.

Mr. Naylor (Defense Research Establishment, Suffield): If I understand you correctly, you are taking the displacements of various parts of the missile stack and subtracting the gross motions of the carrying frame to obtain the differential motions of the missiles in the frame. I have great confidence in your integration methods; but you are subtracting two large quantities, one from the other, leaving a small differential movement, and if you have any errors in your integration process you are going to enhance the supposed motion. Would it not be better to take some kind of linear displacement gage--such as a linear potentiometer--between the frame and the missile, or between extensions of the frame and the missile, to detect the bending or relative displacements?

Mr. Oleson: I will accept this as an indirect compliment to our instrumentation system among other things, whether it was intended that way or not. You are perfectly correct in assuming that we are taking the difference of inertial motions--as measured by accelerometers at different points on the structure--and using this to define deformation. Of the records used as illustrations, you may have noticed two different ones for which the differential displacement trace was scaled at one-half inch per inch on our transcriptions. In one of these instances, the inertial displacement of the measured points was about 15 inches at the end of 200 milliseconds. So we are taking small differences between rather large numbers, and are doing this successfully. I will not say with universal success, but still successfully enough for us. As for using a differential displacement measuring device, I know of no such device which could approach the flexibility and universality of the methods we are employing.

Mr. Naylor: Well, it would seem that we must all use your system in order to get satisfactory results, because I have had no success.

EXPLOSIVE SHOCK

William H. Roberts
Martin Marietta Corporation
Orlando, Florida

Intense shock has proved to be an environment capable of producing widespread damage to missile structure and equipment. A search for the cause of failure shows it resides in dynamics rather than other technologies. The changed waveform which results from introducing abrupt loads to structure generates near resonant response internally. An analogy is found which identifies the portion of the frequency band most highly stressed. This is not the high frequency bands commonly brought under examination but a middle frequency band. Throughout the middle frequency band the stresses are high, in sharp contrast to most dynamic response problems where the stress in higher modes is less than in the adjacent lower frequency mode. The utility of the shock spectrum analysis is demonstrated. The shock spectrum tends to be divisible in three separate frequency bands where nearly constant displacement, velocity or acceleration exist. The change in velocity is the fundamental descriptor of the problem. Increased velocity corresponds to increased stress. The analysis specifically excludes the general view that acceleration is the best measure of stress. Velocity as a measure of shock intensity and damage is developed both through scaling theory and through elementary analysis. In addition the ultimate capability of structural materials to withstand sudden loads is identified and shown to be dependent on velocity. The ultimate capability of the material is used to show the relative limitations of real structure. Equipment and components are limited more drastically relative to material capability. As an absolute number, the limit descriptive of current equipment is surprisingly low.

INTRODUCTION AND DEFINITION OF PROBLEM

Recent attempts to qualify missile structure and equipment to intense shock has proven to be a very difficult task. Numerous failures have occurred in flight and in test.

Explosive shock is a typical causitive source. Explosive devices are used in missile space vehicles to perform a variety of functions including stage separation, jettisoning, launch separation, circuit switching, actuation and propulsion ignition. Because of their power, reliability, and ease of application, 100 or more may be aboard a single vehicle with a complex mission. When one of these devices is exploded, it transmits loads and motions through the entire vehicle structure including secondary structure and equipment. In some cases the loads and motions have been great enough to cause structural failure. In addition, the structure acts as a transmission channel to transfer excessive load to sensitive electronics, guidance, autopilots and instruments. Equipment is designed with its principal function in mind first and its structural integrity second.

Explosive devices generate severe explosive loads. The abrupt load excites both high and low frequency motions. The shock amplitude is more severe when the explosive device is directly coupled to a structure, when sensitive structure and equipment are located near the source, and when damaging stress concentrations and other structural complications are located in the main path of the shock. Response levels depend on the amount of charge, the structural configuration, and the transmission characteristics. Because the abrupt load produces different responses, so the failures it engenders are different, affecting such structural elements as joints, welds, bonds, fasteners, branch structures, and coatings. High frequency responses cover the frequency band of equipment--an unusual feature of explosive shock that differentiates it from mechanical shock with longer pulses and milder gradients. Equipment flexibility causes equipment problems -- relay malfunctions, excessive electrical noise, structural failures in transistors, diodes, capacitors, accelerometers, rate gyros, and failures in connectors and solder joints.

The structural problems of equipment and the structural problems of the primary spaceframe correspond. When equipment fails, as opposed to malfunction of equipment with moving parts, it is usually a failure of the equipment structure. The cause is the same as for the failure of spacecraft structure -- the type of structural inadequacy is the same in both cases. Frequent equipment failures are associated with the greater number of parts, the significantly less design effort per part, and the greater diversity of geometry and materials.

The loads, dynamics, structural response and materials were each examined to ascertain where the current technologies may have been limiting and therefore responsible for the failures. Each technology except dynamics was considered to be adequate for the requirements for information from intense shock. For example the failures were not load related in the sense that unknown static loads may have been present. The structures discipline which transforms external loads to internal loads and stresses appeared free from potential error. And nothing in the dynamics transforms material properties to values significantly different from their static values. With other parts of the problem free from involvement, the analysis becomes a search for the particular dynamic characteristics responsible for failure.

Unfortunately the current technology in dynamics is so inadequate as itself to be a problem. Understanding of the physical mechanisms has been limited and accordingly the engineering effort has been confined mostly to test. Only a small part of vehicle structure may be used in test and the inclusion of equipment and the simulation of major masses is often omitted. Appropriate analytic methods are not available and therefore no analysis in support of design or test are conducted. And analytic predictions of the environment are not constructed for use in equipment design. Equipment is not brought under early development and tests are not run specifically to define the environment for use by suppliers. Thus state of the art developments are badly needed. An improved understanding of the phenomena would depend on knowing:

- The cause of the transient oscillation.
- Usefulness of shock spectrum technique.
- A measure of shock severity.
- A description of the internal events in complex structure and a definition of the problem.
- An answer to the question, can internal structural loads of very short duration produce damage.

DISCUSSION AND RESULTS

Explosive shock is not unique in introducing abrupt loads to structure. Other sources also introduce similar loads which produce similar response at all parts of the frequency band and therefore similar damage. An example was available where one structure was subjected to four strong shocks. The events are:

- Nose closure mechanical impact.
- Explosive opening of cell cover.
- Porting of high pressure gases from launch tube.
- Stage Separation Ordnance.

Figure 1 compares the response of complex missile structure to these various intense shocks and shows the responses have similar shock spectrum shapes.

The data shows a given structure responds to several different kinds of abrupt loads in a similar way and several different loadings are capable of generating high frequency shock.

Next we show three means of analysis and presentation of data for one of the four shocks presented above, the nose impact. The time history, the shock spectrum, and a Fourier spectrum are shown in Figure 2. The time history measured at a point in structure is a decaying transient oscillation not a single pulse even though a single pulse was the external load introduced to structure. The frequency content of the waveform is similar whether given by the shock spectrum analysis or the Fourier series analysis. Comparing amplitudes shows the Fourier spectrum amplitudes are very much less than the time history, and the shock spectrum very much more. The high amplitude of the shock spectrum is due to the many repeated cycles of nearly constant amplitudes occurring in a slowly decaying transient. The many repeated cycles give responses nearly as great as that for steady state vibration resonance. Experience shows the time history cannot be read directly to obtain these significant data and that the supporting analyses are valuable. Naturally the near resonant response greatly increases the likelihood of failure. Thus the transient oscillation is a significant change in waveform.

THE ORIGIN OF THE TRANSIENT

It is worthwhile to consider the origin of the decaying transient. A simple dynamic model for analyzing wave transmission in complex structure was constructed. The model, the accounting system for tracking the waves and the calculation and measured time histories are shown in Figures 3, 4, and 5 respectively. At each impedance change a transmitted and reflected wave is generated. After only a short time, a fraction of a millisecond, the accounting plan shows the presence of many signals for a model containing only three masses. Thus the origin of the oscillating transient arises from dense upstream and downstream signals generated by the many changes in impedance present in complex structure.

A MEASURE OF SHOCK SEVERITY

The problem of determining a proper measure for shock intensity is probably the problem of greatest importance. The most useful information to develop probably would be the portion of the frequency band where damage is produced. To the dynamicist concerned with design support this information is most needed and can be related to other characteristics of the equipment and the decisions to be made regarding it. To do this several routes have been taken. Contributions from elementary analyses are compared to the output of the scaling theory. To compare real structure across the frequency band we are mainly interested in how the designer's real output is related. Generally a change in frequency implies a change in size. Thus it will be necessary to determine more precisely than by frequency alone the relative amount of structure in small sizes to that in corresponding structures in larger sizes.

Elementary analysis shows the form of simple shock spectra and relates the physical variables defining the excitation to the output variables of the shock spectrum. When a simple dynamic system impacts a boundary the shock spectrum which describes this event is a straight line.

$$a = vw$$

a = acceleration
v = velocity
w = frequency

Sketches 1, 2, and 3 illustrate the system for dynamic impact and the associated shock spectra. The shock spectrum in the form of acceleration versus frequency using logarithmic scales shows a characteristic 45° slope for the constant velocity portion.

Thus velocity, the only variable describing the input, defines the event. Velocity acting as the only variable describing the input, also parametrically determines stress or strain in longitudinal impact.

$$e = v/c \quad \text{and} \quad \sigma = \rho c v$$

Where
e = strain; σ = stress
c = speed of sound in the material; ρ = mass density of material
v = velocity of impact

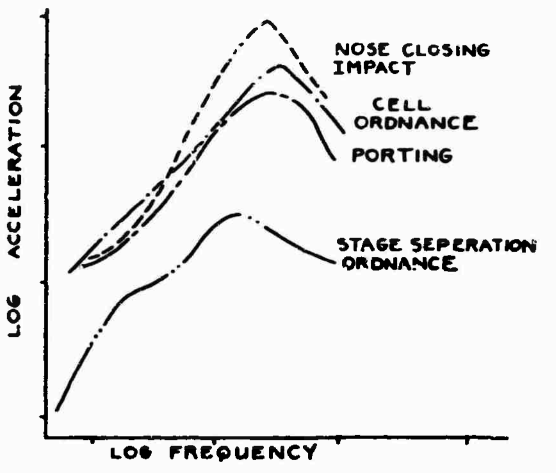

FIGURE 1. FOUR SHOCK SPECTRA COMPARING EFFECTS OF VARIOUS SOURCES.

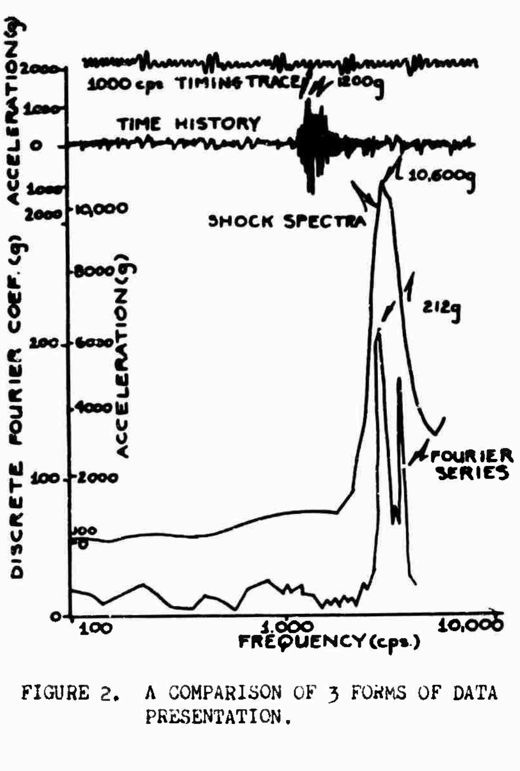

FIGURE 2. A COMPARISON OF 3 FORMS OF DATA PRESENTATION.

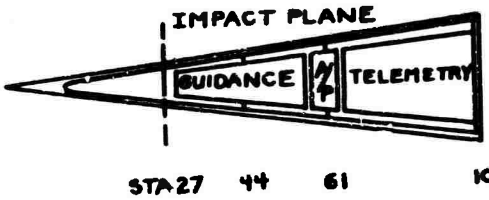

FIGURE 3. DYNAMIC MODEL FOR LONGITUDINAL IMPACT.

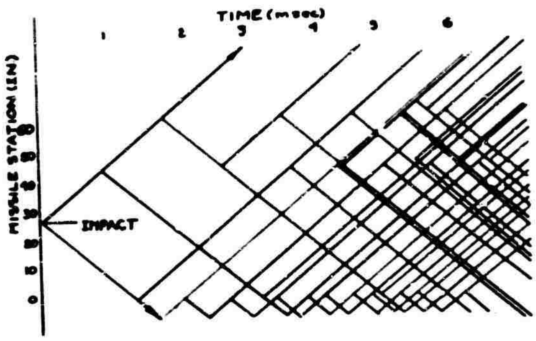

FIGURE 4. TRANSMITTED AND REFLECTED STRESS WAVES.

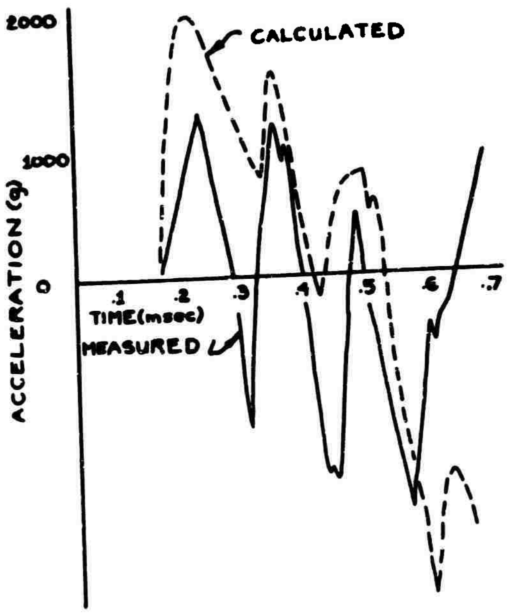

FIGURE 5. CALCULATED AND MEASURED TIME HISTORIES.

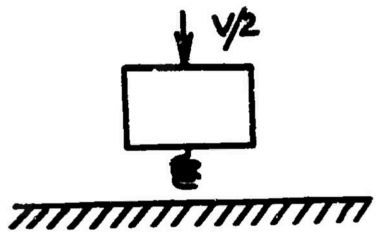

SKETCH 1. SIMPLE DYNAMIC IMPACT.

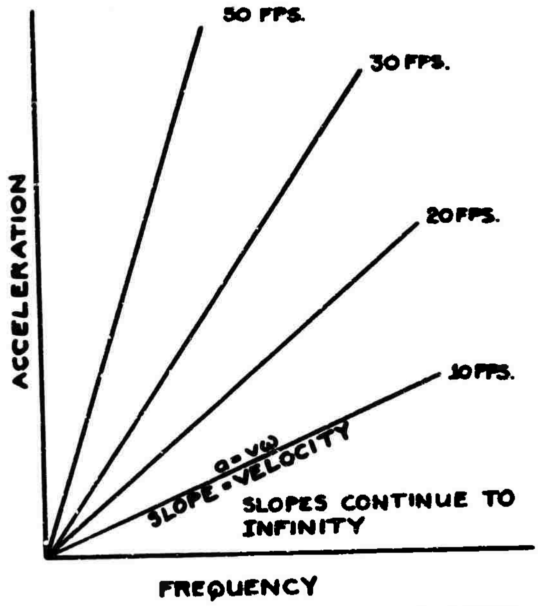

SKETCH 2. SHOCK SPECTRA FROM SIMPLE DYNAMIC IMPACT.

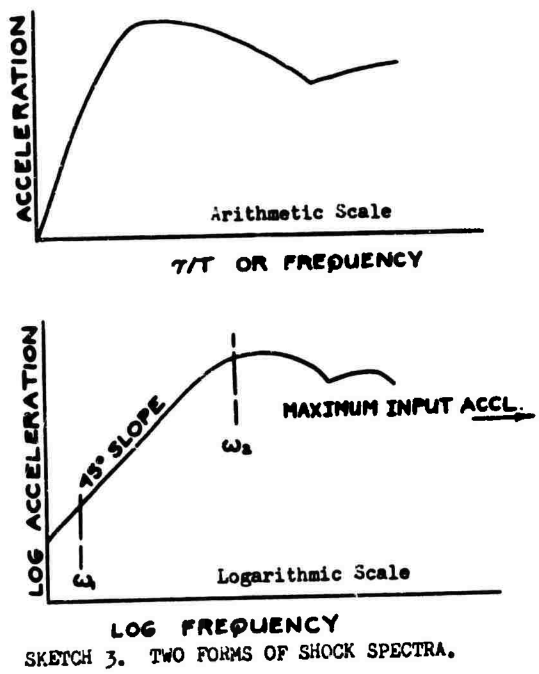

SKETCH 3. TWO FORMS OF SHOCK SPECTRA.

If complex structure exhibits similar response as determined by its shock spectrum over portions of the frequency band, it is a measure of the velocity shock at a particular point of complex structure. Thus, even though a complex transient oscillation may have been the waveform experienced as the internal structural load (from which it would not normally be expected to find a simple response), we ask if the response may be reduced to separate frequency bands of nearly constant displacement, velocity and acceleration. Figure 6 is an examination of five very diverse shocks, each characterized by a transient oscillation. Clearly the response has been simplified by the shock spectrum analysis technique to regions of exceptionally simple responses. The figure shows nearly constant motion, displacement, velocity or acceleration, in successively higher frequency bands. The shock spectra shown in this figure were specially chosen to display this result. However, finding shock spectra with these characteristics was not difficult since approximately ½ those examined at random were as shown. Those not showing these characteristics merely had larger peaks and valleys imposed on an overall tendency similar to that shown. Thus the shapes shown must be considered to be typical for some class of complex structure. To summarize, we have learned then we have a freedom to draw lines of constant displacement, velocity and acceleration through shock spectra for systems whose damping is low, whose response shows strong resonant like characteristics, if the shock spectrum shape permits such equivalent construction. Sketch 4 shows highly resonant response and an estimate of the equivalent velocity.

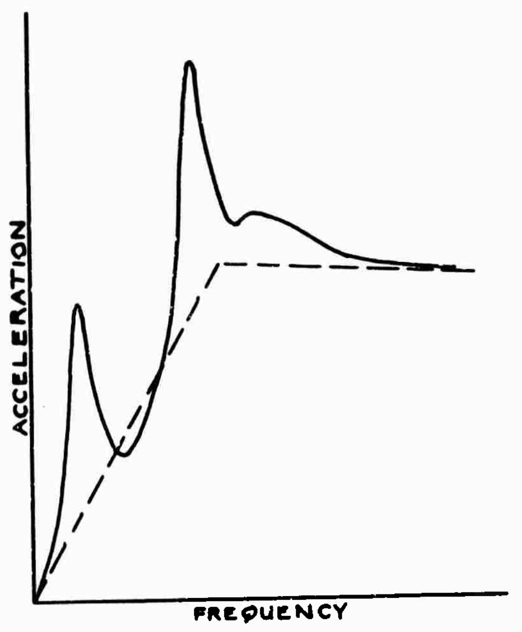

SKETCH 4. SHOCK SPECTRUM CONTAINING TWO NATURAL FREQUENCIES.

The origin of the characteristic shape of the shock spectrum is of interest. The separate extremes may be described by the extremes of the dynamic characteristics: the seismic mass region where the pulse is introduced to the support while the mass remains substantially at rest; the impulse - momentum or velocity shock region; and the equivalent static load region. In order, these extremes yield simple relationships.

$a = w^2\delta_o$ $v = w\,\delta_o$ $\delta = \delta_o$	Mass remains essentially at rest during motion of the support.
$a = v_o w$ $v = v_o$ $\delta = v_o/w$	Mass receives a step change in velocity during a time when deflection remains small.
$a = a_o$ $v = a_o/w$ $\delta = a_o/w^2$	Mass closely follows the support.

The regions are defined by different relationships between the characteristic time which describes the pulse length and the characteristic time describing the natural oscillation of structure.

The delineation of the shock spectrum into component parts is useful on two counts. The shock spectrum becomes an engineering tool which measures the velocity and acceleration at a given point of complex structure under complex loading. And further it could form the basis of prediction.

At this point of the paper preliminary indications are that velocity has fundamental meaning as a measure of shock intensity. Next, we wish to show how a line of constant stress would appear on a shock spectrum. The line of constant stress will indicate which definition of the motion has the greater meaning. To do this the structures modeled by the shock spectrum must be related in a particular fashion. The shock spectrum relates these structures by frequency only. We are mainly interested in how the designer relates large and small structure. The designer conceivably could use load factor to determine the amount of structure introduced throughout the vehicle. This would be a rational and consistent approach to design. Such design would also result in structural dimensions related in an easily identifiable pattern. Alternatively he might relate small items to large by building dynamic models, a different approach, also easily identifiable. Another approach would consist merely of using relatively constant structure, a conservative approach to the design of small items.

Possible Design Approach as Related to Scale	Structural Dimensions Related by
load factor design	$1/n^2$
dynamic model	$1/n$
constant structure	constant

Where our structures and similar items that could be used to compare large and small structures, the structural dimensions were related as shown in Sketch 5. Of most interest is equipment and structure rationally designed to a constant load factor. Consistent use of load factor design would see structure dimensions related by $1/n^2$. Instinctively it is apparent that we do not design with this strenuous an attenuation of structure dimensions for small items. Even the "dynamic model" is not used to the exclusion of other relationships. The sketch shows many small structures use the same skin gauge as correspondingly larger structure, a deviation from scaled design partially due to preserving a minimum gauge.

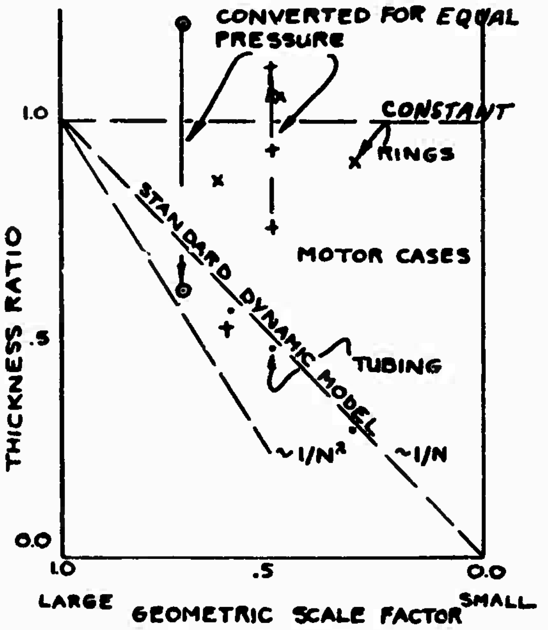

SKETCH 5. A COMPARISON OF STRUCTURAL DIMENSIONS TO GEOMETRIC SCALE FACTOR.

Using the intermediate of these relationships as most representative of how structures are related the lines of constant stress may be defined. Any large structure is scaled to produce a small structure by scaling all structure dimensions proportionate to the geometric scale factor. Such an array of dynamically similar models follows the simplest of scaling laws. For such a relationship the scaling theory shows: (for a 1/2 scale model)

Prototype		Model
1	displacement, length	½
1	velocity	1
1	acceleration	2
1	frequency	2
1	time	½
1	spring rate	½
1	force	¼
1	area	¼
1	stress, pressure	1
1	mass	1/8

This particular structural array leads to the conclusion that equal stress is seen by each structure when a disturbance of equal velocity is imposed. At high frequency where the response velocity decreases the imposed stress decreases. The influence of more nearly constant structural dimensions, would be to rotate lines of constant stress towards lines of constant deflection. Internal stresses can be expected to be high over the frequency band where highest velocity is measured. This permits a judgment to be made as to what part of the frequency spectrum is important.

ACCEPTABLE VELOCITY FOR STRUCTURAL MATERIALS

A theoretical limit of acceptable particle velocity for structural materials exists. The theoretical limit is low (100-200 fps) so that it presents a prominent limitation to structure and equipment that must maintain integrity and preserve function. The limiting velocity in common structural materials is given in Rinehart, Reference 5. The limit is roughly constant for various structural materials except that it is significantly improved as the material is hardened. Examination of the events of Figure 1 on a scale related to the theoretical limit shows complex structure exhibits early failure when compared to the material limit, as one would expect. Experience shows a satisfactory acceptance of particle velocities imposed on structure at the level of 30 fps but numerous failures at 60 fps. Well designed structure, free of stress concentrations, buckling instabilities, eccentricities or other compromises may accept 60 fps. Structures whose details are considerably improved by experience gained from test could accept the higher velocity also.

The problems posed by the design of all manner of mechanical components and equipments which include their structural integrity and their adequacy to accept explosive shock transmitted by structures are formidable. Here the velocity limit may be as low as 5-10 fps, an order of magnitude less than the structural limits and only 5-10 percent of the theoretical limit of the material. Thus equipment failures occur at surprisingly low load levels. To define the problem by defining a limiting velocity is to define an approximate limit which really depends on the fragility of unique items and the amount of improvement accomplished in analysis and test. In practical terms, however, it may be expected that input limitations to this degree apply to structure and equipment.

VIBRATION RESPONSE SPECTRA

Because of the near approach of the waveforms recorded in explosive shock to random vibration waveshapes, and because of the peculiar analytic results obtained for the shock problem, we wished to determine what type response spectrum would result using vibration as an input. Figures 7, 8, and 9 are included to show the spectral response to random vibration is similar to that from the shock transients -- nearly constant velocity and acceleration. It is reasonable to conclude therefore, by analogy to the discussion on the shock spectrum that vibration velocity measures internal stresses, not vibration acceleration.

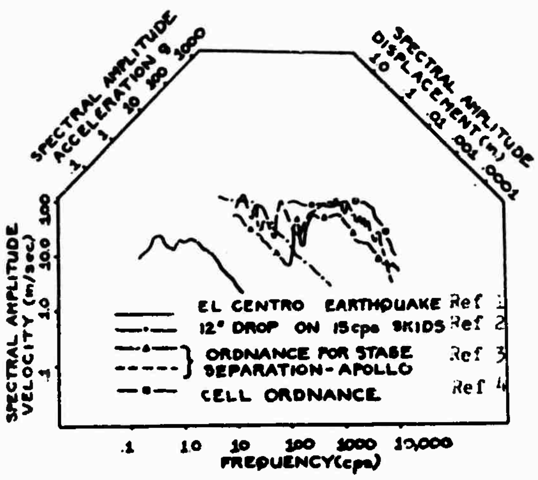

FIGURE 6. RESPONSE SPECTRA FOR VARIOUS EVENTS.

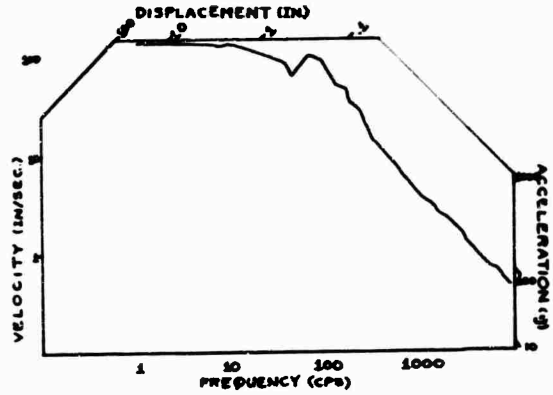

FIGURE 7. EQUIPMENT STRUCTURE RESPONSE SPECTRUM.

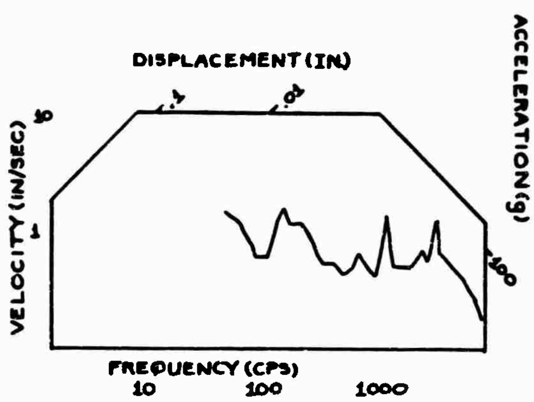

FIGURE 8. EQUIPMENT BASE RESPONSE SPECTRUM.

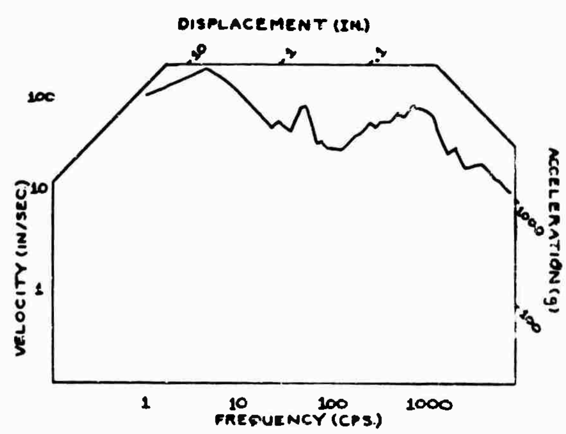

FIGURE 9. PRIMARY STRUCTURE RESPONSE SPECTRUM.

DYNAMIC OVERSTRESS

It is often presumed that a significant material characteristic exists which gives it the capability to accept very briefly high loads of short duration which are unacceptable statically. The presumption presumably is based on material plasticity and material inertia. An examination of available data suggests a material acts in an equivalent static manner within small limits to times shorter than those of interest to the problems being discussed.

References 6, 7, 8, 9, and 10 show negligible rate dependency in the dynamic behavior of materials. The degree of dependency is shown in Figures 10, 11, and 12 where dynamic stress strain relationships are compared to static and where analysis and test of wedge penetration into a thick target are compared. The exceedance of stress due to abrupt load is limited to 25%. The analysis of wedge penetration shows a satisfactory prediction of material dynamic behavior provided work hardening and thermal effects are included. The large deformation plastic behavior as described in Reference 3 follows closely the expression

$$\sigma = \beta_o(1-T/T_m)\epsilon^{1/2} = \beta\epsilon^{1/2}$$

Where $\beta_o = 8.24 \times 10^4$ psi a universal constant and
T_m = melting point temperature
ϵ = strain
σ = stress
a rate independent relationship.

To state as one author does, "The approach that must be used to study behavior under impulsive loading often differs radically from the approach adopted for studies involving conventional loading. Design criteria applicable to static cases often cannot be applied when impulsive loads are involved. The marked differences in behavior under conventional and under impulsive loads are usually traceable to the short duration of the loads", is to gather under one heading a number of dynamic aspects of structure and material behavior with marked differences. The necessity to separate material dynamic behavior proved to be possible and instructive.

Thus, nothing in the dynamics of short duration loading significantly transforms material properties from their static values. Thus, materials considerations and materials-determined structural behavior are nearly independent of the loading duration.

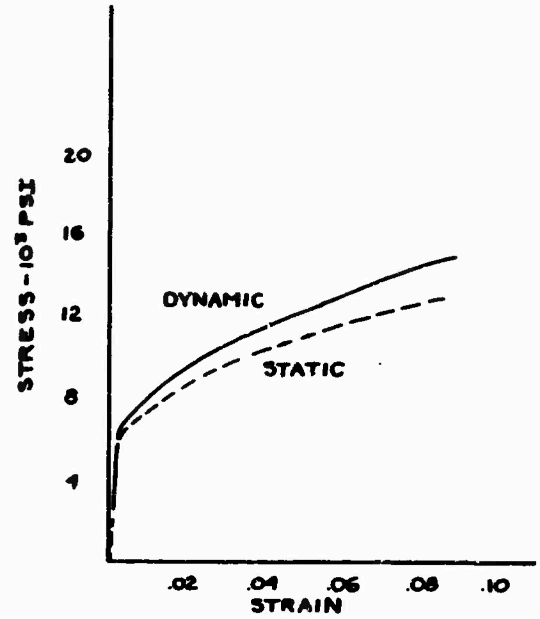

FIGURE 10. COMPARISON OF DYNAMIC AND STATIC STRESS-STRAIN CURVES.

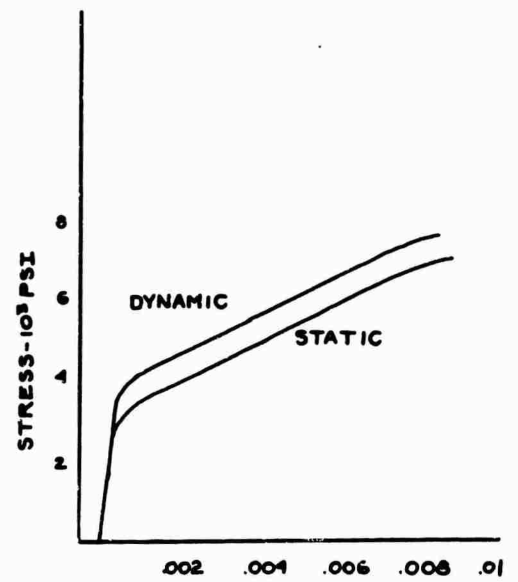

FIGURE 11. COMPARISON OF DYNAMIC AND STATIC STRESS-STRAIN CURVES.

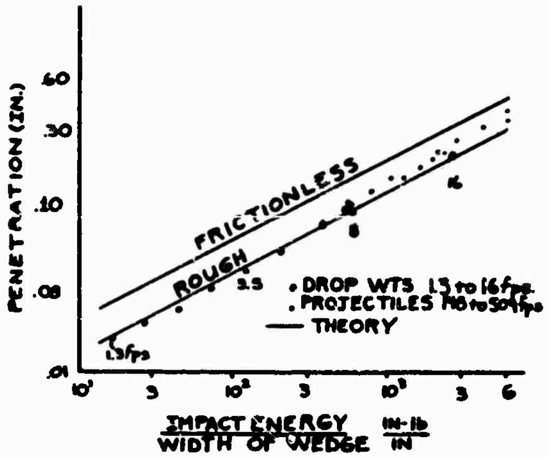

FIGURE 12. WEDGE PENETRATION.

CONCLUSIONS

Structural problems of equipment are the dominant problems impeding straightforward qualification to an intense shock environment. On a measuring scale provided by structural materials the equipment capability is shown to be as small as 5-10% of the ultimate available capability.

The principal dynamic characteristics responsible for failure are

- Imposition of an abrupt load front externally
- An oscillating load transmitted internally through structure whose energy content extends to high frequency.
- Resonant response.
- High stresses at high frequency.

Although the emphasis in this study was on explosive shock it is not a unique loading. Any abrupt loading on complex structure will generate the special dynamic characteristics noted which explain failure.

The origin of the oscillating transient arises from dense upstream and downstream signals generated by the many changes in impedance in complex structure.

A basic shape for a shock spectrum has been identified. It is an unusual result that complex excitation acting on complex structure will generate a response spectra consisting of lines of nearly constant displacement, velocity and acceleration. The basic shape is present for both shock and vibration.

The question of where along the frequency band and where along the shock spectrum the highest internal structural loads may be experienced was resolved by relating large to small structure by "standard" dynamic modeling. The main point of the development was that internal stresses are best given by velocity and not acceleration. Consideration of the motion variable alone does not permit a decision as to which motion variable is important. The structural relationship must also be defined. That is, the ability to define lines of constant stress depends on an auxiliary relationship relating large and small structures across the frequency band. Variations in the manner real structure and equipment are designed in terms of their structure, their masses and stiffnesses suggest lines of constant stress will occasionally agree with lines of constant displacement, at times with constant velocity and at times with lines of constant acceleration. They are related as follows.

Design Approach	Linea of Constant Stress
load factor design	lines of constant accelerstion
dynamic model	lines of constant velocity
constant structure	lines of constant displacement

The limiting velocity as a structural allowable for materials is a prominent design barrier in explosive shock. That the limitation may be simply given as a velocity should be clear. Real structure and equipment are limited to still lower velocity than the materials, equipment to levels only 5-10% of the limit of the material alone.

The portion of the frequency band generating greatest damage is the mid frequency band, not the high frequency band.

REFERENCES

1. J. Blume, N. Newmark, L. Corning, "Design of Multistory Reinforced Concrete Buildings for Earthquake Motions," Portland Cement Association, 1961.

2. Unpublished Pershing Data, Martin Marietta Corporation, Orlando, Florida, 1968.

3. J. Olsen, J. West, H. Himelblau, "Mechanical Shock of Honeycomb Structure from Pyrotechnic Separation," Shock and Vibration Bulletin 37, Part 4, January 1968.

4. NIKE-X SPRINT OR 6879-11, Supplement 1, "Shock, Vibration, and Acoustic Data Analyais (u)," Martin Marietta Corporation and Bell Telephone Laboratories, Inc., Page 3-33, July 1968.

5. J. S. Rinehart and J. Pearson, "Behavior of Metals Under Impulsive Loads," Dover, New York, 1954.

Papers presented at a Colloquim on Behavior of Materials under Dynamic Loading, Winter Meeting ASME, Chicago, Illinois, November 9, 1965. ASME NY, Ref. 6-10.

6. J. F. Bell, "Dynamic Plasticity of Metals at High Strain Rate," an experimental generalization.

7. H. Kolsky, "The Propagation of Mechanical Pulsea in Anelastic Solids."

8. S. R. Bodn[illegible] Strain Rate Effects in Dynamic Load[illegible] of Structure."

9. L. E. Malvern, "Experimental Studies of Strain Rate Effects and Plastic Wave Propagation in Annealed Aluminum."

10. W. G. Soper, "Wedge Penetration in a Thick Target."

DISCUSSION

Mr. Schell (Naval Research Lab.): You did not get into much discussion of actual failures. I know that you were talking about 10,000 g's at 5,000 Hz in the shock spectrum. Could you give some basic idea of what kind of failures these inputs cause?

Mr. Roberts: The electronics is unusual in two respects. There are approximately 9000 electronic components. The electronic components are smaller than standard, but they are not microminiature. Very interestingly, the failures of the equipment are failures that structures people would be vitally interested in if they were to look into the equipment in detail and try to understand the way in which it is designed. These include failures of small internal leads. One of the failures that we obtained involved a seven mil length of wire which was only one mil in diameter. Naturally, soldered joints at these levels are a very critical type of weakness. Other types of failures in general are ones with which you are all familiar in the field of structures. These failures creep into equipment due to inattention to structural details of the design.

MODAL VELOCITY AS A CRITERION OF SHOCK SEVERITY

H. A. Gaberson, Ph. D
Naval Civil Engineering Laboratory
Port Hueneme, California

and

R. H. Chalmers
Naval Electronics Laboratory Center
San Diego, California

An examination of reported spectral shock response data shows the dynamic range of accelerometer data to cover several orders of magnitude; very often the acceleration "g" levels remain the same order of magnitude as the frequency in Hz. No one has explained the damaging effects of high-frequency structural accelerations -- for example, 30,000 g's at 20,000 Hz. To shed light on both problems, this work considers the simple stress mechanisms of longitudinal waves in rods and transverse waves in beams and proves that modal stress is only a function of velocity and independent of frequency. Thus modal velocity singly predicts stress. This analysis cannot take into account failures other than those due to high stress.

The paper in essence urges the development of a more adequate velocity transducer, the use of modal velocity as a severity criterion, and the use of velocity as prime shock-measurement parameter.

INTRODUCTION

Characteristics common to a variety of reported shock spectra, and certain other factors, have led to the conclusion that velocity, suitably interpreted, may be the unifying thread throughout dynamic analysis. The most important considerations are:

1. Existence of a heuristic relationship between shock-induced velocity and damage.

2. Constant velocity tendency of most reported shock spectra.

3. Analytically derived, direct relationship between stress and modal velocity.

Collectively, these factors indicate strongly that shock measurements should be made in terms of velocity, that the much desired correlation between shock-induced motion and structural damage will be found in the velocity spectrum of the shock, and normal mode theory should be used in shock-resistant design.

SHOCK IN TERMS OF ACCELERATION

Current practice in specification of shock tests is to specify the type of shock machine, the shock spectrum, the acceleration-time history, or a combination of these.[1,2] Regardless of how it was specified, the test is nearly always reported by means of acceleration spectrum or acceleration-time history.

Why has acceleration become the predominant shock motion parameter? Does it offer advantages over velocity or displacement?

Yes! Acceleration transducers are inherently smaller and lighter than velocity transducers and, because only small operational motions are required within them, are free of bottoming which is so often incurred in velocity transducers in shock.[3] Contrasted to strain gages, acceleration transducers are easier to install, and they can be removed and used again.

Further, Newton's Second Law of Motion tells us that force equals mass times acceleration, and all engineers have trained awareness that damage to a structure is dependent on forces borne by it.[1]

As a measure of shock severity, however, acceleration levels (without regard to frequency) do not exhibit a straightforward correlation with shock-induced damage. Shock literature contains many discussions on this lack of correlation and on arbitrary measures taken in attempting to establish better correlation.[1,2,4,5] So long as acceleration remains the predominantly used shock parameter, the correlation between shock level and shock-induced damage will remain elusive, as shock-induced accelerations have too wide a dynamic range to allow resolution of all damage-causing accelerations.

J. P. Walsh of the Naval Research Laboratory has pinpointed the problem regarding dynamic range, resolution, and damage correlation. He states:[6]

"On the acceleration-time record the high-frequency component obscured the low-frequency components. The maximum velocity and time to maximum velocity could not be determined because reliable integration was not possible. No information about the displacement-time curve could be found.

"In order to determine the range of the instruments which would be required to record displacement, velocity, and acceleration under shipboard shock conditions, a simple apparatus was studied. It was composed of different parts having high and low natural frequencies and made of brittle and ductile materials. It was shown that a variation in acceleration between 2.45 g and 9×10^3 g combined with displacements varying between 1.9 and 7.6×10^{-4} inches was necessary to produce damage. The extremes of each would damage one part but not affect the others. The extremes of velocity associated with the extremes of displacement and acceleration were 2.5 feet per second and 20 feet per second. This is a narrow range compared with the ranges of displacement and acceleration."

In the case just cited, the dynamic range for damage-causing motions was 3700 to 1, or 71 dB, for acceleration; 2500 to 1, or 68 dB, for displacement; and 8 to 1, or 18 dB, for velocity. Compared to the 40-dB resolution available with current analog tape recorders or oscillographs, it is easily seen that the lower-level damage-causing accelerations (or displacements, for that matter) would not be resolvable with today's instruments and techniques. Note well that damage-causing motions described in terms of velocity spanned only an 18-dB range. Therefore, only the velocity parameter would have permitted recording this shock with inclusion of all of the damaging components.

HEURISTIC VELOCITY - DAMAGE CORRELATION

The above experiment indicates the heuristic relation between damage and velocity; in fact, it is one of the few reported studies of motion parameter and damage. Shipboard shock studies have also indicated this relation. Oleson[7] specifically cites the "empirical correlation" between damage and velocity. Shaw,[8] of the Royal Navy, in explaining choice of velocity transducers, states that they "... could obtain more readily from velocity-time records information on the damaging characteristics of shock..." And in discussing explosively generated ground motions, Hudson[9] has referenced several studies in which "...velocity shows good correlation with damage over a wide range of frequencies."

Thus a great deal of experience leads one to expect a strong correlation between shock-induced velocity and damage.

SHOCK CHARACTERIZED BY CONSTANT VELOCITY SPECTRUM

In addition to the work reported by J. P. Walsh,[6] many other reported shock data reveal a tendency toward a constant velocity spectrum. Figures 1, 2 and 3 are acceleration spectra of response to gunfire shock. Figure 4 presents acceleration spectra from railroad coupling shock, while Fig. 5B is the response of the anvil table of the Navy Medium Weight Shock Machine upon hammer impact.

Even though these spectra are collected from a variety of types of shock, they all exhibit a strong constant velocity tendency. (The single line with a positive 45° slope in Fig. 4 represents a constant 61.4 inches per second.) And the examples included here represent only a few of the shock spectra exhibiting the constant-velocity characteristic. To gain full appreciation of this fact, one should sketch constant velocity lines in any acceleration spectrum he finds. When both acceleration and frequency are plotted logarithmically, drawing the $V = k$ lines is easy. Drawing a straight line through the points where

FROM NOLTR 69-64, FIG. 24

P. S. HUGHES APRIL 1968
ENVIRONMENT SIMULATION DIVISION
NAVAL ORDNANCE LABORATORY
WHITE OAK, MARYLAND – MR. WISARD

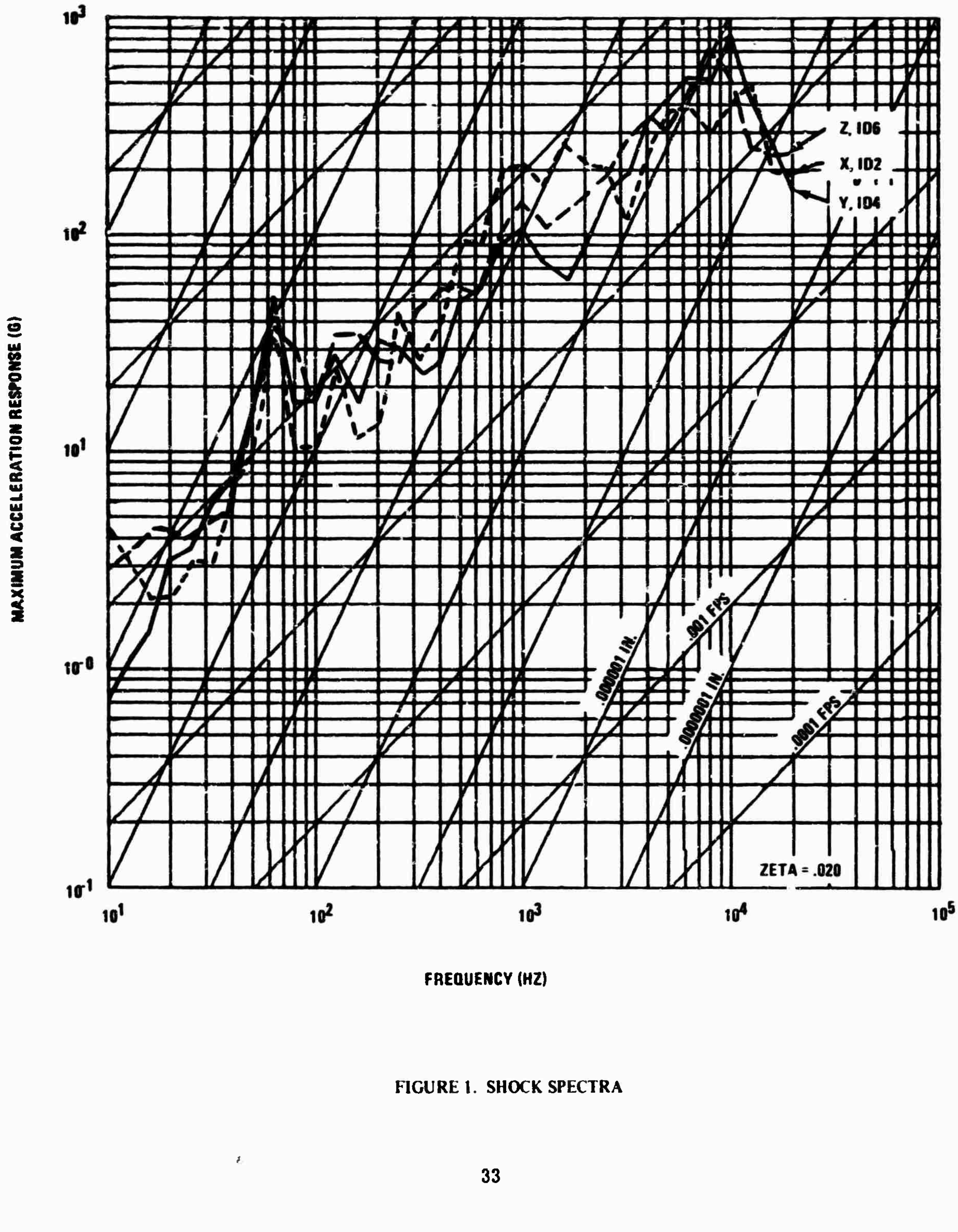

FIGURE 1. SHOCK SPECTRA

FROM NOLTR 69-64, FIG. 25

P. S. HUGHES APRIL 1968
ENVIRONMENT SIMULATION DIVISION
NAVAL ORDNANCE LABORATORY
WHITE OAK, MARYLAND – MR. WISARD

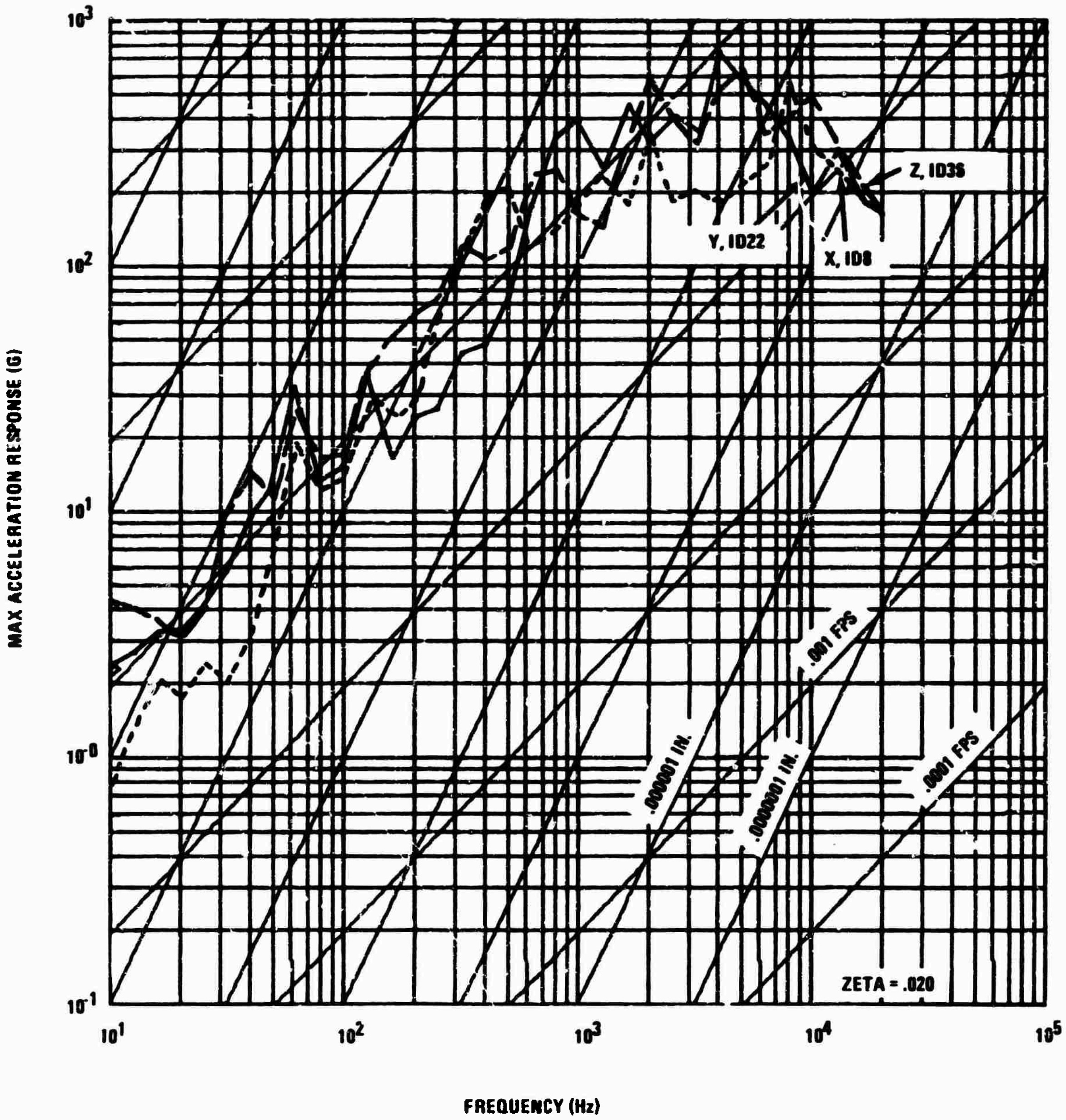

FIGURE 2. SHOCK SPECTRA

FROM NOLTR 69-64, FIG 26

P. S. HUGHES APRIL 1968
ENVIRONMENT SIMULATION DIVISION
NAVAL ORDNANCE LABORATORY
WHITE OAK, MARYLAND – MR. WISARD

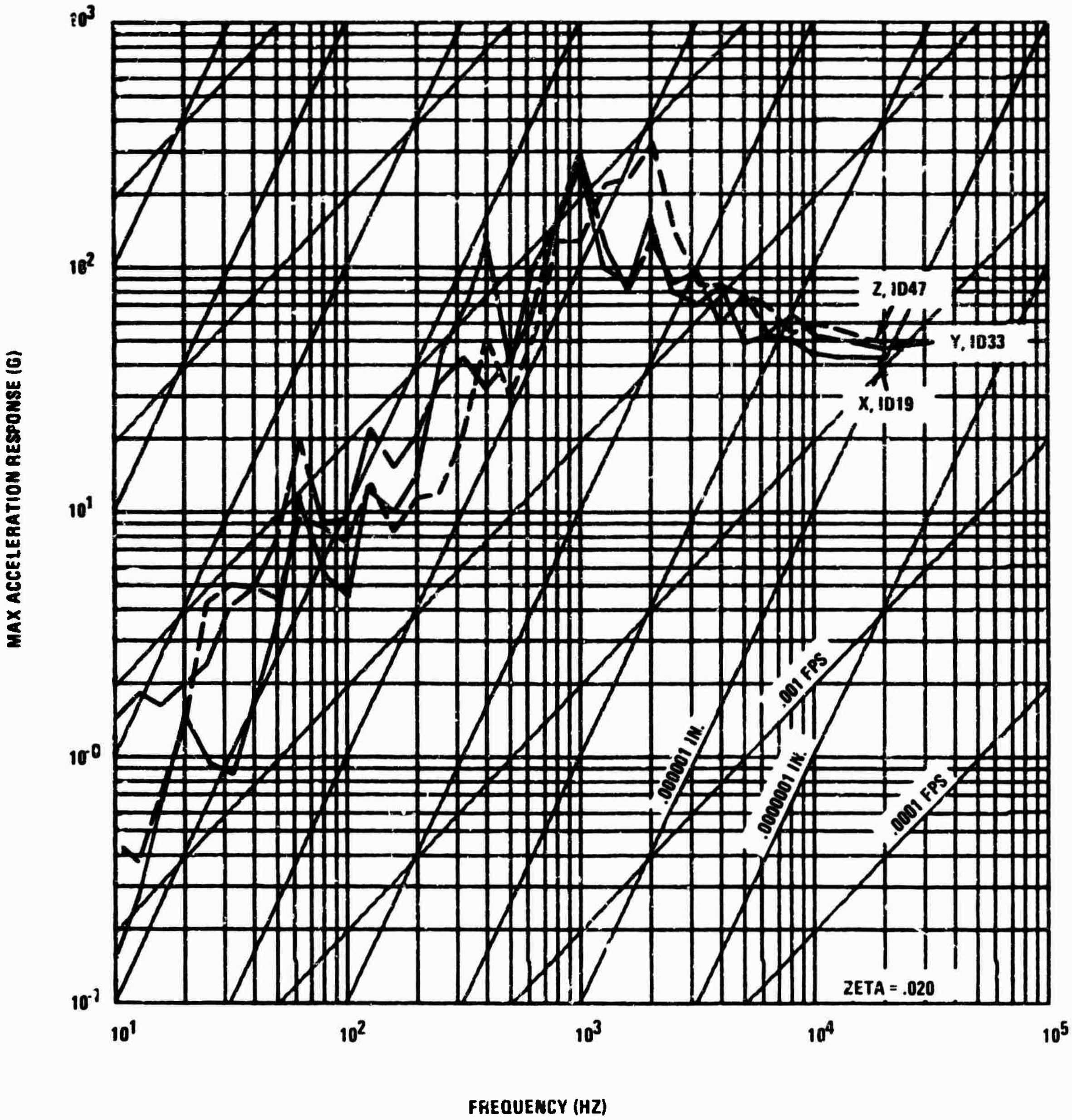

FIGURE 3. SHOCK SPECTRA

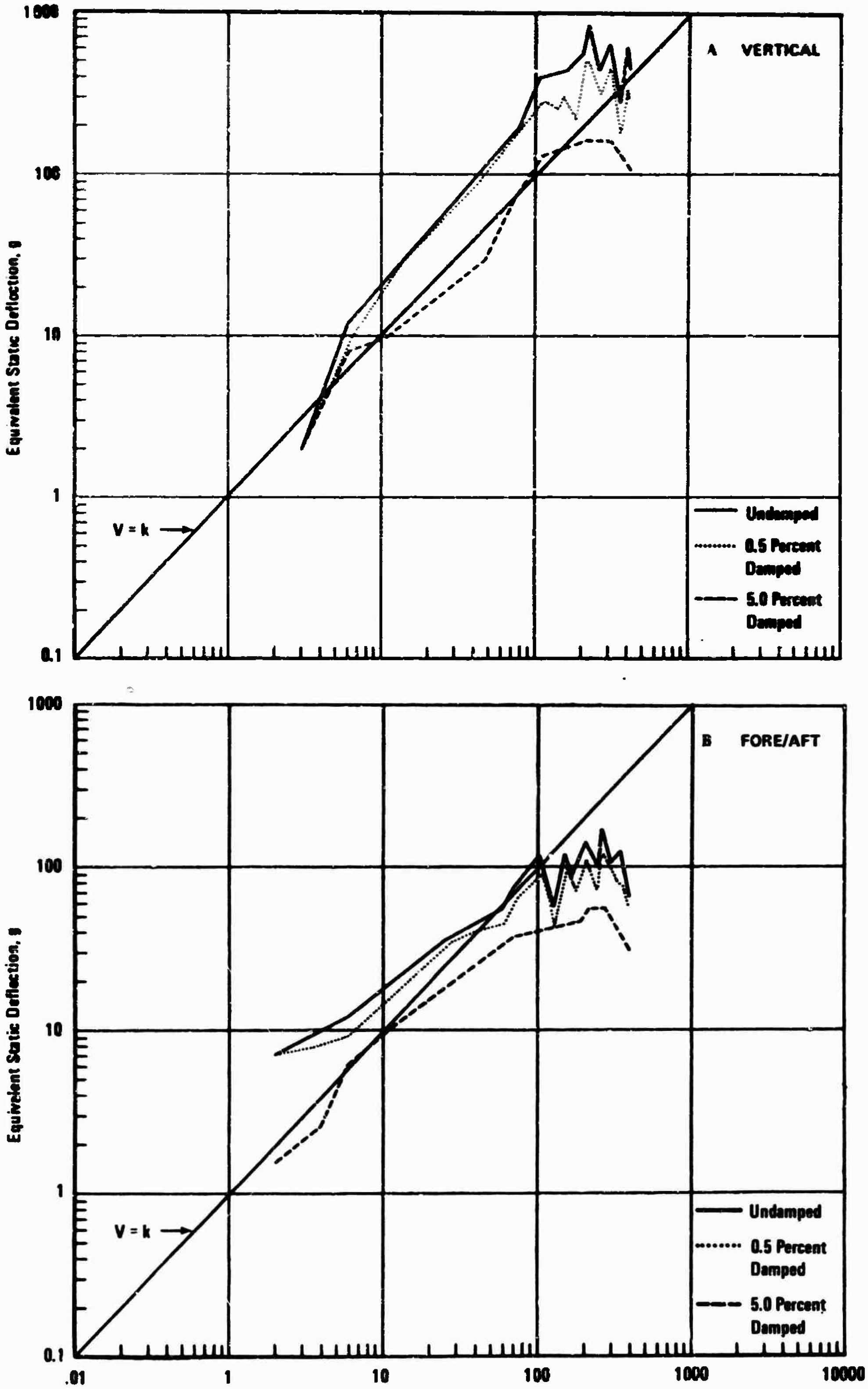

IGURE 4. RAILROAD COUPLING SHOCK SPECTRUM--STANDARD DRAFT GEAR (6.0 MPH) (FROM NAS REPORT 8-11451)

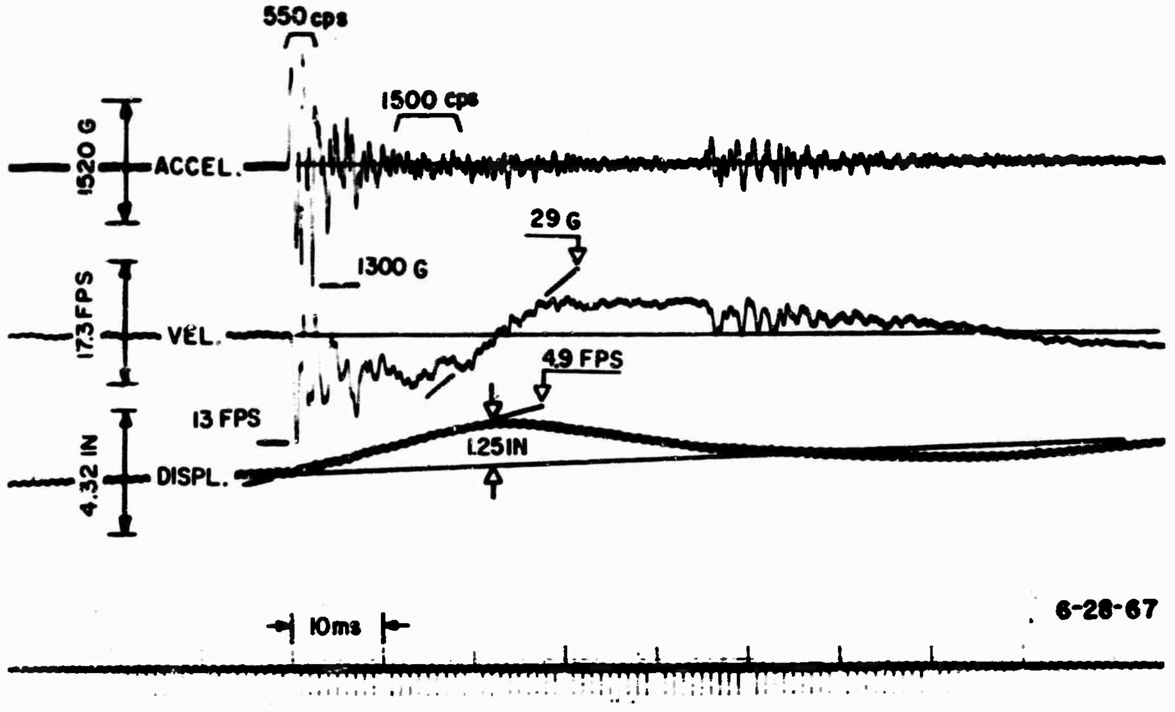

FIGURE 5A. A TAPE RECORDER ACCELEROMETER RECORD, REPRODUCED THROUGH THE SHOCK SIGNAL INTEGRATOR FOR OSCILLOGRAPHIC PRESENTATION. THIS RECORD WAS OBTAINED FROM A SPECIALLY MOUNTED PIEZO-RESISTIVE ACCELEROMETER ATTACHED TO A STANDARD NAVY "LIGHT WEIGHT SHOCK MACHINE." (FROM NRL MEMORANDUM REPORT 1903)

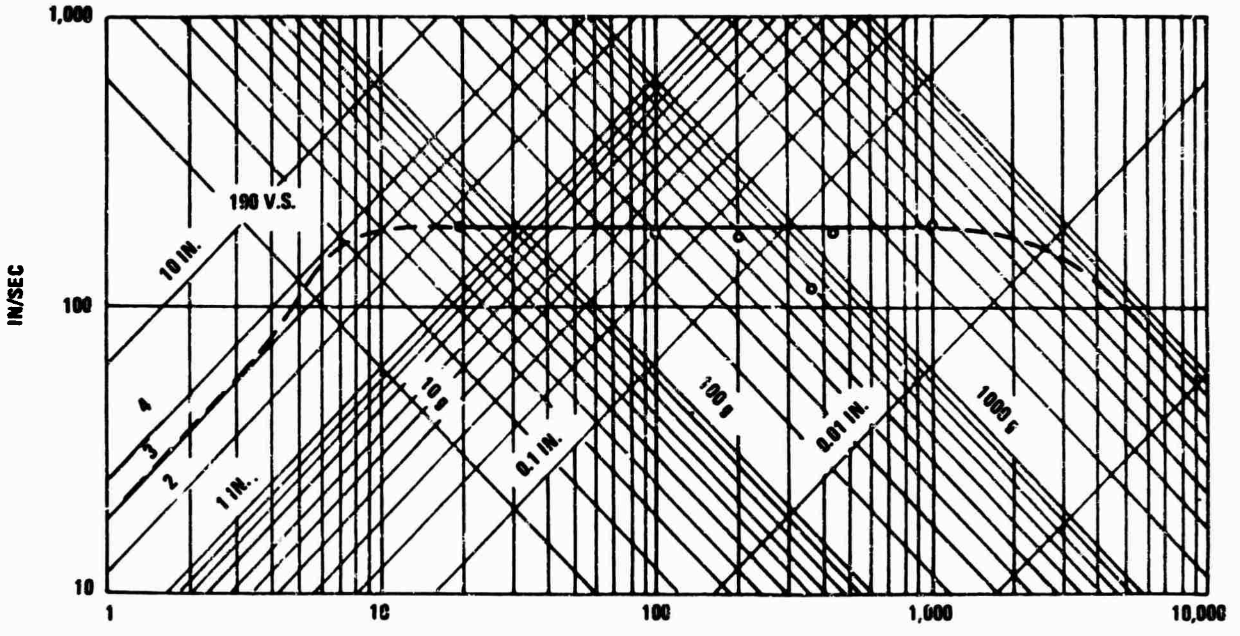

FIGURE 5B. SHOCK SPECTRUM FOR MOTION OF ANVIL TABLE OF HI SHOCK MACHINE FOR MEDIUMWEIGHT EQUIPMENT: 3-FT HAMMER DROP, 3-IN. TABLE TRAVEL, 1115-LB LOAD, 1858 LB ON TABLE, DROP-HEIGHT 150 PERCENT GREATER THAN SPECIFIED (5) FOR CLASS A SCHOCK. (FROM NRL REPORT 5618) acceleration in g's numerically equals the frequency in Hz, one constructs a line where the velocity at all points is 61.4 inches per second. All other parallel lines also represent $v = k$ and their magnitudes can be easily determined. For instance, when the number g's is three times the frequency, velocity is 3 x 61.4 inches per second.

While all shock spectra may not exhibit the strong constant-velocity tendency of the examples cited here, it will be evident that the dynamic range of the velocity spectrum is much less than either acceleration or displacement. It follows that the total vibrational velocity will tend toward constancy more than either acceleration or displacement.

STRESS-VELOCITY CORRELATION

Modal analysis[10] has shown that dynamic structural response of linear undamped systems can be treated as though composed of separate responses of the normal or free vibration modes of the structure. Motion of any point of a structure, where a suitable motion transducer might be located, will yield a time response that is built up of these separate modal motions.

Ideally then, spectral analyses of the motion at this point ought to show distinct, significant amplitudes at the frequencies of all modes which are somewhat antinodal at this point. Thus a shock or Fourier spectrum of a motion, for a linear system at least, indicates the modal makeup of the motion. A spectrum peak at some particular frequency indicates that some mode with that frequency was responding with an amplitude at least that great. If we fortuitously placed the transducer at the maximum amplitude station for that mode, we would know (if we knew the mode shape) the stresses induced throughout the structure for that portion of the response.

However, there is no single antinodal position at which a motion transducer could be placed. This or that convenient mounting position may be antinodal, nodal, or more probably intermediate to the bulk of the modes responding. Thus analysis of motion histories cannot be expected to yield the amplitude of all or even most of the structural modes. The response however will be an indication of the lower limit of the actual modal response. We shall therefore consider the modal response characteristics of some simple structures and theoretically show that maximum modal velocity is a valid indication of maximum modal stress, independent of the frequency and mode shape. Although no generalization for all structures can be made, the results certainly lead one to expect that velocity is the single, most directly damage-related dynamic motion property. Naturally this analysis will in no way explain shock or vibration failures that are caused by effects other than high stress.

Actually, there are only a relatively few classifications of load-carrying mechanisms. There is uniform stress (tension or compression of a member), beam bending, torsion, shear, membrane stresses in plates and shells, bending stresses in plates and shells, and a few others. We shall consider uniform and bending stresses in uniform slender longitudinal members, all with an infinitude of modes, and show that without detailed information one can predict the severity of the resulting stresses.

LONGITUDINAL VIBRATIONS IN RODS

We shall begin by considering the longitudinal free vibrations of a long thin rod. These free vibration shapes are the modes that are excited by a shock input. We confine ourselves to the easiest situation where the longitudinal wavelength is long in comparison with the bar cross-sectional dimensions. For this case the cross sections remain plane with uniform stress and the lateral or "Poisson" deformation has insignificant effects. (See Ref. 11, pp. 297-298.) Let us consider a semi-infinite rod being sinusoidally excited at its end. Since it is semi-infinite no reflections can occur and hence it can (within its elastic limit) vibrate at any amplitude and frequency, thus accepting all inputs. Timoshenko,[11] on page 299 shows that transverse planes in such a rod have the motion

$$u = \left(C \cos \frac{px}{a} + D \sin \frac{px}{a}\right) \left(A \cos pt + B \sin pt\right) \tag{1}$$

where: x = distance down rod

u = displacement of a plane located at x

p = circular frequency

a = wave speed $\equiv \sqrt{E/\rho}$

E = Young's modulus

ρ = density

t = time.

Without loss of generality we may select the rod end as an antinode and begin time such that Eq. (1) becomes

$$u = A \cos \frac{px}{a} \cos pt \tag{2}$$

From elasticity[12] the strain and hence stress is given by

$$\sigma = E\epsilon = E\frac{\partial u}{\partial x} = -EA\frac{p}{a} \sin \frac{px}{a} \cos pt \tag{3}$$

the maximum value of which is

$$\sigma_{max} = \frac{EAp}{a} \tag{4}$$

Note now that the maximum stress for a constant displacement amplitude, A, depends upon the frequency, p. From Eq. 2 the maximum displacement, velocity, and acceleration are

$$\left.\begin{aligned} u_{max} &= A \\ \dot{u}_{max} &= Ap \\ \ddot{u}_{max} &= Ap^2 \end{aligned}\right\} \tag{5}$$

By using V for the maximum modal velocity, Eq. 5 yields

$$V = Ap. \tag{6}$$

The substitution of Eq. 6 into Eq. 4 yields

$$\sigma_{max} = \frac{E}{a} V_{max} \tag{7}$$

Using the value of the wave speed from Eq. 1, Eq. 7 may be conveniently expressed as

$$\sigma_{max} = V_{max} \sqrt{E\rho}. \tag{8}$$

Thus in all semi-infinite rods vibrating longitudinally at any frequency or amplitude within the restrictions set forth above, the maximum modal velocity alone determines the maximum modal stress.

It is significant to note that maximum acceleration does not so simply relate to stress. In fact, a formulation of the expression analogous to Eq. 8 in terms of maximum acceleration from Eqs. 5 and 8 yields

$$\sigma_{max} = \frac{\dot{V}_{max}}{p} \sqrt{E\rho}. \tag{9}$$

Eq. 9 shows that for modes with constant maximum acceleration, the stress is inversely proportional to frequency. Thus, high acceleration at high frequencies does not necessarily indicate high stress. Alternatively, as indicated in Eq. 8, high velocities do indicate high stresses.

We might expect that Eq. 8 would also apply to finite rods and indeed it does. Following Timoshenko (see Ref. 11, pg 299) we consider a rod of length ℓ, with free ends. This rod has the natural frequencies

$$p_i = \frac{ia\pi}{\ell} \tag{10}$$

where $i = 1, 2, 3, \ldots$ and designates the mode.

The complete free (or ringing) solution is

$$u = \sum_{i=1}^{\infty} \cos \frac{i\pi x}{\ell} \left[A_i \cos \frac{i\pi at}{\ell} + B_i \sin \frac{i\pi at}{\ell}\right]. \tag{11}$$

B_i can be made zero by starting time appropriately, hence the modal displacement may be written as

$$u_i = A_i \cos \frac{i\pi x}{\ell} \cos \frac{i\pi at}{\ell}. \tag{12}$$

As above, the stress in the ith mode is given by

$$\begin{aligned} \sigma &= E\epsilon_i = E\left(\frac{\partial u}{\partial x}\right)_i \\ &= -EA_i \frac{i\pi}{\ell} \sin \frac{i\pi x}{\ell} \cos \frac{i\pi at}{\ell}, \end{aligned} \tag{13}$$

the maximum value of which is

$$\sigma_{i\,max} = \frac{EA_i i\pi}{\ell}. \tag{14}$$

From Eq. 12 note that the maximum velocity in the ith mode is

$$V_{i\,max} = \frac{A_i i\pi a}{\ell} \tag{15}$$

and now, as before, substituting Eq. 15 into 14 yields

$$\sigma_{i\,max} = \frac{E V_i}{a} \tag{16}$$

or the result identical to Eq. 7 and again using the definition of a, we find that the maximum stress in any mode is given by

$$\sigma_{max} = v_{max}\sqrt{E\rho}\,. \tag{8}$$

Finally, it is a simple matter to develop a generalized proof to show that the maximum stresses predicted by Eq. 8 apply to all cases of longitudinal vibrations in rods no matter what the end conditions, if the previous restrictions continue to apply. All possible vibrations of the rod are given by Eq. 1. As in Eq. 3, the stress is therefore given by

$$\sigma = E\frac{\partial u}{\partial x} = E\frac{p}{a}\left(-C\sin\frac{px}{a} + D\cos\frac{px}{a}\right)$$

$$(A\cos pt + B\sin pt).$$

In Ref. [13], the maximum values of the quantities in parentheses are shown to be $\sqrt{C^2 + D^2}$ and $\sqrt{A^2 + B^2}$ respectively, hence the maximum value of the stress is

$$\sigma_{max} = E\frac{p}{a}\sqrt{C^2 + D^2}\sqrt{A^2 + B^2}. \tag{17}$$

The particle velocity is found from Eq. 1 to be

$$\dot{u} = \frac{\partial u}{\partial t} = p\left(C\cos\frac{px}{a} + D\sin\frac{px}{a}\right)$$

$$\left(-A\sin pt + B\cos pt\right).$$

Again using the proof of Ref. [13], the maximum value of this velocity is

$$\dot{u}_{max} = p\sqrt{C^2 + D^2}\sqrt{A^2 + B^2}. \tag{18}$$

The substitution of Eq. 18 into Eq. 17 yields the desired result, namely

$$\sigma_{max} = \frac{E}{a}\dot{u}_{max}, \tag{19}$$

which is identical to Eqs. 7 and 16.

Thus it has been proved and illustrated that the maximum stress due to long-wave longitudinal vibrations in rods is completely specified by the material properties and the maximum modal velocity.

TRANSVERSE BEAM VIBRATIONS

Transverse uniform beam vibrations can also be classified according to maximum modal velocities. We shall again consider only the simplest type of vibrations in which the wavelength is long compared to the beam depth. (This neglects the so called rotary inertia and shear effects.) For these cases, simple bending theory suffices; Timoshenko's presentation (See Ref. 11, pp. 324-335) will be used as a foundation. He proves that the free vibrations of the neutral surface of such beams are expressed by the following solution

$$v = (C_1\sin kx + C_2\cos kx + C_3\sinh kx$$
$$+ C_4\cosh kx)\cdot(A\cos pt + B\sin pt), \tag{20}$$

where k, the wave number, and p, the circular frequency, are related by

$$k^4 = \frac{p^2}{\eta^2}\frac{\rho}{E}. \tag{20a}$$

In these equations the following definitions are used:

v = deflection of neutral surface,

x = distance down the beam,

C, A, B = arbitrary constants,

ρ = density,

E = Young's modulus,

η = radius of gyration $\equiv \frac{I}{A}$,

I = cross-sectional area moment of inertia about neutral axis,

A = cross-sectional area

Let us specialize Eq. 20 to consider a semi-infinite beam, which starts at $x = 0$ and continues on out to infinity. Again, since no reflections occur, the semi-infinite beam can accept sinusoidal vibration at all frequencies with amplitudes that do not exceed the elastic limit. The simplest case is that with zero shear and slope at its end, as shown in Fig. 6.

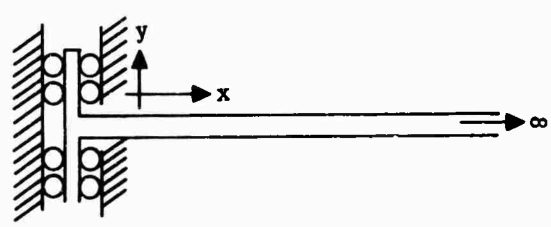

Fig. 6. Semi-infinite beam with zero slope and shear at end.

The boundary conditions to be imposed on Eq. 20 are:

1. The solution remains finite for very large x,
2. Zero slope at $x = 0$; $y' = 0$ at $x = 0$,
3. Zero shear at $x = 0$; $y''' = 0$ at $x = 0$.

The only way in which condition 1 can be satisfied is

$$C_3 = -C_4.$$

Thus the hyperbolic sine and cosine terms from Eq. 20 may be written

$$C_3 \sinh kx + C_4 \cosh kx = C_3 (\sinh kx - \cosh kx). \tag{21}$$

The substitution of the definitions of the hyperbolic functions yields

$$C_3 (\sinh kx - \cosh kx) = C_3 e^{-kx}. \tag{22}$$

Thus the shape portion of Eq. 20 may be written as

$$Y = C_1 \sin kx + C_2 \cos kx + C_3 e^{-kx}. \tag{23}$$

By applying boundary condition 2, we obtain

$$0 = C_1 - C_3,$$

or

$$C_1 = C_3,$$

hence (23) becomes

$$Y = C_1 \sin kx + C_2 \cos kx + C_1 e^{-kx}.$$

Finally, application of boundary condition 3 proves that C_1 must be zero and so for this semi-infinite beam, the shape function is simply

$$Y = C \cos kx. \tag{24}$$

Again without loss of generality, time can be started when the deflection is a maximum, making B zero, in Eq. 20. Thus the deflection of this beam may be expressed simply as

$$y = C \cos pt \cos kx. \tag{25}$$

The maximum stress in any initially straight beam bent to a curvature given approximately by $\frac{\partial^2 y}{\partial x^2}$ is shown in beam theory[14] to be given by

$$\sigma = Eh \frac{\partial^2 y}{\partial x^2}. \tag{26}$$

where

E = Young's Modulus;

h = maximum cross-sectional distance from neutral axis.

Substituting the maximum value of the second derivative of Eq. 25 into Eq. 26 gives the maximum stress to be

$$\sigma_{max} = C E h k^2. \tag{27}$$

Substitution of the value of k^2 from Eq. 20a gives the expression for maximum stress as a function of the maximum deflection, C, to be

$$\sigma_{max} = C h \frac{p}{\eta} \sqrt{E\rho}. \tag{28}$$

Note that in this case the stress is a function of both the deflection, C, and the frequency, p. Now the maximum value of the first time derivative of Eq. 25 shows the maximum velocity, V, to be

$$V = Cp. \tag{29}$$

The substitution of this value into Eq. 28 yields our result:

$$\sigma_{max} = V \frac{h}{\eta} \sqrt{E\rho}. \tag{30}$$

Again the maximum stress for any possible free vibration shape when specified by the maximum velocity does not depend upon frequency, but only on material properties and a beam cross-sectional shape factor, $\frac{h}{\eta}$.

Finally, and as a last example, we shall consider a finite beam to illustrate the previous result is not altered by finiteness *per se*. The bar of length ℓ with hinged ends is chosen, again proceeding from Timoshenko's lead in Ref. [11] on page 331. The general solution for all beams is Eq. 20; the following boundary conditions must be satisfied:

$$\text{At } x = 0,\ y = y'' = 0, \text{ and at } x = \ell,\ y = y'' = 0. \tag{31}$$

These specify zero deflection and moment at the beam ends. Timoshenki[11] shows that these conditions require the shape function of Eq. 20 to reduce to

$$y = C_1 \sin kx,$$

and the modes are such that

$$k\ell = i\pi$$

where i = 1, 2, 3, etc.

Again we may select the starting time in Eq. 20 so that B is zero and hence each mode of the hinged beam is described by

$$y_i = C_i \sin k_i x \cos p_i t \tag{32}$$

where k may only take on the values

$$k_i = \frac{i\pi}{\ell} \tag{32a}$$

where i = 1, 2, 3, etc. and k_i and p_i are related by Eq. 20a.

Application of Eq. 26 shows the maximum stress in any mode to be given by

$$\sigma_{i\,\max} = E h C k_i^2, \tag{33}$$

and the incorporation of Eq. 20a yields

$$\sigma_{i\,\max} = C_i \frac{h}{\eta} p_i \sqrt{E\rho}. \tag{33a}$$

Noting that C is the maximum modal displacement, again the stress in terms of displacement depends upon the frequency, p_i.

From Eq. 32 the maximum velocity of the beam in each mode is

$$V_i = \dot{y}_{i\,\max} = p_i C_i,$$

and the substitution of this value of C_i into 33a yields Eq. 30, once again.

$$\sigma_{i\,\max} = V_i \frac{h}{\eta} \sqrt{E\rho}. \tag{30}$$

It might be commented that a generalized proof for beams is more complicated than the above two examples might lead one to expect. Most boundary conditions will require the presence of hyperbolic sines and cosines in the shape function, e.g., the cantilever beam. This analysis has been done, but it is too lengthy to report here. The above results hold away from the beam ends for modes greater than the second. Simple constants less than 2.0 come into Eq. 30 when root stresses or tip velocities are included.

THE PRACTICAL USE OF THE STRESS-VELOCITY EQUATION

In all the above cases, maximum modal stress is predicted by a single dynamic property, maximum modal velocity. Thus, in order to monitor shock modal response levels that may lead to failures as a result of high stress, modal velocity, at least for these simple cases, is the single, most significant parameter.

Table 1 lists values of the beam shape factor, $\frac{h}{\eta}$, of Eq. 30 for common cross sections. It is interesting to note that the hollow cross sections in bending are only slightly more sensitive than uniform stress.

TABLE 1
Shape Factors, $\frac{h}{\eta}$, for Dynamic Bending Stress

Solid rectangle	=	$\sqrt{3} \approx 1.73$
Solid round bar	=	2
Solid triangle	=	$2\sqrt{2} \approx 2.83$
Thin hollow tube	=	$\sqrt{2} \approx 1.41$
Thin hollow square	=	$\sqrt{6}/2 \approx 1.22$

Eq. 8 and 30 may be used in interpreting the comparative severity of shock spectra. Velocity spectra can be used directly. Acceleration spectra may be used by drawing the constant velocity lines, as mentioned previously. One must compare modal velocities with known damaging values. Severe velocity values may be computed for various metals and beam cross sections. A summary of such properties has been prepared and is included as Table 2. It will be noted that structural steel has the lowest velocity value. This does not indicate steel to be definitely the poorest choice as a shock resistant material. Steel is ductile and local yielding may be an entirely satisfactory behavior. The ideas presented here necessarily depend on a linear stress-strain relation. No similar theory has been developed for the yielding case. When a theory to include the mitigating effects of yielding is developed, shock severity will be much more amenable to evaluation.

TABLE 2
Severe Velocities*

Material	E (psi)	σ (psi)	ρg	v_{max} (ips) $\sigma/\sqrt{E\rho}$	Rectangular Beam v_{max} (ips)
Douglas fir	1.92×10^6	6,450	36 lb/ft^3	633	366
Aluminum 6061-T6	10.0×10^6	35,000	.098 lb/in^3	695	402
Magnesium AZ80A-T5	6.5×10^6	38,000	.065 lb/in^3	1015	586
Structural steel	29×10^6	33,000	.283 lb/in^3	226	130

*(properties taken from Ref. 15)

What has become apparent to us, with respect to complex actual shock motions, is that a broad band of frequencies is invariably present and that a great many of the structural modes are excited. The relative severity of the various frequency components can be assessed via the velocity spectrum of the transient motion. It is to be hoped that further study along these lines may lead us to improved procedures for estimating and testing for shock hardness without actually knowing detailed information about the multitude of possible modes in any real complex structure.

Available Transducers and Methods

Most common of commercially available velocity transducers is the seismic type. They are categorized by employment of a seismically suspended element which remains essentially motionless in space for motions of interest, while a second element of the device is forced to take on the motion of the surface to be measured. If one element has a magnetic field, and the other is a coil of wire, a voltage will be developed in the coil proportional to the relative velocity of the two elements.

Seismic velocity transducers function well, but to insure seismic behavior of the suspended element, internal clearances must exceed the peak displacements of the surface to be measured. If this requirement is not met, the seismic element will "bottom" as peak displacements are reached, and relative velocity between elements will suddenly drop to zero, as will the output voltage.[3,16] A velocity-time history with such "bottoming discontinuities" is exceedingly difficult to decipher.

Seismic velocity transducers are available in a variety of displacement ranges and natural frequencies, but even for the smallest range and highest frequency, the weight of this type of transducer is too high for many applications. Unfortunately, as displacement range increases, or as natural frequency is lowered, weight goes even higher, and area of applicability of the seismic velocity transducer is further limited.[3,16]

Since the arrival of the age of integrated circuits, there is now commercially available a "piezoelectric velocity transducer." Basically an accelerometer, this device contains an integrated circuit within the transducer housing which electronically integrates the acceleration signal to velocity. In size and weight, it is slightly larger than the average accelerometer, and therefore has a distinct advantage over the moving coil type of transducer. A major disadvantage in this approach is the wide dynamic signal range produced by the accelerometer when measuring shock. The electronic integrator is required not only to mechanically tolerate the shock, but at the same time provide satisfactory operation with a 70 dB dynamic range input signal. The "piezoelectric velocity transducers" now available are suitable for vibration measurements, but are too frail and lacking in dynamic range to be useful in any but the lightest shock measurements. Many advances have been made in the field of integrated circuits since these transducers were introduced, and greatly enhanced "piezoelectric velocity transducers" are possible, and may be forthcoming.

M. W. Oleson of the Naval Research Laboratory has reported success in on-line integration of accelerometer signals[7, 17] (see Fig. 5a). His method differs from the "piezoelectric velocity transducer" approach in that his electronic integrators are located some distance from the accelerometers, and are not restricted in size and weight. The freedom from restriction allows increased linearity and lower frequency response for his system, and also permits double integration of the acceleration signal so the shock can be described in displacement if desired.

Mr. Oleson is quite aware that his method has the disadvantage of having to deal with the wide dynamic range of shock acceleration, and has constructed accelerometer mounts which act as low-pass filters and isolate the accelerometers from high-frequency, high-level accelerations.

P. S. Hughes has reported on the use of a digital computer program titled "MR. WISARD" to integrate and double-integrate acceleration signals[18] (see Figs. 7, 8, and 9). In addition, the program computes shock spectra (see Figs. 1, 2, and 3). Assuming that complexity of the program necessitates off-line operation, shock acceleration signals must be recorded for later processing when using this approach. As explained earlier, no present analog-recording medium offers a dynamic range large enough to satisfactorily record shock acceleration. This is a severe limitation on "MR. WISARD."

Another use of digital computers is worthy of mention. G. O'Hara and P. Cuniff have reported on a method of correcting for bottoming discontinuities of velocity transducers.[19] It has been stated that velocity records corrected in this fashion provide information as accurate as the on-line integrated accelerometer approach.

SUMMARY

The basic facts presented in this paper are not new or unique. What is novel is that in this case the facts have been considered collectively rather than singly, and increased understanding of the damage mechanism of shock is the result.

Because of the direct relationship between stress and modal velocity, and the small dynamic range of vibrational velocity in shock, it is apparent that, of the three related parameters, velocity provides maximum measurement efficiency and accuracy.

Since modal velocity, not total vibrational velocity or translational velocity, bears the direct relation to stress, it is also apparent that to obtain shock-severity measurements, a velocity-measuring system need have a lower frequency response a little below the lowest modal frequency of the structure in question. For many usual structures, an instrumentation system with a lower frequency response of 5 Hz would be more than adequate.

Again, because of the direct relationship between modal velocity and stress, the wisdom of using normal mode theory[10] in shock-resistant design is indicated. The Dynamic Design-Analysis Method (DDAM),[20, 22] which is a normal-mode analysis, provides most of what is needed for vastly improved shock-resistant design.

Reviewing current techniques of measuring shock in terms of velocity, it is apparent that a velocity transducer different from ones presently available is needed. While computer correction of bottoming discontinuities appears feasible, it is certainly less than aesthetically satisfying. And use of integrated signals from accelerometers leaves much to be desired, particularly when analog recording must be interposed between accelerometer and integrator.

CONCLUSIONS

Conclusions are:

1. Modal velocity is the best criterion of shock severity.
2. Velocity should be the predominant parameter for shock measurement.
3. Development of an adequate velocity transducer is needed.

FROM NOLTR 61-64, FIG. 22

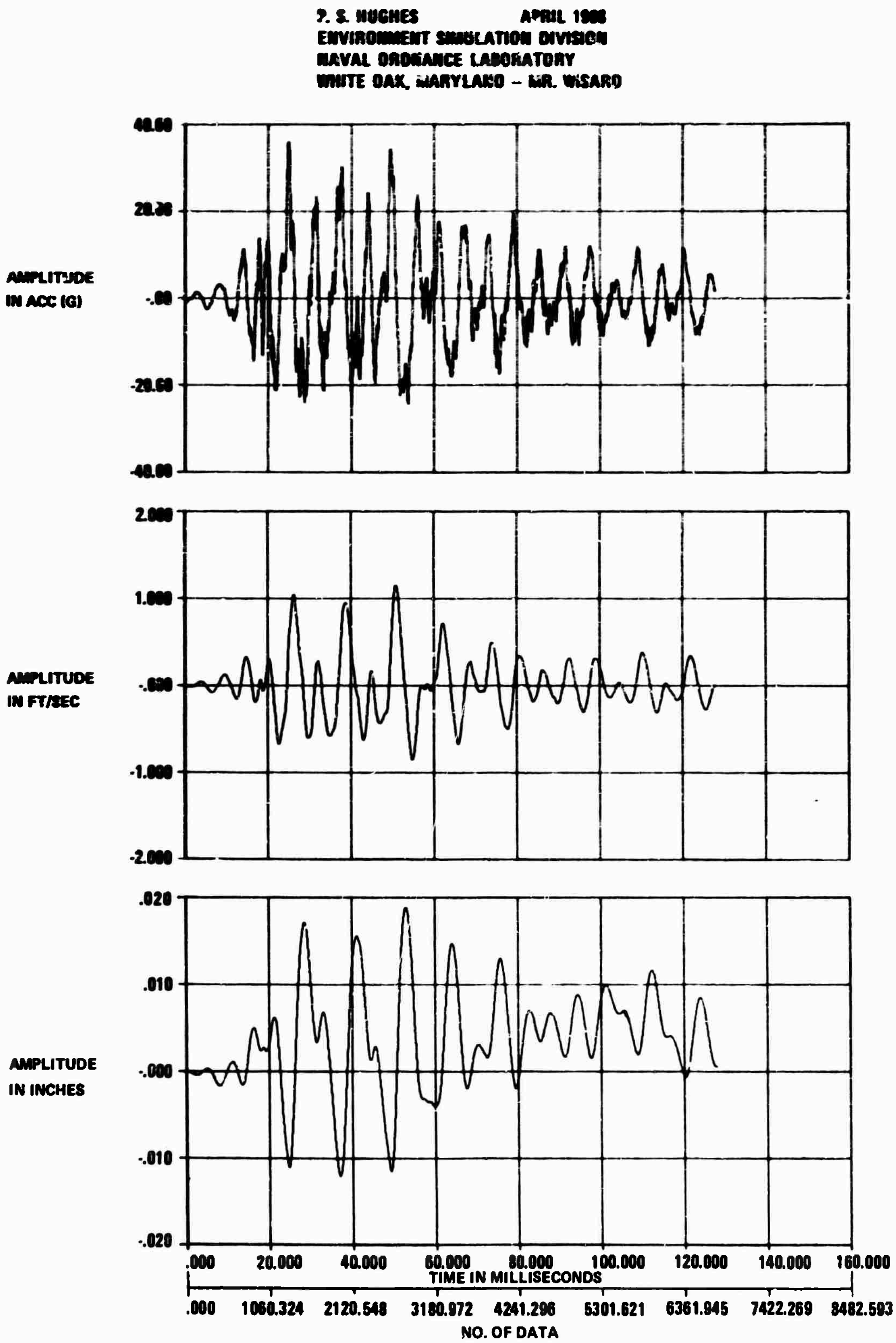

FIGURE 7. A-T, V-T, D-T SIGNATURES

FROM NOLTR 69-64, FIG. 12

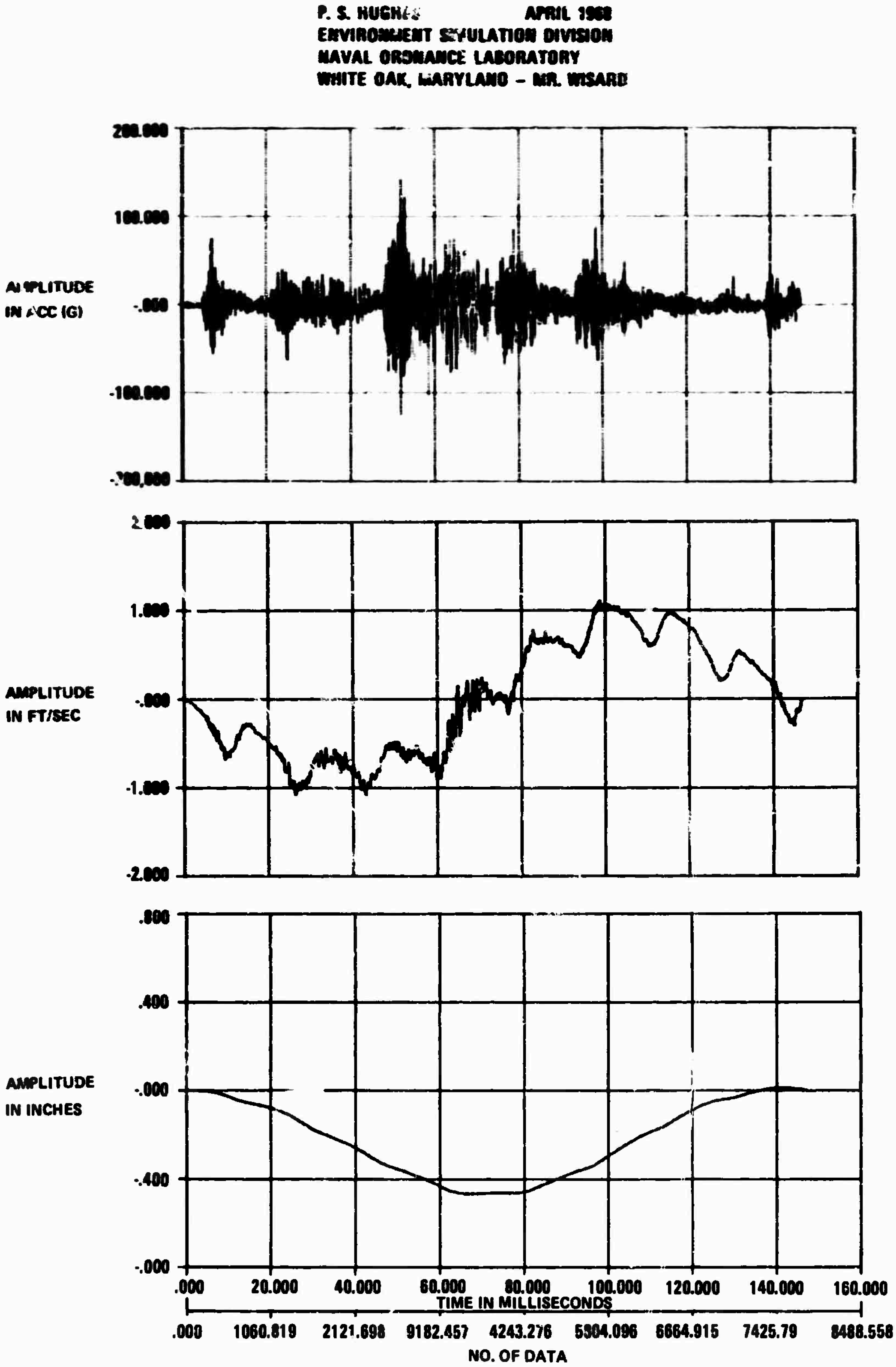

FIGURE 8. A-T, V-T, D-T SIGNATURES

FROM NOLTR 69-64, FIG. 13

P. S. HUGHES APRIL 1968
ENVIRONMENT SIMULATION DIVISION
NAVAL ORDNANCE LABORATORY
WHITE OAK, MARYLAND - MR. WISARO

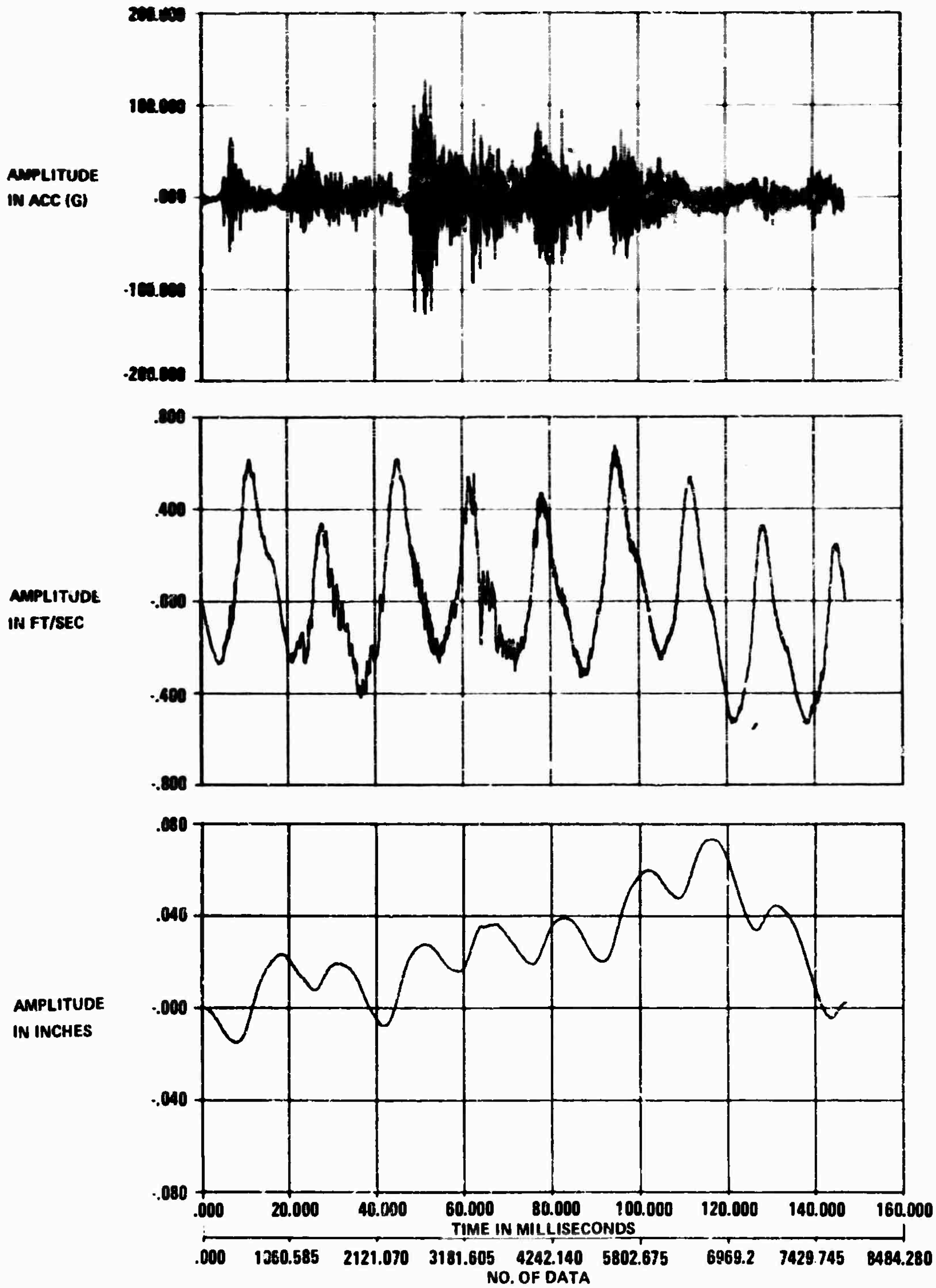

FIGURE 9 . A-T, V-T, D-T SIGNATURES

REFERENCES

1. Blake, R. E., "Problems of Simulating High Frequency Mechanical Shock," Proceedings of the Institute of Environmental Sciences, 1964, p. 145

2. U. S. Army Electronics Command Technical Report ECOM-2647A (Revised), A Mechanical Shock Pulse Survey, by F. Palmisano and L. L. Kaplan, March 1966

3. Vigness, I., "Introductory Remarks on Shock Instrumentation," Shock and Vibration Bulletin, No. 6, Naval Research Laboratory Report No. S3200, p. 92, November 1947

4. Naval Research Laboratory Report No. 0-1965, High Impact Shock Instrumentation and Measurements - First Partial Report, by I. Vigness, p. 20, November 1942

5. Forkois, H. M., "Problems in Getting Consistent Results in Shock Testing," Proceedings of the Institute of Environmental Sciences, 1965, p. 455

6. Walsh, J. P., "A Review of the Report on the Cameron Trials," Shock and Vibration Bulletin, No. 4, Naval Research Laboratory Report No. S-3151, p. 62, July 1947

7. Oleson, M. W., "Components of a New Shock Measurement System," Report of NRL Progress, Naval Research Laboratory, October 1967, p. 16-27

8. Shaw, J. E., "Brief Resume of Recent British Shock Trials in Ships," Shock and Vibration Bulletin, No. 9, Naval Research Laboratory Report No. S-3290, p. 36, April 1948

9. Hudson, D. E., Shock and Vibration Handbook, First Edition, ed. by Harris and Crede, volume 3, p. 50-36 to 50-37, McGraw-Hill Book Co., Inc., New York, 1961

10. Naval Research Laboratory Report No. 6002, Elements of Normal Mode Theory, by G. J. O'Hara and P. E. Cuniff, November 1963

11. Timoshenko, S., Vibration Problems in Engineering, Third edition, p. 297-299, p. 324-335, D. Van Nostrand, Inc., Princeton, New Jersey, January 1955

12. Den Hartog, J. P., Advanced Strength of Materials, p. 172, McGraw-Hill Book Co., Inc., New York, 1952

13. Den Hartog, J. P., Mechanical Vibrations, Fourth Edition, p. 5, McGraw-Hill Book Co., Inc., New York, 1956

14. Higdon, A., Ohlsen, E. H., and Stiles, W. B., Mechanics of Materials, p. 222-225, John Wiley and Sons, Inc., New York, 1960

15. Roark, R. J., Formulas for Stress and Strain, Fourth Edition, McGraw-Hill Book Co., Inc., New York, 1965

16. Oleson, M. W., "Shock Instrumentation Development and Random Vibration Research," Report of NRL Progress, Naval Research Laboratory, July 1963, p. 32

17. Oleson, M. W., "Integration and Double Integration - A Practical Technique," Shock and Vibration Bulletin, No. 35, Part 4, p. 1-10, February 1966

18. Naval Ordnance Laboratory Report NOLTR 69-64, 40 mm Gun Shock Environment Aboard Hydrofoil PCH-1, by P. S. Hughes, 18 March 1969

19. Naval Research Memorandum Report 1489, Velocity Meter Corrections, by G. J. O'Hara and P. E. Cuniff, December 1963

20. Bureau of Ships NAVSHIPS 250-423-30, Shock Design of Shipboard Equipment — Dynamic Design-Analysis Method, May 1961

21. Bureau of Ships NAVSHIPS 250-423-31, Shock Design of Shipboard Equipment — Interim Inputs for Submarine and Surface Ship Equipment, October 1961

22. Applied Technology Associates Report 124, Guide for Users of Dynamic Design-Analysis Method for Shock Resistance Evaluation of Shipboard Equipment, January 1969

DISCUSSION

Mr. Holland (Kinetic Systems): I have done some work for Frankford Arsenal on high frequency cutoff criteria for computing shock spectra. My study looked at simple cantilever beams and simply supported beams, both uniform. I added point masses at the end of the cantilevers and point masses in the middle of the simply supported beams. Using the modal participation factor of easily described structures like these and the fact that my velocity was assumed constant in a small area out to some frequency, I was able to find that my acceleration was constant. It is similar to the Navy shock spectrum where you have three backbones of constant displacement, constant velocity, and constant acceleration. Most of the stresses were contained in the first couple of modes, and by taking these modes I got about 90 percent of the stress in these simple beam structures. The problem that I was trying to solve was where to stop the computation. How high should the frequency be? We came up with the factor of 2000 Hz for some of the stiffnesses that we were looking at in the structure. But when you get into a complex system and have a resonant frequency in the range of 2000 Hz with your shock on the backbone of acceleration, you can easily excite these frequencies. This will create a stress at a higher mode in excess of what you are getting at your lower frequencies, so that you can get out of your velocity range. You had constant velocity, let us say, from 2 Hz to 100 Hz and, if you go down your constant acceleration line, you can easily find higher resonant frequencies where your acceleration is going to produce the failure.

Mr. Chalmers: On the part shown, the constant velocity centered out to 2000 Hz.

Mr. Holland: Your shock spectrum will vary for all different shocks.

Mr. Pakstys (General Dynamics Corp.): I certainly agree with your conclusions about the modal velocity being an important parameter. There is another way to look at this other than just looking at these simple cases. If we look on a mode-to-mode basis, we can look at the modal kinetic energy which then can be related to the velocity squared. Kinetic energy can then be related to strain energy and strain energy can be related to stresses. From that point of view you can rationalize the importance of velocity in a multi-degree-of-freedom system. The velocity does not have to be in the constant velocity range of the spectrum; it can be in the constant acceleration. The importance of the velocity criterion is not diminished.

Mr. Chalmers: That is correct. We are trying to do two things. First, if you are measuring in terms of velocity, insofar as shock is concerned, you have a very much reduced dynamic range required for your measurements. Secondly, Dr. Gaberson has shown that velocity is probably the best descriptor of stress in a simple beam.

Mr. Scharton (Bolt Beranek & Newman): I think the conclusion that much of the data which you have looked at is described by a constant velocity spectrum is very interesting. Two possible explanations of this occurred to me. One would seem to be that, at least in plates in bending and also in a beam in compression or torsion, the modal density is constant with frequency. This means that the frequency separation between modes is constant, so the observation that one has a constant velocity spectrum would be equivalent to saying that each mode of the structure has the same amount of energy. We can then ask, when you put a complex transient into the system does the structure somehow take this energy and distribute it equally among its modes? Also, since yield criteria are commonly related to strain energy, if the shock were so severe that in fact you got local yielding, it might be that the yield phenomenon would damp each mode and automatically bring the level of each mode down to some fixed energy level. Could you comment on that?

Mr. Gaberson: It is very interesting that you bring that up. You have had for a long time a theorem about equal modal density and that just had not occurred to me. I did some studies on what kind of modal distribution you get if you put an impulse on a beam. That gives equal velocity. If you twang it, that gives equal acceleration.

THE SIMULTANEOUS APPLICATION OF TRANSIENT AND STEADY STATE DYNAMIC EXCITATIONS IN A COMBINED ENVIRONMENT TEST FACILITY SIMULATING SHIPBOARD ENVIRONMENTS

T. B. Jones, Jr
Hughes Aircraft Company
Ground Systems Group
Fullerton, California

A design concept has been established for a combined environment test facility in which transient and steady-state dynamic excitations are effected simultaneously by a system of multiple electrodynamic shakers in conjunction with a two-axis gimbaled drive system which effects pitch and roll maneuvers. The facility is designed to simulate Navy shipboard environments and to impose required environmental test conditions on Navy electronic equipments. The subject matter of this paper, is limited to the consideration of design and analysis of the dynamic excitation systems. The systems are designed for a maximum test load of 25, 000 pounds and are capable of effecting shock excitations in the range of 5-20 g's as well as imposing requisite vibratory and oscillatory excitations.

INTRODUCTION

A study, comprising analytical and design efforts, has been conducted for the purpose of assessing the feasibility and practicality of performing combined environment tests. In particular, the inquiry has addressed the problems of performing environmental tests on Navy electronic systems by the device of a shipboard environment simulator with special emphasis being directed toward effecting transient and steady-state dynamic excitations with a common exciter system.

The study on which this paper is based was performed for Naval Electronics Laboratory Center (NELC), San Diego, California, (Contract # N00123-69-C-0066) and has been summarized in a formal report (Reference 1). The study included the consideration of other environments; which factor is reflected in the design features and characteristics of the facility, but which is not otherwise addressed herein.

The objective of establishing a conceptual design for a combined environment test facility is predicated on a desire to account for synergistic effects and to impose test environments which, especially for the case of dynamic excitations, have been determined from actual service environments. Accordingly, mechanical excitation systems (as distinguished from electrodynamic or electrohydraulic shakers) were dismissed from consideration rather early in the study since their responses are more or less fixed and the duplication of programmed random excitations would be virtually impossible.

On this basis, the fundamental problem was to devise a system of exciters (electrohydraulic or electrodynamic) capable of imposing arbitrarily programmed excitations on complete shipboard installations (which were, all the while, being subjected to other simulated shipboard environments) and to effect, simultaneously, the ship's pitching and rolling maneuvers.

It has been established (References 2, 3, 4 and 5) that ganged multiple shakers can be utilized for test systems the sizes and weights of which exceed the load capability of single present day shakers; hence, the study did not involve any assumptions regarding state-of-the-art advancements in shaker load capacity or control.

REQUIREMENTS

The primary requirement imposed by NELC involved simultaneous application of shipboard environments to Navy electronic systems mounted in the confines of a simulated shipboard compartment having 250 square feet of deck area and 8 feet of headroom, from which requirement a 25, 000 pound maximum test load evolved. It was also required that the simulated ships compartment be removable in order to accommodate deck-mounted equipments for test.

Formal performance requirements for the subject test facility were derived, primarily, from MIL-E-16400, a general specification for Navy ship and shore electronic equipments, and other subordinate documents. The basic mechanical excitation requirements relate to transient shock excitation, steady-state vibrations, and low frequency inclinations, i.e., shipboard pitch and roll.

The transient excitations specified for tests of naval equipments are based on those associated with underwater explosions, gun blasts and aerodynamic

THE SIMULTANEOUS APPLICATION OF TRANSIENT AND STEADY STATE DYNAMIC EXCITATIONS IN A COMBINED ENVIRONMENT TEST FACILITY SIMULATING SHIPBOARD ENVIRONMENTS

T. B. Jones, Jr.
Hughes Aircraft Company
Ground Systems Group
Fullerton, California

A design concept has been established for a combined environment test facility in which transient and steady-state dynamic excitations are effected simultaneously by a system of multiple electrodynamic shakers in conjunction with a two-axis gimbaled drive system which effects pitch and roll maneuvers. The facility is designed to simulate Navy shipboard environments and to impose required environmental test conditions on Navy electronic equipments. The subject matter of this paper, is limited to the consideration of design and analysis of the dynamic excitation systems. The systems are designed for a maximum test load of 25,000 pounds and are capable of effecting shock excitations in the range of 5-20 g's as well as imposing requisite vibratory and oscillatory excitations.

INTRODUCTION

A study, comprising analytical and design efforts, has been conducted for the purpose of assessing the feasibility and practicality of performing combined environment tests. In particular, the inquiry has addressed the problems of performing environmental tests on Navy electronic systems by the device of a shipboard environment simulator with special emphasis being directed toward effecting transient and steady-state dynamic excitations with a common exciter system.

The study on which this paper is based was performed for Naval Electronics Laboratory Center (NELC), San Diego, California, (Contract # N00123-69-C-0066) and has been summarized in a formal report (Reference 1). The study included the consideration of other environments; which factor is reflected in the design features and characteristics of the facility, but which is not otherwise addressed herein.

The objective of establishing a conceptual design for a combined environment test facility is predicated on a desire to account for synergistic effects and to impose test environments which, especially for the case of dynamic excitations, have been determined from actual service environments. Accordingly, mechanical excitation systems (as distinguished from electrodynamic or electrohydraulic shakers) were dismissed from consideration rather early in the study since their responses are more or less fixed and the duplication of programmed random excitations would be virtually impossible.

On this basis, the fundamental problem was to devise a system of exciters (electrohydraulic or electrodynamic) capable of imposing arbitrarily programmed excitations on complete shipboard installations (which were, all the while, being subjected to other simulated shipboard environments) and to effect, simultaneously, the ship's pitching and rolling maneuvers.

It has been established (References 2, 3, 4 and 5) that ganged multiple shakers can be utilized for test systems the sizes and weights of which exceed the load capability of single present day shakers; hence, the study did not involve any assumptions regarding state-of-the-art advancements in shaker load capacity or control.

REQUIREMENTS

The primary requirement imposed by NELC involved simultaneous application of shipboard environments to Navy electronic systems mounted in the confines of a simulated shipboard compartment having 250 square feet of deck area and 8 feet of headroom, from which requirement a 25,000 pound maximum test load evolved. It was also required that the simulated ships compartment be removable in order to accommodate deck-mounted equipments for test.

Formal performance requirements for the subject test facility were derived, primarily, from MIL-E-16400, a general specification for Navy ship and shore electronic equipments, and other subordinate documents. The basic mechanical excitation requirements relate to transient shock excitation, steady-state vibrations, and low frequency inclinations, i.e., shipboard pitch and roll.

The transient excitations specified for tests of naval equipments are based on those associated with underwater explosions, gun blasts and aerodynamic

The essential characteristics of the two dynamic actuation systems comprised by the simulator are shown in Figure 2. The framed structure supporting the electrodynamic shakers is rigidly attached to the inner gimbaled drive ring and is designed to support a total weight of 200,000 pounds; which total includes the test system and the shakers. The support frame structure itself would weigh on the order of 6000-12,000 pounds; the actual weight being determined by the overall system natural frequency limits and associated operational cut-off frequencies. The inner gimbaled drive ring is supported by bearings mounted on the outer gimbaled drive ring. The d-c motors actuating the inner gimbaled assembly are supported on frame members attached to the outer gimbaled ring. The outer gimbaled drive ring assembly is supported by bearings resting on a seismic mass.

As shown, the shakers are positioned below the gimbal axis in order to insure stability in the pitch and roll modes; however, this necessitates a reactive system for the overturning moments induced by the four shakers which provide horizontal excitation. Provocation for minimizing this eccentricity also derives from the consideration of the kinetics of the pitch and roll actuation systems since decreases in system inertia accompanying decreases in this eccentricity result in decreased power requirements.

CONTROL AND DYNAMICS

Two problem areas require additional analysis in order to establish the validity of the design concept. These are the matters of control and kinetics.

The problem of control of multiple shakers has been considered in earlier investigations (References 5, 6 and 7). Techniques for controlling multiple shakers in parallel (i.e., with individual power amplifiers and automatic gain controls) have been established and demonstrated for test systems exhibiting cross-coupling no greater than unity (Reference 5). In addition, methods have been described for controlling sinusoidal excitations with multiple shaker systems even when cross-coupling factors exceed unity (Reference 7). At the present time, these circumstances would prescribe performance limitations of (1) operating in frequency domains considerably removed from resonant frequencies, or (2), effecting only sinusoidal excitations.

For steady-state excitations in the range of 1-50 cps as required for naval systems, it is expedient to design the drive fixture and supporting structure such that the relevant stiffness characteristics of the assemblage of test system and supporting structure are sufficiently great to insure cross-coupling factors

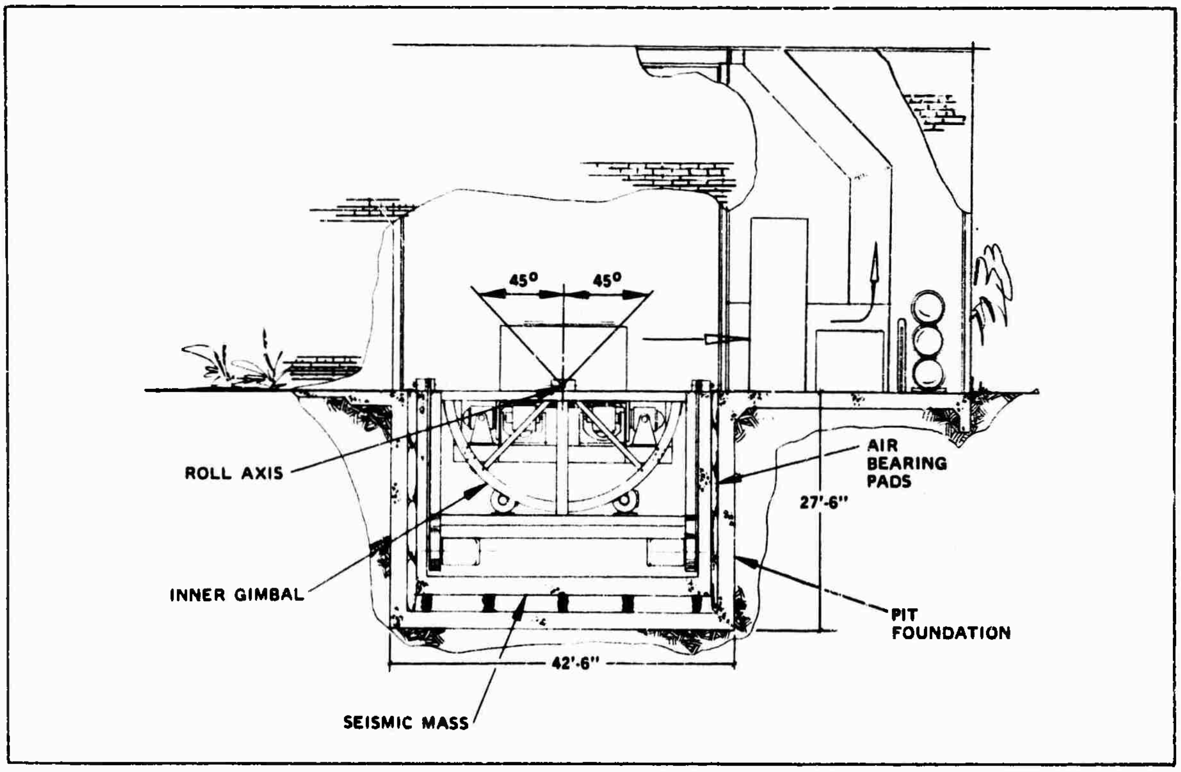

Figure 2. Test Platform

approximating unity. It does not appear that "very soft" support structures are desirable owing to the large size of the test system and the highly localized effects which would result.

As a final note, the results of two analyses made to check essential design characteristics are shown in the following paragraphs.

An analysis was made of the inclination kinematics for the purpose of determining, primarily, the horsepower and torque requirements of the d-c drive motors. Assuming a harmonic driving torque, the maximum steady-state torque, T_o, required is (ignoring friction)

$$T_o = J\,\Theta_o\,\omega_n^2 \left[1 - \frac{\omega^2}{\omega_n^2}\right],$$

wherein J is the system moment of inertia, Θ_o is the maximum inclination, ω is the frequency of driving torque and ω_n is the natural frequency of the system. The maximum horsepower required for the inclination system is

$$H.P. = T_o\,\Theta_o\,\frac{\omega}{2}$$

The torque T_o is shown in Figure 3 for various offset lengths, l, between the system center of gravity and the gimbal axes.

An analysis was also made to determine the influence of stiffness characteristics on the response of the vibratory system and the strength requirements of the support structure. For this purpose a model encompassing three degrees of freedom was considered to represent the combination of the (1) test system, (2) the gimbaled platforms, and (3) the seismic mass. The results of this analysis are shown in Figure 4.

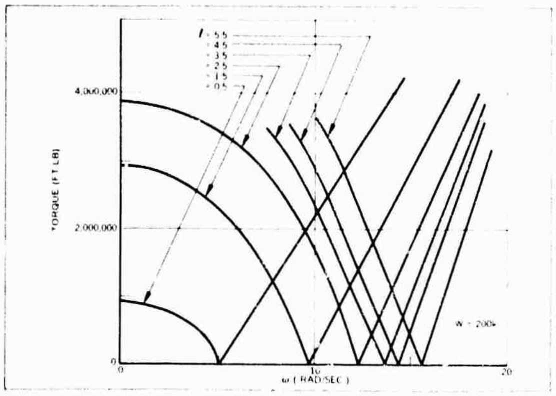

Figure 3. Peak Steady-State Torque to Oscillate Gimbaled Platform

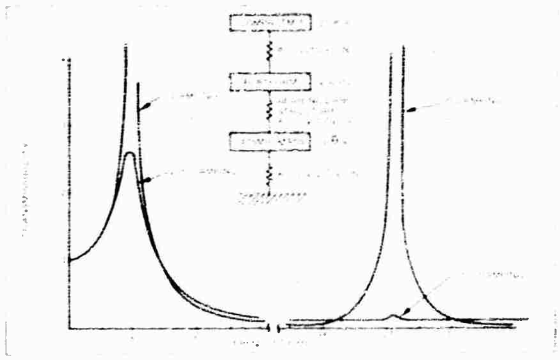

Figure 4. Test Platform Transmissibility

CONCLUSION

The feasibility of the concept described has been established on the basis of conceptual analysis and design efforts.

ACKNOWLEDGEMENT

The author wishes to acknowledge the assistance of Mr. M. L. Ankenbauer who performed some of the calculations for the pitch and roll actuation system dynamics and for the frequency response characteristics of the test platform.

REFERENCES

1. T. B. Jones, "Final Report for Combined Environment Test Facility Study, Phase III," FR 69-10-845, Hughes Aircraft Company, Ground Systems Group, Fullerton, California, July, 1969.

2. V. H. Larson, "The Control of Acceleration by Electrohydraulic Shaker Systems," Technical Bulletin 840.00-1, MTS Systems Corporation, Minneapolis, Minnesota

3. J. G. Helmuth, "Control of Multiple Shakers," Institute of Environmental Sciences, Annual Technical Meeting Proceedings, 1965.

4. D. D. Arnold and T. F. Bogart, "Electrodynamic Shaker Shock Synthesis and Analysis System," Ling Electronics, Anaheim, California

5. J. D. Newton, "Methods of Control of Multiple Shaker Testing Systems," Shock and Vibration Bulletin (35), Part 2, January, 1966.

6. R. A. Arone and P. A. Brock, "Control Techniques for Multi-shaker Vibration Systems," Shock and Vibration Bulletin (36), Part 3, January, 1967.

7. N. F. Hunter, Jr. and J. G. Helmuth, "Control Stabilization for Multiple Shaker Tests," Shock and Vibration Bulletin (37), January 1968.

DISCUSSION

Mr. Rheuble (General Electric Co.): Considering the size of the package and the frequency range of concern, why did you select electrodynamic shakers as opposed to hydraulic shakers? Force is cheap in hydraulic shakers, you know.

Mr. Jones: I am also of the opinion that hydraulic shakers would be cheaper. As to pitch and roll, we chose not to include the hydraulic system because when we traded off the power requirements we would up with a stroke that was so long that it made a very soft link in the whole system. My position regarding the shock and vibration element is not quite so strong. We did consider it and we have shown in our report one concept which included a system of hydraulic shakers. Our experience has been that a hydraulic system does not give as clean a response as the electrodynamic system would. This was the factor that tipped it for me toward the electrodynamic system.

Mr. Rheuble: Of course, we all realize there is a certain restriction on the lower frequency range because it was electrodynamic. Did this give you two axes simultaneously or each axis individually? I could not tell from the gimbal system.

Mr. Jones: We are talking two-axis vibration with the whole thing going at once including pitch and roll. We talked to vendors who have built big electrodynamic shakers such as this and they have assured us that this is practical. They also assured us that the two-axis or multiple-axis excitation could be handled with redesign of the shaker.

Mr. Levin (Naval Ship Engineering Ctr.): I understand that this is a study phase at the moment. Have you tested actual hardware?

Mr. Jones: No sir, we have not.

Mr. Isada (Cornell Aeronautical Lab.): Why did you eliminate heave motion in your simulator?

Mr. Jones: Primarily for the same reason we limited the vibration to two axes. We had to decide on some limit of performance. We settled, after considerable discussion, on the fact that two-axis vibration and shock and two-axis inclination pitch and roll would be about as far as we could go as a practical limit when we traded off cost and the complexity of the system. We sacrificed heave as one of the lesser effects. Certainly the ship's motions do not have a very strong influence on the performance of this system. In the man-machine interface, doubtless they do, but the acceleration levels associated with the ship's motions of roll, pitch or heave would be very low relative to the other excitations.

Mr. Paladino (Naval Ship Systems Cd.): This is a clarification to the audience about this work. Prior to this the Navy has had a great deal of interest in such a facility. This document will be reviewed by various Navy sources. The Navy has to decide whether such a facility is necessary to insure mechanical and service integrity in electronic equipment.

PERIODIC SHOCK EXCITATION OF ELASTIC STRUCTURES

Dusan Krajcinovic
Ingersoll-Rand Res. Inc.
Princeton, New Jersey

and

George Herrmann
Northwestern University
Evanston, Ill.

The dynamic stability of elastic structures subjected to various types of periodic shock excitation is investigated. The paper presents exact and series solution of the linearized problem of parametric resonance. Briefly is outlined also the finite element formulation of the problem. The analysis is illustrated by a thinwalled beam subjected to a transverse pulsating force.

INTRODUCTION

At the present time various classes of problems of elastic structures subjected to dynamic loads continue to attract the attention of numerous investigators because of the abundance of still unresolved problems. In addition to the response problems, the dynamic stability of structures is certainly in timely need of further exploration. The purpose of the present study is to examine analytically one of the aspects of the rather complex dynamic behaviour of elastic structures, subjected to periodic excitation forces, by confining attention to conditions under which excessive parametric motion may occur. The problem is thus formulated as belonging to the class of parametric excitation phenomena which forms a subclass of dynamic stability problems.

The classical problem of parametric resonance of a structure subjected to a harmonic excitation has been studied rather exhaustively in the past [1]. The present paper considers the same phenomenon induced, however, by various types of impulsive periodic forces. This type of loading takes place in numerous applications of technological significance such as in pile driving, marine structural engineering subjected to jerks, in impact tools etc.

FORMULATION OF THE PROBLEM

Consider a continuous linearly elastic structure such as a prismatic bar, plate or shell, with arbitrary boundary conditions subjected to periodic impulsive excitation load. If the lowest natural frequency of the longitudinal motion is large as compared to the lowest natural frequency of the transverse motion and to the frequency characterizing the pulsating excitation force, the spatial dependence of the axial load induced in the structure may be neglected. Hence, the transverse motion may be regarded as being uncoupled from the longitudinal motion for sufficiently small amplitudes. In other words, the unperturbed motion is identified with the undeformed state.

As it is well known, this assumption leads, in the case of a prismatic beam, to the differential equation

$$EI \frac{\partial^4 w}{\partial x^4} + m \frac{\partial^2 w}{\partial t^2} + P(t) \frac{\partial^2 w}{\partial t^2} = 0 \quad (1)$$

where $w(x,t)$ is the transverse deflection, EI the flexural rigidity, m the mass of the beam per unit of length, and $P(t)$ some periodic time dependent load. Appropriate boundary conditions should be supplemented in order to pose the boundary vlaue problem properly. Since only the steady-state problem is considered, no initial conditions are introduced.

It should be understood that since this is not a response problem it is not the solutions of (1) that are sought, but the conditions under which they are stable (bounded).

One seeks the solution of (1) in form of standing waves

$$w(x,t) = \sum_k X_k(x) f_k(t) \tag{2}$$

where $X(x)$ are eigenfunctions of free vibrations, or static stability problems, or simply some preferably orthonormal functions satisfying boundary conditions. The implications of this choice are discussed in [2]. $f(t)$ is an unknown time dependent function.

Substituting relation (2) into (1) and using the property of orthogonality of functions $X(x)$, one obtains the system of coupled linear differential equations governing the problem of parametric excitation

$$\frac{d^2 f_k}{dt^2} + \omega_{kj}^2 [1 - \mu_{kj} P(t)] f_k = 0 \tag{3}$$

where

$$\omega_{kj}^2 = (EI \int X_k'''' X_j dx) / (EI_y \int X_k'' X_j dx) \tag{4}$$

$$\mu_{kj} = (\int X_k'' X_j dx) / (EI_y \int X_k'''' X_j dx) \tag{5}$$

when

$$\int X_k^{IV} X_j \, dx = 0 \qquad (k \neq j)$$

$$\int X_k'' X_j \, dx = 0 \qquad (k \neq j)$$

only $\mu_{kk} = \mu_k$ and $\omega_{kk} = \omega_k$ are different from zero and the system of coupled equations degenerates into an array of independent differential equations

$$\frac{d^2 f_k}{dt^2} + \omega_k^2 [1 - \mu_k P(t)] f_k = 0 \tag{3}$$

When the excitation force is periodic $P(t) = P(t + T)$, equation (3') becomes a Hill's equation with a solution having the property of being unbounded for certain ratios θ/ω. Set of such points in the parametric space (θ, μ) for which the solution is unbounded will be in the sequel referred to as instability region.

EXACT SOLUTION

As it has been shown by same authors [2] in the case of a simply supported beam, hydrostatically loaded ring and a few other extremely simple cases excited by a periodic impulsive load

$$P(t) = P_o + P_t \sum_k \delta(\theta t - k\theta T) \tag{6}$$

an exact solution for the boundaries of instability region may be obtained. In (6) with P_o denoted is the intensity of the constant part of the excitation force, with P_t the amplitude of the time dependent part, with δ the Dirac delta function, with θ the frequency and with T the period of $P(t)$.

Using the apparatus of the Theory of Distributions in conjunction with the Floquet's procedure, one obtains the following relation for the boundaries of the instability regions

$$\Psi(\Omega T) = \left| \frac{P_t}{2(P_{cr} - P_o)} \frac{\Omega_k T}{2\pi} \sin \Omega_k T + \cos \Omega_k T \right| = 1 \tag{7}$$

where

$$\Omega_k = \omega_k \left(1 - \frac{P_o}{P_{cr}}\right)^{\frac{1}{2}} \tag{8}$$

and

$$\omega_k = \frac{k^2 \pi^2}{\ell^2} \left(\frac{EI}{m}\right)^{\frac{1}{2}} ;$$

$$P_{cr} = \frac{k^2 \pi^2}{\ell^2} EI \tag{9}$$

with k = 1, 2, 3, ...

For $\Psi(\Omega T) > 1$, the solution of the equation (3) is unstable.

SERIES SOLUTION

As said before, the applicability

of the exact solution is severly restricted to a very few cases when the problem is essentially governed by a single Hill's equation. Since in general this is not the case, it was essential to develop a procedure for systems governed by several coupled equations.

Out from the several different methods it appears that the solution in form of Fourier series possesses certain computational advantages, and is more frequently used than the other methods.

In order to apply the Fourier series method, all functions appearing in Eq. (3) have to be expanded into trigonometric series. Since the differential equation (3) has indeed periodic solutions, $f(t) = f(t + T)$ (representing actually boundaries of instability regions) one may write for a 2T period

$$f(t) = \sum \left(a_k \sin \frac{k\theta t}{2} + b_k \cos \frac{k\theta t}{2}\right) \quad (k = 1,3,5\ldots) \tag{10}$$

It is known also that every periodic distribution $g(\tau)$ has a Fourier expansion converging in the space of all periodic distributions

$$g(\tau) = \sum_{r=-\infty}^{\infty} G_r \exp(ir\omega\tau)$$

where

$$\omega = \frac{2\pi}{T_1} > 0$$

The constants G_r are of slow growth and as shown in [3] and [4] are given by

$$G_r = \frac{1}{T_1} \int_0^{T_1} g(\tau) \exp(-ir\omega\tau)d\tau \tag{11}$$

Since the periodic delta function is defined by

$$g(\tau) = \sum_r \delta(\tau - 2\pi r)$$

it follows from (11) that the Fourier coefficients are given by

$$G_r = \frac{1}{T_1}$$

such that

$$\delta_T = \sum_{-\infty}^{\infty} \delta(\tau - 2\pi r) = \frac{1}{T_1} \sum_{-\infty}^{\infty} \exp(ir\omega\tau)$$

$$\delta_T = \frac{1}{T_1} + \frac{2}{T_1} \sum_{1}^{\infty} \cos r\omega\tau \tag{12}$$

Finally, for $\tau = \theta t$, $\omega = 2\pi/\theta T$ and $T_1 = \theta T$ one has

$$\sum_{k=-\infty}^{\infty} \delta(\theta t - k\theta T) = \frac{1}{\theta T} + \frac{2}{\theta T} \sum_{n=1}^{\infty} \cos 2n\pi \frac{\theta t}{\theta T} \tag{13}$$

The relation (13) means merely that both series distributionally converge to the same quantity, i.e.

$$\lim \int \sum \delta(\theta t - k\theta T) \cdot \varphi(t)\,dt = \lim \int \left(\frac{1}{\theta T} + \frac{2}{\theta T} \sum_n \cos(n\theta t)\right) \varphi(t)\,dt$$

where $\varphi(t)$ is an arbitrary test function

Substituting relation (13) into eq. (3) yields

$$\frac{d^2 f}{dt^2} + \Omega_1^2 \left(1 - 2\mu_1 \sum_{k=1}^{\infty} \cos k\theta t\right) f = 0 \tag{14}$$

where

$$\Omega_{1,k} = \omega_k \left(1 - \frac{P_o + P_t/2\pi}{P_{cr,k}}\right)^{\frac{1}{2}} \tag{15}$$

$$\mu_{1,k} = \frac{1}{2\pi} \frac{P_t}{P_{cr,k} - (P_o + P_{t/2\pi})}$$

Substituting trigonometric expansion (10) for $f(t)$ into (14) and equating to zero coefficients of like $\sin k\theta t$ and $\cos k\theta t$ one obtains an infinite, homogeneous system of linear, algebraic equations in terms of coefficients a_k and b_k

$$\left(1 + \mu_1 - \frac{k^2\theta^2}{4\Omega_1^2}\right) a_k = 0$$

$$\left(1 - \mu_1 - \frac{k^2\theta^2}{4\Omega_1^2}\right) b_k - 2\mu_1 (1 - \delta_{jk}) \sum b_j = 0 \tag{16}$$

$(j,k = 1,3,5 \ldots.)$

where δ_{jk} is the Kronecker delta symbol.

A nontrivial solution of the homogeneous system (16) exists only if the determinant of the coefficients (known as Hill's determinant) vanishes. This, in fact, represents the condition for the existence of periodic solutions (10) (boundaries separating stable - damped, from unstable - increasing in time solutions) of the differential equation (14).

As a first approximation, off-diagonal terms of the Hill's determinant can be neglected, yielding a simple formula for the boundaries of odd regions of instability, namely

$$\frac{\theta_*}{\Omega_1} \approx \frac{2}{k}\sqrt{1 \pm \mu_1} \quad (k=1,3,5\ \ldots) \quad (17)$$

with the asterisk denoting values of θ on the boundaries of instability retions. Thus, θ_* is the critical frequency of the external load.

If higher accuracy is needed one can substitute (17), for k=1, into the second diagonal term and evaluate θ_* from the second-order determinant. A slightly more accurate formula for the boundaries of the first instability retion is than obtained as

$$\frac{\theta_*}{\Omega_1} = 2\left[1 \pm \mu_1 + \frac{(\mu_1 \pm \mu_1)^2}{8(1 \pm \mu_1)}\right]^{1/2} \quad (18)$$

Since μ_1 does not exceed roughly 0.25, formulas (17) and (18) yield practically identical results.

The more accurate formula for the boundaries of the third instability region obtained from the corresponding second order determinant, using again (17) for k=3, reads

$$\frac{\theta_*}{\Omega_1} = \frac{2}{3}\left[1 \pm \mu_1 \frac{(\mu_1 \pm \mu_1)^2}{\frac{8}{9} \pm \mu_1}\right]^{1/2}$$

In order to establish formulas defining the regions of instability bounded by the periodic solutions of period T, instead of series (10) one uses

$$f(t) = b_o + \sum \left(a_k \sin\frac{k\theta t}{2} + b_k \cos\frac{k\theta t}{2}\right) \quad (k = \text{even})$$

Following the same procedure, the upper and the lower boundaries of the second instability region are obtained as follows

$$\frac{\theta_*}{\Omega_1} = \sqrt{1 + \mu_1} \quad \text{and}$$

$$\frac{\theta_*}{\Omega_1} = \sqrt{1 - \mu_1 - 2\mu_1^2} \quad (19)$$

In case of a simply supported beam even the first approximation formulas provide results accurate enough for all practical purposes. Taking as an example $P_o = 0.25\ P_{cr}$, first three instability regions are computed and plotted in Figure 1.

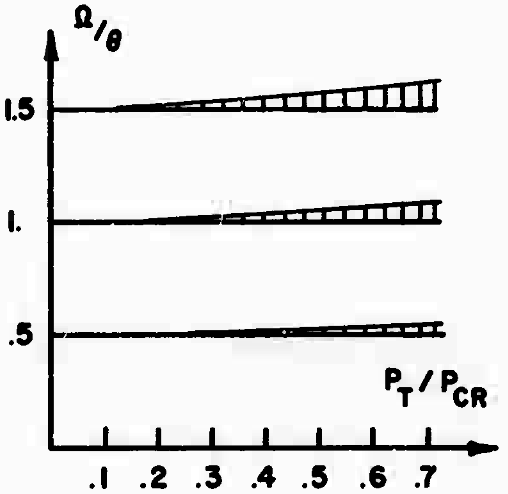

Fig. 1 Three lowest instability regions (shaded areas)

The maximum difference between exact and series solution takes place, as expected, for larger μ and for higher instability regions. Nevertheless, the second approximation formulas were always within 2% of the exact value computed from (7).

The principle merit of the series solution is that it can be applied without further complications to cases when the system of n coupled equations is to be considered. Although it is conceptually possible to eliminate (n-1) variables (since the differential operators are linear), one cannot use standard procedures, since, in general, after separation of variables the system does not reduce to either Mathieu or Hill equations.

Thus, the task is to determine the boundaries of instability regions for the system of differential equations written in matrix form as

$$C\frac{d^2f}{dt^2} + \left[I-\alpha A-\beta\varphi(t)B\right]f = 0 \qquad (20)$$

where A,B and C are matrices with constant elements, I is the identity matrix, α and β two scalars and $f(t)$ unknown vector. $\varphi(t) = \varphi(t+T)$ is a periodic function of time characterizing time dependence of the excitation load.

By analogy to the case of a single equation the solution of (20) with period 2T is sought in form of Fourier series

$$f(t) = \sum(a_k \sin\frac{k\theta t}{2} + b_k \cos\frac{k\theta t}{2}) \quad (21)$$

where a_k and b_k are some unknown vectors with constant components. If $\varphi(t)$ is defined as

$$\varphi(t) = \sum_k \delta(\theta t-k\theta T)$$

one repeats the same procedure as in the case of a single equation to obtain the generalized Hill's equations with matrices rather than scalars as elements.

The first approximation for the boundaries of the first instability region is obtained by equating to zero the first diagonal matrix element of the Hill's determinant

$$\left|I-\alpha_1 A_1 \pm \frac{1}{2}\beta_1 B - \frac{\theta^2}{4} C\right| = 0 \qquad (22)$$

where

$$\alpha_1 A_1 = (\alpha A + \frac{\beta}{2\pi} B) \text{ and } \beta_1 = \frac{\beta}{\pi}$$

The boundaries of the higher instability regions are obtained in much the same way as in the case of a single equation (see Ref. [3]). However, the expressions tend to be rather long and unsuitable for qualitative analysis.

In order to briefly illustrate the procedure a simple example of a beam shown in Figure 2 will be treated. Differential equations governing the problem ([1], [3]) are

$$EI_x v^{IV} - m\ddot{v} = 0$$

$$EI_y u^{IV} + (m_x\varphi)'' + m\ddot{u} = 0 \qquad (23)$$

$$EI_\Omega \varphi^{IV} - GK\varphi'' + M_x u'' + mr^2\ddot{\varphi} = 0$$

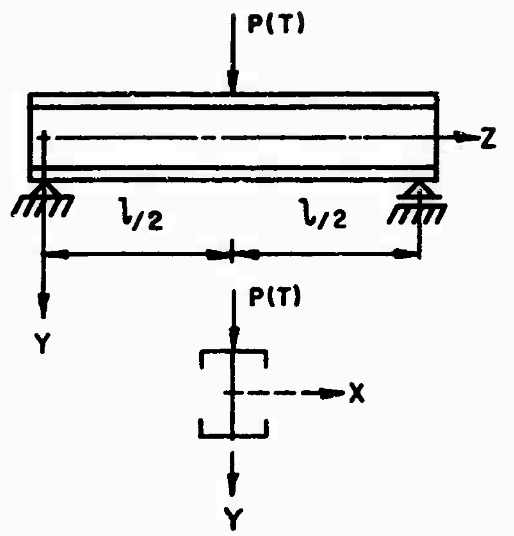

Fig. 2 A thin-walled beam subjected to a concentrated load P(t) at the midspan.

Where u and v are componental displacements and μ angle of rotation about the longitudinal axis EI_x, EI_y are flexural rigidities, EI_Ω sectorial rigidity, GK torsional rigidity and M_x the external bending moment defined by

$$M_x(z,t) = \begin{cases} \frac{1}{2}P(t)z & 0<z<\frac{1}{2}\ell \\ \frac{1}{2}P(t)(\ell-z) & \frac{1}{2}\ell<z<\ell \end{cases}$$

First equation governing the free vibrations in one of the principal equations is uncoupled and may be treated separately. Only two last coupled equations will be treated in sequel.

Assuming solutions in form of series

$$u(z,t) = \sum_n U_n(t)\chi_n(z)$$

$$\varphi(z,t) = \sum_n \Phi_n(t)\psi_n(z),$$

$$\chi(z) = \psi(z) = (\sqrt{2/\ell}) \sin \pi z/\ell,$$

where coordinate functions $\chi(z)$ and $\psi(z)$ are chosen as eigen-functions of the free vibration problem. Making use of Galerkin's method of the last two equations are rewritten in matrix form as

$$m\,\underset{\sim}{F}\,\ddot{\underset{\sim}{f}} + [\underset{\sim}{R}_k - \lambda_0 \underset{\sim}{S} - \lambda_t M(t) \underset{\sim}{S}_t]\underset{\sim}{f} = 0,$$

where

$$\underset{\sim}{F} = \begin{bmatrix} \int \chi^2 dz & 0 \\ 0 & r^2 \int \psi^2 dz \end{bmatrix} = \begin{bmatrix} 1 & 0 \\ 0 & r^2 \end{bmatrix}$$

$$\underset{\sim}{R} = \begin{bmatrix} \kappa_y \int \chi''^2 dz & 0 \\ 0 & \kappa_\omega \int \psi''^2 dz - GK \int \psi \psi'' dz \end{bmatrix} = \begin{bmatrix} EI_y \frac{\pi^4}{4} & 0 \\ 0 & EI_\Omega \frac{\pi^4}{4} + GK \frac{\pi^2}{2} \end{bmatrix}$$

$$\underset{\sim}{S} = \begin{bmatrix} 0 & \int \chi (M\psi)'' dz \\ \int \psi M_x \chi'' dz & 0 \end{bmatrix} = \frac{1}{8} \begin{bmatrix} 0 & \pi^2 - 12 \\ \pi^2 + 4 & 0 \end{bmatrix}$$

$$f = \begin{bmatrix} U_k \\ \Phi_k \end{bmatrix}$$

with all the integrals being taken over the entire length of the member.

The approximate matrix relation defining the first instability region may now be written as

$$\left| \underset{\sim}{R} - \left(P_0 + \frac{P_t}{2\pi} \pm \frac{P_t}{2\pi}\right)\underset{\sim}{S} - \frac{m\theta^2}{4}\underset{\sim}{F} \right| = 0,$$

or

$$\begin{vmatrix} 1 - \frac{\theta^2}{4\omega_x^2} & A_1 \frac{1}{P_x}\left(P_0 + \frac{P_t}{2\pi} \pm \frac{P_t}{2\pi}\right) \\ \frac{A_2}{\ell}\left(\frac{P_0}{P_\varphi} + \frac{P_t}{2\pi P_\varphi} \pm \frac{P_t}{2\pi P_\varphi}\right) & 1 - \frac{\theta^2}{4\omega_\varphi^2} \end{vmatrix} = 0$$

where

$$P_x = \frac{EI_y}{\ell^2}, \quad P_\varphi = \frac{1}{\ell^2}\left(EI_\Omega \frac{\pi^2+4}{\pi^2}\right).$$

Expanding the determinant one obtains the boundaries of two principal instability regions. If $\gamma = \frac{\omega_x^2}{\omega_\varphi^2} \ll 1$ following approximate relations for the first flexural and first torsional instability region are obtained.

$$\theta_* = 2\omega_x \sqrt{1 - \frac{A_1 A_2}{P_x P_\varphi} \frac{1}{1-\gamma} \left(P_0 + \frac{P_t}{2\pi} \pm \frac{P_t}{2\pi}\right)}$$

and

$$\theta_* = 2\omega_\varphi \sqrt{1 + \frac{A_1 A_2}{P_x P_\varphi} \frac{\gamma}{1-\gamma} \left(P_0 + \frac{P_t}{2\pi} \pm \frac{P_t}{2\pi}\right)}$$

In the first of the two instability regions the flexural motion will prevail, while on the second the torsional vibrations will be of principal significance.

In addition to the previously studied loading function (6) the presented technique may be applied if the periodic impulsive excitation force alternates in sign (Fig. 3).

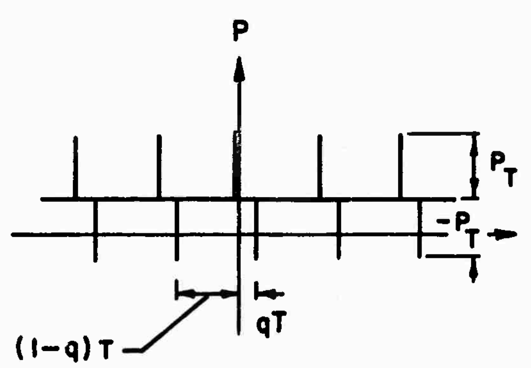

Fig. 3 Alternating impulsive load.

For the sake of simplicity it will be assumed that the intensities of the tensile and compressive force are equal. Varying the parameter q denoting the time distance separating two neighboring tensile and compressive force (Fig. (Fig. 3), one can study the effect of the nature of the excitation force on the width and shape of instability regions.

For q = 0.5 the tensile forces are located midway between two successive compressive forces. The loading function is

$$P_t = P_o + P_t\sum_k \delta(\theta t-k\theta T) - \delta(\theta t - \frac{\theta t}{2} - k\theta T) \qquad (24)$$

For the periodic distribution defined by

$$f(T) = \sum_K \delta(T - \frac{T_1}{2} - kT_1)$$

Fourier coefficients are

$$F_n = \frac{1}{T_1}\int_0^{T_1} \delta(T - \frac{T_1}{2})\exp(-in\omega t)\,dt = \frac{1}{T_1}\exp(-in\pi)$$

Other zeroes of the function f(t) do not fall into the interval $(0,T_1)$ of the integration.

Hence,

$$\sum_{-\infty}^{\infty}\delta(\theta t - \frac{\theta t}{2} - k\theta T) = \frac{1}{\theta T} + \frac{2}{\theta T}\sum_{1}^{\infty}(-1)^n \cos n\theta T \qquad (25)$$

Combining relations (13) and (25) in sense of (24) and substituting it into Eq. (3) one has

$$\frac{d^2f}{dt^2} + \Omega^2(1-4\mu\sum_{n=1}^{\infty}\cos n\theta t)f = 0$$

where

$$\Omega^2 = \omega^2(1 - \frac{P_o}{P_{cr}})$$

$$\mu = \frac{1}{2}\,\frac{P_t}{P_{cr}-P_o}$$

In conjunction with the Hill's determinant following relations for the first instability region are obtained as

$$\theta_* = 2\Omega\sqrt{1 \pm 2\mu} \qquad (27)$$

or more accurately

$$\theta_* = 2\Omega\sqrt{1 \pm 2\mu - \frac{2\mu^2}{-4\pm\mu}} \qquad (28)$$

The boundaries of the second instability region are

$$\theta_* = \Omega \quad\text{and}\quad \theta_* = \Omega\sqrt{1 - \frac{8}{3}\mu^2}$$

Preceeding in much the same way for q = 0.25 the boundaries of the first instability region are found to be

$$\theta_* = 2\Omega\sqrt{1 \pm \mu\sqrt{2}}$$

while for the second instability region one has

$$\theta_* = \Omega\sqrt{1 - 2\mu^2 \pm (2\mu + \mu^3)}$$

In a case when q is infinitely small tensile and compressive force form a dipole in time. The forcing function is then given by

$$\varphi(t) = \sum \dot{\delta}(\theta t-k\theta T)$$

where $\dot{\delta}(\theta t)$ is the dipole or the generalized time derivative of the Dirac delta function. The fourier coefficient can be calculated to be $G_r = ir\omega/T_1$ (with i standing for the imaginary unit), such that

$$\sum_{k=-\infty}^{\infty}\dot{\delta}(\theta t-k\theta T) = -\frac{1}{\pi}\sum_{n=1}^{\infty} n \sin n\theta T$$

The boundaries of the first instability region are now

$$\vartheta_* = 2\Omega\sqrt{1 \pm \mu}$$

while the second instability region is bounded by

$$\theta_* = \Omega\sqrt{1-\mu^2 \pm (2\mu+\tfrac{1}{4}\mu^3)}$$

The whole process is symmetric about $q = 0.5$, i.e. $q = 0.25$ and $q = 0.75$ generate identical instability regions.

Having established all these relations the diagram showing the boundaries of first two instability regions for a simply supported beam, for different q's is plotted in Fig. 4. As expected, the shape of instability regions for $q = 0.5$ resembles the shape for the harmonic load.

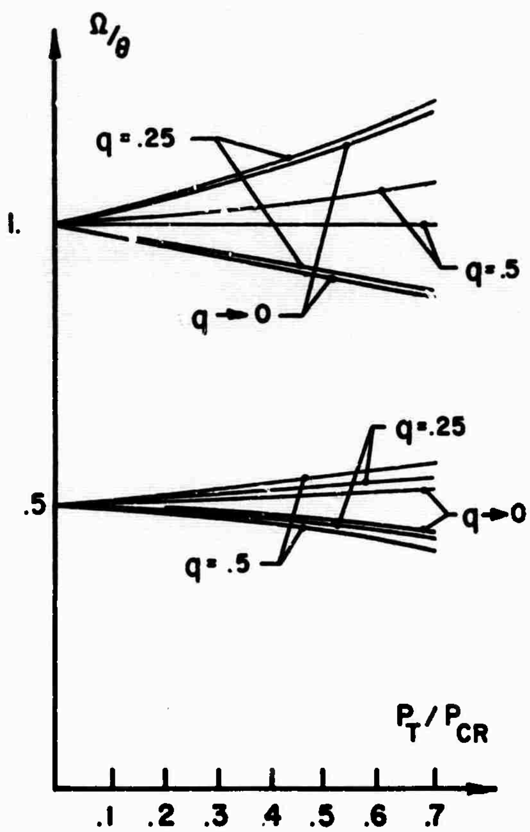

Fig. 4. Instability regions for a simply supported beam subjected to alternating impulsive load.

FINITE ELEMENTS SOLUTION

In order to cope with the problem of complicated geometry, it is necessary to formulate the problem in a way suitable for application of computers.

Writing the unknown generalized displacement $w(x,y,z,t)$ in the form

$$w(x,y,z,t) = \sum_{i=1}^{k} q_i(t)\beta_i(x,y,z)$$

where $q_i(t)$ are some unknown amplitudes and $\beta_i(x,y,z)$ are some given displacement (or influence) functions the differential equation governing the parametric resonance problem (see Refs [5] or [6]) may be written as

$$\ddot{\underset{\sim}{q}} + \underset{\sim}{M}^{-1}\underset{\sim}{K}[\underset{\sim}{I}-P(t)\underset{\sim}{K}^{-1}\underset{\sim}{G}]\underset{\sim}{q} = 0$$

where for the assumed displacement field the mass, stiffness and stability matrices are defined by

$$\underset{\sim}{M} = [m_{ij}] \qquad m_{ij} = m\int \beta_i\beta_j ds$$

$$\underset{\sim}{K} = [k_{ij}] \qquad k_{ij} = EI\int \beta_i''\beta_j'' ds$$

$$\underset{\sim}{G} = [g_{ij}] \qquad g_{ij} = \int \beta_i'\beta_j' ds$$

The approximate relation (derived) from Hill's determinant as before) determining the boundaries of the first instability region reads

$$\left|-\lambda\underset{\sim}{I} + \underset{\sim}{M}^{-1}\underset{\sim}{K} - \alpha\underset{\sim}{M}^{-1}\underset{\sim}{G}\right| = 0 \tag{29}$$

where

$$\lambda = \frac{\theta^2}{4}$$

while the parameter α defining the character of the excitation force is:

for the harmonic force $\alpha = P_0 \pm \tfrac{1}{2}P_t$

for periodic impacts $\alpha = P_0 + \frac{P_t}{2\pi} \pm \frac{P_t}{2\pi}$

As shown in both Refs. [5] and [6], for a simply supported beam idealized by a minimum of two discrete elements the technique yields results of more than satisfactory accuracy.

TRANSVERSE LOAD

When, in addition to the longitudinal periodic excitation force $P(t)$, the structure is subjected to the persistent time dependent periodic transverse load $G(t) = G(t+T)$ the governing equation reads

$$EI\frac{\partial^4 w}{\partial x^4} + P(t)\frac{\partial^2 w}{\partial x^2} - m\frac{\partial^2 w}{\partial t^2} = G(t) \quad (30)$$

If

$$G(t) = \sum X_k(x) g_k(t)$$

then using (2) one has as before

$$\ddot{f}_k + \omega_k^2[1-\mu_k P(t)]f_k = \frac{1}{m}g_k$$

As shown in (7) for the case when g_k/m is bounded in mean, the null solution of (30) which is in the same time the null solution of (3') is stable in the presence of persistent disturbance $G(t)$. Since the continuous system is dealt with, in addition to the boundedness in mean of g_k/m the series for $G(t)$ should also converge.

SUMMARY

The paper is concerned with the linearized problem of the parametric resonance of perfectly elastic structures subjected to various kinds of periodic impulsive forces. The critical frequencies are determined both exactly and approximately. It has been found that the approximate solutions (both series and finite elements) compare favorably with the exact solution.

Comparing different types of im-' pulsive leads, it was also determined that the system of periodic tensile forces superimposed on the system of periodic compressive forces has a destabilizing effect in the sense of enlarging of instability regions. In addition to the forces which are indeed of impulsive nature, the presented analysis may be used for the first approximation in case of periodic forces which are not harmonic.

The evaluation of the influence of various phenonomena such as rotatory inertia, viscous damping and various nonlinearities is not presented herein. Although such a study enriches the overall analysis qualitatively, the phenomena treated do not seem to affect considerably [5] the basic results obtained for the linearized theory as presented herein.

Some additional proofs of mainly mathematical interest, and a more detailed presentation of various examples may be found in our papers [2] and [3].

ACKNOWLEDGEMENT

The work presented herein was supported by the Air Force Office of Scientific Research under Grant AF-AFOSR-100-67.

PARTIAL LIST OF SYMBOLS

E	-	Elastic modulus
I	-	Principal moment of inertia
$f(t)$	-	Time dependence of the deflection function
M	-	Bending moment
m	-	Mass
$P(t)$	-	Time dependent excitation force
P_o, P_t	-	Amplitudes of the static and dynamic part of the excitation force
P_{cr}	-	Static buckling force
T	-	Period of the excitation force
t	-	Time variable
X	-	Free vibration eigenfunction (spatial dependence of the deflection function)
$w(x,t)$	-	Deflection
β	-	Displacement functions (modes)
δ	-	Dirac - delta function
δ_{jk}	-	Kronecker delta symbol
Ω, μ	-	Parameters in the Hill's equation
ω	-	Free vibration frequency
θ	-	Frequency of the excitation force
θ_*	-	Critical frequency
A,B,C	-	Square matrices
I	-	Unit matrix
K,M,G	-	Stiffness, mass and stability matrix

REFERENCES

1. Bolotin, V. V., The Dynamic Stability of Elastic Systems, Holden-Day, Inc., San Francisco, 1964.

2. Krajcinovic, D., Herrmann, G., "Stability of Straight Bars Subjected to Repeated Impulsive Compression", AIAA J., Vol. 6, No. 10, October, 1968. Also, Northwestern Univ., Structural Mechanics Lab, Tech. Report No. 67-8, December,1967 1967.

3. Krajcinovic, D.,Herrmann, G., "Parametric Resonance of One-Dimensional Structures Subjected to Periodic Impacts", Northwestern University, Structural Mechanics Lab, Tech. Report No. 68-1, February, 1968.

4. Zemanian, A. H., Distribution Theory and Transform Analysis, McGraw-Hill, Inc., New York, 1965.

5. Krajcinovic, D., "Dynamic Stability of Elastic Systems Subjected to Periodic Impulsive Loading", Ph.D. Dissertation, Northwestern University, June 1968.

6. Brown, J. E., Hutt, J. M., Salama, A. E., "Finite Element Solution to Dynamic Stability of Bars". AIAA J. Vol. 6, No. 7, July, 1968.

7. Mostaghel, N., Sackman, J. L., "Stability of Some Non-Linear Systems", Structural Engineering Laboratory, University of California, Berkeley, Report No. 68-2.

SHOCK ANALYSIS OF FLUID SYSTEMS USING ACOUSTIC IMPEDANCE AND THE FOURIER TRANSFORM; APPLICATION TO WATERHAMMER PHENOMENA

Arthur A. Winquist, U. S. Air Force, Norton Air Force Base, San Bernardino, California

and

Raymond C. Binder, University of Southern California, Los Angeles, California

The Fourier transform technique is presently used in analysis of electrical and mechanical systems. This technique has not been developed significantly for acoustical and fluid systems. This paper focuses attention on the new problem of the application of the Fourier transform method to fluid systems. From a technical and an educational viewpoint, such application would provide a synthesizing technique to integrate overall understanding of shock and vibration phenomena. An important general problem in practice is the transient response of a liquid system subjected to a shock input, due to a variable constriction or changing valve condition in the line. This type of problem is frequently classed as waterhammer or fluid hammer. Some experimental data are available for various waterhammer cases. Using acoustic impedance and the Fourier transform in a digital computer program, waterhammer excess pressure head resulting from valve closure at the end of a straight pipe was calculated for several cases. Results of this theoretical analysis are compared with experimental data and with results using traditional waterhammer solution techniques. The acoustic impedance-Fourier transform technique proved to be a completely valid method of calculating system excess pressure head for the waterhammer cases discussed. Calculated excess pressure head was closely comparable to the excess pressure experienced in actual experimental tests and the excess pressure head using traditional solution techniques. The Fourier technique satisfies an existing requirement for an alternate approach to the present laborious methods used in calculating waterhammer excess pressures. For one familar with the use of the Fourier transform for the analysis of mechanical and electrical transients, the extension to fluid systems is a relatively simple matter. This method can be applied to various fluid power and control systems, for small or large pipes.

INTRODUCTION

Prior to development of the digital computer, various analytical and empirical methods were used in approaching the solution of vibration and shock problems for mechanical, electrical and fluid systems. Development and use of the digital computer has lead to a quest for development of more general and more suitable methods for the analysis of various shock and vibration problems. Desired is a solution technique which not only would offer technical advantages, but which, from an educational viewpoint, would integrate overall understanding of shock and vibration phenomena. One such synthesizing technique entails use of the Fourier series and Fourier integral.

Fourier series - Fourier integral solution techniques have become well established in analysis of electrical systems and to a somewhat lesser extent have been used for mechanical systems analysis. This method, however, has not been developed significantly for acoustical and fluid systems.

Following are presented theory involved in development of linearized acoustic impedance relationships for liquid and gaseous fluid system elements and Fourier transform computational techniques used in computation of excess pressure induced within a piping system as a result of valve closure. The acoustic impedance--Fourier transform solution technique is then applied to five waterhammer cases to determine the transient excess pressure head resulting at a valve as a result of its closure. These results are compared with experimental results and with computational results obtained by both traditional waterhammer solution techniques and Streeter's characteristic equation technique.

ACOUSTIC IMPEDANCE DEVELOPMENT

The acoustic impedance, Z, of a fluid system subjected to sound pressure wave input is defined as the ratio of fluid excess pressure, p, to the fluid volume velocity, q, resulting from the excess pressure:

$$Z = \frac{p}{q} \quad . \tag{1}$$

The volume velocity is the product of the fluid mean velocity and system cross-sectional area at a given point in the system. The excess pressure, p, is the incremental change in pressure caused by the sound pressure wave.

The acoustic impedance of a system element is developed from the basic differential equations governing fluid flow considering external and internal forces acting on the fluid.

In order to develop useable acoustic impedance relationships for fluid system elements of varying geometry, several simplifying approximations are commonly made in order to preserve analytical linearity. The system must then, of course, satisfy these limitations.

Applicable linearizing simplifications may be enumerated as:

1. The fluid is homogeneous and isotropic.
2. The fluid is elastic.
3. The sound pressure waves are of relatively infinitesimal amplitude.

a. For gases, the magnitude of the excess pressure of the sound pressure wave is small compared with the total pressure, p_t, of the fluid. Such a small magnitude excess pressure, normally requires that $p < p_t/20$ [1].

b. In the case of liquids, pressure magnitudes must not cause fluid cavitation [2].

4. Fluid volumetric changes are small compared with total fluid volume. This assumption generally requires that $\Delta V < V/20$ [1], where V is the total fluid volume and ΔV is the incremental change in fluid volume caused by the magnitude of the excess pressure p.
5. Fluid mean pressure and density are constant. This requirement is valid for fluid mean average flow velocity less than Mach 0.2 to 0.3 [1]. Flow through the system can then be assumed essentially incompressible and consequently does not affect sound propagation.
6. There exists negligible heat exchange in the audible frequency range. During sound propagation, fluid compressions and expansions are essentially adiabatic.
7. Sound is transmitted by plane waves of frequency less than the transverse fundamental frequency; higher order oscillation modes are very rapidly attenuated. This assumption is valid for $ka < \pi/2$, where ka is a non-dimensionalized wave propagation constant equal to the product of ω, the radial frequency, and a, the tube radius, divided by c, the pressure wave propagation velocity.

The general dynamic wave equation of a fluid in a tube may be determined by summing inertial, frictional and pressure forces on a cylindrical volume element as shown in figure 1.

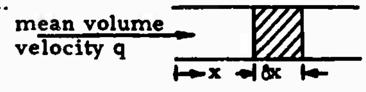

Figure 1. --Cylindrical volume element

The wave equation is then expressed as

$$\rho \frac{\partial^2 q}{\partial t^2} + r_m \frac{\partial q}{\partial t} - B \frac{\partial^2 q}{\partial x^2} = 0 \qquad (2)$$

where ρ is the mean mass density, r_m is the coefficient of mechanical viscous friction per unit area per unit length, B is the fluid bulk modulus of elasticity, and x, δ x, and t signify distance, incremental distance and time.

Viewing the input velocity to be a result of a pressure wave input, the progressive wave solution of this partial differential equation can be written as

$$\dot{\xi} = \dot{\xi}(0)\, e^{j\omega(t \pm \frac{x}{c_1})} = \dot{\xi}(0)\, e^{j\omega t}\, e^{\pm k_d x} \qquad (3)$$

where ξ is the fluid displacement in the pressure wave, $\dot{\xi}$ is the fluid velocity in the pressure wave, and c_1 is the sound pressure propagation velocity in a dissipative fluid. ω is angular frequency, and k_d is the damped wave propagation constant.

Fluid system impedance can be developed initially by considering the force balance on a tube of cross-sectional area S, one end of which is closed with a piston of acoustic impedance Z_L, the other end enclosed with a piston of acoustic impedance Z_p, driven by an arbitrary force $F_o e^{j\omega t}$, figure 2.

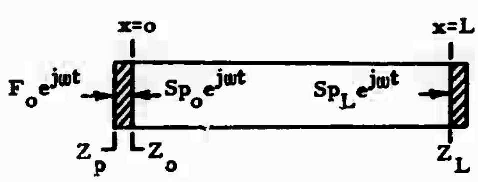

Figure 2.--- Tube impedance

Fluid flow in the tube caused by the externally applied force is governed by the continuity relationship

$$p = -B \frac{\Delta V}{V} = -B \frac{\partial \xi}{\partial x} \qquad (4)$$

and the general dynamic wave equation.

Combining the continuity equation, the dynamic wave equation and the progressive wave equation solution, realizing that $c^2 = B/\rho$, yields

$$p_o = p_L \cosh k_d L + \rho c \dot{\xi}_L \sinh k_d L, \qquad (5)$$

$$\dot{\xi}_o = p_L \frac{1}{\rho c} \sinh k_d L + \dot{\xi}_L \cosh k_d L \qquad (6)$$

when substituting boundary conditions at x = O, x = L and determining coefficients Use of the expressions for p_o and $\dot{\xi}_o$ and evaluation of p_L and $\dot{\xi}_L$ leads to expressions for tube impedance.

The above analysis implies that the tube wall is sufficiently rigid to prevent wall vibration; the tube wall impedance approaches an infinite value. The assumption of infinite wall impedance is valid when the magnitude of the fluid compressibility effect is much greater than the effect of wall elasticity. D'Souza [3] shows that for small diameter pipes subjected to waterhammer pressures the tube walls may be assumed rigid, although in performing calculations, the theoretical speed of sound propagation must be decreased by considering wall elasticity.

Thus in place of c would be substituted c_2, the pressure wave propagation velocity in non-rigid pipe. Parmakian [4] expresses c_2 as

$$c_2^2 = \frac{c^2}{1 + \frac{2abB}{Eh}} \qquad (7)$$

where E is Young's modulus and h is the pipe wall thickness. The pipe mounting factor, b, is shown in figure 3.

b	PIPE MOUNTING CASE
$\frac{5}{4} - \nu$	Straight single pipe supported at one end
$1 - \nu^2$	Straight single pipe supported at both ends
$1 - \frac{\nu}{2}$	Series pipes connected by expansion joint

Figure 3.-- Water pipe mounting factor b as related to Poisson's Ratio ν

The impedance of the tube of figure 2 as viewed from the point of application of the externally applied force, the driving point impedance, is calculated from the pressure, p_o, and the wave velocity, $\dot{\xi}_o$, relationships. Defining Z_{oo} to include both the end piston acoustic impedance Z_p and the tube impedance $Z_o = p_o/S\dot{\xi}$,

$$Z_{oo} = Z_p + \frac{\rho c}{S} \frac{Z_L + \frac{\rho c}{S} \tanh k_d L}{\frac{\rho c}{S} + Z_L \tanh k_d L} \qquad (8)$$

This linearized expression for acoustic impedance is valid for $ka < 0.25$.

The above relationships can be extended to determine the impedances of various acoustical elements such as orifices, frictional elements, cavities, and side branches. Knowing the acoustic impedances of various acoustical elements, the overall acoustic impedance of a composite system may be determined. As an example, the overall impedance of a fluid in a piping system consisting of several segments of pipe in series, each segment with a different diameter and wall thickness, would be calculated by algebraically adding the impedance of each individual segment.

COMPUTATION FEATURES

Fourier transform. The Fourier spectrum of system response to an arbitrary input f(t) can be determined knowing the system impedance $Z(\omega)$ and the Fourier transform $F(\omega)$ of the time input to the system. System time response to an arbitrary input may then be determined from the system frequency response by means of the inverse Fourier transform.

Crede and Harris [5] and Huss and Donegan [6] discuss a numerical integration technique to be used to accomplish the Fourier transform,

$$F(\omega) = \int_{-\infty}^{\infty} f(t)\, e^{-j\omega t}\, dt \qquad (9)$$

and the inverse Fourier transform

$$f(t) = \frac{1}{2\pi} \int_{-\infty}^{\infty} F(\omega)\, e^{j\omega t}\, d\omega \qquad (10)$$

for the situation $f(t) = 0$ when $t < 0$.

The frequency spectrum $F(\omega)$ of the time related input f(t) is calculated from its real and imaginary parts. The function f(t) is fitted with a step function approximation consisting of n intervals with abscissa width Δt and ordinate f_n.

The frequency spectrum $F(\omega)$ is then computed using the equations,

$$\mathrm{Re}\,[F(\omega)] = \Delta t \sum_n f_n \frac{\sin G \cos (2n-1)G}{G}, \qquad (11)$$

$$\mathrm{Im}\,[F(\omega)] = -\Delta t \sum_n f_n \frac{\sin G \sin (2n-1)G}{G}, \qquad (12)$$

$$G = \frac{\Delta t}{2}\,\omega, \qquad (13)$$

$$[F(\omega)]^2 = \{\mathrm{Re}[F(\omega)]\}^2 + \{\mathrm{Im}[F(\omega)]\}^2 \qquad (14)$$

The time input curve may be fitted graphically or it may be approximated numerically using a mathematical relationship such as

$$f_n = \frac{1}{12}\{5[f(t)]_{n-1} + 8[f(t)]_n - [f(t)]_{n+1}\} \qquad (15)$$

which approximates the actual curve with a parabolic fit.

The time response of the system to an arbitrary input is obtained by calculating the inverse transform of the real part of the frequency response $R(\omega)$ of a system of impedance $Z(\omega)$ to an input $F(\omega)$. Re $[R(\omega)]$ is calculated in the frequency domain and is then approximated by a step function consisting of n intervals of abscissa width $\Delta\omega$ and ordinate R_n such that $n \cdot \Delta\omega$ equates to the maximum desired frequency ω_m.

The time response r(t) is determined by the equations,

$$r(t) = \frac{2}{\pi} \Delta\omega \sum_n R_n \frac{\sin G \cos (2n-1)G}{G}, \qquad (16)$$

$$G = \frac{\Delta\omega}{2}\, t. \qquad (17)$$

The frequency response curve may be fitted graphically or as an alternative, numerically by using a parabolic expression such as

$$R_n = \frac{1}{12}\{5[\mathrm{Re}R(\omega)]_{n-1} + 8[\mathrm{Re}R(\omega)]_n - [\mathrm{Re}R(\omega)]_{n+1}\}. \qquad (18)$$

Volume velocity. To apply the Fourier transform technique to water flow through a pipe and gate valve requires consideration of the nature of the actual fluid flow before, during and after control valve movement and the resultant input volumetric flow to the system.

For each of the cases studied, the fluid volume velocity was steady prior to closing the control valve or gate. The source material for each of the cases indicated that the cross-sectional area of the fluid path through the valve varied linearly with time on valve movement, as shown in figure 4, where

$$\tau = \frac{S_g(t) - S_g(T)}{S_g(O) - S_g(T)} .$$

$S_g(O)$, $S_g(T)$ and $S_g(t)$ are respectively the valve cross-sectional area at start of valve movement, at termination of valve movement and at a variable time t between start and termination of valve movement.

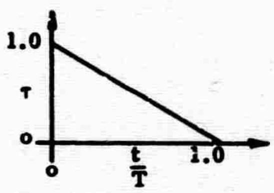

Figure 4. --Variation of valve area with time

Actual fluid flow varies from the initial steady flow before valve closure to the final steady flow after termination of valve movement. The change of volume velocity is of course due to the change of valve cross-sectional area.

The wave equations developed above relate system parameters to an input volume velocity or pressure wave. The resultant volume velocity input for each of the hydraulic system cases studied may be viewed as that input which would be required to decrease the actual fluid flow from the initial steady flow before gate closure to the final steady flow after gate closure. The resultant volume velocity input is derived from the relationship

Initial steady flow + resultant input flow = actual fluid flow. (20)

Thus, the volume velocity input to the system is expressed as the actual volumetric flow rate minus the initial steady-state flow rate.

The relationship between the actual flow rate through the valve, q(t), the initial steady state flow rate, g(O), the final steady state flow rate, q(T), and the resultant input flow rate,

$$\begin{aligned} &q(t) - q(O), \quad O \le t \le T, \\ &q(T) - q(O), \quad T \le t. \end{aligned} \qquad (21)$$

are depicted in figure 5. In figure 5, the initial and actual flow rates towards and through the valve are evaluated as negative since, as shown in figure 6, pipe distance is measured from the valve end of the pipe.

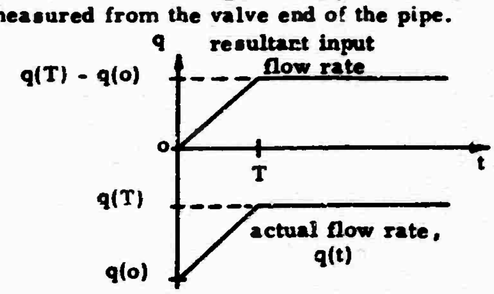

Figure 5.--Determination of Resultant Input Flow Rate

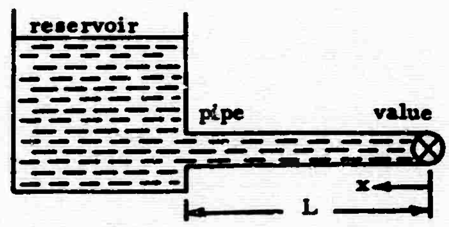

Figure 6. -- Reservoir-Pipe-Valve System Configuration

Two separate categories of waterhammer excess pressure fluctuations during and after gate closure are considered. The first category is that of a straight pipe where the gate closing time, T, is less than or equal to the pressure wave reflection time, RT, the time for the excess pressure wave to travel from the gate to the opposite end of the pipe at the reservoir and then to return to the original starting point at the gate. The second category considered is that of a straight pipe in which the gate closing time is greater than the reflection time.

Volume velocity input, $T \le RT$. For those cases in which the time of valve closing is less than or equal to the reflection time, the fluid volumetric discharge is not effected by pressure fluctuations caused by reflected pressure waves. Using the basic relationship, velocity equals $\sqrt{2gh}$, the volume velocity discharge, q(t), through the gate during the time of gate movement is expressible as

$$q(t) = \frac{S_g(t)}{S_g(O)} \left[\frac{H(t) + \Delta H(t)}{H(t)}\right]^{\frac{1}{2}} q(O) \qquad (22)$$

where $S_g(t)$ is the open gate area at time t. $S_g(O)$ is the initial gate flow area. $\Delta H(t)$ is the time related excess pressure and $H(t)$ is the total steady state head pressure at a given time t. Assuming an essentially linear variation of flow area during gate movement from $t = O$ to $t = T$,

$$S_g(t) = S_g(O) \cdot \tau = S_g(O)\left(1 - \frac{t}{T}\right), \tag{23}$$

this expression becomes

$$q(t) = \frac{T - t}{T}\left[1 + \frac{\Delta H(t)}{H(t)}\right]^{\frac{1}{2}} q(O). \tag{24}$$

As a first order approximation. this equation may be simplified to

$$q(t) = q(O)\,\frac{T - t}{T}. \tag{25}$$

Expressing the actual fluid flow, q(t), as

$$q(t) = \text{AMP}\left(1 - \frac{t}{T}\right) + q(T), O \le t \le T, \tag{26}$$

$$q(t) = q(T), \qquad T \le t, \tag{27}$$

where AMP is the change of fluid volume velocity from start to termination of valve movement, and q(T) is the volume velocity after termination of valve movement, the resultant input to the system becomes

$$f(t) = -\text{AMP}\left(\frac{t}{T}\right), O \le t \le T, \tag{28}$$

$$f(t) = -\text{AMP}, \qquad T \le t. \tag{29}$$

Using a "closed form" solution of the direct Fourier Transform, this time input to the piping system can be expressed in the frequency domain as

$$F(\omega) = AA + j\,BB \tag{30}$$

where

$$AA = \frac{\text{AMP}}{T\omega^2}(1 - \cos\omega T), \tag{31}$$

$$BB = \frac{\text{AMP}}{T\omega^2}\sin\omega T. \tag{32}$$

Volume velocity input, T > RT. When the valve closing time is greater than the pressure wave reflection time, the actual fluid flow is determined from a superposition of the flow resulting from the change of valve cross-sectional area and the flow resulting from the excess pressure head caused by the reflected pressure wave impinging on the gate.

The resultant volume velocity input to the system as a result of the change in the valve area in time T is expressible as

$$f(t) = \text{AMP1}\,\frac{t}{RT}, \quad O \le t \le T, \tag{33}$$

$$f(t) = \text{AMP1}\,\frac{T}{RT}, \qquad T \le t, \tag{34}$$

$$F(\omega) = \frac{\text{AMP1}}{RT\,\omega^2}(\cos\omega T - 1) - j\,\frac{\text{AMP1}}{RT\,\omega^2}\sin\omega T \tag{35}$$

where AMP1 is the positive resultant input amplitude change during the time RT of a single reflection. At the lower frequencies encountered in waterhammer analysis, complete wave reflection may be assumed at the reservoir end of the pipe.

When the initial volume velocity input wave returns to the gate a percentage of its amplitude is reflected off the closed part of the gate. To account for this occurrence a second resultant volume velocity input must be applied at the gate end of the pipe, expressible as,

$$f(t) = \text{AMP1}\,\frac{t - RT}{RT}\,\text{FACTOR}(t), \tag{36}$$

$$RT \le t \le T,$$

$$f(t) = \text{AMP1}\,\frac{t - RT}{RT}, \; T \le t \le \left\{\left[\frac{T}{RT}\right] + 1\right\}RT, \tag{37}$$

$$f(t) = AMPl\left[\frac{T}{RT}\right], \left\{\left[\frac{T}{RT}\right]+1\right\}RT \le t, \quad (38)$$

where FACTOR (t) is a multiplicative factor to account for incomplete pressure wave reflection at the partially open gate, and $\{[T/RT] + 1\}$ RT denotes the first complete reflection time after time T. For those cases where the excess pressure is less than Joukowsky's maximum surge pressure, Billings [7] approximates the reflection coefficient as

$$FACTOR(t) = \frac{1 - \frac{JMS}{2H(O)}\tau}{1 + \frac{JMS}{2H(O)}\tau}, \quad (39)$$

$$JMS = \left| \frac{(c_2)(u)}{g} \right|, \quad (40)$$

where JMS is Joukowsky's maximum surge pressure and H(O) is the static head pressure. A linear variation of τ for valve movement from the open pipe area to the full closed position yields

$$FACTOR(t) = \frac{1 - \frac{JMS}{2H(O)}\left(1 - \frac{t}{T}\right)}{1 + \frac{JMS}{2H(O)}\left(1 - \frac{t}{T}\right)}. \quad (41)$$

The reflective factor may be more simply approximated by

$$FACTOR(t) = \frac{\text{Valve Closed Area}}{\text{Pipe Area}}. \quad (42)$$

For the case where the valve closes linearly from the open pipe area to the full closed position,

$$FACTOR(t) = \frac{t}{T}, \quad 0 \le t \le T. \quad (43)$$

Starting at time equal to twice the reflection time, 2RT, the resultant volume velocity wave superimposed starting at time RT, is reflected off the closed part of the gate resulting in an additional resultant input to be superimposed upon the previous, and written,

$$f(t) = FACTOR(t) \cdot f(t - RT), \; 2RT \le t \le T, \quad (44)$$

$$f(t - RT) = AMPl\,\frac{t - 2RT}{RT}\,FACTOR(t - RT), \quad (45)$$

$$f(t) = f(t - RT), \quad T \le t \le \left\{\left[\frac{T}{RT}\right]+1\right\} RT, \quad (46)$$

$$f(t) = f(T - RT), \; \left\{\left[\frac{T}{RT}\right]+1\right\} RT \le t. \quad (47)$$

Each succeeding reflection time increment RT results in an additional input wave. The effect of each successive input on the excess pressure may be obtained by superimposing each input up to the first complete reflection time after termination of gate movement. For times in excess of $\{[T/RT] + 1\}$ RT, a steady input equivalent to the negative of the change in steady-state fluid volume velocity from start to termination of gate movement accounts for decrease of fluid flow.

System impedance. The driving point impedance, equation (8) was used in computing excess pressure response, where

$$k_d = \frac{r_m L}{2\rho c_2} + j\,kL, \quad (48)$$

$$r_m = \frac{\sqrt{2\rho\mu\omega}}{a}, \quad (49)$$

and μ is the coefficient of viscosity.

For those cases in which the system is composed of a number of pipes of varying diameters and lengths in series, the diameters areas, lengths, wave propagation velocities and impedances of the individual pipes were appropriately dimensioned in the computer programs.

At the reservoir end of the piping system the impedance, Z_L, was expressed as

$$Z_L = \frac{\rho c a}{S} \frac{(ka)^2}{2} + j \frac{\rho c a}{S} \frac{8}{3\pi} ka \tag{50}$$

which is the relationship for a tube with end flange dimension greater than the wavelength and opening into ambient fluid.

APPLICATION

Five cases were studied. In four cases the gate closing time was less than or equalled the acoustic wave reflection time. In one case the pressure wave reflection time was less than the gate closing time. The FORTRAN programs were run on a Honeywell 800 digital computer.

Case 1. Streeter [8] applies the characteristic equation technique to the solution of several waterhammer cases. His systems consist of various straight pipe configurations with different valve closing times. For the case where the gate closing time was less than the reflection time, his system consisted of a straight pipe of 200 feet length with constant diameter of 0.0365 feet and constant 0.00261 feet pipe wall thickness located between the reservoir and the closing valve. The valve clsoing time was 0.022 second as compared to the pressure wave reflection time of 0.0961 second. Steady state velocity before start of valve closure was 2.77 feet per second.

In order to calculate the excess pressure wave propagation velocity, using equation (7), the pipe mounting factor was expressed by

$$\frac{5}{4} - \nu = \frac{5}{4} - 0.30 = 0.95 \ .$$

The resultant volume velocity input to the system was expressed using equations 28 - 32. Equations 8, 48 - 50 were used to obtain the acoustic impedance $Z(\omega)$ of the system.

To numerically determine the inverse Fourier transform of the system response frequency spectrum, each frequency interval equal to the inverse of the reflection time, was divided into 120 increments. The frequency increment was

$$\Delta f = \frac{1}{120} \frac{1}{RT} = 0.0867 \text{ cps} \qquad \Delta ka = 0.239\,(10)^{-5}. \tag{51}$$

To assure computation to a sufficiently high frequency, the numerical integration was performed over 1600 such increments to include up to 138 cycles per second, $ka = 0.00382$.

The excess pressure head as determined by use of the system impedance and the Fourier Transform technique is graphed in figure 7 along with the excess pressure head as determined by Streeter's characteristic equation technique.

To determine the excess pressure from Streeter's graph, the 350 feet static pressure head was subtracted from the total pressure head calculated by Streeter.

For this case, the pressure wave reflection time, RT, was 0.0961 second as compared with the gate closing time of 0.022 second.

Case 2. For the case where the gate closing time equalled the pressure wave reflection time, Streeter's [8] system consisted of a straight pipe of 200 feet length, constant diameter of 0.0365 feet and a 0.00261 feet pipe wall thickness located between the reservoir and closing gate. Steady state velocity before valve movement was 2.77 feet per second. The valve closed in 0.09 second.

The relationships used to determine the pipe mounting factor, the wave propagation velocity, the resultant volume velocity input, the system impedance and the real part of the frequency response are the same as those used for case 1.

Similar to case 1, the frequency increment used to perform the inverse Fourier transform was

$$\Delta f = \frac{1}{120} \frac{1}{RT}$$

which equated to $\Delta f = 0.0885$ cycles per second, $\Delta ka = 0.239\,(10)^{-5}$. Summing over 1600 such increments, frequency response up to 141 cycles per second, $ka = 0.00382$, was considered.

Excess pressure head response as determined by the Fourier transform technique is plotted in figure 8 together with the response as calculated using the characteristic equation technique.

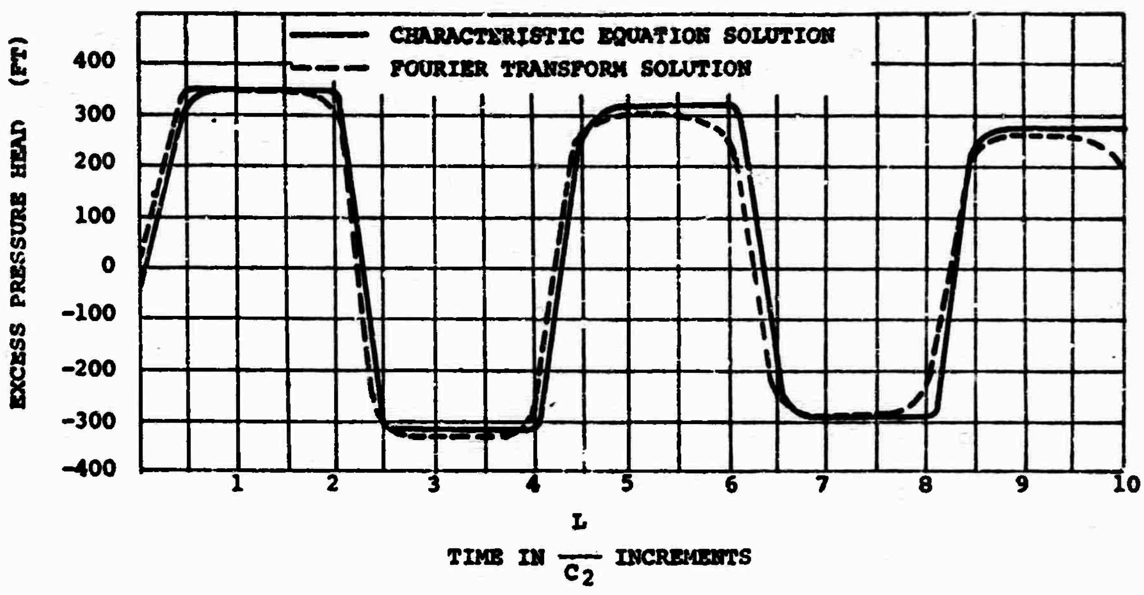

Figure 7. -- Case 1, Excess Pressure Response, T < RT

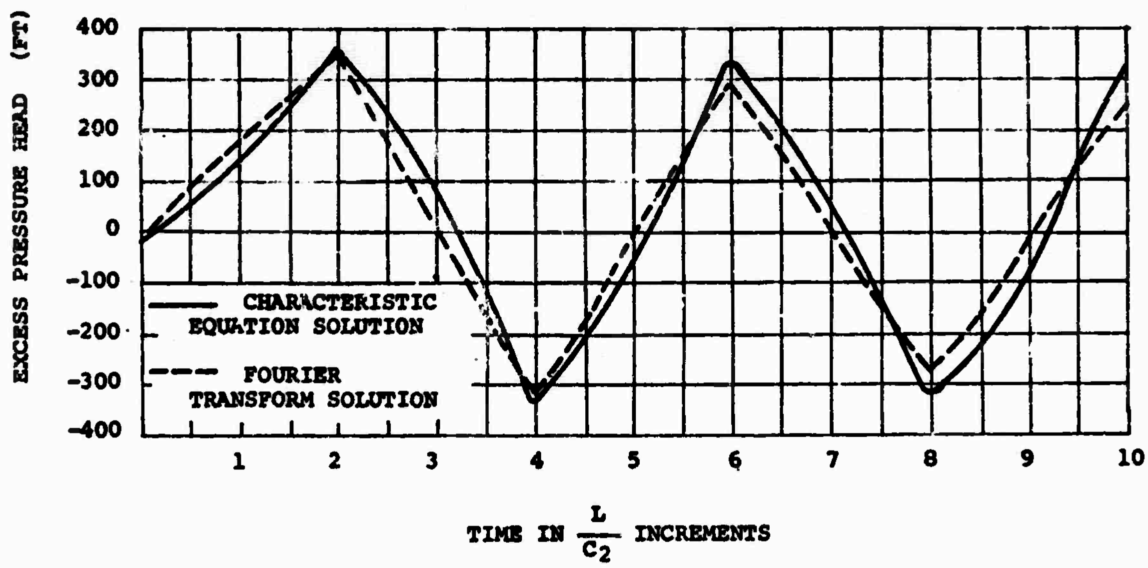

Figure 8. -- Case 2, Excess Pressure Response, T = RT

Case 3. Billings [7] analyzes the waterhammer phenomena occurring at the Serra Penstock number 1 by means of the simultaneous equation technique. Excess pressure as calculated by the Fourier Transform technique is compared with the actual pressure and calculated pressure as presented in the article "High-Head Penstock Design ".

Serra Penstock number 1 consists of pipe of four different diameters and with varying wall thickness anchored at fifteen different points along the 5,335 feet length.

To perform an analysis, the mean wall thickness for the segment of pipe between each anchor was calculated. To determine the excess pressure propagation velocity using the relationship

$$(c_a)_n^2 \le \frac{c^2}{1 + \frac{2a_n bB}{Eh_n}} \qquad (52)$$

where n signifies a selected pipe segment, and to calculate the reflection time for the total pipe length, the pipe was analytically divided into fifteen segments as shown in figure 9. Each segment was chosen to have a constant mean wall thickness and a constant diameter.

Anchor	Length on slope between anchors (feet)	Mean thickness (feet)
–	251	0.175
1	249	0.375
2	200	0.175
3	434	0.460
4	235	0.578
5	277	0.734
6	322	0.846
7	308	1.070
8	448	1.219
9	441	1.219
10	459	1.297
11	342	1.440
12	178	1.580
13	473	1.640
14	238	1.672
15		

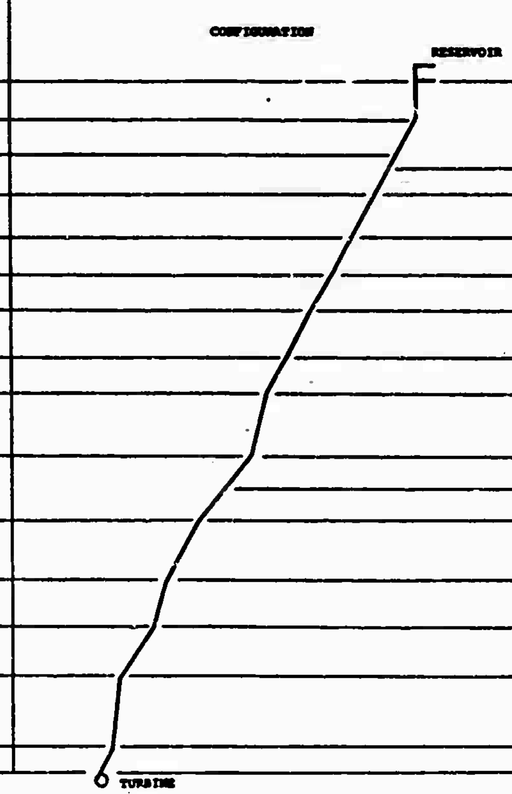

z_n	Length of selected pipe segment (feet)	Diameter (inches)
z_1	640	61.0
z_2	140	55.0
z_3	434	
z_4	235	49.2
z_5	277	
z_6	322	
z_7	308	
z_8	448	
z_9	220	
z_{10}	221	43.1
z_{11}	459	
z_{12}	342	
z_{13}	378	
z_{14}	473	
z_{15}	238	

Figure 9. -- Physical Parameters of Serra Penstock, Number 1

The relationship

$$b = 1 - \frac{\nu}{2} = 0.85 \qquad (53)$$

was used to determine the pipe mounting factor.

System impedance was expressed using the relationship

$$Z_n(\omega) = \frac{\rho(c_2)_n}{S_n} \frac{Z_{n-1} + \frac{\rho(c_2)_n}{S_n} \tanh (k_d L)_n}{\frac{\rho(c_2)_n}{S_n} + Z_{n-1} \tanh (k_d L)_n} \qquad (54)$$

where n varied in units from one to fifteen.

In accordance with the source material, the valve closing time used was 1.010 seconds and the change of volume velocity was 14.20 cubic feet per second.

To perform the inverse Fourier transform each frequency interval equal to 1/RT was divided into 600 increments. Thus, the integration interval Δf was 0.000618 cycle per second, $\Delta ka(15) = 0.164\ (10)^{-5}$. Integrating over 13,000 such increments evaluated frequencies up to 8 cycles per second, ka (15) = 0.02133. Excess pressure as determined by use of the Fourier transform is plotted in figure 10 together with the actual excess pressure and the pressure as analytically determined by Billings.

For this case, the pressure wave reflection time was 2.696 seconds as compared with the gate closing time of 1.010 seconds.

Case 4. Case 4 calculations were performed on the same penstock as case 3. Thus the pipe parameters and mathematical relationships used were the same as those listed for case 3.

The valve closing time was 0.220 seconds and the total change in volume velocity was 15.5 cubic feet per second.

Each frequency interval of 1/RT cycles in the frequency spectrum was divided into 700 segments to yield a frequency segment Δf = 0.000530 cycle per second, $\Delta ka(15) = 0.141(10)^{-5}$. Summing over 13,000 such increments included frequencies up to approximately seven cycles per second, ka(15) = 0.01828.

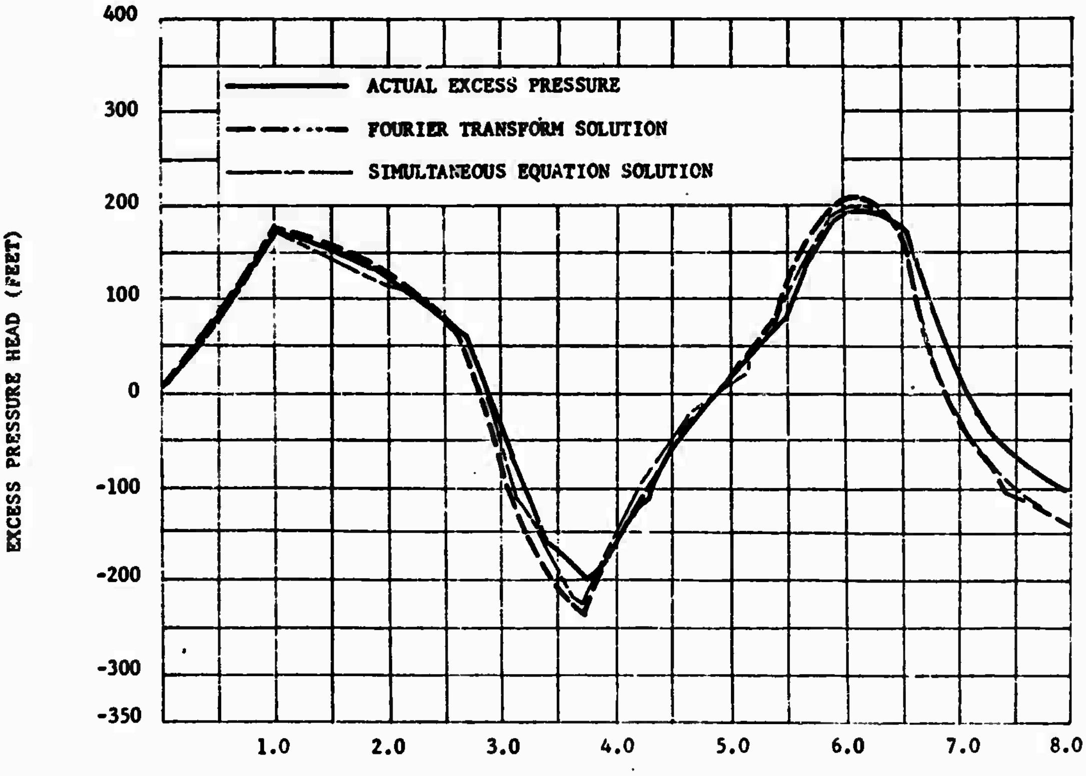

Figure 10.-- Case 3, Excess Pressure, T<RT

Excess pressure calculated is shown in figure 11, along with the actual excess pressure and simultaneous equation derived excess pressure.

Case 5. In discussing waterhammer phenomena where the gate closing time exceeded the pressure wave reflection time Streeter's [8] system consisted of a straight pipe of length 300 feet, diameter 0.0365 feet and wall thickness of 0.0026 feet located between the reservoir and the closing valve.

The resultant volume velocity input to the system was expressed using equations 33 - 38, 42 - 47.

To numerically perform the inverse Fourier transform, the frequency increment used was

$$\Delta f = \frac{1}{200} \frac{1}{RT} = 0.0354 \text{ cps} ,$$
$$\Delta ka = 0.96\ (10)^{-6}. \tag{55}$$

The numerical integration was performed over 1900 such increments up to approximately 67 cycles per second, ka = 0.001816. The calculated excess pressure values are plotted in figure 12, together with the excess pressure head as determined from Streeter's characteristic equation solution technique. The static head pressure was subtracted from Streeter's calculated total pressure to arrive at an equivalent excess head pressure.

For this case the pressure wave reflection time, RT, was 0.1413 second as compared to the gate closing time of 0.2836 second.

DISCUSSION OF RESULTS

Application of acoustic impedance and the Fourier transform technique to the five waterhammer cases considered in this report yielded excess pressure head closely comparable to the excess pressure experienced in actual experimental tests, cases 3 and 4, the excess pressure head as calculated using the simultaneous equation technique, cases 3 and 4, and the excess pressure head determined from application of the characteristic solution technique, cases 1, 2, and 5. The acoustic impedance--Fourier transform technique proved to be a completely valid method of calculating system excess pressure head using algebraic relationships and the resulting simplified computer programming. Continued investigation must be performed to delineate criteria for application of this technique to waterhammer phenomena and to apply the technique to other than waterhammer problems.

Since this technique requires use of a numerical integration technique, it is mandatory that the integration interval be chosen sufficiently small to produce valid results and that the maximum frequency for the inverse Fourier transform be chosen to ensure consideration of all frequencies which would appreciably effect the excess pressure produced. To perform the inverse Fourier transform the frequency increment used for each of the five cases is summarized in table 1. Frequency increments of width substantially greater than those listed did not provide valid excess pressure head results.

Table 1 - Numerical Integration Frequency Increments and Cut-off Frequencies

Case	Δka	Δf (cps)	f_{max} (cps)	ka_{max}
I	$0.239(10)^{-5}$	0.0867	138.78	0.00382
II	$0.239(10)^{-5}$	0.0885	141.57	0.00382
III	$0.164(10)^{-5}$	0.000618	8.04	0.02133
IV	$0.141(10)^{-5}$	0.00053	6.89	0.01828
V	$0.960(10)^{-6}$	0.0354	67.25	0.001816

This analysis did not attempt to maximize the magnitude of the frequency increment required to assure proper system pressure response when performing the inverse Fourier transform nor did it attempt to minimize the maximum frequency to which the inverse Fourier transform should be performed.

The straight pipe systems of cases 1 through 4, for which the pressure wave reflection time is greater than the gate closing time, are both sufficiently simple and sufficiently complex to demonstrate the applicability of the impedance-transform solution technique to a wide variety of straight pipe systems. Additional testing is required to investigate the application of the technique to more complex systems such as parallel piping and branches.

In case 5, although the correlation between the excess pressure head response as calculated using the impedance-transform technique and the excess pressure head response determined by Streeter's characteristic equation solution technique is good for this particular case, many more cases and much additional

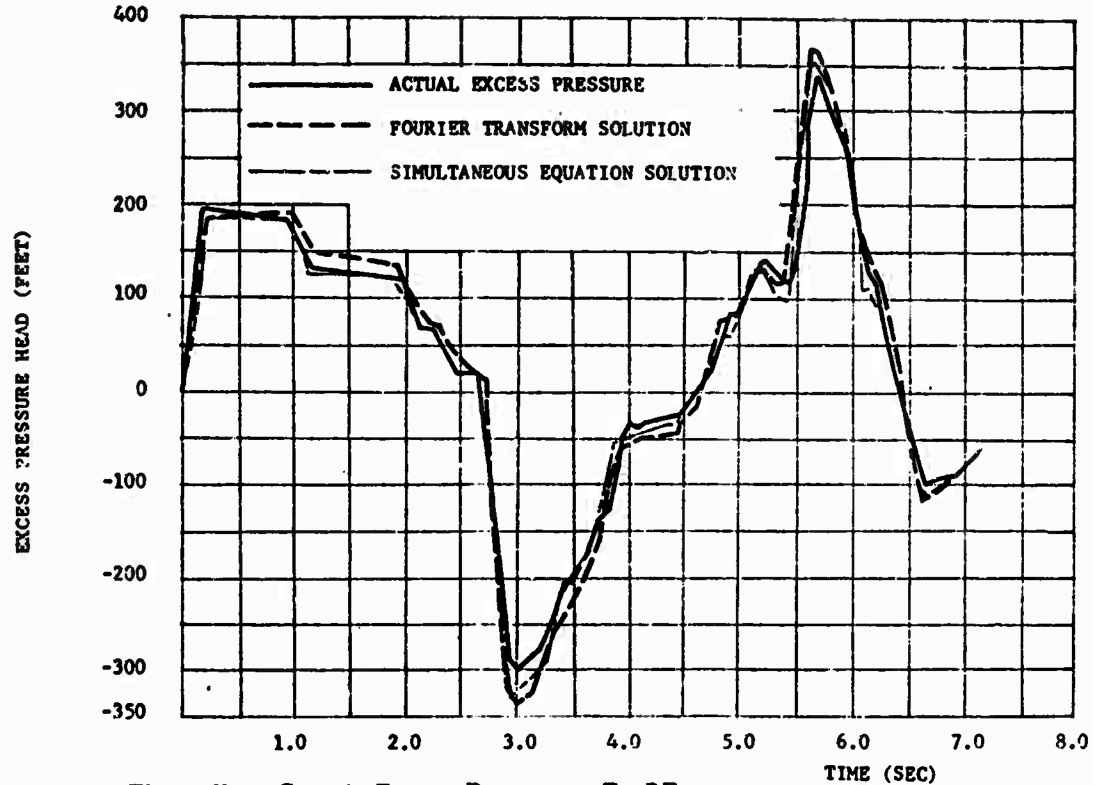

Figure 11. -- Case 4, Excess Pressure, T < RT

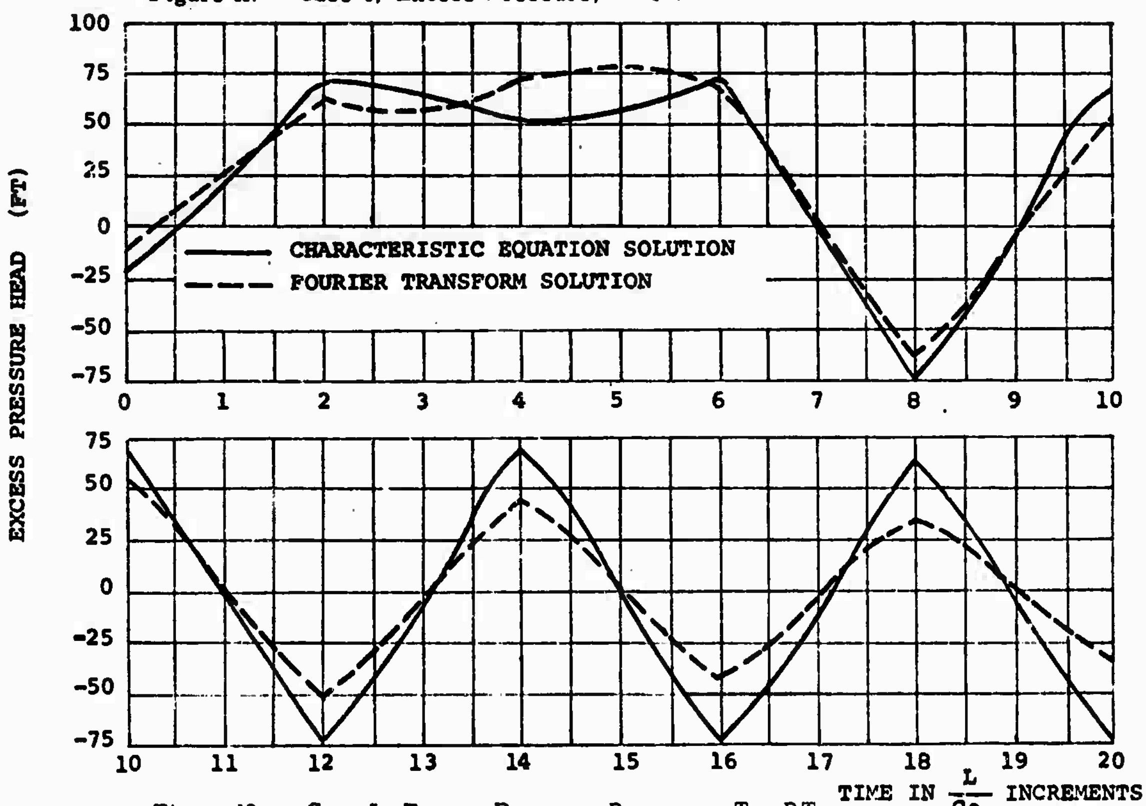

Figure 12. -- Case 5, Excess Pressure Response, T > RT

testing is necessary to validate the theory and to investigate complications introduced by the linear superposition of several reflected waves. It may be seen that as the complexity of a fluid system increases the expression for the fluid volume velocity resultant input can become increasingly complicated.

This paper has discussed the application of the acoustic impedance-Fourier transform technique to waterhammer phenomena since reliable and reproducible waterhammer test data could be readily found in published literature. The theory of application of this technique was, however, developed for a generalized fluid system. The successful application of this technique to waterhammer cases should lead the way to application of the technique to other liquid and gaseous fluid systems.

REFERENCES

1. Goldschmied, F. R., Fox, H. L., and Letham D. C., Analytical Investigation of Fluid Amplifier Characteristics, NASA CR-245, Washington D. C., July 1965.

2. Streeter, V. L. (editor), Handbook of Fluid Dynamics, Section 20, H. M. Paynter, "Transients in Engineering Systems", McGraw Hill Book Co., New York, 1961.

3. D'Souza, A. and Oldenburger, R., "Dynamic Response of Fluid Lines", Journal of Basic Engineering, Transactions ASME, vol 86, 1964, pp 589-598.

4. Parmakian, J., Waterhammer Analysis, Dover Publications, Inc., New York, 1963.

5. Crede, C. E., and Harris, C. M., Shock and Vibration Handbook, McGraw Hill Book Co., New York, 1961.

6. Huss, C. R. and Donegan, J. J., "Tables for the Numerical Determination of the Fourier Transform of a Function of Time and the Inverse Fourier Transform of a Function of Frequency", NACA TN 4073, October 1957.

7. Billings, A. W., Dodkin, D. H., Knapp, F., and Santos, A. Jr., "High-Head Penstock Design", in Symposium on Waterhammer, ASME Committee on Waterhammer, New York, 1949.

8. Streeter, V. L. and Chintu Lai, A. M., "Waterhammer Including Fluid Friction", Transactions ASCE, vol 128, 1963, Part I, pp. 1491-1523.

Mr. Pakstys (General Dynamics Corp.): Did I understand correctly that you did not consider all of the structural effects such as the structural interaction between the pipe and the fluid?

Mr. Winquist: Yes, we did. The written paper will consider the pressure wave propagation velocity along the pipe as a function of the pipe physical structure itself.

Mr. Pakstys: Have all of the effects been considered, including the bending and shell modes of the pipe?

Mr. Winquist: We only considered the bending modes, not the shell modes.

Mr. Dorland (NASA Manned Spacecraft Ctr.): Did you consider the bulk modulus of the fluids in your lines including entrapped air or without entrapped air or air in solution?

Mr. Winquist: No, the criteria we laid down in order to work with linearized acoustic impedances required a continuum of fluid. In other words, there was no trapped air, just one fluid.

Mr. Dorland: Did you try to measure the elasticity of the fluids?

Mr. Winquist: This was strictly an analysis using established experimental data; we did not run any tests ourselves.

Mr. Dorland: I have a similar problem to cope with on a cooling loop in the LEM spacecraft. We find that it is rather severe because we have had to take all the air out of the lines to keep the pumps from cavitating. We find that the theoretical solutions work very well and we are surprised by this. We think the reason is that the actual bulk modulus of the fluid is very close to the theoretical value. These values are close because we deaerate the water for two hours before we put it in. Did you run into any phenomena that might bear on this?

Mr. Winquist: I do not believe so.

DRAG ON FREE FLIGHT CYLINDERS IN A BLAST WAVE

Stanley B. Mellsen
Defence Research Establishment Suffield
Ralston, Alberta, Canada

The free flight method was used to obtain the drag coefficients for circular cylinders in the blast wave from a 500 ton spherical TNT burst. The measurements were made on each of two 3½ inch diameter aluminum cylinders, three feet long, placed at the 12.0 and 8.5 psi peak overpressure locations respectively.

The average drag coefficients obtained over the first 50 milliseconds of the blast wave were 0.67 and 0.48 for the 12.0 and 8.5 psi locations respectively.

NOTATION

- x - horizontal displacement of near end of cylinder
- t - time after shock front hits cylinder
- σ - standard deviation in x
- X - corrected displacement of cylinder
- D - drag force acting on cylinder in blast wave
- m - mass of cylinder
- a - acceleration of cylinder
- V - velocity of cylinder
- U - fluid particle velocity in the blast wave at time t
- U_o - fluid particle velocity directly behind the blast front (t=0)
- p - peak shock overpressure
- p_1 - atmospheric pressure
- c_1 - speed of sound in the air ahead of the blast front
- F - Friedlander pressure decay
- t_+ - positive duration of the blast wave
- a_p - fluid particle acceleration in the blast wave
- C_D - coefficient of drag
- P_D - drag pressure
- q - dynamic pressure at time t
- q_o - dynamic pressure at time t=0
- M - flow Mach number in blast wave
- c_2 - speed of sound in the blast wave at time t
- T_1 - atmospheric temperature ahead of shock front
- R - gas constant
- γ - specific heat ratio
- T_2 - temperature in the blast wave at time t
- T_{2_o} - temperature behind the blast front at t=0
- P_{2_o} - absolute pressure behind shock front at t=0
- P_2 - absolute pressure in the blast wave at time t
- R_e - Reynolds number
- d - cylinder diameter
- ν - kinematic viscosity at time t
- a_c - acceleration coefficient
- a_t - acceleration of fluid relative to cylinder

INTRODUCTION

In August 1968, a 500 ton spherical charge of TNT was detonated at the Defence Research Establishment Suffield. The blast wave, and the effects it produced on various test items, were studied. The overall project was entitled Operation PRAIRIE FLAT.

One of the major Canadian projects in Operation PRAIRIE FLAT was the measurement of the dynamic response of lattice-type masts to blast loading. The masts, which were constructed of aluminum tubing having a circular cylindrical cross-section, were tested in two sizes. Two masts, one 15 feet and the other 30 feet high, were tested at the 12.0 psi location and one mast 15 feet high was tested at the 8.5 psi location. To analyze the response of these structures, it was necessary to know the loading that the blast wave imposed upon them.

A great deal of knowledge has been gained of the aerodynamic drag on cylinders under steady flow conditions, but little is known about it for unsteady flow. Therefore various experiments were devised for measuring aerodynamic drag in Operation PRAIRIE FLAT [1]. One of the methods proposed was the free flight method.

This report describes the results of aerodynamic drag measurements by the free flight method. In the unsteady flow which results from a blast wave of the type produced in Operation PRAIRIE FLAT the aerodynamic drag depends on several flow parameters in a complicated way. As the theoretical prediction or calculation of drag from other measurements is of doubtful accuracy, it is necessary to measure the actual drag at the location of the masts. Hence measurements were made on two circular cylinders fabricated of material similar to that of the masts. The diameter of the cylinders was the same as that of the smallest members of the masts. The other members were only slightly larger and scaling problems were considered unimportant. The cylinders were lightly suspended from the antenna support of each of the two 30 foot masts and their motion in the blast wave was recorded by high speed cine cameras.

The drag coefficients and drag pressures obtained along with the various flow parameters are described herein. A preliminary report [2] on all the aerodynamic measurements made by Suffield in Operation PRAIRIE FLAT has been published.

APPARATUS AND PROCEDURE

Each of the cylinders to be tested consisted of an aluminum alloy pipe 3 feet long and 3.50 inches in diameter with flat metal cover plates fastened to each end. The cover plates were painted so that their quadrants were alternately black and white for easy identification in their photographs. The cylinder on the mast at the 12 psi location weighed 11.19 pounds. The other cylinder weighed 5.58 pounds. The weights of the test cylinders were chosen so that they would travel approximately the same distance in the field of view of the cameras so that maximum accuracy in the displacement data could be obtained for both cylinders. Each cylinder was suspended on two parallel monofilament nylon lines approximately nine feet long which located each cylinder 3.0 feet above the ground in a horizontal position perpendicular to a radial line from the charge centre. Two other monofilament nylon guy lines were used on each cylinder to prevent oscillations due to the wind. These were attached to the antenna support, leeward to the blast, so as not to disturb the cylinder during the blast wave. The suspension system was fabricated from 14 lb. line for the heavier cylinder and 10 lb. line for the lighter cylinder. Preliminary tests indicated that lines of lower strength might fail prematurely.

A 1/4 inch steel marker plate 30 inches high and 36 inches long was anchored in the ground in the vertical plane of the end of each cylinder nearest the camera. These plates were used as a reference from which the cylinder motion was measured. A linear scale three inches wide was painted along the length of the top edge of each marker plate. The scale consisted of alternate black and white stripes each one inch wide. One marker plate along with the corresponding test cylinder suspended in proper position is shown in Fig. 1.

The motion of each cylinder was followed by Fastair cameras running about 600 frames/sec. The cameras were mounted on wooden posts anchored in the ground and gave a field of view slightly over four feet wide with its direction of view along the axis of the cylinder.

DATA ANALYSIS

Film Reading

The film obtained from each of the high speed cameras was read with the aid of a precision film reader to give the total displacement of the cylinder in each frame of the high speed film. The time intervals represented by each frame were 1.80 milliseconds for the experiment nearest ground zero (12.0 psi peak incident overpressure) and 1.54 milliseconds for the other (8.5 psi peak incident overpressure).

The displacement-time data obtained for the two experiments are shown in Figs. 2 and 3. The velocities calculated by dividing the displacement differences by the time intervals between frames are shown in Figs. 4 and 5. Each velocity point is plotted at the mean time at which the corresponding displacement occurred. Also shown in Figs. 6 and 7 are the accelerations obtained by fitting curves to the data. The curve fitting is described in the following subsection.

The cameras were found to oscillate slightly on their mounts. Longitudinal components of the

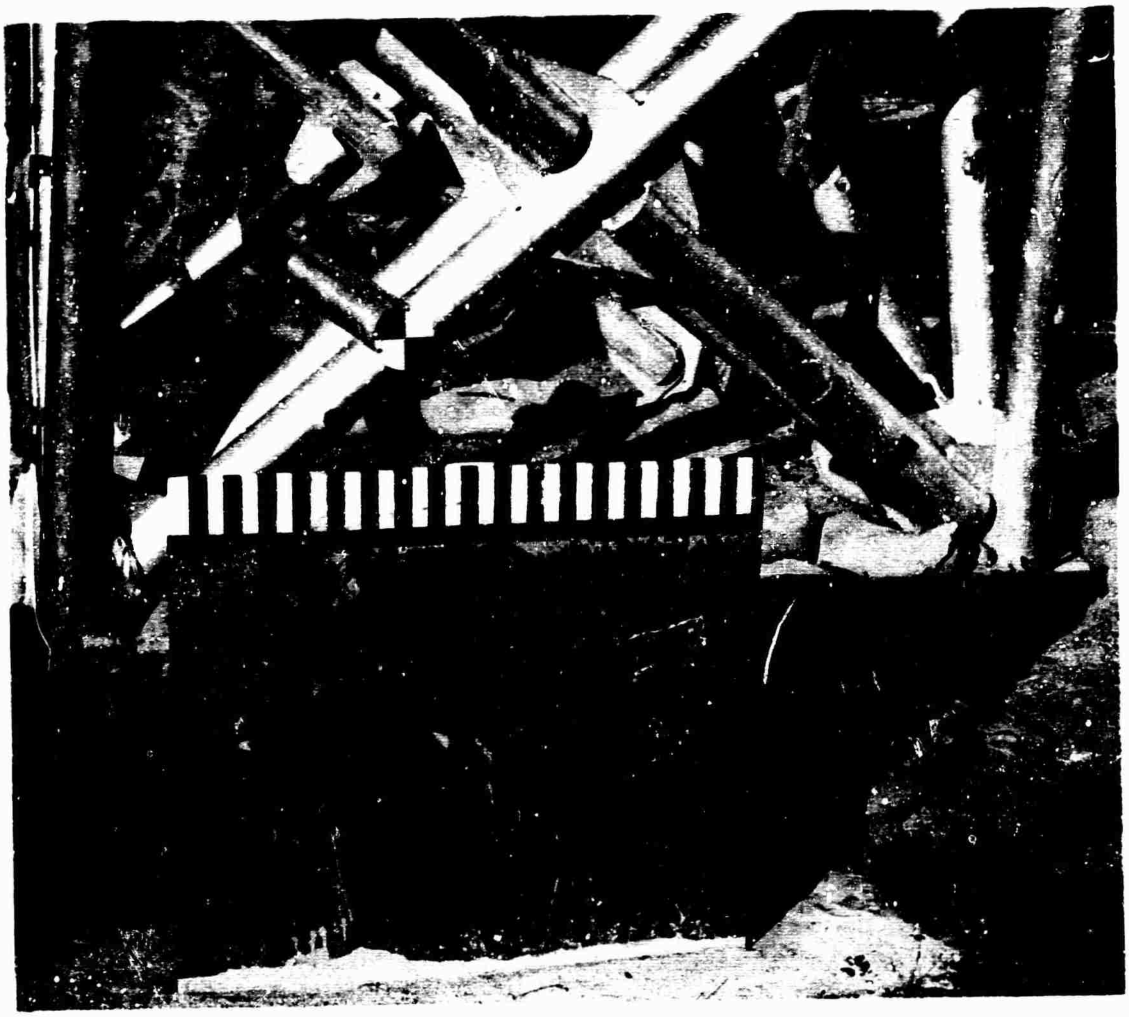

Fig. 1 - Free Flight Cylinder Suspended From Navy Mast - Operation PRAIRIE FLAT

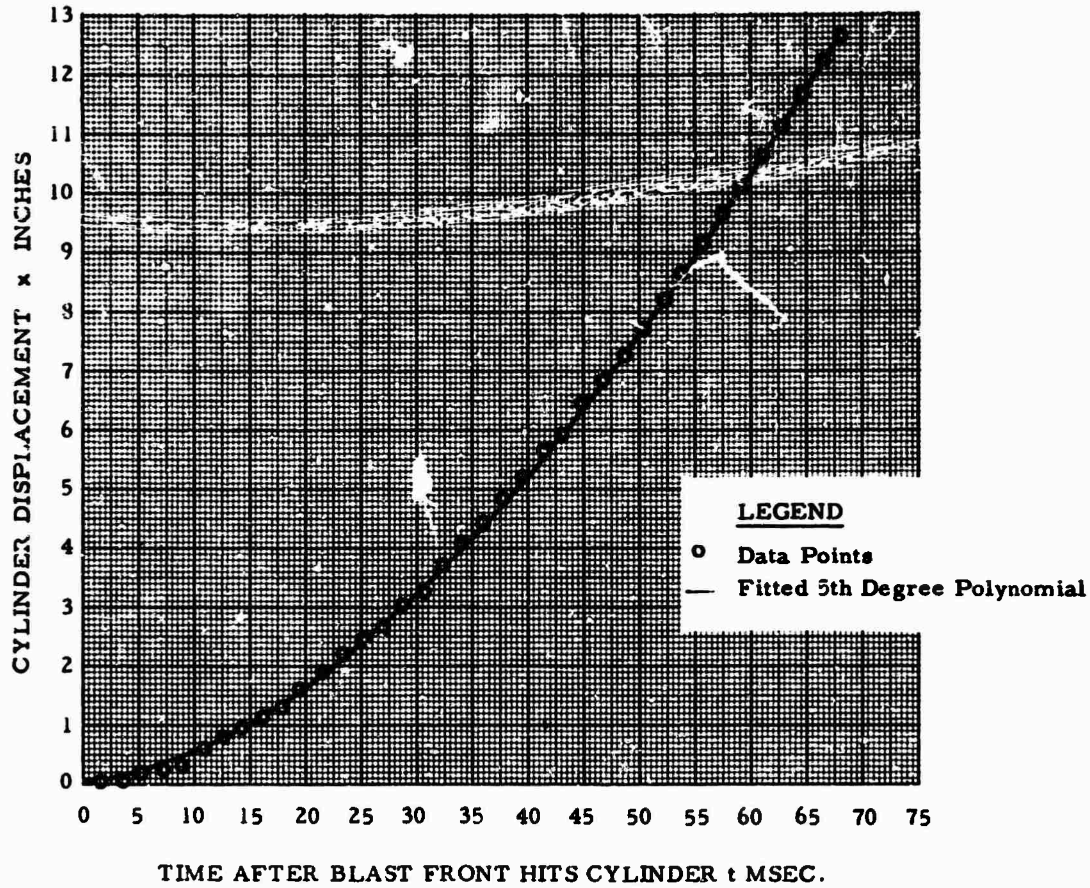

Fig. 2 - Displacement of Test Cylinder at 12.0 PSI Location

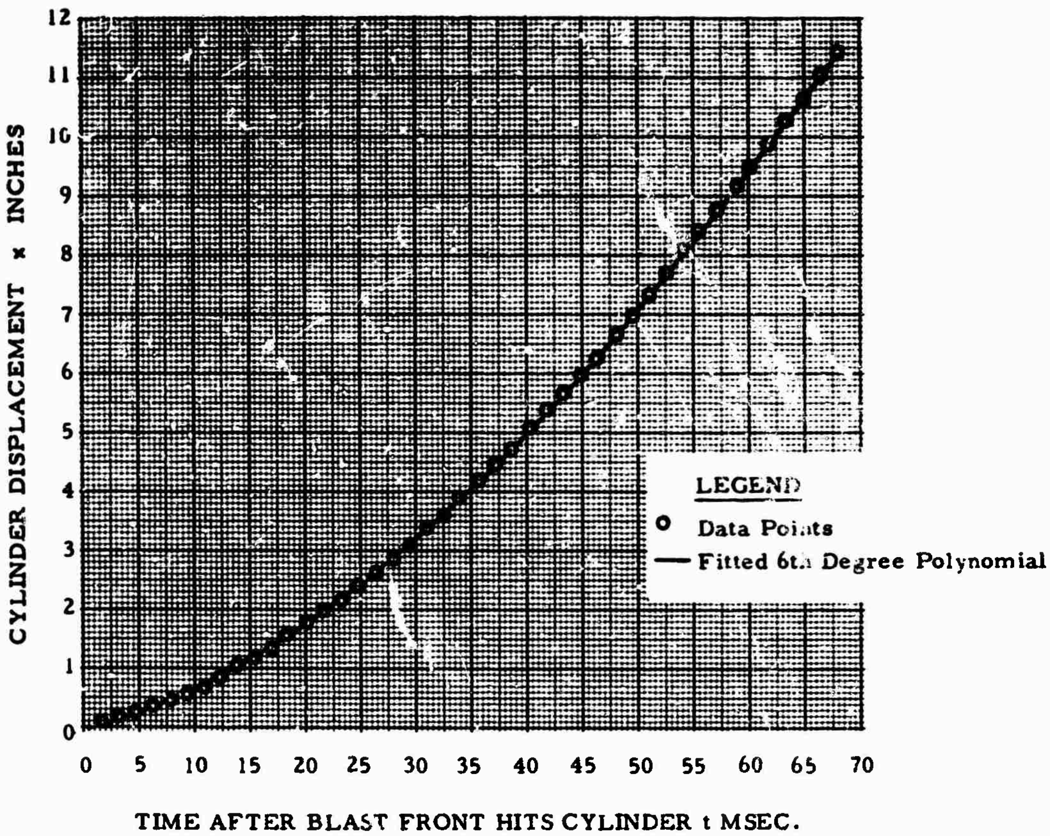

Fig. 3 - Displacement of Test Cylinder at 8.5 PSI Location

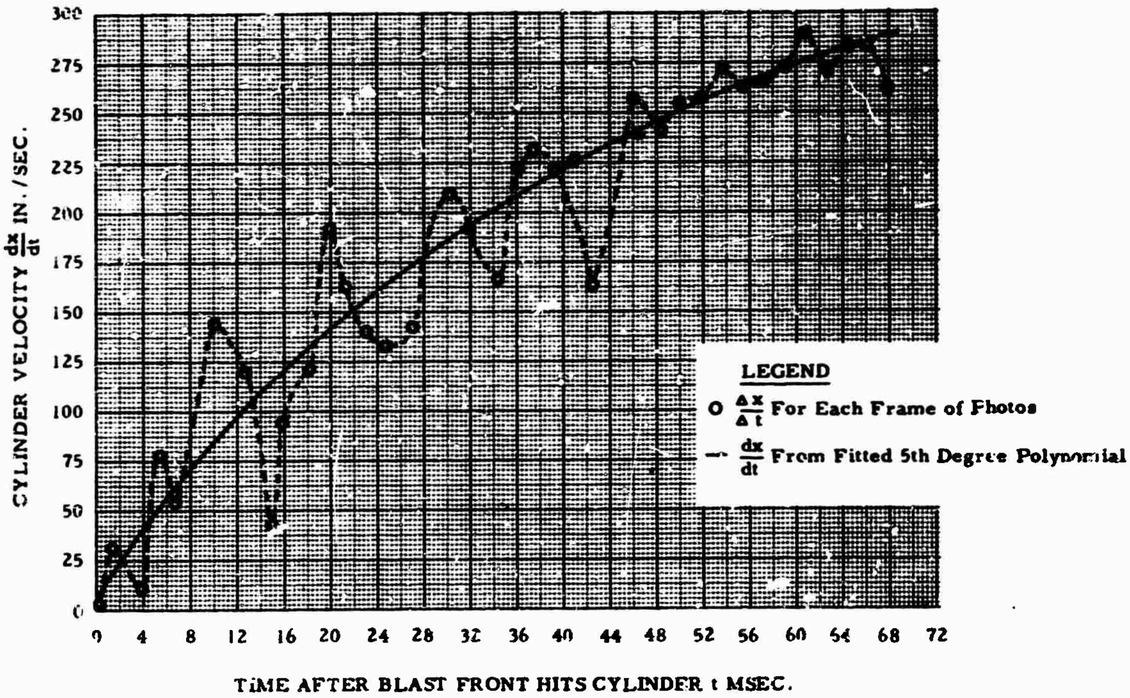

Fig. 4 - Velocity of Test Cylinder at 12.0 PSI Location

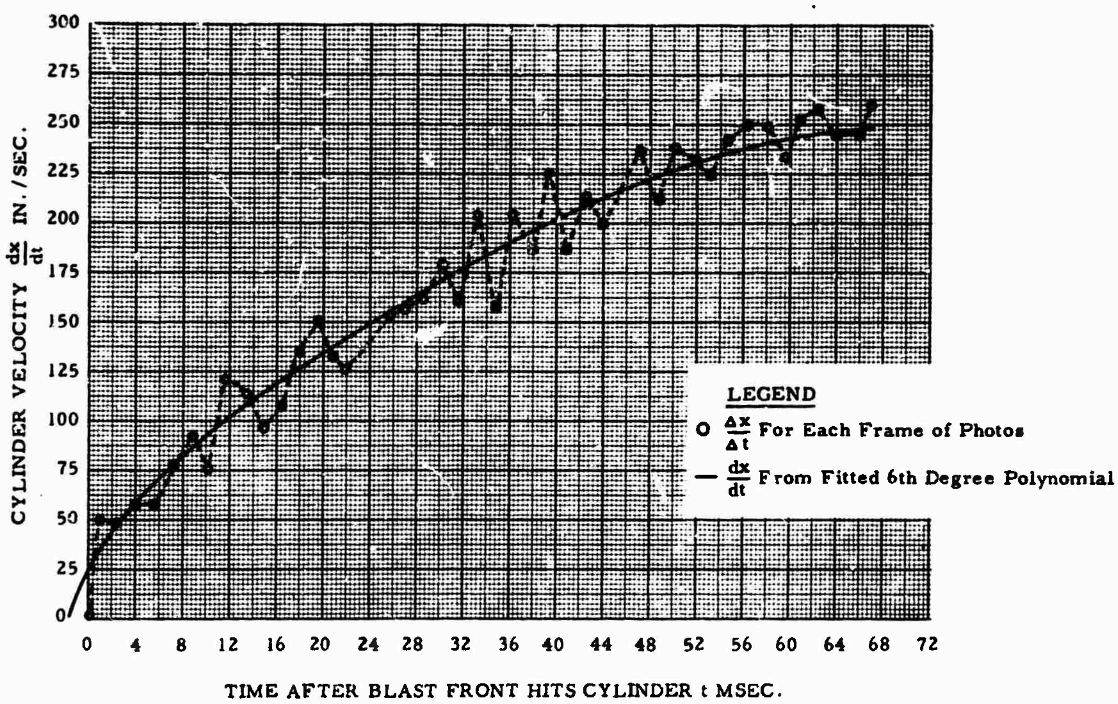

Fig. 5 - Velocity of Test Cylinder at 8.5 PSI Location

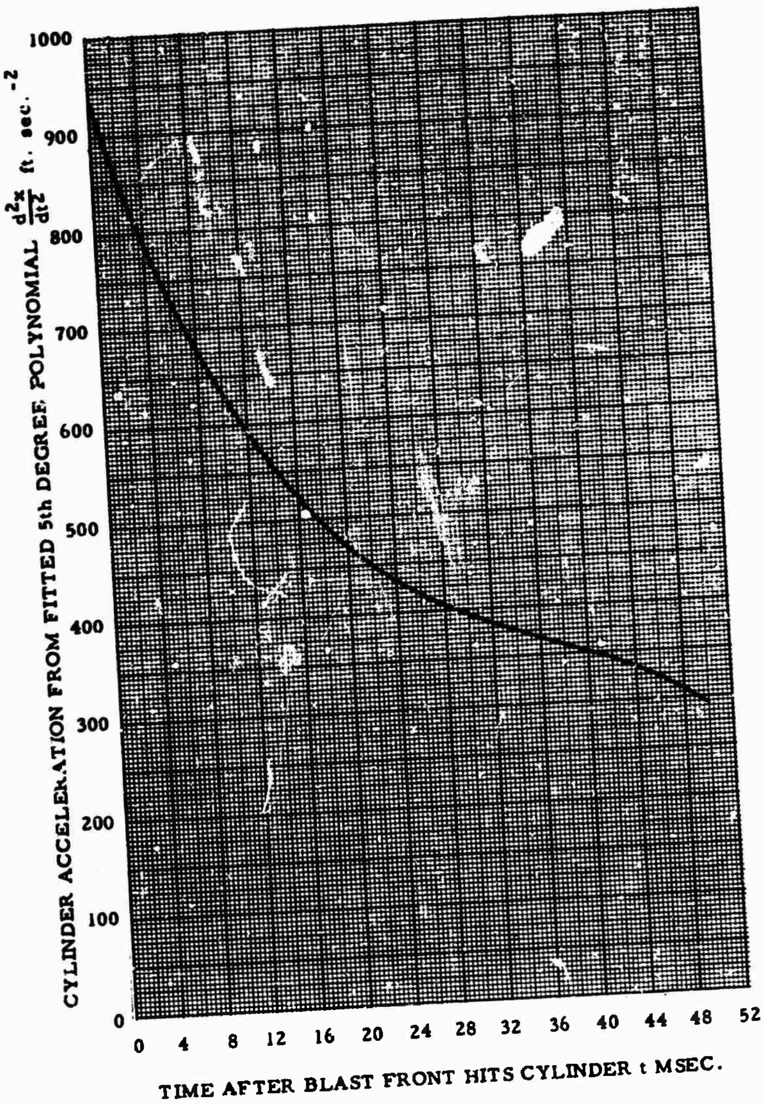

Fig. 6 - Acceleration of Test Cylinder at 12.0 PSI Location

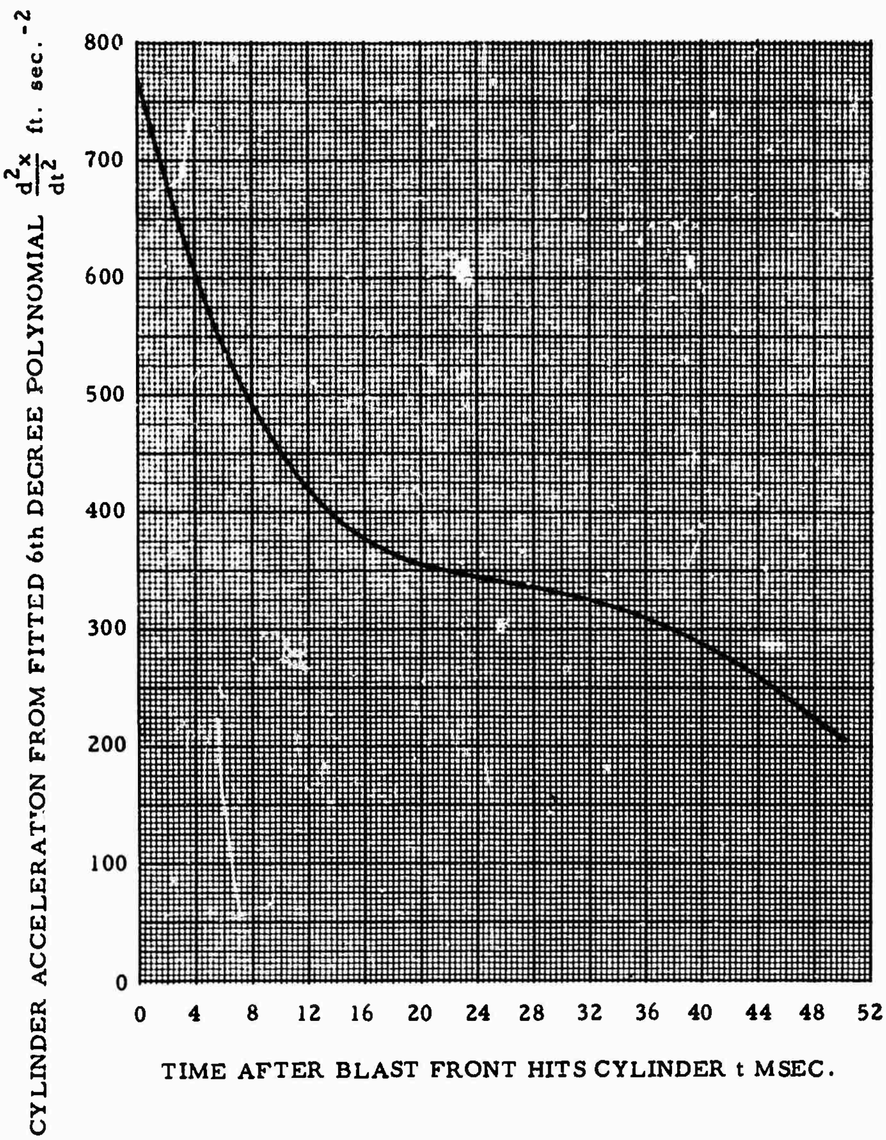

Fig. 7 - Acceleration of Test Cylinder at 8.5 PSI Location

oscillations were effectively eliminated because the plane of the near end of the test cylinder was in the plane of the marker plate, but relative rotary motion between the camera and the marker plate indicated oscillations with frequencies of about 22 and 38 Hz at the 12.0 psi and 8.5 psi locations respectively. These oscillations for each experiment were removed during the film reading by using the top edge of the marker plate as a motionless base line.

The precision of the displacement data at the 12.0 psi location was affected slightly by dust in the air. There was almost no dust visible in the photographs for the 8.5 psi location. The reading precision was approximately ±0.01 inches at each point. Since two points were read to obtain the displacement in each frame, a total error of the order of ±0.02 inches machine units was possible. The film reader was calibrated using the known distances along the marker plate.

Curve Fitting

To obtain velocity and acceleration of any specified time, an algebraic curve was fitted to the displacement time data. The curves obtained are shown in Figs. 2 and 3. Shown in Figs. 4 and 5 are the velocity curves obtained by differentiating the fitted displacement curves. The displacement curves were fitted to the data with the aid of an IBM 1130 computer and a program in the IBM 1130 statistical system entitled "Least Squares Fitting by Orthogonal Polynomials". The type of curve fitted is of the general form

$$x = \sum_{n=o}^{N} a_n t^n$$

where a_n are constant coefficients. The variance of x, also computed by means of the program, is given by

$$\sigma^2 = \frac{\sum\limits_{i=1} d_i^2}{D.F.}$$

where σ is the standard deviation in x

d_i is the residual, i.e., t experimental - t calculated

K is the number of data points

D.F. is the number of degrees of freedom given by D.F. = K - C where C has the value one plus the degree of the polynomial.

The degree of the polynomial used for the fitted curve was determined by trial and error using the criterion that the best fitting polynomial was the one which yielded the smallest variance of x and which satisfied the necessary conditions that the velocity increased monotonically and the acceleration decreased monotonically in the time interval over which the data were recorded. The time intervals over which the variation in drag caused by the initial diffraction of the wave front around the cylinder and the vortex formation and shedding were so short that these features could not be distinguished in the fitting of the displacement time curve.

The resulting polynomials for displacement x in inches and time t in milliseconds are written as follows:

For the 12.0 psi location -

$$x = 0.002428748 + 0.01102118t + 0.004591884t^2 - 0.000063637706t^3 + 0.0000007870470t^4 - 0.0000000043349791t^5 \qquad \text{(Eq. 1)}$$

$$\sigma^2 = 0.0016984 \text{ in.}^2$$

For the 8.6 psi location -

$$x = 0.006780765 + 0.029192391t + 0.003997392t^2 - 0.00008682052t^3 + 0.000001902585t^4 - 0.000000021868201t^5 + 0.00000000009472334t^6 \qquad \text{(Eq. 2)}$$

$$\sigma^2 = 0.00029506 \text{ in.}^2$$

The coefficients are taken directly from the output of the computer. No attempt was made to round them off to correspond to the accuracy of the experiment.

Corrections

Each cylinder was found to have an upward vertical component of motion as well as rotation about a vertical axis in such a way that the far end travelled further than the near end.

The effect of gravity was negligible because for free fall (using $y = 1/2gt^2$ for t = 50 milliseconds) the cylinders could have fallen only 0.5 inches. If the suspension lines did not break in the first 50 milliseconds the maximum possible upward force that they exerted was certainly not greater than 3 times the gravitational force on each cylinder, which corresponds to a maximum possible upward displacement 1.5 inches due to suspension line force. Therefore the vertical motion of the cylinder can be attributed to the drag on the support lines.

The reason for the rotation appears to be that the far end of the cylinder received an initial impulse from the shock wave reflected from the mast. Since the displacement-time data were obtained by measuring horizontal motion of the near end of the cylinder, it was necessary to apply a correction to obtain the motion of the centre of the cylinder. Fortunately both the vertical component and rotation were approximately linear functions of displacement at the 12.0 psi location and the product of the vertical component and rotation was approximately linear at the 8.5 psi location. This means that the corrected value of displacement for each cylinder could be obtained by applying the same constant correction factor to each measured displacement. To obtain the correction due to rotation it was necessary to read the motion of the far end of the cylinder. Since the displacement reference scale was at the near end of the cylinder, the measurement of the far end displacement was affected by foreshortening of the field of view and the changing angle of view of the camera. The correct displacement difference $\Delta x''$ between the far end near ends of the cylinder was then obtained by

$$\Delta x'' = \frac{(L + h)\,\Delta x'}{L} + \frac{xh}{L} \qquad \text{(Eq. 3)}$$

where L is the distance from the lens of the camera to the near end of the cylinder
h is the length of the cylinder
$\Delta x'$ is the measured difference in displacement between the far and near end of the cylinder.

The first term on the R.H.S. side is for the foreshortening of the field of view and the second term is for the changing angle of view. The value of h for both cylinders was 3 feet and the value of L was 50 feet and 42 feet for the 12.0 and 8.5 psi locations respectively.

The corrected values of the displacement data are given by

$$X = 1.217x \qquad \text{(Eq. 4)}$$

for the 12.0 psi location and

$$X = 1.164x \qquad \text{(Eq. 5)}$$

for the 8.5 psi location

Calculations

The drag force D is obtained by

$$D = ma \qquad \text{(Eq. 6)}$$

where m is the mass of the cylinder and

$a = \frac{d^2X}{dt^2}$ is the acceleration obtained from Eq. 1, 2, 4 and 5. The value of the drag force of each cylinder is divided by the frontal area of the cylinder and is shown as P_D, in Tables 1 and 2. Also shown in these tables, for each cylinder, is the drag coefficient C_D, displacement X, velocity V, and acceleration a, of each cylinder along with various flow parameters upon which the drag force is dependent.

The displacement and velocity are obtained by X and $\frac{dX}{dt}$ respectively from Eq. 1, 2, 4 and 5. The fluid velocity U is obtained from the equation

$$U = U_o F \qquad \text{(Eq. 7)}$$

where U_o, the fluid velocity directly behind the blast front (time t = o), is obtained from the Rankine-Hugoniot relations [3]

$$U_o = \frac{5p}{7p_1} \frac{c_1}{\left(1 + \frac{6p}{7p_1}\right)^{1/2}} \qquad \text{(Eq. 8)}$$

where p is the peak shock overpressure
p_1 is the atmospheric pressure
c_1 is the speed of sound in the air ahead of the blast front

$$F = \left(1 - \frac{t}{t_+}\right) e^{\frac{-Kt}{t_+}}, \text{ the Friedlander decay}$$

where t is the time after the blast front has passed the cylinder
t_+ is the positive duration of the blast wave

For the peak incident overpressures which occurred, K has a value of 1, [4]. The fluid particle acceleration a_p is found by differentiating Eq. 7 thus:

$$a_p = \frac{dU}{dt} \approx - \frac{U_o}{t_+} \left(F + e^{-\frac{t}{t_+}}\right) \qquad \text{(Eq. 10)}$$

The drag coefficient is given by

$$C_D = \frac{P_D}{q} \qquad \text{(Eq. 11)}$$

$$\text{where} \quad q = q_o \left(1 - \frac{V}{U}\right)^2 F^2 \qquad \text{(Eq. 12)}$$

where q_o, the dynamic pressure at t = o, obtained from the Rankine-Hugoniot equation [3] is given by

$$q_o = \frac{5}{2} \frac{p^2}{7p_1 + p} \qquad \text{(Eq. 13)}$$

For a stationary cylinder Eq. 12 reduces to $q = q_o F^2$, the Friedlander decay. The Mach number, M of the flow behind the shock front is given by

$$M = \frac{U - V}{c_2} \qquad \text{(Eq. 14)}$$

TABLE 1

Computer Calculations For The 12.C PSI Location

RESULTS FOR T1=24.4 DEG.R.. P=12.0 PSI. [illegible] PSI. AND T=[illegible] MS.

TIME AFTER BLAST FRONT T MSEC.	DISPLACEMENT X INCHES	VELOCITY V FT./SEC.	ACCELERATION A FT./SEC./SEC.	FLUID VEL. U FT./SEC.	FLUID AC. $\dot{U}$ FT./SEC./SEC.
0.0	0.000	0.00	934.3	530.35	-4823.2
2.0	0.051	2.90	857.7	520.57	-4757.8
4.0	0.141	4.55	791.2	511.54	-4693.2
6.0	0.269	6.07	731.6	502.19	-4629.5
8.0	0.432	7.48	678.4	493.02	-4566.4
10.0	0.627	8.79	631.1	483.93	-4504.1
12.0	0.853	10.01	589.4	474.96	-4442.6
14.0	1.107	11.15	552.8	466.16	-4381.8
16.0	1.389	12.22	521.0	457.45	-4321.7
18.0	1.695	13.24	493.4	448.87	-4262.4
20.0	2.023	14.23	469.7	440.4[illegible]	-4203.8
22.0	2.375	15.12	449.4	432.05	-4146.0
24.0	2.748	16.00	432.1	423.82	-4088.8
26.0	3.143	16.85	417.5	415.70	-4032.3
28.0	3.557	17.67	405.0	407.69	-3976.5
30.0	3.991	18.47	394.3	399.79	-3921.4
32.0	4.444	19.25	384.9	392.00	-3866.9
34.0	4.915	20.01	374.4	384.32	-3813.2
36.0	5.404	20.75	368.4	376.75	-3760.0
38.0	5.911	21.48	360.5	369.28	-3707.6
40.0	6.436	22.20	352.2	361.92	-3655.7
42.0	6.977	22.89	343.1	354.66	-3604.5
44.0	7.534	23.57	332.9	347.50	-3554.0
46.0	8.108	24.22	321.0	340.44	-3504.0
48.0	8.697	24.85	307.1	333.48	-3454.7
50.0	9.301	25.45	290.7	326.62	-3406.0

TIME AFTER BLAST FRONT T MSEC.	DRAG P_0 PSI	COEFFICIENT OF DRAG CD	FLOW MACH NO. M	REYNOLDS NO. R=1/100000	ACCELERATION COEFFICIENT AC.
0.0	2.541	0.766	0.433	10.0	0.005
2.0	2.340	0.740	0.423	9.7	0.006
4.0	2.159	0.712	0.415	9.5	0.006
6.0	1.996	0.688	0.406	9.3	0.006
8.0	1.851	0.666	0.398	9.1	0.006
10.0	1.722	0.647	0.390	8.9	0.006
12.0	1.608	0.631	0.382	8.7	0.006
14.0	1.506	0.618	0.374	8.5	0.006
16.0	1.421	0.608	0.367	8.3	0.007
18.0	1.345	0.602	0.359	8.1	0.007
20.0	1.281	0.593	0.352	7.9	0.007
22.0	1.226	0.598	0.345	7.8	0.007
24.0	1.179	0.601	0.337	7.6	0.007
26.0	1.139	0.607	0.330	7.4	0.008
28.0	1.105	0.616	0.323	7.2	0.008
30.0	1.076	0.628	0.317	7.1	0.008
32.0	1.050	0.641	0.310	6.9	0.008
34.0	1.027	0.656	0.303	6.7	0.009
36.0	1.005	0.673	0.296	6.6	0.009
38.0	0.983	0.690	0.290	6.4	0.009
40.0	0.961	0.706	0.284	6.3	0.010
42.0	0.936	0.722	0.277	6.1	0.010
44.0	0.908	0.734	0.271	6.0	0.010
46.0	0.876	0.743	0.265	5.8	0.011
48.0	0.838	0.746	0.259	5.7	0.011
50.0	0.793	0.742	0.253	5.5	0.011

MEAN CD= 0.668

TABLE 2

Computer Calculations For The 8.5 PSI Location

RESULTS FOR T1=524.4 DEG.R., P=8.5 PSI, P1=13.79 PSI, AND T=250 MS.

TIME AFTER BLAST FRONT T MSEC.	DISPLACEMENT X INCHES	VELOCITY V FT./SEC.	ACCELERATION A FT./SEC./SEC.	FLUID VEL. U FT./SEC.	FLUID AC. Ap FT./SEC./SEC.
0.0	0.000	0.00	775.4	401.06	-3213.3
2.0	0.093	4.28	682.9	395.27	-3174.9
4.0	0.212	5.57	606.1	388.96	-3137.0
6.0	0.363	6.72	543.2	382.72	-3099.4
8.0	0.534	7.75	492.4	376.56	-3062.3
10.0	0.731	8.69	451.9	370.47	-3025.5
12.0	0.950	9.56	420.4	364.46	-2989.2
14.0	1.190	10.38	396.3	358.52	-2953.2
16.0	1.449	11.15	378.2	352.65	-2917.6
18.0	1.725	11.90	365.0	346.85	-2882.4
20.0	2.020	12.62	355.4	341.12	-2847.6
22.0	2.331	13.32	348.5	335.46	-2813.1
24.0	2.659	14.01	343.3	329.86	-2779.0
26.0	3.004	14.69	339.1	324.34	-2745.3
28.0	3.365	15.37	335.0	318.88	-2711.9
30.0	3.742	16.03	330.5	313.49	-2678.9
32.0	4.134	16.69	325.1	308.17	-2646.3
34.0	4.543	17.33	318.4	302.91	-2614.0
36.0	4.966	17.96	310.1	297.71	-2582.0
38.0	5.405	18.57	300.1	292.58	-2550.4
40.0	5.858	19.16	288.1	287.51	-2519.1
42.0	6.325	19.72	274.4	282.50	-2488.2
44.0	6.805	20.26	258.9	277.55	-2457.6
46.0	7.297	20.76	242.0	272.67	-2427.3
48.0	7.801	21.23	223.9	267.85	-2397.3
50.0	8.316	21.65	205.2	263.08	-2367.7

TIME AFTER BLAST FRONT T MSEC.	DRAG P_D PSI	COEFFICIENT OF DRAG CD	FLOW MACH NO. M	REYNOLDS NO. Re1/100000	ACCELERATION COEFFICIENT AC.
0.0	1.057	0.615	0.334	7.4	0.007
2.0	0.931	0.571	0.326	7.2	0.007
4.0	0.826	0.527	0.320	7.1	0.007
6.0	0.760	0.491	0.314	6.9	0.007
8.0	0.671	0.463	0.308	6.8	0.007
10.0	0.616	0.461	0.302	6.7	0.007
12.0	0.573	0.427	0.297	6.5	0.007
14.0	0.540	0.418	0.291	6.4	0.008
16.0	0.515	0.415	0.286	6.3	0.008
18.0	0.497	0.416	0.281	6.1	0.008
20.0	0.486	0.421	0.276	6.0	0.008
22.0	0.475	0.429	0.271	5.9	0.008
24.0	0.468	0.440	0.266	3.8	0.009
26.0	0.462	0.452	0.260	5.7	0.009
28.0	0.437	0.465	0.256	5.5	0.009
30,0	0.650	0.478	0.251	5.4	0.303
32.0	0.443	0.489	0.246	5.3	0.010
34.0	0.434	0.499	0.241	5.2	0.010
36.0	0.423	0.507	0.236	5.1	0.010
38.0	0.409	0.511	0.232	5.0	0.011
40.0	0.393	0.312	0.227	4.9	0.011
42.0	0.376	0.508	0.222	4.8	0.011
44.0	0.353	0.500	0.218	4.7	0.011
46.0	0.330	0.488	0.213	4.6	0.012
48.0	0.305	0.471	0.209	4.5	0.012
50.0	0.280	0.650	0.205	4.4	0.012

MEAN CD= 0.477

where c_2 is the speed of sound behind the shock front obtained from

$$c_2 = c_1 \sqrt{\frac{T_2}{T_1}} \qquad \text{(Eq. 15)}$$

where $c_1 = \sqrt{\gamma R T_1}$ is the speed of sound in the atmosphere ahead of the shock front

T_1 is the atmospheric temperature ahead of the shock front

R is the gas constant

γ is the specific heat ratio

T_2 is the temperature of the flow behind the shock front approximated by the isentropic relationship

$$T_2 = T_{2_o} \left(\frac{p_2}{p_{2_o}}\right)^{\frac{\gamma - 1}{\gamma}} \qquad \text{(Eq. 16)}$$

where T_{2_o} is the temperature directly behind the shock front obtained from the Rankine-Hugoniot relations [5] and given as follows:

$$T_{2_o} = T_1 \left(\frac{7 + \frac{p_{2_o}}{p_1}}{7 + \frac{p_1}{p_{2_o}}}\right) \qquad \text{(Eq. 17)}$$

$$p_{2_o} = p + p_1 \qquad \text{(Eq. 18)}$$

$$p_2 \approx p_1 + pF \qquad \text{(Eq. 19)}$$

The Reynolds number is given by

$$Re = \frac{(U - V)d}{\nu} \qquad \text{(Eq. 20)}$$

where d is the cylinder diameter

ν is the kinematic viscosity given by

$$\nu \times 10^6 = \left[\frac{14.7}{p_1}\left(\frac{6 + \frac{p_{2_o}}{p_1}}{1 + 6\frac{p_{2_o}}{p_1}}\right)\left(\frac{p_{2_o}}{p_2}\right)^{0.714}\right]\sum_{n=o}^{N} b_n T^n \qquad \text{(Eq. 21)}$$

where b_n are coefficients obtained by using an IBM 1130 computer applying the same program used for obtaining Eq. 1 and 2 to values of ν known for air at specific temperatures [6]. The values of b_n obtained for T_2 in degrees Rankine were

$b_o = 0.9027754 \times 10^2$ ft.^{2} sec.$^{-1}$

$b_1 = 0.3293413$ ft.^{2} sec.$^{-1}$ deg. R^{-1}

$b_2 = 0.8741066 \times 10^{-3}$ ft.^{2} sec.$^{-1}$ deg. R^{-2}

The quantity in square brackets is the density correction term. The acceleration coefficient, an indicator of the effect on drag of relative acceleration between the fluid and the cylinder [7] is given by

$$a_c = \frac{da_t}{(U - V)^2} \qquad \text{(Eq. 22)}$$

where a_t is the total acceleration defined by

$$a_t = a = a_p \qquad \text{(Eq. 23)}$$

RESULTS

The values of p and t obtained in Operation PRAIRIE FLAT [8] and used in the calculations were:

For the cylinder nearest ground zero

$p = 12.0$ psi $\pm$ 8 per cent

$t_+ = 220$ milliseconds

For the cylinder farthest from ground zero

$p = 8.5$ psi $\pm$ 10 per cent

$t_+ = 250$ milliseconds

The drag and drag coefficient for each cylinder are shown in Tables 1 and 2 along with the corresponding evaluated parameters of the flow and the motion of the cylinders. In the time range studied, the drag coefficient for each cylinder was approximately constant with mean values of 0.67 and 0.48 at the 12.0 and 8.5 psi locations respectively.

DISCUSSION

The values of C_D appear to be approximately constant over the entire time range for each cylinder. The quantity $\frac{V}{U}$ is never greater than 0.08 in the 50 millisecond time range and correspondingly the quantity $1 - \left(\frac{V}{U}\right)^2$ which accounts for cylinder motion in the evaluation of dynamic pressure is less than a 1 per cent correction to the Friedlander decay and does not affect the value of C_D appreciably for a cylinder at rest under the same flow conditions.

The Reynolds number and Mach number appear to vary jointly in such a way that the drag coefficient does not change in the time varying flow of the blast wave. This is also indicated by analysis [9] of some drag measurements made by the Ballistic Research Laboratories at the 15.0 peak incident overpressure location in the 500 ton trial [10] held at Suffield in 1964. This shows that for a 3 inch diameter circular cylinder which is effectively infinitely long, the drag coefficient remains approximately constant over the first 50 milliseconds with a mean value of 0.8.

The acceleration coefficient for each cylinder is never greater than 0.02 in the time range studied. This seems to indicate that fluid acceleration is unimportant because the work of Keim [7] and Selberg and Nichols [11] have shown that the effect of fluid acceleration on the drag coefficient is substantial only when the acceleration coefficient is greater than 0.20.

Experiments done on steady flow around cylinders of various finite lengths [12] show that for length to diameter ratios of about 10 for the test cylinders and Reynolds number and Mach number of 1.3×10^5 and 0.5 respectively, the drag coefficient for steady flow was shown to be about 70% of that of infinitely long cylinders [13]. However, measurements made in a shock tube [14] suggest that for Reynolds numbers greater than 5×10^5, the drag coefficient for finite length cylinders may be greater than that for infinitely long cylinders. It appears that more work needs to be done in this area.

The largest probable error in the results is due to the error in the measurement of peak incident overpressure. The expected error in this measurement is ±8 per cent and ± 10 per cent at the 12.0 psi and 8.5 psi locations respectively. This gives rise to corresponding errors of ±16 per cent and ±20 per cent in the drag coefficients. The remaining probable experimental error is estimated at less than ±10 per cent so that the total tolerance in the drag coefficient at the 12.0 psi location is about ±26 per cent and at the 8.5 psi location about ±30%.

The dust present in the air at the 12.0 psi location would increase the density of the fluid medium and thus increase the drag force. Since the amount of dust was unknown, no attempt was made to account for it in any of the calculations, although its effect is expected to be unimportant, since density measurements indicated that the increase in density due to dust was small.

The velocity-time graphs (Figs. 4 and 5) indicate that oscillations with frequencies between 100 and 350 Hz occurred in the cylinder motion. The causes are unknown but a number of the possibilities can be eliminated as follows:

a. The frequencies of the ground motion which could have produced a motion of the marker plate are much lower than the frequencies which appeared.

b. The fundamental modes of lateral beam vibrations of the cylinders are above the frequency range observed in the velocity-time graphs.

c. Oscillation in the film travel, through the camera, would show up as an apparent oscillation in the cylinder motion. Examination of the film timing disclosed no such oscillation.

d. The only remaining possibility appears to the flow itself, such as reflected shock waves and vortex shedding in the wake of the cylinder.

The frequency of 1'0 Hz at t = 20 ms (Fig. 4) corresponds to a Strouhal number of 0.04. The frequency of 130 Hz at t = 50 ms (Fig. 4) corresponds to a Strouhal number of 0.07. These values of Strouhal number are lower than the value of 0.21 for the same range of Reynolds number in the steady velocity wind tunnel tests [15]. However, the frequency of 315 Hz at t = 40 ms (Fig. 5) corresponds to a Strouhal number of 0.17 which compares favorably to steady flow results.

COMPARISON WITH OTHER EXPERIMENTS

The drag coefficients obtained by the free flight method in Operation PRAIRIE FLAT are plotted against Reynolds number in Fig. 8 along with a value of drag coefficient obtained by analysis [9] of some results obtained by the Ballistic Research Laboratories in Operation SNOWBALL held at DRES [10] in 1964. The Mach and Reynolds numbers shown for these results are the time-averaged values for the first 50 milliseconds of the blast wave. Also shown in the figure is a graph of drag coefficient versus Reynolds number for flow in which compressibility effects are negligible [15] and a graph of drag coefficient for steady flow Mach numbers of 0.4 and 0.5 [13]. The results of the free flight tests are plotted on a larger scale in Fig. 9. Here the drag coefficients are plotted for various instantaneous Mach and Reynolds numbers in the first 50 milliseconds of the blast wave. Also shown in this figure are some results evaluated from direct force measurements in Operation PRAIRIE FLAT [2]. These tests were done on two sets of 3½, 4½ and 5 9/16 inch diameter cylinders, effectively infinitely long. One set was tested at the 8.5 peak incident overpressure location and the other at the 12.0 psi location.

CONCLUSIONS

1. The mean drag coefficient obtained for the 12.0 and 8.5 psi locations were 0.67 and 0.48.

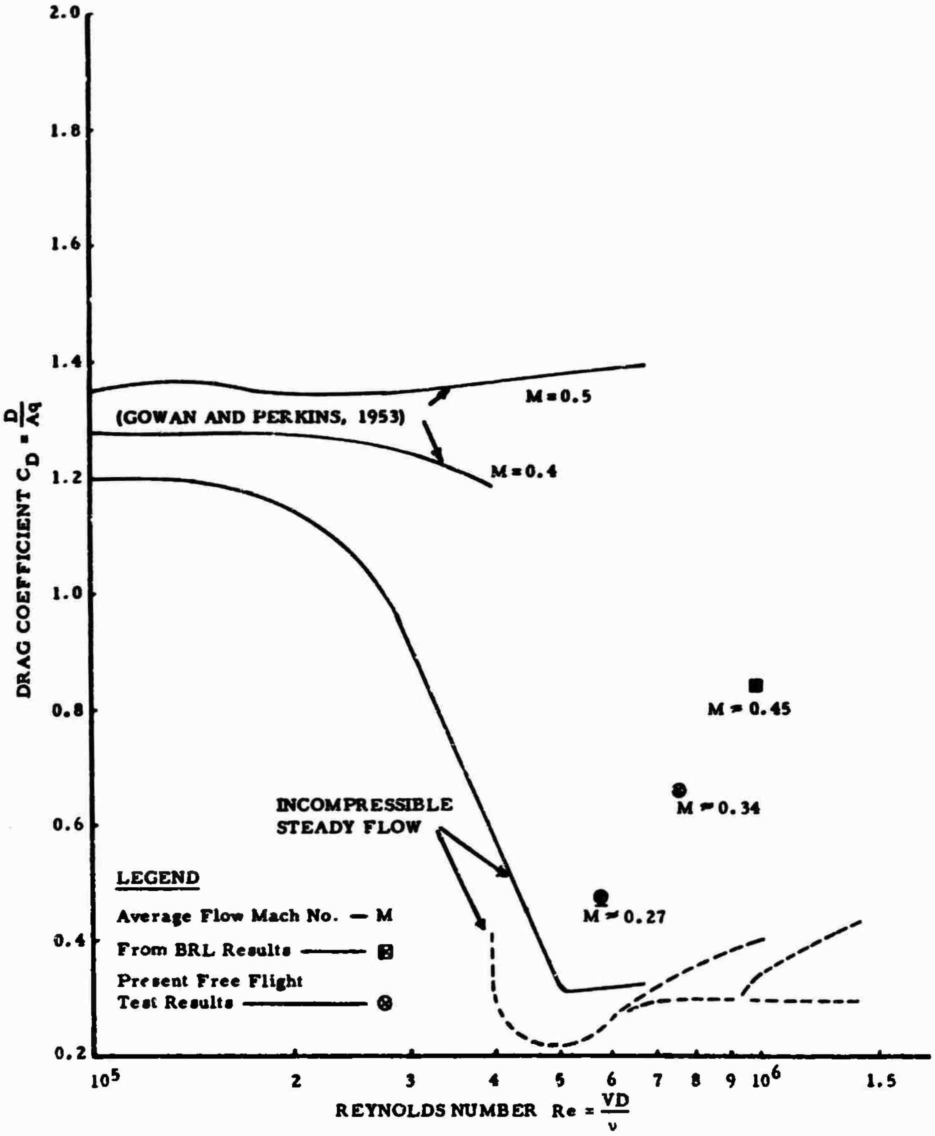

Fig. 8 - Drag Coefficients of Circular Cylinders for Various Mach Numbers

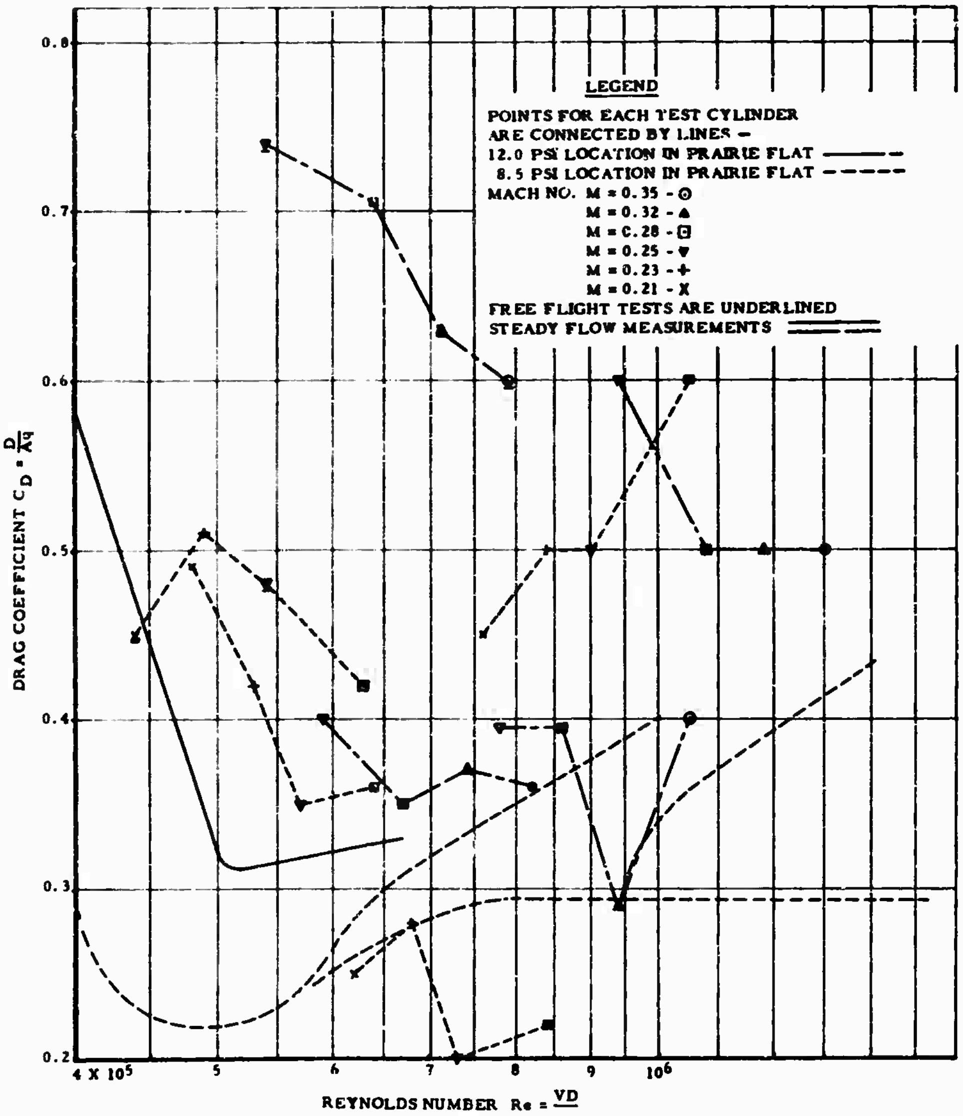

Fig. 9 - Drag Coefficients of Circular Cylinders From Operation Prairie Flat

2. The drag coefficient in the range from 8.0 to 15.0 psi peak incident overpressure in the first 50 milliseconds of the blast wave from a 500 ton TNT surface charge appears to be approximately constant for a $3\frac{1}{2}$ inch diameter circular cylinder when calculated from

$$C_D = \frac{F_D}{q}$$

where

$$q \approx q_o \left(1 - \frac{t}{t_+}\right)^2 e^{\frac{-2t}{t_+}} \quad \text{from the}$$

Friedlander decay.

3. Reasonable agreement was shown between the free flight and direct force results. Also the results obtained from the blast waves correlated well with the drag coefficient curves for steady flow.

REFERENCES

1. G.H.S. Jones, "Final Operational Manual of Canadian Projects Operation PRAIRIE FLAT", Suffield Memorandum No. 42/68, 1968

2. A.M. Patterson, "Preliminary Report on Programme A, Basic Air Blast Measurements Operation PRAIRIE FLAT", Suffield Memorandum No. 115/68, 1968

3. S. Glasstone, "The Effects of Nuclear Weapons", prepared by the United States Department of Defense, published by the United States Atomic Energy Commission, 1957

4. R.B. Harvey and T. Fisher, "The Effect of an R.C. Circuit on a Friedlander Blast Wave", DRES Internal Report, 1968

5. H.W. Liepmann and A. Roshko, "Elements of Gasdynamics", John Wiley and Sons, 1957

6. H. Schlicting, "Boundary Layer Theory", McGraw Hill Book Co., Inc., 1960

7. S.R. Keim, "Fluid Resistance to Cylinders in Accelerated Motion", Proceedings of the American Society of Civil Engineers, Journal of the Hydraulics Division, Vol. 82, HY6, Paper 113

8. B.R. Long, "The Behavior of Two Simple Framed Structures Under Blast Loading", Suffield Memorandum No. 110/68, 1968

9. S.B. Mellsen, "Development of the Free Flight Method for the Measurement of Drag on Cylinders in Operation PRAIRIE FLAT", Suffield Memorandum No. 119/68, 1968

10. N.H. Ethridge, Private communication, Ballistic Research Laboratories, Aberdeen Proving Ground, Maryland

11. B.P. Selberg and J.A. Nichols, "Drag Coefficient of Small Spherical Particles", AIAA Journal, Vol. 6, No. 3, March, 1968

12. Clement J. Welsh, "The Drag of Finite-Length Cylinders Determined From Flight Tests at High Reynolds Numbers for a Mach Number Range from 0.5 to 1.3", NACA Technical Note 2941, 1953

13. Forrest E. Gowen and Edward W. Perkins, "Drag of Circular Cylinders for a Wide Range of Reynolds Numbers and Mach Numbers", NACA Technical Note No. 2960, 1953

14. Valerie C. Martin, K.F. Mead and J.E. Uppard, "Blast Loading on a Right Circular Cylinder", AWRE Report No. 0-93/65, U.K. Atomic Energy Authority, 1965

15. Anatol Roshko, "Experiments on the Flow Past a Circular Cylinder at Very High Reynolds Number", Journal of Fluid Mechanics Vol. 10, 1961

ANALYTICAL AND EXPERIMENTAL RESULTS OF

LATTICE TYPE STRUCTURES SUBJECTED TO A BLAST LOADING

BY

Robert Geminder
Mechanics Research, Incorporated
Los Angeles, California

This technical paper presents the results of a program in which three antenna mast structures were designed, fabricated, and subjected to a detonation of 500 tons of TNT. The masts were instrumented, and the experimental data was compared with the analytical predicted results. A final analytical result was obtained which integrated the experimental results with the analytical predictions.

INTRODUCTION

An experimental program was conducted to measure the response of three antenna masts subjected to a 500 ton TNT blast. This free-field blast trial was known as Operation Prairie Flat and was conducted on August 9, 1968, at the Defense Research Establishment Suffield (DRES) range at Suffield, Alberta, Canada.

The purpose of this program was to develop the analytical design method for shipboard antenna masts and to modify this method with empirical data. In order to verify the analytical design study, three masts were selected. Two masts of unequal size (30 foot and 15 foot) were placed at one overpressure location, and a third mast (30 foot) was placed at a significantly lower overpressure location. (Figures 1 and 2 show the mast locations and the blast, respectively.) Thus, the effect of mast size and the effect of two different mast loadings with respect to the analytical design could be evaluated. These masts experienced a blast loading equivalent to 12 psi and 8.5 psi overpressure.

The three antenna mast structures were instrumented to obtain response and forcing function test data. The instruments used were strain gages, pressure transducers, accelerometers, and drag probes. They were located so as to obtain an optimum amount of data with a fixed number of instrumentation channels. Approximately 120 channels of data were multiplexed and recorded. A description of the instrumentation system used, along with a description of a dynamic "Twang" calibration performed on all the masts, is presented. The dynamic calibration on all masts established the damping ratio and the first two modes of frequency for each antenna mast.

This paper presents the theoretical considerations used regarding the foundation, the masts, the antenna, the drag loading, as well as a summary of the computer programs used for the analysis.

The results of the experimental program yielded a general formula for the design force.

$$F_t = Kq_o \sum AC_D$$

where:

F_t = maximum response load, lbs., as a function of time

K = dynamic amplification factor

q_o = peak dynamic pressure, psi

A = member projected area, including shading effects, in^2

C_D = member peak drag coefficient as a function of time

The force F_t, represents the maximum dynamic load in the structure and can be used as an equivalent static load for purposes of design and analysis. The location of the force is dependent on the C_D and A of the individual members; that is, it is the resultant of the forces on each member.

The above parameters are dependent upon the structural dynamics of the mast, upon the geometry of the mast, and upon the blast environment. A discussion of the parameters is presented in this paper.

In general, there was close agreement

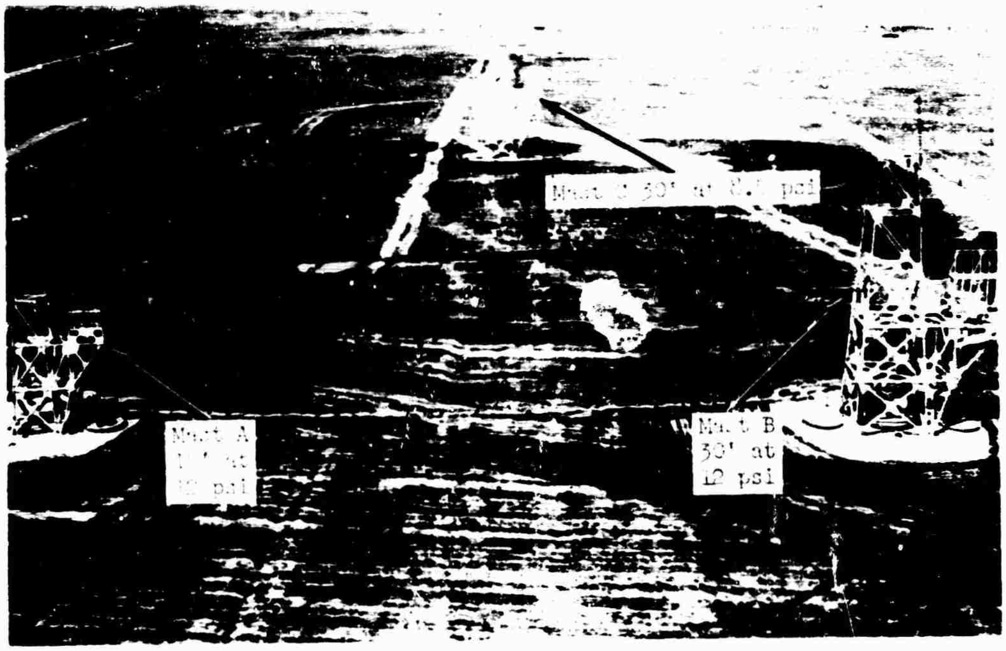

Figure 1. Antenna Masts Locations

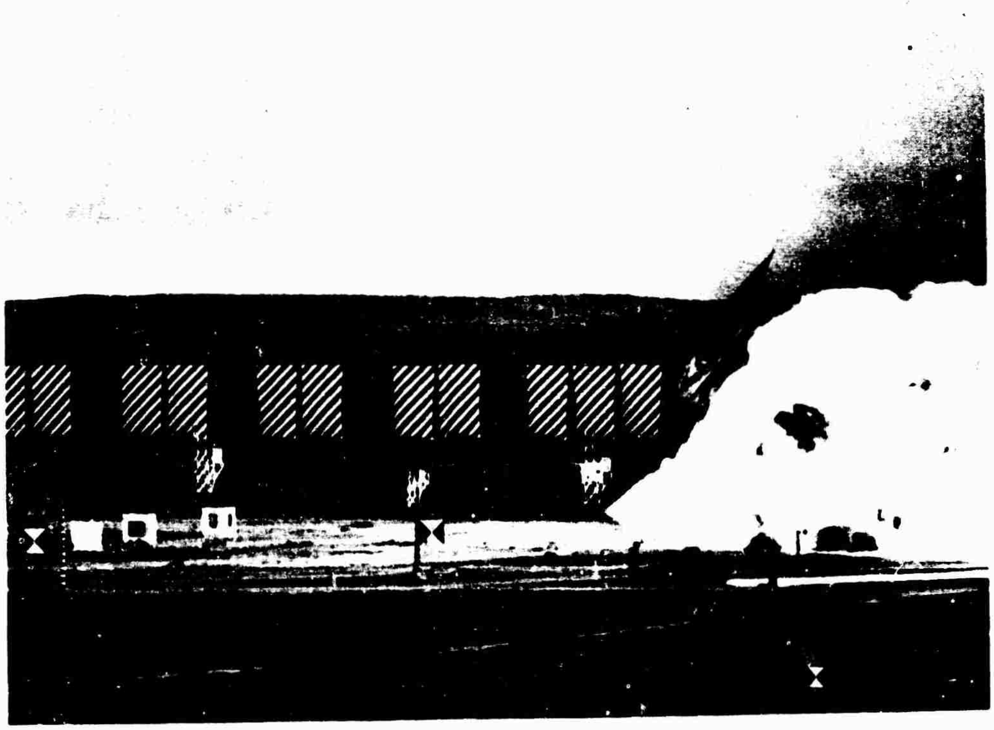

Figure 2. Operation Prairie Flat

between the experimental and analytical results. The consistency of the ratio between experimental and computer results indicates a factor which can be used for mast design purposes.

For this particular program, that is, this type of structure and blast, the design force can be considered:

$$F_t = 1.67\ Kq_o \sum AC_D$$

where K is equal to the impulse response value of $4\pi f_n$ and the factor 1.67 is an experimental factor obtained for all three masts.

THEORETICAL CONSIDERATION

The purpose of the project was twofold: (1) to develop an analytical design method for determining the dynamic loading of a typical shipboard antenna mast subjected to a blast environment, and (2) to design test antenna masts and provide instrumentation plans for test verification of the design approach.

The preliminary analysis showed that a typical shipboard antenna mast can be adequately represented by the following four basic components. (Figure 3)

FOUNDATION DESIGN CONSIDERATIONS

The design of adequate foundations to support the 15' and 30' masts used in the tests of Operation Prairie Flat was based on the theoretical dynamic response of the foundations embedded in the soil of the experiment station. The determination of foundation size was based primarily on the soil mechanics properties determined at the test site.

The foundation was sized by considering the equivalent elastic springs of the soil supporting the foundation, together with equivalent linear damping, with the foundation dynamically responding to the shear and overturning moment time varying loads transmitted by the mast. The foundation natural frequencies were then determined, and the response of the foundation to the mast which transmitted the time varying shear and overturning moment was calculated.

The foundation designs for the 30' mast at lower overpressure and for the 15' mast were determined by rationing the dynamic loads to one-half and one-third, respectively, of the reference design. The foundations were sized in accordance with these loads.

A preliminary analysis of the antenna mast design showed that the mast foundation was dynamically uncoupled and would not influence the dynamic response of the antenna mast. Consequently, a rigid base for the antenna mast response analysis was assumed.

The determination of the amount of motion of the foundation due to the 500 ton surface explosion of Operation Prairie Flat was desired. This information provides insight into the response of buried foundations to ground shock and provides knowledge of the amount of base motion input to the antenna mast. The foundation response was to be measured by accelerometers mounted at specified locations on the concrete block. These accelerometers were emplaced on mounting studs located within steel boxes. A minimum of six accelerometers were utilized to provide all three translational components and all three rotational components of acceleration.

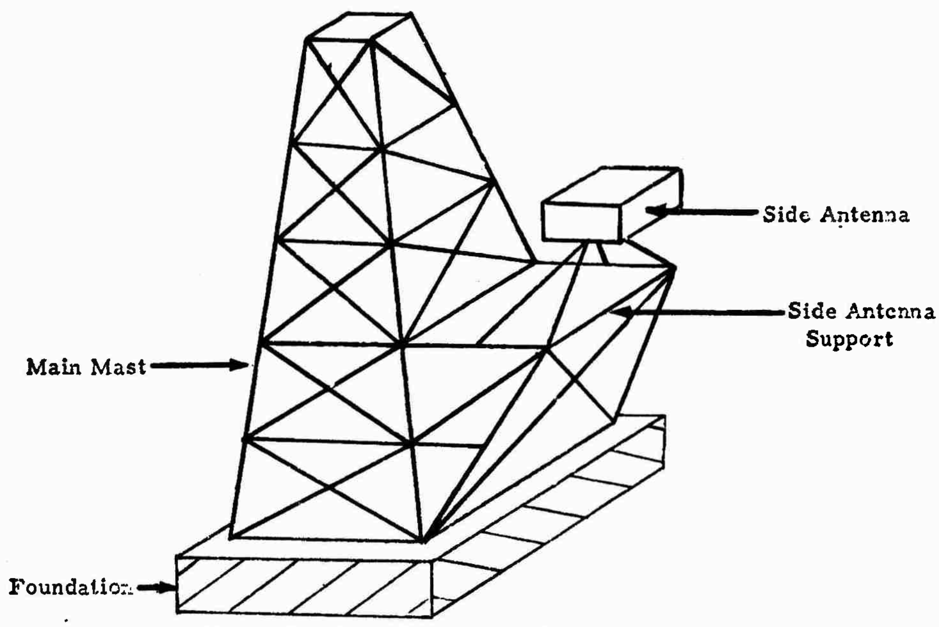

Figure 3. Basic Components of Mast Program

MAIN MAST AND SIDE ANTENNA
SUPPORT DESIGN CONSIDERATIONS

After having identified the basic components, the following design parameters were frozen to initiate detail design and construction of the test antenna mast and method of instrumentation:

- three separate main masts, one 15' mast and two 30' masts
- a square base configuration
- a simulated side antenna of pipe frame construction with a drag area ratio of 0.3 (ratio of antenna projected area to structure projected area)
- two overpressure locations: 8.5 psi (30' mast) and 12.5 psi (15' and 30' masts).

A mathematical model of the antenna mast structure was developed. In the model, the antenna mast was assumed to have rigid joints and was mounted on a rigid foundation. The joints were allowed six degrees of freedom and were connected by weightless elastic bar members. The weight and inertia of the structure were located at the joints. The geometrical and elastic properties of the structure were represented by the line bar members. In obtaining the dynamic response, the external forces and moments due to the blast were applied at the joints.

The vibration characteristics of the antenna masts were calculated by the Stardyne computer program. These calculated modes were later verified by a twang test on the actual structure.

ANTENNA DESIGN CONSIDERATIONS

The geometry and basic design of the two simulated antennas were determined in the analysis.

The 15' antenna was fabricated with four equal frontal bays separated from one another by vertical plates. Two 1-1/2" nominal diameter tubes were located vertically in each bay. The bays were separated into two horizontal sections by three 2-1/2" nominal diameter tubes.

Due to higher drag force data obtained from references prior to the blast, the antenna was modified by removing two of the bays. The primary reason for the modification was that the theoretical drag predictions were considerabl_ higher than anticipated. Consequently, the antenna frontal area was reduced.

In the structural model, the antenna was represented by a single joint at the antenna center of gravity and was connected by four bar members to the side antenna support. The antenna's inertial properties at the c.g. about the three axes were calculated and used in the structural model. The antenna weight, inertia and drag area were modified in the structural model to correspond with the actual antenna tested.

DRAG CONSIDERATIONS

Prior to the test, it was determined analytically that drag loads, rather than diffraction loading or ground motion caused by the blast, produce the most significant loads on the antennas and on the masts. The important parameters affecting the drag overpressure load include:

- the time history of the drag overpressure
- the drag coefficient (C_D)
- the projected area of the structure, including shading effects
- the effects of gussets
- the Reynolds number.

The most difficult parameter to determine was the drag coefficient. Several concepts were studied before a satisfactory analytical model was derived. The original concept considered the steady state drag coefficient to be equal to 1.2, with no aerodynamic shading of the aft members by the front members in the antenna mast structure. The load distribution was based on the bar members' projected area and was a function of the dynamic pressure. Reynolds number effect and the gussets area were not used and were assumed to be accounted for by the drag coefficient conservatism.

The concept was later revised to include the gussets area with the bar member area, in addition to taking into account the effects of aerodynamic shading and Reynolds number on the drag coefficient. An overall effective drag coefficient of 0.56 was calculated for a quick look at the mast responses. On the basis of this comparison, a final pretest analytical calculation was made for the individual effective drag coefficients. Again, the aerodynamic shading and Reynolds number effects were included. All flat plates used a value of C_D of 1.6. These values were used with the appropriate values of dynamic pressure and area to derive the forcing function used in the pretest dynamic response analysis.

The data selected which best represented the drag time history was measured by the 3" cylinder located at 8.5 psi. This data was normalized and used as the drag-time history curve for all the dynamic response calculations. (Figure 4).

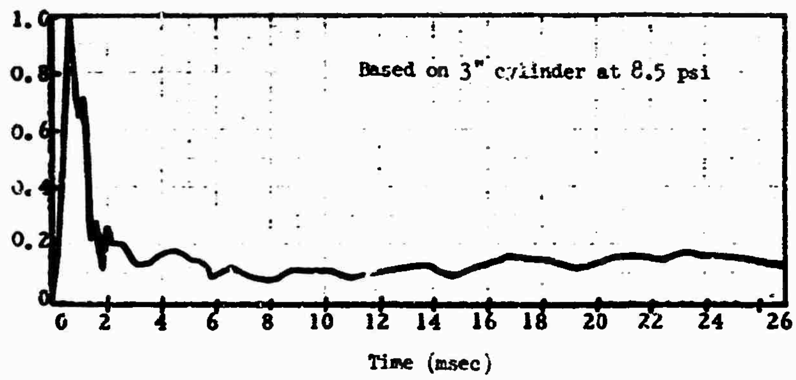

Figure 4. Normalized Drag-Time History

COMPUTER PROGRAMS

The determination of the dynamic response for a simple one, two or three degree-of-freedom system subjected to a mathematically simple time variation load can be accomplished by a rigorous or closed form method. However, actual dynamic problems almost always have many degrees of freedom and a complex load-time variation.

To obtain the internal design loads in a typical antenna mast due to a blast generated overpressure, calculations based on the rigorous method are very difficult, or impossible, and a numerical analysis is required. Consequently, the calculations in this analysis were performed with a series of digital computer programs designed to analyze linear elastic structural models. The method of analysis using the computer program is illustrated by the simple flow diagram in Figure 5 on the following page.

The computer programs used for the mast analysis are briefly described below:

PREP

The first in this series of computer programs is the preprocessor. Primarily, the functions of this program are to read the arbitrarily coded input data, check for modeling and coding errors, and optimize the joint numbering scheme to insure the most efficient use of computer time.

STARDYNE

This is a large order finite element program based on the "Stiffness Method" or "Displacement Method". The program has two distinct functions that are applicable to this study: a modal analysis and a static analysis.

Modal Analysis

Once the mathematical model of the mast-antenna structure has been defined, STARDYNE calculates the stiffness matrix and mass matrix along with their resulting dynamic matrix. The mode shapes and frequencies are obtained by one of the following methods: (1) Inverse Iteration Method, (2) Classical Jacobi Extraction, (3) Householder Tridiagonalization and Q-R extraction. In addition, the program computes the generalized weights, the participation factor and the internal forces on the members associated with each mode.

Static Load Analysis

Given the mathematical model of the mast-antenna structure, STARDYNE calculates the reaction to any general type of static load. The displacements of the system, as well as the internal forces of the members in the system due to the given external static load, are calculated by STARDYNE.

DYNRE-1

This is a computer program designed to analyze the time dependent response of linear elastic structural models subjected to dynamic loadings. The "Normal Mode Method" is used to obtain the response. The system's joint forces are calculated at several discrete time points. These loads are punched on cards for input into the STARDYNE static load analysis.

INSTRUMENTATION SYSTEM

The mast-antenna measuring system consisted of transducers, signal conditioning equipment, and a recording system. The transducers were capable of measuring strain, vibration, pressure, and drag forces. The data acquisition system is shown in the photograph of Figure 6 on the following page.

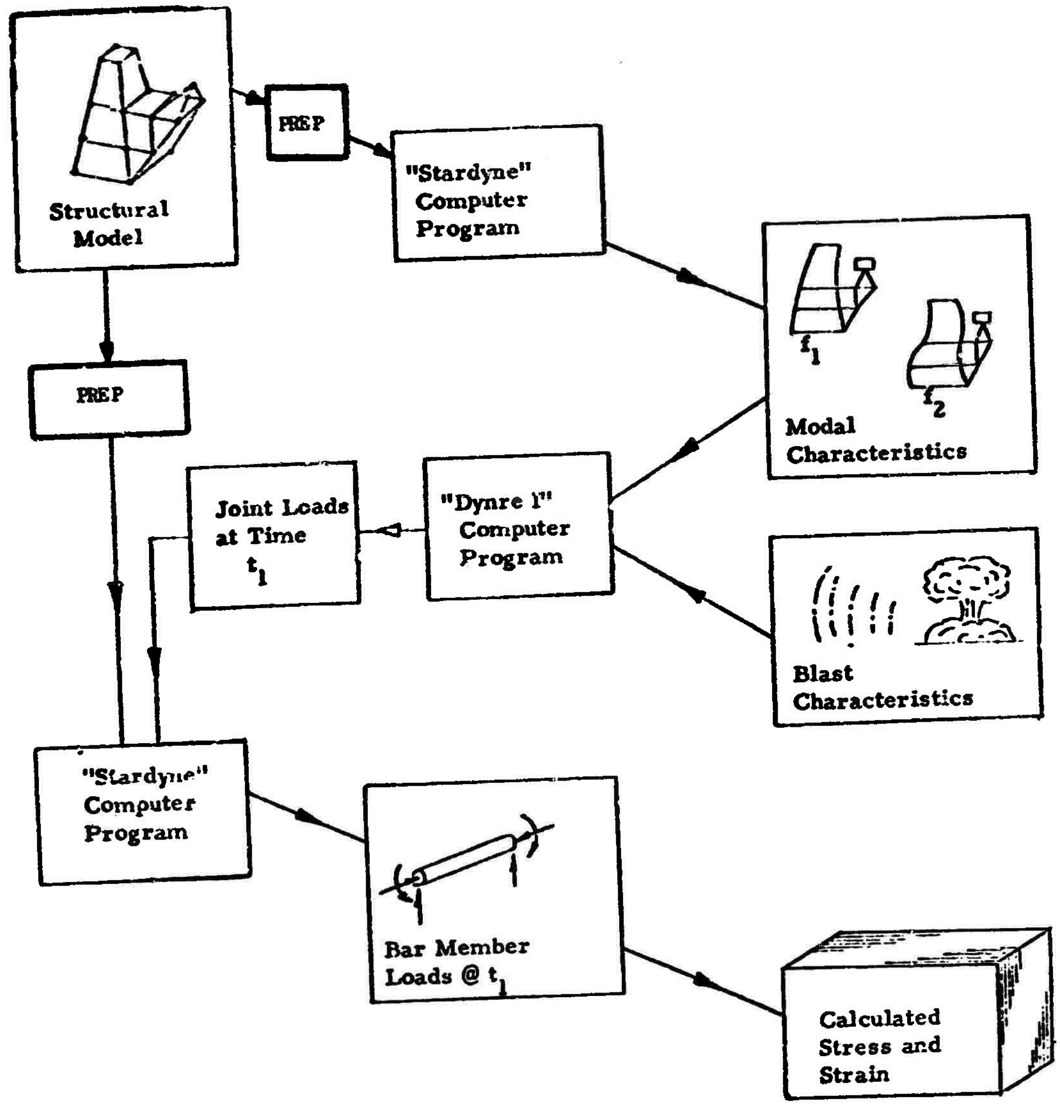

Figure 5. Strain Calculation Flow Diagram.

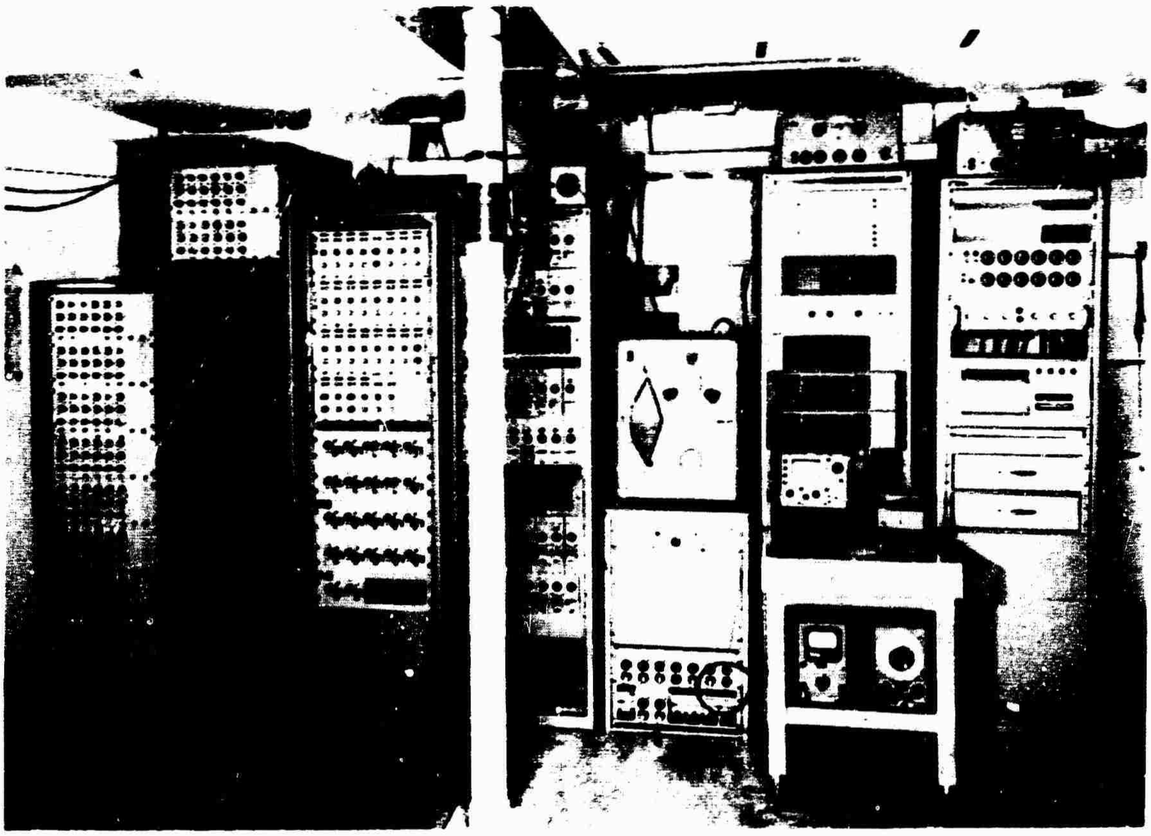

Figure 6

Photograph of the Data Recording and Data Playback System

The data recording system consisted of four data multiplexers and a magnetic tape recorder. The data playback system consisted of an eight channel demultiplexing unit and an oscillograph recorder. The transducers used for the mast measurements were strain gages, accelerometers, pressure gages, and strain drag gages. Locations are shown in Figure 7. To obtain a complete picture of the force in the mast at the mast-foundation interface, strain gages were placed on the lower member legs. These members were instrumented for axial loading. Accelerometers were placed on the foundation and on the mast, as shown in Figure 7. Six accelerometers were mounted on each foundation. Additional accelerometers were placed on the masts to obtain the first mode behavior of the mast. Drag gages were mounted near each 30' mast at each overpressure location. Two types of drag gages were used: strain gaged force measuring gages and free flight cylinders. Three pressure transducers were located on each mast.

TWANG TEST

At the conclusion of the installation of all the transducers, a mechanical twang test was performed on each of the masts. This test consisted of applying a known load to the structure. The load was applied in three steps of approximately 10,000 lbs. each, to a value of 30,000 lbs. At the latter value, the load was released with a quick release system, allowing the masts to oscillate. The twang test system is shown in the photograph of Figure 8 on the following page.

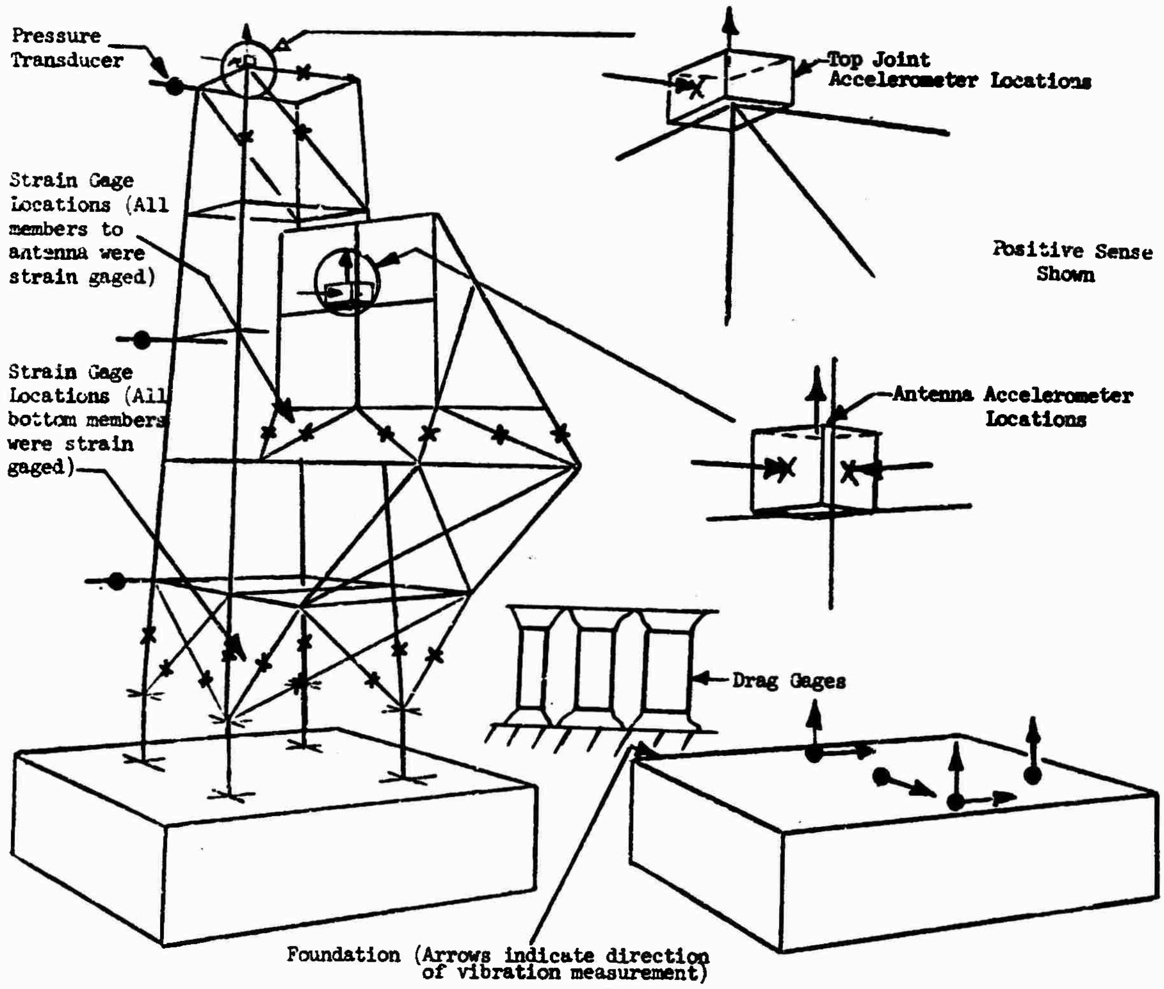

Figure 7

Tranducer Locations on Antenna Masts

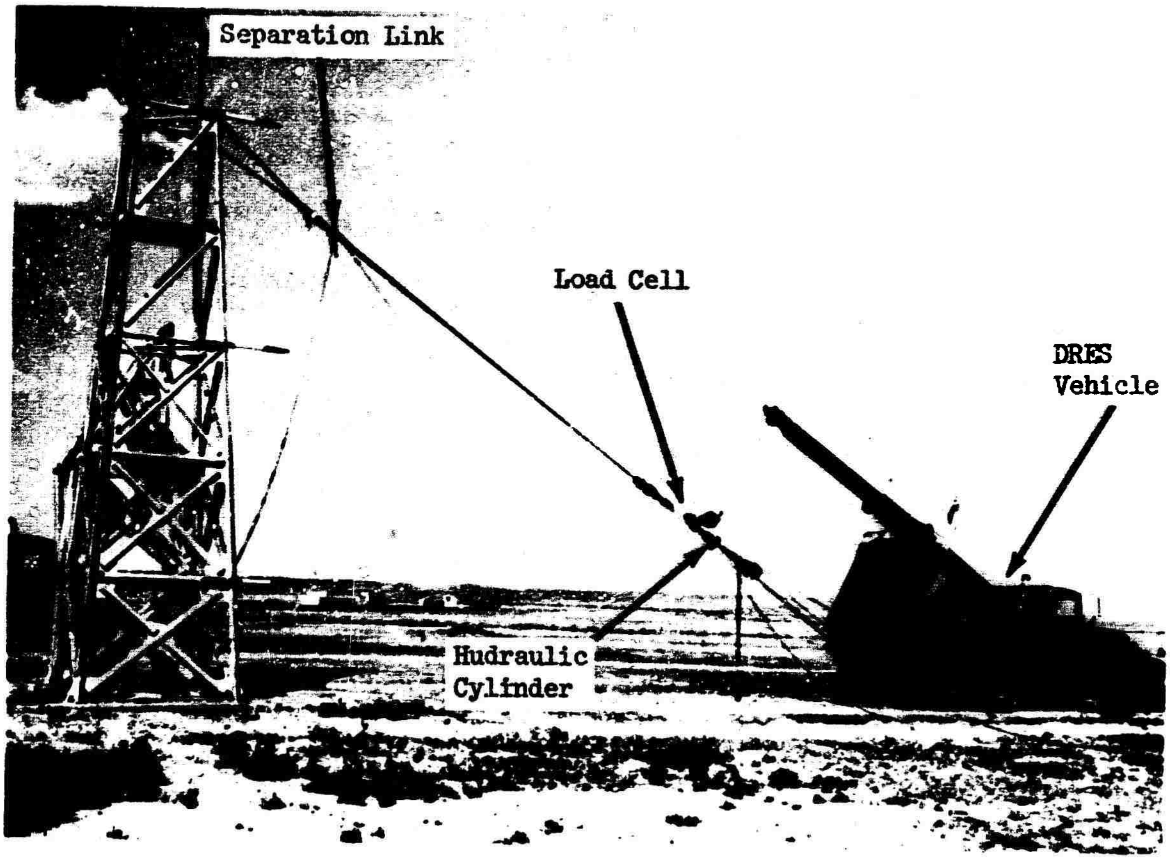

Figure 8

Twang Test Setup

[illegible]

[illegible] objectives of the twang tests [illegible]:

(1) to verify the analytical model of the [illegible] and to confirm [illegible] lengths.

(2) to measure the strain in the instrumented members in order to determine the amount of prestress and to ascertain that the [illegible] occurred in the linear region of the [illegible] strain curve,

(3) to verify repeatability of results,

(4) to check all instrumentation channels.

All test objectives were realized with the twang tests.

Objective 1. The analytical models of the 30' and the 15' masts were verified. The modal frequencies were compared with the experimental frequencies obtained during the twang tests, and the actual damping of the masts was calculated.

The modal frequencies were obtained from the experimental results both by filtering the data recorded on magnetic tape and by the use of a digital computer program. The latter method was more accurate, as some of the modes were too close in frequency to be separated by experimental methods. The results from one of the channels are shown in Figure 9.

The modal frequencies in the blast direction were compared, and the first and second mode frequencies obtained experimentally agreed with predicted computer results.

In the theoretical predictions, a damping ratio of zero was used. The critical damping ratios obtained from the twang tests were 2% to 4%.

The static strain values obtained from the computer output were checked against the experimental results. The data agreement was very good (with differences of less than 20%) for most of the channels.

Objective 2. The strain values caused by the applied static load during the twang tests indicated that the loading was in the linear region of the load-strain curve.

Objective 3. The repeatability of the strain outputs for a given load was checked by applying similar loads to the same mast. The data from this test indicates that data repeatability was obtained.

Objective 4. Instrumentation channels were checked during the twang test loading. Three channels were found inoperative. They were repaired, so that data was obtained from these stations during the actual blast.

In conclusion, the twang tests indicated agreement between predicted computer responses and experimental responses. The variaion in frequency for the first two modes between analytical and experimental results was only 7%, and the variation in strain values for mast members between analytical and experimental results was 15% to 20%.

RESULTS

Utilizing the results from the twang tests, new analytical predictions were obtained. Time history plots for the member joints, mode frequency values, and axial strain values for each member were obtained. These analytical predictions were derived from the previously described computer programs.

The experimental data was reduced to amplitude-time histories and to the amplitude-frequency spectra domain. The peak axial strain values were reduced and tabulated for each member.

The dominant frequencies obtained from spectrum analysis of the blast data agree favorably with the values obtained from the modal analyses of the structures. Frequency agreement was obtained for the first six modes.

A comparison of the maximum experimental axial strain with the maximum calculated axial strain for instrumented tubular members of the antenna mast structures indicates that the calculated axial strain is about 60% of the experimental axial strain.

The duration of the analytical input pulse spike is approximately 2 milliseconds. The masts respond primarily in the first mode, as shown by both computer and experimental

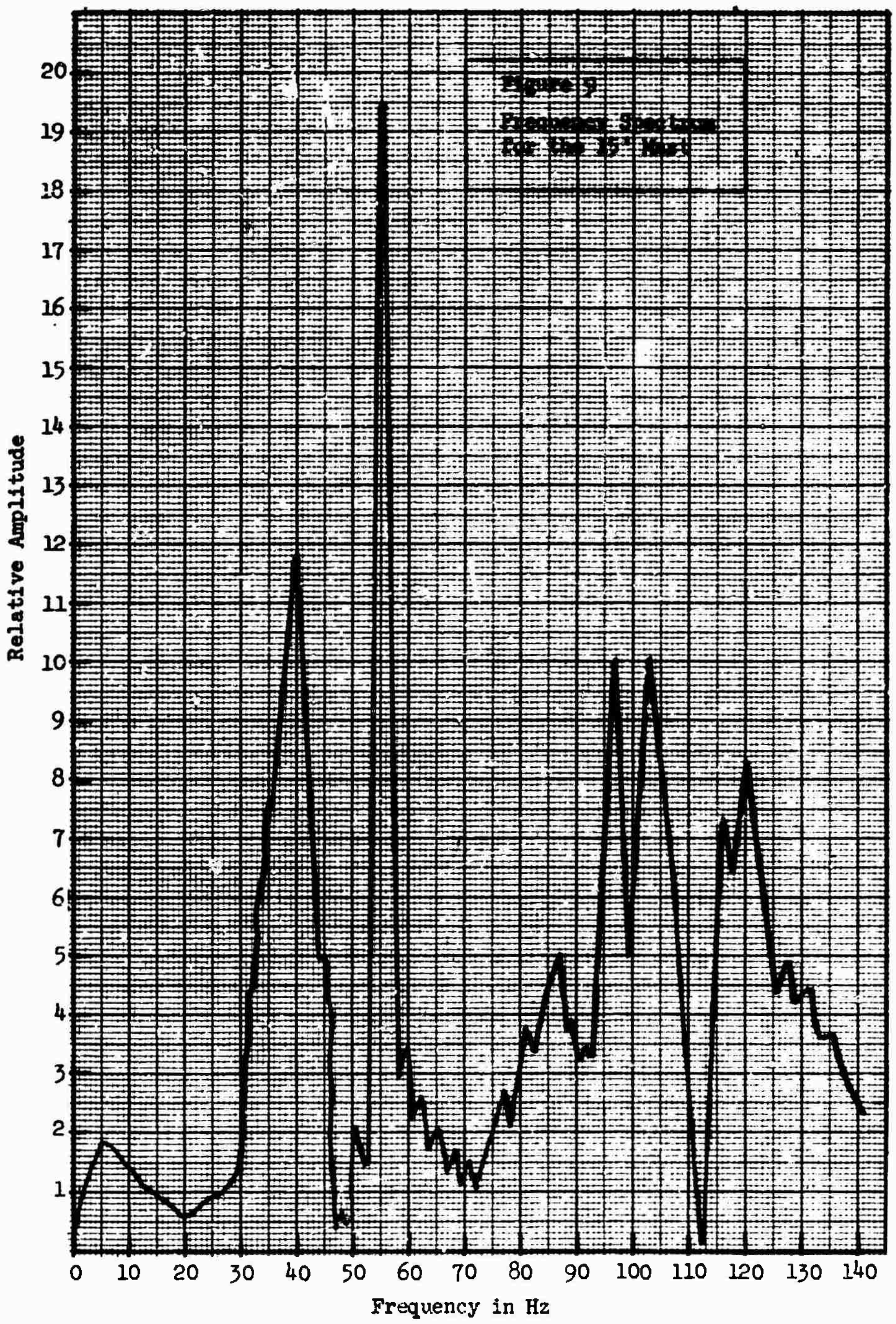
Relative Amplitude
20
19
18
17
16
15
14
13
12
11
10
9
8
7
6
5
4
3
2
1
0
10
20
30
40
50
60
70
80
90
100
110
120
130
140
Frequency in Hz

results. The system can be approximated as a single-degree-of-freedom system for purposes of studying the effect of pulse duration. For values of τf_n less than 0.2 the impulse of the shock becomes more important than the shape. In this "impulse region" the value of the amplification factor (for all pulse shapes), can be approximated by:

$$A_m = 4\tau f_n$$

The table on the following page shows agreement between the single-degree-of-freedom amplification factor, A_m, and the ratio of response to input forces from the computer analyses. This is a further indication of the significance of the first mode with regard to the mast structual response. The equation for A_m is an accurate approximation of the amplification factor (in this case, attenuation factor). It can be concluded that changes in the actual shock pulse duration will change the response loads in the masts proportionally. Therefore, the duration of input pulse has a significant influence on the loads.

CONCLUSIONS

The experimental program verified the assumption of the theoretical predictions. The conclusions obtained from the experimental program are stated below.

1. The behavior of the masts clearly establishes the quasi-single-degree-of-freedom dynamic behavior of antenna mast structures.

2. The foundation will slightly lower the dominant mode frequency of the antenna mast. Thus, it is sufficiently accurate to predict that future designs of antenna masts will assume a rigid base.

3. Dynamic analysis must be performed for any new mast design. The above conclusion is still deemed necessary in order to establish the modal frequencies and to find the load distribution throughout the masts.

4. Ground shock loads are negligible, amounting to approximately one tenth of the loads which result from the drag overpressure.

5. The computer programs utilized enable very precise predictions to be made of modal frequencies for antenna mast structures.

6. The computer predictions are adequate for masts of different sizes and at different overpressure locations.

BIBLIOGRAPHY

1. "RCN Antenna Mast Study", A. Britt, A., MRI Report TR-C181-1, March 15, 1967.

2. "Foundation Designs for Ships' Masts Subjected to Air Blast", including drawings 1, 2, and 3, Bartholomew, R., MRI Report C216-TR-1, Sept. 1, 1967.

3. "Literature Survey - Blast Loads on Cylinders and Flat Plate Antenna Components", Wolkovitch, J., MRI Report C0255-TR-1, June 26, 1968.

4. "Proposed Antenna Mast Suffield Experimental Station - Report on Subsoil and Foundation Conditions", Materials Testing Laboratories, Ltd., August, 1967.

5. "Dynamics of Bases and Foundations", D.D. Barkan, McGraw-Hill Book Company, Inc., New York, N.Y. 1960.

6. "The Vibration of Foundations with Various Types of Subgrade Support", N.E. Funston, Ph.D. Thesis, Urbana, Illinois, 1965.

7. "The Effects of Nuclear Weapons", U.S. Department of Defense and Atomic Energy Commission, 1962.

8. "Principles and Practices for Design of Hardened Structures", Air Force Design Manual, AFSWC 62-132, December 1962.

9. "Hypersonic Aerodynamics", R.W. Truitt, Ronald Press Corp., New York, N.Y., 1969.

10. "Nuclear Handbook" - Effects of Nuclear Weapons, S. Glasstone, Ed, U.S. Atomic Energy Commission, April 1962.

11. "Lift and Drag Forces on a Circular Cylinder in a Flowing Fluid", R.E.D. Bishop and A.Y. Hassian, Proc. Roy. Soc. (A), p. 32, January 1964.

12. "The Interaction of a Long Duration Friendlander Shaped Blast Wave with an Infinitely Long Right Circular Cylinder", Bishop, V.J., U.K. Atomic Energy Authority, Atomic Weapons Research Establishment, September 1965.

13. "Drag Measurement on Cylinder by the Free Flight Method-Operation Prairie Flat", Mellsen, S.F., DRB Project No. D-16-78-07.

14. "Canadian Blast Simulation Facilities", Patterson, A.M. DRB Project No. D52-99-10-38, January 1967.

TABLE 1

Dynamic Amplification (Attenuation) Factors			
	MAST A	MAST B	MAST C
Theoretical single-degree of freedom system:			
τ pulse duration	.002 sec	.002 sec	.002 sec
f_n, natural frequency (1st mast mode)	40.4 Hz	23.7 Hz	23.7 Hz
$A_m = 4\tau f_n$	.323	.19	.19
Computer Analysis			
Computer Peak Input Force, F_{1N}, lbs.	230,429	463,167	217,507
Equivalent Force, F_T, lbs. (Response Load)	72,800	106,000	49,600
Amplification factor $= \frac{F_T}{F_{1N}}$	.317	.229	.228

Mr. Hughes (Naval Weapons Evaluation Facility): You mentioned the determination of damping by your twang test. Can you give us the damping coefficient?

Mr. Geminder: Yes, it was of the order of 0.2 or 0.3 for the first mode.

Mr. Naylor (Defense Research Establishment, Suffield): Your value of about 0.6 of the computed results to experimental results showed a deficiency in estimating the drag loads. When you inserted your experimental forcing function did you include the whole of it or just the initial spike? Recently we have done more tests with drag cylinders in the 6 ft. shock tube and we found that at these very low overpressures the initial spike had roughly the same impulse as the succeeding drag for the next few milliseconds. So than, as you pointed out, the initial spike is of great importance, but this does not account for all of the impulse applied. We estimated that if you add the drag load to its initial spike then your computed results would be very close.

Mr. Geminder: You asked whether we put the whole time history in. Yes, we did. Our forcing function input is not just a number; it is actually a time history input.

Mr. Naylor: I thought you said that you just applied this initial spike.

Mr. Geminder: No, I made the statement that the initial spike has the most effect, just as you pointed out, but the actual time history shown was what was placed. And not only that, that drag coefficient was merely a representative plot. It changed as a function of tube size from 3 1/2 to 6. We changed it as a function of overpressure. We delayed the time from the front to the rear. We delayed the time around each of the cylinders because it was different. All of this was put into the computer program and this 0.6 was based on all of these inputs.

Mr. Roberts (Martin Marietta Corp.): Would you speculate for our benefit as to what the difference is between the computer result and the measured case history?

Mr. Geminder: The computer results are based on strictly a computer model. The only experimental data that was placed into the model was the forcing function, which is this drag that we kick around. In other words, we do not know what force to put in there. As I pointed out, when you have six cylinders and the cylinders at 12 psi give you a lower drag coefficient than the ones at 8 1/2, they are suspect. The fact that we had fairly close (10-20 percent) agreement on our member loads on each of the masts, and that the model agreed frequencywise, made the forcing function suspect.

Mr. Naylor: As the Reynolds number decreases you get an abrupt increase of drag coefficient. Now these 3 1/2 inch cylinders at the low pressures were very close to this abrupt rise. Thus it is possible for the drag coefficient to be higher at 8 1/2 psi than at 12 because of the dip in the Reynolds number curve.

Mr. Geminder: I agree with you. This is a very critical region.

Voice: I do not think the total drag could be higher at the 8.5 psi location, but it is possible at the higher pressure level that the drag coefficient dropped as the cylinder size increased. That is, the slope of the curve is such that your drag coefficient decreases as Reynolds number increases. I would say the drag coefficient could drop from about 0.6 conceivably down to as low as 0.4 just by increasing the size of the cylinder.

LATERAL RESPONSE OF SLIGHTLY CURVED COLUMNS UNDER LONGITUDINAL PULSE LOAD

Thomas L. Anderson
Department of Civil Engineering
University of Idaho
Moscow, Idaho

and

Martin L. Moody
Department of Civil Engineering
University of Colorado
Denver, Colorado

This paper presents response spectra for the transient lateral vibrations of columns of slight initial curvature. The bending vibrations are induced parametrically by the following longitudinal pulse loads: 1) zero rise-linear decay, 2) linear rise-linear decay, 3) rectangular, and 4) linear rise-constant. Selected individual transient solutions are shown, and certain nonlinear effects to account for large displacements and the effect of a mass attached to the end of the column are included and compared with the linear case. Under certain conditions, the addition of damping to the system is found to result in an increased response.

INTRODUCTION

Considerable attention has been given to the parametric vibration of columns loaded by axial periodic loads. The purpose of this paper is to present a portion of the results of an unpublished study [1] which investigated, in part, the transient lateral response of an initially curved column under a variety of single axial pulse loads. The column under consideration supports an initial static axial load and then is subjected to a time dependent pulse load. Meier [2], Koning and Taub [3] and Taub [4] have all investigated the linear form of this problem, but treat only a rectangular longitudinal pulse load. Transient solutions are presented in the form of dimensionless response spectra curves for four different longitudinal pulse forms. These response spectra represent the absolute maximum lateral column displacement at any time as a function of a characteristic frequency of the system. The make-up and use of these plots in analysis and design are discussed at length in the literature [5, 6].

BASIC EQUATIONS

In the presentation that follows it is assumed that the longitudinal force in the column is constant throughout its length at any given time. For practical loading velocities, this assumption is generally accepted [2, 7,8] owing to the speed of propagation of the longitudinal stress waves. In addition, it is assumed that the slight initial column crookedness and the time dependent lateral displacements of the column are defined by a one-half sine wave. These assumptions have been justified analytically [3] and experimentally [9] for similar problems. The development of the differential equation governing the lateral displacement of an initially curved column under time dependent longitudinal load is available in the literature [1, 10, 11] and will not be repeated herein. The column is assumed to be initially curved in one principal plane, of constant cross-section, stressed below the proportional limit, and simply supported as shown in Fig. 1. Considering the nonlinear effect of elasticity (large displacements) and inertia of an end mass results in the following dimensionless equation of motion:

$$\ddot{f} + 2\zeta\dot{f} + \left(1 - \frac{P_1^*}{1-P_o^*}\right) f + \gamma\,[f\,\ddot{f} + (\dot{f})^2]\,f$$

$$+ \frac{\pi^2}{(1-P_o^*)\ 8\ (L/r)^2}\, f^3$$

$$= \frac{a}{r}\left(\frac{P_o^* + P_1^*}{1 - P_o^*}\right) - \frac{a}{r}\,\gamma\,[f\,\ddot{f} + (\dot{f})^2] \qquad (1)$$

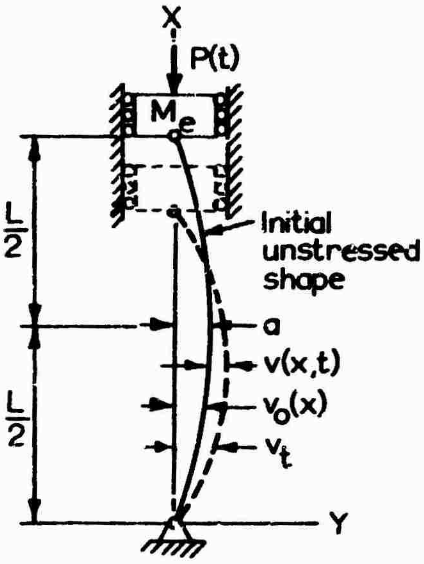

Fig. 1 - Initially Curved Column on Simple Supports

Wherein the following dimensionless parameters are to be considered:

$$P_o^* = \frac{P_o L^2}{\pi^2 EI} \qquad P_1^* = \frac{P_1 L^2}{\pi^2 EI}$$

$$\gamma = \frac{W\pi^4}{2(L/r)^2} \qquad \varepsilon = \frac{c}{2m\Omega} \qquad (2)$$

$$f = \frac{v}{r} \qquad W = \frac{P_o}{mgL}$$

The damping parameter ε in Eq. 2 represents the fraction of critical damping. The independent dimensionless parameters in the equation for dimensionless dynamic lateral displacement f are as follows: damping ε, dynamic load P_1^*, static load P_o^*, slenderness ratio L/r, ratio of static load to weight of column or weight ratio W, and initial mid-span displacement a/r. In this paper one value of initial imperfection is used (a/r = 0.1), and one value of slenderness ratio (L/r = 100) is used initially. Nonlinear terms in Eq. 1 in which γ appears are due to the end mass, and the terms with f^3 result from an approximate nonlinear curvature expression for large deflections.

The column is assumed to be "at rest," initially, therefore f(o) = 0, and the initial dimensionless mid-span displacement is

$$f(o) = \frac{a}{r}\left(\frac{P_o^*}{1 - P_o^*}\right) \qquad (3)$$

which corresponds to a column deflection under the static load P_o^*.

SOLUTIONS

Transient solutions of Eq. 1 for four different pulse over-loads were obtained on a digital computer. The equation was integrated numerically using Runge-Kutta formulas of order h^5. A time interval of 0.2π, corresponding to one-tenth the fundamental period, was used. The four dynamic load pulse shapes considered are shown in Fig. 2. They are a) zero rise-linear decay, b) linear rise-linear decay, c) rectangular and d) linear rise-constant. The dimensionless parameter α represents the ratio of pulse duration to fundamental period. The numerical values for the parameters in Eq. 2 were selected to represent values of practical interest.

The primary purpose of this paper is to determine the maximum lateral deflections which occur during or after the application of the pulses considered. To accomplish this goal sufficient transient solutions were obtained to define typical response spectra for each of the pulse shapes. The spectra are plotted for zero, ten and fifty percent of critical damping. Response spectra are shown for two different initial axial loads, P_o^* = 0.20 and P_o^* = 0.50. These values are assumed to be of practical interest since most design specifications contain requirements which limit the axial load for a column to less than one-half of the Euler load. Finally,

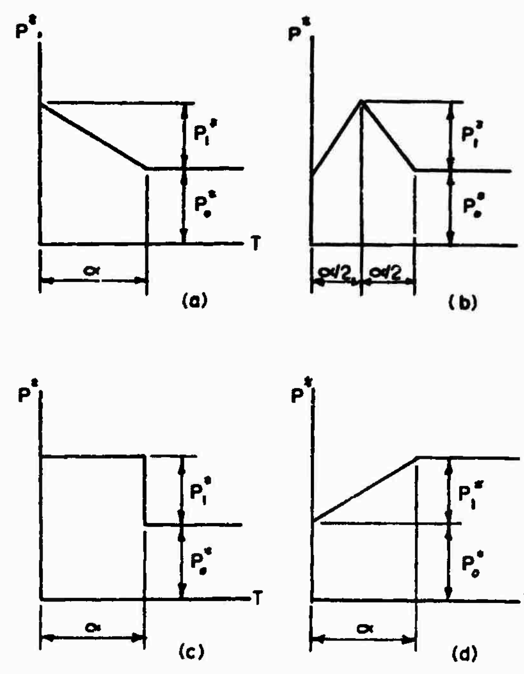

Fig. 2 - Force-Time Characteristics for Pulse Shapes Studied

the dimensionless weight ratio W was taken as 270 for $P_o^* = 0.5$, and for $P_o^* = 0.2$ a weight ratio of 108 was used which corresponds to four-tenths of the above weight ratio. This represents the same column section but under a reduced initial static load.

The response spectra are shown plotted as a function of dimensionless pulse duration α. The ordinate MF, called magnification factor, is defined as

$$MF = \frac{f_{max}}{f(o)} \qquad (4)$$

which is the ratio of maximum dynamic displacement to initial static displacement.

<u>Zero Rise - Linear Decay</u> - The response spectra for this pulse shape are shown in Figs. 3 and 4. The effect of decay of force on maximum displacement was neglibile as α became large. The maximum magnification factors indicated on these figures were obtained by direct solution of the linear form of the basic equation of motion using a rectangular pulse load variation. The undamped spectrum curves are asymptotic to these maximum ordinates. It is evident from this spectra that for load combinations near the Euler load a short pulse duration, vis., $\alpha = 2$, will result in a MF of less than half the maximum possible. These spectra were not affected by a change in weight ratio W from 108 to 270 for $P_o^* = 0.2$, therefore the remaining solutions were obtained for W=108 when $P_o^* = 0.2$ and W = 270 when $P_o^* = 0.5$. These figures also reflect response spectra for the linear form of the basic equation of motion. There is a difference, between the linear and nonlinear spectra for one case shown in Fig. 4, wherein the total static plus dynamic overload ap-

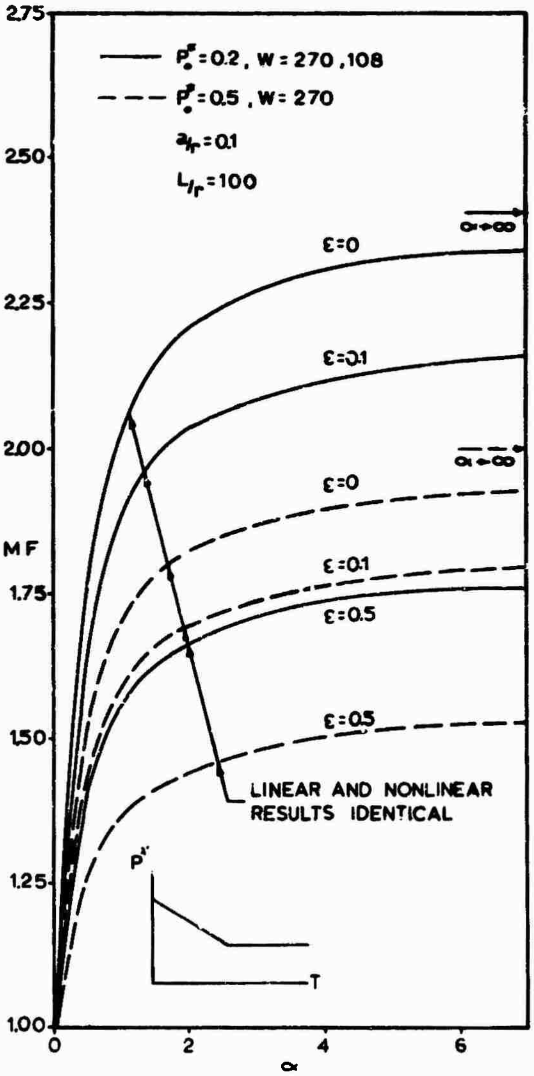

Fig. 3 - Response Curves for Mid-Span Column Displacement, $P_1^* = 0.1$

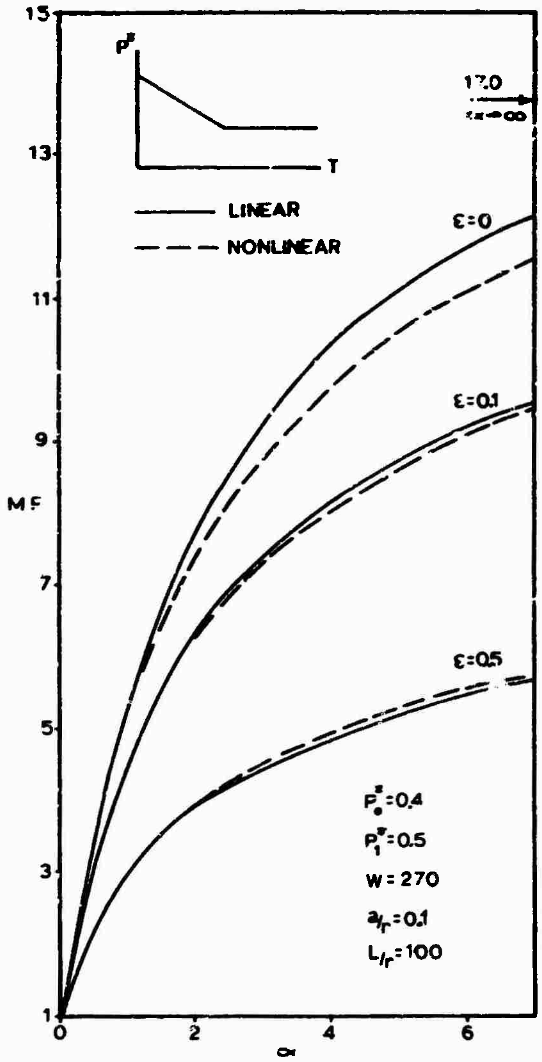

Fig. 4 - Response Curves for Mid-Span Column Displacement

proaches the Euler buckling load for the column, i.e., $P^*_o + P^*_1 = 0.9$. For these load parameters the column displacements are large which is to be expected. This difference between the linear and nonlinear spectra can be attributed, in part, to the nonlinear aspect of column curvature. Yet as the damping parameter ε is increased the nonlinear solutions produce larger displacements but to a lesser degree. For a practical problem with some damping, the difference in maximum response might reasonably be neglected without appreciable error. Transient solutions for this situation are shown in Fig. 5.

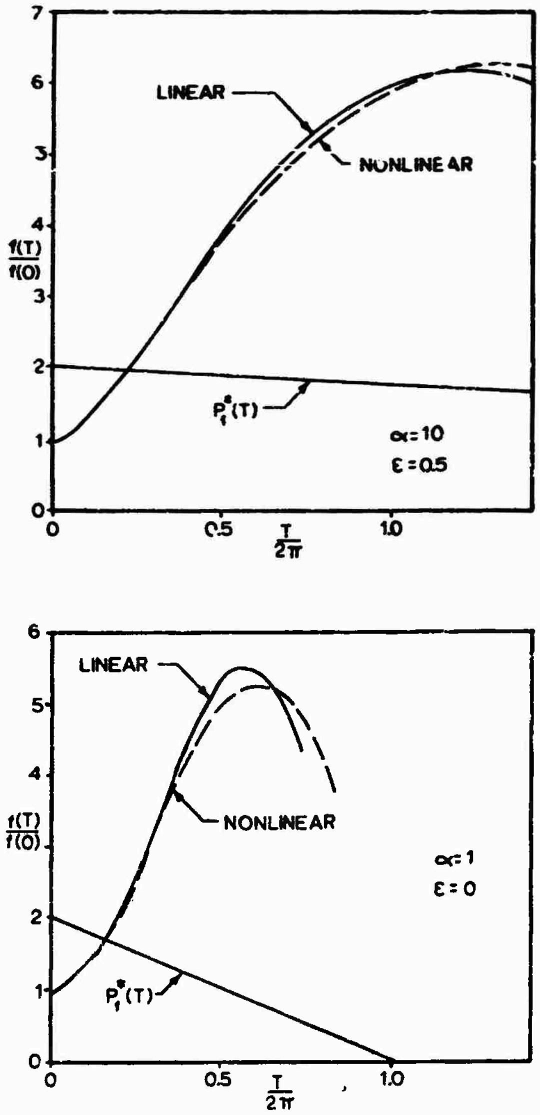

Fig. 5 - Linear and Nonlinear Transient Solutions for Linear Decay Pulse, $P^*_o = 0.50$, $P^*_1 = 0.4$

<u>Linear Rise - Linear Decay</u> - The response spectra for this pulse shape are shown in Figs. 6 and 7. It may be observed that, in general, the maximum magnification factor occurs when the pulse duration is approximately equal to the free lateral vibration period under the influence of the static load. The notable exception is seen in Fig. 7 for load parameters $P^*_1 = 0.5$ and $P^*_2 = 0.4$. For these loads the maximum MF occurs when α is large. The response spectra for a damping parameter ε of 0.5 are always less than the MF at $\alpha = \infty$. The magnification factors as $\alpha \to \infty$ were computed using Eq. 3 since for an infinitely slow rise times no vibrations will occur. Thus, P^* in that equation may be replaced by $P^*_o + P^*_1$ to evaluate the displacement at $\alpha = \infty$. Observe that for certain pulse durations the MF is nearly the same as if the load were applied statically, and for certain pulse durations the damped response is greater than the undamped response.

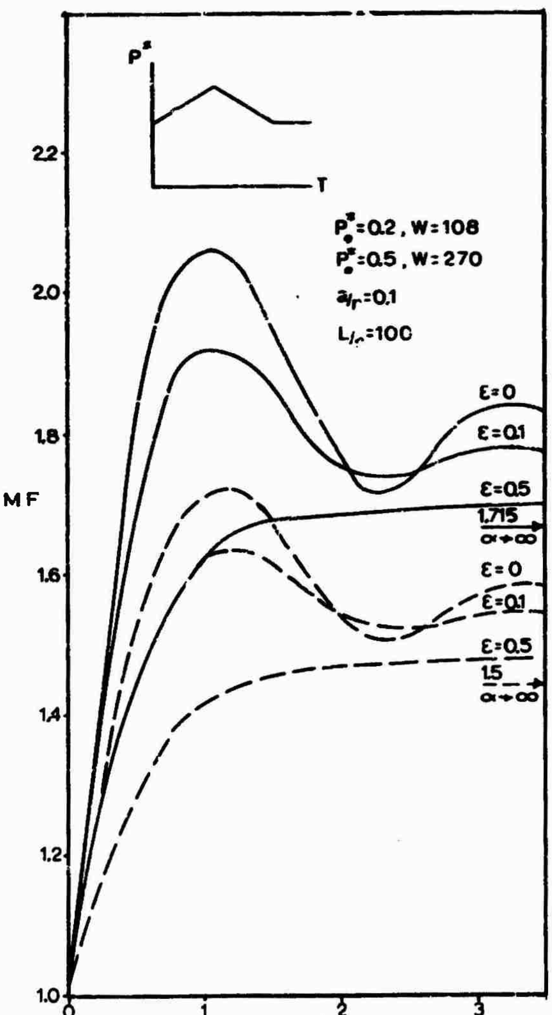

Fig. 6 - Response Curves for Mid-Span Column Displacement, $P^*_1 = 0.1$

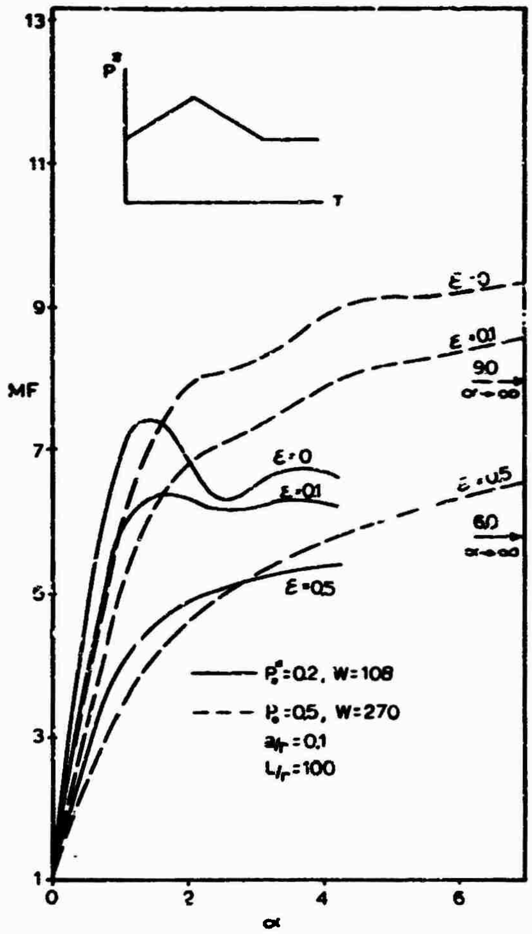

Fig. 7 - Response Curves for Mid-Span Column Displacement, $P_1^* = 0.4$

Rectangular - The response spectra for this pulse are shown in Figs. 8 and 9. It may be observed that for a small dynamic overload ($P_1^* = 0.1$) in Fig. 8 and when $\alpha > 0.6$, the maximum response is the same as if the load duration had been infinite. For $P_1^* = 0.4$ this is true for $\alpha > 2$. These spectra reach a different maximum for each damping parameter considered whereas for the other three pulse shapes considered the spectra reached a common asymptotic maximum as $\alpha \to \infty$ regardless of ε.

Linear Rise - Constant - The response spectra for this pulse are shown in Figs. 10 and 11. For long pulse durations it may be observed that the response simply follows the gradually applied load with little dynamic effect. These spectra are asymptotic to the same values of MF as $\alpha \to \infty$ as those shown in Figs. 6 and 7, and they were obtained in the same manner. Rise times α less than one-fourth produce magnification factors essentially the same as for the suddenly applied (rectangular) load. Thus, one may justifiably ignore the effect of rise time for this pulse shape when $\alpha < 1/4$ and treat it as a rectangular pulse of infinite duration

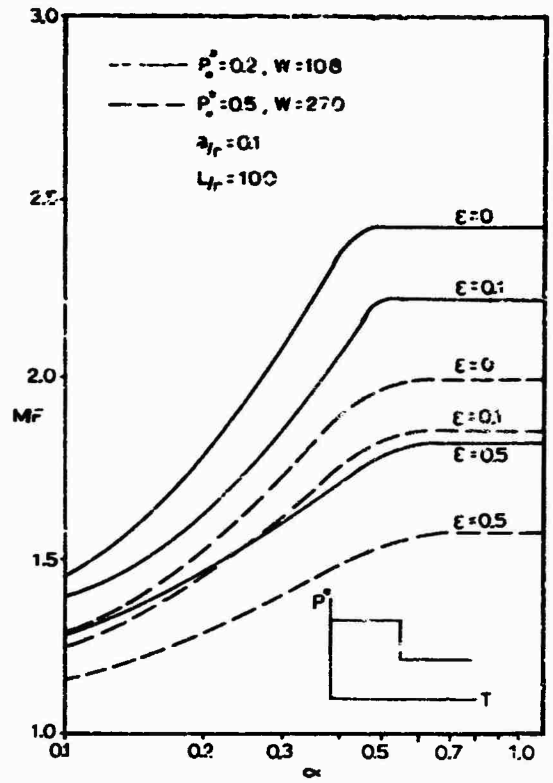

Fig. 8 - Response Curves for Mid-Span Column Displacement, $P_1^* = 0.1$

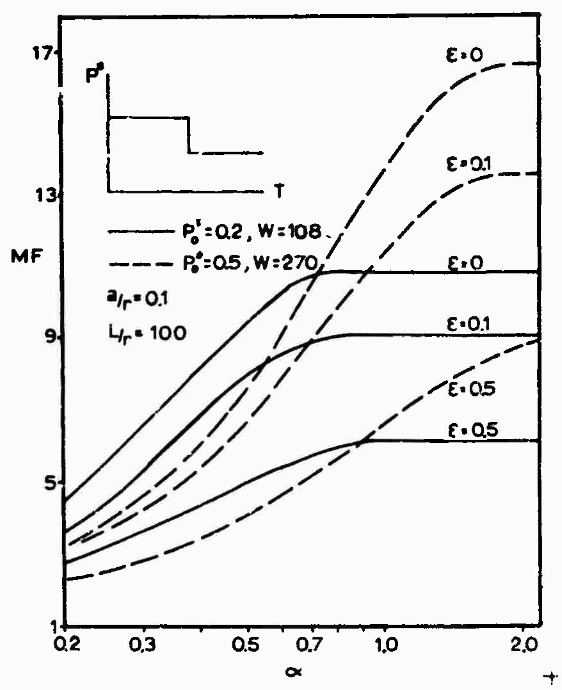

Fig. 9 - Response Curves for Mid-Span Column Displacement, $P_1^* = 0.4$

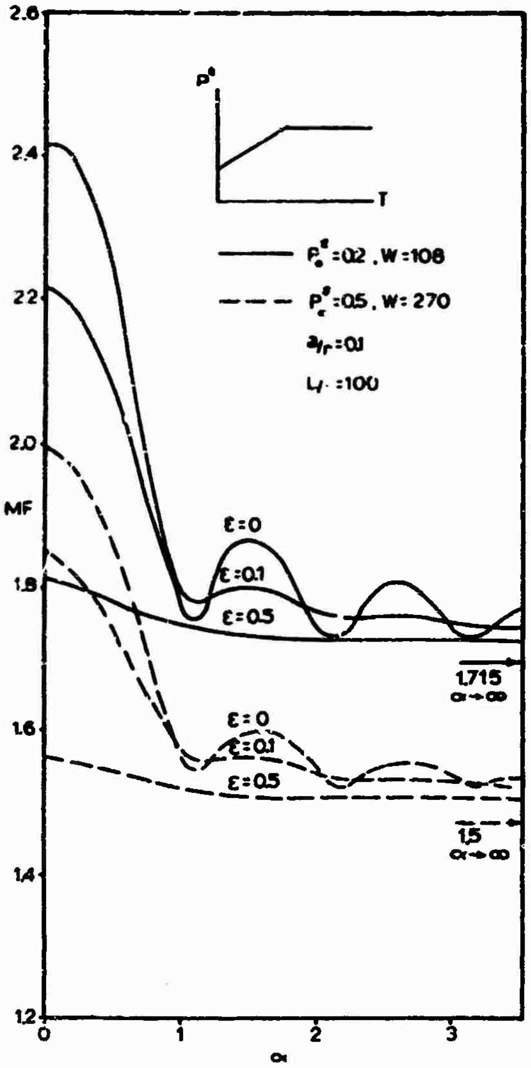

Fig. 10 - Response Curves for Mid-Span Column Displacement, $P_1^* = 0.1$

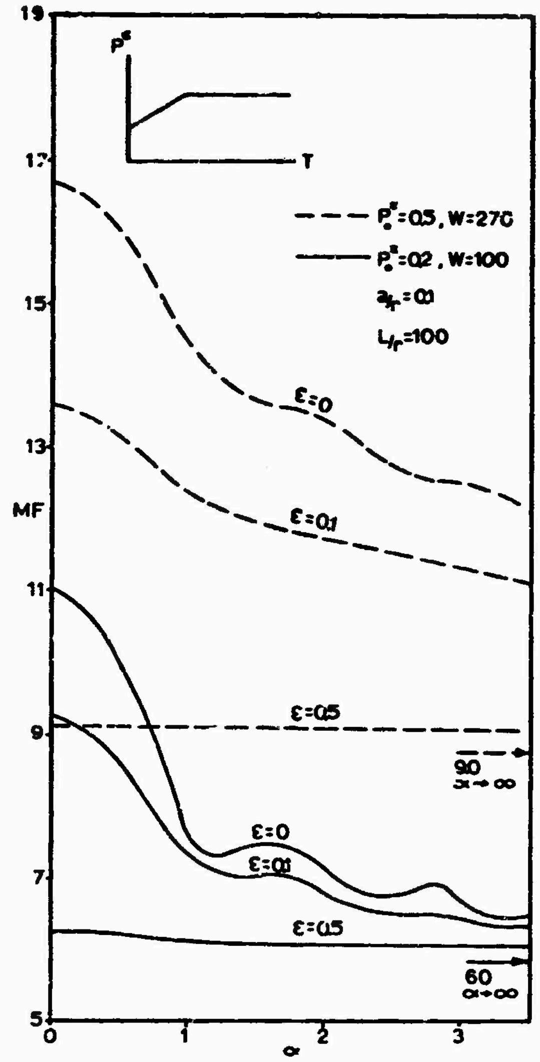

Fig. 11 - Response Curves for Mid-Span Column Displacement, $P_1^* = 0.4$

NONLINEAR PARAMETERS

The question naturally comes to mind regarding the influence of the nonlinear parameters, W and L/r, on the magnification factor. It should be pointed out that the selection of L/r = 100, W = 270 when $P_o^* = 0.5$ and W = 108 when $P_o^* = 0.2$ for use in obtaining the spectra was to a degree arbitrary. The authors, however, believe they represent practical values to be found in design practice. To study, in part, the influence of variation of the parameters on the magnification factor, additional undamped solutions were obtained for the rectangular pulse load. These comparative results are shown in Table 1 as magnification factors for P_1^* equals 0.4 and two values for P_o^* of 0.2 and 0.5. For each dimensionless static load two pulse durations are shown; one in which the maximum displacement occurred during the pulse and one in which the maximum displacement occurred after the pulse. Magnification factors are shown for various combinations of the parameter a/r, L/r and W. In addition the magnification factors obtained by closed-form analytic solution [1] of the linearized form of the equation of motion have been included.

Consider first the data for $\alpha \geq 1$. These data reflect little difference between the linear and nonlinear magnification factors as well as little change caused by variation of the parameter a/r, L/r and W. The greatest reduction, only 4%, occurred as a result of an increase in initial column crookedness a/r. In all cases the nonlinear magnification factors are smaller than those obtained by the linear solution. On the

TABLE 1
COMPARISON OF MAGNIFICATION FACTORS FOR RECTANGULAR-PULSE OVERLOAD

			Magnification Factors (MF) for $P_1^* = 0.4$			
			$P_o^* = 0.2$		$P_o^* = 0.5$	
$\frac{a}{r}$	$\frac{L}{r}$	W	$\alpha = 0.1$	$\alpha = 1.0$	$\alpha = 0.1$	$\alpha = 2.0$
0.1	50	108	2.844	10.85	2.105	16.38
0.1	100	108	2.855	10.96	2.188	17.00
0.1	200	108	2.858	10.98	2.211	16.88
0.05	100	108	2.858	10.98	2.211	16.88
0.10	100	108	2.855	10.96	2.188	17.00
0.25	100	108	2.836	10.81	2.050	16.25
0.1	100	50	2.857	10.98	2.213	16.86
0.1	100	108	2.855	10.96	2.188	17.00
0.1	100	200	2.853	10.93		
0.1	100	500	2.843	10.83	2.163	16.60
LINEAR			2.598	11.00	2.037	17.00
MAXIMAX OCCURS:			AFTER PULSE	DURING PULSE	AFTER PULSE	DURING PULSE

other hand consider the data for short pulse duration (α = 0.1). Here, the nonlinear solution resulted in larger maximum amplitudes compared with the linear results. The maximum difference is 16% for P^* = 0.2. For all the pulse durations shown the behavior of MF due to changes for the parameters was similar, for example, an increase in W caused a reduction in MF.

For the rectangular pulse data shown one can conclude that the rectangular pulse spectra could be justifiably utilized without modification over a range of parameters of the following: $0 < \frac{a}{r} \leq 0.25$, $50 \leq \frac{L}{r} \leq 200$, and $0 \leq W \leq 500$. On the basis of the above discussion one may reasonably utilize the spectra for the other three pulse shapes considered in this study for at least a limited range of the parameters a/r, L/r and W near the numerical values used to generate the spectra.

CONCLUSIONS

Using a nonlinear analysis, response spectra were obtained to define the absolute maximum transient lateral displacements at mid-span of a simply supported column carrying a static load and subject to four different single pulse dynamic overloads. These spectra may be used for analysis and design. The interpretation of the spectra to represent vertical ground accelerations is also possible [1]. The general influence of damping on the spectra was to reduce the dynamic amplification of the displacement except for some problem variables where the addition of damping increased the maximum transient dynamic displacement.

ACKNOWLEDGEMENT

The authors wish to acknowledge the Civil Engineering Department, University of Idaho, for their financial help in making the computer solutions possible.

NOTATION

E = modulus of elasticity

I = moment of inertia of column cross-section about axis of bending

L = unsupported column span

M_e = mass supported on the displaced end of the column

MF = ratio of absolute maximum dynamic column displacement to initial static displacement, $MF = f(T)_{max}/f(0)$

P = general axial column load

P^* = dimensionless ratio of axial column load to Euler buckling load

P_o = initial static portion of column load

P_1 = dynamic overload portion of column load as a function of time

P_o^* = dimensionless ratio of initial static axial load to Euler buckling load

P_1^* = dimensionless ratio of dynamic overload to Euler buckling load

T = independent dimensionless time variable equal to Ωt

W = dimensionless load ratio equal to P_o/mgL

a = initial unstressed column displacement at column mid-span

c = coefficient of linear velocity damping, a constant

f = dimensionless time dependent displacement at column mid-span, $f = v/r$

$\dot{f}$, $\ddot{f}$ = first and second derivatives respectively of f with respect to T

g = acceleration of gravity

m = mass of column per unit length

r = radius of gyration of column cross-section about axis of bending

t = independent time variable

v = dynamic lateral column displacement measured from the initial unstressed curvedaxis of the column

v_o = initial unstressed lateral column displacement measured from the a straight line between supports

v_t = total column displacement $v_o + v$

α = dimensionless ratio of load pulse duration to fundamental vibration period when acted on by static load P_o

γ = nonlinear coefficient in basic equation of motion (see Eq. 2)

ε = per cent of critical damping

Ω = free lateral vibration frequency of a simply supported column loaded by a constant axial force P_o

REFERENCES

1. T. L. Anderson, "Response Spectra for Parametric Vibration of Initially Curved Columns," unpublished Ph.D. Thesis, University of Colorado, 1967.

2. J. H. Meier, "On the Dynamics of Elastic Buckling," Journal of Aeronautical Sciences, Vol. 12, pp. 433-440, 1945.

3. C. Koning and J. Taub, "Impact Buckling of Thin Bars in the Elastic Range Hinged at Both Ends," Technical Memorandum of the National Advisory Committee on Aeronautics, No. 748, June, 1934.

4. J. Taub, "Impact Buckling of Thin Bars in the Elastic Range for Any End Conditions," Technical Memorandum of the National Advisory Committee on Aeronautics, No. 749, July, 1934.

5. R. D. Mindlin, "Dynamics of Package Cushioning," Bell System Technical Journal, Vol. 24, pp. 353-451, 1945.

6. D. Young, M. V. Barton, and Y. C. Fung, "Shock Spectra for Nonlinear Spring-Mass Systems and Their Applications to Design," American Institute of Aeronautics and Astronautics Journal, Vol. 1, No. 7, pp. 1597-1602, 1963.

7. A. F. Schmitt, "A Method of Stepwise Integration in Problems of Impact Buckling," Journal of Applied Mechanics, pp. 291-294, June, 1956.

8. H. R. Bailey, "Dynamic Bending of Elastic Columns," Proceedings, ASCE, Vol. 89, No. ST4, Part 1, pp. 95-107, 1963.

9. H. H. Somerset and R. M. Evan-Iwanowski, "Experiments on Parametric Instability of Columns," Proceedings of Second Southeastern Conference on Theoretical and Applied Mechanics, Atlanta, Ga., pp. 503-525, March, 1964.

10. V. V. Bolotin, "The Dynamic Stability of Elastic Systems" (in Russian), Gostekhizdat, Moscow, 1956, translated by V. I. Weingarten, L. B. Greszczuk, K. N. Trirogoff, and K. D. Gallegos, Holden Day, San Francisco, pp. 104-107, 1964.

11. M. L. Moody, "The Parametric Response of Imperfect Columns," Proceedings Tenth Midwestern Mechanics Conference, Fort Collins, Co., pp. 329-346, 1967.

RESPONSES OF AIRCRAFT STRUCTURES SUBJECTED TO BLAST LOADING

Nelson M. Isada, Cornell Aeronautical Laboratory, Inc.
and Associate Professor of Engineering, State
University of New York at Buffalo, Buffalo, New York

and

Richard K. Koegler, and Donald O. Bliven
Cornell Aeronautical Laboratory, Inc.
Buffalo, New York

The responses of aircraft structural elements subjected to blast loading were studied. The nature and extent of damage of concern for representative aircraft structures were established to define the specific regions and load distributions to be investigated. After this was done, it was found feasible to use both a linear and a nonlinear (to consider the plastic effects) dynamic response analysis in predicting the transient blast loading required to cause to fail specified structural components. The prediction is carried out by means of structural isodamage curves that were constructed for this study and discussed in this paper.

INTRODUCTION

In evaluating the airblast vulnerability of aircraft, several factors must be considered. The response of the aircraft structural elements under impulsive, dynamic, and quasi-static loading must be studied. The nature and extent of damage of concern for representative aircraft structures also must be established to define the specific structural regions and load distributions to be investigated. When these were done, it was decided to use for this purpose a linear dynamic response analysis plus moderate corrections for plastic effects in predicting the transient blast loading required for failure of specified structural components - as discussed below.

To develop a reliable blast analysis technique, information is needed on: (a) the importance attached to varying degrees of damage, (b) the geometrical and structural configuration of the pertinent components or regions, (c) the loadings (usually static ultimate) and load factors to which the components are designed, (d) the steady load-deflection characteristics of the components, (e) the dynamic characteristics of the structure (e.g., natural frequencies), (f) the nature of the blast failures (e.g., regions of plasticity and rupture), and (g) the nature of the blast loading (e.g., peak blast pressure, duration, rise time, etc.).

On the basis of the information needs enumerated above, the nature of the necessary shock analysis, and anticipated future efforts, the study was divided into the following parts: (1) selection of aircraft vulnerable areas and structural dynamic characterization by a mathematical model, (2) selection of blast wave forms, (3) formulation of the governing equations for the elastic response of the model to the blast waves, (4) determination of the elastic isodamage response relations (ratio of blast load for failure to the elastic strength of the structure in terms of the blast load duration), and (5) determination of the plastic isodamage response relations.

SELECTION OF AIRCRAFT VULNERABLE AREAS AND STRUCTURAL DYNAMIC CHARACTERIZATION

For this study a cantilever beam, which represents the major vulnerable element in failures of significant portions of aircraft tails, wings, etc., was chosen. The loading case considered was the one most likely to cause a major failure (i.e., a bending failure at the root), which subjects the cantilever beam to a uniform blast pressure, Fig. 1. A simple dynamic model system, Fig. 2, consists of a rigid body in rotation and an equivalent rotational spring.

The moment-rotation characteristics of a physical example of a yielding rotational spring is shown in Fig. 3a. Note that in Fig. 3a there are three significant points, namely, the elastic limit, the ultimate strength, and

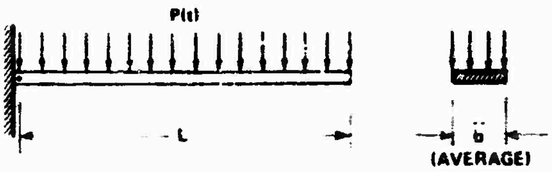

Figure 1 A CANTILEVER BEAM SUBJECTED TO A UNIFORM BLAST PRESSURE

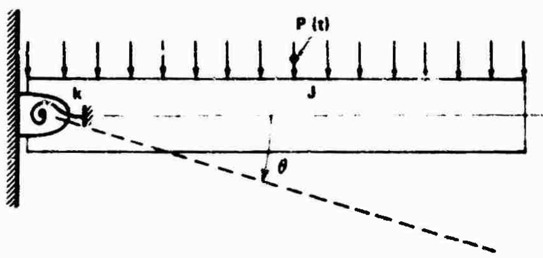

Figure 2 AN EQUIVALENT SINGLE DEGREE OF FREEDOM MODEL

the fracture point. But, results of tests performed on actual aircraft structures indicate that the yielding of the composite aircraft structures of the cantilever type is much less than the yielding of a simple shape such as a spring, and its residual strength after reaching its ultimate strength also is quite different - see Fig. 3b. Therefore, in the model, the three points in Fig. 3a must be made to match the corresponding points in Fig. 3b so that the use of the spring analogy is symbolic but not physical.

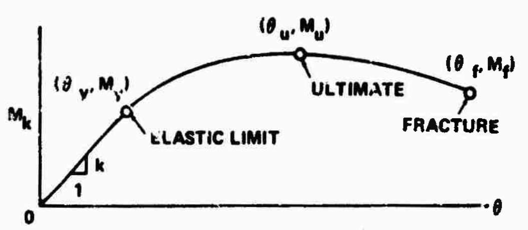

Figure 3a MOMENT-ROTATION CHARACTERISTIC OF AN EQUIVALENT SPRING

Also, the model must simulate the dynamic properties of the beam under impulsive loads of varying duration relative to the natural oscillation period of the cantilever. The crude simulation used is justifiable because (1) the curvature of the beam is relatively unimportant for the magnitudes of distributions of these loadings (i.e., surface velocities of the surface with beam motions are small compared to blast wave speeds, etc.) and (2) the only location on the beam in which there is interest in bending moment and failure for the problem being studied is at the beam root. Therefore, for the case of interest the model needs only to simulate the fundamental natural frequency of the actual aircraft component and the effects of its inertial dynamics on beam root bending moments.

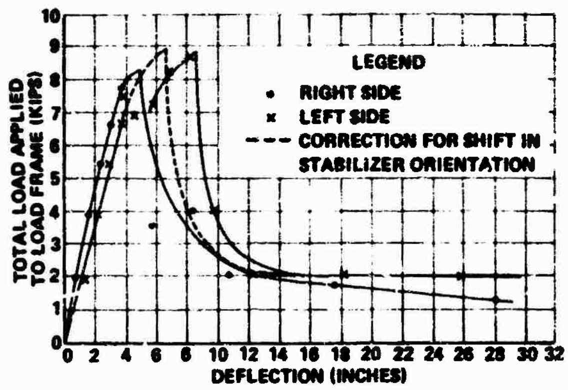

Figure 3b TOTAL LOAD APPLIED TO LOAD FRAME VS. DEFLECTION AT STATION 70 FOR STATIC TEST OF INTERNALLY REINFORCED F-80 HORIZONTAL STABILIZER (FROM REF. 6)

If in future cases there is interest in bending moments and failures at other stations, possibly as a consequence of special inertia distributions along the span, more complete models would be needed. Examples of possible models for such purposes are given in Fig. 4.

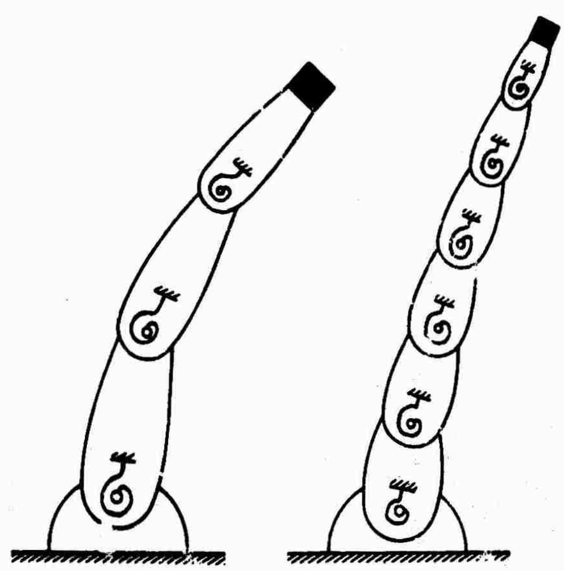

Figure 4 POSSIBLE DYNAMIC MODELS OF A CANTILEVER BEAM WITH TIP WEIGHT

SELECTION OF BLAST WAVE FORMS

For this phase, the wave forms chosen were simple representations of the essential features of the blast wave. The representation, when used with the simplified model which represents beam motions and inertial reactions in the mode involved in major failures, yields solutions comparable to those which would result if the irregular character of the higher frequency components of actual blasts were included. On the basis of work of Morton, [1] it was decided to use a triangular pulse with zero rise time as the approximation of the effective pressure-time curve. This is shown in Fig. 5a. The equation for this pulse is

$$P(t) = P_b\left(1-\frac{t}{\tau}\right)S(t)\,, \qquad +0 \le t \le \tau$$
$$= 0 \qquad , \qquad t \ge \tau \tag{1}$$

where $P(t)$ = effective blast pressure acting on the structure, psi

P_b = effective peak blast pressure acting on the structure, psi

τ = blast duration, sec

t = time, sec

$S(t)$ = unit step function, dimensionless

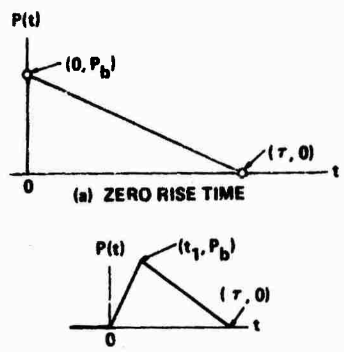

(b) FINITE RISE TIME

Figure 5 A TRAINGULAR BLAST PRESSURE HISTORY

Another wave form considered was a symmetrical triangular pulse, i. e., a triangular wave form (Fig. 5b) with rise time, t_1, equal to one-half of the blast duration. Such a shape might represent a partly developed shock front or a wave impinging on a highly curved surface.

Other wave forms which should be given consideration in a continuation study are shown in Figs. 6a and 6b. One is the "letter N" shaped wave of a fully developed blast wave at large standoffs, and the other might be obtained by timed double explosions at moderate standoffs.

FORMULATION OF THE GOVERNING EQUATIONS FOR CANTILEVER BEAM

The equation of motion for the equivalent single-degree-of-freedom system shown in Fig. 2 is

$$J\ddot{\theta} + M_R(\theta) = M(t) \tag{2}$$

where

J = mass moment of inertia about the axis of rotation, lb-in. -sec^2

$M_R(\theta)$ = resisting moment, lb-in.

$M(t)$ = excitation moment, lb-in.

The excitation moment is obtained from the beam dimensions and blast pressure and is equal to (for the pressure pulse in Fig. 5a)

$$M(t) = M_0\left(1-\frac{t}{\tau}\right)S(t)\,, \qquad 0 \le t \le \tau \tag{3}$$
$$= 0 \qquad , \qquad t \ge \tau$$

In the foregoing equation, M_0 is the peak blast moment and is equal to

$$M_0 = AeP_b = L\bar{b}eP_b \tag{4}$$

where A = blast surface area, in.^{2}

e = moment arm of resultant blast force, in.

L = length of cantilever beam, in.

$\bar{b}$ = average width of cantilever beam, in.

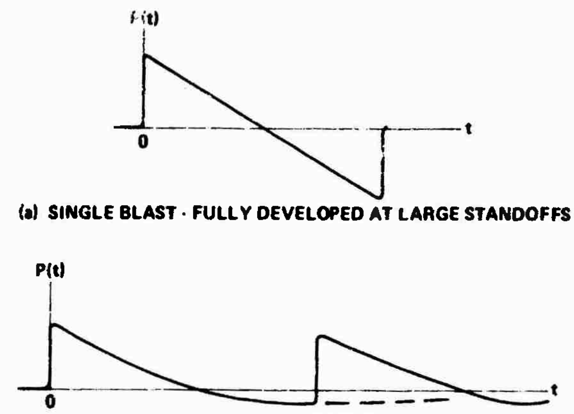

(b) MULTIPLE TIMED BLASTS

Figure 6 OTHER POSSIBLE BLAST PRESSURE HISTORIES

Similar expressions for the triangular pulse with rise time, t_1, can be developed. These expressions are:

$$M(t) = M_0\left(\frac{t_1}{\tau}\,t\right)S(t)\,, \qquad 0 \le t \le t_1$$

$$= M_0\left(\frac{\tau}{\tau - t_1} - \frac{t}{\tau - t_1}\right), \qquad t_1 \le t \le \tau$$

$$= 0 \qquad , \qquad t \ge \tau$$

ELASTIC RESPONSE

Selection of Damage Mechanism Definitions

The question of vulnerability requires a definition of damage mechanism. In the initial (elastic response) phase of the methodology development critical damage is defined as that which occurs when the maximum distortion energy (energy absorbed by the structure) is equal to the energy at the elastic limit of the structure, i.e.,

$$\left(\int M_R(\theta)d\theta\right)_{max} = \frac{1}{2}M_y\theta_y = \frac{1}{2}k\theta_{max}^2 = \frac{1}{2}\frac{M_y^2}{k} \tag{5}$$

where $M_R(\theta)$ = resisting moment, lb-in.

M_y = yield or elastic limit moment, lb-in.

θ_y = yield or elastic limit distortion, rad

Note that the yield or elastic limit moment for a cantilever beam subjected to a uniform blast pressure is

$$M_y = AeP_y \tag{6}$$

where P_y is the pressure at yield or elastic limit.

Since the damage criterion used above is energy absorbed by a material, it is defined as failure at "elastic limit toughness." In the subsequent plastic response phase of method development the elastic response was extended to the point of failure and other measures of toughness were investigated such as failure at "ultimate strength toughness." As a necessary first step, the basic elastic model had to be developed. The results obtained from the use of elastic models are very interesting because they can be applied directly to aircraft construction and those materials which experience essentially brittle failures under these loadings (e.g., built-up wood-plywood components, many plastics, etc.). Also, with so little plastic deformation of built-up aircraft components the elastic response reveals many of the essential features of the blast failure of such structures.

Deflection Time History Response Solutions of Equations

The time history response of an undamped single-degree-of-freedom system in the elastic range which is subjected to a triangular pulse with zero rise time is known to be

$$\theta(t) = \frac{M_0}{k}y(t) \tag{7}$$

where

$$y(t) = \left[1 - \frac{t\omega_n}{\tau\omega_n} + \frac{1}{\tau\omega_n}\sin\omega_n t - \cos\omega_n t\right], \quad 0 \le t \le \tau$$

$$= \left[-\frac{1}{\tau\omega_n}\sin\omega_n(t-\tau) + \frac{1}{\tau\omega_n}\sin\omega_n t - \cos\omega_n t\right], \quad t \ge \tau \tag{8}$$

k = elastic spring constant, lb-in./rad

$\omega_n = \sqrt{k/J}$ = undamped natural circular frequency, rad/sec and the remaining notations as defined previously.

The time-history response for the triangular pulse with finite rise time is also known [2, 3]. The response can be thought of as comprising three successive events, namely, (1) pulse rise time, (2) the pulse decay, and (3) the residual vibration.

Construction of Elastic Isodamage (Blast-to-Steady-Pressure Ratio for Failure) Curves

As pointed out in the early part of this paper, structural vulnerability will depend upon the dynamics of the structure and damage mechanism. The damage equation derived in the previous section will now be converted into a structural isodamage (blast to steady pressures for failure) equations by using the blast moment defined previously and the dynamic response in this section as follows:

$$\begin{aligned}
\frac{1}{2}k\theta_{max}^2 &= \frac{1}{2k}M_y^2 \\
\frac{1}{2}k\left(\frac{M_0}{k}y_{max}\right)^2 &= \frac{1}{2k}M_y^2 \\
M_0^2 y_{max}^2 &= M_y^2 \\
(AeP_b)^2 y_{max}^2 &= (AeP_y)^2 \\
\frac{P_b}{P_y} &= \frac{1}{y_{max}}
\end{aligned} \tag{9}$$

The construction of the graphs of Figs. 7a and 7b for the foregoing structural isodamage equation will now be discussed. The values of y_{max} as a function of the nondimensionalized blast duration, τf_n (equal to the period ratio, τ/T), were obtained from the response spectra published by Jacobsen and Ayre [3]. Some of these values are given in Table 1. With these tabulated values, the nondimensionalized critical pressures, P_b/P_y were calculated and are plotted against the nondimensionalized blast durations as shown in Figs. 7a and b. Note that the critical pressure ratio approaches 0.5 (or a magnification factor of 2) as a limit. This to be expected because the blast pressure has a vertical front and the dynamic model is assumed to be an undamped single-degree-of-freedom elastic system, i.e., the dominant response is due to the fundamental frequency of the structure and the blast wave.

The structural isodamage curve for the case where the rise time is one-half the blast duration is also shown in Fig. 7a. Note that this curve shows a quasi-resonance phenomenon.

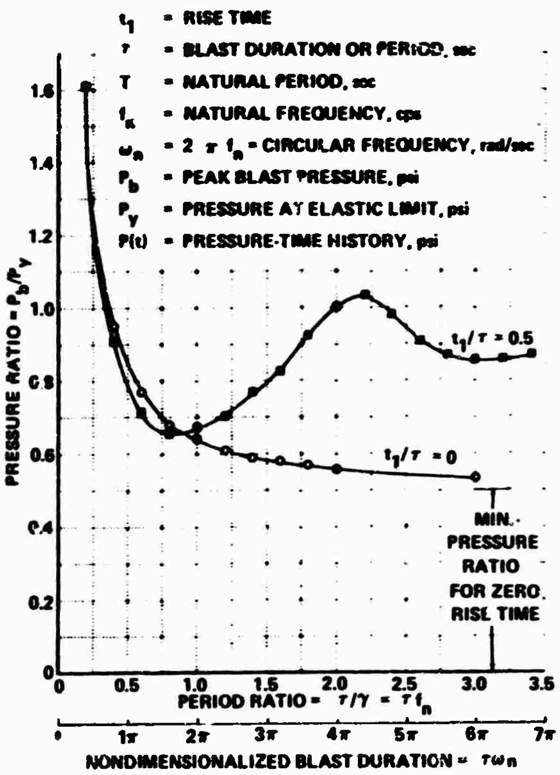

Figure 7a NONDIMENSIONAL STRUCTURAL ISODAMAGE CURVES AT ELASTIC LIMIT FAILURE

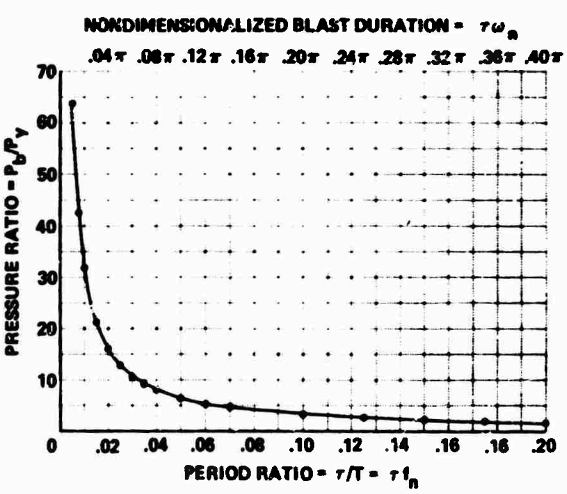

Figure 7b LOWER PERIOD RATIO RANGE OF NON-DIMENSIONAL STRUCTURAL ISODAMAGE CURVES AT ELASTIC LIMIT FAILURE

TABLE I

Undamped Single-Degree-of-Freedom Response Spectra (zero rise time)

Period Ratio	Normalized Maximum Displacement,
0.2	0.62
0.4	1.05
0.6	1.30
0.8	1.46
1.0	1.56
1.2	1.63
1.4	1.68
1.6	1.73
1.8	1.77
2.0	1.80
2.5	1.84
3.0	1.87
3.5	1.89
4.0	1.90

To present the results in the same form as standard practice, the structural isodamage equation derived in the previous section will now be converted in terms of the impulse. This is done by expressing the normalized blast duration in terms of the impulse as follows. The impulse is

$$I = \int_0^{\tau} P(t)\,dt \tag{10}$$

For a triangular pulse, the impulse is

$$I = \frac{1}{2}\tau P_b \tag{11}$$

Division by P_y will yield

$$\frac{I}{P_y} = \frac{\tau}{2}\frac{P_b}{P_y} \tag{12}$$

Multiplying and dividing the right hand side of the above equation by the natural frequency, f_n, will yield

$$\frac{I}{P_y} = \frac{1}{2f_n}(\tau f_n)\frac{P_b}{P_y} \tag{13}$$

The normalized impulse, I/P_y (pressure-impulse) is obtained from the values of τf_n and P_b/P_y in the nondimensionalized curve plotted in Figs. 7a and b and by specifying natural frequencies. The results can be plotted as a family of curves as shown in Fig. 8. The choice of natural frequencies is based upon published data [4] on aircraft structures. Note that damage at elastic limit depends not only upon the peak blast pressure and impulse, but also, because this quantity is not nondimensionalized, upon the natural frequency of the structure. For each blast shape, however, only one curve is required in the nondimensionalized representations.

The family of pressure-impulse curves for the case where the rise time is one-half of the blast duration is shown in Fig. 9. Here again, the quasi-resonance phenomenon can be observed. This quasi-resonance phenomenon appears to be consistent with the plots of test data on the collapse-hinge failure of 6061-T6 aluminum tubing [5] as shown in Figs. 10 and 11.

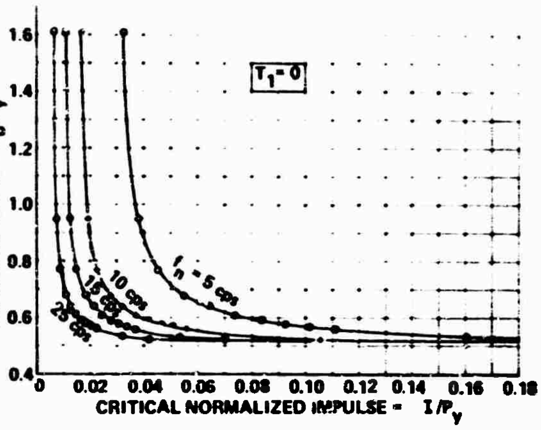

Figure 8 NORMALIZED PRESSURE-IMPULSE STRUCTURAL ISODAMAGE CURVES AT ELASTIC LIMIT FAILURE

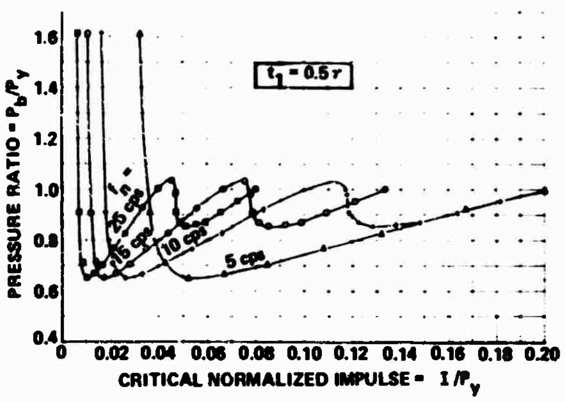

Figure 9 NORMALIZED PRESSURE-IMPULSE STRUCTURAL ISODAMAGE CURVES AT ELASTIC LIMIT FAILURE

PLASTIC RESPONSE

Selection of Damage Mechanisms

In this phase of method development, critical damage beyond the elastic limit is defined as that which occurs when the deformation at the ultimate strength (or moment) is reached (Fig. 3a). The main reasons behind this choice are: (1) static tests of aircraft structures show that the resistance drops sharply once the ultimate strength is reached, (2) aerodynamic loads would most likely be able to break the structure after it had exceeded its ultimate strength and started to deform drastically, (3) criteria are relatively simple to specify numerically, and (4) the static breaking strength of aircraft structures is a primary design requirement so that these strengths are available in aircraft structural analyses.

The consequence of the above definition is a resisting moment-rotation characteristic of the type shown in Fig. 12. In this figure, there are two axes, namely, an absolute resisting moment, M_R, vs. an absolute displacement, θ, and a relative resisting moment, $m = M_R - M_y$, vs. a relative displacement, $\beta = \theta - \theta_y$. Note that in this figure the moment-rotation relation is linear up to the elastic limit, M_y or θ_y, and is characterized by a cubic equation in β beyond the elastic limit. The main

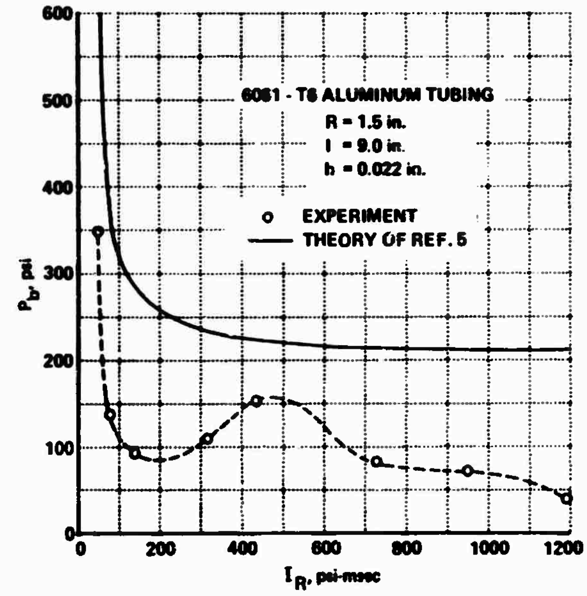

Figure 10 PRESSURE-IMPULSE STRUCTURAL ISODAMAGE CURVES FOR COLLASPE-HINGE FAILURE

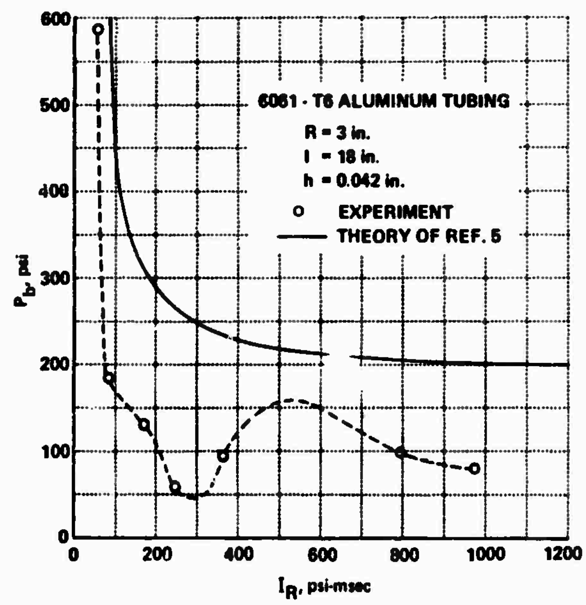

Figure 11 PRESSURE-IMPULSE STRUCTURAL ISODAMAGE CURVES FOR COLLASPE-HINGE FAILURE

reasons for this choice are: (1) to make the characteristic as realistic as possible without undue complexity, (2) to use data (see Fig. 3b) which show that the characteristic is linear up to the elastic limit, (3) to make the slope continuous at the elastic limit, and (4) to simplify the amount of static structural data needed.

On the basis of the above description and the notations in Fig. 12, the moment-rotation characteristic can then be expressed as follows:

$$M_R(\theta) = k\theta \qquad , 0 \le \theta \le \theta_y$$

$$= k\left[\theta + \frac{-2+4\alpha\lambda}{\mu\theta_y}\beta^2 + \frac{1-4\alpha\lambda+\lambda}{\mu^2\theta_y^2}\beta^3\right], 0 \le \beta \le \mu\theta_y \quad (14)$$

$$= 0 \qquad , \beta > \mu\theta_y$$

where

$\beta = \theta - \theta_y$

$\alpha = m_m / m_u$

$\lambda = k_2 / k$

$\mu = \beta_u / \theta_y$

θ_y = deflection at the elastic limit

Deflection Time-History Response Solutions of Equations

Using the above resisting moment-rotation characteristic, the equation of motion then becomes

$$J\ddot{\theta} + M_R(\theta) = M(t) \quad (15)$$

which can be normalized into the following form

$$\ddot{\theta} + \omega_n^2 \frac{M_R(\theta)}{k} = \omega_n^2 \frac{M_o}{k} m(t) \quad (16)$$

where

$$\omega_n^2 = k/J \quad (17)$$

$$m(t) = M(t)/M_o \quad (18)$$

In order that solutions be more generally applicable, the above equation is nondimensionalized by using a dimensionless time variable, $\hat{t}$, defined as:

$$\hat{t} = \omega_n t \quad (19)$$

which results in the following relationship

$$\ddot{\theta} = \omega_n^2 \frac{d^2\theta}{d\hat{t}^2} = \omega_n^2 \theta''(\hat{t}) \quad (20)$$

Hence, the dimensionless differential equation of motion is

$$\theta''(\hat{t}) + M_R(\theta)/k = \frac{M_o}{M_y}\theta_y m(t) \quad (21)$$

where M_y is the moment at the elastic limit. The above equation when expanded becomes

$$\theta''(\hat{t}) + \theta(\hat{t}) = \frac{M_o}{M_y}\theta_y m(t) \qquad , 0 \le \theta \le \theta_y$$

$$\theta''(\hat{t}) + \theta(\hat{t}) + \frac{-2+4\alpha\lambda}{\mu\theta_y}\beta^2 + \frac{1-4\alpha\lambda+\lambda}{\mu^2\theta_y^2}\beta^3 = \frac{M_o}{M_y}\theta_y m(t),$$

$$0 \le \beta \le \mu\theta_y$$

$$\theta''(\hat{t}) = \frac{M_o}{M_y}\theta_y m(t) \qquad , \beta > \mu\theta_y \quad (22)$$

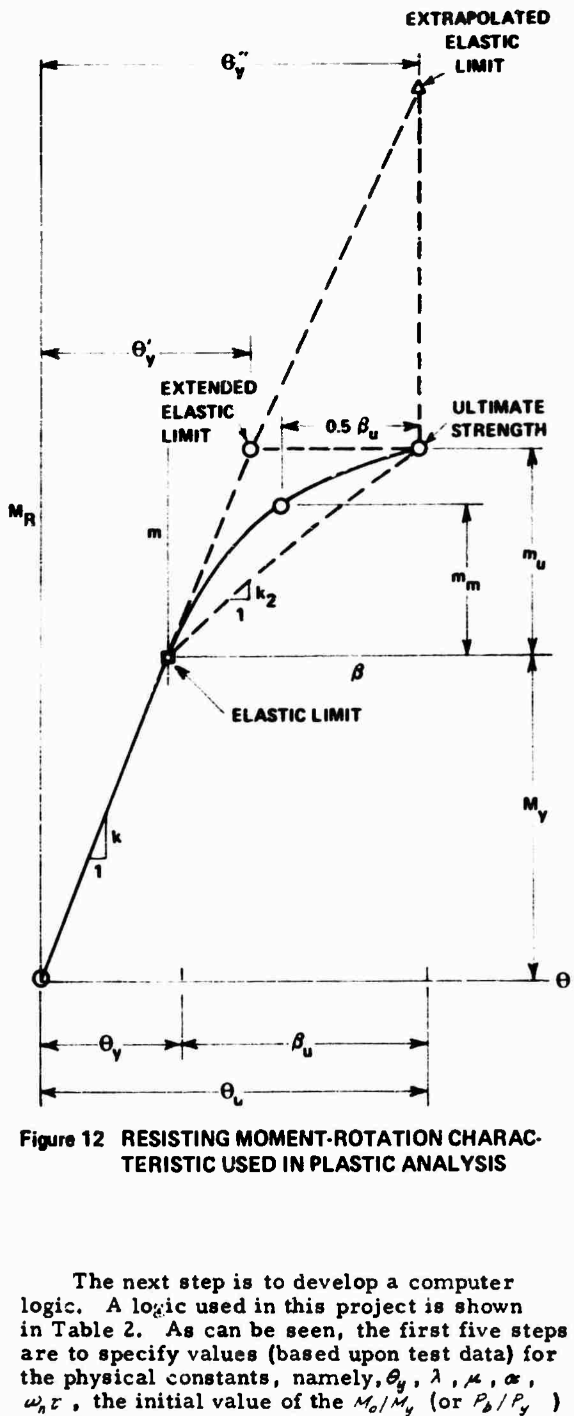

Figure 12 RESISTING MOMENT-ROTATION CHARACTERISTIC USED IN PLASTIC ANALYSIS

The next step is to develop a computer logic. A logic used in this project is shown in Table 2. As can be seen, the first five steps are to specify values (based upon test data) for the physical constants, namely, θ_y, λ, μ, α, $\omega_n\tau$, the initial value of the M_o/M_y (or P_b/P_y) and the final value of M_o/M_y . The next step is to solve the differential equation, followed by print-out of the time-history solutions. The subsequent step is to increment the moment ratio, M_o/M_y (or pressure ratio, P_b/P_y) and the steps are repeated until the final value of the moment ratio is reached. The calculations are then repeated for new values of $\omega_n \tau$.

TABLE 2

Computing Logic for Plastic Analysis

1. Specify values for θ_y, λ , μ and α.
2. Specify value for $\omega_n \tau$.
3. Specify initial value for M_o/M_y (or P_b/P_y).
4. Specify final value for M_o/M_y (or P_b/P_y).
5. Solve the differential equation.
6. Output time-history solutions.
7. Increment M_o/M_y.
8. Go to step 5 if the new M_o/M_y is less than the final, otherwise stop the calculations.
9. Repeat the computations for other values of $\omega_n \tau$.

Construction of Structural Isodamage Curves Based on Ultimate Strength

The construction of the critical structural isodamage curves will now be discussed. The values of the maximum displacement, θ_{max} , corresponding to a particular pressure ratio, P_b/P_y , are read off from the tabulated computer output of the displacement time-history solutions. These maximum responses are plotted against the pressure ratio and are shown as a family of curves in Fig. 13, with the normalized blast duration as the third parameter. It can be seen from these curves that the normalized blast duration is a very significant parameter.

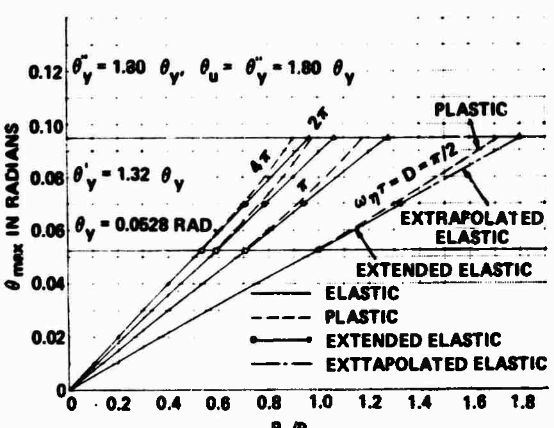

Figure 13 EFFECT OF PLASTICITY ON THE MAXIMUM DISPLACEMENT BLAST RESPONSE SPECTRA

A critical structural isodamage curve can now be constructed based upon the necessary pressure ratio to cause the structure to fail at its ultimate strength, i.e., the pressure ratio necessary to produce a maximum structural response equal to θ_u . These pressure ratios are read off the intersection between the response curves shown in Fig. 13 and the line θ_u = 1.80 θ_y . These values of P_b/P_y and $\omega_n \tau$ are plotted in Fig. 14, labeled PLASTIC, θ_u = 1.80 θ_y , the second curve from the top.

Other critical structural isodamage curves are also shown in Fig. 14. These curves are based upon the necessary pressure ratio to reach the elastic limit, θ_y , to cause failure at an extended elastic limit, θ_y' = 1.32 θ_y or at an extrapolated elastic limit, θ_y'' = 1.80 θ_y . Note that these curves are based upon linear elastic and equivalent linear elastic moment-rotation characteristics shown in Fig. 12.

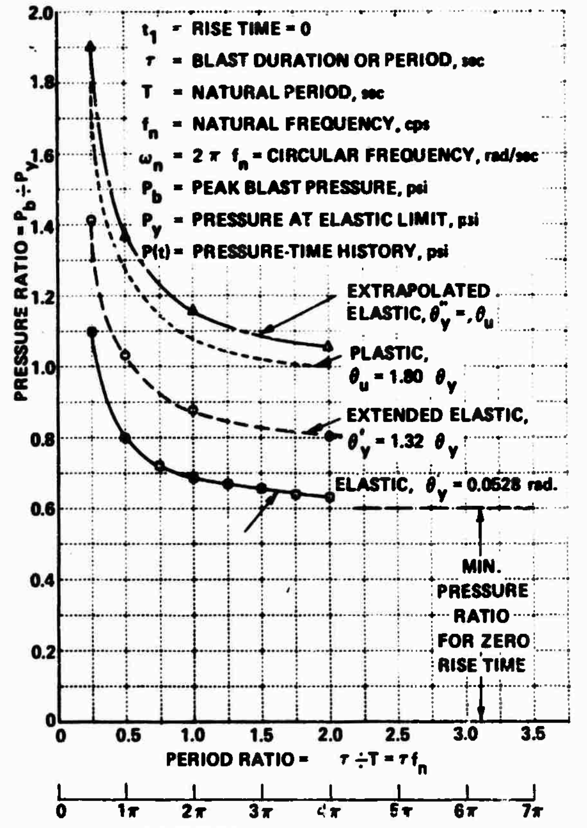

Figure 14 NONDIMENSIONAL STRUCTURAL ISODAMAGE CURVES

It appears from Fig. 14 that for the fundamental-mode type of failure of cantilever-type aircraft structures, the structural isodamage response curves for the extrapolated elastic-limit type of failure is slightly conservative, but the effect of the conservative results will be lessened if the resistance beyond the ultimate strength, material damping, etc., are taken into account.

Finally, it appears that a simple correction factor could be defined because the proportion of the structure undergoing large plastic or buckling distortions is small for cantilever-type aircraft structures.

SUMMARY AND CONCLUSIONS

Results of an initial study on the responses of aircraft structures subjected to blast loading have been presented. The final results, presented as structural isodamage curves, have been obtained after studying the nature and extent of damage of representative aircraft structural elements, the load distributions due to blast, mathematical models, time-history solutions and damage mechanisms. The structural isodamage curves (see Figs. 7, 8, 9 and 14) in conjunction with static structural data (natural frequency, pressure at yield or elastic limit, and pressure at ultimate strength) and blast pressure characteristics (blast pressure shape and duration) can be used to scale from blast test data on built-up aircraft cantilever structures the necessary blast loading to fail specified aircraft structural components with similar characteristics, i.e., those treated in this initial study. For other types of structure, slight modifications of the methodologies discussed in this paper would have to be developed.

ACKNOWLEDGMENT

The authors would like to thank the U.S. Naval Weapons Laboratory, Dahlgren, Virginia for permission to publish this work.

REFERENCES

1. H.S. Morton, "Scaling the Effects of Air Blast on Typical Targets," APL Technical Digest, September-October 1967, p. 209

2. N.M. Isada, "Lecture Notes in Vibration and Shock," School of Engineering, State University of New York at Buffalo, Buffalo New York, 1965

3. L. Jacobsen and R. Ayer, "Engineering Vibrations," McGraw-Hill, New York, 1958, pp. 167-170

4. E. F. Bruhn, "Analysis and Design of Flight Vehicle Structures," Tri-State Offset Company, Cincinnati, Ohio, 1965, p. A 4.13

5. Kaman Nuclear, "The Collapse-Hinge Failure of Blast Loaded Cylinders," U. S. Army Ballistic Research Laboratories Contract No. DA-18-001-AMC-1047(X), Aberdeen Proving Ground, Maryland, August, 1967, pp. 27-28

6. R. D'Amato, "Destruction Tests of Aircraft Structural Components," WADC TR 54-365, Part 1, June 1955

NOMENCLATURE

A = blast surface area, in.^{2}

$\bar{b}$ = average width of cantilever beam, in.

D = $\omega_n T$ = normalized blast durations, dimensionless

e = moment arm of resultant blast force, in.

f_n = natural frequency, cps or Hz

I = pressure impulse, psi-sec

J = mass moment of inertia about the axis of rotation, lb-in.-sec^2

k = equivalent rotational spring constant, lb-in/rad

k_2 = plastic spring constant, lb-in./rad

L = length of cantilever beam, in.

M_f = fracture moment, lb-in.

M_u = ultimate strength moment, lb-in.

M_y = yield or elastic limit moment, lb-in.

$M(t)$ = excitation moment, lb-in.

$M_R(\theta)$ = resisting moment, lb-in.

M_o = peak blast moment, lb-in.

m = $M_R - M_y$ = relative resisting moment, lb-in.

m_m = relative resisting moment at one-half of plastic strength, lb-in.

m_u = $M_u - M_y$ = available plastic strength, lb-in.

$m(t)$ = $M(t)/M_o$, normalized excitation moment, dimensionless

$P(t)$ = effective blast pressure acting on the structure, psi

P_b = effective peak blast pressure acting on the structure, psi

P_y = pressure at yield or elastic limit, psi

$S(t)$ = unit step function, dimensionless

T = natural period, sec

t = time, sec

t_1 = rise time of pulse, sec

$\hat{t}$ = normalized time, dimensionless

$y(t)$ = normalized displacement, dimensionless

y_{max} = maximum normalized displacement, dimensionless

α = m_m / m_u , dimensionless

β = $\theta - \theta_y$ = relative angular displacement, rad

β_u = $\theta_u - \theta_y$ = available plastic deformation, rad

θ = angular displacement, rad

θ_y = angular displacement at elastic-limit, rad

θ_y' = angular displacement at extended elastic limit, rad

θ_y'' = angular displacement at extrapolated elastic limit, rad

θ_u = angular displacement at ultimate strength, rad

θ_f = angular displacement at fracture point, rad

$\ddot{\theta}$ = angular acceleration, rad/sec^2

$\theta(\hat{t})$ = normalized angular displacement, rad

$\ddot{\theta}(\hat{t})$ = normalized angular acceleration, rad

λ = k_t / k , dimensionless

μ = β_u / θ_y , dimensionless

π = 3.1416, dimensionless

τ = unit step function, dimensionless

ω_n = $\sqrt{k/J}$ = undamped natural circular frequency, rad/sec

DISCUSSION

Mr. Addonizio (Gibbs & Cox): In your determination of p sub y, did you use the dynamic yield or the static yield?

Mr. Isada: This is the static yield. In other words, we tried to use data which are normally available, either through tests or design specifications for static structural analysis of these structures.

Mr. Addonizio: Are you saying that no rapid strain rate test results were available to you?

Mr. Isada: Well, I could argue as far as rapid strain rate tests are concerned. When we talk about time we need dynamic methods.

PREDICTION OF BLAST-VALVE RESPONSE USING MODELS

R. G. McCoy, G. Nevrincean, and E. F. Witt
Bell Telephone Laboratories
Whippany, New Jersey

A louver blast valve has been developed for use in Bell System underground communication buildings to prevent air blast from possible nuclear detonations from entering air entrances and exits. Because of the complex blast flow and resulting stresses during valve closure, the valve principle was demonstrated using a 1/4-scale model in the Bell Laboratories Chester shock tube. Extensive data were obtained on stresses and closing times and compared well with subsequent data from tests on full-size valves in a 6-foot-diameter shock tube. Improved prototype valves were then tested successfully in Operation Prairie Flat (a simulated nuclear detonation), demonstrating the value of prior shock-tube testing.

The Bell System is hardening critical elements of its extensive communications network against the effects of nuclear weapons. Numerous underground buildings, used for network power and switching purposes, require large amounts of air; some of the larger buildings use over 200,000 cubic feet of air per minute. Therefore, blast valves with large air-flow capacities are needed to prevent blasts from entering the building air entrances and exhausts. Also, the valves prevent contaminated air from entering the building and endangering personnel.

The valves, in addition to having a large air capacity, must also close rapidly so that an efficient detection system can be used for closure before air-blast arrival at the building. And, of course, as in all systems, the requirements should be met at a low cost.

Many of the buildings are designed to withstand nuclear-weapon effects associated with a peak free-field overpressure of 50 psi. This produces an incident shock of 23 psi in the vertical air shafts in which the valves are mounted. This shock reflects from the bottom of the shaft and subsequently loads the valve with a 70-psi overpressure.

A louver valve, shown in Figure 1, was developed by Bell Telephone Laboratories to satisfy the needs of the underground buildings.

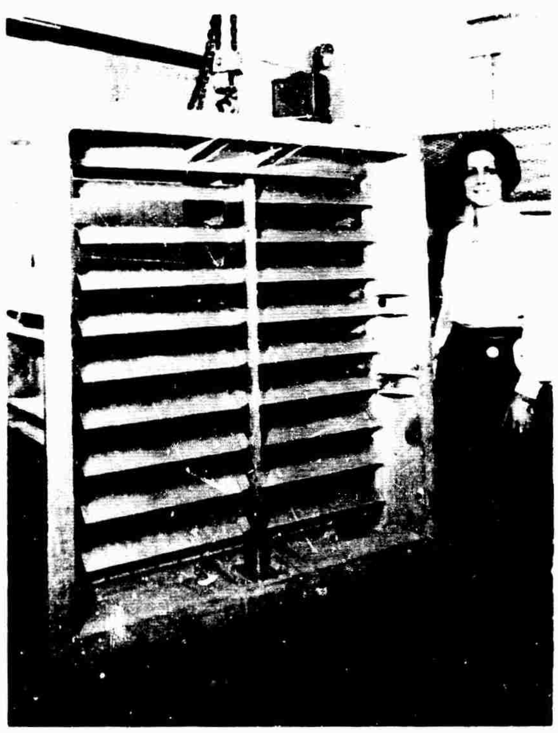

Fig. 1 - Louver Blast Valve

The opening of the valve is approximately 44 inches square and is controlled by nine center-hinged louvers, as shown in Figure 2. These louvers are controlled by a common actuating link, shown in the center of the valve in Figure 1, and the motion of this link is controlled by an actuator at the bottom of the valve. The actuator contains a motor drive, to open the valve against a spring force, and a trigger mechanism which holds the valve in the open position. The trigger is held engaged by a solenoid. Normal electrical closing of the valve is accomplished by de-energizing the solenoid; the trigger then releases the spring, which closes the valve in approximately 50 milliseconds.

The valve can also be closed directly by blast forces. The high-velocity flow through the valve induced by the overpressure in the air shaft causes an aerodynamic torque on the blades which is transmitted to the actuating mechanism. A linkage then uses this force to

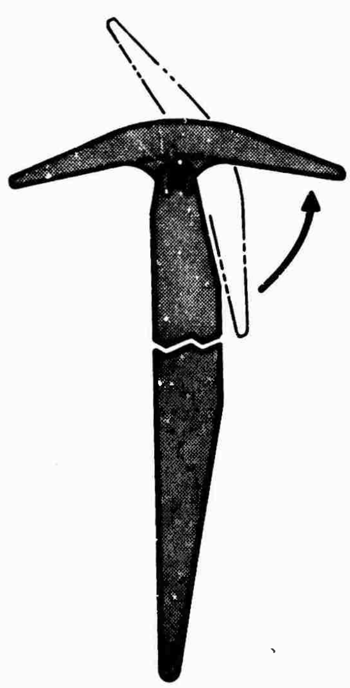

Fig. 2 - Detail of Louver Action

overpower the solenoid, which causes the valve to trip. Subsequently, the valve closes under the spring and aerodynamically induced forces. In this case, for the highest overpressure environment, the valve closes in approximately 10 to 14 milliseconds.

Because of the complexity of the valve mechanism, the shock interaction, and the resulting flow through the valve, it was decided to test the valve principle in a shock tube using a one-quarter scale model, shown in Figure 3. These tests provided measurements of valve stresses and closing times under blast loading. The effects of various orientations of the valves were also observed.

The quarter-scale model did not have a scaled actuating mechanism or trigger. The valve was closed by a spring released when a restraining cord was severed by a cutter triggered by a pressure switch. As a result, the blast-tripping threshold of the valve, i.e., the lowest pressure that would cause the valve to self-trip, was not obtained.

The Bell Telephone Laboratories shock tube at its Chester laboratory was used for the tests. This shock tube, shown in Figure 4, is driven by high-pressure air. Shocks of up to 50 psi can be produced in the 12-inch-ID section of the tube. The model louver valve was mounted in a special test section with a 16-inch cross section at the end of the shock tube, in the foreground in Figure 4. Peak pressures attainable in this section were approximately 35 psi, which were more than adequate for the test.

In performing scale experiments, it is desirable to use as large a model as practical; in this case, quarter scale was used. This modest scaling provided a good simulation of full-scale conditions, and a model of this size was relatively easy to fabricate and handle. Also, it wasn't so small as to make the strain-gage installation unduly difficult. The scaling scheme used for this model was straight geometric scaling which maintained the same ratio

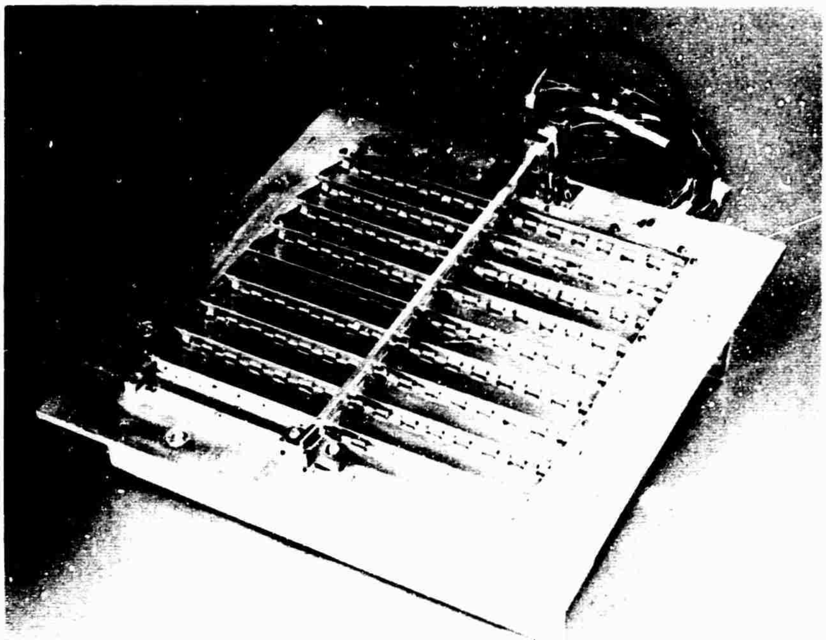

Fig. 3 - Quarter-Scale Model of Louver Valve

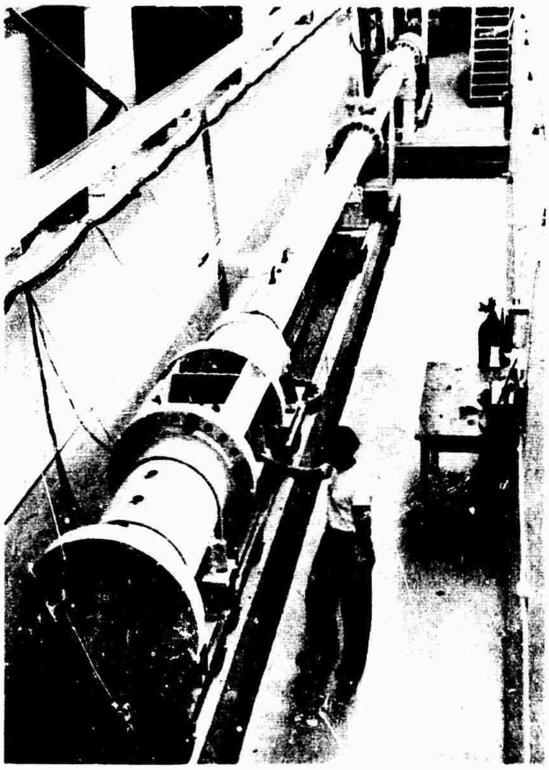

Fig. 4 - Bell Laboratories Chester Shock Tube

of stress to pressure. Of course, as a result of the scaling, time scaled directly as the linear dimensions of the model, and acceleration inversely as the linear dimensions. Since gravity was not an important factor in these tests, scaling was expected to be valid.

Pressure loading on the valve was a result of shock defraction around the valve and the resulting drag forces due to the high-velocity flow through the valve. The shock loading on the quarter-scale valve would have the same peak value as on a full-scale valve, because the same incident overpressures were used and defraction would be very closely simulated in the quarter-scale tests. The validity of the scaling for shock defraction can be seen in Figure 5, where the pressures in square cross-section vertical air shafts subjected to free-field blast pressures are shown for full-scale and 1/30-scale tests. The peak values and waveforms are very similar. This adds considerable confidence to the use of scale tests of this nature.

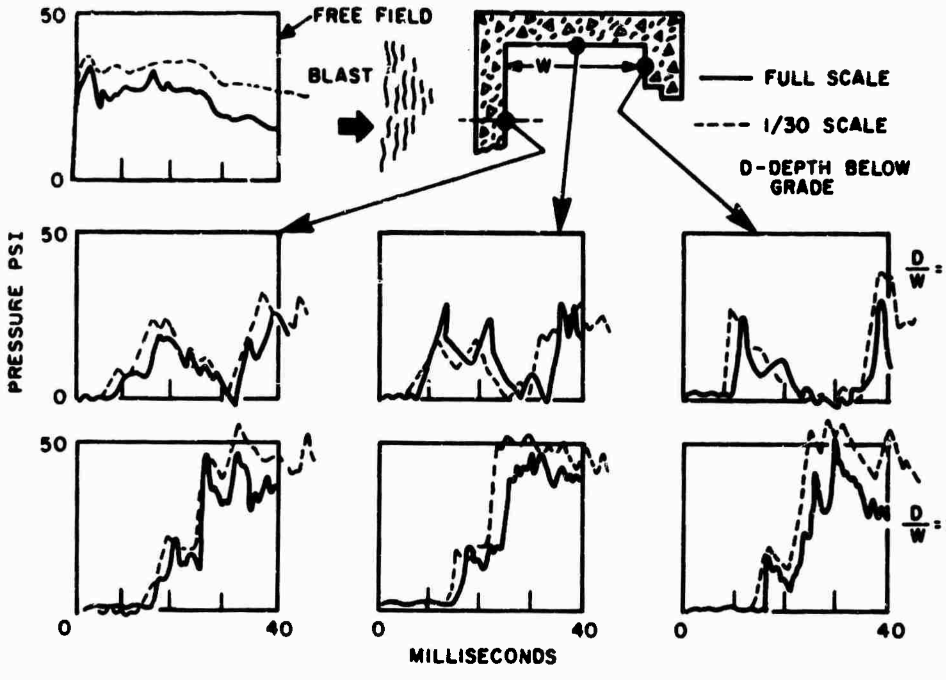

Fig. 5 - Comparison of Overpressures in Air Shaft, Full-Size and 1/30 Scale Models

Another factor in the loading of the valve was the aerodynamic force resulting from high-velocity flow through the valve. This flow was generally in a transonic region, and because the same pressures were maintained, the same flow velocities and, as a result, the same Mach numbers, would be maintained. However, the Reynolds number for the scale test was one quarter of that for the full-size test. This was not expected to be important.

The shape of the louvers was determined from low-velocity tests on a shape similar to the louvers. These tests indicated that a closing torque would be induced on the blades by the flow through the valve. The quarter-scale tests were to check the performance of the louver shape; if a different shape were required, it would be a simple matter to install different louvers in the valve. The shape of the louver in the original model proved to be quite satisfactory,* and the same shape was maintained through subsequent tests and is now incorporated in the production unit.

The valve was tested in various orientations in the shock tube, as shown in Figure 6. Further, it was tested closed before blast arrival and also blast-closed, i.e., closing during the period of blast loading. For the tests with the valve closed, a comparison can be made between calculated and measured stresses divided by the inducing pressure. This comparison is shown in Figure 7 for various locations, indicated as R( ) and B( ), on the valve blade and rib. The blade was primarily stressed in bending about the center hinge, and strain gages were positioned accordingly. The ribs were stressed as beams with end supports, and gages were located to measure longitudinal strains. The measured values are averages obtained from all tests run on the quarter-scale valve when loaded with an essentially static pressure. The measured values on the rib are consistently slightly higher than the calculated values, but agreement is quite good. There is also good agreement for some

*Further shock-tube tests, not reported here, on various louver shapes did not indicate a better cross section.

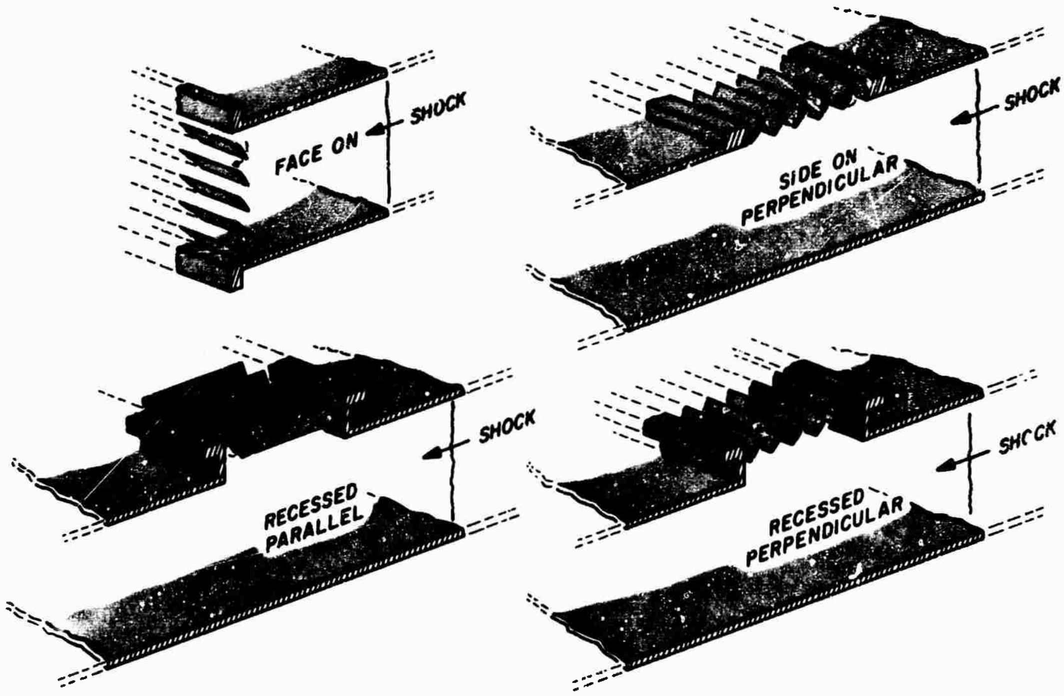

Fig. 6 - Test Orientations of Valve

locations on the blade, but for several other locations differences between the measured and calculated values are as great as 2 to 1.

Table 1 presents all values for stress divided by pressure for the various tests performed on the quarter-scale valve, and a considerable consistency can be seen in the results. For example, for the B4 location, almost all the stress-to-pressure ratios are around 40, where the calculated value is 20. It would be very difficult to explain this type of difference by experimental error. Rather, it may be due to anomalies in loading of the blade. For example, the blades were not exactly straight, so that initial contact was over only local areas; this could have induced greater stresses in certain areas than in others. In addition, the crank which connects the blade to the linkage could have restrained the blade and, as a result, higher stresses may have been induced in the blade because it was not freely floating as was assumed in making calculations.

The values used in Figure 7 were obtained from the peak pressure in the shock tube which corresponds to point M on the pressure/time curve shown in Figure 8. At this point, the pressure in the tube was varying only slightly and was of very long duration compared to the natural frequency of the components of the valve. As a result, the average strain during this period could be considered a static strain produced by the pressure at point M. With this used as the static value for the ratio of stress divided by pressure, the dynamic stress factor for the incident and reflected pressure loading was calculated: The stresses caused by the incident and reflected pressures were divided by their respective pressures. These ratios were then divided by the static stress-to-pressure ratio. These dynamic stress factors are presented on the small drawings on the valve rib and blade shown in Figure 8.

For the case where the shock wave sweeps across the valve, there is a distinct reflected

TABLE 1

Blade and Rib Stresses for Pressure Plateau in Shock Tube

Valve Orientation	Incident Overpressure (psi)	Valve Open	σ_M/p_M* Gage Position†							
			R1	R2	R3	B1	B2	B3	B4	B5
Face-on	21		100	82	150	54	42	-	42‡	34
	25		90	73	130	65	27	33	44‡	37
	23	X**	89	76	-	-	25	29	41	-
	20	X	97	87	-	-	27	48	43	46
Side-on	27		88	71	120	82	-	40	42‡	48
	12	X**	82	70	-	-	-	-	39	-
	17	X**	97	68	-	-	-	-	58	-
	9	X	92	65	150	-	43	76	60	-
Recessed Perpendicular	15	X	81	72	142	-	20	53	70	-
	20	X	76	72	120	-	-	43	76	-
	23	X	79	64	130	-	-	32	81	-

*σ_M = stress and p_M = pressure, corresponding to point M on pressure traces in Figure 8.
†Gage positions are shown in Figure 7.
‡From strains on a different blade.
**Absorber used.

wave on the valve, caused by a reflected wave from the closed end of the shock tube. The dynamic-load factor for the rib is considerably higher for the incident pressure than for the reflected pressure, which is reasonable because the reflected pressure loading does not start from zero as does the incident pressure loading. The same situation is not consistently obvious in the dynamic-load factors on the blade.

For the case where the shock wave hit the valve face on, there was no separate delayed reflection because reflection occurred immediately. It is interesting to note that the dynamic-load factors for the rib, in this case, were consistently somewhat less than they were for the incident wave hitting the valve in the sweeping condition. However, the dynamic-load factors in the blade appear to be approximately the same within the scatter of data.

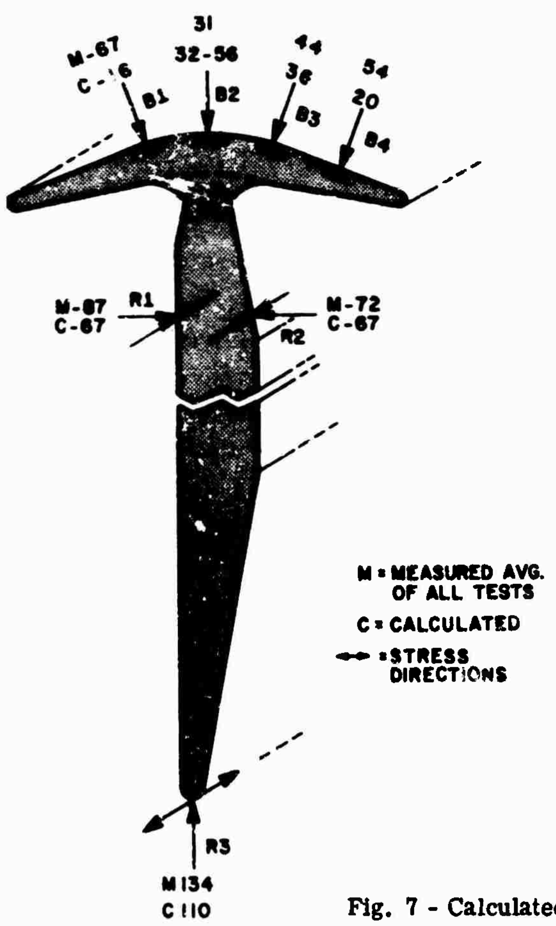

Fig. 7 - Calculated and Measured Stresses in Quarter-Scale Model

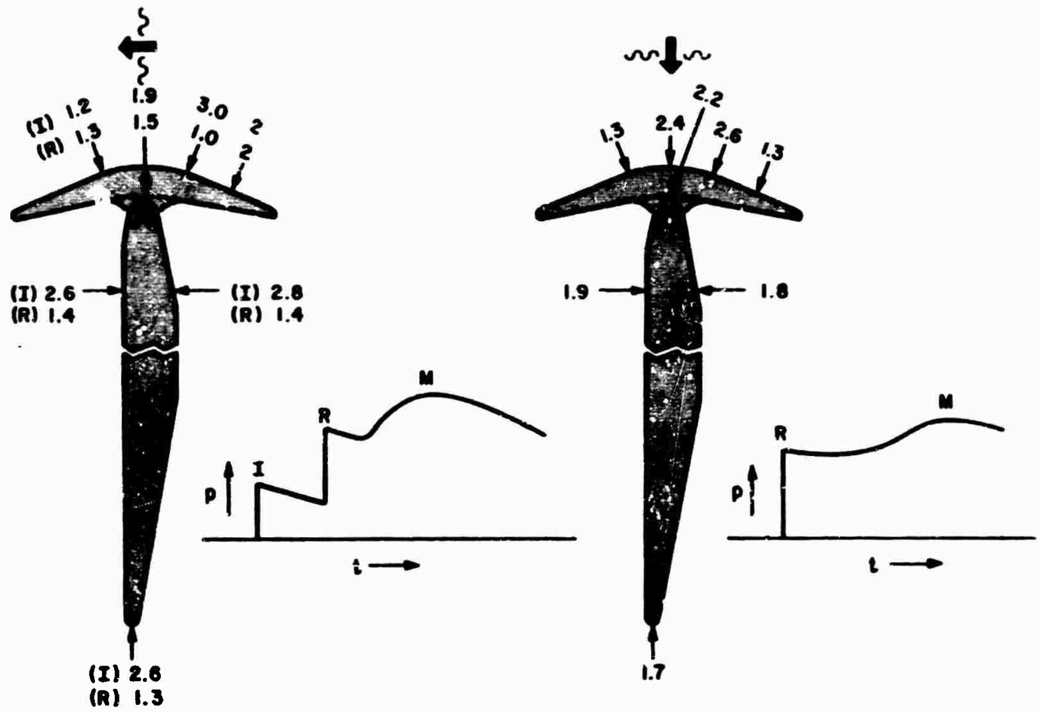

Fig. 8 - Dynamic Stresses in Quarter-Scale Model

The data in Figures 7 and 8 were obtained with the valve closed before the arrival of the shock wave. When the valve was blast-closed, there was a combination of stresses due to two factors: one, the overpressure loading on the valve, and the other, due to impact of the blades when they close. Figure 9 shows the effects of this impact for the valve oriented in the face-on position. The circles represent the stresses caused only by pressure loading when the valve was closed. The squares represent the stresses on the blade caused by blast closing but with an absorber cushioning the last portion of the stroke. The triangles show the stresses induced on the blade without any absorber. This data has a reasonable interrelationship. The stress on the upper surface of the blade was tensile as a result of pressure loading: The blade impacting against its neighboring blade caused an additional tensile force on the blade and thus would increase the stresses on that section of the blade. On the left section of the blade, the impact would come from the opposite direction and the stresses on the upper surface of the blade would be compressive and would subtract from the stress due to the overpressure. Since there are no data for this region, the curves in Figure 9 are not extended. However, it is probable that the stress levels in this section would not be appreciably less than the peak stress levels caused by the overpressure alone because, shortly after impact, the stress would again reach the value caused by the overpressure alone.

There was very little change in stress at the center of the blade. Along the top surface of the blade, a tensile stress propagating from the right and a compressive stress propagating from the left met at the center of the blade; the net result should have been a zero change in stress, which appears to be verified by the test data. This also indicates that very little stress reflection would occur.

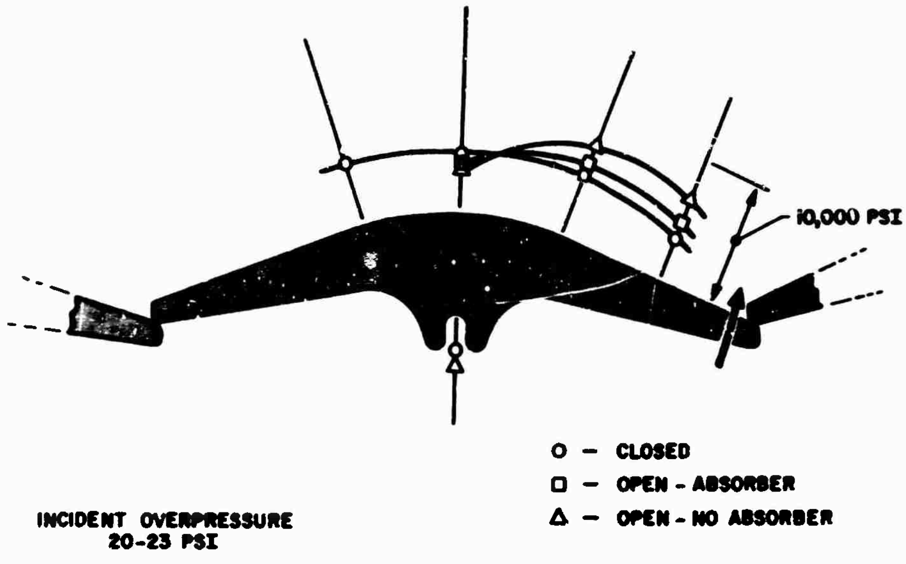

Fig. 9 - Blade Stresses Due to Impact

The impact stresses in Figure 9 apply only to the face-on orientation. Other orientations result in different impact stresses, as shown in Figure 10. The impact stress is taken as the difference between maximum stress at impact and stress caused by the same overpressure acting on a closed valve. (The average of impact stresses at locations B3 and B4 are plotted.) This corresponds to the distance between the curves in Figure 9. Impact stress should be a function of the velocity at impact which, in turn, should be a function of the total closing time of the valve. For all orientations except the recessed perpendicular orientation, a reasonable relationship existed between impact stress and closing time. However, for the recessed perpendicular case, which is the most common mounting, the data was quite different. Stresses were very high, but the valve closed quite slowly. There has been no satisfactory explanation for this data, but since it occurred for three separate tests, it is not an anomalous condition; it merely indicates the rather complex situation which exists when these valves are blast-closed.

Because the force for blast closing is produced largely by aerodynamic forces and not by spring forces, as evidenced in these tests, one would expect the closing time to be a function of the incident overpressure. The data shown in Figure 11 indicates that this is not generally the case. Valve orientation seems to have a much stronger effect on valve closing time than the incident overpressure.

The quarter-scale tests demonstrated that the louver-valve principle was sound and would meet the design overpressure requirements in any orientation. Stresses induced in the valve by blast closure, even without a shock absorber, were not excessive. However, the data did demonstrate that there were some rather complex interactions that were not easily explainable.

The next step in the development of the louver valve was a full-size test in the shock tube at the Defence Research Establishment, Suffield, Alberta, Canada. This test was to investigate further valve characteristics. A complete valve, including the actuator, the linkage between the actuator and the valve mechanism, and the trigger, would be subjected to blast loading. Use of the trigger provided data on the blast threshold level, i.e., the lowest pressure which would cause self-tripping of the blast valve.

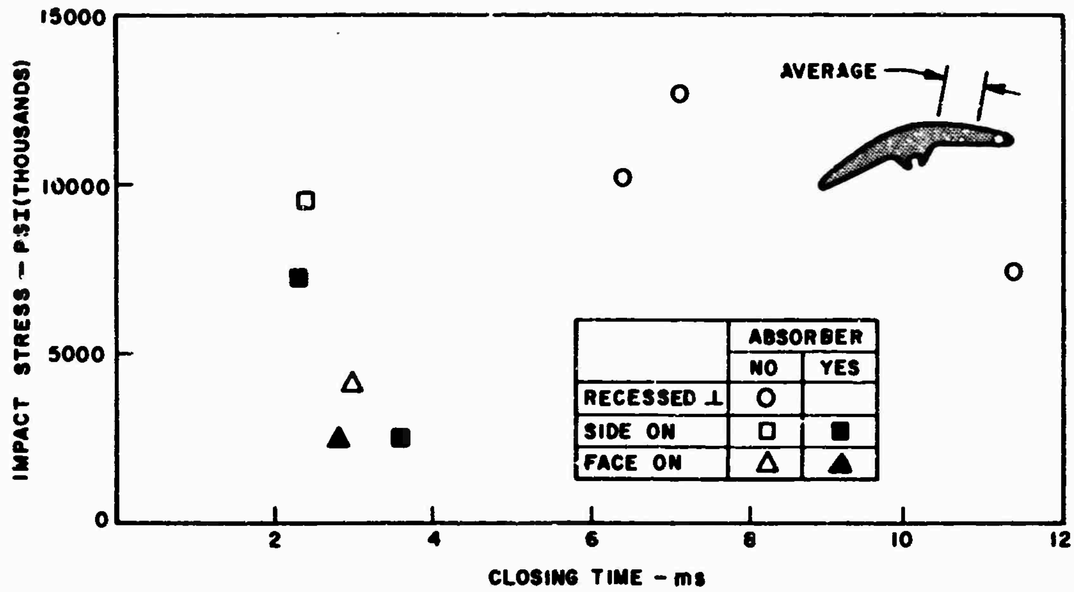

Fig. 10 - Impact Stresses Related to Closing Times

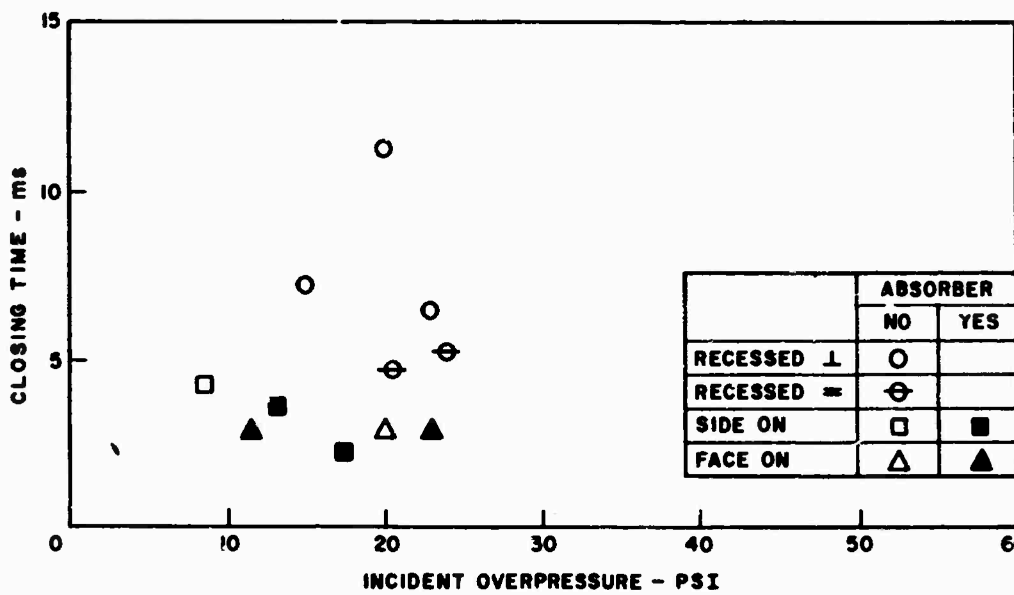

Fig. 11 - Valve Closing Times for Various Pressures

The test setup is shown in Figure 12, with the valve shown in the side-on recessed mounting. The valve was tested with the louvers vertical and horizontal at that location. It was also tested in a face-on position at the end of the shock tube, where it was fitted into the square assembly visible through the end of the shock tube in Figure 12. The Suffield shock tube is driven by high explosives, contrasting with the high-pressure air used for the Chester shock tube. Up to 20 pounds of explosives were used in this test series. The tube has a recoilless construction so that no horizontal loads are transmitted to the shock-tube foundations. This was the reason for mounting the test vehicle on rails.

Some of the most interesting information obtained in the full-scale test was the comparison of this test data with that obtained from the quarter-scale test. The full-scale test did not have as extensive strain-gage instrumentation. However, one location on the ribs and one location on the blade were instrumented so that a comparison could be made with data from gages at the same locations on the quarter-scale valve. The comparison is summarized in Table 2. In the case where the valve was closed before blast arrival, the stress levels were quite similar, especially for the side-on and recessed perpendicular cases. The comparison is made for the side-on valve in the quarter-scale test and the recessed perpendicular valve for the Suffield test because no flush side-on tests were made at Suffield. Comparison is not quite as good for the face-on condition.

Similar correlation is generally evident in the tests where the valve was blast-closed. For the recessed case where the louvers were parallel to the axis of the shock tube, the closing times between the quarter-scale and full-scale tests were within 3 milliseconds. (The closing time for the quarter-scale tests had been

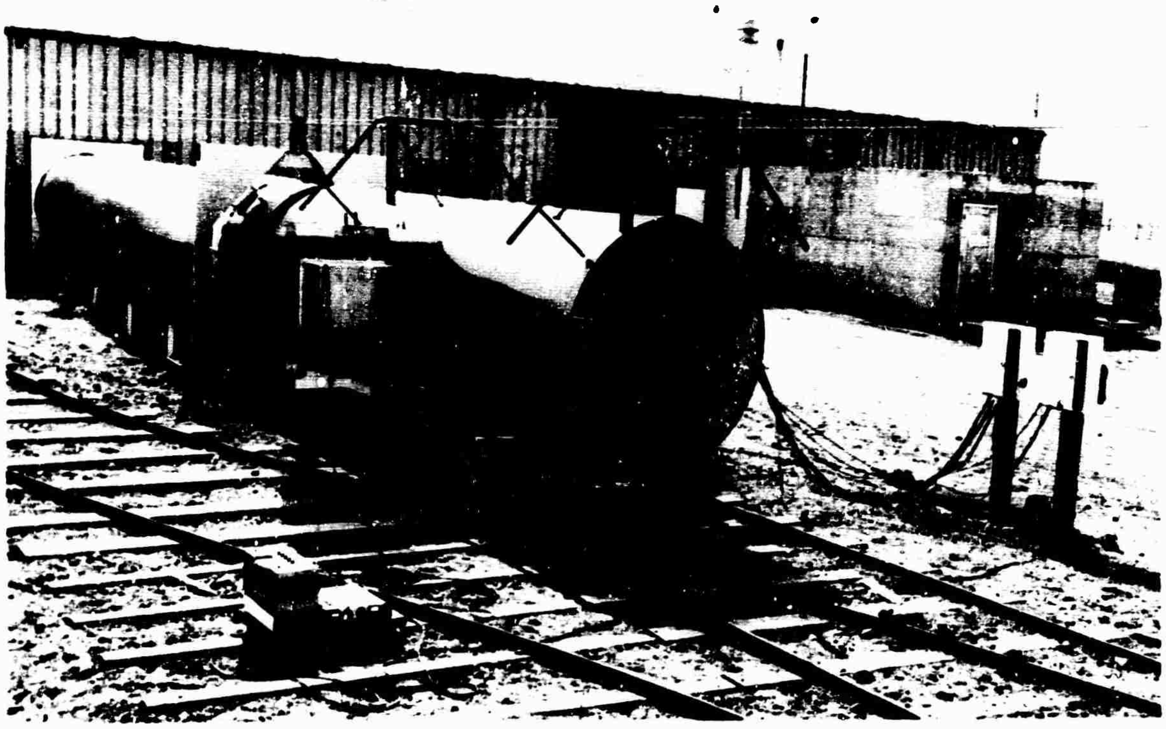

Fig. 12 - Suffield Shock Tube

TABLE 2

Comparison of Quarter-Scale and Full-Size Test Data

Valve Orientation	Incident Pressure (psi)		Rib Stress Location R3 (psi)		Blade Stress Location B3 (psi)		Closing Time (ms)	
	1/4	1	1/4	1	1/4	1	1/4*	1
Closed before blast arrival:								
Side-on and Recessed Perpendicular	21	23	10,000	9,700	4,200	4,500	-	-
Face-on	25	27	17,000	-	6,100	8,500	-	-
Blast-closed:								
Recessed Parallel	20†	19†	-	6,900‡	3,000†‡	4,600†‡	19†‡	16†‡
Face-on	20 23†	22†	-	10,800‡	5,800‡ 7,400†	6,100†‡	11.2‡ 11.6†	10†‡
Recessed Perpendicular	23	23	12,500	8,300 6,300‡	11,300	9,400 7,900‡	26	10 20‡

*Actual values multiplied by 4.
†Data compared in Figures 13 and 14.
‡Absorber used.

multiplied by four to compensate for scaling factors.) The blade stress, however, was somewhat less in the quarter-scale test. Comparison of these blade stresses is presented in Figure 13. The waveforms are quite similar, but the stresses are generally higher for the full-scale test. This can be attributed to the reflected pressure in the full-scale test; this was not present in the quarter-scale test, as can be seen in the overpressure waveforms. In the full-size test, the geometry of the test arrangement simulated the pressure environment for a valve located near the bottom of a vertical air shaft and, as a result, the reflected wave would interact with the blast valve during blast closure. For the quarter-scale test, this geometry was not considered and, as a result, the reflecting end of the shock tube was too far back to cause the reflected pressure to interact with the blast valve during closure.

For the face-on case, closing times and blade stresses were very similar and, as can be seen in Figure 14, the waveforms for blade stresses are also quite similar. The overpressure traces for these tests show separate incident and reflected shocks, because the transducer was approximately 24 inches from the valve in both cases. However, the valve itself saw only a reflected pressure. The comparison made in Figure 14 is for a quarter-scale valve with no absorber and a full-scale valve with an absorber. Table 2 presents a comparison between the closing time and blade stress for a similar quarter-scale test made with an absorber, and the peak values are also quite similar. The data most difficult to interpret were obtained in the recessed perpendicular orientation. This is the same orientation that produced the very high impact stresses and long closing times noted earlier. There is similar data on a full-scale valve without a shock absorber which closed in 10 milliseconds,*

*This was one of the tests in which the valve was damaged.

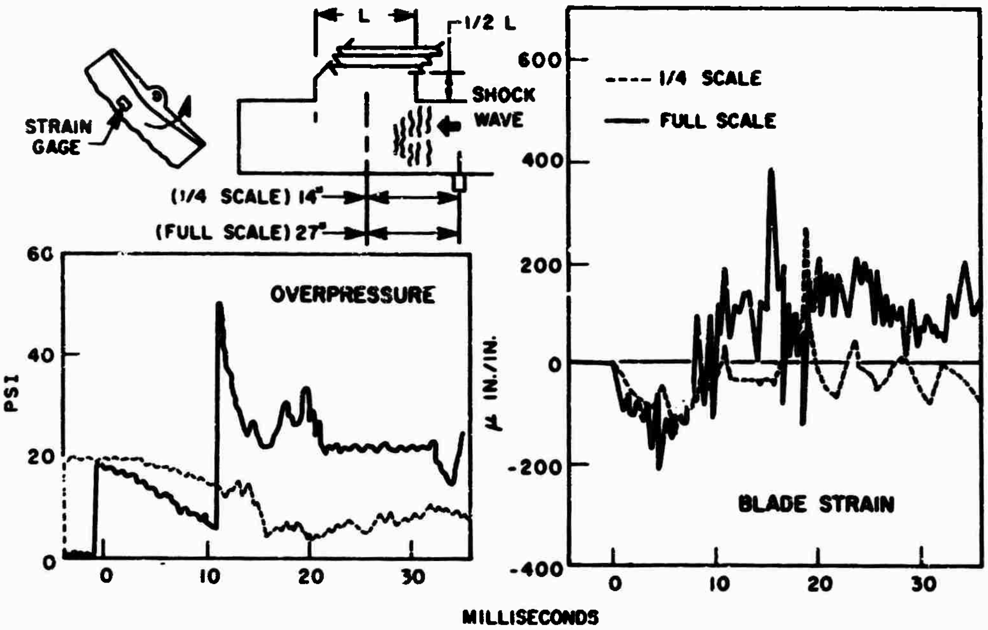

Fig. 13 - Comparison of Stresses in Quarter-Scale and Full-Size Models in Recessed Orientation

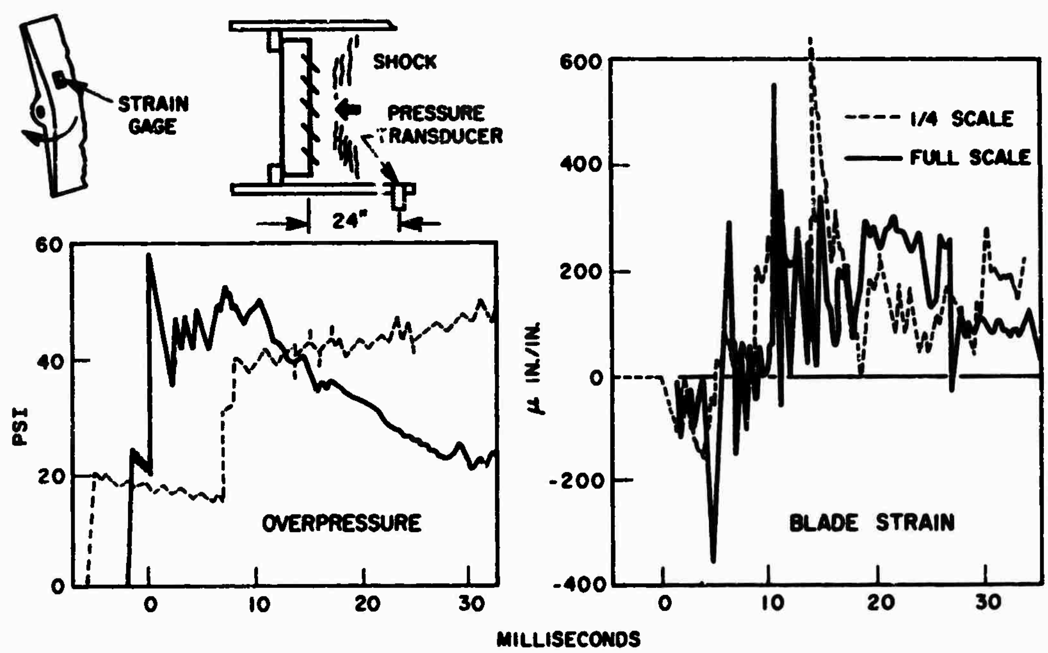

Fig. 14 - Comparison of Stresses in Quarter-Scale and Full-Size Models in Face-on Orientation

as compared with the 26 milliseconds indicated by the quarter-scale tests. Stresses, however, were much closer than would be indicated by the difference in closing times. There is also data on a full-scale test with a shock absorber, and the closing time is more compatible with that predicted by the quarter-scale test. But the stresses are considerably less: almost one half the values observed in the quarter-scale test.

These full-size tests indicated weaknesses in the linkage between the actuating bar and the actuator. The parts were modified and retested in the shock tube to prove their performance. Also, the blast-threshold tripping level for the valve was determined to be approximately 2 psi for the various orientations.

Perhaps the most useful information obtained in the full-scale test was the good correlation between the quarter-scale and full-scale data, indicating the validity of using scale testing for blast-valve performance.

Final test of the louver valve was made in Operation Prairie Flat, a free-field detonation of 500 tons of TNT which simulated the blast and ground-shock effects from a nuclear detonation. The valves tested in this operation were essentially the same as those tested at the shock tube but were fabricated to reflect production techniques. Also, the modifications dictated by the shock-tube tests were made and, in addition, an improved trigger mechanism was used in the valve. The valves were mounted in a simulated, essentially full-scale air shaft,* as shown in Figure 15, to reproduce as closely as possible the actual blast environment that would result from a nuclear detonation. The upper valve was blast-closed, that is, closed by the aerodynamic forces on the valve. The lower valve was closed before blast arrival. This required a control system to electrically trip the valve. The control system was itself tripped by a pressure switch located upstream of the valve test structure.

Both valves performed perfectly during the field test and were completely operational afterwards. The success of the field test is attributable to the extensive shock-tube test program performed on the valve and demonstrates the value of shock-tube tests before an expensive, one-shot field test.

*The full-scale data shown in Figure 5 was obtained in this shaft.

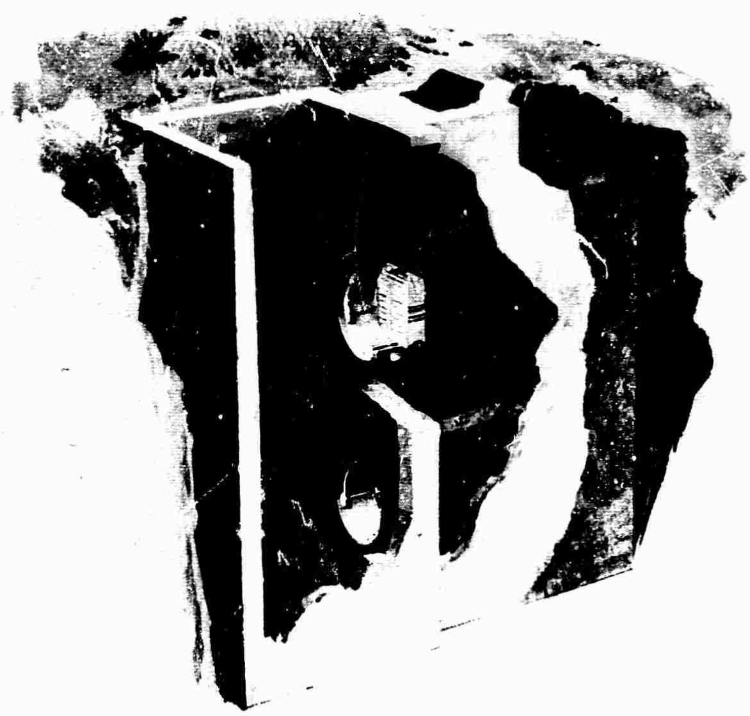

Fig. 15 - Air-Shaft Installation of Louver Valve Tested in Operation Prairie Flat

Mr. Fay (TRW Systems): What are the requirements and performance relating to the down stream pressures that are allowable or seen?

Mr. Witt: Normally, this valve is supposed to be closed before blast arrival at the building. That is, for these underground communication buildings, we have a sensing system which causes these valves to be closed before shock arrival. So essentially there is no pressure down stream in this mode. In the blast closing mode we had no requirements on this, but we made some measurements during Operation Prairie Flat. We tested some of these valves in an actual airshaft and found that the peak pressure down stream of the valve was about 7 psi for a free field pressure of about 33 psi. For normal air conditioning ducting and air filters, such pressure levels would be intolerable.

TESTING THE RESPONSE OF GAS TURBINES TO AIR BLAST

J.C. Muirhead, R. Naylor and C.G. Coffey
Defence Research Establishment Suffield
Ralston, Alberta

The effect of blast on gas turbine engines is of interest to the Canadian Forces because of the use of gas turbines in a new series of destroyer. Exploratory experiments used an Orenda 8 engine, which was subjected to blast waves from a valve-operated, compressed air driven shock tube. No significant effects were caused by inlet loadings, but blast waves impinging on the exhaust caused compressor stall and flame-out at low RPM. A general review of the program is given.

INTRODUCTION

The Canadian Forces are using Pratt and Whitney FT-4A-2 and FT-12A-3 gas turbine engines as the prime movers in a new class of destroyer. The former has a dual axle, 15-stage compressor. The latter has an 8-stage, single axle compressor. Both have 2-stage turbines.

An effort is being made to incorporate some degree of blast hardness into these destroyers. The complexity of the equipment is such that it is impractical to harden all components to a specific level. Thus, certain critical components have received special attention. Among these is the propulsion system.

The Defence Research Establishment Suffield was requested to obtain information concerning the ability of these engines and their associated ducting systems to withstand blast loadings. Studies on the response of the ducting and demister systems have been reported (Ref. 1-3). The effect of blast on the engines is reported herein.

No theoretical models, and little background data were available. This, combined with a requirement for a rapid acquisition of information, prompted the initiation of a program of exploratory experimentation. As marine power units were not available for test, our experiments employed an Orenda 8 gas turbine of the type which was used in the CF-100 interceptor. It has a 10-stage single axle compressor, with a single stage turbine. It was chosen because of its general similarity to the marine turbines, and because of ready availability.

SHOCK TUBE FACILITY

Two basic choices were available in selecting a source of blast waves with which to load the engine; large free-air explosions, and shock tubes. Large (up to 500 tons of TNT) blast trials are a regular feature of the DRES research program. They offer the opportunity of testing large equipment under realistic conditions. However, these trials are of infrequent occurrence, whereas shock tubes may be operated several times during a single day.

The basic system chosen was a 17 inch internal diameter shock tube. This device, which is described in Ref. (4), is driven by compressed air, which is released by a flexible diaphragm shock wave valve, similar in principle to the valves described in Ref. (5). The method of operation of this valve is illustrated in Fig. 1.

The driver gas is contained in an annular compression chamber which surrounds the upstream length of the expansion chamber. Additional compressed air in the actuating chamber acts to seal the nylon reinforced Hypalon diaphragm against the entrance to the expansion chamber.

Upon release of air from the actuating chamber (through a conventional bursting

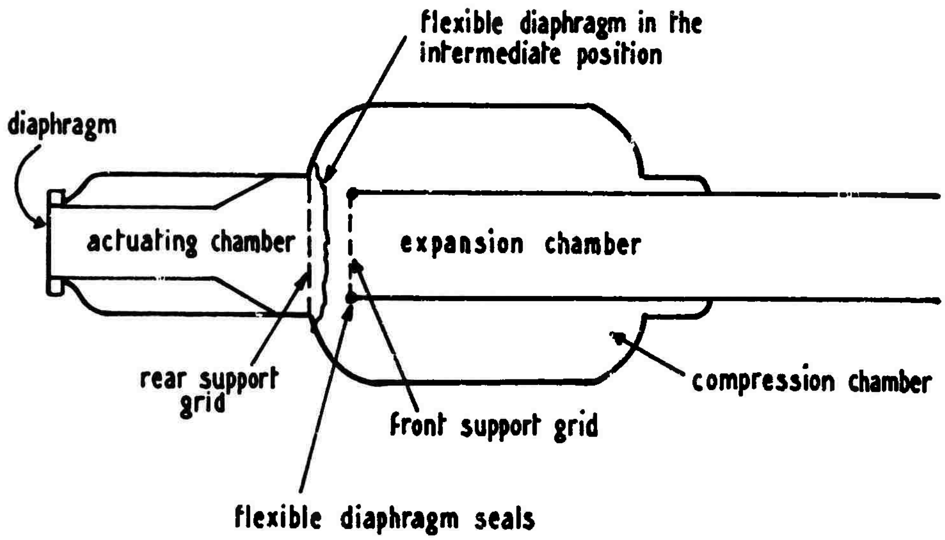

Fig. 1 - Shock Tube Driving System

diaphragm), the flexible diaphragm moves backward, allowing the compression chamber gases to exhaust into the expansion chamber.

An external view of the compression chamber-valve system is given in Fig. 2.

Major advantages of this type of shock tube include the avoidance of the residue which is normally associated with frangible diaphragm operated shock tubes, and the absence of gaseous impurities which are associated with explosively driven shock tubes. Either of these could severely affect the operation of a gas turbine engine.

The 17 inch shock tube is capable of handling compression overpressures of up to 200 psi, and of producing shock waves having overpressures of up to 45 psi with positive durations of up to 200 msec.

Modifications were needed to allow this shock tube to fire into the engine. An important requirement of any modification was that it be capable of delivering blast waves to the engine, but that its presence should not interfere with the normal engine operation. For blast loading of the inlet, the 17 inch tube was fired into a 36 inch diameter tube, which led to the turbine inlet. This is illustrated in Figs. 3 and 4.

The exhaust was loaded by firing the 17 inch tube into a 24 inch tube which led to the turbine exhaust. This arrangement is illustrated in Figs. 5 and 6.

Both of these systems worked well, although the maximum blast overpressure available for delivery to the turbine was only 20 psi. Details on the development and performance of these modified shock tubes are described in Ref. (6).

INSTRUMENTATION

The engine was mounted in a CF-100 airframe, which was mounted on a concrete pad. All operational instrumentation was left intact in the cockpit, and parallel circuits were taken to the control room. With the aid of remote controls and video coverage of the cockpit control panel, all aspects of the engine operation following start-up were conducted from the control room.

A variety of instrumentation was used to monitor the behaviour of the aircraft during blast loading, and to check the transmission of blast waves through it. Locations of these are indicated in Fig. 7.

The pressure transducers used were piezoelectric types of DRES design and manufacture where the local temperatures did not exceed

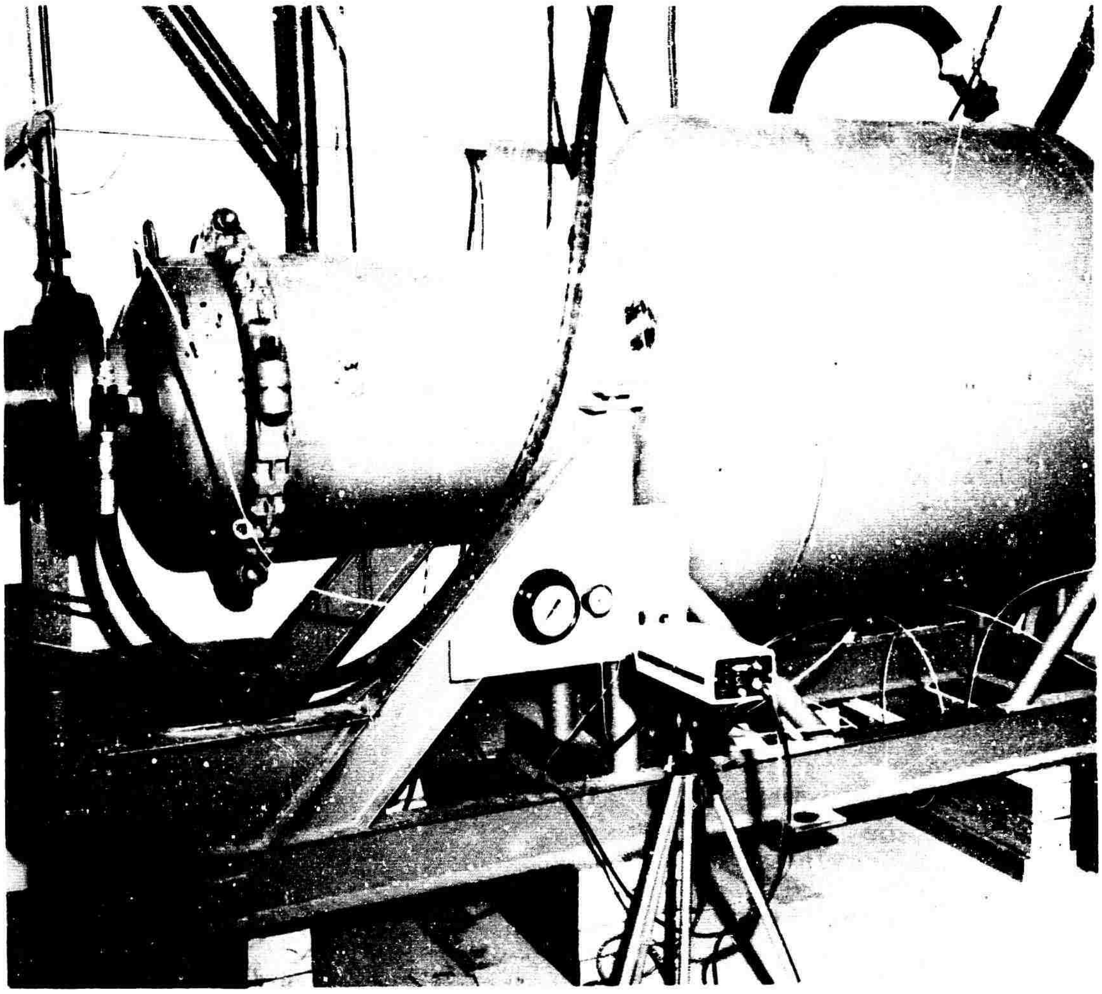

Fig. 2 - Shock Tube Driving System

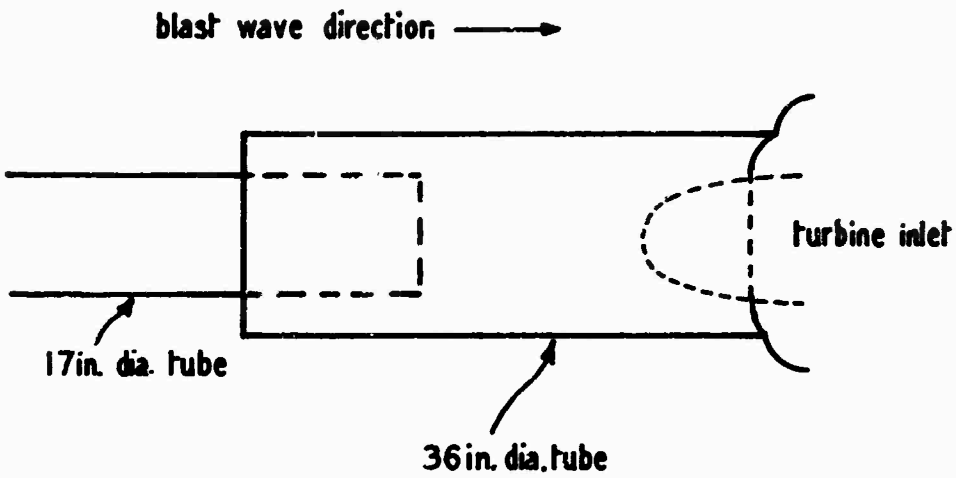

Fig. 3 - Shock Tube Geometry For Inlet Loading
(not to scale)

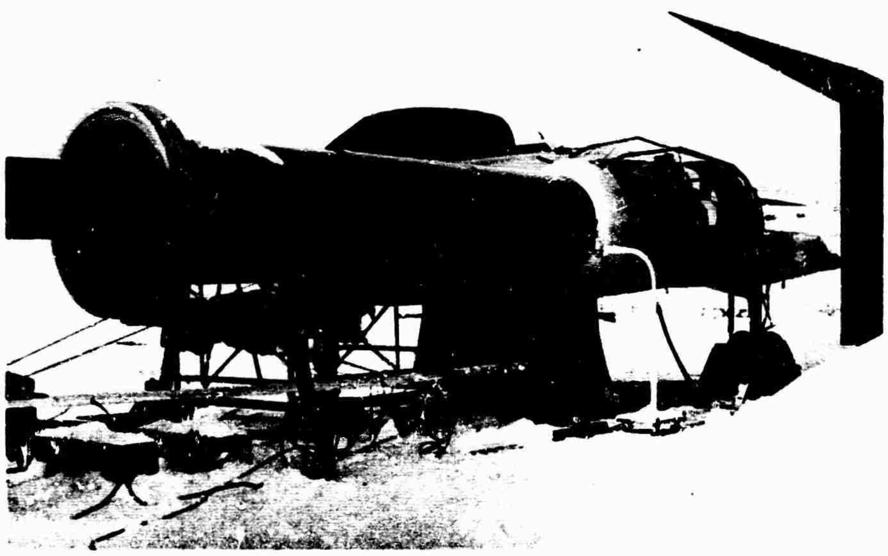

Fig. 4 - Shock Tube For Inlet Loading

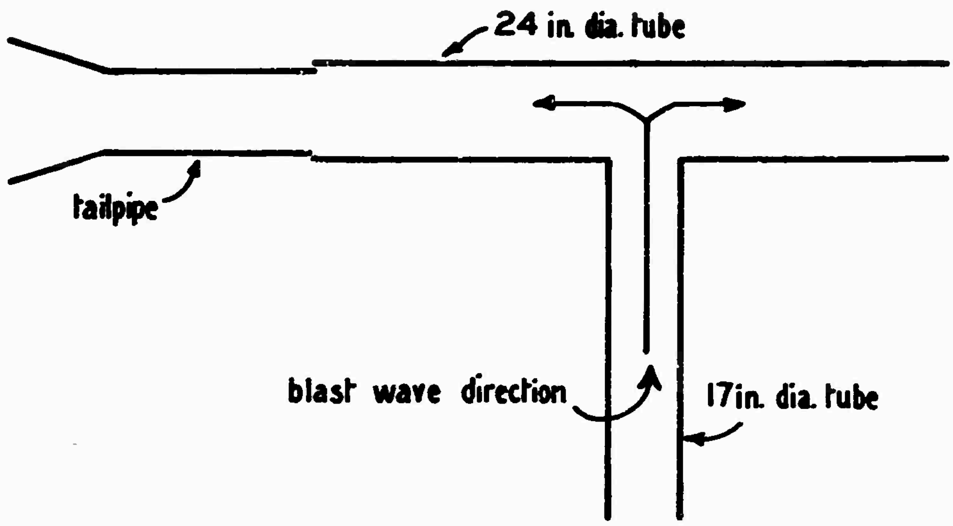

Fig. 5 - Shock Tube Geometry For Exhaust Loading
(not to scale)

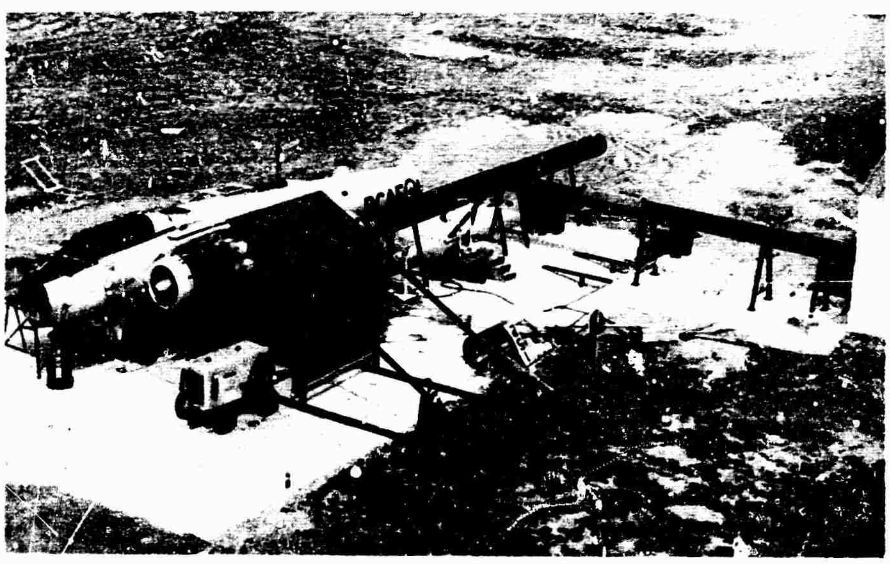

Fig. 6 - Shock Tube For Exhaust Loading

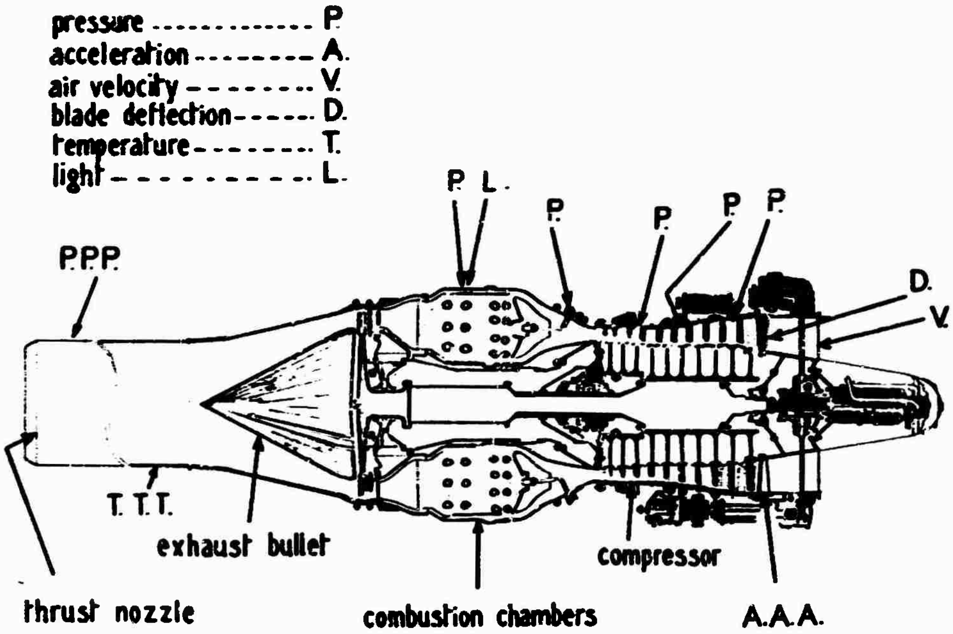

Fig. 7 - Instrumentation Locations

about 80°C and Bytrex strain gauge type where temperatures were higher than 80°C. Satisfactory results were obtained with the latter up to 150°C. Where temperatures were higher as in the combustion chambers or tail-pipe, water cooled mounts of DRES design and manufacture were used. Iron-constantan thermocouples were used for auxiliary tail-pipe temperature measurements.

A constant-temperature thermistor bead sensed the air velocity at the inlet, while a Bently-Nevada proximity coil sensed the gap of the first stage compressor blades.

Endevco strain gauge accelerometers sensed the vibration of the front of the engine in the three principal axes. Their output was electrically integrated to velocity as an indication of engine roughness; higher frequencies than first engine order were attenuated by use of low-pass filters on the field lines.

All tests were recorded on FM tape recorders and a video tape recorder. The latter recorded indications from the cockpit instruments for subsequent analysis.

PROCEDURE

The inlet of the turbine was subjected to blast waves on 12 occasions, while the exhaust was loaded 20 times. These tests were conducted with the engine stationary, and operating at a variety of speeds ranging from 38% to 100% of its maximum speed of 7800 RPM. Blast waves having overpressures of up to 13 psi were applied to the inlet and up to 20 psi on the exhaust. The thrust nozzle (Fig. 7) was removed for the exhaust loading experiments. No attempt was made to apply blast waves to the inlet and exhaust simultaneously.

RESULTS - Front End Loading

Blast loading of the inlet of the engine caused small (less than 2%) transitory changes in engine RPM. However, no mechanical damage of any kind was observed. There was no evidence of compressor stall, nor of any disruption of the combustion processes.

Considerable data were accumulated on the transmission of blast waves through the turbine.

A summary of the average pressure measurements is given in Table 1. These are expressed in dimensionless form as a ratio to the incident overpressure (in the 36 inch expansion section).

TABLE 1

Summary of Peak Overpressures Measured During Inlet Loading Experiments: Overpressures Are Expressed as Ratios to the Incident Overpressure

Turbine RPM (% of Max)	Compressor			Burner Cover Plate	Tailpipe
	Stage 2	Stage 5	Stage 8		
0	1.5	1.2	0.9	0.3	0.6
38	1.7	1.8	1.6	0.7	—
93	1.7	2.0	1.8	1.5	—
100	1.7	2.0	1.9	1.6	—

The overpressure of the blast wave is increased upon entry into the compressor. This increase is a result of the reduction in the area of the available flow channels, which compresses the blast wave. For example, the flow area at the 8th stage is about 150 square inches, compared to 850 square inches in the shock tube. An increase in overpressure is also associated with an increase in engine RPM. Presumably, this increase is related to the velocity of the air flow through the engine. These pressure transmission results are reviewed in greater detail in Ref. (7).

RESULTS - Rear End Loading

Blast loading of the engine exhaust resulted in flame-out, compressor stall, and some mechanical damage. The damage occurred to the exhaust bullet, and consisted of longitudinal buckling. The bullet, whose location is indicated in Fig. 7, was manufactured of 321 stainless steel, and contained reinforcing ripples. These were aimed at increasing the resistance of the bullet to radial compression, but tended to weaken it against longitudinal compression. A damaged bullet is illustrated in Fig. 8.

Flame-out occurred at 38% and 58% RPM, with incident overpressures of 10 and 11 psi respectively, however flame-out could not be achieved at higher RPM. The results of these experiments are illustrated in Fig. 9. This indicates the incident overpressures which were used, and whether or not flame-out resulted. While the projected curve is speculative, it is clear that flame-out requires increased pressures at higher RPM.

The mechanism of flame-out appears to involve compressor stall and disruption of the combustion process. Analysis of photographic records obtained in the combustion chamber, pressure records obtained in the compressor, and of the inlet air velocity measurements indicated a pattern of flame disruption, which was marked by an intense brightening of the flame, followed (after about 150 msec) by a rapid drop in flame intensity. Simultaneously, a stall (marked by a strong "negative" pressure signal) was observed in the compressor, and the inlet air velocity dropped markedly.

If the compressor recovered from its stall before extinction of the flame occurred, the engine kept running. If, however, stall (and the resulting drop in air flow) continued until the flame had been extinguished, then the engine stopped. Extinction of the flame, therefore, appears to have resulted from enhanced combustion (and enhanced oxygen consumption) caused by the initial disruption of the flame by the blast wave, followed by oxygen starvation which resulted from the compressor stall.

A typical set of transducer records is presented in Fig. 10. Here, a common absolute time base is used so that the relationship among various parameters may be observed.

Considerable data were again obtained on the transmission of blast waves through the engine. This is summarized in Table 2. As in Table 1, these data are presented in dimensionless form, as ratios to the incident overpressure (in this case, in the 24 inch tube).

A more detailed review of these data is given in Ref. (8).

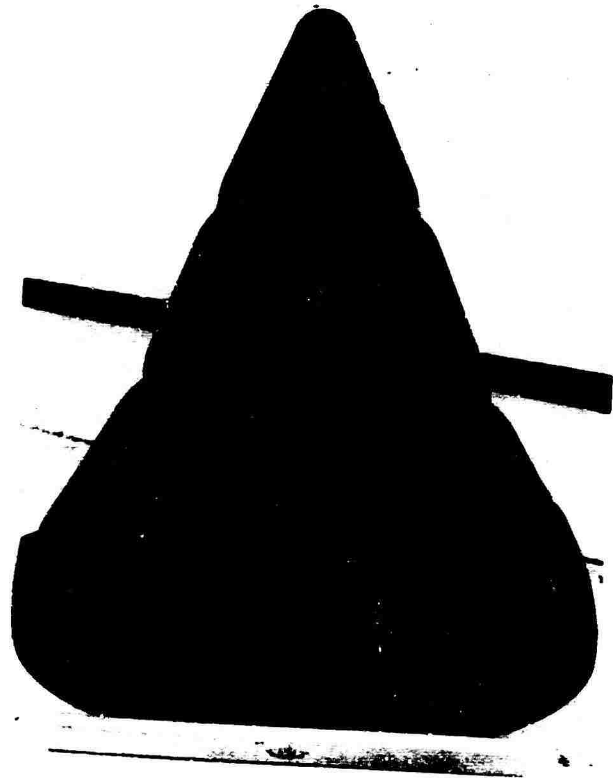

Fig. 8 - Damaged Bullet

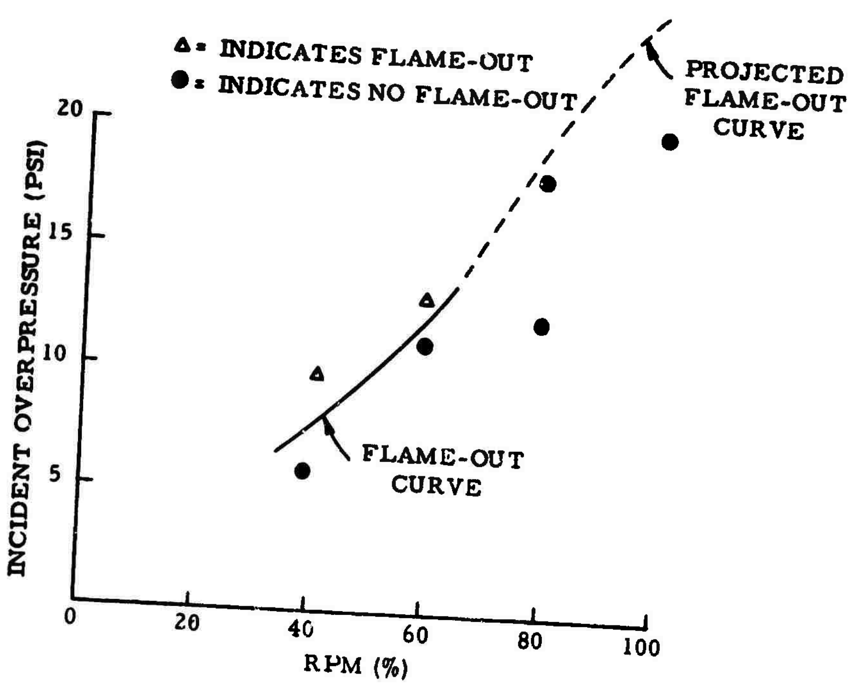

Fig. 9 - Overpressure Vs RPM For Flame-Out

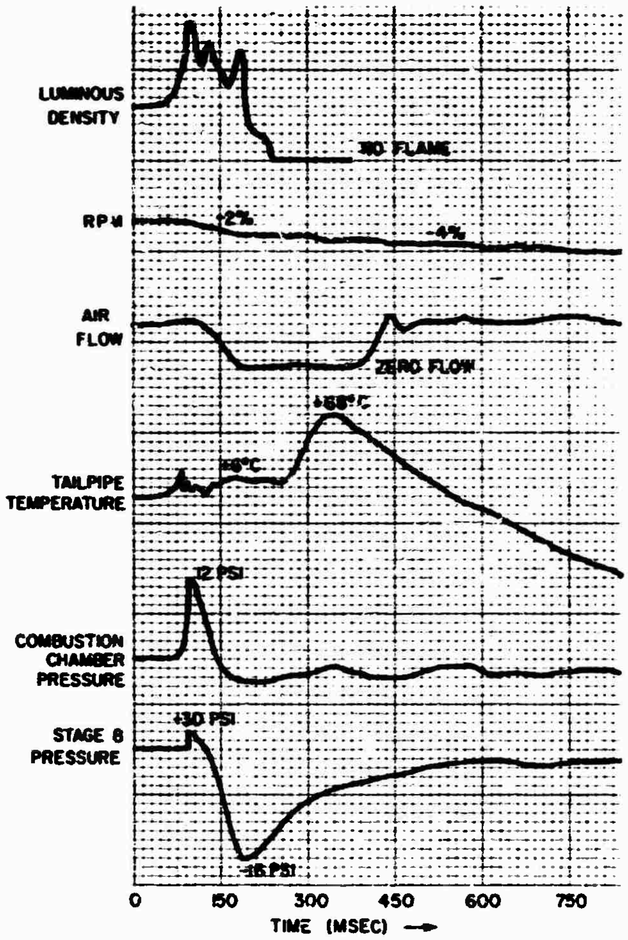

Fig. 10 - Typical Transducer Records

TABLE 2

Summary of Peak Overpressures Measured During Exhaust Loading Experiments: Overpressures Are Expressed as Ratios to the Incident Overpressure

Turbine RPM (% of Max)	Tailpipe	Combustion Chamber	Burner Cover Plate	Compressor	
				8th stage	5th stage
38	1.0	0.9	1.0	0.8	0.4
58	0.9	1.1	0.8	0.5	0.2
79	0.9	0.6	0.5	0.3	0.06
100	0.9	0.7	0.2	0.3	0.06

It is clear that with increased RPM, the blast wave finds it increasingly difficult to travel upstream.

DISCUSSION

These experiments illustrate that the particular Orenda 8 engine which was involved in these tests is a rugged and stable machine, and is relatively insensitive to blast loadings. It was subjected to more than 32 blast waves, and operated in an open air test stand at temperatures ranging from -40 to +90°F. With the exception of the exhaust bullet, no evidence of damage could be detected by visual inspection, or from vibration analyses.

Blast loading of the exhaust caused interference with the combustion process and compressor stall, phenomena which were not observed during blast loadings of the inlet. It may be instructive to note that blast loading of the exhaust tends to oppose the normal pattern of air flow through the engine, whereas blast loading of the inlet tends to reinforce this flow.

It is hoped to apply the facilities and background knowledge which have been established by this program to the prediction of the effects of blast on the marine power units which were discussed in the Introduction.

REFERENCES

(1) J.S. Watson and W.A. Jones, "Response of DDH 280 Demister Pads to Blast Waves", Suffield Memorandum No. 33/69, 1969

(2) A.M. Patterson, "Air Blast Tests of a Proposed Demister Unit for DDH 280 Air Filtration System", Suffield Memorandum No. 149/69, 1969

(3) W.A. Jones and F.L. McCallum, "Progress Report DDH 280 - FT4 Ducting: Modification of the Reflected Wave Profile", Suffield Memorandum No. 15/69, 1969

(4) W.A. Jones, F.L. McCallum and L.W. Tamke, "Construction and Evaluation of a 17 Inch Flexible Diaphragm Shock Wave Valve", Suffield Memorandum No. 32/68, 1968

(5) J.C. Muirhead and W.A. Jones, "Shock Wave Valves", Rev.Sci.Instr. 35, 1, p.119, 1964

(6) J.C. Muirhead and C.G. Coffey, "Shock Tube Facilities for the Study of Blast Effects on Gas Turbine Engines", Suffield Technical Note No. 261, 1969

(7) J.C. Muirhead, R. Naylor and G.D. Felt, "The Transmission of Blast Waves Through an Orenda 8 Engine", Suffield Technical Note No. 219, 1969

(8) J.C. Muirhead, R. Naylor and G.D. Felt, "The Transmission of Blast Waves Through an Orenda 8 Engine From Exhaust to Inlet", Suffield Technical Note No. 265, 1969

TRANSIENT WAVEFORM CONTROL OF ELECTROMAGNETIC TEST EQUIPMENT

John D. Favour and Jay M. LeBrun
The Boeing Company
Seattle, Washington

and

Joseph P. Young
NASA Goddard Spaceflight Center
Greenbelt, Maryland

This paper discusses a technique by which electromagnetic exciters are controlled to produce specific time-history transient waveforms. The technique utilizes an "on line" digital computer in a near-real-time configuration. A recently developed Fast Fourier Transform algorithm forms the operational foundation of the technique. A prototype transient waveform control system was assembled and tested. That prototype system and its performance are discussed.

INTRODUCTION

Shock testing in the aerospace industry has been somewhat schizophrenic, torn between a confusing mixture of opinions concerning the test device and imposed motion time history. Test devices take the form of impact machines, electromagnetic exciters, and the shock producing device itself. Specified time histories have ranged from a simple pulse, to complex decaying transients, to slow sine sweeps, to fast sine sweeps, to short random bursts, and to creation of the actual shock producing event.

One common ground of agreement has been the desirability of being able to use an electromagnetic exciter to produce specific transient waveforms with the same degree of convenience that exciters are used to produce sine and random vibration environments. During the past five years, a number of investigators have reported on efforts to utilize the shaker for shock testing [1-6] . These efforts have followed two distinct paths. Use of the shock spectrum as a standard of comparison is common for one group, whereas, the other group has concentrated on producing a specific time history waveform. Without having to become embroiled in the merits and demerits of the shock spectrum, the specified time history path certainly provides greater simulation realism. Even for the case where a specified shock spectrum is the basic criterion for simulation, some time history can be associated with the shock spectrum. Therefore, the ability to produce a specified time history encompasses both of the simulation criteria. This fact, coupled with the increasing capability to predict transient time histories [7,8], promoted an effort to produce a near-real-time, on line, transient waveform control system for use on electromagnetic exciters. The first results of this effort are presented in this paper. As can be seen, there remains more work to be done to fully explore the limits of this control system.

TECHNIQUE

The successful implementation of Transient Waveform Control depends upon the test system being a time-invariant linear system. The test system is defined to include the power amplifier, exciter and specimen mounting fixture, with the specimen acting as system load*. The general approach to this transient waveform control system is to:

1) Develop an accurate definition of the test system transfer function, $H(\omega)$;

2) Develop the Fourier transform of the required waveform, $F(\omega)_R$, and divide it by the test system transfer function;

3) Inverse Fourier transform the quotient, developed in 2) above, into the time domain.

*This assumes the test system output is at the fixture-specimen interface.

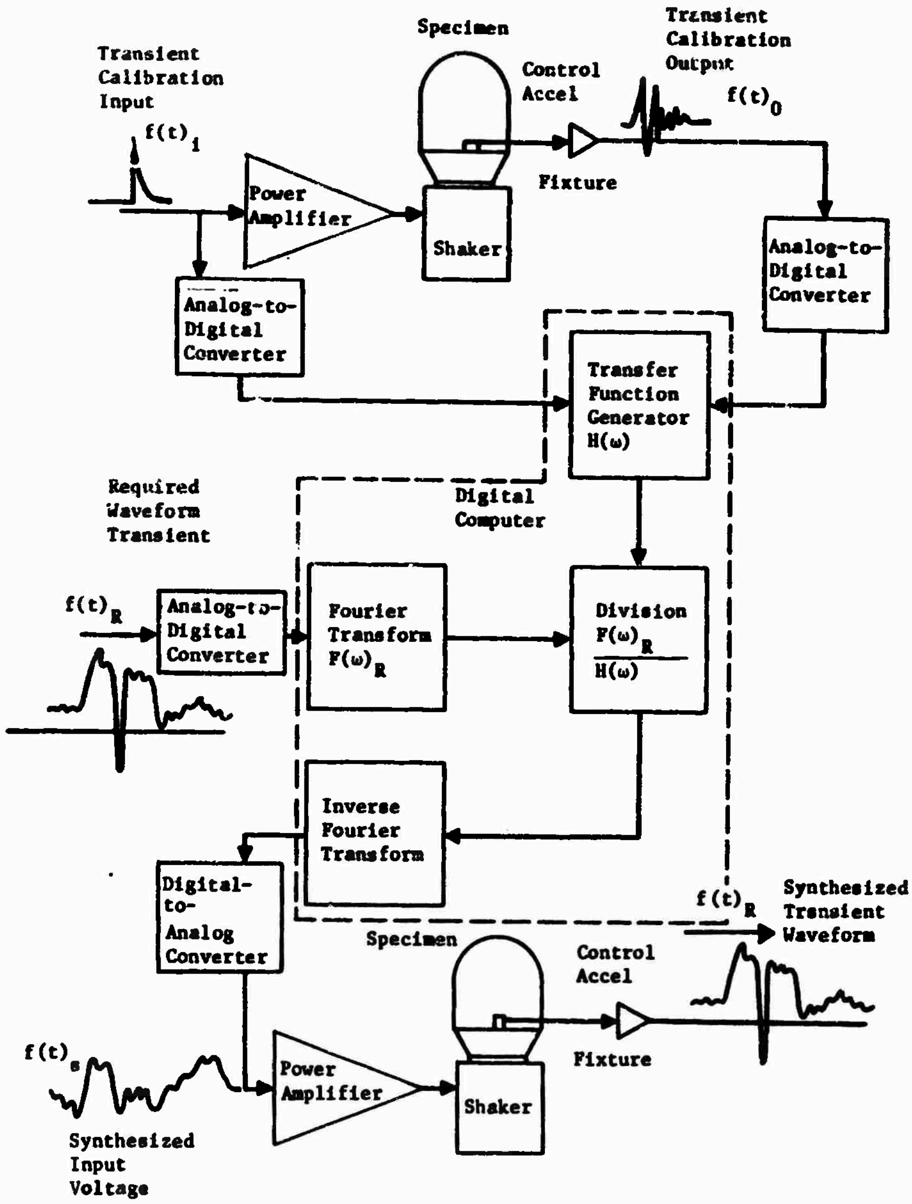

Figure 1: TRANSIENT WAVEFORM CONTROL, LOGIC DIAGRAM

This computer-generated time domain function represents a voltage that, when applied as an input to the test system, will cause the required waveform to be generated at the control system output. The entire concept is schematically illustrated in Figure 1.

The Transient Calibration Input signal, $f(t)_i$, must be of a form such that its frequency content completely saturates the entire operating bandwidth of the system. Currently a pulse of the form,

$$f(t)_i = K e^{-\alpha t} \quad \text{for } t > 0 \tag{1a}$$

$$f(t)_i = 0 \quad \text{for } t < 0 \tag{1b}$$

is used as the calibrating transient. Its Fourier transform is of the same form as a first order, low pass filter, with a corner frequency of f_c, where,

$$f_c = \alpha \tag{2}$$

Refer to Figure 2.

Both the transient calibration input, $f(t)_i$ and the transient calibration output, $f(t)_o$, signals are passed thru identical analog to digital converters (ADC), and the digital information stored in the computer memory. From this digital information, the respective Fourier transforms, $F(\omega)_i$ and $F(\omega)_o$, are computed and then ratioed to produce the test system transfer function,

$$H(\omega) = \frac{F(\omega)_o}{F(\omega)_i} \quad . \tag{3}$$

Prior to the time the test system is calibrated, the digital description of the required transient waveform, $f(t)_R$, is read into the computer and its Fourier transform, $F(\omega)_R$, is computed. This transform is then divided by the test system transfer function to synthesize the frequency domain description,

$$F(\omega)_S = \frac{F(\omega)_R}{H(\omega)} \quad . \tag{4}$$

$F(\omega)_s$ is then "inverse" Fourier transformed into the time domain and the digital data passed thru a digital to analog converter, (DAC), to produce $f(t)_s$.

This technique is based upon the capability to accurately, economically, and rapidly compute Fourier transforms of transient time functions into frequency functions, and "inverse" Fourier transforms of synthesized frequency functions into continuous, useable functions of time.

In 1965, a new algorithm for computing a discrete Fourier transform was described by Cooley and Tukey [9,10] . This algorithm is known as the "Fast Fourier Transform" (FFT). Assuming a time history is described by N discrete data points, the FFT will compute the Fourier transform in $N\log_2 N$ operations whereas previous or conventional algorithms required N^2 operations. For example, assuming N equals 4096 data points, the FFT algorithm would compute a transform 341 times faster than the conventional algorithm.

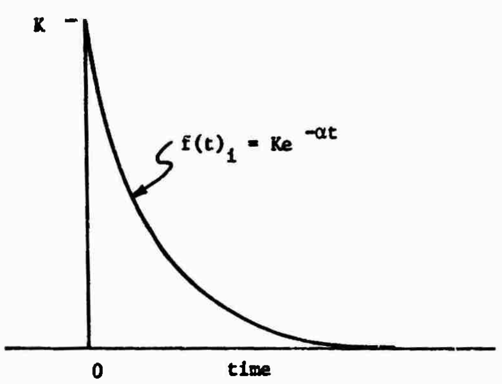

Figure 2a: TRANSIENT CALIBRATION INPUT SIGNAL

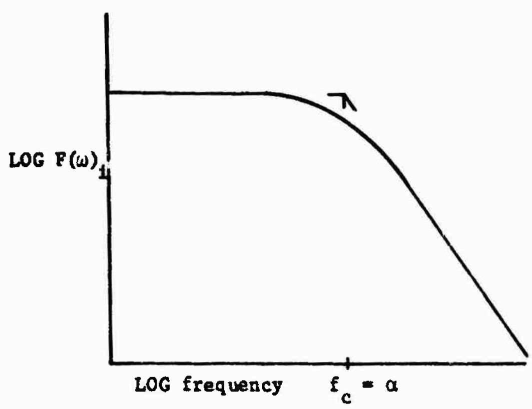

Figure 2b: FOURIER TRANSFORM MODULUS OF TRANSIENT CALIBRATION INPUT

Figure 2: TRANSIENT CALIBRATION INPUT

The FFT is a discrete Fourier transform based upon the following reciprocal equations of the Fourier Transform [10] ,

$$A(n) = \frac{1}{N}\sum_{k=0}^{N-1} X(k)\, e^{-j2\pi nk/N} \quad , \qquad (5)$$

and the inverse Fourier transform,

$$X(k) = \sum_{n=0}^{N-1} A(n)\, e^{j2\pi nk/N} \quad . \qquad (6)$$

The quantities A(n) and X(k) represent number sets only. N equals the number of data values in each set. The summation counters are n and k. In this form, they are not restricted to a time-frequency domain relationship.

Equations (5) and (6) are used to compute discrete Fourier transforms in units of time and frequency by inclusion of the sampling increments, Δt and Δf, and use of the following theorem.

If x(t) (a continuous time function for $-\infty < t < \infty$) and a(f) (a continuous frequency function for $-\infty < f < \infty$) are a Fourier integral transform pair,

$$x(t) \longleftrightarrow a(f),$$

then $TX_p\ (k\Delta t)$, k = 0, 1, 2, ... N-1

and $A_p\ (n\Delta f)$, n = 0, 1, 2, ... N-1

are a discrete Fourier transform pair, where,

$$\Delta f = \frac{1}{N\Delta t} = \frac{1}{T} = \frac{\Delta\omega}{2\pi}$$

and N = number of time data points,

Δt = time sampling interval,

T = time duration of total signal ($N\Delta t$),

Δf = frequency sampling internal.

The resulting transform pair are,

$$A_p\ (n\Delta f) = \Delta t \sum_{n=0}^{N-1} X_p(k\Delta t)^{-j2\pi nk/N} \quad ,$$

and

$$X_p\ (k\Delta t) = \Delta f \sum_{n=0}^{N-1} A_p(n\Delta f)^{j2\pi nk/N} \quad ,$$

where,

$A_p(n\Delta f)$ = nth complex frequency sample

$X_p(k\Delta t)$ = kth time sample

N = total number of time/frequency samples

$j = \sqrt{-1}$

PROTOTYPE TRANSIENT WAVEFORM CONTROL SYSTEM

A prototype control system, corresponding to the Transient Waveform Control - Logic Diagram, Figure 1, was developed and evaluated in the Environmental Test Laboratory of The Boeing Company Aerospace Group. The primary elements are illustrated in Figure 3. The digital computer and its peripheral equipment (not all shown) was designed to provide data processing support for vibration, acoustic, and shock test operations and is geared to provide large volume production analysis capability for random and transient data [11] .

Communication between the vibration test laboratory and the computer is accomplished with a remote computer test station located at the vibration console (Figures 4 and 5). The computer is controlled by the vibration test system operator using six thumb wheel switch positions on the remote station. The software "Inter-overlay Operational Logic Versus Remote Test Station Switch Position" is shown in Figure 6. A synopsis of the switch positions and their functions are as follows:

Position 1 allows the computer operator to enter and transform the required transient waveform, $f(t)_R$.

Position 2 instructs the computer only to send the transient calibration input pulse, $f(t)_i$, without recording or computation. This allows for adjustment of the excitation level.

Position 3 instructs the computer to send the transient calibration pulse, $f(t)_i$, record $f(t)_i$ and $f(t)_o$, and calculate the test system transfer function, $H(\omega)$.

Position 4 instructs the computer only to send the synthesized input voltage, $f(t)_s$, without recording. This allows inspection of $f(t)_s$ while the test system amplifier is down.

Position 5 instructs the computer to send $f(t)_s$, and record and plot* the test system output waveform

*Many plot options are available for additional operation inspection and test qualification.

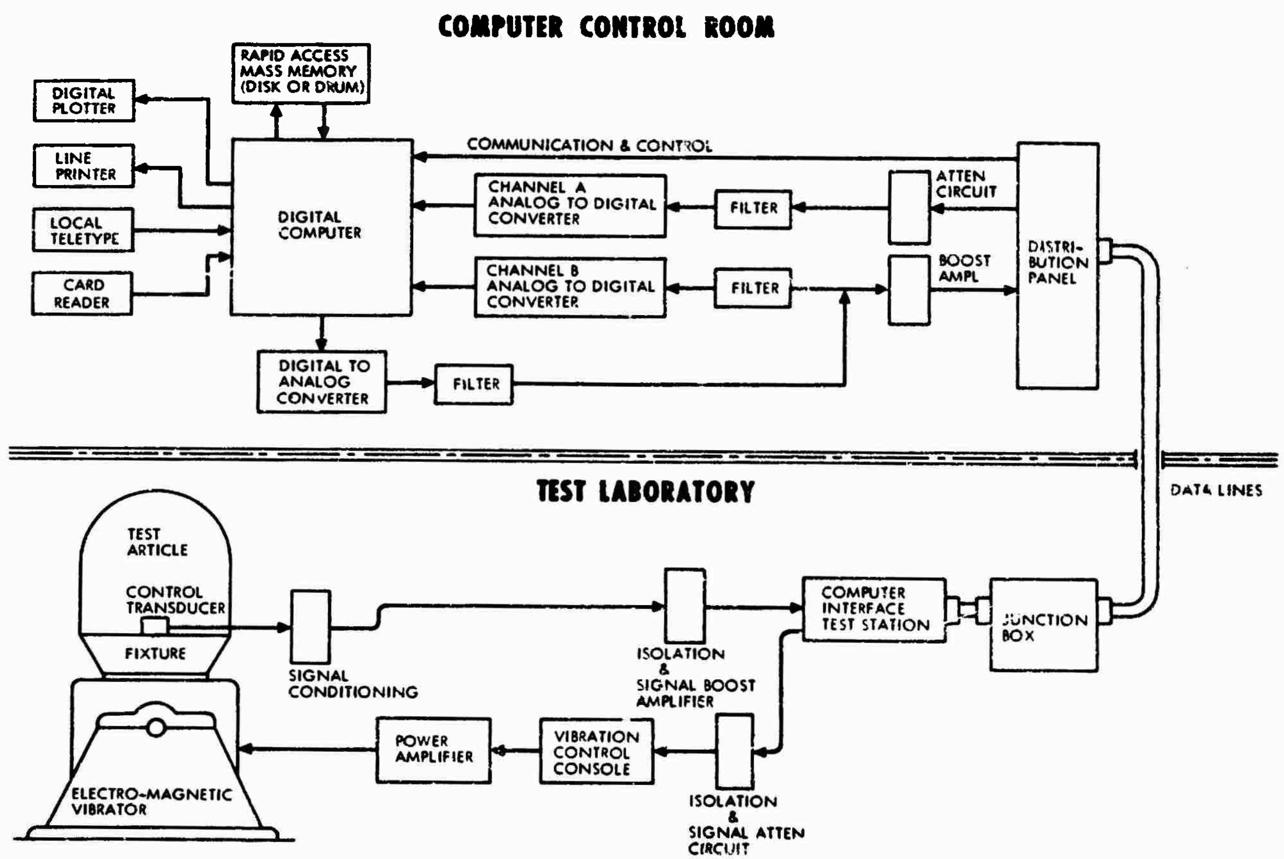

Figure 3: CONCEPTUAL DESIGN - TRANSIENT WAVE FORM CONTROL SYSTEM

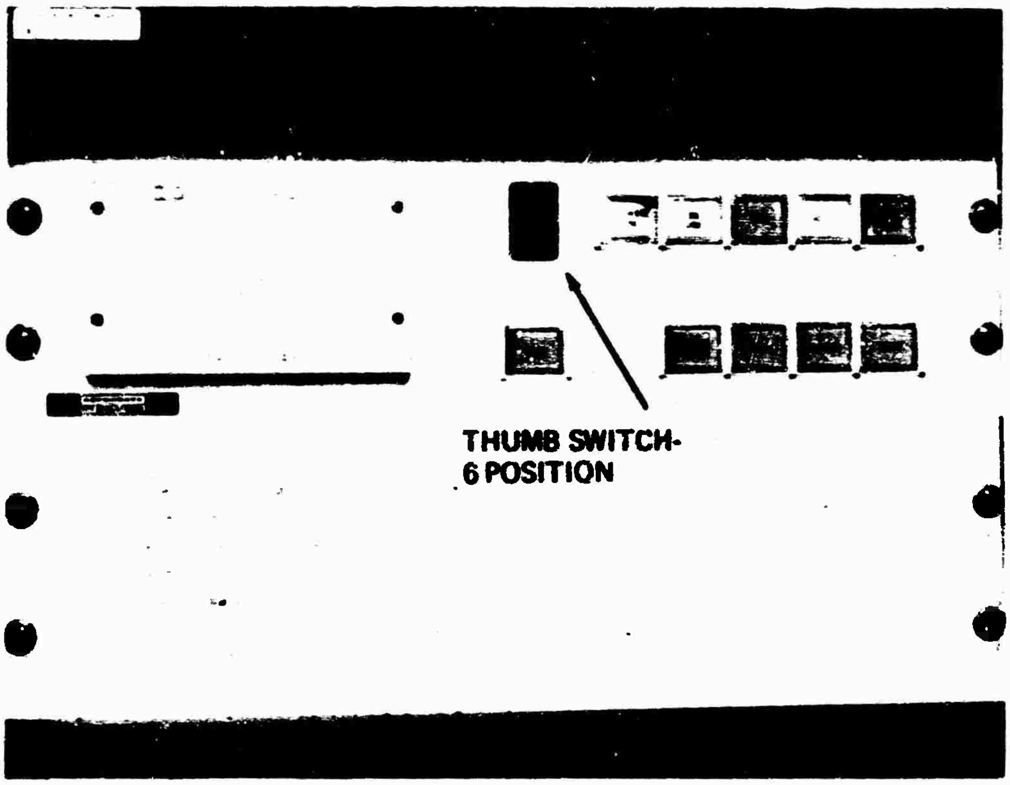

Figure 4: TEST STATION FUNCTIONAL LAYOUT

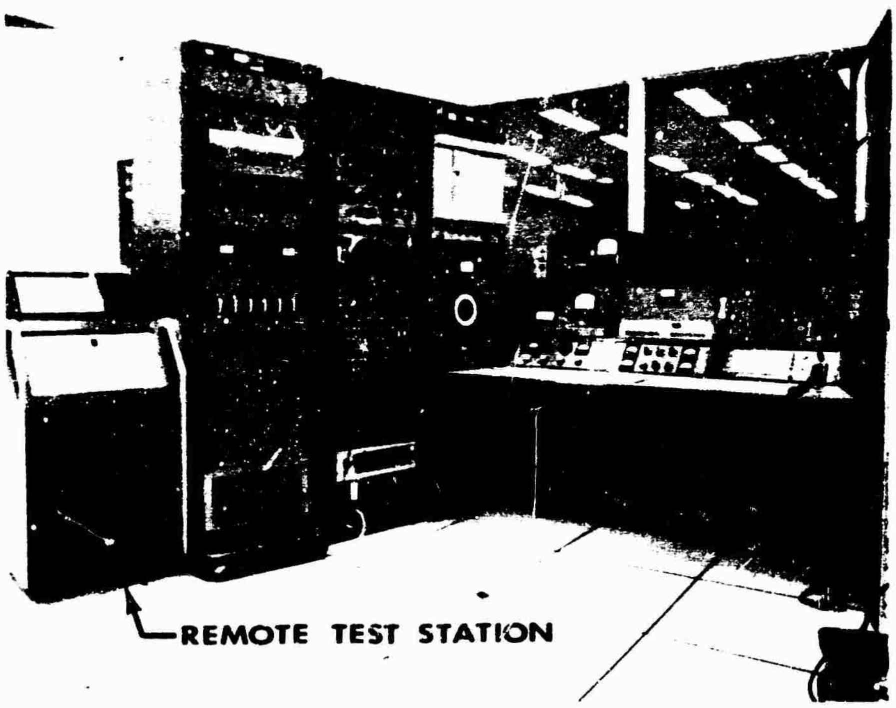

Figure 5: TEST STATION LOCATION AT VIBRATION CONTROL CONSOLE

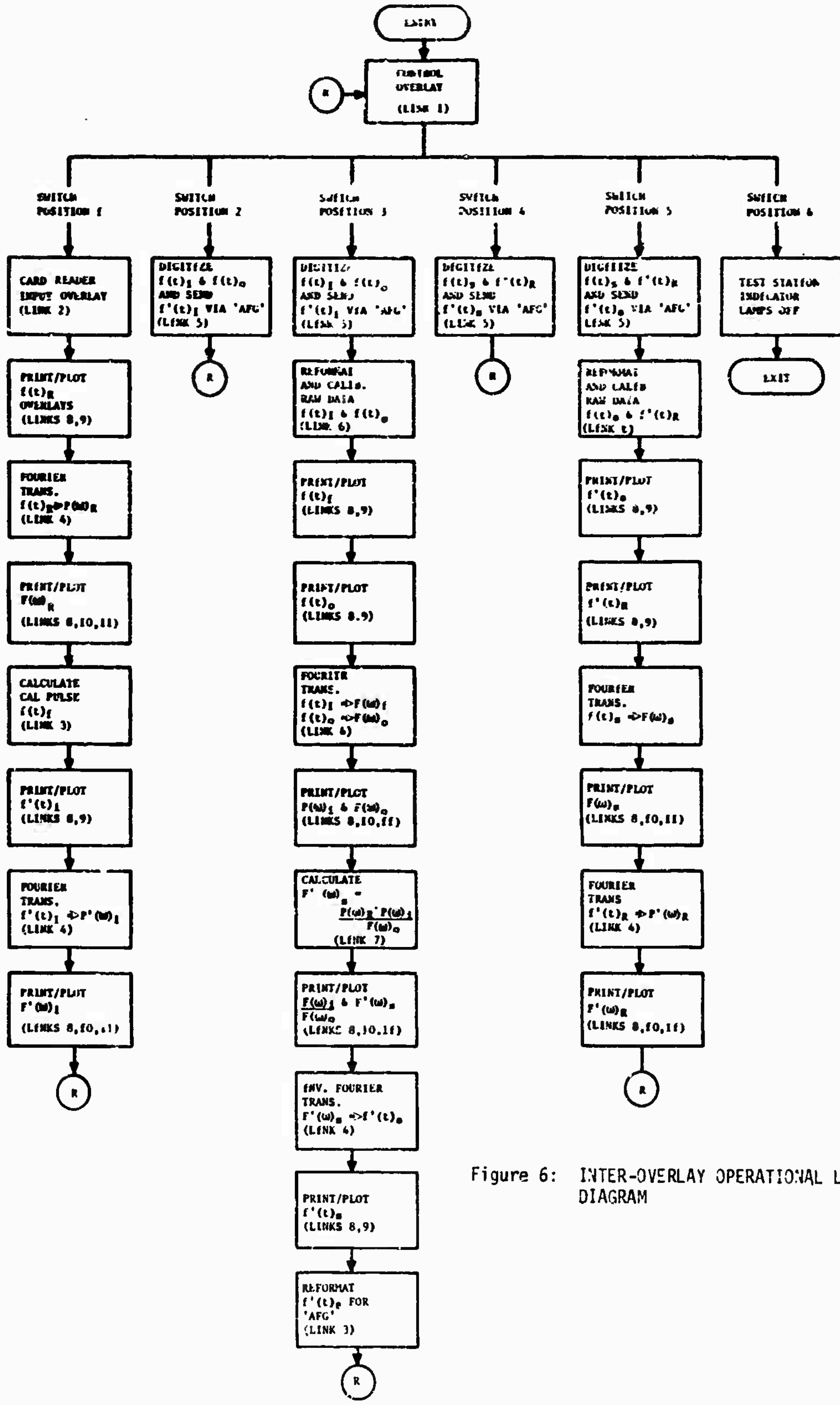

Figure 6: INTER-OVERLAY OPERATIONAL LOGIC DIAGRAM

$f'(t)_R$ which should match the required transient waveform, $f(t)_R$.

Position 6 instructs the computer program to exit.

The test operator is free to rotate the computer control from position 5 back to position 1, 2 or 3 for additional testing.

The prototype control system was evaluated to determine its performance. The prototype control system characteristics during evaluation were:

1) The word size for both the analog to digital and digital to analog converters was 10 bits plus sign (11 bits).

2) The sampling and up-date rates were both 20,000 samples per second.

3) The anti-aliasing filters in front of the ADC's and the smoothing filters on the output of the DAC were identical 6 pole Butterworth low pass filters cutoff at 5 KHz (system bandwidth is 2 - 5000 Hz).

In its present configuration, the prototype control system, when operating on a 4096 data point description of the required waveform, requires a cycle time, from system calibration to controlled waveform, of 16 minutes. Included in that cycle time is time spent to produce a digital plot of the synthesized input voltage $f(t)_s$. The cycle time of a special purpose control system computer could be reduced to less than two minutes.

Detailed knowledge of the required transient is fundamental to correct control. This requires that:

a) The transient is physically realizable within the capability of the vibration equipment,

b) The digital description of the transient is within the capability of the computational equipment (i.e. storage requirements for long duration, high frequency transients).

Three examples of transient waveform control are illustrated and discussed below. The waveforms selected were:

1) A 20 g terminal peak sawtooth designed to meet MIL SPEC 810-B requirements for component shock testing.

2) and 3) Two waveforms derived from the TAT/Agena-D launch vehicle (OGO-D) spacecraft* [12] considered typical of staging transients eligible for simulation on laboratory test apparatus.

The experiments were conducted on a Ling 249 (30,000 force-pound) vibrator driven by a Ling PP 120/150 KVA amplifier. The test specimen was a 450 pound plate.

Figure 7 illustrates the performance of the prototype control system operating on the terminal peak sawtooth. Figure 7a is a digital plot of the required terminal peak sawtooth in ordinate units of millivolts**. The transducer calibration was 50 mv/g, therefore the required peak was 20 g's. Figure 7c is the Fourier transform (modulus only) of the required terminal peak sawtooth. Figure 7b illustrates both the a) synthesized input voltage to the test system and b) the controlled terminal peak sawtooth acceleration function monitored on top of the 450 pound plate. Figure 7d is the Fourier transform of the controlled terminal peak sawtooth pulse. A visual comparison of Figures 7a and 7b indicate excellent agreement in the time domain while Figures 7c and 7d demonstrate excellent agreement in the frequency domain. The one obvious discrepancy in the comparison of Figures 7c and 7d is in the low frequency domain. This discrepancy was caused by biased quantization errors produced in the analog-to-digital conversion process. This discrepancy can be reduced by using ADC's having a larger word size or by using a statistical unbiasing scheme. One such scheme has been developed but not implemented into the prototype control system yet.

Figure 8 illustrates the performance of the prototype control system simulating a typical flight transient. Figure 8a is the digital plot of the required transient waveform and represents telemetered transient data from an OGO-D spacecraft transducer [12] (PL 30 at T + 234.5). Figure 8c is the Fourier transform of the required transient waveform, and demonstrates the fact that the majority of the energy lies well below 1000 Hz. Because of this, this transient is considered a low frequency type of transient. Figure 8b is a digital plot of the controlled waveform simulating the actual flight transient. Figure 8d is the Fourier transform of the controlled transient. Visual comparison between Figures 8a and 8b and between Figures 8c and 8d, again demonstrate the excellent performance of the prototype system. In addition to this visual comparison, a comprehensive statistical study was made from digital listings of the two transients to put some "figure of merit" on the performance. This study is discussed at the end of this section.

* TAT is an augmented Thor/Agena-D Launch Vehicle and OGO-D is the Orbiting Geophysical Observatory.

** The rectangular undershoot was programmed so that the terminal velocity would equal zero.

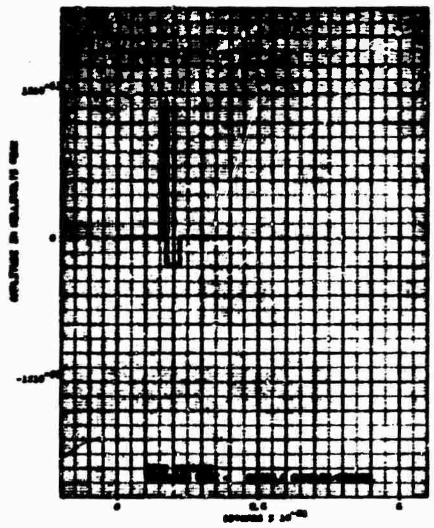

Figure 7-A: TERMINAL PEAK SAWTOOTH SPECIFICATION (MIL810-B) 50 MV/G

Figure 7-B: SHOCK SYNTHESIS ON VIBRATION TEST SYSTEM

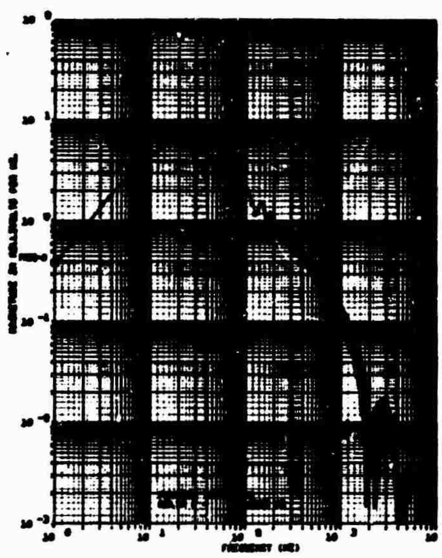

Figure 7-C: FOURIER TRANSFORM MODULUS OF SPECIFIED TERMINAL PEAK SAWTOOTH

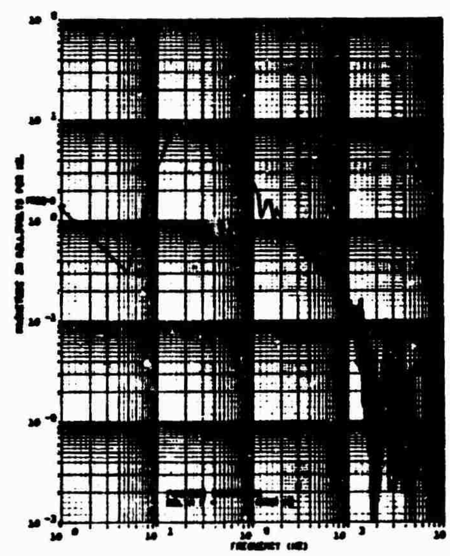

Figure 7-D: FOURIER TRANSFORM MODULUS OF SYNTHESIZED WAVEFORM (Control Accelerometer Response)

Figure 7: TRANSIENT WAVEFORM CONTROL APPLIED TO MIL810-B SHOCK TEST REQUIREMENTS

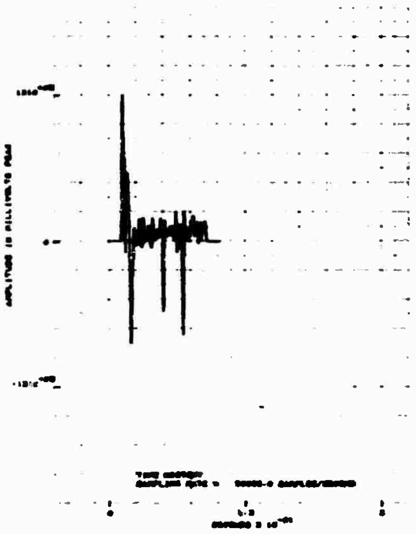

Figure 8A: TIME HISTORY OF REQUIRED WAVEFORM PL-30, $f(t)_R$

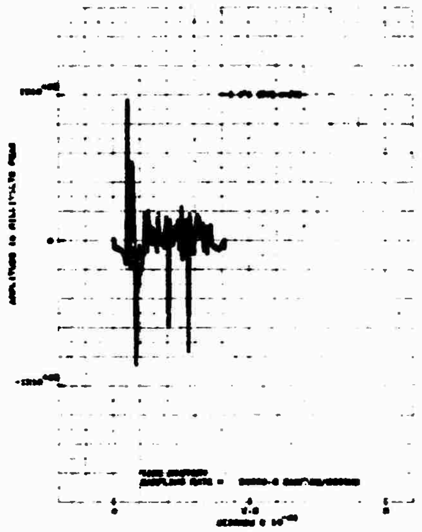

Figure 8B: TIME HISTORY OF SYNTHESIZED WAVEFORM PL-30, $f'(t)_R$

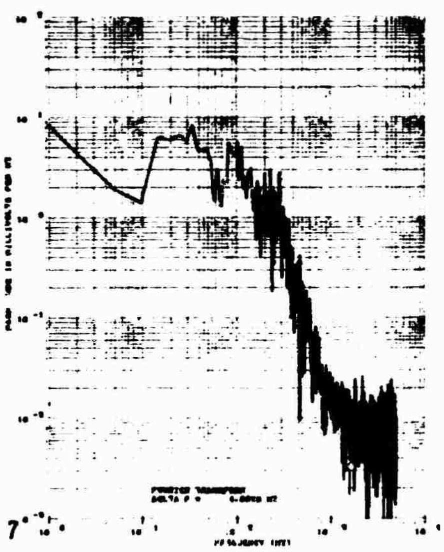

Figure 8C: FOURIER TRANSFORM MODULUS OF REQUIRED WAVEFORM PL-30, $F'(\omega)_R$

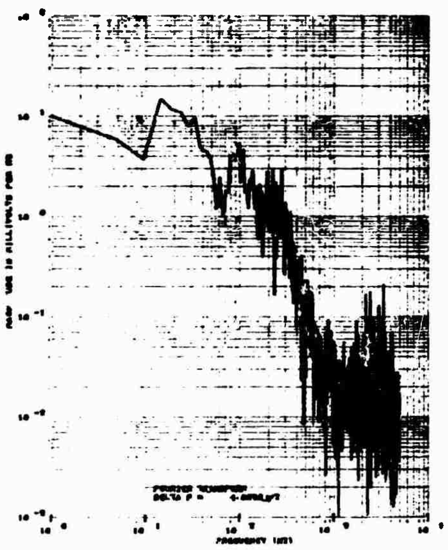

Figure 8D: FOURIER TRANSFORM MODULUS OF SYNTHESIZED WAVEFORM PL-30, $F'(\omega)_R$

Figure 8: TRANSIENT WAVEFORM CONTROL APPLIED TO SPACECRAFT FLIGHT TRANSIENTS
L249 Vibrator, PP120/150 Amplifier, Specimen Weight 450lb

Figure 9 illustrates the performance of the prototype control system simulating another flight transient. Figure 9a is the digital plot of the required transient waveform and represents telemetered transient data from another OGO-D spacecraft vibration transducer [12] (PL 20 at T + 234.5). Figure 9c is the Fourier transform of the required transient. From this transform it can be seen that this third required transient waveform contains high frequency information out to and beyond 5 KHz. This transient, therefore, is a severe test of the prototype control system performance. Figures 9b and 9d are the digital plots of the controlled transient and its Fourier transform. Since Figure 9b can only demonstrate "envelope similarity" due to the high frequency content, the test was rerun and computer listings of both the required transient and the controlled transient produced. From this listing, an expanded time domain overlay of the two transients was produced. See Figure 10. In this figure, only the first 19 milliseconds are plotted; however, that time span covers the first main burst of energy in the transient.

From the digital listings of the transient sets illustrated in Figures 8 and 9, the following error analysis was developed. A statistical error term, E_n, was defined as the difference in amplitude between the required and synthesized waveform at corresponding discrete points in time

$$E_n = f(t)_R - f'(t)_R$$

Operating on approximately 400 equally distributed data points, the following statistical parameters are used to further describe the error term. The mean of the error term,

$$\mu_e = \frac{1}{N}\sum_{n=1}^{N} E_n \quad ,$$

indicates the zero frequency or non-alternating component of the error term and the variance of the error term,

$$\sigma_e^2 = \frac{1}{N-1}\sum_{n=1}^{N} (E_n - \mu_e)^2 \quad ,$$

indicates the mean squared value of the alternating component of the error term. The results of this analysis are tabulated in the table below.

Both sets of statistics were derived from approximately 400 equally distributed data points over the "transient" interval. Assuming a chi-squared distribution of the error term, E_n, there is a .99 probability that the time domain variance of the control system is equal to or less than 13 percent.

STATISTICAL PARAMETER	PL-20, ILLUSTRATED IN FIGURE 9, UNITS OF G's	PL-30, ILLUSTRATED IN FIGURE 8, UNITS OF G's
Error Mean, μ_e	-6.4×10^{-4}	.231
Error Variance, σ_e^2	2.283	.0827
Mean of the Required Waveform, μ_R	.117	.263
Variance of the Required Waveform, σ_R^2	18.87	.715
Variance of Test System Noise, σ_n^2	.27	.0625
Time Domain Variance, in Percent, $\sigma_e^2/\sigma_R^2 \times 100$	12.0%	11.6%

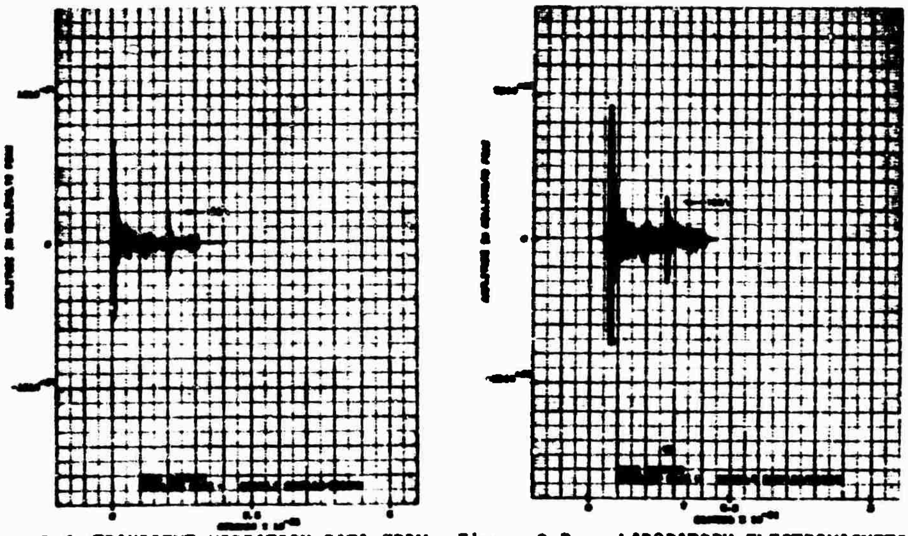

Figure 9-A: TRANSIENT VIBRATION DATA FROM THE TAT/AGENA-D LAUNCH VEHICLE (OGO-D Spacecraft), PL20 AT T+234.5

Figure 9-B: LABORATORY ELECTROMAGNETIC TEST EQUIPMENT SYNTHESIS OF OGO-D FLIGHT TRANSIENT

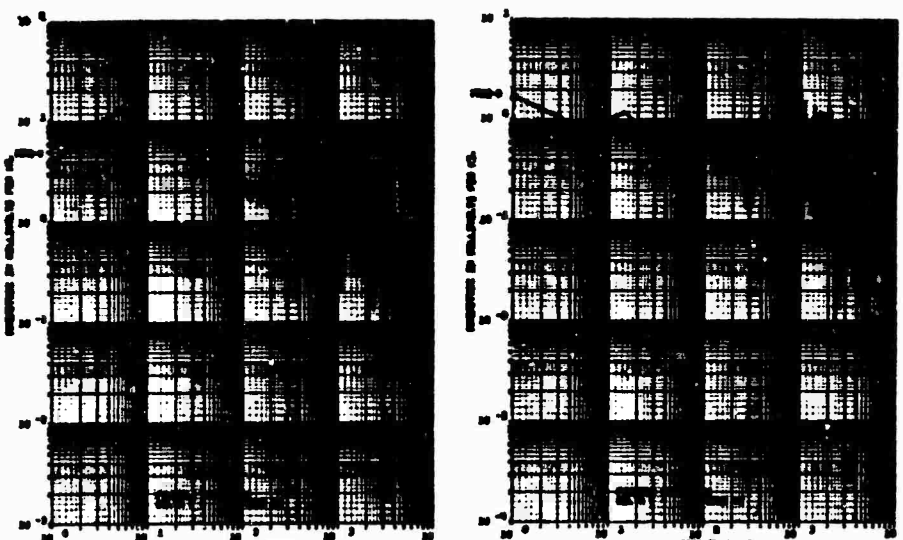

Figure 9-C: FOURIER TRANSFORM MODULUS OF OGO-D SPACECRAFT RESPONSE PL20 AT T+234.5

Figure 9-D: FOURIER TRANSFORM MODULUS OF LABORATORY SYNTHESIZED OGO-D FLIGHT TRANSIENT

Figure 9: TRANSIENT WAVEFORM CONTROL APPLIED TO SPACECRAFT FLIGHT TRANSIENTS
L249 Vibrator, PP120/150 Amplifier, Specimen Weight 450lb

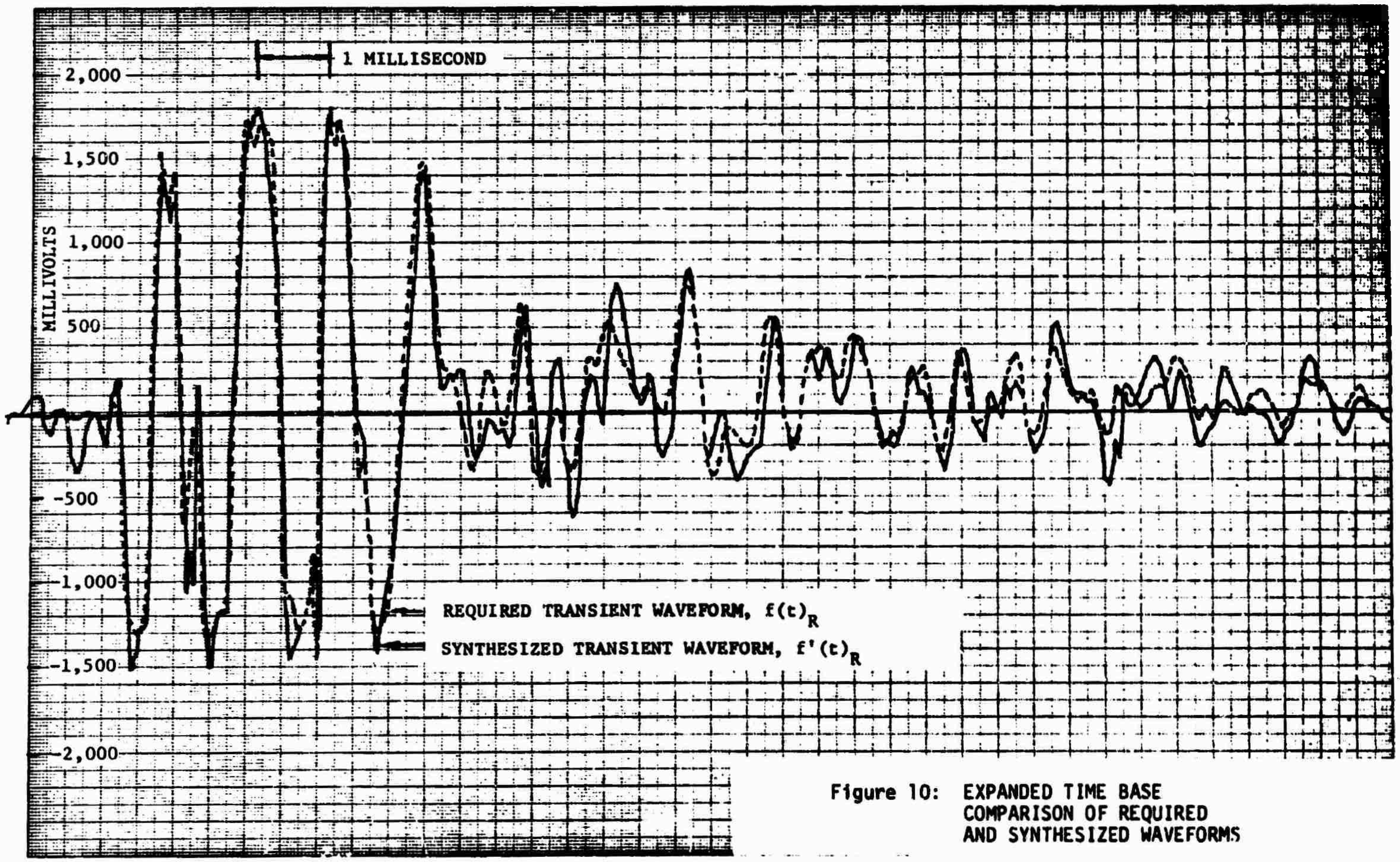

Figure 10: EXPANDED TIME BASE COMPARISON OF REQUIRED AND SYNTHESIZED WAVEFORMS

CONCLUSIONS

This control concept represents one of the first marriages of an on-line digital computer, using modern computing algorithms, to an electromagnetic virator in an environmental testing laboratory to meet a transient motion control requirement in near-real time. Experimental results using the prototype control system demonstrated controlability with a time domain variance of less than 13 percent. The fidelity measurement for laboratory transient waveform synthesis requires

- time history,

- Fourier transform modulus,

- Fourier transform phase spectrum

representations of the data. Error variance figures can be employed to specify test criteria.

ACKNOWLEDGEMENTS

The work on which this paper is based has been sponsored by the National Aeronautics and Space Administration, NAS5-15171. The authors would like to express their thanks to James Brown, The Boeing Company, for his contribution toward the successful implementation of this technique.

REFERENCES

1 Miller, R.W., "Shaping Shock Acceleration Waveforms for Optimum Electrodynamic Shaker Performance", LTV Ling Electronics Division, Anaheim, Calif., 34th Shock and Vibration Bulletin, 19[illegible].

2 Young, F.W., "Shock Testing with Vibration Systems", Radiation, Incorporated, Melbourne, Florida. 34th Shock and Vibration Bulletin, 1964.

3 Fandrich, R.T., "Shock Pulse Time History Generator", Institute of Environmental Sciences Proceedings, 1969.

4 Regillo, D.A., "Shock Testing with an Electrodynamic Exciter and Waveform Synthesizer", M.I.T. Lincoln Laboratory, 39th Shock and Vibration Bulletin, 1969.

5 Fagan, J. and Sincavage, J., "Shock Testing and Analysis: A New Laboratory Technique", RCA Astro-Electronics Div., Princeton, New Jersey, 39th Shock and Vibration Bulletin, 1969.

6 Fitzgerald, T.E., and Kula, L.C., "Transient Vibration Simulation", The Boeing Company, New Orleans, La., 37th Shock and Vibration Bulletin, 1968.

7 Jones, G.K., and On, F.J., "Prediction of Interface Random and Transient Environments Through the Use of Mechanical Impedance Concepts", NASA Goddard Spaceflight Center, Greenbelt, Maryland, 40th Shock and Vibration Symposium, 1969.

8 Trubert, M.R., "A Fourier Transform Technique for the Prediction of Torsional Transients for a Spacecraft from the Flight Data of Another Spacecraft Using the Same Booster", Technical Memorandum 33-350, Jet Propulsion Laboratory, Pasadena, California, October 1967.

9 Cooley, J.W., Tukey, J.W., "An Algorithm for the Machine Calculation of Complex Fourier Series", Math. of Comp., Vol. 19, No. 90, pp. 297-301 (1965).

10 Cooley, J.W., Lewis, P.A.W., Welch, P.A., "The Fast Fourier Transform Algorithm and Its Applications", IBM Research Report RC 1746, 1967.

11 Michellich, M.O., "Dynamic Data Analysis System", The Boeing Company, Seattle, Washington, 40th Shock and Vibration Symposium, 1969.

12 Munson, A.N. Jr., "Flight Shock and Vibration Data from the TAT/AGENA-D Launch Vehicle (OGO-D Spacecraft)", Report No. 681-10 Test and Evaluation Division - Goddard Space Flight Center, Greenbelt, Maryland, 1968.

BIBLIOGRAPHY

1 LeBrun, J.M., Favour, J.D., Final Report, "Feasibility and Conceptual Design Study - Vibration Generator Transient Waveform Control System", NAS5-15171. 1969.

DISCUSSION

Mr. Fandrich (Radiation Inc.): By using an impulsive input to establish a system transform it is necessary to assume amplitude linearity. Did you find that this assumption was warranted? If this assumption was not warranted, have you considered using the data from the first trial to update the transfer function?

Mr. Favour: To answer your first question, generally the assumption of linearity was warranted. The systems are mildly nonlinear, and therefore we can set the calibration pulse so that the response is at approximately the same level as the desired output. In general, the systems have been sufficiently linear; however, we had one problem in the test program this past spring with a grease lubricated slip plate that exhibited nonlinearity, therefore we had to use other means.

Mr. Fandrich: The second part of my question was have you considered using the data from the first try to update the transfer function? In other words, you are trying to establish a time history; after your first try you would be able to establish amplitude nonlinearities in your system transfer function.

Mr. Favour: No, we have not done that. We have not felt it was necessary.

Mr. Ballard (National Bureau of Standards): How do you handle phase, or are you automatically handling the phase of the frequencies in the system through your Fourier transform?

Mr. Favour: This is automatically handled in the algorithm.

Mr. Ballard: How about the high frequency response in reference to the shaker? You have a DC that you cannot handle, so how high in frequency can you go in the synthesis in reference to the ability of the shaker to respond?

Mr. Favour: We have conducted tests out to approximately 5000 Hz.

Mr. Ballard: What is the resonant frequency of the shaker system which you used to conduct tests to 5000 Hz?

Mr. Favour: The first axial resonance of that shaker system was approximately 1700 Hz.

Mr. Stathopoulos (Naval Ordnance Lab.): What do you consider the advantage of using the shaker over conventional shock testing procedures?

Mr. Favour: Economics. We do not have to build another fixture for the shock testing. We use the same fixture that is used for vibration testing. Furthermore, in a test program conducted this past spring, we had eleven separate specimens, and each one was given eighteen separate shocks; this is a matrix of about 200 shocks, and the entire program was completed in less than a month by using this technique. We have documented savings of the order of $17,000 over conventional shock testing techniques.

AN IMPROVED ELECTRODYNAMIC SHAKER SHOCK TECHNIQUE

J.R. Moser and D. Garner
Texas Instruments Incorporated
Dallas, Texas

Many investigators have been working to improve techniques for performing shock testing on standard laboratory vibration facilities. The result of this work shows (1) that the shaker system response is inherently frequency dependent and (2) suggests methods for modifying the real-time input pulse to the shaker amplifier using transient synthesizers, such that the shaker response conforms to specified pulse shapes. This paper details how we have frequency-compensated our shaker/amplifier system response such that, to achieve the same pulse at the output, only the required real-time pulse at the system input is needed. We will demonstrate how it is possible to use standard laboratory pulse generators rather than the cumbersome waveform synthesizers in use throughout the country. The time required to do the test is estimated to be one-third of that required using the present state-of-the-art technique. A circuit will be presented which will allow for in-lab construction of the required inverse shaping filter. This circuit is quite simple, using a solid-state linear integrated circuit. Discussion will be included in support of performing full-sine shock testing because of inherent shaker mechanical limitations. Recommendations will be made for including a full-sine shock pulse in MIL-STD-810B as an option when performing shock tests on electrodynamic shakers.

INTRODUCTION

The advantage of shock testing on electrodynamic vibration machines is the resultant savings in fixture costs and test time. Optimally effective test techniques have not been fully developed at this time. Nevertheless, many environmental engineers are realizing the advantages and are specifying an increasing portion of shock tests to be done on vibration machine facilities. The purpose of this paper is to discuss an aspect of shaker shock testing which has not been discussed adequately in shock and vibration literature. A technique for frequency-compensating an electrodynamic shaker system will be presented. It will be shown how compensation will allow generation of a shaker pulse response which is nearly identical in duration and shape to the input pulse of the shaker amplifier. Discussion will be specifically directed toward the creation of the 11-millisecond half-sine shock pulse of MIL-STD-810B, but the principles developed herein are general and will be of value in generating pulses of any arbitrary shape on vibration machines.

FREQUENCY COMPENSATION OF SHAKER SYSTEM

It is highly desirable to be able to produce a specified acceleration pulse G(t) at the shaker head by injecting an identical voltage pulse v(t) at the shaker preamplifier. The system transfer relationship can be stated symbolically:

$$G_0(\omega) = V_i(\omega)H(\omega)H'(\omega) \qquad (1)$$

where

$G_0(\omega)$ = the Fourier transform of the desired shock pulse G(t) (output)

$V_i(\omega)$ = the Fourier transform of the voltage pulse v(t) to the shaker preamplifier (input)

$H(\omega)$ = shaker/amplifier system frequency response without compensation

$H'(\omega)$ = compensation amplifier response (=1 for uncompensated system).

The Fourier transform of a real-time pulse is uniquely paired to that pulse. Therefore, if two Fourier spectra are shown to be identical, they represent identical pulses. Therefore, if

$$v(t) = k\,G(t)$$

compensation must be accomplished by making $H(\omega)H'(\omega)$ of Equation (1) independent of frequency. Figure 1(a) shows a typical shaker/amplifier system response $H(\omega)$ versus frequency. Each response point was obtained by driving the shaker preamplifier with a sinusoidal voltage of fixed amplitude and by observing the corresponding output acceleration level. The figure shows the response $H(\omega)$ to be very frequency- and mass-load-dependent below 100 Hz. But what then is the range of frequency over which one must compensate? Figure 2 shows relative spectral (Fourier) distributions of (1) a half-sine pulse of 11 milliseconds

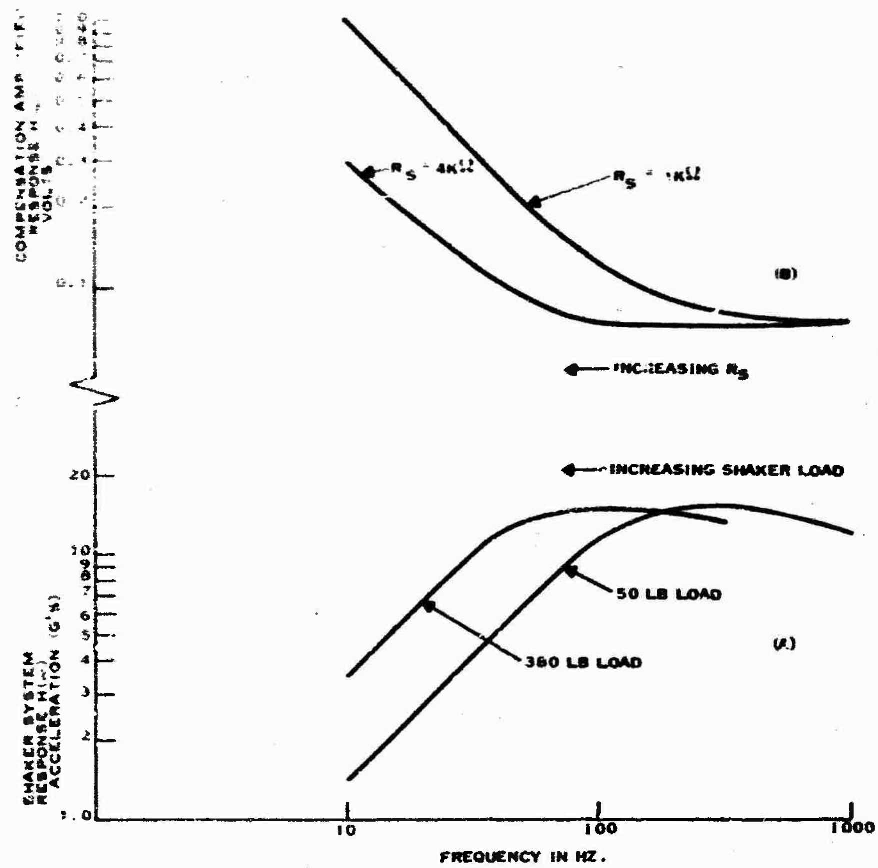

Figure 1. Vibration System Response H(ω) Versus Frequency and Compensation Amplifier Response H′(ω) Versus Frequency

duration, (2) a full-sine pulse of 22 milliseconds duration, and (3) a practical pseudo-half-sine pulse of 11 milliseconds duration. The latter pulse conforms to the limits of method 516, Figure 516-2 of MIL-STD-810B, and is typical of the pulse shape obtainable on an electrodynamic shaker. The half- and full-sine distributions were obtained using a voltage-controlled generator (VCG) triggered by a 30-Hz sine-wave oscillator. The pseudo-half-sine pulse was generated by a waveform synthesizer. Both half-sine pulses were of 11-millisecond duration and 1-volt zero-to-peak amplitude. The full-sine pulse was of 2.2-millisecond duration and 2-volt peak-to-peak amplitude. The magnitude of each spectral line was observable by scanning the output of the VCG (or waveform synthesizer for the pseudo-half-sine pulse) with a wave analyzer having a 7-Hz bandwidth. For plotting purposes, the time scale was multiplied by 10, yielding the Fourier spectral amplitudes of the various 11-millisecond pulses. Note that the above is equivalent to analyzing the output of a loop of magnetic tape containing the desired pulse but played back at 10 times the recording speed and such that the tape loop travels at 30 revolutions per second. Only the loci of the spectral component peaks are plotted in Figure 2. The relative spectral amplitude distribution of the three pulses would remain unchanged as the pulse repetition rate is reduced to zero (single pulse) and the Fourier spectra become continuous. The results for the half-sine and full-sine pulses are consistent with those of Gertel and Holland.[1] It is clear from the figure that the significant portion of the spectra for the half- and full-sine pulses lies within a frequency interval determined by

$$0 \leq f \leq 2/\tau$$

where τ is the pulse duration. For the 11-millisecond half-sine pulse of MIL-STD-810B, this corresponds to a frequency interval from dc to 182 Hz. With this and the shaker response [Figure 1(a)] in mind, it is clear that the shaker must be compensated over the same frequency interval for good pulse transmission fidelity. In general, shorter pulse durations would require frequency compensation over a wider frequency inteval to keep H(ω) H′(ω) independent of frequency over the principal portion of the Fourier spectrum of the pulse.

To make H(ω) H′(ω) independent of frequency, a compensating amplifier having an amplitude versus frequency response inverse to that of H(ω) is required in the system. The compensation amplifier of Figure 3 is designed to have the required response H′(ω) by using the noninverting input

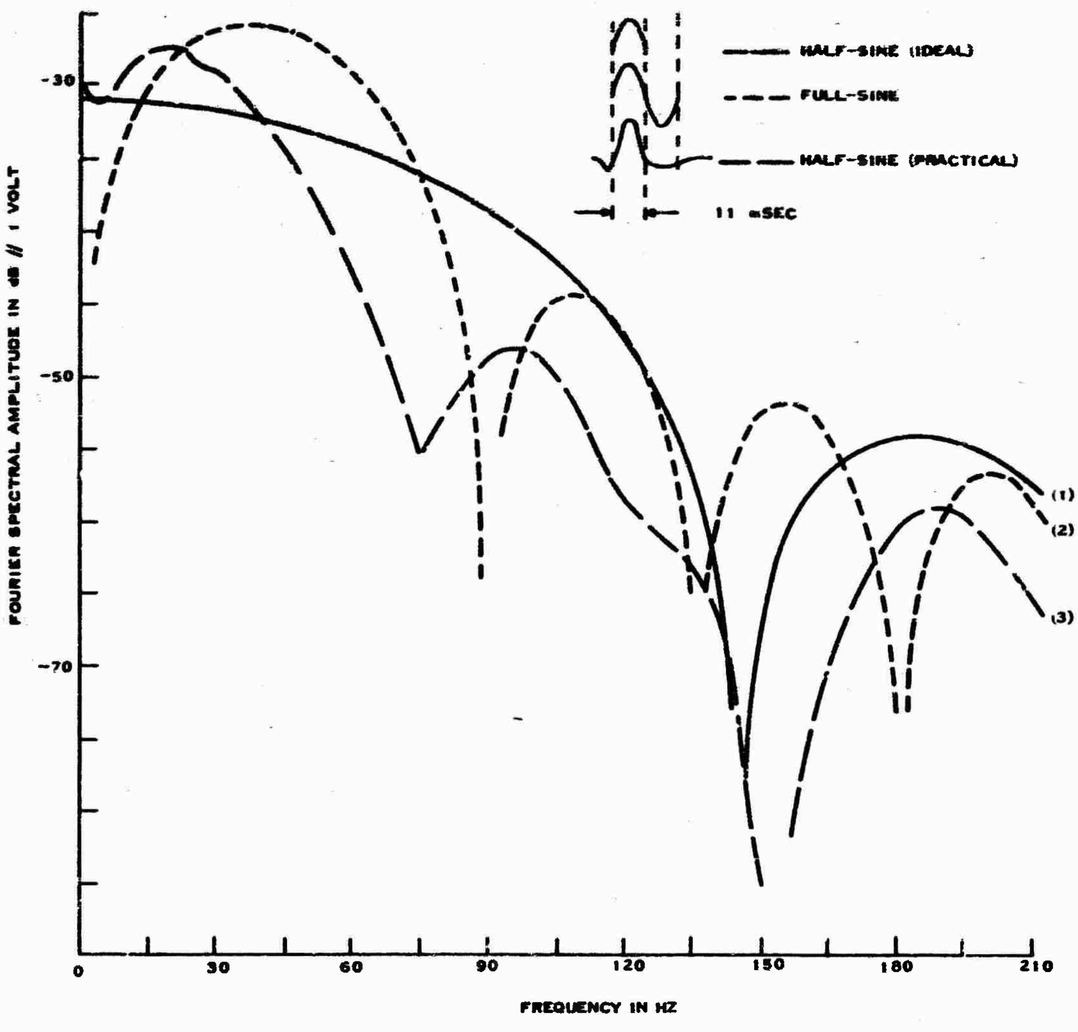

Figure 2. Relative Fourier Spectra of Various Shock Pulses

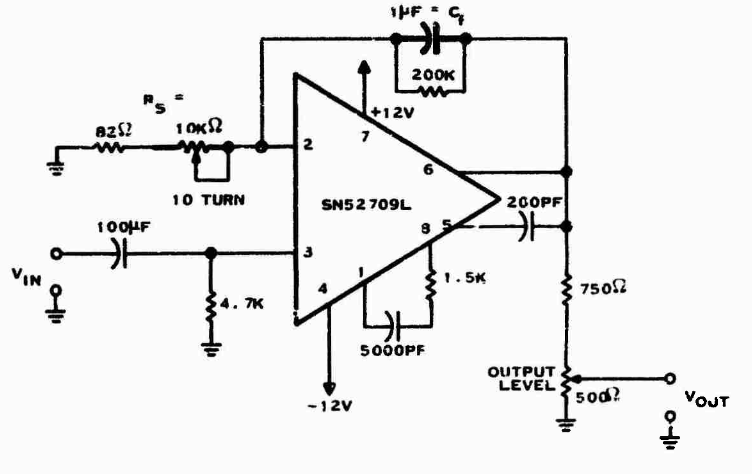

Figure 3. Schematic Diagram of Compensation Amplifier

of the SN52709 linear operational amplifier integrated circuit. The gain of this circuit is equal to[2]

$$1 + Z_f/R_s = 1 + 1/j\omega C_f R_s \qquad (2)$$

R_sC_f can be chosen to give the desired response as shown in Figure 1(b) such that the product of both the uncompensated system responses $H(\omega)$ and the compensation amplifier response $H'(\omega)$ (or the sum if these responses are expressed dB) is independent of frequency over the desired frequency interval. By varying R_s, the knee of the inverse filter response can be moved in frequency to correspond to the knee in the frequency response of the vibration system shown in Figure 4. Figure 1(a) shows that, as the shaker load increases, the knee in the shaker frequency response characteristic $H(\omega)$ decreases in frequency. The circuit of Figure 3 is capable of compensating the vibration system for all loads tested to date for shock pulses of 11-millisecond duration.

Figure 5 is the circuit diagram for the triggering circuit used in the system (Figure 4). It is composed of an SCR switch for positive-action single-pulse triggering and a unijunction multivibrator for repetitive triggering. The latter is used while adjusting R_s of Figure 3 for optimum compensation at a low G level.

RESULTS

The limitations of performing half-sine shock pulses on vibration systems have been discussed before.[3,4,5,6] For this unidirectional acceleration pulse, the armature velocity is monotonically increasing during the pulse to a maximum when the pulse has passed. Since the velocity is maximum when control is removed, the armature maximum displacement limit is exceeded for relatively small G levels. Clearly, longer duration half-sine pulses more severely limit the maximum G-level obtainable on a given vibration system. Figure 6 is a photograph of the largest 11-millisecond half-sine (like) acceleration pulse obtainable using a compensated 15,000 force-pound shaker. This acceleration pulse is clearly outside the acceleration pulse envelope specified in MIL-STD-810B. Figure 7 is a photograph of the pulse obtained under the same conditions except that the vibration system is uncompensated. This pulse in no way resembles a half-sine acceleration pulse. Inspection of Figure 7 clearly indicates the differentiating characteristic in the critical frequency range of the uncompensated vibration system used. All shaker systems are transformer coupled, so their response near dc is necessarily quite limited. No amount of compensation found is adequate for controlling the 50-millisecond undershoot shown in Figure 8.

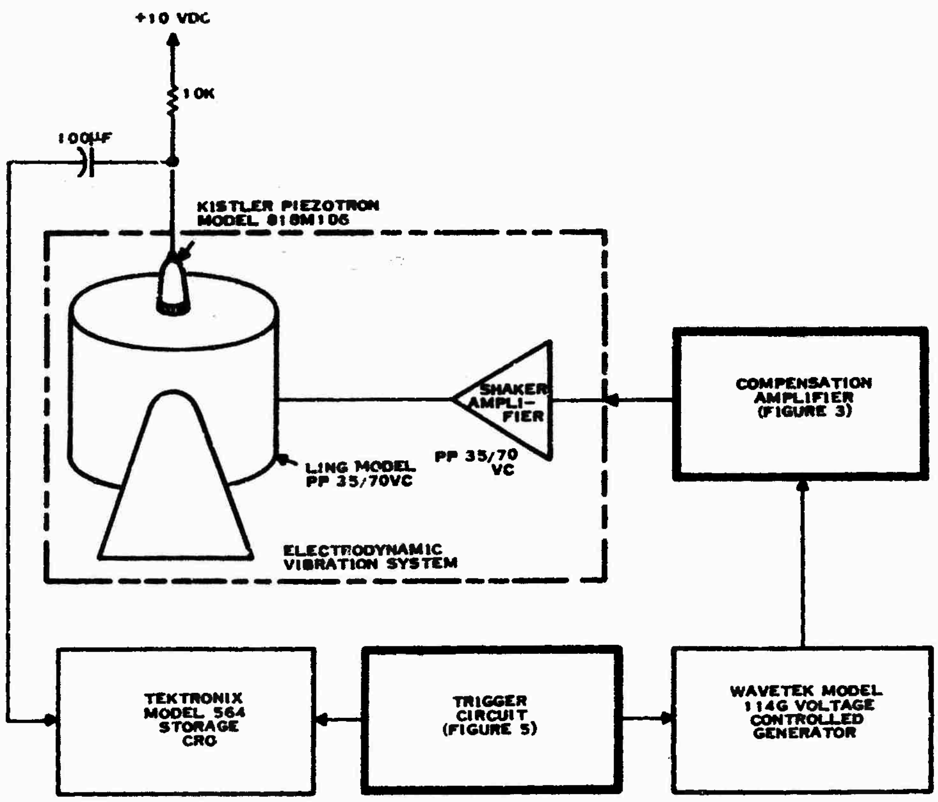

Figure 4. Diagram of Compensated Electrodynamic Shaker for Shock Testing

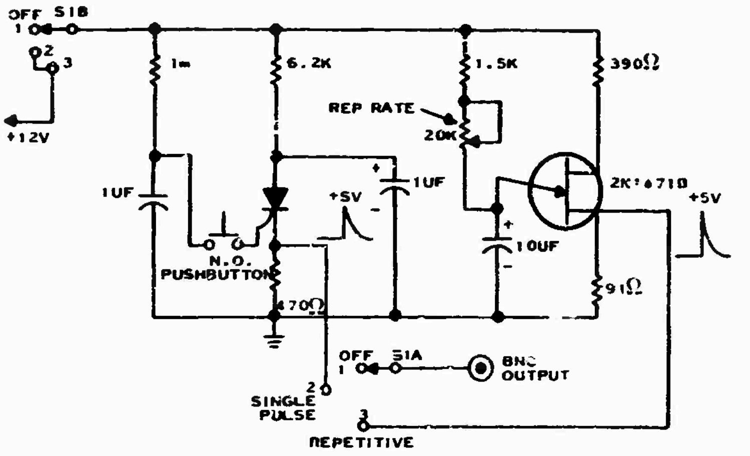

Figure 5. Schematic Diagram of Trigger Circuit

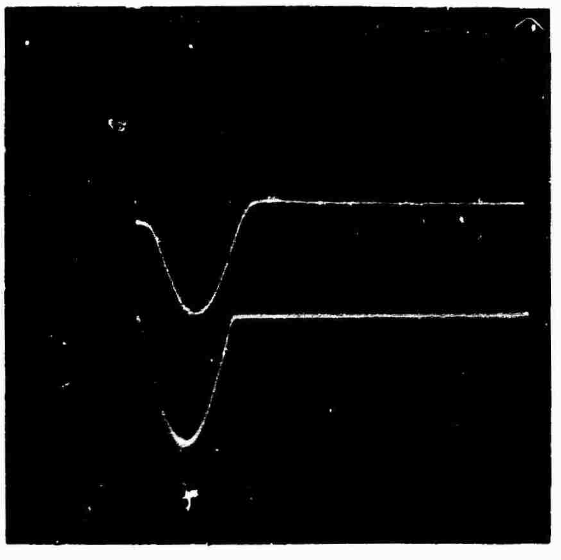

ARMATURE LOAD = 50 LBS
BOTTOM TRACE IS IDEAL HALF SINE VOLTAGE INPUT
TOP TRACE IS COMPENSATED SYSTEM RESPONSE
HORIZONTAL SWEEP = 5 MSEC/CM
VERTICAL SENSITIVITY = 5G/CM (INVERTED)

Figure 6. Half-Sine Shock Pulse from Compensated Shaker

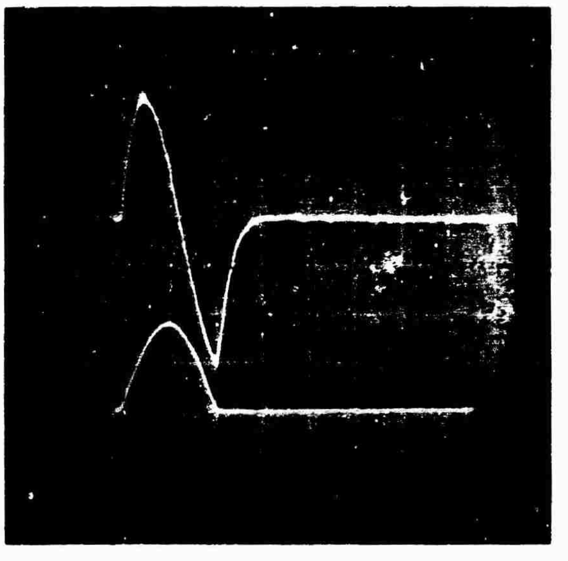

ARMATURE LOAD = 50 LBS
BOTTOM TRACE IS IDEAL HALF SINE VOLTAGE INPUT
TOP TRACE IS UNCOMPENSATED SYSTEM RESPONSE
HORIZONTAL SWEEP = 5 MSEC/CM
VERTICAL SENSITIVITY = 5G/CM

Figure 7. Half-Sine Shock Pulse from Uncompensated Shaker

Some investigators have increased the half-sine G-level capability by prestressing the armature one way, then by reversing the drive to the shaker to form the "desired" pulse, and then by controlling the undershoot such that the net signed area under the acceleration versus time curve is near zero.[3,4] They have been partially successful in finding a combination that would both satisfy the G-level requirement and fit within the specified bounds of, for example, MIL-STD-810B (apparently ignoring the requirement on the velocity change ΔV). Schell[7] has demonstrated the major effects of variations in the real-time acceleration pulse shape on the Fourier and shock spectra. The reader should again compare the Fourier spectra of the ideal half-sine pulse and the "practical" half-sine pulse (which lies within the envelope of MIL-STD-810B) of Figure 2.

ADVANTAGES OF USING A FULL-SINE ACCELERATION PULSE

How can shock testing be accomplished in a controlled and repeatable fashion using an electrodynamic shaker? The best method is to control the undershoot required to keep the net velocity change zero by specifying in method 516 of MIL-STD-810B an optional full-sine acceleration pulse, such as the one given in Figure 9. Figures 10 and 11 are examples of how near to ideal the full-sine pulse can be produced with

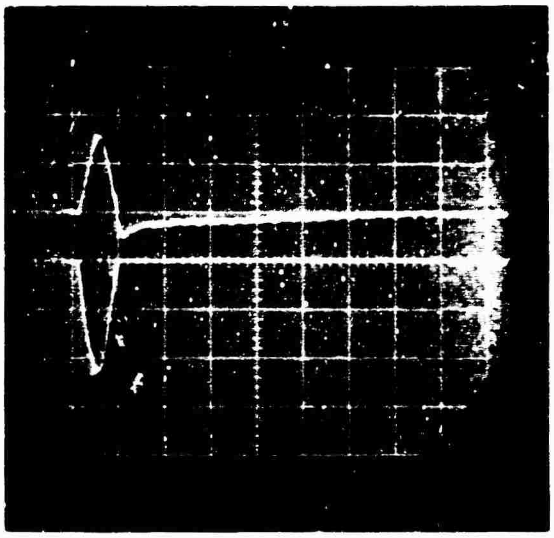

ARMATURE LOAD = 50 LBS
BOTTOM TRACE IS IDEAL HALF-SINE VOLTAGE INPUT
TOP TRACE IS COMPENSATED SYSTEM OUTPUT
HORIZONTAL SWEEP = 10 MSEC/CM
VERTICAL SENSITIVITY = 5G/CM (INVERTED)

Figure 8. Half-Sine Shock Pulse from Compensated Shaker Showing 50-msec Duration Undershoot

the compensated electrodynamic vibration system. These pulses would easily fit within the bounds of Figure 9. From Figure 2 the Fourier spectra of the half- and full-sine pulses are commensurate in distribution, the main difference being below 75 Hz.

Figures 12 and 13 show the system full-sine shock pulse capability before compensation. The lightly loaded table (Figure 12) gives the poorest results without compensation. This result is consistent with Figure 1. Below 200 Hz, the variation of H(ω) with frequency is greatest for the lightly loaded shaker.

CONCLUSION

We have shown how frequency-compensating an electrodynamic vibration system allows for greatly improved single pulse generation. Instead of compensating the real-time input voltage pulse to the shaker amplifier by using cumbersome waveform synthesizers, classical shock pulses can be generated by standard voltage-controlled generators. The input voltage pulse closely characterizes the output acceleration pulse. Thus, even those required to use pulse waveform synthesizers for generating arbitrary pulse shapes will find the compensation techniques presented herein of benefit in reducing setup time and optimizing pulse shape. Arguments have been made for addition of an optional full-sine acceleration pulse to method 516 of MIL-STD-810B, thereby making shock testing on vibration systems much more uniform and repeatable.

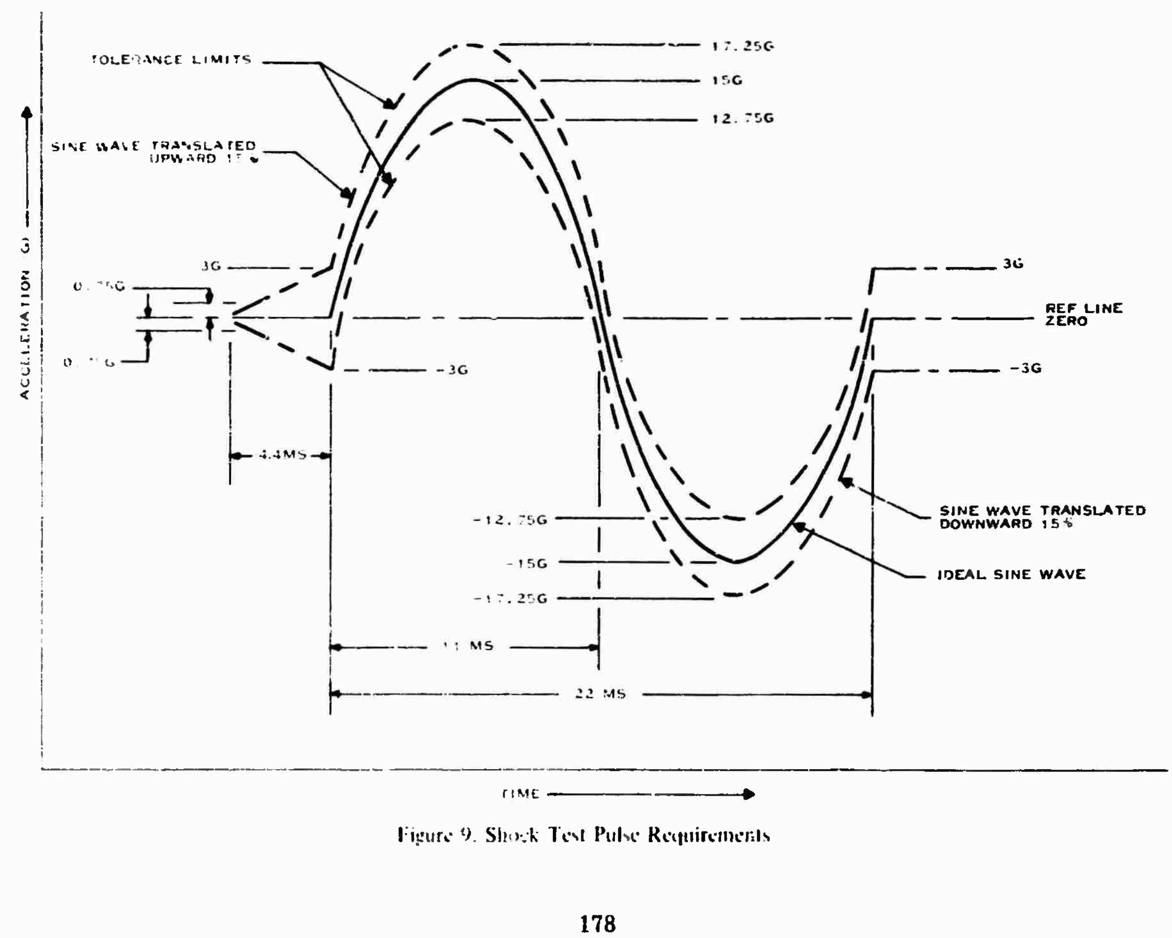

Figure 9. Shock Test Pulse Requirements

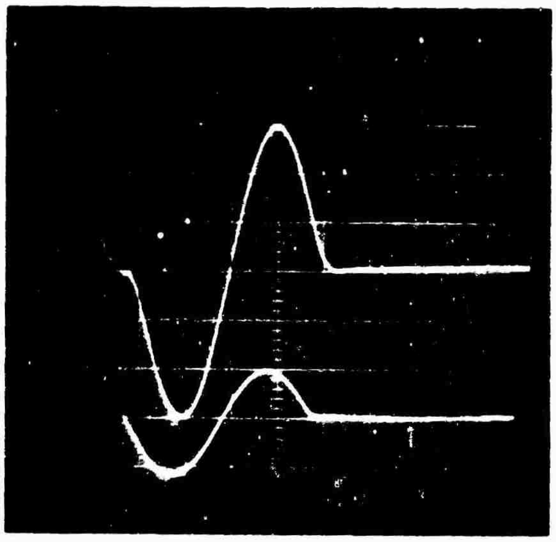

ARMATURE LOAD = 50 LBS
BOTTOM TRACE IS IDEAL FULL SINE VOLTAGE INPUT
TOP TRACE IS COMPENSATED SYSTEM OUTPUT
HORIZONTAL SWEEP = 5 MSEC/CM
VERTICAL SENSITIVITY = 5G/CM

Figure 10. Full-Sine Shock Pulse from Compensated Shaker with 50 Pound Load

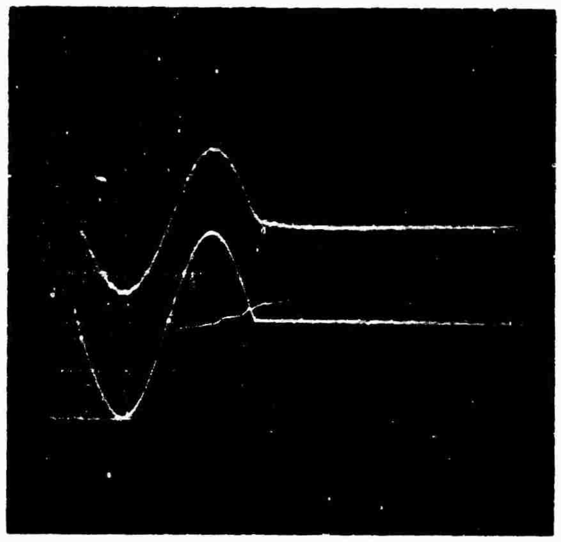

ARMATURE LOAD = 400 LBS
BOTTOM TRACE IS IDEAL FULL SINE VOLTAGE INPUT
TOP TRACE IS COMPENSATED SYSTEM OUTPUT
HORIZONTAL SWEEP = 5 MSEC/CM
VERTICAL SENSITIVITY = 10G/CM

Figure 11. Full-Sine Shock Pulse from Compensated Shaker with 400 Pound Load

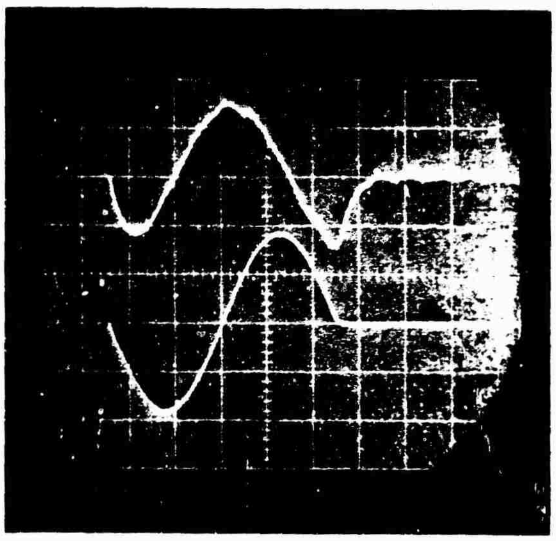

ARMATURE LOAD = 50 LBS
BOTTOM TRACE IS IDEAL FULL SINE VOLTAGE INPUT
TOP TRACE IS UNCOMPENSATED SYSTEM RESPONSE
HORIZONTAL SWEEP = 5 MSEC/CM
VERTICAL SENSITIVITY = 5G/CM

Figure 12. Full-Sine Shock Pulse from Uncompensated Shaker with 50 Pound Load

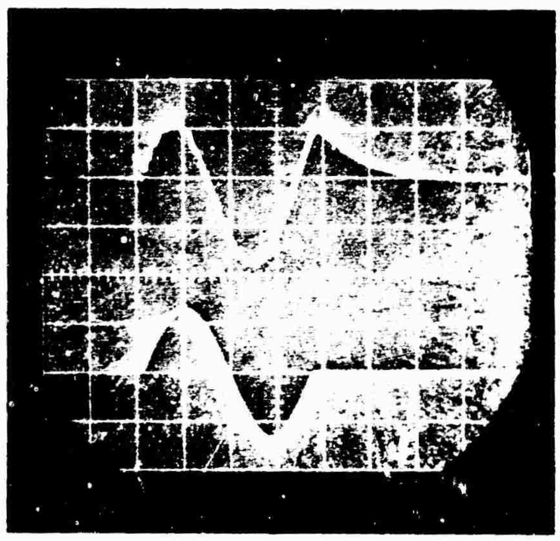

ARMATURE LOAD = 400 LBS
BOTTOM TRACE IS IDEAL FULL SINE VOLTAGE INPUT
TOP TRACE IS UNCOMPENSATED SYSTEM OUTPUT
HORIZONTAL SWEEP = 5 MSEC/CM
VERTICAL SENSITIVITY = 5G/CM

Figure 13. Full-Sine Shock Pulse from Uncompensated Shaker with 400 Pound Load

REFERENCES

[1] M. Gertel and R. Holland, "Definition of Shock Design and Test Criteria Using Shock and Fourier Spectra of Transient Environments," The Shock and Vibration Bulletin, No. 35, Part 6 pp. 252-253, April 1966.

[2] RCA Linear Integrated Circuit Fundamentals, pp. 70-72, Radio Corporation of America, Harrison, N.J., 1966

[3] W.R. Miller, "Shaping Shock Acceleration Waveforms for Optimum Electrodynamic Shaker Performance," The Shock and Vibration Bulletin, No. 34, Part 3, pp. 345-354, December 1964

[4] F.W. Young, "Shock Testing with Vibration Systems," The Shock and Vibration Bulletin, No. 34, Part 3, pp. 355-364, December 1964

[5] H.J. Schwabe, "An Approach to Polaris Flight Shock Simulation by Electrodynamic Shaker," Shock, Vibration and Associated Environments, No. 31, Part 2, pp. 144-163, March 1963

[6] G.W. Painter and H.J. Parry, "Simulating Flight Environment Shock on an Electrodynamic Shaker," Shock, Vibration and Associated Environments, No. 33, Part 3, pp. 85-96, March 1964

[7] E.H. Schell, "Spectral Characteristics of Some Practical Variations in the Half-Sine and Sawtooth Pulses," The Shock and Vibration Bulletin, No. 34, Part 3, pp. 223-251, December 1964

DISCUSSION

Mr. Verga (Hazeltine Corp.): I was very much encouraged by the simplicity of your block diagram, compared with the one in the previous paper. Of course, you were aiming for a sinusoidal pulse and the previous paper was concerned with a much more complicated pulse. Still, in your simple diagram there were many things which were not familiar. Given an electrodynamic system which enables you to perform a sinusoidal vibration test, what is the basic additional equipment required for the synthesis of a sinusoidal pulse?

Mr. Moser: The basic equipment is the $4.95 SN-52709 operational amplifier with the circuit I showed. It is in the paper, and I think the concept could be extended to other pulse shapes. I did not try it for this study. Eighty to ninety percent of our testing is to the half sine.

Mr. Ames (Frankford Arsenal): You mentioned about adding something to MIL-STD-810 I believe that requires you to go both positive and negative, so why could you not use the full sine wave rather than modifying it? I would think this would be within the requirements.

Mr. Moser: The requirements actually outline an envelope. The full sine pulse would not fit within the envelope because of the requirements for 0.4 sec before the pulse and a long period after the pulse.

Mr. Ames: Even if you consider that you have to go both positive and negative? They do not say you have to have some finite time between them.

Mr. Moser: Well, I hope you are right because then it is less difficult to sell the full sine pulse. Frankly, I have been thinking along these lines, not trying to sell it as fitting within that envelope, but thinking it would be the way to go.

Mr. Schell (Naval Research Lab.): Basically, while you do have two half sine pulses, one starts out with zero velocity and the other with a very high initial velocity. We also have the system still responding to the first half sine, therefore the second half sine would not produce the same response. These are theoretical arguments against letting such a test represent the application of a half sine shock in both directions. I do not necessarily mean to imply that this could not be done in MIL-STD-810; I am just citing one of the reasons why you might run into some objections. The responses to the two pulses would be quite different. Whether either one of the pulses is more realistic as far as the environment is concerned is debatable.

PROTUBERANCE EFFECTS ON LIMITER-EQUIPPED HARD LANDING PAYLOADS

John L. McCarty and James T. Howlett
NASA Langley Research Center
Hampton, Virginia

An analytical and experimental study was conducted to evaluate the effects of surface protuberances, such as rocks, on impact limiters for hard landing payloads. The analytical phase of this study consisted of extending an existing analysis to include protuberances and the application of this extended analysis to establish the effect of protuberances on impact limiter design. The experimental phase was undertaken to validate the analysis and consisted of impacting full-scale (for a prospective Mars mission) hard lander configurations, equipped with balsa wood as an impact limiter, onto a rigid planar surface having cylindrical and conical protuberances. The experimental test results substantiate the capability of the analysis to predict the effect of surface protuberances on the design and behavior of the impact limiter.

INTRODUCTION

One possible technique for exploring an extraterrestrial body is that of hard landing survivable scientific instruments on the surface of the body. This technique is attractive because landing, guidance, and control systems can be simpler and less expensive than those required for soft landing techniques. However, one of the major problem areas associated with this concept is that of designing an impact limiter which will attenuate landing accelerations to levels acceptable to the scientific instruments. Much work, both analytical and experimental, has been done toward evaluating various materials and devices suitable for impact limiter applications. Crushable materials such as foams, balsa, and honeycombs have been examined for their shock alleviation characteristics and analyzed when applied to various payload shapes (spheres and disks, for example) [1-9]. Other impact energy absorbing techniques such as frangible metal tubing [10] and inflatable gas bags [11] have also received some attention. These studies have concentrated upon planar impacts wherein the target is effectively a flat rigid surface. However, one significant aspect which has received very little attention in the hard lander approach is the effect of surface protuberances, such as rocks, on the design and behavior of the impact limiter. In particular, no analysis exists, substantiated by experiment, which treats this effect.

The purpose of this paper is to present the results of an analytical and experimental study to evaluate the effects of protuberances on impact limiters for hard landing payloads. The analytical phase of the study consisted of the extension of the analysis of Cloutier [5] for planar impacts to include the presence of protuberances, and the application of this extended analysis to establish the effect of protuberances on impact limiter design. The experimental phase was undertaken to validate the analysis.

DESIGN PHILOSOPHY

To accomplish the objectives of this study, certain parameters had to be established to define the hard lander configuration, the target protuberances, and the impact conditions. Since this project was conceived in 1968 in support of considerations of a hard landing instrument payload for the scientific exploration of the planet Mars, the selected parameters were based upon that prospective mission. The chosen Mars mission defined a scientific payload of 300 pounds having a 3000g tolerable shock loading, a nominal impact velocity of 150 fps, and surface protuberances as high as 5 inches. Further, the payload was required to survive regardless of its orientation upon impact. Although other shapes, relying upon rather unique shock attenuation devices, have been proposed for a hard lander configuration, it was apparent that the objectives of this study could best be achieved by using the design configuration illustrated in Fig. 1.

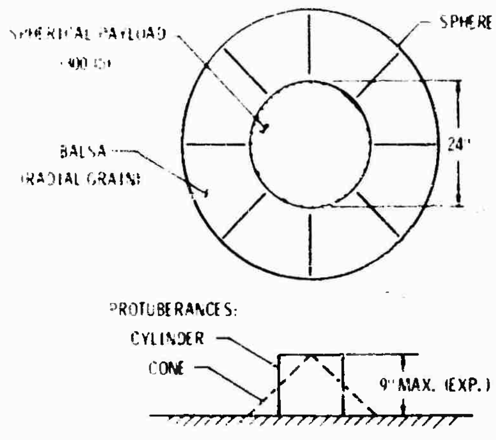

Fig. 1 - Analytical design configuration

This design consisted of a full-scale spherical payload completely encapsulated within a crushable impact limiting material. Assuming the density of the payload (scientific instruments, supporting equipments, and packaging structure) to be approximately 70 lb/ft^3, the diameter of the payload was fixed at 24 inches.

Radial grain balsa wood was selected as the impact limiter material although other materials such as plastic foams and metallic and phenolic honeycombs were considered. Balsa has a high energy absorbing capability per unit weight, is easy to shape, and is economical and available. Furthermore, preliminary calculations based upon estimated hard lander sizes and impact conditions of this study indicated that the crushing strength of balsa would maintain impact accelerations below the tolerable 3000g level.

A maximum experimental protuberance height of 9 inches was selected because it appeared to be a reasonably severe test inasmuch as 5-inch protuberances were postulated for the Mars mission. From the many possibilities for protuberance shapes, the protuberances for this study were restricted to those which provided symmetrical impacts; that is, to those protuberances which were symmetrical about an axis coincident with the velocity vector of the impacting hard lander. The shapes selected, a circular cylinder and a cone, were felt to bracket the extremes of symmetrical impacts.

ANALYSIS

Equations of motion were developed to describe the impact of a spherical body, which consisted of a payload encapsulated within a crushable balsa wood limiter, with the targets of this study. These equations are a straightforward extension of the analysis of Cloutier [5] for impact of a crushable sphere on a planar surface to that of impact on rigid symmetrical protuberances. The necessary assumptions and the analytical approach for the development follow.

Assumptions.- 1. Variations in the mass undergoing deceleration are neglected.

2. Effects attributed to shock waves generated in the balsa limiter are neglected.

3. All limiter crushing occurs at the impact surface and parallel to the direction of impact.

4. The balsa is of uniform density and has completely radially oriented grain.

5. Balsa crushes up to 20 percent of its original length.

6. The variation in balsa crushing strength, σ, with grain angle, θ, is given by

$$\sigma(\theta) = \sigma_c\left(1 - \frac{2.7}{\pi}\theta\right)$$

where σ_c is the crushing strength of balsa parallel to the grain and is assumed to remain constant during crush. Limited available data [1 and 5, for example], including the results of tests performed in conjunction with this study, indicate that this expression is a reasonable first approximation for values of θ up to $\pi/3$.

Approach.- Consider the impact of a crushable sphere with an arbitrary symmetrical protuberance as illustrated in Fig. 2. The general equation of motion for this system is of the form

$$m\ddot{y} = F(y) = \int_A dF$$

where m is the mass of the sphere, y is the distance from the planar surface to the center of gravity of the sphere, and F is the force exerted on the sphere by the crushing balsa wood.

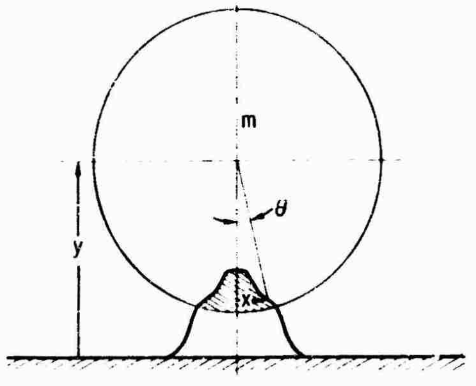

Fig. 2 - Analytical impact model

The last term of this expression is the integral of the force over the entire surface area of contact between the impacting body and the target. Since

$$dF = \sigma(\theta)\, dA$$

the equation of motion for any protuberance can thus be written

$$m\ddot{y} = \int_A \sigma(\theta)\, dA$$

Hence, for a specific protuberance, the final equation of motion is obtained by integrating the right-hand side of this expression over the area of contact. For example, in the case of a cylindrical protuberance, the motion is divided into three phases: the initial phase where the sphere is in contact with a portion of the upper surface of the cylinder; the second phase, during which the cylinder is penetrating into the sphere and the integration is over the entire upper surface of the cylinder; and the final phase, which commences when the impacting body contacts the planar surface and the area over which the integration is performed includes both that of the second phase and the appropriate area of the plane. For some protuberance shapes, the cylinder being an example, the integration over the surface can be done in closed form; for others, a numerical integration may be required. However, a numerical integration over the surface of some protuberances can be avoided, as was done for the cone, for example, by approximating the expression for dA by $2\pi X\, dX$, the area of an annular strip of radius X (see Fig. 2) and width dX, and expressing X as a function θ.

The analysis was used to determine the amount of balsa wood limiter required to protect the payload of this study during impact with the various protuberances. The procedure consisted of the arbitrary selection of a limiter thickness and the computation of the response of the body as it impacted a specified target. The process was repeated for different thicknesses until, following impact, the clearance which remained between the payload and the target was the minimum acceptable on the basis of 80 percent balsa wood crush-up. The analysis defined a limiter thickness of 9.5 inches for impacts on a planar target and a thickness of 21.5 inches for impact on a 9-inch-high protuberance projecting from a planar surface. (To introduce some conservatism into the design, the impact velocity for these calculations was assumed to be 175 fps rather than the nominal test velocity of 150 fps.)

EXPERIMENTAL TESTS

The impacting body configuration for the experimental tests on protuberances is shown in Fig. 3 and consisted of a simulated payload equipped with a hemispherical shell of radial-grain balsa wood. Seven impacting body configurations were fabricated — six configurations, 67 inches in diameter, to study the impact response to protuberances and one, 43 inches in diameter, to study the impact with a planar target. The testing technique

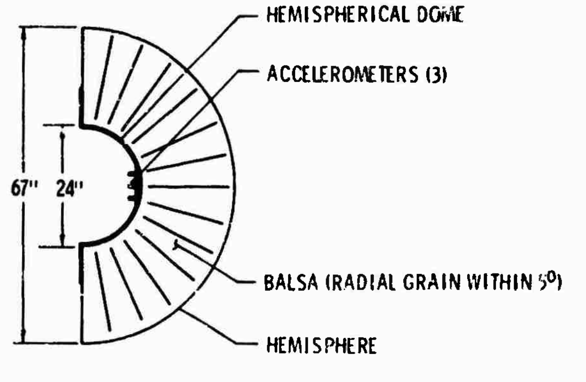

Fig. 3 - Experimental test configuration for impact on protuberances

provided the bodies with a fixed attitude at impact which eliminated the need for omni-directional protection of the test payload and thus the more formidable task of fabricating completely spherical limiters. In the fabrication of the impacting bodies, a steel hemispherical dome 1/2 inch thick and 24 inches in diameter served as the payload to which was bonded the balsa limiter. The balsa was applied in sections to provide a grain orientation within 5^{o} of the radial and then covered with fiberglass layers to act as a sealant and to minimize fragmentation during impact. Each body was instrumented with three piezoresistive accelerometers of different sensitivity to provide both redundancy and a better definition of the impact accelerations. These accelerometers were attached to a mounting plate welded within the hemispherical dome and oriented along the impact axis. Signals from each accelerometer were routed through a cable to an oscillograph recorder.

The test configuration was mounted to the launching apparatus by means of a three-arm support structure which was bolted to the flange of the hemispherical dome. This structure and load-distributing plates fastened to the rear face of the limiter provided ballast which effectively equated the mass of the hemispherical impacting body to that of the analytical sphere of the same diameter. Figure 4 is a photograph showing the installation of an impacting body to the outrigger sting of the high-speed carriage at the Landing Loads Track Facility [12]. The bodies, centered in the 8-foot-wide, 6-foot-deep channel which parallels the track, were propelled to the desired velocity by the carriage and released upon impact with the targets located in the test region of the channel. The targets consisted of the various protuberances attached to a 64-ton concrete backstop fronted by a sheet of 1/2-inch-thick boiler plate.

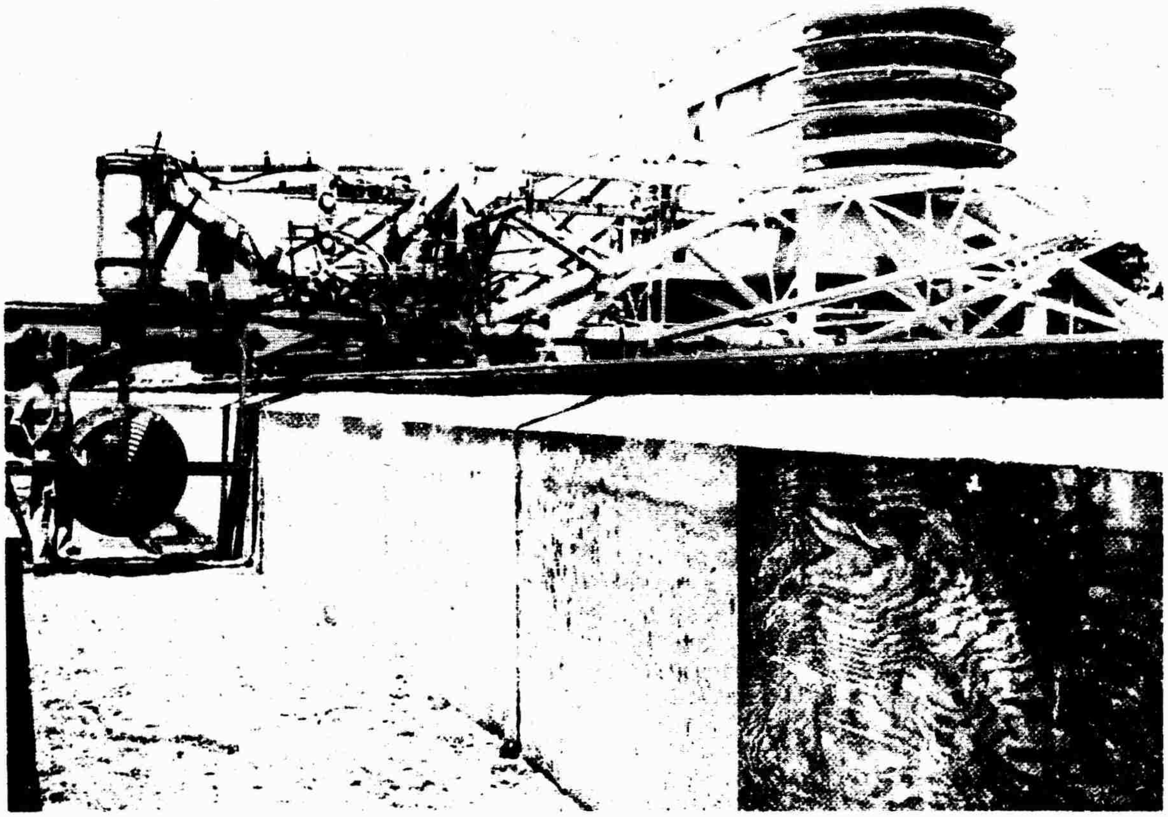

Fig. 4 - Installation of impacting body on sting of propelling apparatus

RESULTS AND DISCUSSION

Figure 5 is a reproduction of an oscillograph record showing typical responses of the accelerometers during impact with a protuberance. The protuberance for the record illustrated is a 9-inch-high cone having a total included angle of 100°. The signals contained a high-frequency response which, it was determined, corresponded to a natural frequency of the steel hemispherical dome and were faired as shown. To arrive at

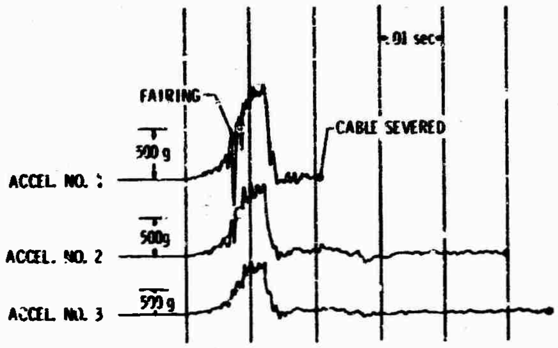

Fig. 5 - Typical impact response of accelerometers (100° conical protuberance)

a single impact acceleration time history for each test, the outputs from the three accelerometers were faired independently and compared. The reported acceleration time history was the mean of the outputs from the accelerometers of lower sensitivity, where the high-frequency noise level was less. One such faired experimental acceleration time history is presented in Fig. 6 together with that developed analytically. The protuberance of this figure is a 15-inch-diameter cylinder, 9 inches high and purposely selected to differ from that of the previous figure to illustrate the difference in the shape of the time histories during penetration of the protuberance. The analytical acceleration time history of this figure ceases when the velocity of the impacting body is computed to reach zero, whereas the experimental time history is shown to continue until the acceleration reaches zero and includes the restitution which was observed. The overall agreement between the experimental and analytical acceleration time histories, typified by that of Fig. 6, is considered good, particularly in view of the possible variations in physical properties of the

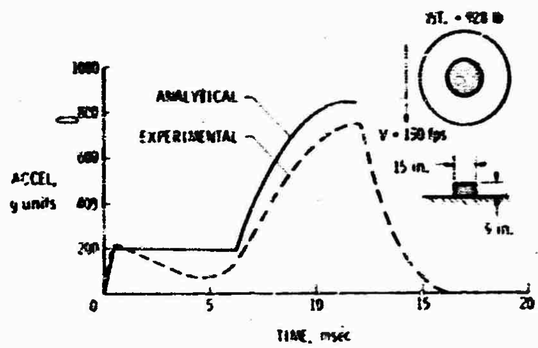

Fig. 6 - Typical impact acceleration time history for cylindrical protuberance

individual balsa wood segments from which the limiters were fabricated. The analytical acceleration time histories were based upon an assumed balsa crushing strength parallel to the grain of 1232 psi — an average value determined experimentally [1] which corresponds to the gross density of the balsa employed in the fabrication of the impacting bodies. The use of a somewhat lower value of crushing strength for the case illustrated would appear to better correlate the experimental acceleration time history.

Effects of Protuberance Geometry

The next two figures further illustrate the agreement between the analytical and experimental results and simultaneously indicate trends associated with protuberance geometry. The impact characteristics illustrated are payload maximum acceleration and the extent of limiter crush depth and are considered to be the most significant characteristics from the standpoint of impact limiter design. Figure 7 shows the variation in these characteristics as a function of the diameter of a cylindrical protuberance 9 inches high at a nominal impact velocity of 146 ft/sec. Experimental data are presented for protuberance diameters of 5, 15, and 22 inches, whereas the analytical results are extended to a diameter of 40 inches. The experimental data are shown to verify the analytical trends. The figure shows that with increasing protuberance diameter, the maximum acceleration decreases, reaches a minimum (for the impact conditions considered) at a protuberance diameter of approximately 22 inches, and then increases for larger

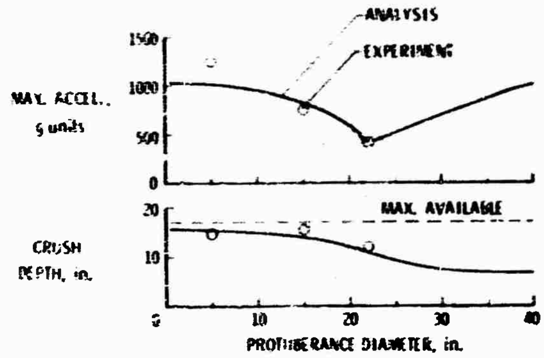

Fig. 7 - Effect of cylindrical protuberance diameter on impact characteristics (Protuberance height = 9 in.; impact velocity = 146 fps)

protuberances. At diameters below 22 inches, the entire protuberance penetrates the limiter and the maximum acceleration occurs when the body impacts the planar surface. Thus, for smaller protuberances, less energy is removed from the impacting body by the protuberance and hence the accelerations during impact with the plane are greater. As the protuberance diameter increases beyond 22 inches, less and less of the protuberance penetrates the body and the protuberance begins to resemble a planar surface. Calculations show that the maximum acceleration increases in this region until the protuberance diameter is roughly 65 percent of the body diameter (for the configuration considered), beyond which the maximum acceleration is identical to that for an actual planar surface. When the protuberance gives the appearance of a plane, the maximum acceleration occurs during impact of the body with the face of the protuberance and not with the target surface to which the protuberance is mounted. For impacts where the protuberance does not resemble a planarlike surface, the extent of penetration, and hence the extent of crush depth, is a function of the amount of impact energy absorbed during penetration of the protuberance. Thus, as the diameter of the protuberance increases, the limiter crush depth decreases to a value corresponding to that for impact with a plane surface. The difference between the crush depth for very small and for very large diameter protuberances is equal to the protuberance height. The maximum available crush depth denoted on the figure corresponds to the 80-percent allowable crush depth assumed for balsa wood and is shown to provide the configuration design with approximately a 1.5-inch clearance. This minimum clearance occurs in the region where the protuberance diameter is extremely small and the impact energy absorbed by the protuberance during penetration is practically nil.

Similar trends are noted in the variation of maximum acceleration and crush depth with the included angle of a conical protuberance as presented in Fig. 8 for the same impact conditions and protuberance height. The figure indicates that, for these conditions, a conical

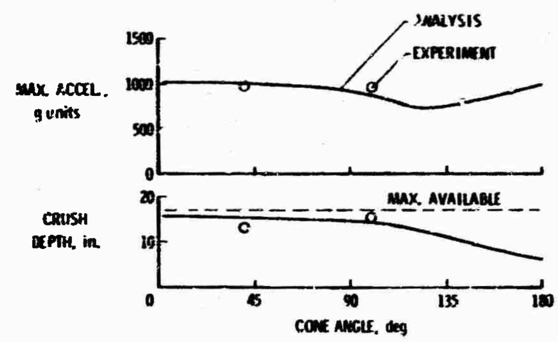

Fig. 8 - Effect of protuberance cone angle on impact characteristics (Protuberance height = 9 in.; impact velocity = 146 fps)

protuberance begins to resemble a planar surface at a cone angle of approximately 120°. At 120° the peak acceleration is a minimum and the crush depth, only slightly affected at lower angles, is definitely influenced by cone angle changes. The acceleration for impacts on a 180° cone is analytically identical to that for cone angles approaching 0°, since both are essentially plane surfaces. However, as the shape of the cone approaches a flat plate, penetration of the protuberance into the limiter decreases until at a cone angle of 180°, the crush depth is exactly 9 inches (protuberance height) less than that which occurs at very small cone angles. The results from experimental impact tests on 40° and 100° conical protuberances at approximately the same impact conditions are shown to agree favorably with the analytical results.

As shown in Figs. 7 and 8, as would be expected, the maximum impact accelerations are greatest when the protuberance, regardless of shape, gives the appearance of a planar surface; that is, either when the protuberance is small in cross section and thus absorbs a negligible amount of impact energy or when the protuberance itself presents a planar surface to the impacting body. However, from the standpoint of limiter crush depth, the most severe protuberance is one which has a small cross section regardless of shape. Hence, in the design of a limiter for a hard lander to accommodate protuberances, it is apparent that height is the critical protuberance dimension.

Application of Analysis to Limiter Design

Having established that the analysis is capable of predicting with reasonable accuracy the response behavior of a hard landing configuration during impact with specified protuberances, the analytical technique was used to study the interdependent effects of protuberance height, limiter thickness, and impact velocity on limiter design. For purposes of this study, the payload was assumed to be a 2-foot-diameter sphere weighing 300 pounds, and the impact limiter to be of balsa wood having a density of 6.5 lb/ft^3 and a crushing strength 1232 lb/in^2 parallel to the grain. The protuberance selected was a cylinder, 1 inch in diameter, which would imply, from the previous analytical results, a severe impact which requires a limiter design that is appropriate to any protuberance shape.

Figure 9 presents the thickness of balsa wood limiter necessary to protect the payload during impact at 150 fps with protuberances ranging in height up to 20 inches. Similar curves can be derived from the analysis for other velocities, payloads, and limiter materials. At limiter thicknesses less than those described by the thickness (t) curve, the limiter "bottoms out" and the payload itself effectively strike a rigid target which results in greatly increased accelerations and possible damage to the payload structure. Also included on the figure is a curve which represents the sum of the protuberance height, h, and the limiter thickness, t_0, required for a planar impact. A comparison of the two curves indicates that a limiter thickness in excess of the protuberance height is necessary to provide for the increase in kinetic energy of the impacting body resulting from the larger body mass.

Figure 10 shows the thickness of limiter material required to protect the payload as a function of the velocity at impact on a protuberance of fixed height. The protuberance height selected for this figure is approximately 10 inches, however, similar curves can be developed from the analysis for other heights as well as other payloads and limiter materials. The figure shows that, as expected, the greater the impact velocity, the more limiter material is required to absorb the increased energy of the impacting system. A hard lander with an omnidirectional limiter, such as the one under consideration here, suffers a severe mass penalty, particularly at the higher impact velocities, since limiter material must be applied over the entire spherical surface. For example, at 100 fps, the weight of the limiter for the hard lander is approximately 370 lb; whereas at 250 fps, the weight of the required limiter is 1100 lb.

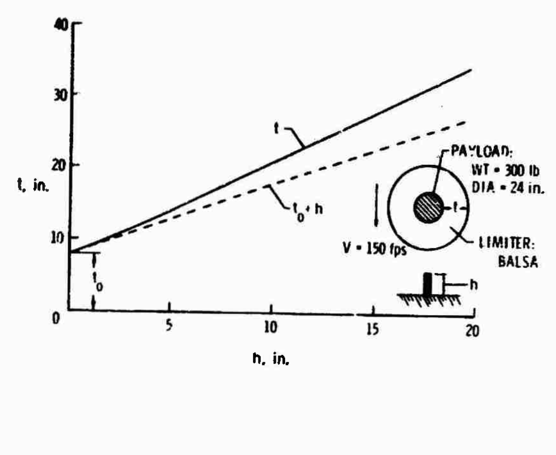

Fig. 9 - Effect of protuberance height on limiter thickness

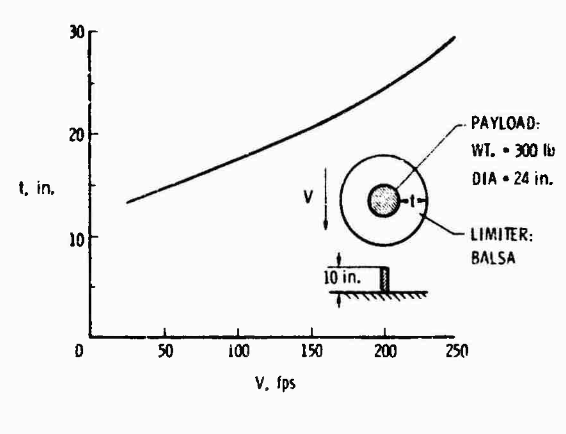

Fig. 10 - Effect of impact velocity on limiter thickness

The effect of protuberance height on the allowable impact velocity of a fixed configuration design is illustrated in Fig. 11. The impact limiter for the fixed configuration was based upon an impact velocity of 150 fps and a protuberance height of nearly 10 inches which described an overall configuration 64.8 inches in diameter weighing 809 pounds. The curve of this figure was obtained by computing the maximum impact velocity for which the limiter of the design configuration affords protection to the payload against protuberances ranging in height up to approximately 16 inches. Thus, in effect, any point on this curve would design the same hard lander configuration. For combinations of impact velocity and protuberance height which fall below the curve, the payload is provided with ample protection: for those combinations which fall above, insufficient limiter is available and the payload "bottoms out" and effectively impacts a rigid target. The figure shows that, as expected,

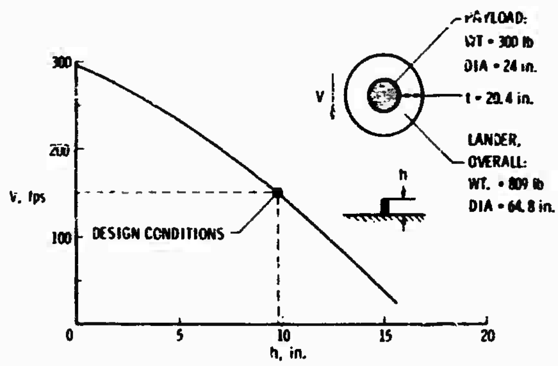

Fig. 11 - Effect of protuberance height on impact velocity for fixed hard lander design

for protuberances higher than that for which the hard lander is designed, the impact velocity must be reduced for the payload to survive; and similarly, if the impact velocity is higher than the design velocity, the limiter will only provide adequate protection for protuberances shorter than those for which the configuration was designed. It would appear that in a hard lander application, curves similar to that of Fig. 11 would be useful in assessing the probability of a successful landing on a surface of unknown protuberance sizes for missions where some control is provided over the impact velocity.

CONCLUDING REMARKS

The results from experimental impact tests demonstrated the capability of an analysis for planar impacts, extended to include protuberances, to describe the impact behavior of hard landing payloads on various protuberances. The analytical expressions predict with good accuracy both the accelerations sensed by the payload and the extent of limiter crush during impact. The application of the analysis to limiter design indicates that limiter thickness and mass penalties are associated with an increase in either protuberance height or impact velocity.

REFERENCES

[1] Daigle, D. L.; and Lonborg, J. O.: "Evaluation of Certain Crushable Materials," Tech. Rept. No. 32-120, Jet Propulsion Lab., California Inst. Technol., Jan. 13, 1961.

[2] Anon.: "RF Transparent, Energy Absorbing, Structural Elements," Phase II, Final Report No. 64SD4329 (prepared for Jet Propulsion Lab. under Contract No. 950564). General Electric Co., Aug. 17, 1964.

[3] Anon.: "Impact Technology Document," Volumes I and II, Publication No. U-3031 (prepared for Jet Propulsion Lab. under Contract No. 950996). Aeronutronic Division of Philco Corp., Feb. 25, 1965.

[4] Conn, Andrew F.: "Impact Energy Absorption Properties of Crushable Materials." RM-315, Martin Company, Oct. 1966.

[5] Cloutier, Gerald J.: "Landing Impact Energy Absorption Using Anisotropic Crushable Materials," J. of Spacecraft, Vol. 3, No. 12, pp. 1755-1761, Dec. 1966.

[6] Meyers, William M.: "Development of Energy-Dissipating Plastic Honeycomb," Final Report No. 68SD4264 (prepared for Jet Propulsion Lab. under Contract No. 951172). General Electric Co., June 14, 1968.

[7] Knoell, A. C.: "Analysis of the Crushing of a Dovetail Phenolic Honeycomb Spherical Impact Limiter," Tech. Rept. No. 32-1287, Jet Propulsion Lab., California Inst. Technol., July 1, 1968.

[8] Knoell, A. C.: "Structural Development of an Impact Limiter System for a Mars Landing Vehicle." AIAA 2nd Aerodynamic Deceleration Systems Conference, AIAA Paper No. 68-961. September 23-25, 1968.

[9] Berkowitz, Harvey M.; and Rodriguez, David A.: "Dynamic Analysis and Development of Response Histories and Tradeoff Study Charts for Spherical Impact Limiters," J. of Spacecraft, Vol. 6, No. 1, pp. 50-58, Jan. 1969.

[10] McGehee, John R.: "A Preliminary Experimental Investigation of an Energy-Absorption Process Employing Frangible Metal Tubing," NASA TN D-1477, 1962.

[11] Ross, R. G., Jr.; and Layman, W. E.: "The Design and Testing of an Inflated Sphere Impact Limiter," Tech. Rept. No. 32-1037, Jet Propulsion Lab., California Inst. Technol., December 15, 1966.

[12] Joyner, Upshur T.; Horne, Walter B.; and Leland, Trafford J. W.: "Investigations on the Ground Performance of Aircraft Relating to Wet Runway Braking and Slush Drag," AGARD Rept. No. 429, 1963.

DISCUSSION

Mr. Hughes (Naval Weapons Evaluation Facility): I wonder if you can come up with a rule of thumb for the optimum design of your balsa wood impacting sphere? I noticed that you had some dips. You could have combined the last two slides and come up with an optimum diameter and an optimum length required to reduce the number of g's. Have you done this?

Mr. McCarty: You are speaking primarily with respect to protuberance height, are you not?

Mr. Hughes: Height and diameter of the sphere.

Mr. McCarty: Of course, the most critical protuberance, as you saw on the slide, would be a needle, although this may not be very realistic in practice. Not knowing the impact velocity or what the limiter material is going to be, it is rather difficult to come up with a rule of thumb that would tell you how much limiter material is required to protect the payload for that protuberance.

Mr. Hughes: I just happened to notice that on the third from the last slide you had a marked dip. In that case, the diameter of the protuberance was about one-half the diameter of the impacting sphere.

Mr. McCarty: About one-third. I might also point out that in the case of conical protuberances, where we varied the included angle of the cone, we had a similar dip. You begin by absorbing energy for a real small cone and then, as the cone angle increases, the amount of energy being absorbed in penetration increases. It began to resemble a plane impact at an included angle of about 120°.

IMPACT TESTS OF NUCLEAR FUEL MATRICES USING A VACUUM TUBE LAUNCHER

H. W. Nunez
Sandia Laboratories
Albuquerque, New Mexico

This paper discusses a Vacuum Tube Launcher (VTL) and its operation. The VTL uses the small difference between atmospheric pressure and a vacuum as the force to propel a piston through a tube. The interesting features of the work described are the radioactive nuclear fuel being tested and the precautions necessary to handle the fuel. The method of obtaining the required impact conditions is discussed as are the calibration shots used to determine the functional parameters of the VTL and to verify the attitude of the nuclear fuel puck at impact.

INTRODUCTION

As part of a test program aimed at studying the safety aspects of nuclear-powered fuel devices when impacted onto a hard surface, Sandia Laboratories received a request to perform a series of tests to subject both simulated and live fuel matrices to a shock environment representative of impact after reentry. The live fuel matrices contained 239 PuO_2 (approximately 2 to 6 curies) compressed into the form of a disc about 1.5 inches in diameter and 0.5 inch thick. Because of its size and shape, it was referred to as a fuel puck. Due to the radiation hazard of the nuclear material, and because all pieces of the material had to be recovered for analysis after impact, it was essential that the fuel pucks be enclosed in thick-walled steel containers. This assembly was referred to as a fuel capsule.

These fuel capsules were fabricated by the Los Alamos Scientific Laboratories (LASL) and by Battelle Memorial Institute (BMI). The simulated fuel pucks (fabricated by the same agencies) were similar to the live pucks in size and shape but were made of a compressed ceramic material.

Requirements of the test were to develop impact velocities of the fuel puck relative to its container ranging from 100 to 150 feet per second and to have the container essentially at rest (zero velocity) when the impact of the fuel puck occurred. The fuel puck was to be held flat against the inside upper surface of the container during travel and then to impact flat against the inside lower surface. No adhesive or restraining device could be used to hold the puck in position.

Another important requirement of the test, from the standpoint of safety, was that the fuel capsule impact area be in an enclosed chamber so that in the event a capsule did rupture and expose the radioactive fuel material, this material could be trapped by an absolute filter system. These requirements indicated that a Sandia Laboratories test facility called a Vacuum Tube Launcher (VTL) could be used.

VACUUM TUBE LAUNCHER THEORY

In principle, a vacuum launcher is extremely simple and not very costly. Figure 1 shows the essential parts of a typical system. A long tube is sealed at the ends by a close-fitting piston and a diaphragm or an impact block. Since flexible nylon flanges can be used to seal the ends of the piston, the tolerances on the inside of the tube are not critical. The piston is held by some form of restraint and the pressure on the interior of the tube is reduced by means of a vacuum pump.

When a predetermined differential between interior pressure and atmospheric pressure is reached, the restraint is removed and the atmospheric pressure accelerates the piston through the tube. A reservoir opening into the tube receives the air being compressed ahead of the piston. The size of the reservoir can be large enough to ensure that the piston does not decelerate as it pushes the air ahead of it in the tube, or its size may be selected so that the piston will slow down prior to impact. The piston may be allowed to break through the diaphragm and go into free flight, or it may impact against a block used to seal the end of the tube.

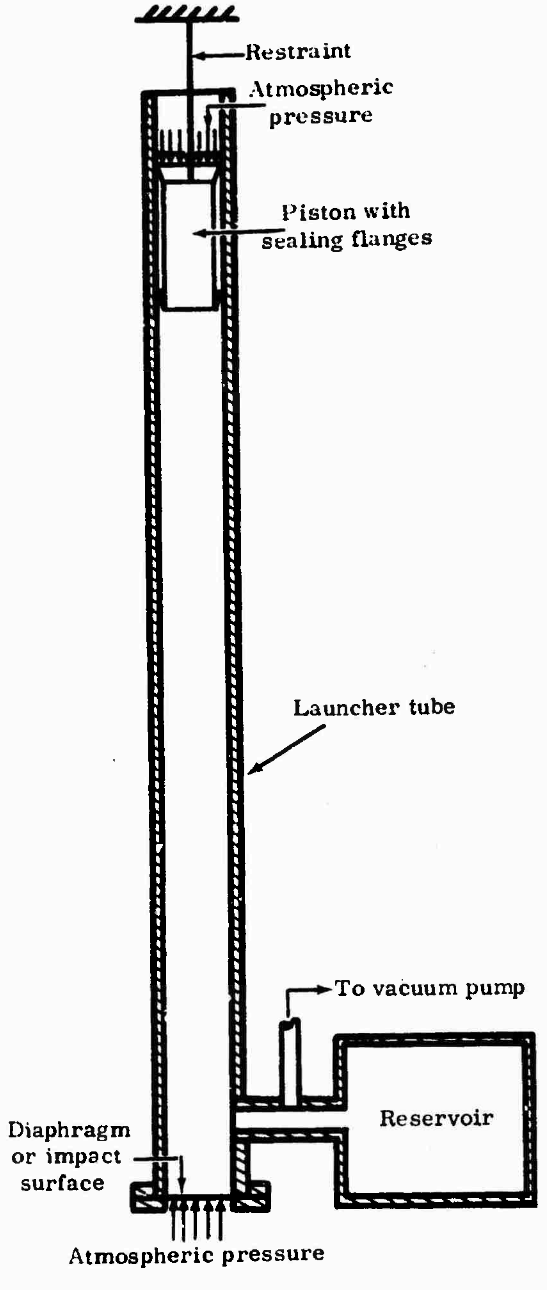

Fig. 1 - Diagram of a typical vacuum launcher

The object being tested may be mounted to or inside the piston or may be on the impact block and be hit by the piston.

Impact velocities in the VTL are functions of the weight of the piston, the length and diameter of the tube, the differential pressure, the reservoir volume, and the friction between the piston and the tube wall.

The mathematical analysis of a VTL is presented below. While the general analysis appears rather complicated, for a given VTL setup it is reducible to a fairly simple statement that lends itself readily to nomographic solution. A computer solution has also been programmed.

MATHEMATICAL ANALYSIS OF VACUUM TUBE LAUNCHER

The analysis of a vacuum system such as the VTL is very similar to that of a high pressure open-end air gun with the following exceptions:

1. In an open-end air gun, the high pressure behind the projectile is decreasing and the pressure ahead of the projectile remains atmospheric; while in a vacuum system, assuming no flow restrictions, the pressure behind the projectile remains the same (usually atmospheric) and the pressure ahead of the projectile is increasing.

2. In an air gun, the volume behind the projectile is increasing and the volume ahead of the projectile is infinite; while in a vacuum system, the volume behind the projectile remains infinite and the volume ahead of the projectile is decreasing.

Figure 2 is a simplified diagram of a general vacuum system showing the piston in its initial condition and the condition after piston release. If the air ahead of the piston is assumed to be an ideal gas compressing isentropically, then

$$P_o V_o^k = P_x V_x^k$$

or

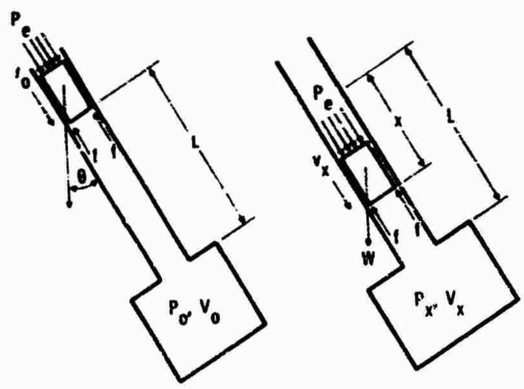

W = total weight of piston assembly
θ = angle tube makes with vertical
L = total length of travel in tube
P_e = external pressure (atmospheric) driving piston
A = piston area
k = specific heat ratio for gas in tube, = c_p/c_v = 1.4 for air
v_o = initial piston velocity
v_x = piston velocity after piston travels x distance
P_o = initial internal pressure in tube
P_x = internal pressure after piston travels x distance
V_o = initial volume of tube (and reservoir)
V_x = volume of tube (and reservoir) after piston travels x distance
ΔP = initial pressure differential = $P_e - P_o$
f = total frictional force on tube
$x, \dot{x}, \ddot{x}$ = distance, velocity, and acceleration of piston at any time

Fig. 2 - Diagram of a general vacuum system

$$P_x = \frac{P_o V_o^k}{V_x^k} . \qquad (1)$$

Also

$$V_x = V_o - Ax .$$

Therefore:

$$P_x = \frac{P_o V_o^k}{(V_o - Ax)^k} . \qquad (2)$$

Summing the forces acting on the piston at any given time:

$$\Sigma F = P_e A - P_x A + W \cos \theta - f = \frac{W}{g} \ddot{x} . \qquad (3)$$

Assume that the tube is vertical ($\cos \theta = 1$) and let the frictional force equal the piston weight. Then:

$$W = f$$

and Eq. (3) becomes

$$P_e A - P_x A = \frac{W}{g} \ddot{x} . \qquad (4)$$

Substituting the value of P_x from Eq. (2) into Eq. (4):

$$P_e A - AP_o V_o^k (V_o - Ax)^{-k} = \frac{W}{g} \ddot{x} . \qquad (5)$$

For the purpose of integration, introduce a dummy variable:

$$y = \dot{x} .$$

Then:

$$\dot{y} = \ddot{x} = \frac{dy}{dx} \dot{x} = \frac{dy}{dx} y .$$

Therefore, Eq. (5) becomes

$$P_e A dx - AP_o V_o^k (V_o - Ax)^{-k} dx = \frac{W}{g} y dy .$$

Then, by integration:

$$P_e A + \frac{P_o V_o^k}{1 - k} (V_o - Ax)^{1-k} = \frac{W}{2g} y^2 + C . \qquad (6)$$

But initially when $x(o) = 0$, $y(o) = v_o$

$$C = 0 + \frac{P_o V_o^k}{1 - k} (V_o - 0)^{1-k} - \frac{W}{2g} v_o^2$$

$$= \frac{P_o V_o^k (V_o)^{1-k}}{1 - k} - \frac{W}{2g} v_o^2$$

$$= \frac{P_o V_o}{1 - k} - \frac{W}{2g} v_o^2 . \tag{7}$$

Now substituting the value of C from Eq. (7) into Eq. (6) and also replacing the dummy variable y with $\dot{x}$:

$$P_e Ax + \frac{P_o V_o^k}{1 - k} (V_o - Ax)^{1-k}$$

$$= \frac{W}{2g} \dot{x}^2 + \frac{P_o V_o}{1 - k} - \frac{W}{2g} v_o^2 ,$$

$$P_e Ax + \frac{P_o V_o^k (V_o - Ax)^{1-k} - P_o V_o}{1 - k}$$

$$= \frac{W}{2g} (\dot{x}^2 - v_o^2) ,$$

or

$$P_e Ax + \frac{P_o V_o}{1 - k} \left[\left(1 - \frac{Ax}{V_o} \right)^{1-k} - 1 \right]$$

$$= \frac{W}{2g} \left(\dot{x}^2 - v_o^2 \right) . \tag{8}$$

If the initial velocity $v_o = 0$, then the square of the piston velocity at any instant in the tube is

$$\dot{x}^2 = \frac{2g}{W} \left\{ P_e Ax + \frac{P_o V_o}{1 - k} \left[\left(1 - \frac{Ax}{V_o} \right)^{1-k} - 1 \right] \right\} \tag{9}$$

which indicates that for a given VTL setup, the velocity is a function of only four variables:

1. W = the piston weight
2. X = the length of travel in the tube
3. P_o = initial pressure in the tube
4. P_e = atmospheric pressure, which for practical purposes can be assumed constant for a particular location.

Letting

$$\Delta P = P_e - P_o \quad \text{or} \quad P_o = P_e - \Delta P \tag{10}$$

and substituting this value of P_o into Eq. (9)

$$\dot{x} = \left\{ \frac{2g}{W} \left[P_e Ax + (P_e - \Delta P)(R) \right] \right\}^{0.5} \tag{11}$$

where

$$R = \frac{V_o}{1 - k} \left[\left(1 - \frac{Ax}{V_o} \right)^{1-k} - 1 \right] .$$

Rearranging Eq. (11) and solving for ΔP, the differential pressure required to achieve a given velocity,

$$\Delta P = \frac{P_e R + P_e Ax - \frac{W\dot{x}^2}{2g}}{R} . \tag{12}$$

The maximum piston velocity, V_m, possible in any given test setup is:

$$V_m = \left\{ \frac{2g}{W} \left[P_e AL + (P_e - \Delta P)(R) \right] \right\}^{0.5} \tag{13}$$

where L is the length of the launcher section of the tube and $\Delta P \leq$ one atmosphere.

This empirical solution has been developed using the assumption that the frictional force between the piston and the tube is equal to the weight of the piston. This implies that the piston will not slide down a vertical tube under its own weight. The correct value of this frictional force and all other losses should be determined experimentally for any given test setup.

VACUUM TUBE LAUNCHER DESCRIPTION

Figure 3 is an overall view of the VTL as it was set up for the impact tests of the fuel pucks. The VTL consisted of three sections of steel tube, each 9 in. OD x 8 in. ID x 200 in. long, with flanges at each end. The three sections can be bolted together in line to form a continuous tube 50 feet long with a separate

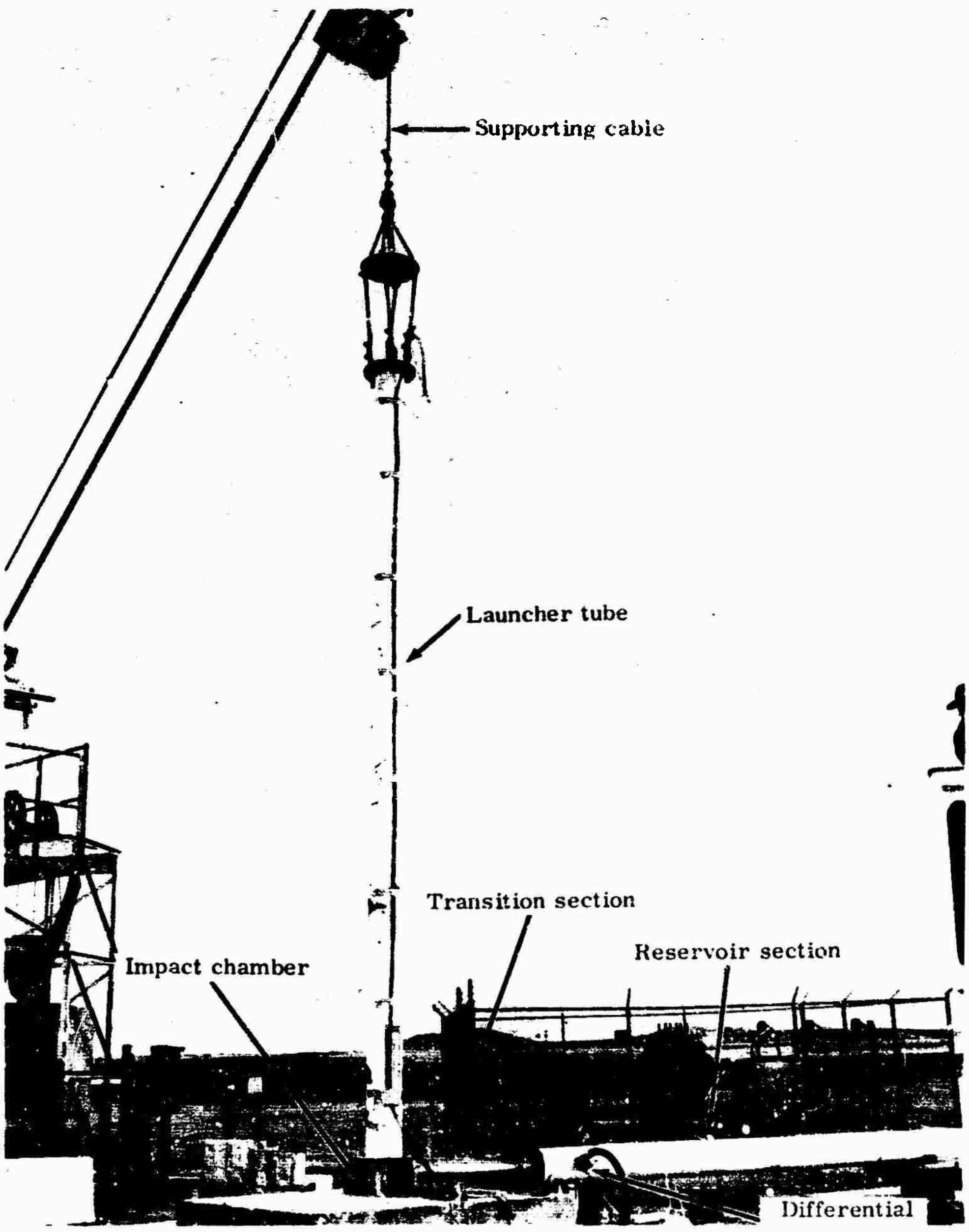

Fig. 3 - Vacuum tube launcher (VTL) setup for impact tests of fuel pucks

reservoir provided. However, in this case, by using a transition section, one length of tube was used vertically as the launcher tube and the other two sections were used horizontally as the reservoir. A vacuum pump was attached to the tube, and a differential-type pressure cell was used to monitor the difference between atmospheric pressure and the pressure inside the tube.

Three wires were inserted through the wall of the launcher tube at known distances apart. As the leading edge of the piston passed these wires, they were bent down against the tube wall completing a circuit and causing a voltage change which was recorded on a tape recorder. This permitted the calculation of the piston velocity just prior to impact.

The piston was held in the upper portion of the tube by a cable loop between the piston and the supporting cable. When the desired differential pressure was reached, this cable was cut by means of an explosive cable cutter fired from a remote location. The piston then accelerated down the tube to the impact chamber.

PISTON DESCRIPTION

Figure 4 shows a typical VTL piston used during calibration tests. A typical piston and capsule containing a fuel puck are shown in Figure 5. The pistons consisted of foam cylinders (approximately 6 lb/ft^3 density) fitted at the top and bottom with nylon flanges. These flanges were slightly larger than the ID

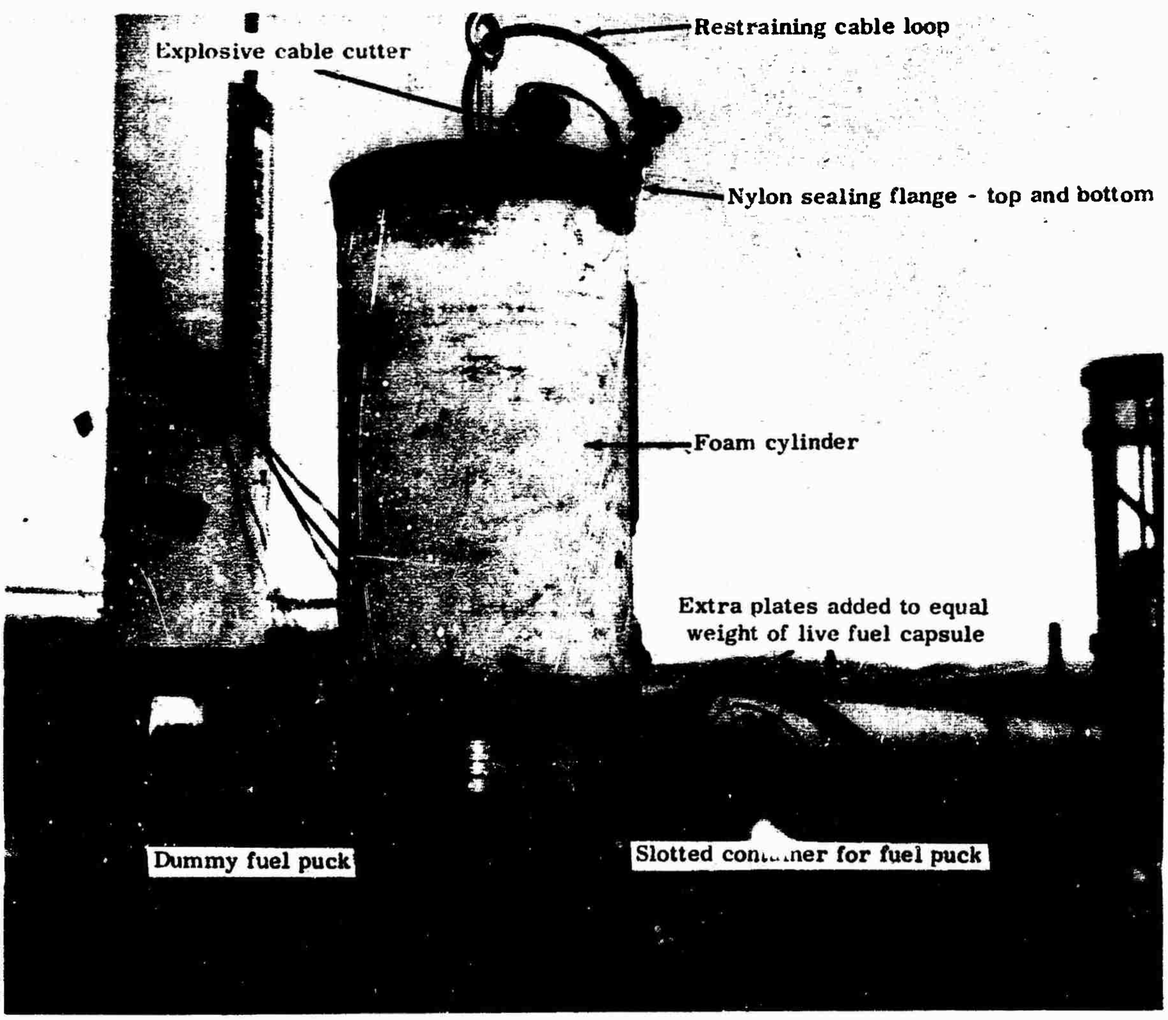

Fig. 4 - Typical piston used during calibration tests

of the launcher tube and formed a seal around the inside. Cover plates and tie-rods held the assembly together. The fuel capsule was bolted to the bottom cover plate.

The main purpose of the foam was to provide a piston of minimum weight to load the capsule during impact and to hold the sealing flanges apart a distance approximately 1.5 times the tube ID. The foam was usually crushed during impact.

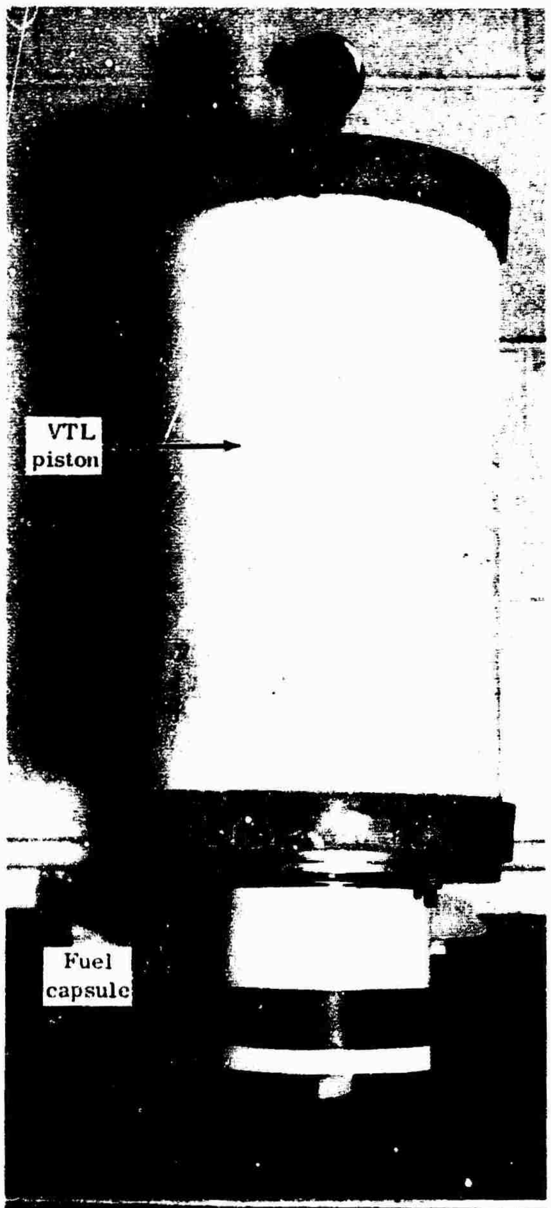

Fig. 5 - Typical piston and fuel capsule

CAPSULE DESCRIPTION

Figure 6 is a diagram of a typical fuel capsule containing a fuel puck. After the fuel puck was placed in the container, the plug was screwed in place and the cap welded in. This assembly was done either at LASL or BMI. At the time of assembly of the fuel capsules, several empty containers were also fabricated to be used as proof-test containers prior to impacting the live fuel capsules. Also during fabrication, live fuel pucks were placed in some of the containers, and simulated fuel pucks were placed in others. All of these capsules were fabricated at the same time and under exactly the same conditions. Each capsule weighed approximately 15 pounds.

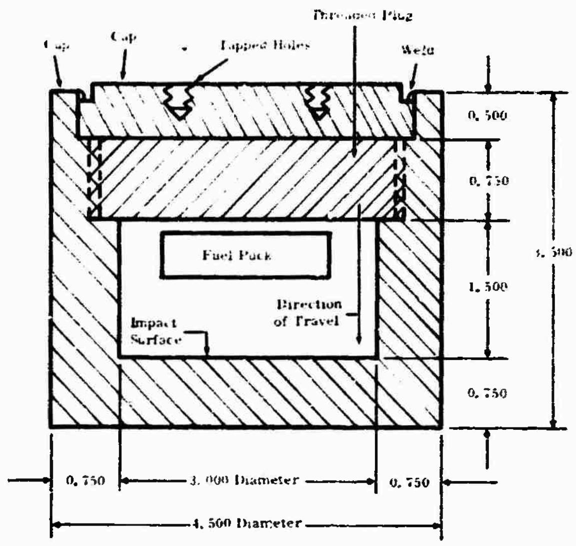

Fig. 6 - Diagram of typical fuel capsule

The proof-test containers were impacted at approximately 155 feet per second, the maximum velocity obtainable on the VTL; whereas the containers with live or simulated fuel pucks were impacted at either 100 or 125 feet per second velocity. All of the fuel capsules were returned to either LASL or BMI for opening and analysis.

Figure 7 shows a special slotted container used during the calibration shots of the VTL. This container was the same size as the LASL and BMI containers, but it had several cutouts in the side walls to permit photographing a dummy fuel puck during the tests. A plywood disc served as a dummy fuel puck. Additional weight was added to the piston to compensate for the difference in weight of the

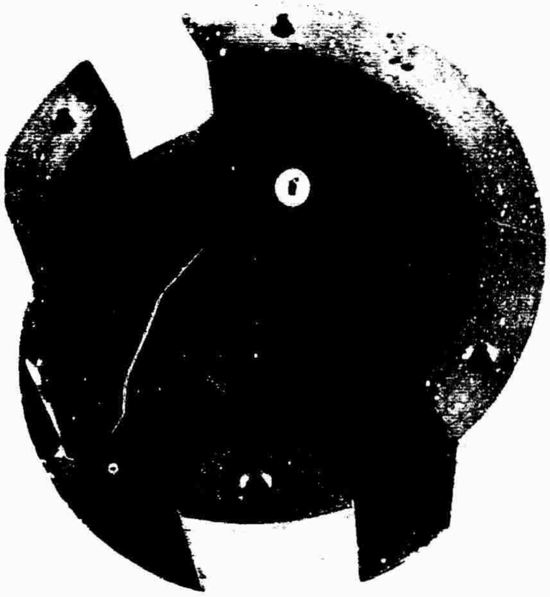

Note: Top of container
has been removed.

Fig. 7 - Slotted container used with dummy puck

two capsules (see Figure 4). A typical piston and fuel capsule weighed approximately 18.75 pounds and was approximately 16 inches long.

IMPACT CHAMBER

In order to provide photographic verification of the fuel puck behavior during impact, a special chamber was designed for use in conjunction with the slotted fuel capsule and dummy fuel puck just described. Three of the walls of this chamber were of 1-1/2-inch thick plexiglass, and the fourth wall formed the opening to the transition section between the launcher tube and the reservoir. The bottom of the impact chamber was a 2-inch thick steel plate bolted to a heavy concrete block. The bottom flange of the launcher tube was bolted to this plate. This impact chamber is shown in Figures 8 and 9.

The lead cones shown in these two photos were selected as the impact medium for the piston assembly. Previously, considerable work has been done at Sandia on the deflection and energy-absorbing properties of these lead cones. Computations indicated that if the fuel capsule could impact on seven cones arranged as shown in Figure 9, the flow of the lead during deformation would cause the capsule and piston to decelerate and come to a stop in about 1 inch and then begin to rebound. The impact chamber was designed so that its height would permit the slotted calibration container to come into view during the impact, but the container would be stopped and rebound would begin before the lower flange had left the tube.

An important safety requirement for the test was that the pressure in the impact chamber during and immediately after the test had to be less than atmospheric to prevent any leakage of radioactive material. The vacuum pump used to evacuate the launcher prior to the test also had to be off and the valve closed. It was then necessary to provide a controlled leakage from the launcher past the piston, through the reservoir, and through an absolute filtering system.

To do this, the end of the reservoir section of tube was fitted with a spring-loaded flap valve and a length of 6-inch diameter flexible hose that led through an absolute filter (99.97 percent retention of 0.3 micron particles) to a filter pump. The flap valve was held closed by pressure close to atmospheric before before and during a shot. After a shot, as the pressure rose on the reservoir side of the flap valve, the spring opened the valve, and the filter pump pulled the air from the tube past the piston, through the reservoir into and through the filter. A diagram of this flap valve and filter section is shown in Figure 10. Personnel experienced in radiation monitoring examined this filter and the entire setup after

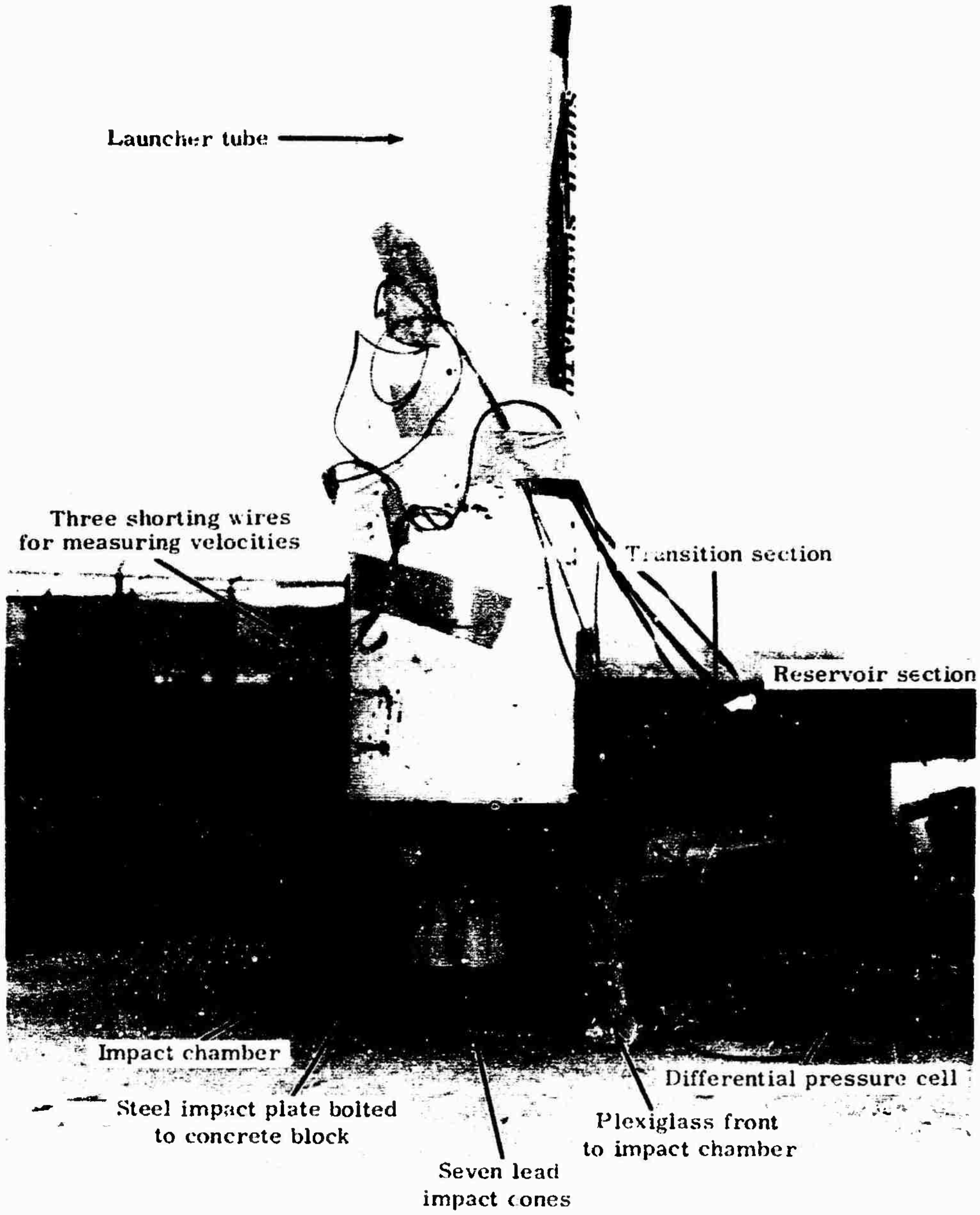

Fig. 8 - View of the VTL impact chamber

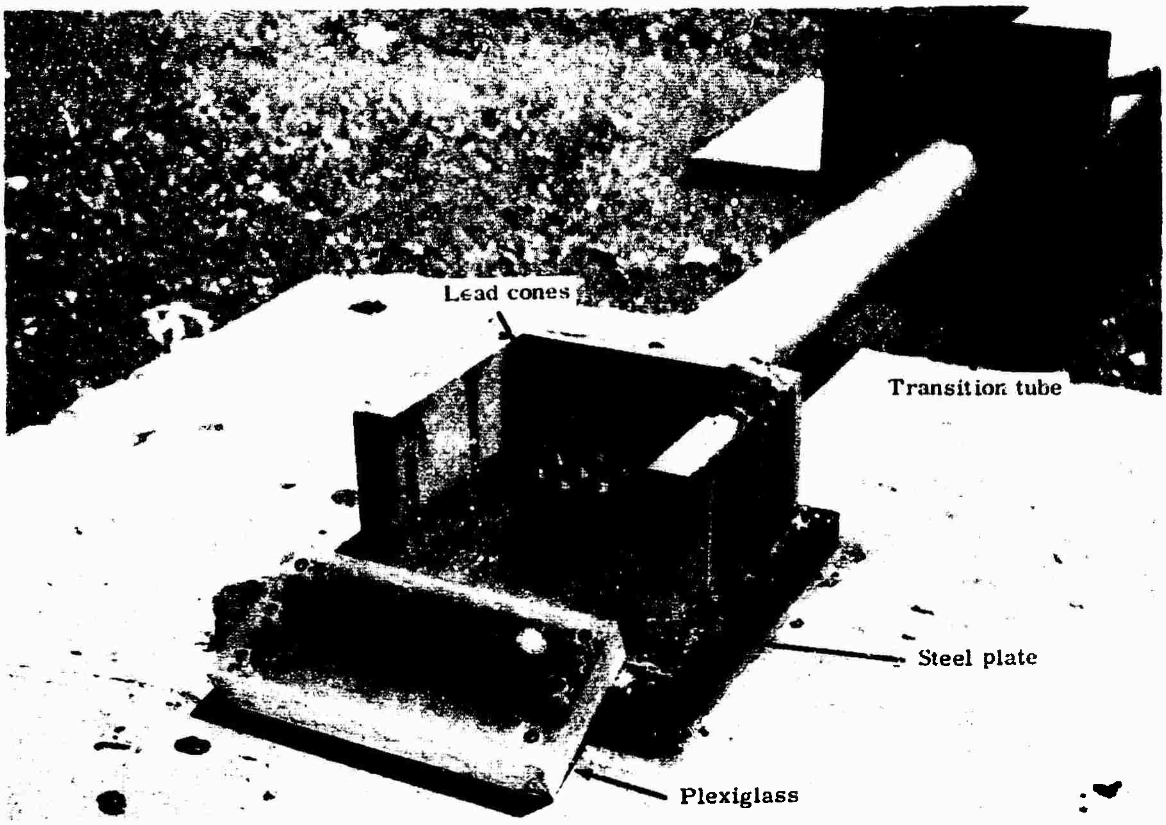

Fig. 9 - View of opened impact chamber

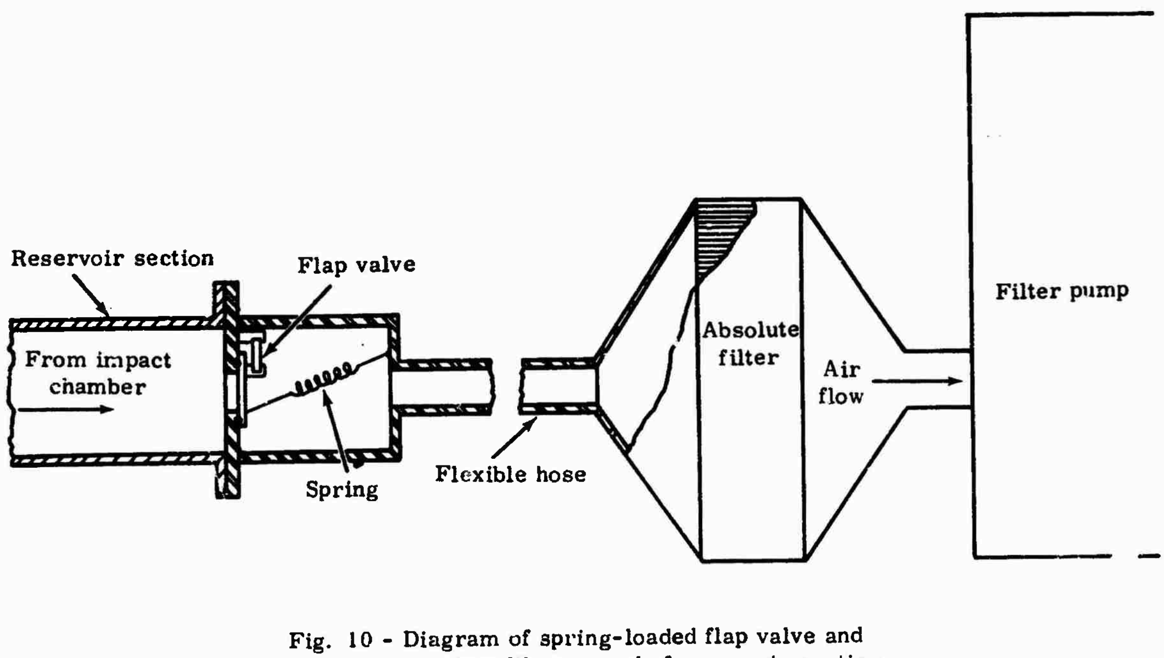

Fig. 10 - Diagram of spring-loaded flap valve and absolute filter at end of reservoir section

each test of a live fuel capsule to determine if any radioactive material had escaped from the capsule.

FACILITY CHECKOUT

The initial checkout of the VTL facility was made using the standard piston assembly fitted with the slotted fuel container and the dummy puck. Several shots were made at different differential pressures to establish a correlation between theoretical velocity and actual velocity; i. e., to determine a value for friction and other losses in the tube. At the same time, high-speed motion pictures were made to study the behavior of the dummy puck. These films indicated that the puck behaved exactly as predicted.

During transit down the tube, the puck was forced against the inside upper surface of the container. As the container crushed the lead cones, it was brought to a stop. During the short period of time that the container was at rest and before rebound started, the puck impacted against the inside bottom surface of the container. The velocity of the fuel puck at this point was the same as the velocity of the container before it hit the cones.

The calibration shots indicated that at the maximum differential pressure possible with this setup (approximately 11.5 psi), the measured velocity (155 fps) was about 89 percent of the theoretical velocity. At lower differential pressures (approximately 7.0 psi), the measured velocity (98 fps) was about 80 percent of the calculated velocity. By using Eq. (12) to determine the theoretical differential pressure for a given velocity and "correcting" that pressure by the "friction factor" appropriate to the velocity range, it was possible, in the later shots, to achieve velocities within 2 percent of the desired values.

The use of streak camera techniques also played an important part in the checkout of the VTL facility. Figure 11 is an enlargement of a portion of the streak camera film taken during one of the calibration shots. This picture shows the entry into the field of view of the fuel container and the dummy puck. The impact of the container onto the lead cones and the impact of the puck onto the inside bottom surface of the container are also shown. Figure 12 is a diagram explaining the various features shown in Figure 11.

The streak camera was used as a backup system of piston velocity measurement on all tests. This camera and the high-speed motion picture camera were excellent tools for studying the impact of the fuel pucks.

TEST RESULTS

A total of 18 shots were made in the Vacuum Tube Launcher (VTL) for this test. Seven of these were calibration shots to determine parameters of the VTL and to define the impact medium necessary to assure the required impact conditions. Five of these calibration shots used the slotted container and a plywood puck. One calibration shot used the slotted container and a ceramic puck. (This test was run to provide photographic documentation of the breakup of a fuel puck.) The final calibration shot was made using an empty welded container and was shot to achieve maximum impact velocity.

Of the other 11 shots, seven were fired to proof-test either an empty container or a container with a simulated fuel puck, and four were fired with live fuel pucks.

None of the containers showed any signs of damage after testing. There was no escape of radioactive material from a container. Reports from LASL and BMI indicated that the fuel pucks impacted as desired and broke up in an anticipated manner.

Fig. 11 - Enlargement of portion of film from streak camera

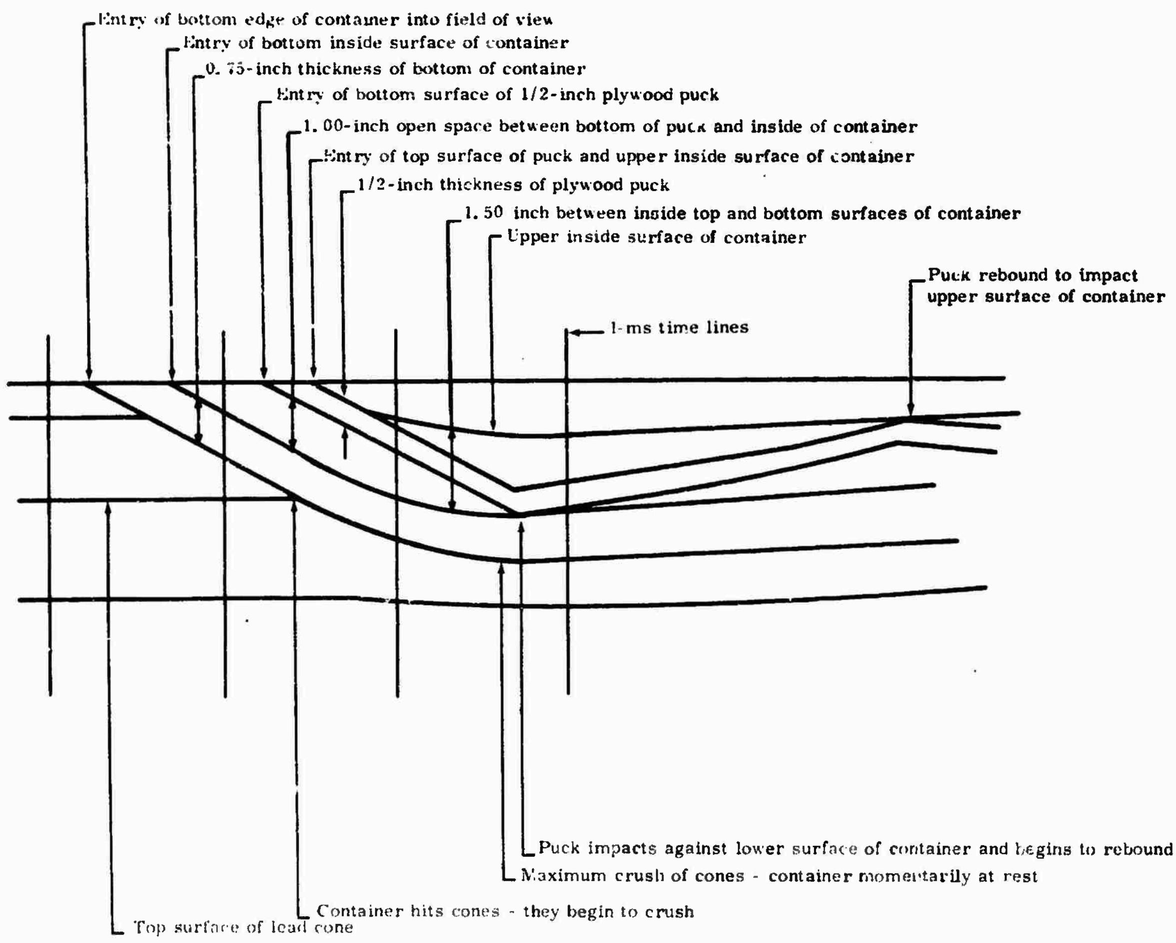

Fig. 12 - Diagram explaining features shown in Figure 11

DEVELOPMENT OF 100,000 g TEST FACILITY

Robert L. Bell
Endevco
Pasadena, California

A mechanical amplifier was built to produce high accelerations - on the order of 100,000 g - for survival testing of accelerometers. Theoretical calculations underlying the design of the facility are included. Data and results of the actual testing show reasonable agreement between experiment and theory. Absolute calibration of the apparatus has not been undertaken as yet. Accelerometers calibrated by the comparison technique at low g's have been used to indicate the output. These devices have indicated accelerations in excess of 100,000 g can be generated by the shock bar.

INTRODUCTION

Modern technology has created a need to monitor high levels of acceleration. In general, the highest accelerations are produced in shock environments. The aerospace industry with pyrotechnic explosions can and does produce acceleration pulses and ringing with a 1-10μsec rise time and peak amplitudes over 50,000 g. Because of the great expense of these activities, monitoring systems must be tested to assure reliability in survival and measurement in this environment. For this reason a feasibility study was begun in 1968 which has culminated in the creation of a test facility capable of generating in excess of 100,000 g.

The choices available for development would seem to fall mainly into the category of cannon devices. A slingshot shock machine has been used to accelerate a projectile to high velocity. The projectile then impacts a specially designed impact anvil and can produce accelerations greater than 20,000 g (1). Another group has an air gun facility which works in the same fashion as the slingshot gun, but which generates higher velocities and hence higher acceleration levels, up to 100,000 g (2). In yet another scheme, an electromagnetic field is used to propel a projectile. One problem with all these techniques is the high velocities attained. High pressures, large electrical currents, and dangers from explosions are also possible hazards to technicians. Space limitations and lack of noise isolation facilities at Endevco make an alternate technique attractive.

One approach had not been tried. Mechanical amplification of a stress wave traveling through a shock bar would allow low impact velocities to produce high accelerations. A shock bar would have the advantages of 1) no explosive potential; 2) low impact velocities; 3) a length sufficient to prevent ringing to interfere with the impact pulse. It was decided to attempt to build a shock bar with an integrable amplifier section to give an amplification of sixteen. If an impact of 10,000 g could be obtained, then a peak acceleration of 160,000 would result.

DESIGN OF THE FACILITY

The Appendix presents the theoretical argument basic to the mechanical amplifier. A model of the shock bar to be proposed was needed to experimentally support the theoretical arguments. An exponentially tapered aluminum bar 2 in.long was fabricated. It was attached by means of a 1/4-28 threaded bolt to another aluminum bar 7in. long. An accelerometer, ENDEVCO® Model 2225, was mounted on the small end of the amplifier section. A 2in. diameter steel ball was dropped from a height of three feet. The average acceleration measured was 17,000 g for four drops. Next, the amplifier section was removed and the accelerometer mounted directly on the end of the aluminum bar. The average recorded acceleration level was 8,800 g.

Theoretically, the model amplifier should have produced an amplification of four. However, the contact between the aluminum bar and the amplifier was less than perfect. Mismatches in areas and roughness of both mating surfaces could have caused considerable reflection and the apparent loss in amplification. Noting the probable causes for the failure of the model to attain better than an amplification of two, the shock bar design was begun.

Several assumptions were made concerning the impact and stress wave. From the Hopkinson bar tests we found the impact ball does not rebound to a first approximation. If we also assume that no inelastic deformations take place, then it follows that the entire energy of the impact must be traveling through the shock bar in the form of a stress wave. For reasons of simplicity and from experimental data, it was assumed that the impact would produce a half-sine compression wave. It was important that the impact would produce sufficient acceleration to allow the bar to reach 100,000 g. Therefore, a theoretical calculation was needed to help specify the parameters, e.g., material for shock bar and impact ball, needed impact velocity, cross sectional area of bar, and mass of the ball. Using the assumptions above and the conservation of energy and momentum, the appropriate differential equations can be solved.

E	=	energy associated with the stress wave
V	=	volume
T	=	stress
e	=	strain
Y	=	Young's modulus
w	=	characteristic frequency of sinusoidal stress wave
c	=	wave propagation velocity
A	=	cross sectional area of shock bar
m	=	mass of impact ball
P	=	momentum of stress wave
p^1	=	mass density of shock bar
U_o	=	impact velocity of the ball
t	=	pulse duration

The energy density of a stress wave is:

$$\frac{\partial E}{\partial V} = Te \quad . . . (1)$$

Since the stress wave has a sinusoidal shape and $T = Ye$, we have

$$\frac{\partial E}{\partial V} = Ye_o^2 \sin^2\left(\frac{wx}{c}\right) \quad . . . (2)$$

$$E = \int Ye_o^2 \sin^2\left(\frac{wx}{c}\right) dV \quad . . . . (3)$$

The area is constant so that $dV = Adx$

$$E = YAe_o^2 \int_o^{\frac{3.14c}{w}} \sin^2\left(\frac{wx}{c}\right) dx \quad . . (4)$$

$$E = \frac{YAe_o^2 c}{w}\left(1.57\right) \quad . . . . (5)$$

The energy of the stress wave must equal the energy of the impact ball.

$$1/2\ mu_o^2 = 1.57\frac{YAe_o^2 c}{w} \quad . . . . (6)$$

$$\frac{e_o^2}{w} = \frac{mu_o^2}{(3.14)YAc} \quad . . . . (7)$$

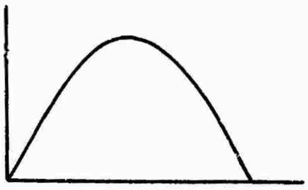

Fig. 1 - Compression Wave

The momentum density of a stress wave is:

$$\frac{\partial P}{\partial V} = p^1 \frac{du}{dt} \quad . . . . (8)$$

Since $e = \frac{1}{c}\frac{du}{dt}$ we have with Eq. (8)

$$\frac{\partial P}{\partial V} = p^1 ce \quad . . . . (9)$$

$$P = \int p^1 ce dV \quad . . . . (10)$$

$$P = p^1 cAe_o \int_o^{\frac{3.14c}{w}} \sin\left(\frac{wx}{c}\right) dx \quad . (11)$$

$$P = \frac{2p^1 Ac^2}{w} e_o \quad . . . . (12)$$

The momentum of the impact ball must be equal to the momentum in Equation (12).

$$mu_o = \frac{2p^1 Ac^2 e_o}{w} \quad . . . . (13)$$

$$\frac{e_o}{w} = \frac{mu_o}{2p^1Ac^2} \quad \ldots (14)$$

Equations (13) and (14) can be solved to give e_o and w.

$$e_o = \frac{U_o}{(1.57)c}$$

$$w = \frac{2p^1Ac}{(1.57)m} \quad \ldots (15)$$

$$t = \frac{(2.44)m}{p^1Ac}$$

The maximum acceleration is $a_{max} = wce_o$.

$$a_{max} = \frac{p^1Au_oc}{(1.22)\ m} \quad \ldots (16)$$

Acceleration doubling takes place at the end of the bar, hence

$$a_{max} = \frac{(1.64)p^1Au_oc}{m} \quad \ldots (17)$$

Equation (17) will then give the peak acceleration expected whenever the initial assumptions are satisfied and the properties of the materials, impact velocity, and impact ball mass are known. The validity of this equation was tested by applying it to a 12 foot, 3/4" diameter Hopkinson bar. The measured and known parameters are:

$p^1 = 8\ gm/cm^3$

$A = 2\ cm^2$

$c = 5 \times 10^5\ cm/sec$

$u_o = 200\ cm/sec$

$m = 250\ gm$

From Equations (15) and (17), we have:

$t = 77\mu sec$

$e_{max} = 10,000\ g$

These calculations are within 20% of the actual measured values.

The final design of the shock bar incorporated the following choices:

$p^1 = 8\ gm/cm^3$

$A = 2.85 \times 10^2\ cm^2$

$c = 5 \times 10^5\ cm/sec$

$u_o = 200\ cm/sec$

$m = 120\ lbs. = 5.45 \times 10^4\ gms$

From Equations (15) and (17) again we have:

$t = 120\mu sec$

$e_{max} = 440\mu in/in$

$a_{max} = 12000\ g$

With an amplification factor of 16 the acceleration level at the small end of the shock bar should theoretically be 190,000 g.

The actual construction of the shock bar was quite difficult. To keep the reflections small the entire bar was to be one piece. By choosing the smallest mounting area commensurate with our needs, we could arrive at the diameter for the final end of the amplifier section. This diameter would have to be multiplied by 16 to achieve the necessary amplification. The small diameter was chosen to be 3/4", meaning the large diameter would have to be 12".

The lengths of the sections of the shock bar were also important. The large diameter must continue for a reasonable length to allow the stress wave to become fairly uniform. A long amplifier section was attractive because more length meant a lower cutoff frequency and lower cutoff frequency would put more energy into the small end where the tests would be conducted. At the small diameter end the longest length possible would give a more planar uniform stress front at the test interface. In general, then, it would appear that the longest bar would be the best. However, several structural reasons exist for keeping the individual and total dimensions smaller than would otherwise be expected. If the test end were made too long, then bending strains could become very great in the horizontally hung bar. Also, if the amplifier section and/or impact section were very long, then the bar would weigh enough to make it unwieldly both to move and to adjust.

Compromise lengths of 18 in., 24 in., and 30 in. were chosen for the impact, amplifier, and test sections respectively. The total length of 6 feet would give a ring frequency of only 1.4 k Hz, if no reflections occur at the interfaces between sections. The uninterrupted pulse duration would be twice the time it would take the wave to travel the length of the bar - approximately 600μsec. This would be enough time to take the data of interest from the initial shock pulse.

The end result of the above logic is a shock bar with a diameter ranging from 12 in. to 3/4 in., 6 feet long, and weighing approximately 850 lbs. in its finished form. See Figure 2. The rough shape of the bar was forged out of 4340 steel. In testing the forging for cracks with an ultrasonic transducer a large forge burst was found in the center. A new forging was made to slightly larger dimensions and was found free of defects. Next, the new forging was machined to final dimensions. The machined part was magnafluxed and then heat treated to 220,000 psi tensile strength or 53 Rockwell C Hardness. Following the quenching, the part was again magnafluxed. The impact surface was then lapped to .0002 flatness. The mallet also went through the hardening and lapping process. Its impact surface was hardened to 180,000 psi yield strength and lapped to .0003 flatness. One hole was drilled and tapped into the side of the mallet to accept a 1/2-20 bolt, which would act as a pendulum arm.

Fig. 2 - 100,000 g Shock Bar

The superstructure was built from standard weldable pipes. The shock bar was hung by four steel cables with turnbuckles to allow adjustment of the alignment. A pendulum arm was attached to two pillow blocks which were in turn bolted to the superstructure. At the rear of the superstructure a winch was placed to pull the mallet to its drop height. The release mechanism consisted of a Ball-lok® release pin and receptacle.

The electronics consisted of a set of charge amplifiers, two band pass filters, a strain gage power supply and amplifier, a "memo" oscilloscope, and a photoelectric trigger circuit. In general, two charge amplifiers were used to monitor the output from accelerometers mounted on the impact and test ends of the shock bar. Outputs from the accelerometers were amplified, filtered, and recorded on the memoscope. The photoelectric circuit triggered when the mallet cut off the light source from a detector. The strain gages were mounted two feet from the test end. Two strain gages were used; one mounted on top and the other below. Using a full bridge circuit, the sensitivity was 10^{-3} in./in. per 10 mV. The strain gages were mounted to the bar using high temperature cement so that the heat involved in testing accelerometers at temperature would not destroy the bond between strain gage and bar.

SHOCK BAR TESTING

Certain problems exist in measuring shock motions of 100,000 g, not the least of which is keeping measuring devices in one piece. Another major problem is to keep the high g, high frequency components of the acceleration wave from ringing the accelerometer. Lastly, it is difficult to calibrate any measurement system to 100,000 g. No absolute calibration is built into the present facility. Possible means of absolute calibration exist in the techniques of interferometry and ultra-high speed photography. These techniques are being contemplated for tests in the near future, but for now the only available methods of calibration are to use calibrated accelerometers and strain gages. Strain gage output must be differentiated and multiplied by the appropriate constants to give the output acceleration.

The accelerometers used most in evaluation of the facility were ENDEVCO® preproduction prototypes, Model 2291, which had a resonance frequency of 250 k Hz and a designed dynamic range from 1,000-100,000 g. The piezoelectric material used, PIEZITE® P-10, is identical to that used in the ENDEVCO® 2225M5 accelerometers which have been tested linear to 100,000 g by Sandia Corporation. Several other types of accelerometers were used, including 2225M5's, 22[illegible]1's, 2222C's and 2270's. The nature of the acceleration wave in the shock bar causes large amplitudes in both positive and negative directions. The 2225M5 has and can successfully measure 100,000 g shocks in the positive direction, but failure in the negative direction occurs below 50,000 g when the mounting threads in the stainless steel case collapse. Also, the resonance frequency of 80 k Hz and minor resonance at 40 k Hz present problems in working with the short pulse duration. Each of the other accelerometers mentioned failed for lack of high resonant frequency and/or strength.

The 2291 weighs only 1.3 gm and mounts in a 1/4-28 threaded hole. This small weight and large thread allows the unit to survive acceleration levels well in excess of 100,000 g in both positive and negative directions. Its sensitivity is nominally .0034 pC/g. Calibration of this sensitivity was by comparison technique using the ENDEVCO® Shock Calibrator Model 2965C with drops from 1,000 g to 15,000 g. See Figure 3.

It was hoped that the output of the 100,000 g shock bar would be similar to the Hopkinson bar's, as shown in Figure 4. The actual output is pictured in Figures 5 through 10. Note that there is a very predominant ringing at about 5 k Hz in Figures 5 through 10. The shock bar had to be the source of the ringing. Other accelerometers, 2225 and 2220, were mounted on the 100,000 g shock bar and they too recorded the same 5 k Hz ring. Apparently, the amplifier section was not transmitting all of the stress wave and reflections were taking place. The specific frequency involved could be associated with several different path lengths. Large strips of butyl rubber were wrapped around the different sections and taped snugly. It was hoped the damping would be sufficient to decrease the amplitude of the ringing but not affect the pulse to any great extent. No improvement was noted in the peak pulse amplitude to ring amplitude ratio.

Fig. 3 - 2291 Accelerometer
Magnified 2.5 Times

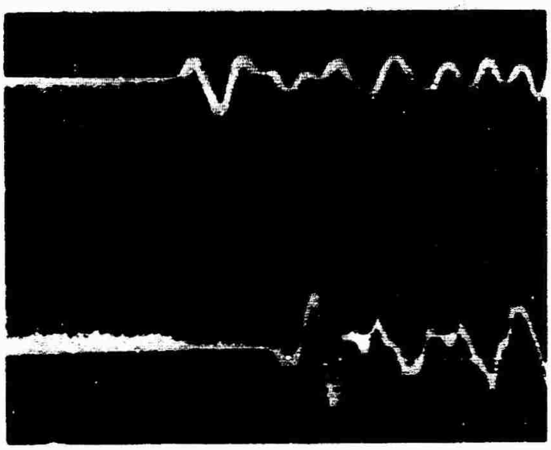

Fig. 5 - Low Level Shock Bar Output
Vertical Scale: 33,000 g/div. (Test)
4,000 g/div. (Impact)
Horizontal Scale: 200μsec/div.
Test: 33,000 g peak
Impact: 2,200 g peak

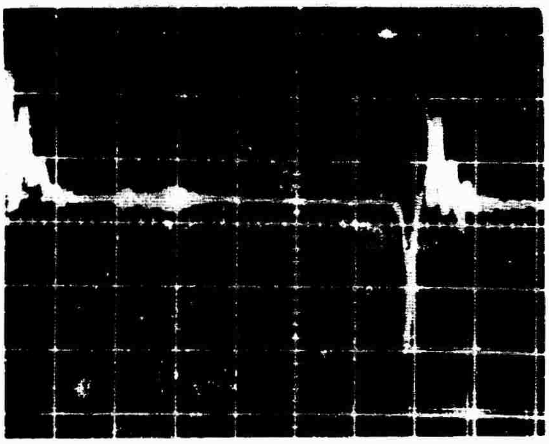

Fig. 4 - Typical Hopkinson Bar Output
Vertical Scale: 4,000 g/div.
Horizontal Scale: 200μsec/div.
9,400 g peak

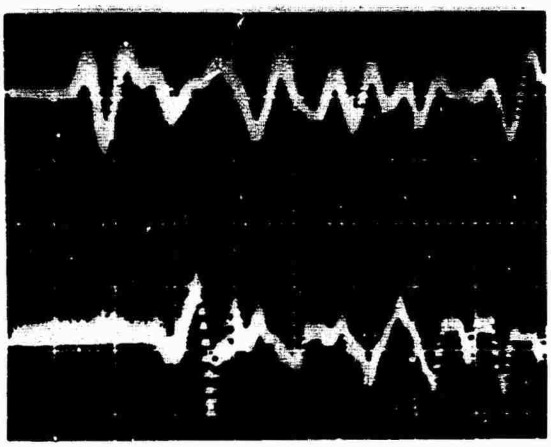

Fig. 6 - Moderate Level Shock Bar Output
Vertical Scale: 60,000 g/div. (Test)
4,000 g/div. (Impact)
Horizontal Scale: 200μsec/div.
Test: 76,000 g peak
Impact: 3,800 g peak

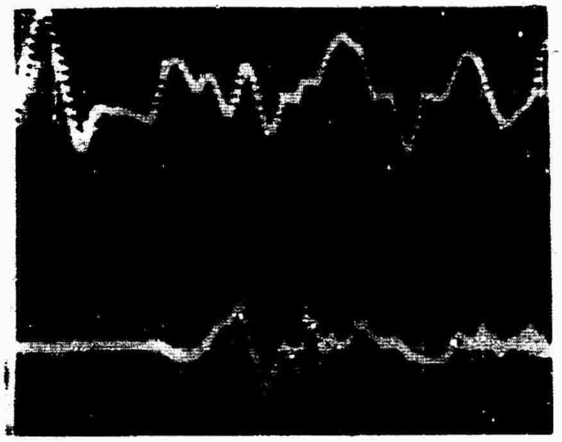

Fig. 7 - High Level Shock Bar Output
Vertical Scale: 120,000 g/div. (Test)
5,000 g/div. (Impact)
Horizontal Scale: 100μsec/div.
Test: 102,000 g peak
Impact: 6,500 g peak

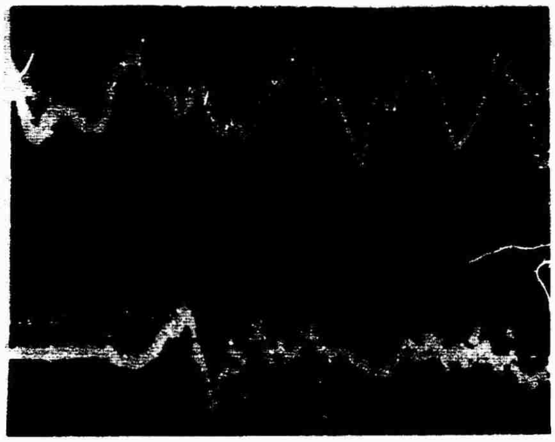

Fig. 8 - High Level Shock Bar Output
Vertical Scale: 120,000 g/div. (Test)
5,000 g/div. (Impact)
Horizontal Scale: 100μsec/div.
Test: 114,000 g peak

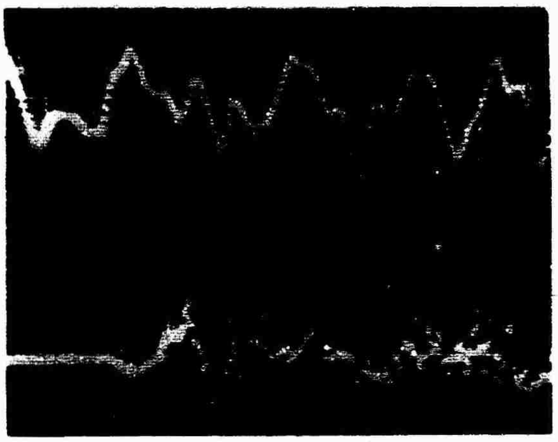

Fig. 9 - High Level Shock Bar Output
Vertical Scale: 120,000 g/div. (Test)
5,000 g/div. (Impact)
Horizontal Scale: 100μsec/div.
Test: 138,000 g peak

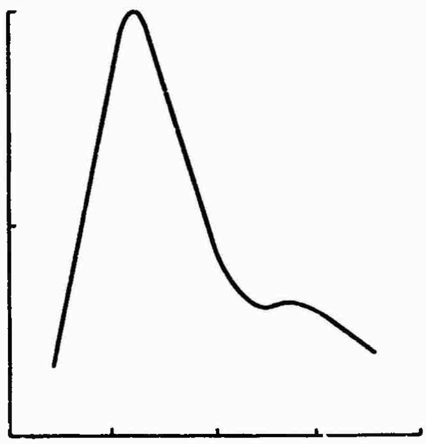

Fig. 10 - Frequency Content of Shock Bar Output
Vertical Scale: Normalized to peak of unity
Horizontal Scale: 5 k Hz/div.

The measured pulse duration is 210μ sec. There are some distinguishing characteristics of the pulse shape. Large positive and negative accelerations have been measured by the impact and test accelerometers. However, the test accelerometer shows an initial acceleration which is smaller than that which appears in the impact accelerometer output, i.e., the ratio of the initial pulse amplitude to the peak pulse amplitude varies from an extreme of 85 per cent at the impact accelerometer to 20 per cent at the test accelerometer. The time lapse between initiation of the impact and test outputs is 310μsec. In a steel bar, the compression wave should travel with a velocity of about 5,800m/sec, and, therefore, if the first output arises from a compression wave, then the time lapse should have been 315μsec. This indicates that the first pulse is a compression wave, as would be expected.

The ringing begins about 230μsec after the initial pulse begins in both the impact and test outputs. The characteristic length associated with this time interval is 134cm or 52.5 in. There is also a 16 k Hz ring superimposed on a 5 k Hz ring. The 5 k Hz may be the major resonance of a section of the bar and the 16 k Hz may be a third harmonic which is being excited by the impact. Unfortunately, none of the section lengths correspond exactly to the characteristic length. There are two possible explanations for this behavior. One is that the wave velocity is lower in some sections of the bar than in others. Another is for the reflecting surface to be located somewhere in the middle of a section.

Alignment of the impact surfaces of the shock bar and mallet was very critical and has been a major problem. The original pendulum arm was not torsionally strong enough to limit oscillations of the mallet after release. A redesign produced a much stronger arm which kept alignment for impacts producing less than 40,000 g. Refinement and strengthening of the new arm still does not allow us to produce more than 50,000 g without a misalignment resulting from each impact.

The amplitudes obtained to date have been lower than calculations predicted. The main reason for this was the decrease in impact acceleration level from increasing the mass of the impact mallet. Another major contributor to the lower performance is the dispersion in the large diameter section of the shock bar. The highest acceleration level measured using the 2291 accelerometer was 144,000 g. Most high drops, two feet, produce an output between 90,000 g and 120,000 g depending upon the specific impact.

A series of tests conducted at the 18 inch drop height produced a very repeatable output of 94,000 g with a standard deviation of only ±5 per cent. See Table I.

Table I - A Series of 100,000 g Tests Using a 2291 Accelerometer

Acceleration: Impact	Acceleration: Test
7,500 g	93,000 g
8,000 g	90,000 g
8,000 g	90,000 g
8,500 g	95,000 g
6,500 g	85,000 g
7,500 g	110,000 g
6,500 g	90,000 g
7,000 g	90,000 g
6,750 g	90,000 g
6,000 g	105,000 g

As soon as absolute methods of calibration are developed for this facility these findings will be verified more fully.

APPENDIX

The following discussion will establish a differential equation and solve it. Consider a solid horn with a cross sectional area $A=A(x)$, Young's modulus Y, density p', pressure $P=P(x)$, and displacement $u=u(x)$. Assuming axial symmetry of the cross sectional area, the force density is:

$$p' \frac{d^2u}{dt^2} = \frac{dP}{dx} \qquad \text{. . .(18)}$$

$$\frac{d^2u}{dt^2} = \frac{1}{p'} \frac{dP}{dx} \qquad \text{. . .(19)}$$

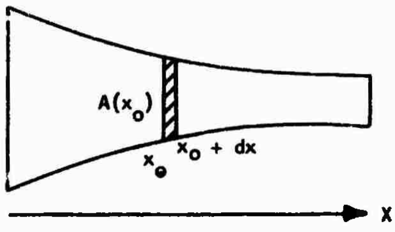

Fig. 11 - Solid, Tapered Horn

The stress at any distance x from the end of the horn is Young's modulus times the strain.

$$P(x) = Y \frac{d(Au)}{Adx} \qquad \text{. . .(20)}$$

$$\frac{dP(x)}{dx} = Y \frac{d}{dx}\left[\frac{1}{A}\frac{d(Au)}{dx}\right] \quad \text{. . .(21)}$$

Using Equations(18) and (20) and after much algebra, we get:

$$p' \frac{d^2u}{dt^2} = \frac{Y}{A}\frac{dA}{dx}\frac{du}{dx} - \frac{Y}{A^2}\left(\frac{dA}{dx}\right)^2 u + \frac{Y}{A}\frac{d^2A}{dx^2}u + Y\frac{d^2u}{dx^2} \quad \text{. . .(22)}$$

Assuming that the displacement is sinusoidal in time, rearranging terms, dividing by Y, and substituting the wave velocity, c, for $(Y/p')^{1/2}$ yield --

$$\frac{d^2u}{dx^2} + \frac{1}{A}\frac{dA}{dx}\frac{du}{dx} + \left[\frac{1}{A}\frac{d^2A}{dx^2} - \frac{1}{A^2}\left(\frac{dA}{dx}\right)^2 + \frac{w^2p'}{Y}\right]u = 0 \quad \text{. . .(23)}$$

There is no general analytical solution for Equation (23). However, for some variations of cross sectional area, Equation (23) reduces to a linear second order differential equation which can be solved. Letting the cross sectional area vary exponentially results in a simplified differential equation.

$$A(x) = A_o \exp\left[-Gx\right] \quad \text{. . .(24)}$$

Equations (23) and (24) yield

$$\frac{d^2u}{dx^2} - G\frac{du}{dx} + \frac{w^2}{c^2}u = 0 \quad \text{. . .(25)}$$

Differentiating Equation (25) with respect to time and interchanging differential operators since the solution will be separable, we get:

$$\frac{d^2u'}{dx^2} - G\frac{du'}{dx} + \frac{w^2}{c^2}u' = 0 \quad \text{. . .(26)}$$

where $u' \equiv \frac{du}{dt}$

Assuming a solution of the form $u' = u_o' \exp\left[(ia + b)x\right]$, substituting into Equation (26), and doing some algebra, gives:

$$ia + b = \frac{G}{2} \pm \left[\left(\frac{G}{2}\right)^2 - \left(\frac{w}{c}\right)^2\right]^{1/2}, \quad u' \neq 0 \quad \text{. . .(27)}$$

If we require the solution to be sinusoidal with respect to x, the term under the square root must be negative.

$$\left.\begin{aligned} a &= \pm\left[\left(\frac{w}{c}\right)^2 - \left(\frac{G}{2}\right)^2\right]^{1/2} \\ b &= \left(G/2\right) \end{aligned}\right\} \quad \text{. . .(28)}$$

We will designate $\left[\left(\frac{w}{c}\right)^2 - \left(\frac{G}{2}\right)^2\right]^{1/2}$ as Q. Then the solution u'(x) can be written:

$$u'(x) = \exp\left[Gx/2\right]\left\{A_1 \exp\left[iQx\right] + A_2 \exp\left[-iQx\right]\right\} \quad \text{. . .(29)}$$

For a traveling wave u' = iwu and the stress, T, is

$$T(x) = \frac{iY}{w}\frac{du'}{dx} \quad \text{. . .(30)}$$

$$T(x) = \frac{iY}{w}\exp\left[Gx/2\right]\left\{\left[\frac{G}{2} + Q\right]A_1 \exp\left[iQx\right] + \left[\frac{G}{2} - Q\right]A_2 \exp\left[-iQx\right]\right\} \quad \text{. . .(31)}$$

At x = 0, the stress is zero, hence

$$A_1 = \frac{iQ - \left(\frac{G}{2}\right)}{iQ + \left(\frac{G}{2}\right)} A_2 \quad \text{. . .(32)}$$

$$T(x) = \frac{2iY}{w} A_2 \left\{\frac{G}{2} - iQ\right\}\left\{\exp\left[Gx/2\right] \sin\left[Qx\right]\right\} \quad \text{. . .(33)}$$

The result of tapering the horn is shown by Equation (33). There is an amplification of the stress by the factor $\exp\left[Gx/2\right]$ for frequencies greater than $\left(\frac{Gc}{12.6}\right)$. Those frequencies below this cutoff frequency do not have sinusoidal wave shapes with respect to distance. Using similar reasoning, the stress can be calculated for frequencies less than cutoff.

$$T(x) = \frac{iA_1Y}{w}\left[Q + \frac{G}{2}\right]\exp\left[(Q + G/2)x\right] \times \left\{1 - \exp\left[-2Qx\right]\right\}, \text{ w less than or equal to } G/2 \quad \text{. . .(34)}$$

REFERENCES

1. J. W. Shipley, "Analysis of Problems Related to Slingshot Shock Machine High Velocity Shock Testing", JPL Technical Report 32-1342, California Institute of Technology, June, 1969.

2. Dove, R.C., Butler, R.I., Duggin, B.W. "Calibration and Evaluation of Accelerometers in the 10,000 g to 100,000 g Range", Instrument Society of America Preprint Number 17.3-1-65, Los Angeles, California, October, 1965.

BIBLIOGRAPHY

Mason, W.P. Physical Acoustics & the Properties of Solids, pp 156-166. D. Van Nostrand Company, Inc., Princeton, New Jersey, 1958.

DISCUSSION

Mr. Hughes (Naval Weapons Evaluation Facility): What is your explanation of the initial negative output from your accelerometer, the one that looked like about 20 percent of the first high peak in the positive direction.

Mr. McWhirter (Sandia Corp.): The little dip before it goes up.

Mr. Bell: That is the initial dip that you see. In other words, you see a sine wave on the top one and it is the same thing on the lower accelerometer only for some reason the first swing is attenuated. I do not have an explanation for it.

Mr. Hughes: I might suggest you look into the possibility of using manganin wire gage or manganin foil gage as a calibration technique as opposed to your laser interferometer. It is much simpler and I think it might give you some good answers.

Mr. Bell: Do you actually think that we can calibrate this particular strain gage?

Mr. Hughes: This is not a strain gage per se; these are used for measuring solid wave propagation rise times of less than one tenth of a microsecond.

Mr. Bell: Are you talking about a pressure bar?

Mr. Hughes: It is similar to the x-cut quartz gages.

Mr. Ramboz (National Bureau of Standards): I believe that this effort into this fairyland area of 100,000 g requires more than one calibration method because you are not sure that any one method would give you the correct result. I do not think you pointed out, for example, that this particular accelerometer which you are using has something like a microvolt per g sensitivity which almost prohibits any other lower g calibration; other than up in the several-thousand-g land.

Mr. Bell: That is true, but calibrations up into the several thousand g realm are done more or less routinely these days.

Mr. Ramboz: One of the other little subtleties that does not show up immediately when you look at this very small accelerometer, which is buried within the material, is that the actual mounting interface is not as well defined as it is for an accelerometer that has a definite base. I am not quite sure where one might want to define the mechanical input to that accelerometer, and I am sure that if you mount that in different materials at these frequencies the sensitivity will be a function of the mounting material. I think a lot of attention will have to be paid to the nature of the tapped hole and the interface.

Mr. Bell: I do not really agree with this but that is something we cannot correlate or discuss at this time. Maybe at some later time we can discuss that more fully.

Mr. Ramboz: I have some comments on your oscillograms. I noticed fairly wide traces compared to the pulse amplitude. Was there any reason why you did not run the scope gain up enough to obtain the resolution you needed to look at this better?

Mr. Bell: That was the best Memoscope we had. We did not open up the camera and just let one trace go by. That is a Memoscope reproduction of it and we just took pictures at our leisure. When one uses the Memoscope one obtains wider traces because the screen widens them.

Mr. Ramboz: What kind of noise levels did you obtain prior to impact?

Mr. Bell: You mean if you just trigger the scope and measure the noise level?

Mr. Ramboz: Yes.

Mr. Bell: Just the width of the line.

Mr. Ramboz: I estimated that to be something like 10,000 g's.

Mr. Bell: Yes, 10 percent.

Mr. Carpenter (Goodyear Aerospace): I was curious whether you used the one accelerometer for repetitive testing, and about the little blips on the first peak. Have you investigated the air gap which is left after you mount your accelerometer? That is, you do not have a continuous rod at the end now. You have an air gap which you must now traverse in both directions which would affect the acceleration on the end of that rod.

Mr. Bell: In other words, when you put the accelerometer in there, is there some distance to the end of the tapped hole that is not filled up, and how does this affect the calculations?

No, the actual percentage area taken out by that hole is rather small, and I do not think it makes much difference in the calculations, although that could be a partial cause for a few of these problems.

Mr. Matteson (Naval Ordnance Lab.): Are you familiar with the VHG tester that recently has been developed at the Naval Ordnance Laboratory?

Mr. Bell: No.

Mr. Matteson: It is a pressurized system where a piston is fired into an anvil thereby inducing high acceleration levels, and one of our big problems is recording the accelerations because we have reached a point where the accelerometer disintegrates at about 160 or 170 thousand g's, and we cannot record any higher than that unless we protect the accelerometer mechanically.

Mr. Bell: What kind of accelerometer are you using?

Mr. Matteson: It is a crystal type--I am not sure of the number--but it is a very high frequency type--Endevco, I am sure.

Mr. Bell: That is good, but I am skeptical that any products currently on the market would take acceleration levels like that in both positive and negative directions.

ON THE INTERPRETATION AND APPLICATION OF SHOCK TEST RESULTS IN ENGINEERING DESIGNS

Chi-Hung Mok
General Electric Company
Philadelphia, Pennsylvania

A theoretical study of the characteristics of a shock spectrum which is measured in a shock test of equipment is presented. For this purpose, the machine and the equipment are represented by two systems connected in series; an upper and a lower bound of the spectrum of the shock motion at the interface of the two systems are found using the Fourier transform and impedance method. The spectrum is shown to be affected by the characteristics of both systems. It is demonstrated that in a system containing negligible damping, hills would occur in the spectrum at the resonant frequencies of the combined system whereas valleys (spectrum dips) would appear in the neighborhood of the fixed-base resonant frequencies of the equipment. The possible effects of damping and of the variation in the characteristics of the system on the phenomenon are also discussed. The results support, at least in the case of systems with low damping, the current design practice of the Navy in which an envelope of a group of the dips of measured spectra is used in creating a design spectra for similar equipment. The analysis developed here would also be useful in understanding the behavior of vibration absorber and other shock phenomena.

INTRODUCTION

In the design of equipment or buildings which are subject to shock loading, analyses can be performed easily using normal mode theory and shock spectrum [1, 2, 3]. A shock spectrum is a plot of displacement or velocity amplitudes at various frequencies and can be interpreted as the maximum absolute values of the relative displacement or velocity generated by the shock load in a set of massless-single-degree-freedom systems of various natural frequencies. Once the magnitudes of shock spectrum are specified at the fixed-base resonant frequencies of the equipment, the extreme response at any position of the equipment can be estimated by combining the contributions from all normal modes which are weighted according to the shock spectrum values at the natural frequencies. This design practice is very simple to use. Nevertheless, the difficulty lies in the specification of the shock spectrum. Since a shock motion is always transmitted into an equipment through another medium which usually has finite impedance compared to that of the equipment, the form of the shock spectrum would depend on the characteristics of both the foundation and the equipment. The spectrum for design purposes, therefore, must be obtained in the field under conditions which, however, do not exist until the equipment is designed. One of the methods being employed in the U.S. Naval Research Laboratory to overcome this difficulty is to perform shock tests on structures similar to those to be designed [4]. In each test the motion of the interface between the equipment and the test is measured, and a shock spectrum is derived from it. The spectra from several tests are then put together in one graph, and an envelope of these spectra is chosen as the spectrum for design which is usually called the design spectrum to be distinguished from the test shock spectra. Since the upper envelope represents the worst possible conditions, the practice of using it for design purposes would seem to be a logical one if the Navy's research workers had not found that the practice often leads to extremely over-conservative designs. In searching for an explanation, O'Hara [5], has shown experimentally that a valley often occurs in the test shock spectrum in the frequency range close to a fixed-base resonant frequency of the structure being tested. Since only those magnitudes of the shock spectrum which correspond to the fixed-base resonant frequencies of the equipment are needed for the design of the structure, the use of the upper envelope of test spectra, which tends to pass through all the peaks rather than the dips of the spectra, would undoubtedly lead to an over-conservative design. Accordingly, they have suggested that the lower instead of the upper envelope of the test spectra should be used for design.

O'Hara, Blake, and Belsheim attributed the test-spectrum dip at the fixed-base resonant frequencies to the interaction between the equipment and the test machine in view of the fact that the relation between a testing machine and an equipment is very similar to the one existing between a vibrating machine and its shock absorber. They have attempted to show, theoretically, the existence of the spectrum dip [6,7,8] . Nevertheless, their arguments do not appear to be sufficiently explicit and physical intuition is needed to understand them. This paper is intended to present another theoretical approach which is able to show the spectrum dip directly from the basic characteristics of the transfer function of a testing-machine-equipment system. Recently, Cunniff and Collins made numerical studies of the phenomenon in a system of several degrees of freedom [9]. Their results are in agreement with these of this study obtained for the most general "machine-equipment" system.

In the following sections, the characteristics of the transfer function of two systems connected in series will be studied first. A lower and an upper bound are then obtained, and the results are used to explain the spectrum dip phenomenon in shock testing. The possible effect of the damping of the equipment and of the machine on the shock spectrum are also discussed. Finally, a numerical example using a two-degree freedom model is presented to demonstrate the general theoretical conclusions.

TRANSFER FUNCTION OF TWO SYSTEM IN SERIES

In studying the mechanics of shock testing, the equipment specimen and testing machine in a shock test* can be considered simply as two systems connected in series (Figure 1), and a shock load $\ell(t)$ is transmitted through one of the systems, namely, the machine into the other, the specimen, or the equipment in designers' language. The motion at the interface of the two systems is usually measured during a test, and shock spectrum is then derived from it by obtaining the maximum absolute value of the following integral for various frequencies, ω_n:

$$\delta(t, \omega_n) = \frac{1}{\omega_n} \int_0^t a_2(t') \sin \omega_n (t - t')\, dt', \qquad (1)$$

*The same evaluation is applicable to a piece of equipment attached to a supporting structure rather than testing machine.

where $a_2(t')$ is the acceleration at the interface point 2 or 3 in Figure 1. Instead of acceleration shock spectrum can also be defined in terms of velocity or other parameters representing the shock load [10]. Nevertheless, spectra derived based on these various definitions can be mutually related; thus the discussion presented here will apply equally well to shock spectrum defined otherwise.

If the mechanical impedances of both systems, namely, the equipment and the machine are known, the Fourier transform of the acceleration at the interface, i.e., $a_2(t)$, in (1) can be predicted from that of the input load at point 1 [11]; i.e.,

$$A_2(p) = T_{21}(p)\, L_1(p) \quad . \qquad (2)$$

In this equation as well as in the rest of the paper, the functions denoted by capitalized letters are the Fourier transforms or spectra of the functions represented by the lower case of the same letters; thus, A_2 and L_1 are corresponding to a_2 and l_1, respectively:

$$A_2(p) = \int_0^\infty a_2(t)\, e^{-pt}\, dt \quad , \qquad (3)$$

$$a_2(t) = \frac{1}{2\pi j} \int_{-j\infty}^{j\infty} A_2(p)\, e^{pt}\, dp \quad . \qquad (4)$$

Accordingly, the Fourier transforms are functions of a purely imaginary variable, $p = j\omega$, where ω, a real quantity, is the frequency. L_1 in (2) is the shock load at point 1 and can be the velocity or other parameters; T_{21} is usually called a transfer function and is a function of the impedance of the two systems.

For any system, four components of the inverse of the mechanical impedance, i.e., mobility can be defined between two points, say, 1 and 2 in the systems. The first component, M_{11} is the ratio of the velocity to the force at point 1 when a sinusoidal force is applied at point 1 and when point 2 is free of constraint.

$$M_{11} = \left. \frac{V_1}{F_1} \right|_{F_2 = 0} \quad . \qquad (5)$$

The other three components are similarly defined as follows:

$$M_{22} = \left.\frac{V_2}{F_2}\right|_{F_1 = 0} \quad ; \qquad (6)$$

$$M_{12} = \left.\frac{V_1}{F_2}\right|_{F_1 = 0} \quad ; \qquad (7)$$

$$M_{21} = \left.\frac{V_2}{F_1}\right|_{F_2 = 0} \quad . \qquad (8)$$

Equations (5) to (8) lead to the following relations between the velocity and force at two points of a system:

$$V_1 = F_1 M_{11} + F_2 M_{12} \quad , \qquad (9)$$

$$V_2 = F_1 M_{21} + F_2 M_{22} \quad . \qquad (10)$$

The velocity of a linear system to a sinusoidal force input,

$$F = F_o e^{pt} \quad , \qquad (11)$$

can be written as

$$V = V_o e^{pt} \quad , \qquad (12)$$

where F_o and V_o are amplitudes at $t = 0$. For a realistic system, where the response is governed by equations having real coefficients, V_o should be a real function of F_o and p; thus the mobility components of such a system are always real functions of the frequency variable p. Moreover, the mobility components M_{12} and M_{21} should be equal for a bilateral system in which a force can be transmitted equally well in both directions, namely, from 1 to 2 and from 2 to 1.

Since a Fourier spectrum of a shock is essentially the amplitude of its sinusoidal components, the mobilities can also be used to relate the Fourier spectra of the velocity response and of the input shock load. Consequently, the T_{21} in (2) should be a function of the mobilities of the two connecting systems. Using the definitions in (5) to (8) and the relation between the Fourier integrals of velocity and acceleration, i.e.,

$$A = pV, \qquad (13)$$

the transfer function T_{21} can be found; i.e.,

$$T_{21} = \frac{pM_{12} M_{33}}{M_{11} M_{33} - M_{12}^2 + M_{11} M_{22}} \qquad (14)$$

for a velocity input at location 1, and

$$T_{21} = \frac{pM_{12} M_{33}}{M_{22} + M_{33}} \qquad (15)$$

for a force input. In (14) and (15), the mobility components M_{11}, M_{12}, ..., etc. are defined when the two connecting systems are independent of each other. The transfer function T_{21} also possesses the property of reciprocity or of symmetry, i.e., $T_{12} = T_{21}$, as a result of the same property of M_{12} and M_{34}. If the machine is infinitely rigid compared to the equipment, i.e. $M_{33} \to \infty$, equations (14) and (15) will reduce to the following forms:

$$T_{21} = \frac{pM_{12}}{M_{11}} \quad , \qquad (16)$$

and

$$T_{21} = pM_{12} \quad . \qquad (17)$$

Therefore, in these cases (when the machine is much more rigid than the equipment), the output of the testing machine is not affected by the characteristics of the equipment but only by the properties of the machine, i.e., M_{11} and M_{12}, as one would have expected. Nevertheless, the situation, $M_{33} \to \infty$, would occur only at a few frequencies; for most frequencies, M_{33} is finite and may even be equal to zero at the fixed-base resonant frequencies of the equipment, as will be shown later in this paper. Therefore, the interaction between machine and equipment is always present in shock and vibration testing.

When the exact mass-spring-dash-pot representation of the connecting systems I and II is known, the transfer function T_{21} can be expanded further and expressed completely in terms of the frequency ω, the mass m, the spring constants k and the damping coefficient c [11]. As an example, the transfer function for a two-degree-freedom system shown in Figure 2 has the following mobility components:

$$M_{11} = \frac{c_2 + [c_2^2 - k_2 (pm_2 + k_2/p)/p]/pm_2}{c_2^2 - (k_2/p)^2} \quad ; \qquad (18)$$

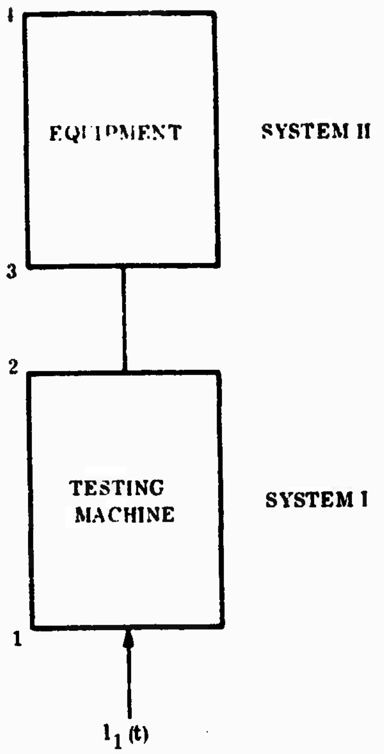

Figure 1. Schematic Representation of Shock Testing

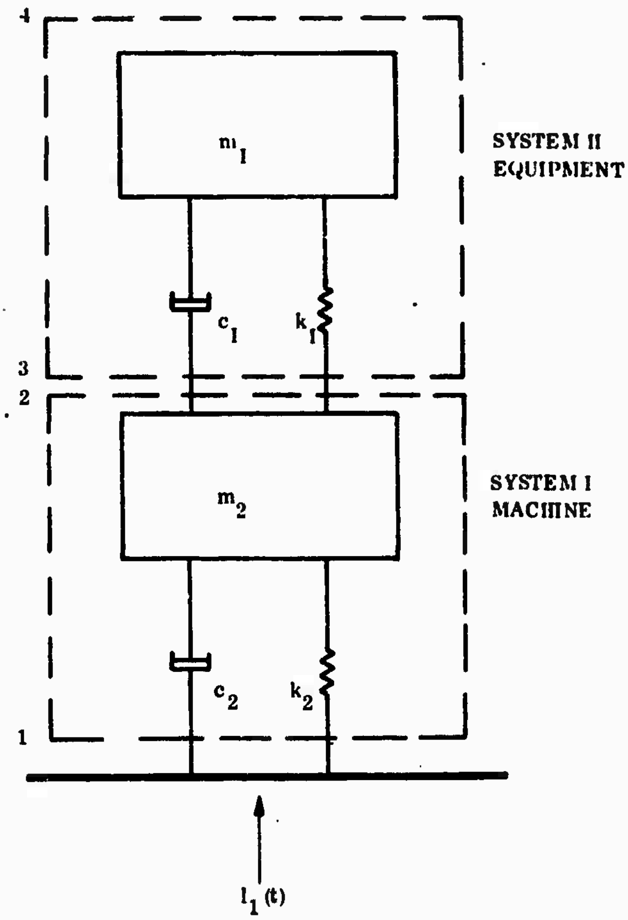

Figure 2. Two-Degree-Freedom Representation of Shock Test Arrangements

$$M_{12} = M_{22} = \frac{1}{pm_2} \quad ; \tag{19}$$

and M_{33} is also given by the right-hand side of (18) if the subscript 2 of k, c and m is replaced by 1. Using this information, the transfer function in (14) for a velocity-forcing function can be derived; denoting

$$\alpha = (k_1/m_1)^{1/2} \quad , \quad \beta = (k_2/m_2)^{1/2} \quad , \tag{20}$$

$$\mu = m_1/m_2 \quad , \quad \zeta_2 = c_2/2\beta m_2 \quad ; \tag{21}$$

the transfer function for the case where $c_1 = 0$ but $c_2 \neq 0$ is

$$T_{21} = \frac{2\beta\zeta_2\,(p + \beta/2\zeta_2)\,(p^2 + \alpha^2)p}{p^4 + 2\beta\zeta_2 p^3 + [\beta^2 + (1+\mu)\,\alpha^2]\,p^2 + 2\beta\alpha^2\zeta_2 p + \alpha^2\beta^2} \; . \tag{22}$$

Similarly, the transfer function for the reverse case, i.e., $c_2 = 0$ but $c_1 \neq 0$ is

$$T_{21} = \frac{\beta^2(p^2 + 2\alpha\zeta_1 p + \alpha^2)p}{p^4 + 2\alpha\zeta_1(1+\mu)p^3 + [\beta^2 + (1+\mu)\alpha^2]p^2 + 2\alpha\zeta_1\beta^2 p + \alpha^2\beta^2} \tag{23}$$

where ζ_1 is equal to $c_1/2\,\alpha\, m_1$. For the undamped case, when $\zeta_1 = 0$ and $\zeta_2 = 0$, both transfer functions in (22) and (23) should reduce to the same form.

ZEROS AND POLES OF TRANSFER FUNCTION

It is noted in (22) and (23) that the transfer function T_{21} is a quotient of two real polynomials of p. This is just a direct consequence of the fact that all the mechanical mobilities of a realistic system are real functions of p. The real polynomials possess real and complex conjugate roots. Those of the numerator are the zeros while those of the denominator are the poles of the transfer function. As in an electrical system [12], it can be shown that all the zeros and poles have either zero or negative real parts if the system is a stable one. These general properties can be observed in the results for the two-degree-freedom system. The transfer function in (23) has two zeros at

$$z_{1,2} = -\alpha\zeta_1 \pm j\alpha\left(1-\zeta_1^2\right)^{1/2}$$

$$= -\omega_1\zeta_1 \pm j\omega_1\left(1-\zeta_1^2\right)^{1/2} \quad , \tag{24}$$

and four poles at

$$p_{1,2} = \frac{\alpha\zeta_1\left[\beta^2 - (1+\mu)\omega_2^2\right]}{\omega_2^2 - \omega_3^2}$$

$$\pm j\omega_2\left\{1 - \frac{\alpha^2\zeta_1^2\left[\beta^2-(1+\mu)\omega_2^2\right]^2}{\omega_2^2\left(\omega_2^2-\omega_3^2\right)^2}\right\}^{1/2} , \tag{25}$$

$$p_{3,4} = -\frac{\alpha\zeta_1\left[\beta^2 - (1+\mu)\omega_3^2\right]}{\omega_2^2 - \omega_3^2}$$

$$\pm j\omega_2\left\{1 - \frac{\alpha^2\zeta_1^2\left[\beta^2-(1+\mu)\omega_3^2\right]^2}{\omega_3^2\left(\omega_2^2-\omega_3^2\right)^2}\right\}^{1/2} . \tag{26}$$

In these equations,

$$\omega_1 = \alpha \quad , \tag{27}$$

$$\omega_{2,3}^2 = \frac{1}{2}\left[\beta^2 + (1+\mu)\alpha^2\right]$$

$$\mp \frac{1}{2}\left\{\left[\beta^2 + (1+\mu)\alpha^2\right]^2 - 4\alpha^2\beta^2\right\}^{1/2} . \tag{28}$$

Letting the damping ζ_1 approach zero, the results in (24) to (26) will reduce to the following:

$$z_{1,2} = \pm j\omega_1 \quad , \tag{29}$$

$$p_{1,2} = \pm j\omega_2 \quad , \tag{30}$$

$$p_{3,4} = \pm j\omega_3 \quad . \tag{31}$$

ω_1 is the undamped fixed-base resonant frequency of the equipment system II, while ω_2 and ω_3 are those of the combined equipment-machine system [13] . Thus, (29) to (31) state that when damping is not present, the resonant frequency of the equipment is a zero, while that of the whole machine-equipment system is a pole of the transfer function T_{21}. As shown in the following paragraphs, this conclusion also holds for any two linear bilateral systems connected in series.

Considering that the system II in Figure 1, i.e., the equipment is fixed at its base position 3, and a sinusoidal force is applied to point 4, the ratio of the driving force to the velocity response at point 4 can be found using (9) and (10); i.e.,

$$\frac{F_4}{V_4} = \frac{M_{33}}{M_{33}M_{44} - M_{34}^2} \quad . \tag{32}$$

When the equipment is at resonance, the velocity response to a driving force of finite amplitude will become infinitely large:

$$\frac{F_4}{V_4} = 0 \quad , \tag{33}$$

This requires that either

$$M_{33} = 0 \quad , \tag{34}$$

or

$$\frac{1}{M_{33}M_{44} - M_{34}^2} = 0 \quad . \tag{35}$$

The latter condition leads to a trivial solution as can be seen from (9) and (10). Thus, (34) is the only condition for the occurrence of resonance in the equipment. Comparison of this equation with the expression for T_{21} in (14) and (15) shows that the roots of this equation are also the zeros of the transfer function. Therefore, the equipment will be in resonance at some of the zeros of T_{21}. Nevertheless, since the resonance so defined in (33) can only occur in an undamped system, the zeros or the roots of (34) should be purely imaginary numbers for the case of an undamped system but will be either complex or purely real numbers for a damped system. The absolute value of the zeros for an undamped case will correspond to the undamped fixed-base resonant frequencies while those of the damped case should approach, and be equal to in the limit, these frequencies when damping decreases. The relation between the zeros of transfer function T_{21} and the undamped resonant frequencies of the equipment, as demonstrated above using the two-degree-freedom system, is thus verified for the most general system.

Similar arguments can be used to demonstrate the relation between the poles of T_{21} and the resonant frequencies of the combined machine-equipment system. When the base of the machine-equipment system, i.e., point 1 shown in Figure 1, is fixed, the velocity response to a sinusoidal force applied at location 4 is

$$V_4 = \frac{M_{11}(M_{44}M_{33} - M_{34}^2) + M_{44}(M_{11}M_{22} - M_{12}^2)}{M_{11}(M_{22} + M_{33}) - M_{12}^2} F_4 \tag{36}$$

Accordingly, the conditions for resonance, i.e.,

$$F_4/V_4 = 0 \quad , \tag{37}$$

is either

$$\frac{1}{M_{11}} = 0 \quad , \tag{38}$$

or

$$\frac{1}{M_{44}} = 0 \quad , \tag{39}$$

or

$$M_{11}(M_{22} + M_{33}) - M_{12}^2 = 0 \quad , \tag{40}$$

after excluding the trivial conditions which are similar to the one in (35). As it is evident in the form, the first two conditions are associated with the resonance either of the equipment or of the machine alone. The third condition is thus the only one governing the resonance of the combined machine-equipment system; its roots, which are also the poles of the transfer function T_{21} in (14), are therefore related to the undamped fixed-base resonant frequencies of the whole system in the same manner as just discussed for the zeros. Similarly, one can also show that the poles of the transfer function T_{21} in (15) are related to the free-base resonant frequencies of the whole system. Accordingly, the transfer function can be written in a general form,

$$T_{21} = \frac{N(p)\ (p-z_1)\ (p-z_2)\ldots\ldots(p-z_m)}{D(p)\ (p-p_1)\ (p-p_2)\ldots\ldots(p-p_n)} \quad , \tag{41}$$

where $N(p)$ and $D(p)$ are polynomials of p; $z_1, \ldots, z_m$ are zeros related to the fixed-base resonant frequencies of the equipment, and $p_1, \ldots., p_n$ are poles related to the resonant frequencies of the combined machine-equipment system. The foregoing interesting properties of the transfer function will be utilized in the following section to study the spectrum dip phenomenon.

LOWER AND UPPER BOUNDS OF SHOCK SPECTRUM

A lower and upper bound can be found for the shock spectrum and will be sufficient for the study of the spectrum dip phenomenon. A lower bound has been given by Rubin [10] based on the facts that the shock spectrum defined in (1) is actually the maximum displacement response of a one-degree-freedom system subject to an acceleration shock, $a_2(t)$ at the base and that the maximum residual response of the system is equal to the absolute value of the Fourier spectrum of the input shock evaluated at the fixed-base resonant frequency of the one-degree-freedom system. Since the residual response consists of only the response after the input shock subsides, its maximum value can only be less than or equal to the absolute maximum of the entire response. The Fourier spectrum of the shock, therefore, furnishes a lower bound for the shock spectrum; i.e., using (2) and denoting $q = j\omega_n$

$$S_L(q) = \left|\frac{1}{q} A_2(q)\right| = \left|\frac{T_{21}(q)}{q}\right| \; |V_1(q)| \leq S(q). \quad (42)$$

An upper bound of the shock spectrum can be obtained by taking the Fourier transform of (1); thus,

$$\Delta(p,q) = A_2(p) \frac{1}{p^2 - q^2} = \frac{T_{21}(p)}{p^2 - q^2} V_1(p). \quad (43)$$

Using the factorial form of the transfer function T_{21} in (41) and Heaviside's inversion formula for a factorial Fourier transform [14], the following form is obtained for the shock spectrum, in terms of the poles of the transfer function:

$$\text{Max}\,|\delta(t,q)| = \text{Max}\left|\frac{1}{2q} A_2(q)\, e^{qt} + \frac{1}{2\bar{q}} A_2(\bar{q})\, e^{\bar{q}t} + \sum_{\ell=1}^{n} \frac{T'_{21}(p_\ell)\, V_1(p_\ell)}{(p_\ell^2 - q^2)}\, e^{p_\ell t}\right| \quad (44)$$

where $q = j\omega_n$ and $\bar{q} = -j\omega_n$; p_ℓ, is a pole of the transfer function T_{21}, and

$$T'_{21} = \lim_{p \to p_\ell} [T_{21}(p)\,(p - p_\ell)]. \quad (45)$$

As a confirmation of previous discussions on the poles, the requirement for a negative real part of the pole can be clearly seen here. If any of the poles had a positive real part, the term $e^{p_\ell t}$ would increase indefinitely and the shock spectrum would have infinite value for all frequencies. Taking the absolute value of both sides of (44), an upper bound is defined for the shock spectrums; i.e.,

$$S_U(q) = S_L(q) + \sum_{\ell=1}^{n} \frac{|T'_{21}(p_\ell)|\; |V_1(p_\ell)|}{|p_\ell^2 - q^2|} \geq S(q). \quad (46)$$

It can be noted in (46) that the difference between the upper and lower bounds given here does not remain a constant but varies inversely, to a large extent, with the factor $|q - p_\ell|$ where p_ℓ is the pole of the transfer function whose magnitude is closest to the value of q. Local maximum value of $S_U - S_L$ will, therefore, tend to appear at a frequency close to a pole of the transfer function.

GENERAL CHARACTERISTICS OF SHOCK SPECTRUM

Equations (42) and (46) show that the shock spectrum at the interface depends on both the Fourier spectrum of the input shock and the transfer function. The variation of the shock spectrum with frequency, therefore, reflects the characteristics of both quantities. Since the magnitude of the transfer function would experience large variations as the frequency variable q goes through the zeros and poles of the transfer function, corresponding large variations would also appear in the shock spectrum. The amplitude of variation will be determined mainly by the relative position between the frequency variable q and its neighboring zeros and poles of the transfer function; i.e., the determining factor will be $|q - q_o|$ where q_o is a zero or pole whose value is nearest to the variable q.

When damping does not exist in the system, q, as shown in the foregoing section, will be a purely imaginary number, and thus q can be identically equal to q_o. Consequently, the shock spectrum will have an infinite magnitude when q assumes the value of one of the poles: i.e., when, for an undamped system, the frequency is at a resonant frequency of the machine-equipment system. On the other hand, the shock spectrum will have a finite and probably a near zero magnitude at one of the zeros of the transfer function T_{21}, i.e., at a fixed-base resonant frequency of the equipment. In short, for a machine-equipment system of little or no damping, the shock spectrum measured at the interface will show hills at the resonant frequencies of the whole system and valleys at the fixed-base resonant frequencies of the equipment.

When damping is present in the system, the zeros and the poles of the transfer function T_{21} will be complex numbers and thus can never be equal to the frequency variable, which is always a purely imaginary number. The minimum magnitude of $|q - q_o|$ will be different from zero and increase with increasing damping. As a result, as damping in the machine-equipment system increases, the amplitude of the hills at the resonant frequencies of the combined system will decrease while the level of the valleys (or dips) corresponding to the resonant frequencies of the equipment will be raised. Consequently, the "oscillations" in the shock spectrum might eventually disappear at a sufficiently high damping. Nevertheless, if the damping is not in the equipment, the zeros of the transfer function which correspond to the resonant frequencies of the equipment will not be affected by the damping and will remain purely imaginary quantities; thus, the magnitude of the shock spectrum at the fixed-base resonant frequencies of the equipment will stay small compared to that at the resonant frequencies of the whole system. Consequently, in this case, dips might still appear in the shock spectrum at the resonant frequencies of the equipment, even for a very high damping in the machine (or equipment-supporting structure).

The extent of the oscillations in the shock spectrum will also depend greatly on the degree of separation between the neighboring zero and pole. This can be shown by considering the change of the value of the transfer function in the neighborhood of a pole and of a zero when the distance between the pole and the zero is reduced. For a frequency q in the neighborhood of a zero z_1, the absolute value of the transfer function and, in turn, of the shock spectrum, will increase as one of the neighboring pole p_1 approaches z_1. This is due to a decrease in the value of factor $|q - p_1|$ in the denominator of the transfer function. Similarly, for a frequency in the neighborhood of a pole, the value of the shock spectrum will decrease with decreasing distance between the pole and its neighboring zeros. The effects of reducing the separation between poles and zeros on the shock spectrum is thus similar to that of increasing damping. The effects will be greater when more poles are converging simultaneously towards a zero or vice versa. All the above results can be clearly observed in the numerical example presented later in this paper.

Based on the foregoing results, one can expect that the oscillations in the shock spectrum tend to appear more distinctly in the high frequency than in the low frequency range, since the separation between a zero and a pole would probably be larger at high frequencies; i.e., the separation $|z_\ell - p_\ell|$ can be larger compared to the differences between the frequency q and the zero and between the frequency and the pole; namely, $|q - z|_{min}$ and $|q - p|_{min}$. This conclusion is, of course, arrived at with the assumption that the effects of the damping on the zeros and poles will be independent of the frequency; i.e., $|q - z_\ell|_{min}$ and $|q - p_\ell|_{min}$ will remain nearly constants for all frequencies.

NUMERICAL EXAMPLE

The two-degree-freedom representation of a machine-equipment system, depicted in Figure 2 and discussed previously, will be analysed further here in order to demonstrate numerically the foregoing results concerning shock spectrum dip. It is considered that a velocity shock of constant Fourier spectrum is transmitted through the testing machine. The transfer function is given in (22) for the system where damping exists only in the machine system, and in (23) for the case where damping exists only in the equipment. Based on this information, the bounds of the shock spectrum of the system can be obtained numerically from (42) and (46). The results for the case of a damped equipment is shown in Figure 3 for several magnitudes of damping. It can be seen that a distinct spectrum dip exists in the neighborhood of the undamped fixed-base resonant frequency of the equipment when the damping is small. However, when the damping increases, the appearance of the valley in the spectrum becomes less distinct and finally disappears completely, when ζ is at the value of 0.2. Therefore, a spectrum dip at the fixed-base resonant frequency of the equipment may not appear when the damping in the equipment being tested is very large. On the other hand, when the damping in the equipment is negligible comparing to that in the machine, spectrum dip may not disappear at large damping. This result, which was obtained using (22), is demonstrated in Figure 4.

As discussed in the foregoing section, the spectrum dip effect also depends on the separation between the poles and the zeros of the transfer function; i.e., between the resonant frequencies of the equipment and of the whole "machine-equipment" system. When the two resonant frequencies are closer together, the spectrum dip would appear less prominent provided the damping remains constant. This fact is depicted in Figure 5 for the present system. The magnitude of the quantity S_L/S_U, shown in Figure 5, is an inverse measure of the extent of the spectrum dip; i.e., the larger the magnitude of S_L/S_U, the less pronounced is the dip at the fixed-base resonant frequency of the equipment. It can be seen in the figure that this situation occurs when the resonant frequencies ω_2 and ω_3 of the whole system approach that of the equipment, namely, ω_1. For this extreme situation, the value of the shock spectrum at ω_1 can even become much higher than those at ω_2 and ω_3, i.e., $S_L/S_U > 1$. This extreme situation occurs in the case $m_1/m_2 = 0.01$ when both ω_2 and ω_3 are about equidistant from ω_1; i.e., $\omega_2/\omega_1 \approx 0.95$ and $\omega_3/\omega_1 \approx 1.05$. It is, however, noticed that this situation does not appear in the case of $m_1/m_2 = 0.1$. The reason is that in this case, when the frequencies ω_2, ω_3 simultaneously approach the frequency ω_1, they cannot approach each other closer than for the case of $m_1/m_2 = 0.01$. For the case of $m_1/m_2 = 0.1$, the maximum magnitude of S_L/S_U occurs for two occasions, i.e., when $\omega_2/\omega_1 \approx 0.834$ and $\omega_3/\omega_1 \approx 1.17$; also when $\omega_2/\omega_1 \approx 0.915$ and $\omega_3/\omega_1 \approx 1.28$. These values can be compared to the corresponding one cited above for the other case of $m_1/m_2 = 0.01$.

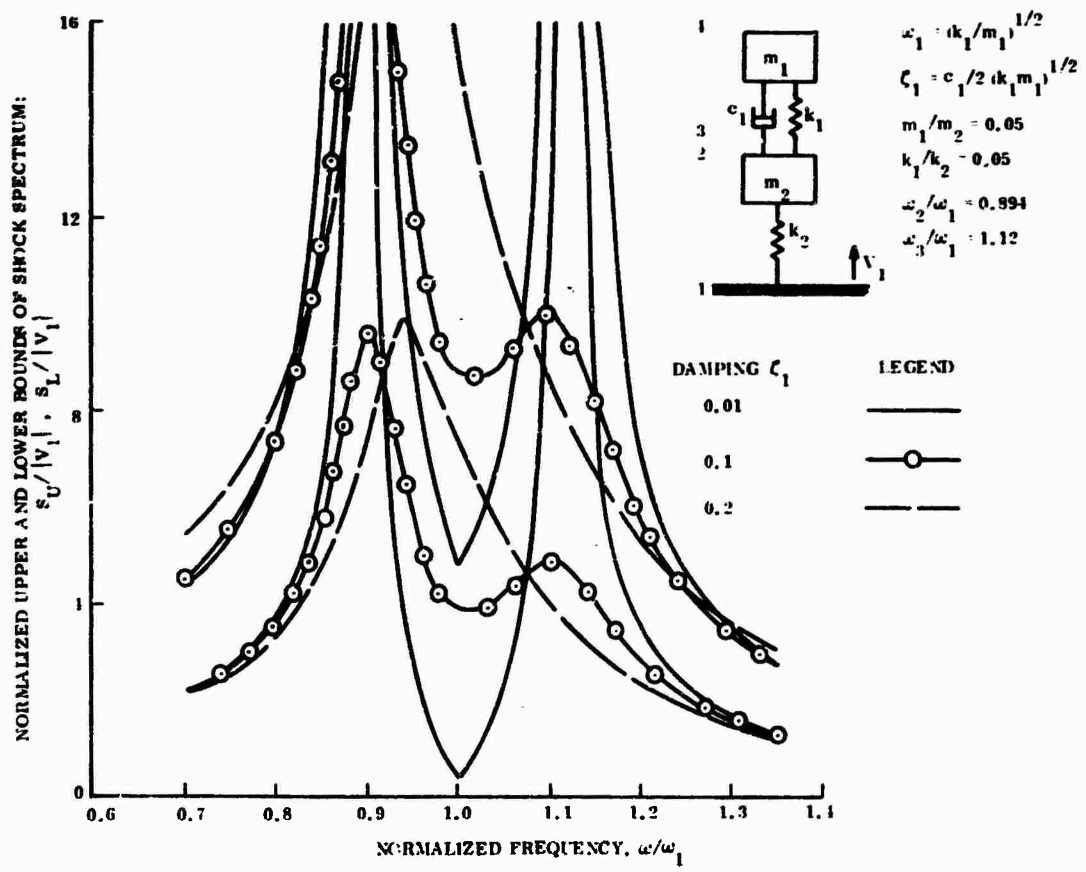

Figure 3. Effects of Equipment Damping on Upper and Lower Bounds of Shock Spectrum of Machine-Equipment System

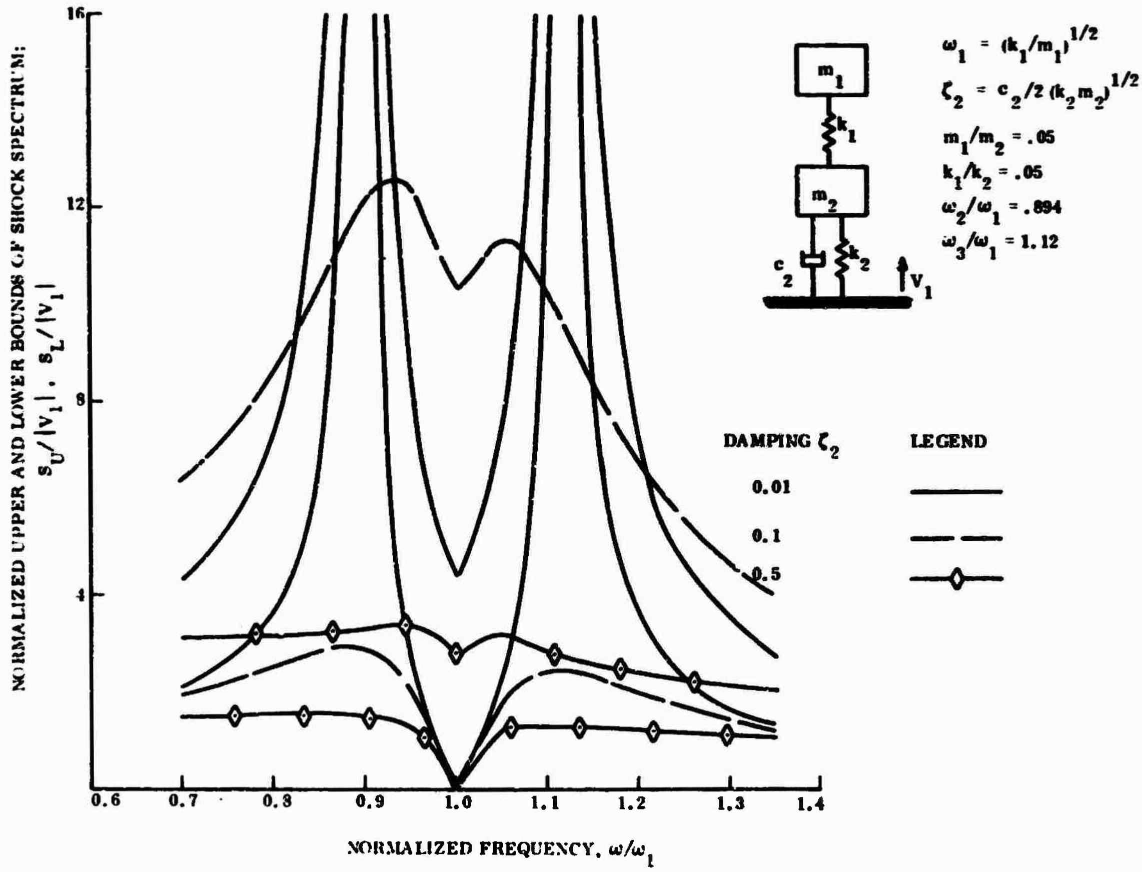

Figure 4. Effects of Machine Damping on Upper and Lower Bounds of Shock Spectrum of Machine-Equipment System

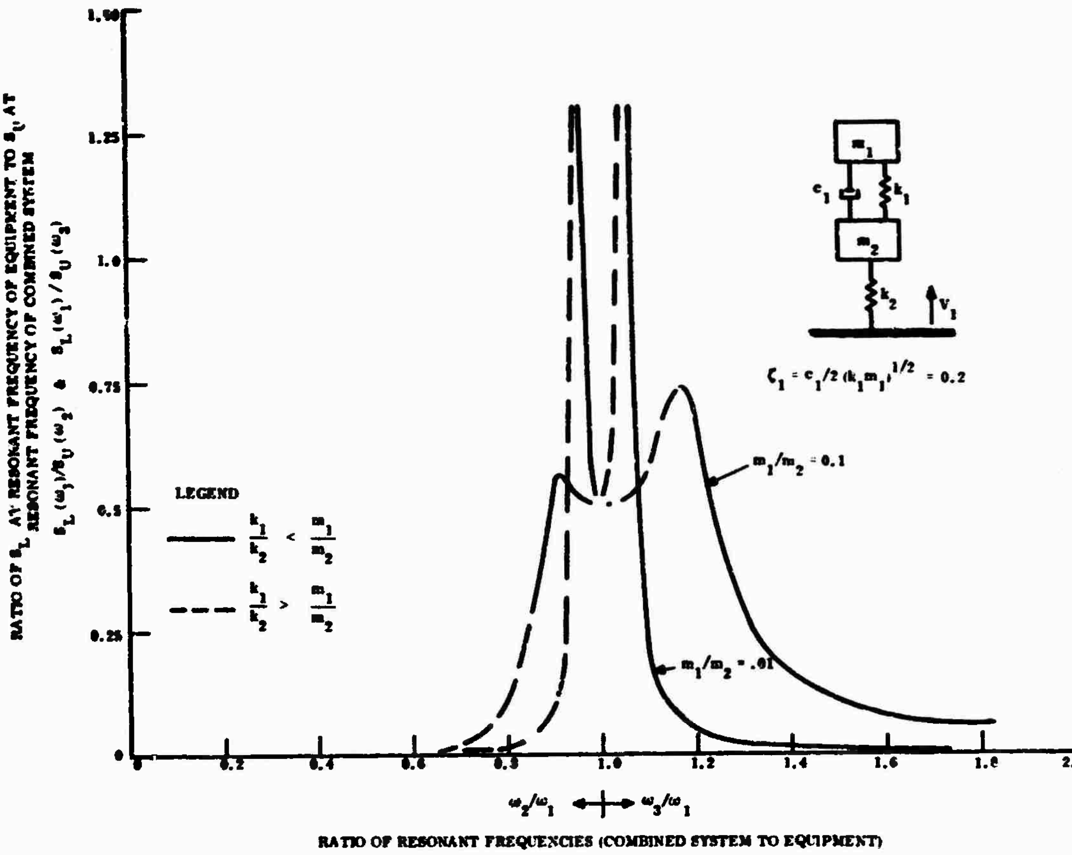

Figure 5. Effects of Separation between the Resonant Frequencies of Equipment and Machine-Equipment System on the Extent of Spectrum Dip

CONCLUSIONS

It has been shown using an impedance method that hills and valleys (peaks and dips) always appear in the shock spectrum of a shock motion which is transmitted through one linear bilateral system to another similar system of negligible damping. The valleys would appear near the fixed-base resonant natural frequencies of the "receiving" system while the hills would occur at frequencies close to the resonant frequencies of the whole system. This phenomenon is a direct result of the characteristics of the transfer function of the shock motion. The "oscillation" in the shock spectrum can be shown to decrease with increasing damping in the receiving system and with decreasing separation between the resonant frequencies of the receiving system and of the combined system.

The present results have an immediate application in the interpretation of test shock spectra for design purposes. In this case, the equipment under a shock test is the receiving system and the testing machine or supporting structure is the transmitting system. In the light of the present results, the magnitude of the shock spectrum at the fixed-base resonant frequency, which is needed for design against the input shock, are always closer to the magnitudes at valleys than at the hills of test spectrum. Consequently, in constructing a design spectrum from the test spectra of a similar system subject to similar loading, an envelope which connects the bottoms of the valleys could be used as has been suggested by O'Hara, Blake, Belsheim, et al. One of the current practices which makes use of the upper envelope passing through the peaks of the hills tends to provide an unnecessarily large margin of safety. This is particularly true according to the present results when the damping in the equipment is very small, and when the resonant frequencies of the machine are quite different from those of the equipment. The present results suggest that a design of reasonable economy and considerable margin of safety can be achieved by using an envelope which connects the dips of the shock spectra for some similar pieces of equipment that have higher damping than the equipment being designed.

ACKNOWLEDGEMENTS

The author wishes to express his special appreciation to Dr. A. L. Ross, who suggested this work and provided the author with the necessary knowledge about current design practices. The author is also indebted to A. H. Garber for encouraging this work and to L. Chaump for suggesting possible applications of this work. Thanks are also due to Dr. Stephen Ching, Associate Professor of Electrical Engineering at Villanova University, for providing necessary information concerning impedance methods, and to Mrs. R. Jones for preparing the manuscript.

REFERENCES

1. A. L. Ross, "Direct Application of Shock Spectra in Dynamic Analysis of Structures," GE, RS, Structural Mechanics Technical Memo No. 8159-018, February 1968

2. G. J. O'Hara and P. F. Cunniff, "Elements of Normal Mode Theory," U.S. Naval Research Laboratory, NRL Report 6002, November 1963

3. M. A. Biot, "Analytical and Experimental Methods in Engineering Seismology," ASCE Transaction, v. 108, p. 365, 1943

4. G. J. O'Hara, "Background for Mechanical Shock Design of Ships Systems," U.S. Naval Research Laboratory, NRL Report 6267, March 1965

5. G. J. O'Hara, "Effects Upon Shock Spectra of the Dynamic Reaction of Structures," Experimental Mechanics, v. 1, p. 145, 1961

6. G. J. O'Hara, "Impedance and Shock Spectra," J. Acoust. Soc. of Am., V. 31, p. 1300, 1959

7. G. J. O'Hara, "Shock Spectra and Design Shock Spectra," U.S. Naval Research Laboratory, NRL Report 5386, November 1959

8. R. E. Blake and R. O. Belsheim, "The Significance of Impedance in Shock and Vibration," Mechanical Impedance Method for Mechanical Vibration, edited by R. Plunkett, ASME, New York, p. 101, December 1958

9. P. F. Cunniff and R. P. Collins, "Structural Interaction Effects on Shock Spectra," J. Acoust. Soc. Am., v. 43, p. 239, 1968

10. S. Rubin, "Concept in Shock Data Analysis," Shock and Vibration Handbook, C. M. Harris and C. E. Crede (Ed.), McGraw-Hill Book Company, Inc., New York, v. 2, p. 23-1, 1961

11. E. L. Hixson, "Mechanical Impedance and Mobility," Shock and Vibration Handbook, C. M. Harris and C. E. Crede (Ed.), McGraw-Hill Book Company, Inc., New York, Vol. 1, p. 10-1, 1961

12. J. S. Bendat, Principles and Applications of Random Noise Theory, John Wiley and Sons, Inc., New York, 1958

13. F. E. Reed, "Dynamic Vibration Absorbers and Auxiliary Mass Dampers," Shock and Vibration Handbook, C. M. Harris and C. E. Crede (Ed.), McGraw-Hill Book Company, Inc., New York, Vol. 1, p. 6-1, 1961

14. Y. H. Ku, Transient Circuit Analysis, D. Van Nostrand Company, Inc., New York, 1961

METHODS OF COMPUTING STRUCTURAL RESPONSE OF HELICOPTERS TO WEAPONS' MUZZLE AND BREECH BLAST

W. E. Baker, S. Silverman, P. A. Cox, Jr., and D. Young
Southwest Research Institute*
San Antonio, Texas

In this paper, the authors consider methods of computing response of helicopter structures to muzzle and breech blast from weapons located on or near the aircraft. They review the current state of knowledge in this field and then present techniques for applying existing response analyses and for developing new analysis methods where existing ones are inadequate. Finally, they describe computer codes for prediction of response in the elastic and plastic regimes of various elements and major components of helicopter structures.

INTRODUCTION

The importance of the helicopter in tactical military operations has been demonstrated by the Vietnam war. Many of these versatile aircraft have proven to be very effective weapon platforms--so effective that several new types of helicopters are being specifically designed as helicopter gunships. Whenever a helicopter is employed as a weapons platform to mount machine guns, grenade launchers, cannon, recoilless rifles, rockets, or it functions as a prime mover for artillery which can be fired in its vicinity, the helicopter is subjected to blast waves from the muzzle or breech of weapons. These blast waves have the potential of causing significant structural damage. In arming existing helicopters which are not designed to withstand muzzle blast, one must either limit the weapons which may be carried or strengthen structural members to resist the blast. In the development of new helicopter gunships, blast effects should be considered from the outset in the design.

In order to consider the effects of muzzle and breech blast from weapons on helicopter structures, one must first define the characteristics of the blast field about all types of weapons. Although many blast measurements have been taken near various weapons, few systematic attempts have been made to predict the blast field about weapons from a knowledge of gun and ammunition characteristics. Westine [1]† has recently reviewed past efforts in this area and developed a procedure for predicting the blast field about guns in general and for making reasonable estimates of the transient load imparted to various helicopter structural components.

From a knowledge of the transient load applied to a helicopter, the response of the structure and the effects of this response on structural integrity of the aircraft can be determined. In the past, the empirical approach of mounting the weapon on a helicopter, firing it, and observing the results, has dramatically demonstrated the compatibility or lack of compatibility between a helicopter and a weapon system. The analytical approach offers another technique for establishing mathematical models to analyze the dynamic response of helicopter structural components for both elastic and plastic deformations. In the past, few attempts have been made to adopt the analytical approach to this problem because of the extreme complexity of most helicopter structures. In this paper, the applicable digital computer solutions from

*The work reported here was performed under contract to the U.S. Army Ballistics Research Laboratories.
†Numbers in brackets refer to the references at the end of this paper.

previous work have been applied to this helicopter problem and new computer solutions developed to assist in analyzing the elastic and plastic response of helicopter structural components subjected to muzzle and breech blast. The work reported here is a condensation of a comprehensive effort reported in Reference 2.

REVIEW OF PAST WORK

A comprehensive review of past studies on interaction of blast waves with structures and on response of structures and structural elements to such waves is presented in Reference 2. Only those studies which bear directly on the problem of weapons blast, loading, and response of helicopter structures will be discussed here.

Interaction of Blast Waves with Helicopters

Measurements of the actual transient loads on rotary-wing aircraft or portions of these aircraft from weapon blast are so sparse as to be almost nonexistent, and the geometry of these aircraft or their component parts is so complex that data obtained for loading of simpler structures must be applied with caution. Let us discuss such information as is available for various parts of helicopters.

If fuselages of rotary-wing aircraft could be assumed to be an assemblage of simple geometrical shapes such as cylinders and rectangular blocks, and if sources of blast energy were located reasonably far from the fuselages, then data obtained from shock-tube and field studies such as References 3 through 6 would probably prove adequate for estimation of fuselage loads. But, most rotary-wing aircraft fuselages are distressingly irregular in shape, and the sources for weapons blast loading are so close to the structure that such data will be of little use. For completeness, however, let us describe the data available in the literature.

Some portions of fuselages can be approximated by right circular cylinders. Unfortunately, the diffracted loading on such type cylinders is extremely complicated, and, therefore, all past efforts have been devoted to a cylinder oriented with its axis either parallel or perpendicular to the direction of propagation of the shock front (References 3 through 6). The most severe loading occurs for the axis perpendicular to the direction of propagation of the shock; for the axis parallel, "free-air" blast parameters will apply. Based upon the discussion contained in Reference 7, the best approach for determining the pressure distribution on the cylinder seems to be that given by Norris, et al., in Reference 5. The range of Reynolds and Mach numbers for which the simple expressions presented in Section 3.2 of Reference 5 are valid is unknown. In Reference 3, the results of some carefully performed experiments are reported. It was concluded that the computed drag coefficients, except for the initial shock-interaction phase, are of the same order of magnitude as the steady-state values obtained for comparable Reynolds and Mach numbers. This is significant in that the drag coefficients presented in Reference 5 are based upon steady-state values.

Reference 5 should be consulted for details of the blast load prediction technique. Steady-state drag coefficients must be employed since more accurate coefficients are not available. The loads computed by this technique are "overall" loads applied to the fuselage. Data and methods of prediction of transient pressures on all sides of rectangular block structures are also given in References 4 and 5.

In predicting structural response of fuselages to blast loading, we may in many cases be interested in loading small portions of the structure such as skin panels between stringers and frames, skin plus stringers between longerons and frames, windows, etc. These structural elements can be small enough that the surrounding structure acts as a reflecting surface, and diffraction effects are not important. Because the blast source may be close to the structure, such panels will usually be loaded by a blast wave which impinges on them at some changing angle of obliquity, so that the wave sweeps across, changing in intensity and duration as it does so. Data are available in quantity for the limiting cases of either normal or side-on incidence of the wave, provided one assumes that the weapons blast source is equivalent to a conventional source. Reference 8 is an excellent source for such data. Limited data are available in Reference 4 (Figure 3.71b) for the variation of reflected overpressure with a single angle of obliquity and additional data for blast from guns are presented in Reference 1.

Most rotary-wing aircraft employ small nonrotating airfoils for stability in forward flight, and some compound aircraft also utilize stub wings for lift in forward flight. These airfoil structures are usually thin enough that data for blast loading of stationary flat plates can be utilized to estimate loading from weapons blast, for certain limiting cases. If the blast source lies in the plane of the foil, then the wave will engulf the foil with little or no perturbation, and the crushing blast loading on both sides will be defined by a wave with side-on airblast parameters sweeping over the foil with the shock front velocity. If the source lies on a normal to the foil, then diffracted blast loads can be estimated with reasonable accuracy for front and rear surfaces (and also for net transverse loading) by methods described in References 4 and 9. If the aircraft is moving at a great enough forward velocity, the diffracted blast loading of nonrotating airfoils is seriously altered, as indicated in References 10 through 13. We will now discuss the data that exist for blast loading of moving airfoils.

There have been two series of investigations pertaining to blast loads normally incident on translating airfoils. In the first series [10, 11], blast-induced loads on the wing and horizontal foil of an airplane model were determined at low Mach numbers (<0.7). An important characteristic of the loading was shown to be the travel of a leading edge vortex, generated by blast loading, aft along the foil surface and a consequent time-varying lift and moment change. Subsequently, the blast-induced vortex movements about a wing in subsonic flow were investigated experimentally and theoretically in an effort to understand more completely how the blast wave interacts with the foil [12, 13]. Experimental investigations of blast-induced loading on an airfoil in Mach 0.7 airflow were conducted in References 14 and 15. Chordwise pressure time histories were measured and used to calculate lift and moment coefficients.

There has been only one reported experimental investigation of the response of a rotating helicopter rotor blade to blast loading from high explosive [16]. In an unreported experiment, O. T. Johnson, of Ballistic Research Laboratories, Aberdeen Proving Ground, Maryland, detonated a 20-lb explosive charge which was placed beneath a tethered H-21 which had its rotor blades in motion. The blast caused a blade to oscillate so violently that it collided with the helicopter fuselage. In neither of these experiments were there any attempts to measure details of loading on the moving rotor blades. It therefore appears that no data whatsoever exist on blast loads on helicopter rotors.

Response of Structures and Structural Elements

Many analyses have been developed for elastic and plastic response of relatively simple structural elements to transient loads such as those produced by muzzle blast from weapons, and a very few for response of more complex structures typical of entire airframes or large portions of airframes. Also, a number of computer codes exist for dynamic response of aerospace structural elements and structures. In addition, there are limited test results for aircraft or aircraft components subjected to blast loading, and much more extensive data on simple structural elements under such loading. We will discuss here the past unclassified work in this area.

Very few analyses have been made in the past of either elastic or plastic response of aircraft structures to blast or other transient loading. Most aircraft manufacturers do indeed perform complex dynamics analyses, generally using matrix techniques, as typified by Sciarra's paper [17] describing an analysis of the CH-46 helicopter, but these are usually limited to determination of the mode shapes and frequencies for elastic vibration and do not include computation of response to transient forces. The status of analysis methods for helicopter rotor blade response to time-varying forces is apparently typified by Reference 18, wherein the blade response is computed based on elastic flapwise bending only. Several reports deal with methods predicting elastic and post-failure response of fixed airfoils. These include Reference 19, which presents a lumped-parameter dynamic analysis, and References 20 and 21, which present a modified modal analysis.

In contrast to the paucity of work in response to transient loads of complex aircraft structures, there are many analyses of both elastic and plastic response of simple structural elements. A review of such analyses is given in Reference 2. We will cite here only two general papers, one which discusses MIT finite-difference computer codes [22] and another general discussion of analysis methods for simple structures [23].

In reviewing the literature, we found a number of solutions to problems in elastic response of rectangular plates and membranes which could represent portions of helicopter structures. These are cited in Reference 2. There were, however, very few solutions for plastic response or permanent deformation. Greenspon [21, 24] has applied membrane analysis for large deformations, as have Baker and Hoffman [25]. An analysis of the plastic bending behavior of plates by means of variational approach is also presented by Greenspon in Reference 26. Plastic deformation theory is employed (as opposed to flow theory), and the plate may be of a sandwich type or stiffened type of construction. The chief disadvantages of this approach are that a deformation pattern must be assumed, and, for other than the simplest pattern, the calculations are extremely tedious.

As compared to beams and plates, the theory for determining the dynamic response of such shells as exist in helicopters is poorly developed. The vast majority of the work deals with shells of revolution loaded axisymmetrically whereas, in practice, few helicopters components can be so idealized. The tail boom on some of the smaller helicopters is cylindrical, but often is not a shell of revolution and is of stringer/rib construction, thus hopelessly complicating the problem. Many of the helicopter components may be approximated by portions of cylindrical and spherical shells. However, the boundary conditions for these shell segments are not well defined. The outward curvature of the helicopter components dictates that dynamic buckling be considered. Unfortunately, it is well known that such buckling is extremely difficult to predict even for very idealized shell structures. Further difficulties arise in predicting the blast loading, as pointed out in Reference 1 and earlier in this paper. Since few of the papers reviewed seem appropriate, we will not discuss them here. A limited discussion is presented in Reference 2. In Reference 2 may also be found further discussion of literature on elastic and plastic response of structures. Included is a listing of computer programs which were uncovered in available references.

Experiments on Aircraft and Components, and Related Tests on Structural Elements

A number of empirical blast damage experiments have been conducted on a wide variety of aircraft, but the results of these tests are, almost without exception, classified because they relate specified levels of blast loading to vulnerability of specific military aircraft. Discussion of such tests will, therefore, not be given here. We can state here, however, that almost none of these tests were instrumented and also that the investigators were usually concerned with producing severe damage to the aircraft, rather than the relatively superficial damage which concerns us in our study of muzzle blast effects on helicopters.

Essentially all of the experimental data on dynamic response of simple structures and structural elements are unclassified. But, in contrast to the plethora of response analyses for simple elements, there are surprisingly few experiments to corroborate or negate these analyses. This may be in part due to the difficulty and expense of conducting carefully instrumented dynamic response tests.

More experimental data exist for response of blast- or impulsive-loaded beams than any other simple structural elements. Locklin and Mills [27] present data for simply-supported and cantilever beams and undergoing elastic deformation when subjected to normal blast loading. Considerable data on maximum elastic response and permanent deformation of slender cantilevers subjected to diffracted blast waves are reported by Baker, et al., [9]. A number of the papers by staff members from Brown University, notably References 28-30, report data for impulsively-loaded beams. Humphreys [31] reports some careful experiments on impulsively-loaded clamped beams, and Florence and Firth [32] give data for an extensive series of both clamped and simply-supported beams under similar loading. A number of impulsively loaded beam and ring experiments are also reported by Clark, et al., [33], and these experimental results were comparable to computer code predictions by Balmer and Witmer [34] using the MIT DEPROSS Codes. The conclusion in this last study was that the DEPROSS codes yielded predictions which were in much better agreement with experiment than rigid-plastic theories--even those rigid-plastic theories which considered strain-rate and strain-hardening effects.

We could find <u>no</u> experimental data on rectangular plates, or indeed on any plates of geometry other than circular.

In contrast to the paucity of data on blast response of plates, there exist considerable data on blast or impulsive response of shells. Most of the results are on cylindrical shells, with some on conical shells. Schuman has conducted an extensive program on blast-loaded cylindrical shells of a variety of materials and dimensions. His work is summarized in Reference 35. Abrahamson and Goodier [36] present some data on thin cylindrical shells subjected to uniform radial impulses, as do Anderson and Lindberg [37]. Results of an extensive series of blast loading tests of short cylindrical and conical shells are also given by Lindberg, et al., [6]. Baker, et al., [38] gives data on permanent deformations under impulsive loading of a wide variety of simple and composite cylinders. Finally, Baker and Westine [39] have conducted a series of experiments involving the dynamic loading, by means of spray explosive, airblast from HE, and airblast from a shock tube, of cantilever beams and cylindrical shells fabricated from a wide variety of materials. But, very few dynamic response measurements are included in these references.

Summary

Our review of the current state of knowledge regarding interaction of blast waves with aircraft structures and structural elements reveals that: one must probably rely on very approximate methods for estimating blast loading; one may have considerable difficulty choosing an appropriate analysis or computation method for simple structural elements; one cannot expect to have the chosen analysis methods corroborated by existing experimental data; and one has no acceptable techniques for computing plastic response of the entire complex aircraft structure available. Although this overall assessment is quite pessimistic, many specific subproblems in structural response can indeed be handled quite adequately with existing methods or by modification of existing methods.

In general, both elastic and plastic response of beams or beam-like structures is in the best state and can be handled with existing methods or relatively minor modifications of these methods. Most of the literature on theory of plates is confined to axisymmetric response of circular plates, and the only data for impulsively loaded or blast-loaded plates are confined to this geometry, which is seldom applicable to helicopter response problems. For rectangular plates and membranes, the response problem is somewhat more difficult, but, for elastic behavior, a number of practical problems have been solved. There is no solution for the plastic behavior of rectangular plates, except for that presented in [2].

In shell response methods, most analyses to date, including involved computer codes, treat only axisymmetric motion of shells of revolution.

We can see, therefore, that much remains to be done before one can, with confidence, predict response of helicopter structures to muzzle blast loading.

DEVELOPMENT AND APPLICATION TO HELICOPTERS OF TECHNIQUES FOR LOADING AND RESPONSE

Methods of Estimating Blast Loading

As indicated earlier in this paper, the general problem of prediction of blast loading of helicopters from weapons blast is so complex that one cannot hope to solve it completely; i.e., one cannot predict the time history of pressure at all points on the surface of the helicopter. But, for various components of the structure whose response may be critical in determining compatibility of a given weapon with a given helicopter, the loadings can perhaps be predicted with sufficient accuracy. We will now discuss techniques for estimating transient blast loads for various structural elements.

If the structural element which we are considering is a flat or slightly curved panel which constitutes a small part of a much larger surface which is subjected to the blast wave, and if the blast source is a closed-breech weapon, then the loading can probably be predicted with reasonable accuracy from the empirical data and scaling laws generated in Reference 1.

The geometry for loading of a flat panel is shown in Figure 1. A nearly spherical shock front emanates from a point A some distance r_0 ahead of the weapon muzzle and impinges on the flat surface which is a distance h beneath the muzzle. At the particular instant in time depicted in the figure, a circular area of the surface, including one corner of the panel, is loaded, and the shock has just arrived at point B on the panel. The incident shock 1 has impinged on the surface, and the reflected shock 2 has been generated by the reflection. The general character of the pressure variation is shown graphically in the figure. As the shock front expands, a circular area centered on the point C will be loaded, with the pressure at the front attenuating and the velocity of passage over the panel decreasing. The length of the pressure pulse also increases. So, one can see that, in general, the panel loading can be described as a complex nonseparable function of time and space coordinates which nearly defies analytical description. This complexity does not, however, prevent a reasonably accurate numerical description of the loading at any specific time or for any specific sequential time steps. Such description is possible, based on techniques described in Reference 1, provided the geometric parameters of Figure 1 are known and provided one knows the effective blast energy W for the weapon, the gun caliber c and the barrel length ℓ. A limitation is that the line of fire must be parallel to the panel.

For two limiting cases, the loading is relatively simple. If the panel is located directly under the point A and if the largest dimension b of the panel is much less than h,

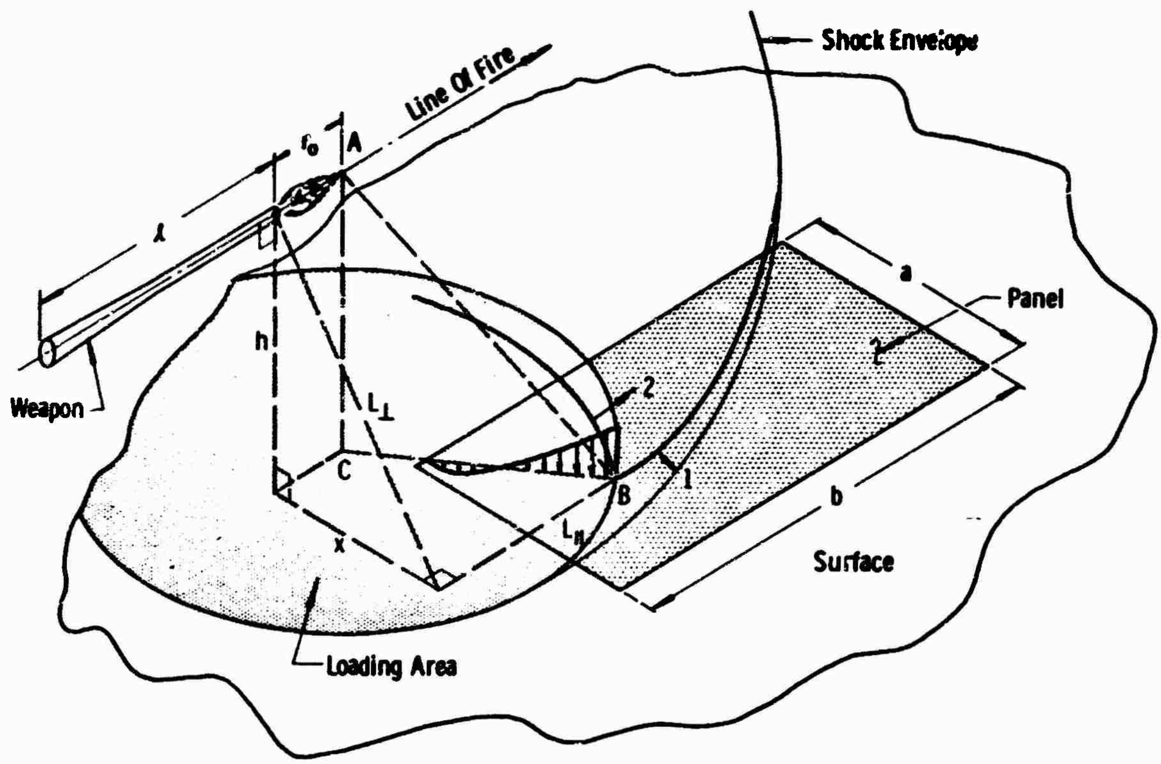

Figure 1. Geometry of Shock Loading of Panel

then the shock wave undergoes essentially normal reflection and the loading is a function of time alone. If the panel is located far from A and if the weapon muzzle is close to the surface, i.e., BC >> AC, then the shock front moves across the panel as the plane front at a constant velocity essentially equal to Mach 1.0 and the pressure pulse does not change in character while passing over the panel.

No general procedure can be evolved for prediction of loading of curved panels which form a small part of a larger surface unless the radii of curvature are large enough for the curved panel to be considered essentially flat, in which case the methods described for flat panels will apply. If a curved panel has double curvature, there is no good rational or empirical method of defining the blast loading with reasonable accuracy, but a technique is presented in Reference 5. The loading can be defined for a panel with single curvature which is part of a cylindrical or nearly cylindrical surface, for two limiting cases. For a blast source far ahead of or behind the cylinder, the panel will be loaded by a travelling wave moving along its length at nearly constant velocity and with essentially unchanging characteristics which can be determined from the "free-air" blast wave properties discussed in Reference 1. For a blast source normal to the cylinder axis, panels on the side struck first by the blast front will be the most heavily loaded, and they will have a shock running rapidly across from one side to the other, with varying velocity, intensity, and duration. An approximate method of estimating the loading presented by Lindberg, et al., (Reference 6) is to ignore the "travelling" load and assume that the transient pressure can be given by a separable loading function.

$$p(\theta, t) = f(\theta)p_o(t)$$

where

$$f(\theta) = \begin{cases} (P_r - P_i)\cos^2\theta + P_i, & -90° < \theta < 90° \\ = P_i & 90° < \theta < 270° \end{cases} \quad (1)$$

and

$$p_o(t) = e^{-t/T}$$

In these equations, P_r and P_i are reflected and incident overpressure, θ is angle measured between the point of first contact of the shock front with the cylinder to the point of interest, and duration T is adjusted so that the blast wave impulse agrees with experiment. Although loading estimated from Equation (1) is considerably oversimplified, it may prove adequate for response calculations of panels. It will probably prove adequate for all cases where total loading duration T is significantly greater than time of shock front travel across the panel.

Tail booms and fixed airfoils are structural components of helicopters which fall in the category of fixed, beam-like structures. For one special loading case, we can devise methods of estimating the time history of loading on these elements. (We are interested here in defining loading which affects overall bending and torsional response of a beam-like structure rather than response of local panels in such a structure, which we have already covered.)

The particular case which we consider is that of a blast source located some distance from, and on a normal to, a relatively flat structural element such as an airfoil, or some distance off the side of an approximately cylindrical structure such as a tail boom. The shock front is then essentially plane, and the shock wave diffracts around the structure, producing a net transverse loading. Procedures based on shock tube experiments have been developed for predicting this loading. These are reported in References 3-5 and a specific application to thin cantilever beams is given in Reference 9.

Let us consider a slender beam-like structure, viewed from the direction of approach of the shock wave, as in Figure 2(a). An element of this structure will have a net transverse pressure applied to it which can be approximated by the time history shown in Figure 2(b), with a diffracted phase of duration T_1, followed by a drag phase which completes the loading in total time T. The amplitude P_r of the diffracted phase can be obtained from sources of compiled blast data such as Reference 8, once the effective blast energy W of the explosive source and its standoff distance R are known. The duration T_1 of the diffracted phase may be expressed as

$$T_1 = \frac{2w}{U} \qquad (2)$$

for either a flat or cylindrical structure, where w is the width of the structure at a given station along its length [Figure 2(a)], and U is the shock front velocity, which can also be obtained from a source of compiled blast data. The amplitude of the drag phase, $C_D q_s$,

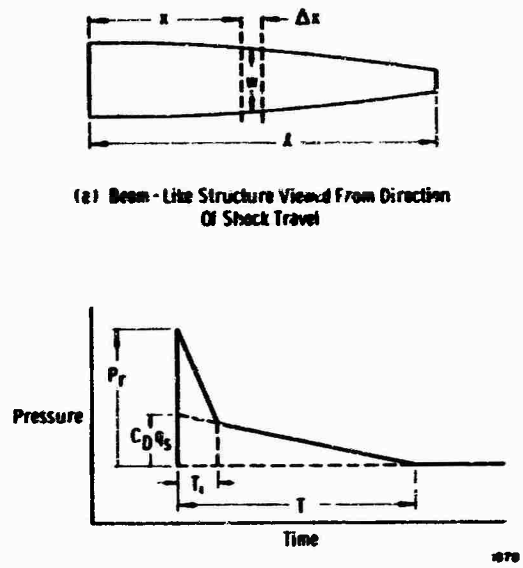

(a) Beam-Like Structure Viewed From Direction Of Shock Travel

(b) Time History Of Net Transverse Pressure On Beam-Like Structure

Figure 2. Time History and Shock Wave on Beam-Like Structure

is composed of a drag coefficient C_D which is a function of the beam geometry, u, Reynolds number, and the peak drag pressure,

$$q_s = \frac{1}{2} \rho u^2 \qquad (3)$$

where ρ and u are peak density and particle velocity immediately behind the shock front. $C_D = 2.0$ for a flat beam, and $C_D = 1.0$ for a cylinder. Values for q_s, or for ρ and u from which q_s can be computed, are also obtainable from sources of blast data such as References 4, 8, and 40. The duration T for the drag phase must be modified from drag duration data in the literature because we have assumed a linear decay of pressure, while the pressure in actuality decays as a modified exponential. We suggest that T be estimated by the formula

$$T = \frac{2I_i}{P_i} \qquad (4)$$

where P_i and I_i are the peak incident overpressure and impulse for a "free-air" blast wave.

The method of estimating loading which we have presented here should give reasonably accurate estimates for relatively weak blast waves, i.e., $P_i \leq 25$ psi. For stronger blasts, complications occur, as indicated in Reference 7, and these techniques may be inaccurate. The reader is cautioned not to use the methods for estimating loads on cylindrical structures presented in Reference 4 as they are considerably in error for the stated range of overpressures.

Estimation of the blast loading of moving rotor blades is an exceedingly complex problem, much more so than estimation for airfoils which are simply translating, as would be the case for fixed-wing aircraft. For a fixed-wing machine, the airflow over the foil at time of blast intercept is essentially constant velocity, while, for a helicopter rotor in forward flight, the airflow velocity varies along the length of the blade and even reverses in direction over a portion of a retreating blade. A torque-balancing tail rotor is an even more complex flow field, which nearly defies description. Even the geometry of the blast wave intercept with a rotating main blade is complex for the case of a blast source mounted on or near the helicopter. But, because blade response may prove to be critical, we have attempted to generate methods for estimating the loading. The methods developed require description of the complex geometry of blast wave intercept with the rotating blades, division of the blade into spanwise elements, and integration of pressures during passage over these elements based on linear fits to data from Reference 15 to obtain normal force F_N and moment M on each element. The procedure is described in considerable detail in Reference 2.

Response Methods

From the review of past analysis of structural response given in the first section of this paper, it is apparent that many investigators have presented analysis methods for elastic and/or plastic response of certain structural elements to blast or impulsive loading, and very few have done so for complex structures. We must here apply those methods which already exist to our problem of response of helicopter structures to muzzle and breech blast or generate new methods where existing ones appear to be inadequate. The problem of overall response of the entire helicopter is quite forbidding, particularly for plastic deformation. Because of this and also because of the localized nature of structural damage which will probably be of concern in muzzle blast effects, we will not attempt to attack the complex overall problem but will instead limit ourselves to those subproblems which are amenable to analysis.

Of the various substructures into which helicopters can be divided, flat panels are potentially one of the most critical elements in response to blast loading. The panels can represent sections of fuselage skin between stringers and frames, panels of fuselage including stringers between longerons and frames, sections of airfoil skin between spars and ribs, flat or slightly curved acrylic resin windows, etc. Generally, in helicopter construction, the skin gages are quite light and flat panels deforming under blast loading will develop appreciable In-plane (membrane) stresses as well as bending stresses, and will also undergo elastic or plastic deformations which are large compared to skin thickness. We feel, therefore, that some of the analysis methods which one uses to predict response of flat panels must include the effects of membrane as well as bending stresses, and perhaps must also include effects of large deformations.

Depending on the dimensions of the panels, different theories may yield acceptable predictions of response. The simplest conceptual theories are so-called "strip-theories," wherein the panel is assumed to be an assemblage of parallel strips, each of which is analyzed as a beam responding to the blast or impulsive loading. Strip theories will probably yield acceptable response predictions for long, narrow panels, if the strips are assumed to run across the narrow dimension of the panel. Such theories can perhaps also be used to predict response of stringers plus attached skin between fuselage frames. Usually, the boundary conditions for the strips are symmetric and can be approximated as clamped or modified simple-support (pinned ends--rotation possible, but translation impossible). The best available method for computing response of strips, under the assumptions noted in the beginning of this paragraph, is that developed by Balmer, et al., [21] at MIT. Using their methods, large deformations of clamped-clamped or simply-supported strips under symmetric impulsive loading can be computed, with reasonably accurate accounting for elastic and plastic material properties, plus strain-hardening and strain-rate effects. The particular computer program employed for these calculations is called DEPROSS 1 (see Reference 42). Using the MIT code, one can predict elastic, incipient plastic, or large plastic deformation.

From the above discussion, one can see that none of the existing analysis methods is capable of handling the most general case of a strip subjected to blast loading, i.e., large-deflection elastic-plastic response to a transient pressure loading which varies both in space and time. Conceptually, the best approach to solution of this problem would be to generalize the MIT technique, to include loading other than impulse, and response other than symmetric about the midspan of the strip. But, this approach would undoubtedly generate a computer program of great complexity and running time, and we could not, therefore, consider it seriously in this program. We have developed a somewhat more limited program for beam response which can be used to predict plastic deformation of strips to more arbitrary loads than the MIT programs. Strips are a degenerate case for this program, so we will defer discussion of it until later.

Membrane theories are appropriate for flat and perhaps slightly curved panels which are thin as compared to the other panel dimensions. Since plate theory is also applicable to these panels, the analyst and/or designer must decide which theory is appropriate. For large panel deflections, membrane forces must be accounted for and classical plate theory can be excluded on this basis. In the following, three membrane theories are discussed. It is suggested that these theories be employed for membrane calculations.

For a constant thickness rectangular membrane, subjected to suddenly applied, uniformly distributed, linearly decaying pressure, the response is presented by Baker and Hoffman in Reference 25 (see also Ref. 2). The usual restrictions of membrane theory hold, i.e., elastic material behavior, small deflections, and constant in-plane membrane force. The solutions for an arbitrarily decaying pressure loading may be readily derived from the information presented. The solution for an isotropic, cross-stiffened or sandwich membrane subjected to a suddenly applied, arbitrarily distributed pressure loading is presented by Greenspon in Reference 26. Plastic material behavior, but small lateral deflections, was assumed. The most versatile approach to the membrane problem is that developed by D. Young and presented in Reference 2. With this program, the membrane is approximated by means of a pin-jointed frame. Essentially, the large deflection equations of motion for the pin-jointed frame are solved numerically by means of a computer. The stress-strain behavior for each member is assumed to be bilinear with hysteretic recovery. Time-dependent applied forces having linear decay may act at the joints. In the elastic range, the program gives results which agree well with those of Baker & Hoffman [25] for the case of a square membrane. This program is called DANAXX5.

*See Reference 2 for more detail.

Because none of the solutions or computer programs for rectangular plate response include plastic deformation, we developed our own program called DANAXX6*. In this program, the linear equations for plate bending are cast in finite-difference form, with moment-curvature relationships assumed to be bilinear with hysteretic recovery, as shown in Figure 3(a). For the finite-difference analysis, the plate is divided into a network of nodal stations, as in Fig. 3(b).

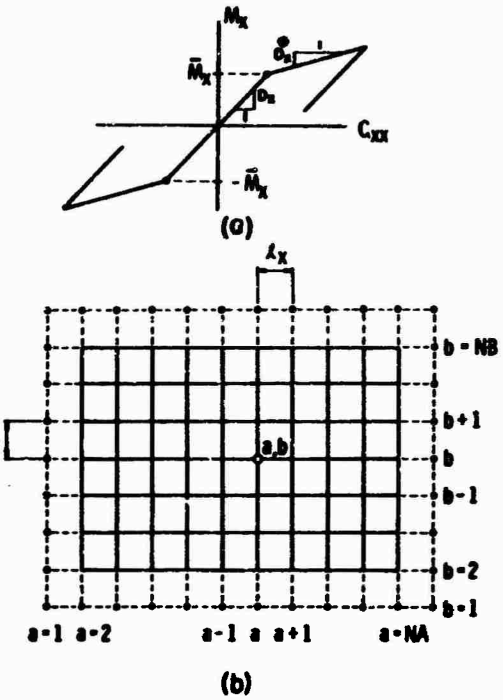

Figure 3. Plate Lumped--Mass Model

The actual boundaries of the plate are along vertical rows a = 2 and a = NA and along horizontal rows b = 2 and b = NB. The outside nodal points (along dashed lines) are fictitious points that are introduced in order to establish boundary conditions. The accelerations of the nodal points are computed and used in a step-by-step numerical integration scheme to obtain the time history of the response. Boundary conditions for simply-supported, clamped, free and guided edges can be used in any desired combination. No interaction in the plastic range between orthogonal moments M_x and M_y was assumed. If a plate theory which employs an interaction between the moments is desired, then the only choice currently available is to follow the technique employed at MIT (Refs. 24 and 30) and develop another computer program.

The fixed beam-like structures common to most present-day helicopters included large airframe assemblies such as tail booms, horizontal and vertical stabilizers, as well as small airframe components such as stringers, longerons, and frames. Generally, these structures have irregular cross sections, are nonuniform over their length, and are composites of more than one material. The overpressures on these structures resulting from weapons fired nearby may vary in intensity and duration along their length. When the structure is irregular in shape, like a tail boom, the blast loads can cause twisting as well as bending of the structure. Thus, determining the response of helicopter beam-type structures to blast loads presents formidable problems.

Past analyses which treat the response of beam-like structures to impulsive and transient loads are discussed earlier in this paper. None of the analyses discovered in the literature are general enough to handle the most complex response problem encountered in this study; that is, the elastic-plastic response of a nonuniform beam in bending and torsion when subjected to a nonuniform force-time history. Consequently, SwRI developed a computer program general enough to treat all of the beam-type response problems we have encountered. This program is entitled DANAXX4. It calculates the time history of the response of a beam to applied force pulses and applied torque pulses. The beam is represented by a lumped-parameter system which is essentially equivalent to the finite-difference approximation of the governing equations. In addition to solving the general case of coupled bending and torsion, the program can be used for uncoupled bending and torsion, for torsion alone, and for bending alone.

As shown in Figure 4(a), the beam is divided into a number of segments which do not have to be equal in length. The mass of the beam is lumped at the nodal stations. For coupled bending-torsion problems, the center

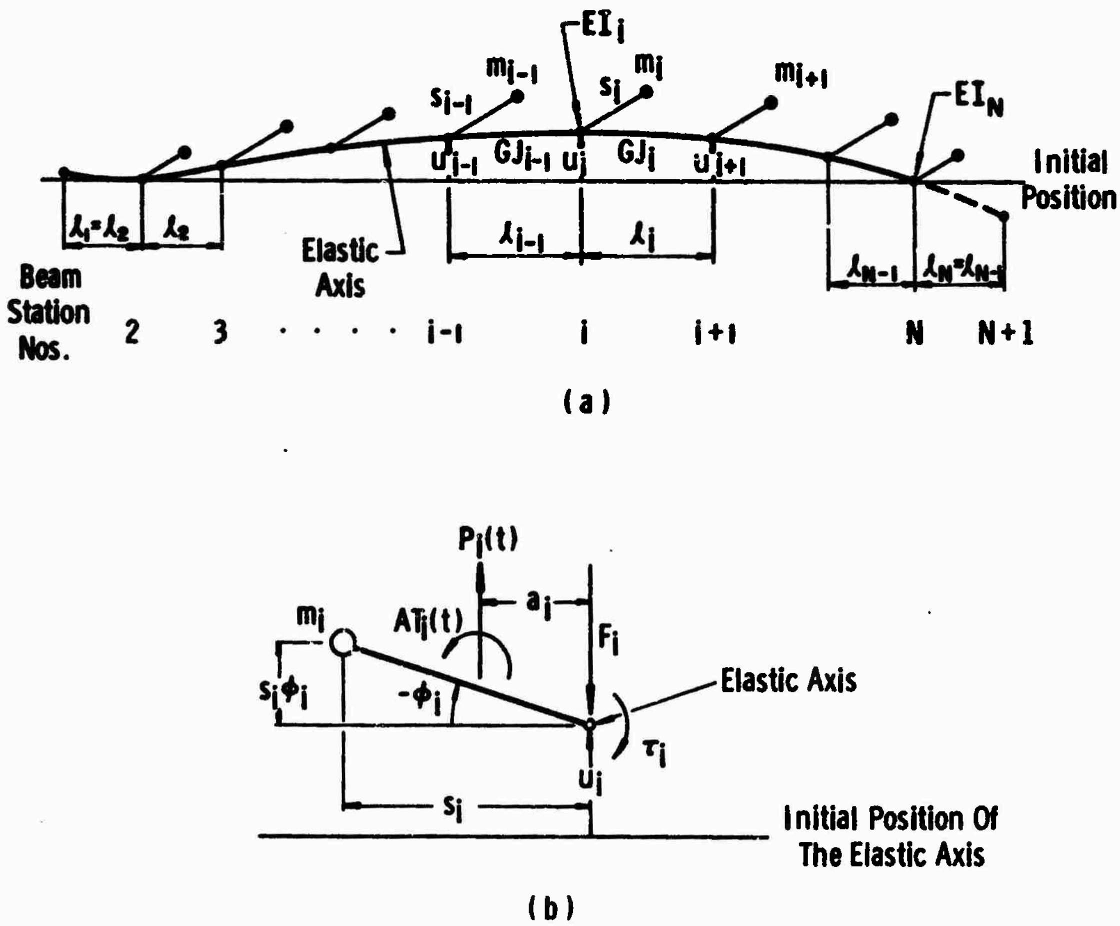

Figure 4. Beam Lumped-Mass Model (Shown with Clamped-Hinged Ends)

of gravity of each nodal mass m_i is offset a distance s_i from the elastic axis. The applied forces and applied torques are taken as acting on these offset arms (Figure 4(b)).

The program provides for any combination of the four differential flexural boundary conditions--hinged, clamped, free or guided. The beam is assumed to be fixed against torsional rotation at hinged, clamped, and guided ends.

The applied forces, $P_i(t)$, and the applied torques, $AT_i(t)$, are functions of time. Subroutines are available for a number of different pulse shapes. Subroutines for other pulse shapes can be prepared when needed. The present program requires that the type (shape) of the applied torque pulse must be the same as that of the force pulse. The program can be modified if the need arises to have different pulse shapes for torques and forces.

The program provides for inelastic behavior by assuming that both the moment-curvature relation and the torque-angle of twist relation are of the bilinear type with hysteretic recovery. The fact that these two relations are interdependent is neglected.

The effect of shear on deflections is neglected. No damping is included. Rotatory inertia effects in the plane of bending are not included.

The response is determined with a step-by-step integration of the equations of motion using the linear acceleration method. To prevent instability of the numerical integration, it is necessary to take the integration time step, Δt, about one-fifth or less of the smallest period of vibration of the system, that is, the period corresponding to the highest natural frequency of the system. Since the actual magnitude of the smallest period of vibration may not be known, it is often necessary to try a series of successively smaller values of Δt until there is no significant change in the calculated response curve as Δt is decreased.

In our survey of the literature, no solutions directly applicable to the aeroelastic response of rotor blades to blast loading were discovered. Although several analytical techniques have been developed for studying the aeroelastic behavior of rotary wings, the emphasis has been on the aerodynamic performance of rotor blades in forward flight and rotor blade response to control inputs. A good survey of this work is given in a paper by Lemios, et al., [41].

To study the response of rotor blades to blast loading, SwRI has developed a computer code based on the same approach as noted above for fixed beams. The program solves for the coupled bending-torsion response of the blade to blast-induced forces and torques. Elastic and inelastic material behavior, including strain-hardening and hysteretic recovery, is taken into account. This program is called ROTOR 10.

The blade is represented by a lumped parameter system as shown in Figure 5. The blade is divided into segments of equal length, ℓ. The mass of the beam is lumped at the

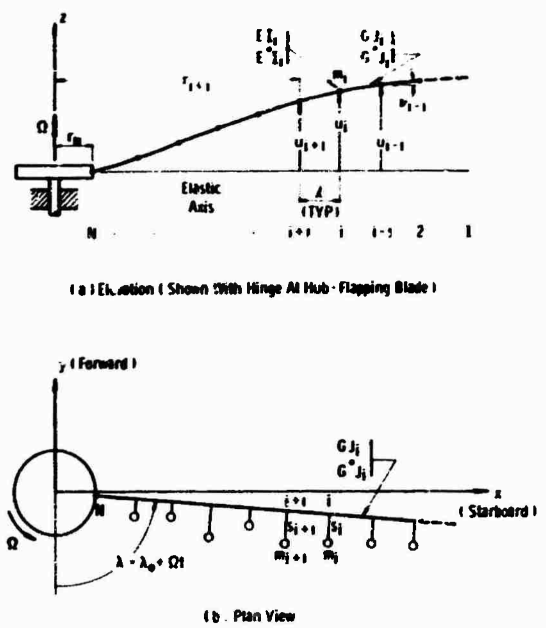

Figure 5. Blade Lumped- -Mass Model

nodal points joining the blade segments, but the CG may be offset a distance s_i from the elastic axis as required. The external forces are assumed to act on these offset arms as shown in Figure 6.

The blast load, $B_i(t)$, is a function of time. Different pulse shapes can be handled by the program. The aerodynamic loads, A_i and M_{Ai}, depend on blade motions. The overall rotor blade geometry and the blade section geometry pertinent to the airload calculations are shown in Figures 7 and 8. Bilinear relationships for moment versus curvature and torque versus twist are incorporated in the program, as shown in Figure 9. These simulate elastic-plastic deformation with hysteretic recovery.

The response is determined in the same manner as for program DANAXX4.

COMPUTER PROGRAMS FOR RESPONSE

In previous sections, we have discussed several computer programs developed for predicting elastic-plastic dynamic response of portions of helicopter structure to weapons' blast loading. Much more details on all of these programs, including complete program listings, are given in Reference 2. To summarize, we list these programs together with short descriptions in Table 1. All have been written in FORTRAN IV language for use on a CDC 6600 computer.

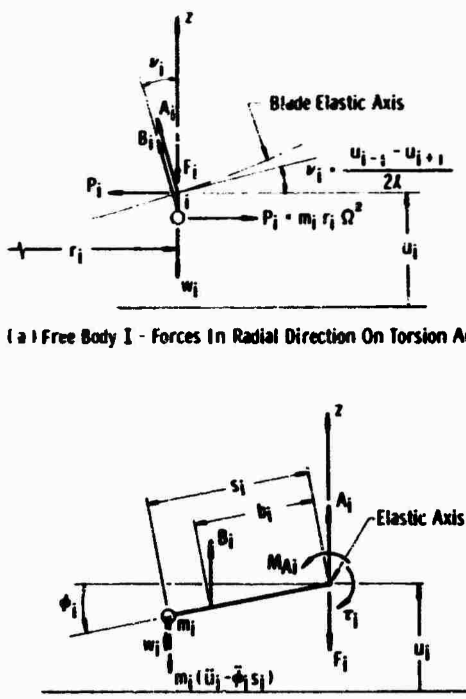

(a) Free Body I - Forces In Radial Direction On Torsion Arm

(b) Free Body II - Forces In Vertical Direction On Torsion Arm

Figure 6. Sketch Showing Position of External Loads on Blade

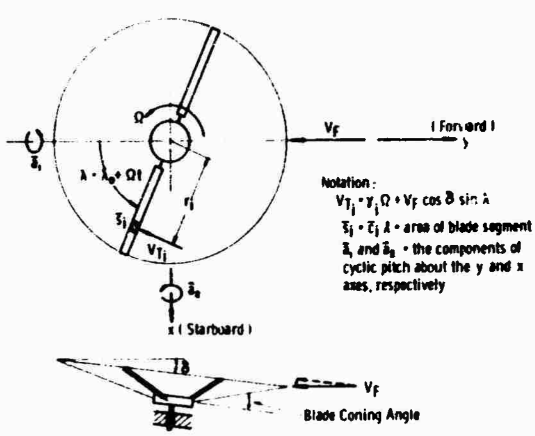

Figure 7. Overall Rotor Geometry

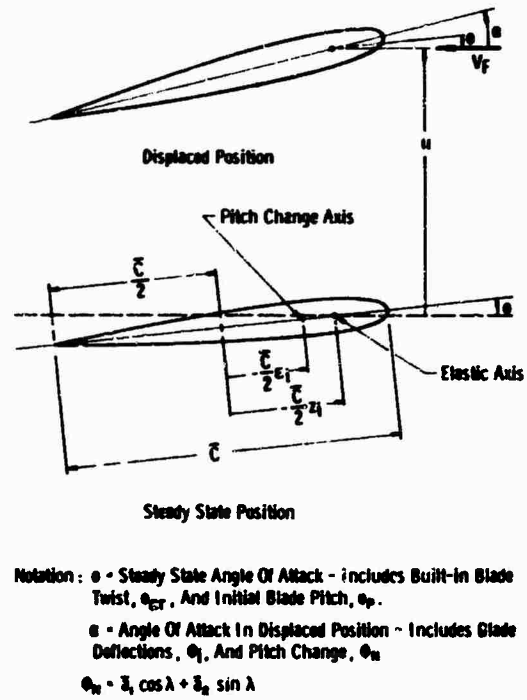

Figure 8. Blade Section Geometry

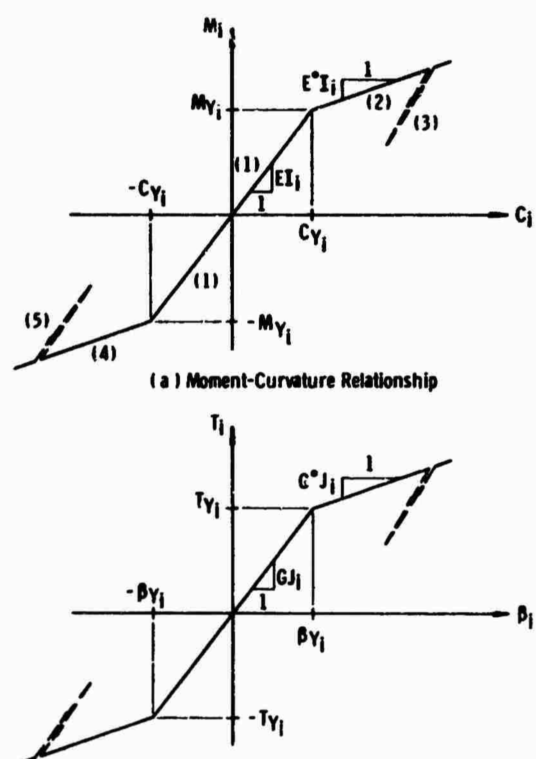

Figure 9. Moment-Curvature and Torque-Twist Relationships

Table 1. Listing of Computer Programs Developed at SwRI

Program Number	Title	Description
1	VIBRATE	This program sums the infinite series solution for response of an elastic rectangular membrane to blast loading given in Reference 27. Blast loading is restricted to a normally incident wave of triangular shape.
2	DANAXX 4	This program computes the time history of response of a nonuniform beam to applied force and torque pulses. Elastic-plastic relationships for moment-curvature and torque-twist are included. A variety of shapes of force and torque pulses can be accommodated. In addition to solving for the general case of coupled bending and torsion, the program can be used for uncoupled bending and torsion, bending alone, or torsion alone.
3	DANAXX 5	This program computes the out-of-plane response of a pin-jointed framework to force pulses. The framework may be employed to approximate a rectangular membrane. Capability for simulation of various force pulses and elastic-plastic deformation is the same as for DANAXX 4. Travelling blast waves can be easily handled in the program.
4	DANAXX 6	This program computes the elastic-plastic response of a rectangular plate to a travelling blast wave. Plates can be stiffened or uniform. A variety of boundary conditions can be handled. Capability for simulation of force (pressure) pulses is the same as for DANAXX 4.
5	ROTOR 10	This program calculates the coupled bending-torsion response of a moving rotor blade to applied blast loads. Aerodynamic forces and rigid-body motions are included, as well as blade bending and torsion as in DANAXX 4.

REFERENCES

1. P. S. Westine, "The Blast Field About the Muzzle of Guns," Shock & Vibration Bulletin, Bulletin 39, Part 6, pp 139-149, March 1969.

2. W. E. Baker, S. Silverman, P. A. Cox, Jr., and D. Young, "Structural Response of Helicopters to Muzzle and Breech Blast, Vol. II of Final Technical Report, Structural Interaction and Response to Blast," Southwest Research Institute, San Antonio, Texas, March 1969, AD 850081.

3. V. J. Bishop and R. D. Rowe, "The Interaction of a Long Duration Friedlander-Shaped Blast Wave with an Infinitely Long Right Circular Cylinder. Incident Blast Wave 20.7 psi, Positive Duration 50 ms, and a 16 cm Diameter Cylinder," AWRE Report No. 0-38/67, Atomic Weapons Research Establishment, Aldermasten, Berkshire, April 1967.

4. The Effects of Nuclear Weapons, prepared by U. S. Department of Defense, Pub. by U. S. Atomic Energy Commission, Rev ed, February 1964.

5. C. H. Norris, R. J. Hansen, M. J. Holley, J. M. Biggs, S. Namyet, and J. K. Minami, Structural Design for Dynamic Loads, McGraw-Hill Book Company, Inc., Harmer E. Davis, ed, 1959.

6. H. E. Lindberg, D. L. Anderson, R. D. Firth, and L. V. Parker, "Response of Reentry Vehicle-Type Shells to Blast Loads," Final Report for Lockheed Missiles and Space Co., P.O. 24-14517 Under Contract No. AF 04(694)-655, SRI Project FGD-5228, September 30, 1965.

7. W. E. Baker, "Additional Comments on Reference Data for Blast Loading on Cylinders," David Taylor Model Basin, Structural Mech. Lab., Ship Protection Div., Tech. Note SML 740-52, July 1964.

8. H. J. Goodman, "Compiled Free-Air Blast Data on Bare Spherical Pentolite," BRL Report No. 1092, February 1960, AD 235278.

9. W. E. Baker, W. O. Ewing, Jr., J. W. Hanna, and G. E. Bunnewith, "The Elastic and Plastic Response of Cantilevers to Air Blast Loading," in Proceedings of the Fourth U. S. National Congress of Applied Mechanics, pp 853-866, June 1962.

10. H. B. Pierce and T. D. Reisert, "Initial Experimental Investigation of the Aerodynamic Load on the Wing of a Model Caused by a Blast-Induced Gust That Increases the Angle of Attack into the Stall Region," NACA RM L55H22b, December 19, 1955.

11. H. B. Pierce and R. J. Spahe, "Experimental Investigation to Determine the Loads on a Horizontal Tail of a Model Caused by a Blast-Induced Gust," NACA RM L57A28a, March 29, 1957.

12. D. R. McFarland and P. W. Huber, "Investigation of Vortex Movements About a Wing in Steady Subsonic Flow Undergoing a Large Angle-of-Attack Change in a Blast-Induced Gust," NASA RM L57K04, January 22, 1958.

13. D. R. McFarland, "Investigation of Vortex Movements About a Wing in Intermediate and High Subsonic Flow Undergoing a Large Angle-of-Attack Change in a Blast-Induced Gust," NASA TN D-1283, April 1962.

14. H. B. Pierce and J. C. Manning, "Experimental Investigation of Blast Loading on an Airfoil in Mach Number 0.7 Airflow with Initial Angle-of-Attack Change of 20°," NASA TN D-1603, February 1963.

15. J. C. Manning, "Experimental Investigation of Blast Loading on an Airfoil in Mach 0.7 Airflow with Initial Angle-of-Attack Change of 28°," NASA TN D-2876, June 1965.

16. T. Coyle and W. R. Harris, "The Effect of Blast Against Helicopter Rotor Blades (U)," BRL Tech. Note No. 1342, September 1960.

17. J. J. Sciarra, "Dynamic Unified Structural Analysis Method Using Stiffness Matrices," AIAA/ASME Seventh Structures & Materials Conference, pp 94-111, April 1966.

18. J. C. Balcerak, "A Method for Predicting the Aerodynamic Loads and Dynamic Response of the Rotor Blades of a Tandem-Rotor Helicopter," USAAVLABS Tech. Rept. 67-38, June 1967.

19. E. S. Criscione, N. P. Hobbs, and E. A. Witmer, "Outline of a Method for Calculating the Elastic and the Post-Buckling Responses of an F-80 Horizontal Stabilizer to Blast," WADC TN 56-137, May 1956.

20. J. E. Greenspon, "Dynamic Elastic-Plastic Behavior of Beams and Lifting Surfaces," Journal of the Aerospace Sciences, 29, 6, pp 633-640, June 1963.

21. J. E. Greenspon, "Plastic Behavior of Control Surfaces and Plates Subjected to Air Blast Loading, Part 2," Tech. Rept. No. 2, Contract DA-034-ORD-3081 RD, March 1962.

22. E. A. Witmer, H. A. Balmer, J. W. Leech, and T. H. H. Pian, "Large Dynamic Deformations of Beams, Rings, Plates and Shells," AIAA Journal, 1, 8, pp 1848-1857, August 1963.

23. S. B. Menkes, "Improved Methods for the Approximate Prediction of Large Deformation of ICBM Structures for Use in Lethality Analysis, Vol. I," The City College of the City University of New York, Report CUNY TR 67-10, July 1967.

24. J. E. Greenspon, "Plastic Behavior of Control Surfaces and Plates Subjected to Air Blast Loading, Part 1, Simplified Theoretical Relations," Tech. Rept. 1, Ballistic Research Laboratories, Aberdeen Proving Ground, Maryland, November 1960, AD 248639.

25. W. E. Baker and A. J. Hoffman, "The Shapes of Circular and Square Membranes Under Air Blast Loading," Memorandum Rept. No. 556, Ballistic Research Laboratories, Aberdeen Proving Ground, Maryland, April 1951.

26. J. E. Greenspon, "Elastic-Plastic Response of Structures to Blast and Impulse Loads," Tech. Rept. No. 7, Under Contract No. DA-18-001-AMC-1019(X), Ballistic Research Laboratories, Aberdeen Proving Ground, Maryland, March 1967, AD 651051.

27. R. G. Locklin and S. N. Mills, Jr., "Dynamic Response of Thin Beams to Air Blast," BRL Report No. 787, September 1951.

28. S. Bodner and P. S. Symonds, "Experimental and Theoretical Investigation of Cantilever Beams Subjected to Impulsive Loading," Journal of Applied Mechanics, 29, Series E, p 719, December 1962.

29. P. S. Symonds and T. J. Mentel, "Impulsive Loading of Plastic Beams with Axial Constraints," Journal of Mechanics & Physics of Solids, 6, p 186, 1958.

30. S. R. Bodner, "Deformation of Rate-Sensitive Structures Under Impulsive Loading," Engineering Plasticity, Cambridge University Press, pp 77-91, 1968.

31. J. S. Humphreys, "Plastic Deformation of Impulsively Loaded Clamped Beams," Journal of Applied Mechanics, 32, Series E, 1, pp 7-10, March 1965.

32. A. L. Florence and R. D. Firth, "Rigid-Plastic Beams Under Uniformly Distributed Impulses," Journal of Applied Mechanics, 32, Series E, 2, pp 481-488, September 1965.

33. E. N. Clark, F. H. Schmitt, D. G. Ellington, R. Engle, and S. Nicolaides, "Plastic Deformation of Structures, Vol. I, Plastic Deformation of Beams, Vol. II, Plastic Deformation of Rings," Tech. Doc. Report FDL-TDR 64-64, Picatinny Arsenal, Dover, New Jersey, May 1965.

34. H. A. Balmer and E. A. Witmer, "Theoretical-Experimental Correlation of Large Dynamic and Permanent Deformations of Impulsively-Loaded Simple Structures," FDL-TDR-64-108, Aeroelastic and Structures Research Lab., Massachusetts Institute of Technology, Cambridge, Massachusetts, July 1964, AD 605215.

35. W. J. Schuman, Jr., "A Failure Criterion for Blast Loaded Cylindrical Shells," Report No. 1292, Ballistic Research Laboratories, U.S. Army Materiel Command, Aberdeen Proving Ground, Maryland, May 1965, AD 628289.

36. G. R. Abrahamson and J. N. Goodier, "Dynamic Plastic Flow Buckling of a Cylindrical Shell from Uniform Radial Impulse," Proceedings of the 4th U.S. Congress of Applied Mechanics, ASME, New York, pp 939-950, 1962.

37. D. L. Anderson and H. E. Lindberg, "Dynamic Pulse Buckling of Cylindrical Shells Under Transient Lateral Pressures," AIAA Journal, 6, 4, pp 589-598, April 1968.

38. W. E. Baker, S. Silverman, and F. O. Hoese, "Impulsive Loading of Simple and Composite Cylinders," Final Tech. Rept. Contract DAAD05-67-C-0160, Southwest Research Institute, February 1969.

39. Wilfred E. Baker and Peter S. Westine, "Modeling the Blast Response of Structures Using Dissimilar Materials," Final Technical Report on SwRI Project 02-1940, Southwest Research Institute, March 1968, AD 832056.

40. R. R. Mills, Jr., F. J. Fisch, W. B. Jezek, and W. E. Baker, "Self-Consistent Blast Wave Parameters," Prepared as AAI Engineering Report ER-3589, Aircraft Armaments, Inc., Cockeysville, Maryland, and as DASA-1559 (UNCLASSIFIED), Defense Atomic Support Agency, October 1964, AD 450022.

41. A. Z. Lemnios, A. F. Smith, and A. Berman, "The Aeroelastic Behavior of Rotary Wings in Forward Flight," Final Rept. No. R-585 and No. R-585-1, 2 Volumes: 1--Analysis, 2--Correlation with a Servo-Flap Rotor System, Kaman Aircraft Corp., Bloomfield, Connecticut.

42. H. A. Balmer, "Improved Computer Programs--DEPROSS 1, 2, and 3--To Calculate the Dynamic Elastic-Plastic Two-Dimensional Responses of Impulsively-Loaded Beams, Rings, Plates, and Shells of Revolution," ASRL-TR-128-3, Aeroelastic and Structures Research Lab., Department of Aeronautics and Astronautics, M.I.T., Cambridge, Massachusetts, August 1965, AD 471940.

SHOCK TESTING FOR EQUIPMENT IN PROTECTIVE STRUCTURES

M. M. Dembo and C. C. Huang
US Army Engineer Division, Huntsville
Huntsville, Alabama

This paper presents a new shock test system which has been developed to simulate the predicted shock environment induced by nuclear weapons. The test system was developed as part of the SAFEGUARD Facility Equipment Test Program directed by the US Army Engineer Division, Huntsville, Corps of Engineers. The induced environment was predicted by dynamic analysis performed by the Ralph M. Parsons Company, Los Angeles, California. The shock test system consists of an electrohydraulic exciter and complex waveform synthesizer. The system was developed at Wyle Laboratories, Norco, California.

INTRODUCTION

Protective structures are designed to withstand all nuclear weapons effects, including ground shock and air blast, and to protect housed equipment and personnel. The critical equipment, which must maintain normal functioning during and after attacks, are required to survive laboratory tests simulating the shock environment induced by the exterior shock loads on the structure. This paper presents a shock test system which has demonstrated its capability in providing close simulation for testing such equipment.

The induced shock environment predicted by analytical methods for a protective structure designed to withstand specified shock loads is presented in terms of time-history and shock spectrum. The acceleration time-history provides a basis for the development of a test system that can best simulate the motion; the shock spectrum defines the specification for equipment testing.

The system which has been used for testing the equipment consists of a complex waveform synthesizer, servo-hydraulic exciter and shock spectrum analyzer. Several items of equipment have been tested by this system with satisfactory results. What has been done, however, is only the beginning of a continuing effort directed toward the operation of a full scale testing program. The equipment items which have been planned for testing vary over a wide range in weight, size, dynamic properties and functional requirements. For a system which would be adaptable to testing such a variety of equipment on production basis, repeatability of simulated motion, reliability of test equipment, and economy in operation and maintenance are all important factors. Evaluation of this test system will give insight into finding further innovations so that it can be developed to the full stature of a system capable of fulfilling the demand of production runs.

PREDICTION OF SHOCK ENVIRONMENT

The induced shock environment within a protective structure was predicted by use of the classical dynamic analysis with the aid of a digital computer. The parameters that define the exterior shock environment were specified in a criteria document which controlled the basic design of the structure. The specified shock loads were then used as the excitation for the structure. The structure, for which the interior shock environment was predicted, is a partially buried, multi-story, heavy concrete building. Its model used for dynamic analysis, shown in Fig. 1, contains 71 mass points, with a total number of 142 dynamic degrees of freedom. The mass points which represent the mass distribution are interconnected by elastic elements which simulate the stiffness and damping characteristics of the structural elements, as well as the soil elements that support and surround the structure. The shock loads are applied to the structure in the vertical and the horizontal planes and the horizontal load can be in any direction with respect to the orientation of the building. Accordingly, the process of predicting the peak interior shock environment requires numerous computations to embrace all possible variations of the parameters involved. The results of such computations provide time functions of displacement, velocity, and acceleration for each of the mass points of the model. From the time functions, shock spectra have been generated.

The induced motion is a transient whose characteristics -- the peak level of severity, pattern and duration of motion -- can be found in its acceleration time-history. The energy distribution can be determined from a power spectral density derived from the time-history.

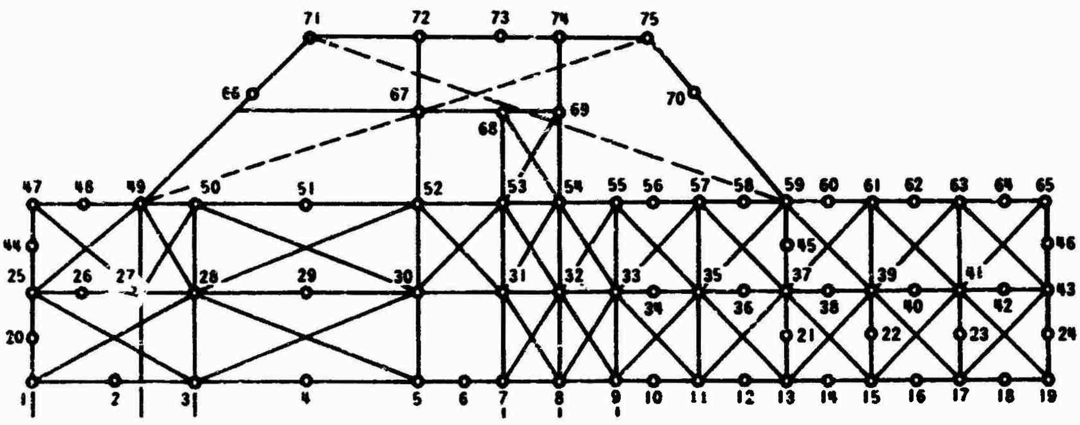

Figure 1. Mathematical model of structure.

A typical calculated acceleration time-history, Fig. 2, depicts the induced acceleration at a mass point on the second floor of the building. The pattern of the transient is characterized by a slow, oscillatory motion of relatively low acceleration, followed by an abrupt increase in acceleration as well as frequency. The total duration lasts several seconds, but the portion dominated by high frequencies lasts only a fraction of a second. This is the type of motion a piece of equipment located in the proximity of that mass point would experience. The transient excitation provided for testing equipment in laboratories, therefore, should have a close similarity to this motion.[1]

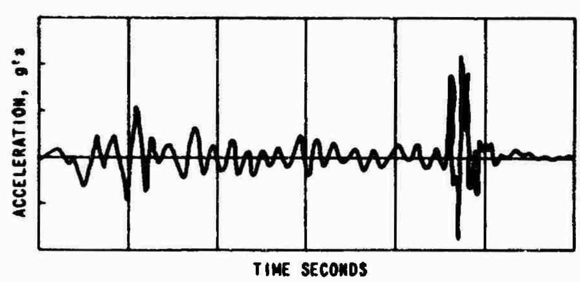

Figure 2. Calculated acceleration time-history.

For simulating the transient, another important parameter is needed; namely, the frequency range of excitation. Fig. 3 indicates the energy distribution of the transient and Fig. 4 the percentage of the total energy for various frequency ranges. These curves indicate that the predominate energy content lies in the region between a frequency range of 0 Hz to 35 Hz.

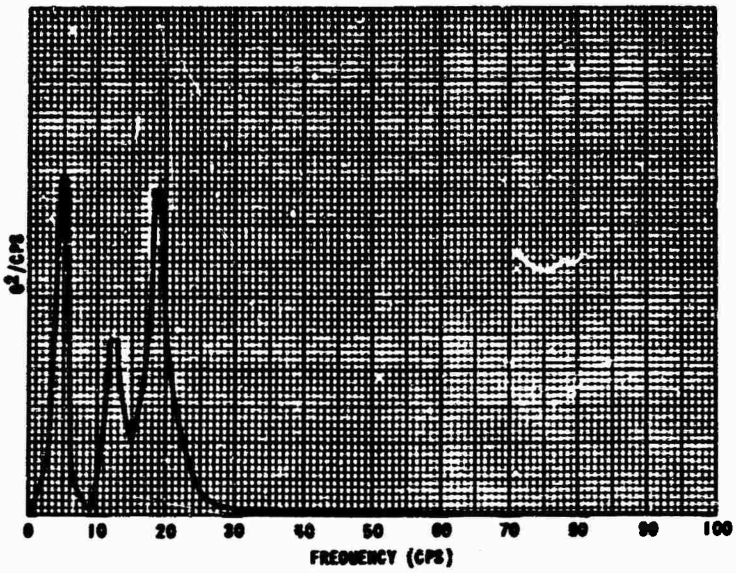

Figure 3. Power spectral density of vertical motion at a mass point on second floor.

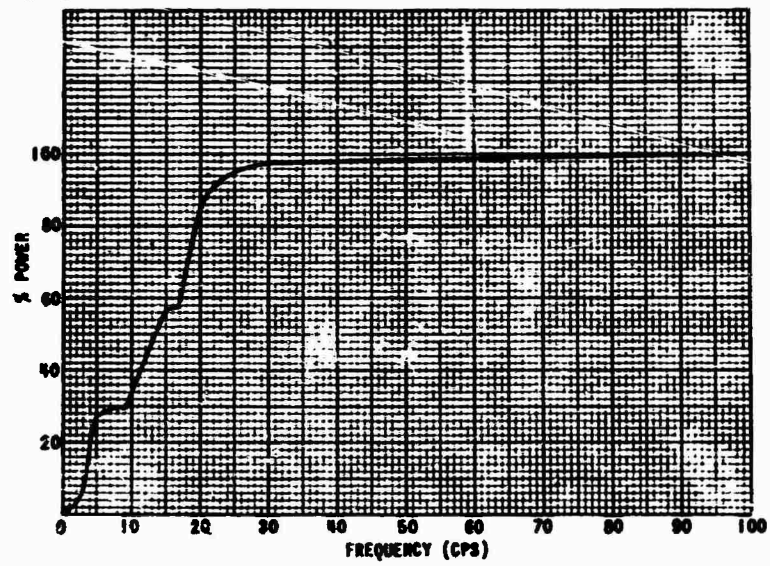

Figure 4. Vertical motion percent power vs. frequency.

The discussion, so far, has been concerned with the in-structure induced motion which is also the excitation for the equipment. Nothing has been said about the effects of such excitation which can be related to the damage or malfunction of the equipment. Such effects can best be represented by shock spectra.[3] A shock spectrum is defined for this test program as the peak response of an array of undamped oscillators to a transient excitation. Therefore, the shock environment at each mass point can be represented by a shock spectrum. Fig. 5 is an envelope of all the shock spectra for the mass points modeled for the second floor of the building. This envelope was accepted as the test shock spectrum for all the equipment mounted on that floor. Similar envelopes had been prepared to represent the shock environment for the other floors, walls and roof. They, too, became the test specifications for the equipment located in their respective areas.

Two aspects of the test specifications (Fig. 5) need clarification. First, apparent over testing may result from using the enveloped shock spectra. The environment required by the test specification is clearly more severe than that calculated for the various specific locations at which the equipment will actually be mounted. Second, the frequency range of the test shock spectrum, as indicated in Fig. 5, has been extended to 200 Hz which is beyond the range of predominate energy content, 0 to 35 Hz, discussed previously. Both modifications to the calculated predictions have been considered necessary in order to provide a margin for compensating the uncertainties due to inevitable assumptions and practical limitations involved. For example, the physical phenomena about the application of air blast

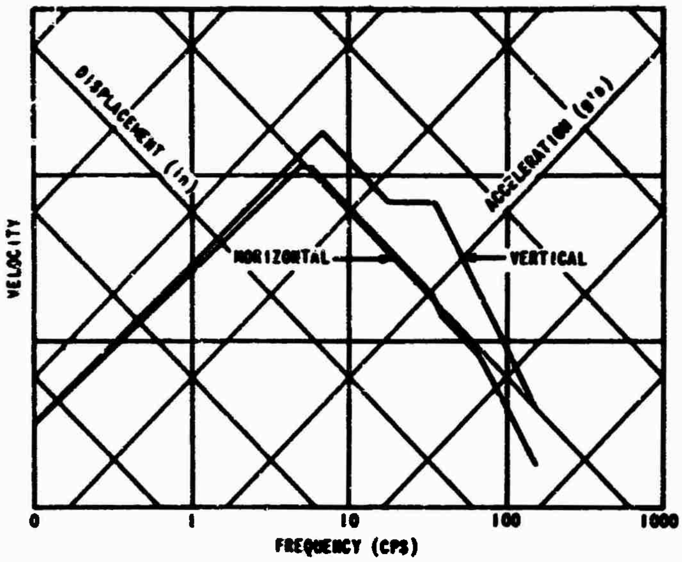

Figure 5. Vertical and horizontal shock spectra for the second floor.

pressure on the exposed surfaces, and about the interaction between the structure and its surrounding ground were idealized for mathematical treatment. It is reasonable to expect that if a more refined model were used, variations in the peak acceleration for various mass points might have occurred. Similarly, more high frequency content might have appeared.

TEST SYSTEM

The critical equipment contained in this building may be divided into two groups based on their source of supply. One group contains equipment which is especially developed to withstand the predicted shock environment. The other group contains industrial equipment which has not been designed and built to meet such a shock requirement. The objective of this test program is, then, to determine whether several equipment items selected from the latter group will survive the shock.

There are three general approaches to accomplishing a shock test: (1) testing made on a specified testing machine, (2) testing made with a specified excitation and (3) testing to a specified shock spectrum requirement. Discussions concerning pros and cons on each of the above approaches, from various viewpoints, have been documented abundantly in literatures and will not be repeated here. The third approach of using shock spectrum as test specification was adopted for this test program. However, specifying a shock spectrum alone without additional requirement for the type, duration and range of frequency of excitation still lacks the complete definition of a desired simulation. It is well known that there is no single, unique excitation associated with a specified shock spectrum. The requirements for the test system used in this test program were designed to bridge the gap and can be summarized as follows:

(1) The excitation should be a transient complex waveform having the characteristics similar to Fig. 2.

(2) The test system must be capable of producing, with each single shock application, a shock spectrum which closely matches the specified shock spectrum, Fig. 5.

(3) The test machine must be capable of testing specimens weighing up to 1,000 pounds.

The above requirements pointed to the fact that a shaker system might be a promising candidate. Investigations were made on the applications of electrohydraulic and electrodynamic shakers. An electrohydraulic shaker system was finally selected for its inherent suitability for application in the frequency range of interest, as well as its adaptability for providing the required long stroke.

In order to meet the first two requirements, the choice of excitation waveform was limited to the use of a combination of transient sinusoids.[1,3] The waveform synthesizer then available at the testing agency was capable of generating arbitrary complex waveforms consisting of superimposed transient sinusoids. The transient sinusoids were generated from pulse-excited 1/3 octave filters. However, the lowest center frequency of the 1/3 octave filters was only 12.5 Hz. Since a large percentage of energy does exist below this frequency as shown in Fig. 4, it was necessary to modify the synthesizer by adding more 1/3 octave filters to cover the frequency region below 12.5 Hz. Since modification, the synthesizer has contained two banks of 1/3 octave filters: 1.25 Hz to 10K Hz and 12.5 Hz to 40K Hz.

Figure 6 is a block diagram of the test system. The shaker was a Wyle Model W250 D-3 equipped with a 200 gpm servovalve. Operating with a 3,000 psi 120 gpm hydraulic power supply, the shaker accepted the synthesized waveform and produced the desired excitation to the specimen. The accelerometer mounted on the fixture, adjacent to the specimen, provided signals from which acceleration time-histories of the shaker were recorded on tape for subsequent shock spectrum analysis. The spectrum analyzer and the ancillary equipment are standard commercial items capable of plotting responses at 1/6 octave frequency intervals.

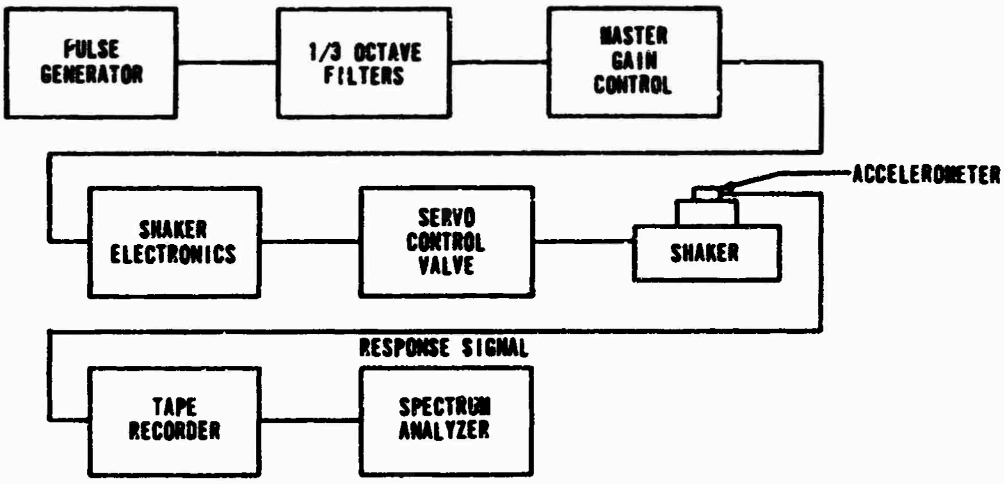

Figure 6. Simplified block diagram.

Typical acceleration and displacement time-histories of the excitation generated by the shaker system are shown in Fig. 7 and Fig. 8.

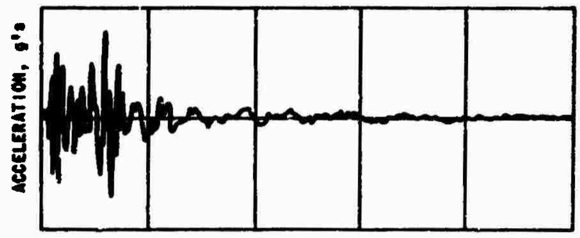

Figure 7. Acceleration time-history generated by test machine.

The pattern of the acceleration time-history generated by the test machine (Fig. 7) appears as if a mirror image of the calculated time-history shown in Fig. 2. This is the peculiarity of the synthesizer used; that is, the high frequency predominates at the start and successively lower frequencies predominate as time continues. Nevertheless, the duration of excitation and level of peak acceleration were closely simulated. The effect on damage potential to the equipment resulting from transposing the early arrival of low frequencies with high frequencies has yet to be investigated, but instead, plans have been made to investigate further modifications to the synthesizer to reverse the pattern of the motion by producing low frequencies at start followed by high frequencies.

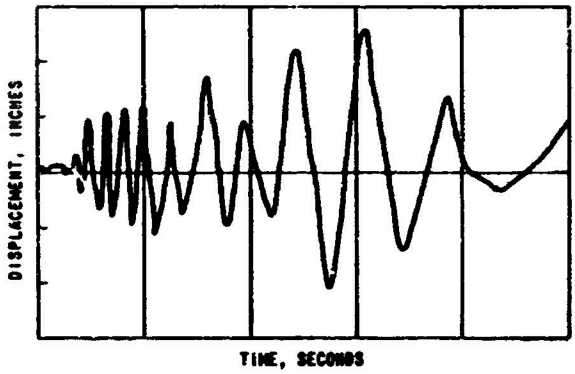

Figure 8. Displacement time-history generated by test machine.

The shock spectra generated by the test system (Q = 100) are shown in Fig. 9 and Fig. 10. These spectra match fairly well with those specified. All of the tests were made on a single shaker head and the excitations were made in one direction at a time.

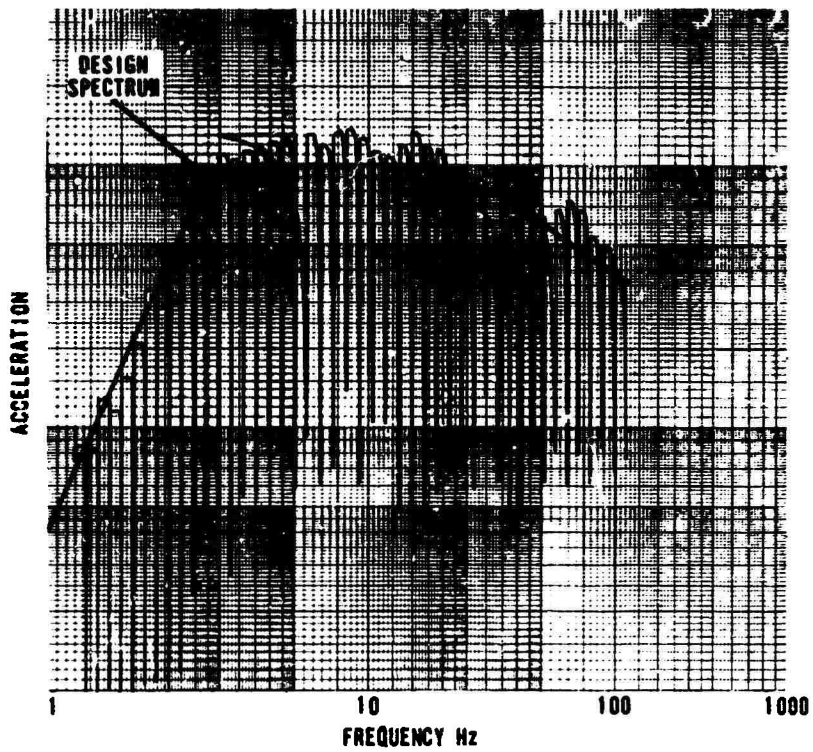

Figure 9. Comparison of design and test response spectra, horizontal axis.

Eight items of equipment have been tested by this shaker system. The test set-ups for two of the items tested are shown in Fig. 11 and Fig. 12. The motor control center (Fig. 11) failed the test, because the relays inside the cabinet dropped from "on" to "off" due to contact chatter while the shock was being applied. The pump (Fig. 12) survived the tests without damage or malfunction caused by shock. It was noted that hydraulic pressure fluctuations existed in the piping loop during shock but damped out quickly after the shock stopped.

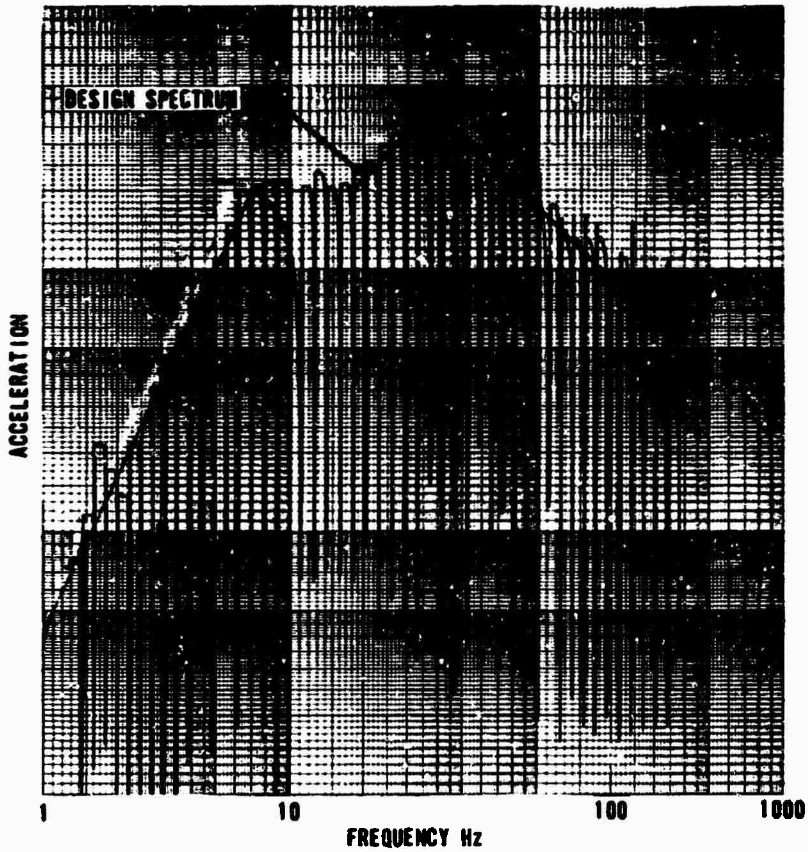

Figure 10. Comparison of design and test response spectra, vertical axis.

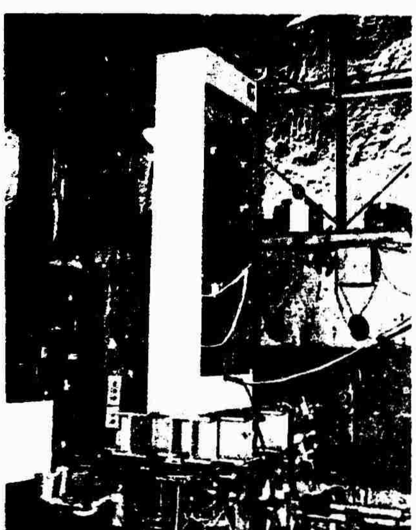

Figure 11. Motor control center mounted on test machine.

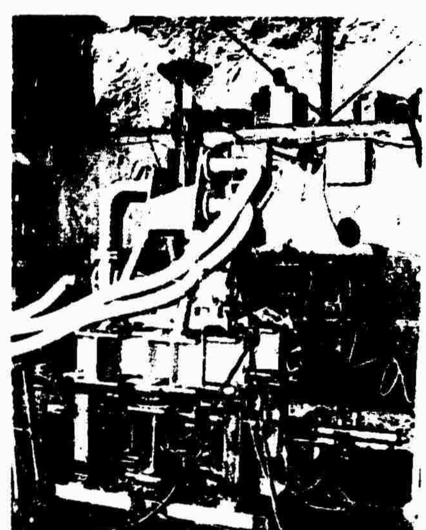

Figure 12. Pump and valve assembly mounted on test machine motion.

CONCLUSION

This paper has described a shock test system which has met the shock spectrum requirements formulated by the dynamic analysis for a protective structure. This test system has laid the foundation for further innovations so that its improved version will be able to fulfill future demands of testing heavier and larger specimens and to meet a variety of shock spectrum requirements.

The innovations envisioned for investigation include: (1) increasing the test system capacity by use of a multi-shaker arrangement for specimens up to 15,000 pounds in weight, (2) exciting the specimens simultaneously in two orthogonal axes with different waveforms, and (3) improving the techniques of synthesizing waveforms in (a) simulating acceleration time-histories of various durations and different arrival times of varying frequencies, (b) improving repeatability and establishing tolerances for the shock spectrum generated by the system.

REFERENCES

[1] Kenneth J. Metzar, "A Test Oriented Appraisal of Shock Synthesis and Analysis", Institute of Environmental Sciences 1967 Proceedings.

[2] R. A. Eubanks and Bernard R. Juskie, "Shock Hardening of Equipment", Shock, Vibration and Associated Environments Bull. No. 32 Part III (December 1963) pp 23-47.

[3] G. W. Painter and H. J. Parry, "Simulating Flight Environment Shock on an Electrodynamic Shaker", Shock, Vibration and Associated Environments, Bull. No. 31 Part III (March 1964) pp 85-97.

GPO 885-410